LPI, Inc. Consulting Engineers
Advanced Analysis & Fitness for Service
Failure & Materials Evaluation
Nondestructive Engineering
Est. 1885

LA181690-R-002 REV. 1

ROOT CAUSE AND FITNESS-FOR-SERVICE ASSESSMENTS OF TPG3 FRACTURED GIRDERS SALESFORCE TRANSBAY TRANSIT CENTER SAN FRANCISCO, CA

NOVEMBER 12, 2019

PREPARED FOR

DENNIS TURCHON

TRANSBAY JOINT POWERS AUTHORITY
425 MISSION STREET, SUITE 250
SAN FRANCISCO, CA 94105

PREPARED BY

LPI, INC.

ROBERT S. VECCHIO, PH.D., P.E.
CHIEF EXECUTIVE OFFICER

ANDREW SMYTH, P.E.
PRINCIPAL ENGINEER

JULIA GROGAN
SENIOR ENGINEER

EVAN SCHICKEL
SENIOR ENGINEER

EXECUTIVE SUMMARY

LPI, Inc. (LPI) was requested by the Transbay Joint Powers Authority (TJPA) to provide engineering services in the root-cause and fitness-for-service (FFS) assessments of the TPG3 girders at the Transbay Transit Center (TTC) in San Francisco. The bottom flanges of the two TPG3 girders (D.4 and E.6 lines) located above Fremont Street fractured, originating at and propagating from weld access holes[1] located adjacent to hangers at three locations. Onsite examination revealed that the north and south sides of the north girder (D.4 line) and the south side of the south girder (E.6 line) had fractured, and that the fractures had extended from the weld access holes across the entire half-width of each flange. The Fremont Street weld access holes were thermally cut into the bottom flange plates to facilitate complete joint penetration (CJP) groove welding of the flanges. In contrast, the First Street weld access holes were thermally cut after the CJP groove welding had been completed.

To assess the nature and root cause of the girder fractures, four T-shaped samples were removed from each Fremont Street girder, such that the samples consisted of sections of the flange and vertical stiffener plates. In addition, four 3-in. diameter core samples were removed from the bottom flanges of the First Street girders and one 3-in. diameter core from each of the hangers at both Fremont and First Streets. All samples were removed under the supervision of representatives from LPI and the Engineer of Record, Thornton Tomasetti (TT), and shipped to LPI's New York facility for evaluation.

Detailed metallurgical evaluation and testing of the girder and core samples were performed in accordance with a mutually-agreed-upon testing protocol. To this end, a joint examination with all interested parties was held at LPI November 13-15, 2018. All results of the joint examination and subsequent testing were provided to all parties.

Results of the metallurgical analyses revealed that the TTC TPG3 girder flange fractures initiated from pre-existing cracks that developed during thermal cutting of the weld access hole radii and subsequent welding of the flange CJP groove welds prior to service, as follows:

- Initially, shallow surface microcracks developed during thermal cutting of the weld access holes in the highly hardened and brittle martensitic surface layer.

[1] The use of the term "weld access hole" is consistent with contract document RFI-2003 [1], in which the Contractor (Webcor/Skanska) and the Structural Engineer of Record (Thornton Tomasetti) used the term to refer to this feature (i.e., the termination of the 4-in. thick flange CJP groove weld at the vertical hanger plate) prior to fabrication.

- Thereafter, larger pop-in cracks formed in two of the four flanges during CJP groove welding of the flange plates.
- Rapid, low-energy fracture of the flanges initiated from these pre-existing fabrication-induced cracks, as the girder was subjected to service loading in addition to the normal residual stresses due to welded fabrication.
- Dark, tenacious, high temperature oxide present on both the shallow microcracks and the larger pop-in cracks, confirmed that both crack types formed at elevated temperatures, which only occur during fabrication processes.
- CVN testing was performed on all flange samples at the top and bottom surfaces, ¼ and ¾ thicknesses, and the ½ thickness (mid-thickness). Although the ¼ thickness CVN results were found to be consistent with the project specification and girder plate mill certifications, the mid-thickness toughness levels were substantially lower than the ¼ thickness toughness and unacceptable from a performance perspective.
- The fracture origins were located in the mid-thickness of the flange where the fracture toughness was exceptionally low. That is, the mean ½ thickness CVN toughness level at 50ºF, the approximate temperature at which the fractures occurred, was only 11 ft-lb and the lower bound toughness was less than 5 ft-lb. This level of toughness provides little or no resistance to fracture from pre-existing cracks such as the observed microcracks and pop-in cracks.

In order to establish the driving force for the flange fractures and assess the design stresses under factored loading, finite element (FE) models of both the Fremont and First Street TPG3 girders were developed and stress analyses were performed using loads provided by TT. Stress analyses of Fremont Street were based on the expected loads at the time of D.4 bottom flange fracture initiation, which provided input for the root-cause assessment fracture mechanics calculations. First Street FE analyses were performed for factored loading (1.2(DL+SDL) + 1.6(LL)) in order to perform a FFS assessment of the TPG3 girders and to validate the proposed reinforcement plan.

From the results of the detailed FE and fracture mechanics analyses and bottom flange fracture sequence assessment, it can be concluded that:

- Pop-in cracks initiated from shallow surface microcracks due to the CJP groove weld-induced residual stresses.
- Pop-in crack propagation of Fremont Street D.4-NW arrested at a depth of 0.38 in.
- Fremont Street D.4-NW bottom flange brittle fracture initiated from the pop-in crack due to normal service stresses and the CJP groove weld-induced residual stresses.
- Once Fremont Street D.4-NW fractured, the stresses at D.4-SW increased significantly with a corresponding high loading rate, which resulted in an apparent

lower fracture toughness at D.4-SW. The combination of higher stress and lower toughness induced fracture of D.4-SW from a significantly smaller microcrack.

- After Fremont Street D.4 completely fractured, the imposed loads were shed throughout the adjacent structure. This redistribution increased stresses in the E.6 girder sufficiently to initiate fracture from a relatively large pop-in crack in the E.6-SW bottom flange. However, there was insufficient driving force remaining after load shedding to initiate fracture from the small microcrack in E.6-NW.
- Due to a combination of the absence of long-term oxidation (rusting) on the fracture surfaces (along with no evidence of fireproofing), the TT determined loading timeline, and lower steel fracture toughness at colder temperatures, the Fremont Street girder fractures occurred between the end of February 2018 and the end of April 2018.

It can be further concluded that:

- Yield strength level residual stresses at the weld access hole radius surface, induced by CJP groove welding, were required to initiate the pop-in crack from the 0.06 in. deep microcracks. These weld-induced residual stresses decreased rapidly as the distance into the bottom flange from the weld access hole radius surface increased.
- Normal service-induced stresses, based on the TT-determined loads at the time of fracture, were not sufficient to initiate the bottom flange fracture from the pre-existing 0.38 in. deep x 1.2 in. long pop-in crack located at the weld access hole radius surface, in the mid-thickness of the 4-in. thick bottom flange, where the fracture toughness (K_{1C}) was approximately 55 to 60 ksivin. at 50°F – the most likely temperature at the time of the fractures.
- Rapid, low-energy fracture of the Fremont Street bottom flanges occurred as the girders were subjected to normal service-induced stresses combined with typical residual stresses already present due to CJP groove welding of the bottom flanges.

Additionally, FFS assessments of the Fremont and First Street TPG3 girders determined that:

- The First Street and Fremont Street TPG3 girder weld access hole stress states due to service loading are approximately the same.
- The First Street and Fremont Street TPG3 girders are adequately designed for the factored design load case from a stress perspective.
- Thermal cutting of the weld access holes after CJP groove welding of the bottom flange plates relieved a notable fraction of the CJP groove weld-induced residual stresses.

- Fracture of the First Street TPG3 girders did not occur because of lower CJP groove weld-induced residual stress magnitude and the absence of pop-in cracks in the weld access hole radii.
- Based on factored loading the reinforcement is fit for the intended service at both Fremont and First Streets.
- The bottom flange hanger slots are not susceptible to fracture in the presence of an assumed 0.38 x 1.2 in. pop-in crack when subjected to the factored design loads.
- The hanger is not susceptible to fatigue crack propagation due to expected cyclic loading from bus traffic.

TABLE OF CONTENTS

1. INTRODUCTION

LPI, Inc. (LPI) was requested by the Transbay Joint Powers Authority (TJPA) to provide engineering services in the root cause and fitness-for-service (FFS) assessments of the TPG3 girders at the Transbay Transit Center (TTC) in San Francisco. The bottom flanges of the two TPG3 girders (D.4 and E.6 lines) located above Fremont Street fractured, originating at and propagating from weld access holes[2] [1] located adjacent to hangers at three locations. Onsite examination revealed that the north and south sides of the north girder (D.4 line) and the south side of the south girder (E.6 line) had fractured, and that the fractures had extended from the access holes across the entire half-width of each flange. In contrast to the TPG3 girders above Fremont Street, the two TPG3 girders (D and F lines) above First Street did not fracture. It was reported that the 4-in. thick bottom flange plates were fabricated from ASTM A572, Gr. 50 structural steel.

2. WORK SCOPE

The root cause and FFS assessments of the TTC TPG3 girders consisted of the following scope of work:

- On-site visual and nondestructive examinations (NDE)
- Metallurgical analysis of the fractured girder flanges
  - Visual and optical stereomicroscopic examination
  - Wet fluorescent magnetic particle testing (FMT)
  - Scanning electron microscopy (SEM) and energy dispersive x-ray spectroscopy (EDS)
  - Micro- and macro-section examination
  - Microhardness testing
- Fracture mode assessment
- Analysis of girder steel
  - Charpy V-Notch (CVN) toughness testing
  - Tensile testing

[2] The use of the term “weld access hole” is consistent with contract document RFI-2003 [1], in which the Contractor (Webcor/Skanska) and the Structural Engineer of Record (Thornton Tomasetti) used the term to refer to this feature (i.e., the termination of the 4-in. thick flange CJP groove weld at the vertical hanger plate) prior to fabrication.

- Macro-section hardness testing
- Surface hardness testing
- Compositional analysis

- Development of TPG3 finite element (FE) models
  - Fremont Street D.4 girder
  - Fremont Street D.4 girder with northwest and southwest fractures included
  - Fremont Street D.4 girder with the pop-in crack mesh included
  - First Street F girder
  - First Street F girder with proposed improvements
  - First Street F girder with crack meshes included
  - First Street F girder with repair included
  - Local weld access hole submodels used for residual stress calculations
- Calculation of detailed stress distributions in TPG3 girder fracture-critical areas due to service loading using FE analysis
- Estimation of residual stress distributions due to bottom flange CJP groove welding from fracture mechanics and FE analysis calculation
- Determination of fracture toughness from Charpy V-Notch data
- Fracture mechanics calculations for each stage of the Fremont Street girder bottom flange fractures
- Determination of root cause of Fremont Street TPG3 girder fractures
- FE simulations of various improvement considerations
- Fracture mechanics calculations of postulated cracks located within the hanger and within the hanger slot
- FE simulation of final First Street repair configuration

3. METALLURGICAL ASSESSMENT

3.1 Site Inspections

3.1.1 Initial Site Inspection

An initial site inspection of the fractured girders was performed by LPI on October 1, 2018. Onsite examination revealed that the north and south sides of the north girder and the south side of the south girder had fractured, as shown in Fig. 1 through Fig. 5. The fractures were oriented transverse to the longitudinal axes of the girders and extended

from the weld access holes at the bottom (see Fig. 3 and Fig. 5) across the entire half-width of each flange. It was evident that the access holes had been thermally cut into the flange plates to facilitate complete joint penetration (CJP) groove welding of the bottom flange plates, adjacent to the hanger.

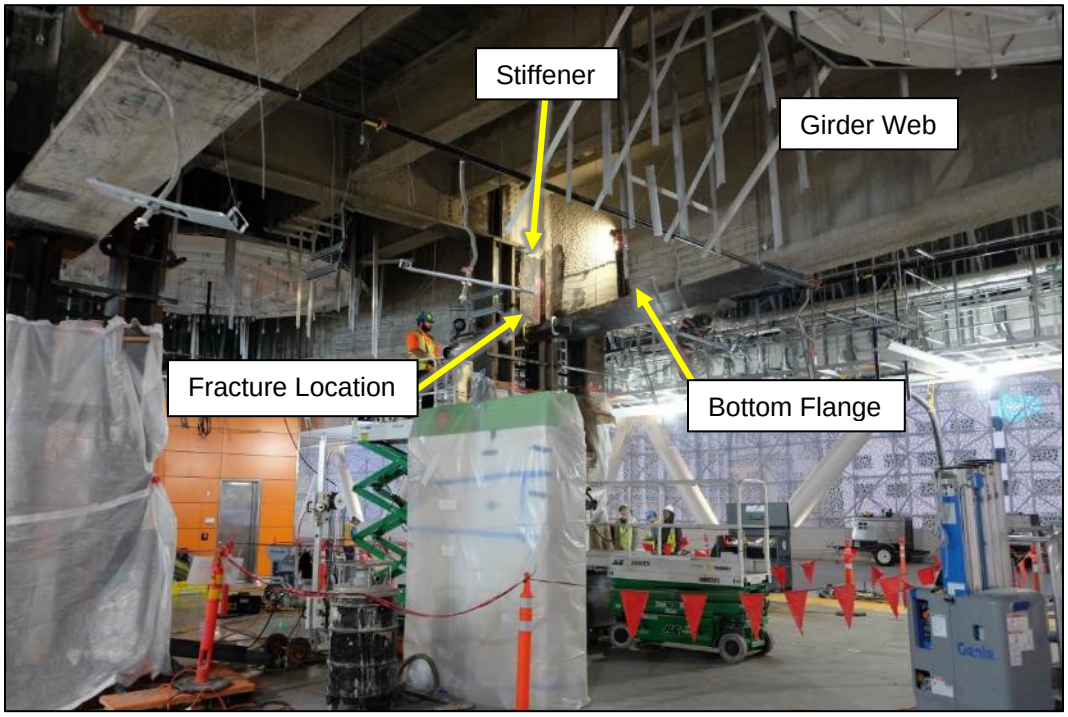

Fig. 1. Fractured girders above Fremont Street

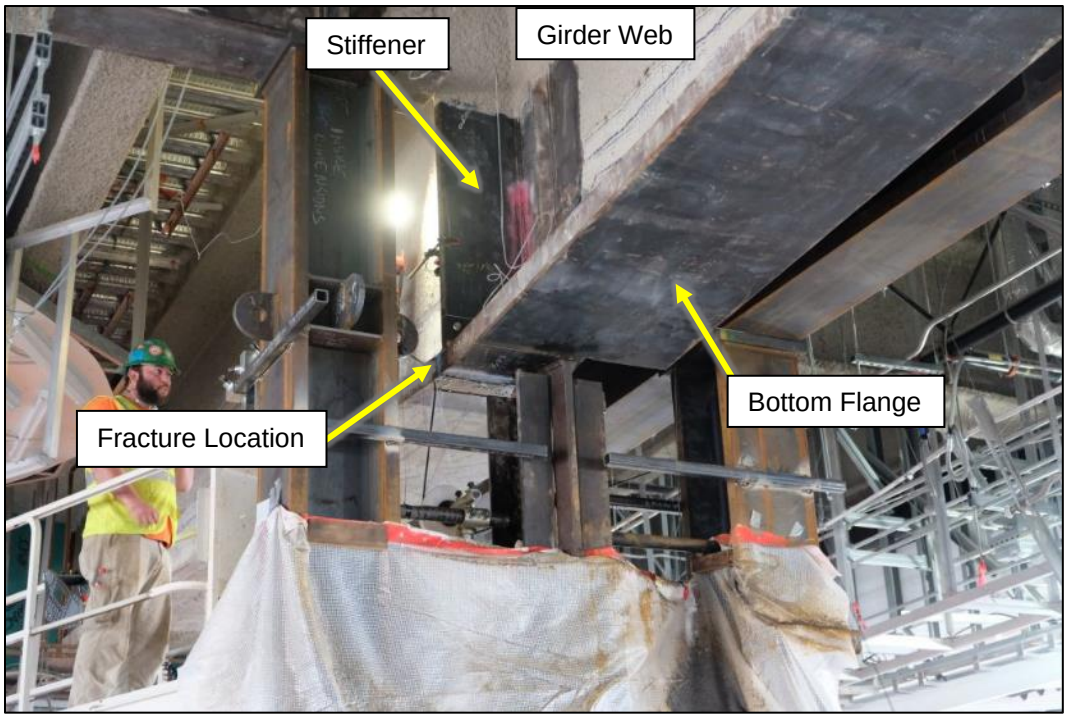

Fig. 2. North side girder flange fracture location above Fremont Street.

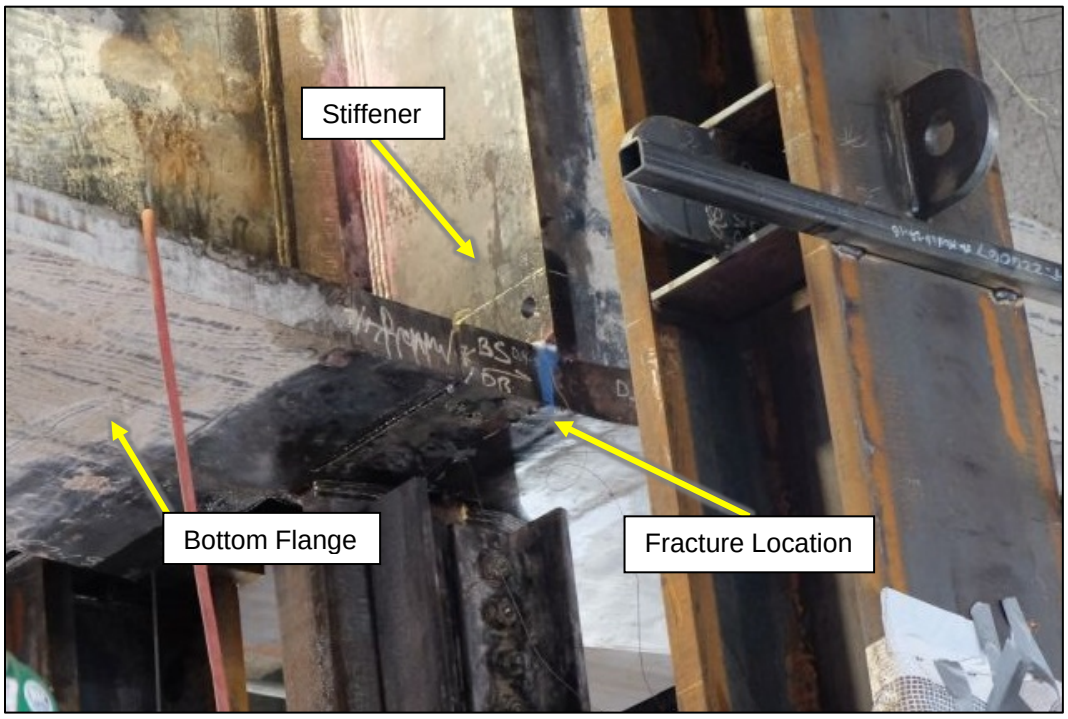

Fig. 3. Typical location of north side girder fracture, where the fracture was protected with silicone prior to flange sample removal.

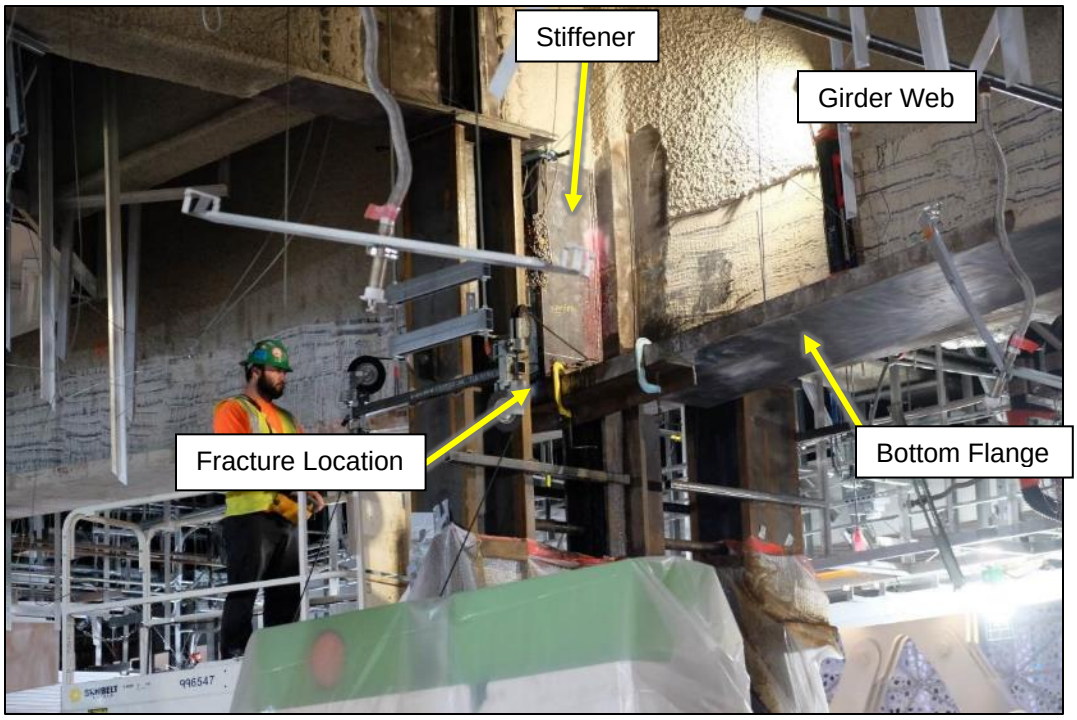

Fig. 4. Flange sample removal of the north side girder by wire cutting.

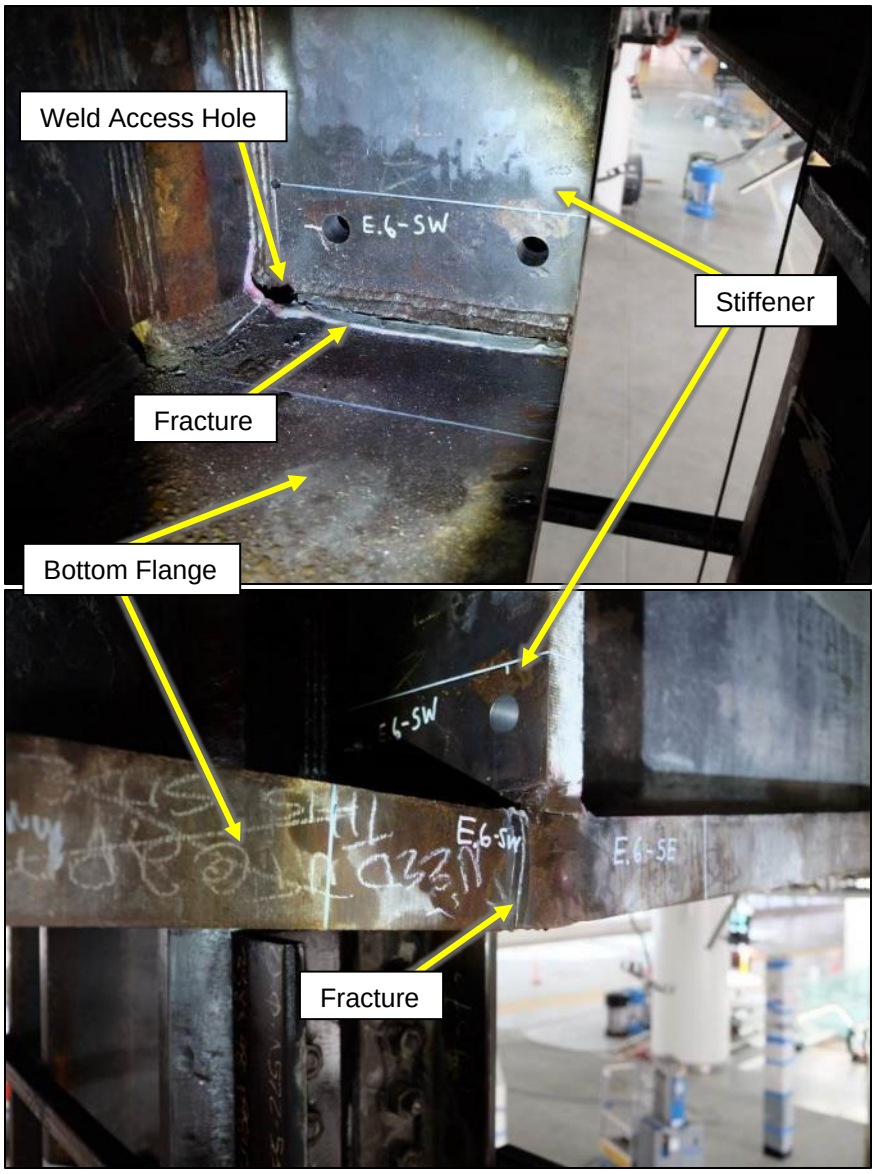

Fig. 5. South side girder fracture, where the fracture was protected with silicone prior to flange sample removal.

3.1.2 Onsite Nondestructive Assessment

Ultrasonic testing (UT) of TPG3 girder welds and bolts was performed December 10, 2018 through December 14, 2018 by an LPI technician certified in accordance with the guidelines of the American Society for Nondestructive Testing. Specifically, the CJP groove welds on girder D.4 and E.6 located 20 feet east and 20 feet west of Fremont Street were evaluated and found to be acceptable. The same 20-ft welds in the First Street girders were also inspected by UT. Results of the UT inspections did not reveal

any rejectable indications as summarized in the LPI field UT inspection reports given in Appendix A.

In addition, fifty 1-1/4 in. diameter bolts on the east end connection of Fremont Street girder D.4 and five 1-1/2 in. diameter bolts on the west end connection of Fremont Street girder D.4 were evaluated visually and by straight beam UT. Fifty-five 1-1/4 in. diameter bolts at the east and west ends of the Fremont Street girder E.6 were similarly evaluated. Results of the visual and UT examinations determined all bolts to be acceptable, that is, the bolts were tight and did not exhibit any detectable cracks as summarized in the LPI field report provided in Appendix B.

3.2 Sampling

LPI facilitated and supervised, jointly with Thornton Tomasetti (TT), the Engineer of Record for the TTC, the removal of all samples by In-Place Machining Company, LLC from October 23, 2018 through January 25, 2019. The removed girder flange, girder core, and hanger core samples were packaged under LPI's supervision, and shipped to LPI's New York facility for analyses. Additionally, girder sample removal was reviewed and witnessed by all interested parties, including the Metropolitan Transportation Commission (MTC).

3.2.1 Girder Sample Removal

To assess the nature and cause of the girder fractures, four T-shaped samples were removed from each girder, such that each sample consisted of flange and vertical stiffener sections, as shown in Fig. 6. Three of the four girder samples contained the three fractures, whereas the fourth sample, which was removed from the north side flange of the south side girder, did not contain a fracture.

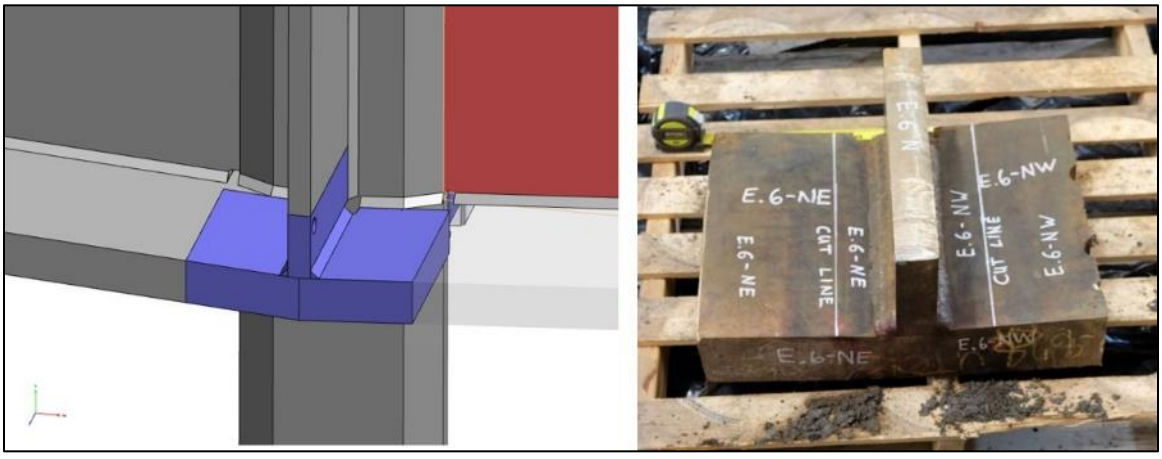

Fig. 6. Girder model (left) showing girder sample geometry and location. Typical girder sample after removal (right).

The girder samples from the north girder were identified **D.4-N** (north girder flange) and **D.4-S** (south girder flange). Similarly, the girder samples from the south girder were identified **E.6-N** (north side girder flange) and **E.6-S** (south side girder flange). The two flange sections in each sample were further identified as **W**(est) and **E**(ast), as given in Table 1.

The girder samples are shown in Appendix C, Fig. 177 through Fig. 184 following removal from the TTC and as-received at LPI. Girder samples D.4-S and E.6-S separated in two sections during removal from the girder without the application of any undue force. Girder sample D.4-N separated during handling at LPI's facility without the application of any undue force.

Table 1 – Girder Sample Identification

North Side Girder				**South Side Girder**			
D.4				E.6			
North Side Flange		**South Side Flange**		**North Side Flange**		**South Side Flange**	
D.4-N		D.4-S		E.6-N		E.6-S	
West Side Flange Section	**East Side Flange Section**	**West Side Flange Section**	**East Side Flange Section**	**West Side Flange Section**	**East Side Flange Section**	**West Side Flange Section**	**East Side Flange Section**
D.4-NW	D.4-NE	D.4-SW	D.4-SE	E.6-NW	E.6-NE	E.6-SW	E.6-SE

3.2.2 Core Sample Removal

As part of the repair procedure and fitness-for-service assessment of the First Street girders, four 3-in. diameter, full flange-thickness core samples were removed from the bottom flange of the north and south girders for Charpy V-notch toughness testing, as shown in Fig. 7. As identified in Table 2, the 3-in. diameter cores were removed from the north and south girder flanges above First Street, approximately 18 to 20 ft east and west of the hanger centerlines. These samples correspond to the same TPG3 flange plates that exhibited the fractures at Fremont Street.

Additionally, four 3-in. diameter core samples were removed from hanger plates of the north and south girders located above Fremont Street and First Street. The hanger core samples were removed approximately 12 in. below the girder top flange, at the center of the hanger plate, as shown in Fig. 8. One core sample was removed from each hanger plate, as identified in Table 3.

The core samples are shown in Appendix C, Fig. 185 through Fig. 190 following removal from the TTC and as-received at LPI.

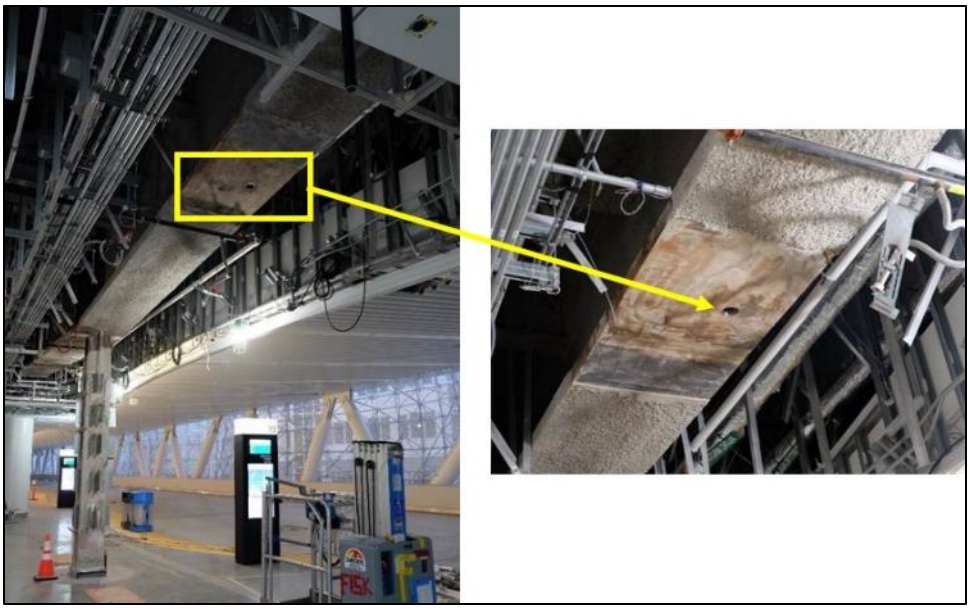

Fig. 7. Typical location of the 3-in. diameter core samples removed from girder flanges above First Street.

Table 2 – Girder Flange Core Sample Identification

First Street North Side Girder		First Street South Side Girder	
West	East	West	East
NW-18	NE-18	SW-18	SE-18

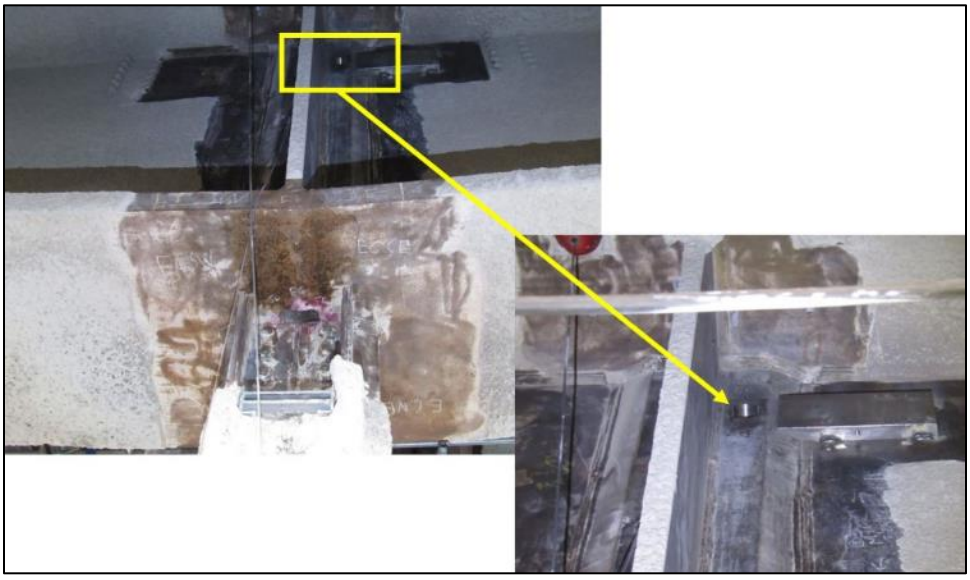

Fig. 8. Typical location of the 3-in. diameter core samples removed from girder hangers above both Fremont and First Streets.

Table 3 – Girder Hanger Core Sample Identification

Fremont Street Girders		First Street Girders	
North	South	North	South
N-26	S-26	N-18	S-18

3.3 Girder Sample Testing Protocol

Upon arrival at LPI's New York test facility, evaluation of the girder and core samples was performed in accordance with a mutually agreed upon testing protocol. A joint examination was held at LPI during the time period of November 13-15, 2018. The following tasks were completed and are detailed in Section 5.0:

- Preparation of samples for joint lab examination, including as-received photographs, cleaning of fracture surfaces with mild hand detergent and nylon fiber brush, as-cleaned photographs, and sectioning of girder samples to separate the fracture surfaces from the sections to be used for mechanical testing.
- Visual and stereomicroscopic examination of fracture surfaces and other areas of interest on the girder samples.
- Nondestructive examination (NDE) of the weld access holes by fluorescent magnetic particle testing.
- Scanning electron microscopy (SEM) of fracture surfaces, along with energy dispersive X-ray spectroscopy (EDS) of areas of interest.
- Metallographic examination of specimens prepared through the fracture surfaces and access holes.
- Microhardness testing of cross-sectioned specimens prepared through the fracture surfaces and access holes.
- Charpy V-notch (CVN) fracture toughness testing of samples sectioned from girder flange plates and core samples.
- Tensile testing of samples sectioned from girder flange plates.
- Hardness testing of macro-sections prepared through girder samples and surface hardness testing of weld access hole surfaces.
- Compositional analysis of samples sectioned from girder flange plates.

3.4 Metallurgical Analysis of Fractured Girders

3.4.1 Visual and Optical Stereomicroscopic Examination

Visual examination of the fractured girder samples, D.4-NW, D.4-SW and E.6-SW, revealed similar fracture morphologies. That is, all fractures were oriented transverse to the longitudinal axis of the girder flange and initiated at the weld access holes adjacent

to the hanger plate. Further examination of the fracture surfaces revealed a relatively shiny surface appearance with varying degrees of superficial corrosion due to exposure to the environment following fracture, and little or no associated inelastic (plastic) deformation, as is characteristic of rapid, low-energy (brittle) fracture. The fractures also exhibited chevron marks on the fracture surfaces that identified the fracture origins, which in all cases similarly occurred at the surface of the access hole radii, as shown in Fig. 9 through Fig. 11. Chevron marks are V-shaped features that develop on low-energy (brittle) fracture surfaces and point back to the fracture initiation site.

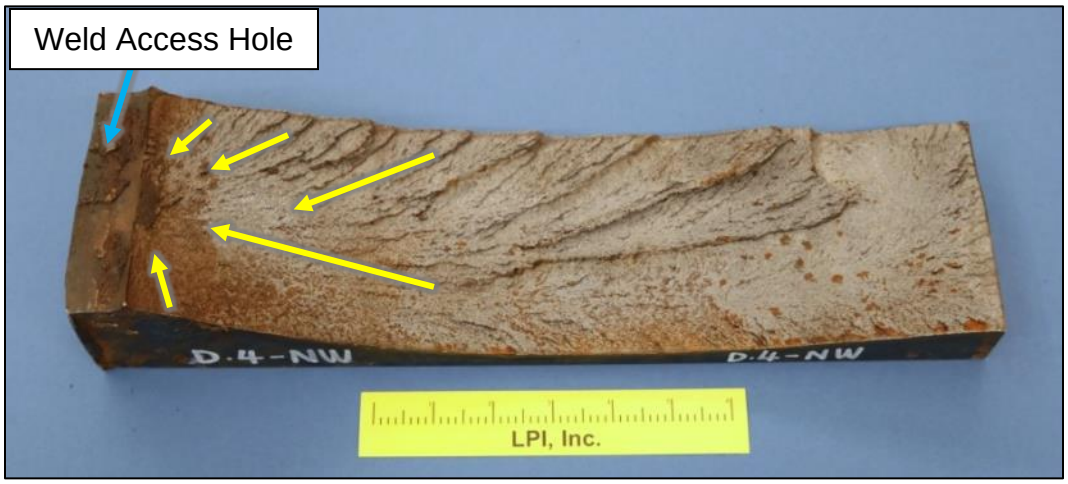

Fig. 9. Chevron marks (yellow arrows) on the fracture surface of girder sample D.4-NW reveal the fracture origin to be adjacent to the weld access hole.

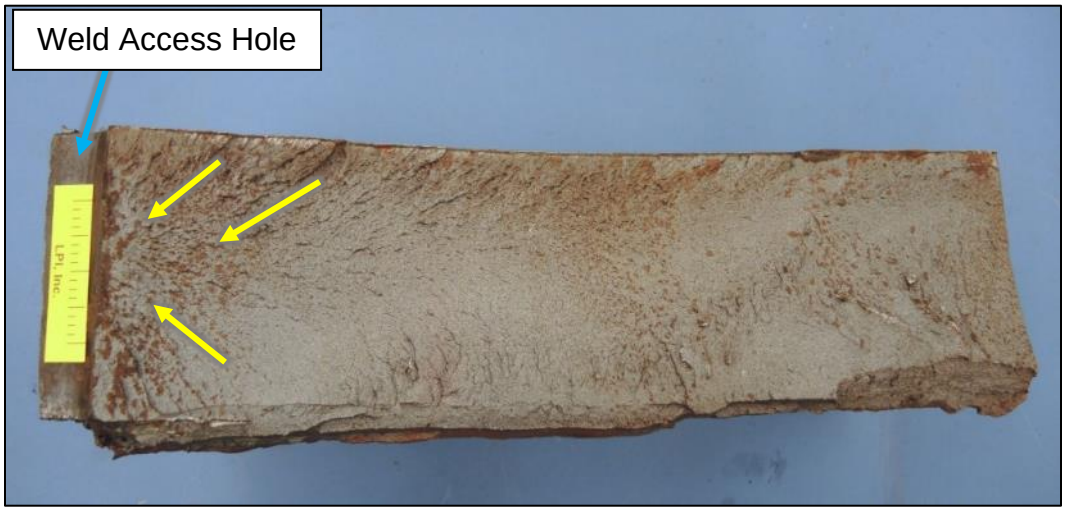

Fig. 10. Chevron marks (yellow arrows) on the fracture surface of girder sample D.4-SW pointing towards the origin at the edge of the weld access hole.

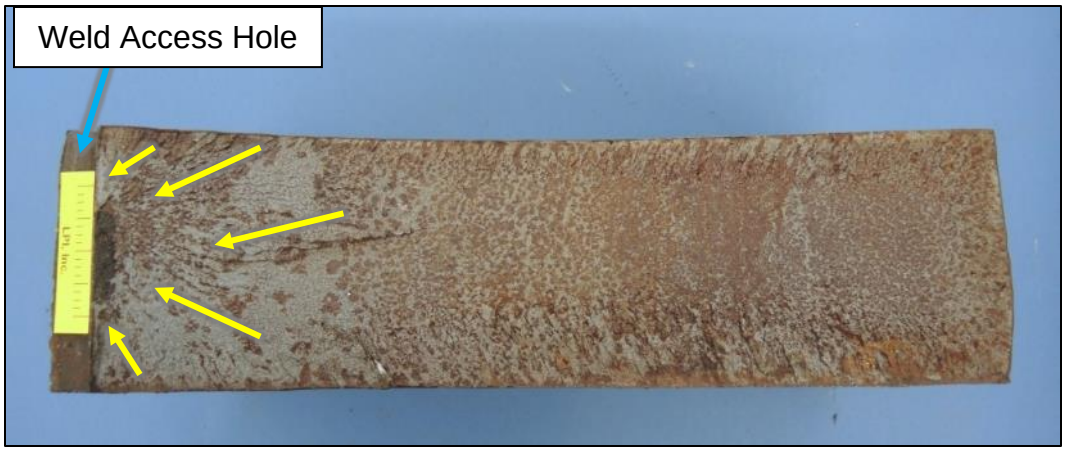

Fig. 11. Chevron marks (yellow arrows) on the fracture surface of girder sample E.6-SW pointing towards the origin at the edge of the weld access hole.

Further examination of the fracture surfaces from girder samples D.4-NW and E.6-SW revealed semi-elliptical crack-like features that were covered with dark, tenacious oxides, as shown in Fig. 12 and Fig. 13. These semi-elliptical crack-like features were located at the edge of the flange fractures coincident with the radii of the access holes, near the mid-thickness of the flange plates. Dimensional examination revealed that the semi-elliptical crack on D.4-NW measured approximately 0.38 in. deep x 1.2 in. long and the crack on E.6-SW measured 0.32 in. deep x 1.41 in. long. The fracture origin of girder sample D.4-SW was relatively small (approximately 0.04 in. deep) compared to the elliptical origins of girder samples D.4-NW and E.6-SW; however, this narrow crack-like band also exhibited a dark, tenacious oxide layer adjacent to the radius surface, along the edge at the access hole, as shown in Fig. 14. Closer examination of samples D.4-NW and E.6-SW also revealed the presence of narrow, dark oxide-filled cracks immediately adjacent to the access hole radii surface. The narrow band oxide-filled cracks were nearly identical in appearance and varied in depth from the radii surface from approximately 0.020 in. to 0.060 in. (hereafter referred to as microcracks). The dark, tenacious oxide present on the elliptically shaped and narrow band microcracks are typical of oxides that formed at elevated temperatures, typically greater than about 350°F [2].

Fig. 12. Dark oxide covered elliptical pop-in crack fracture origin at the weld access hole (top) of girder sample D.4-NW.

Fig. 13. Dark oxide covered elliptical pop-in crack fracture origin at the weld access hole (top) of girder sample E.6-SW.

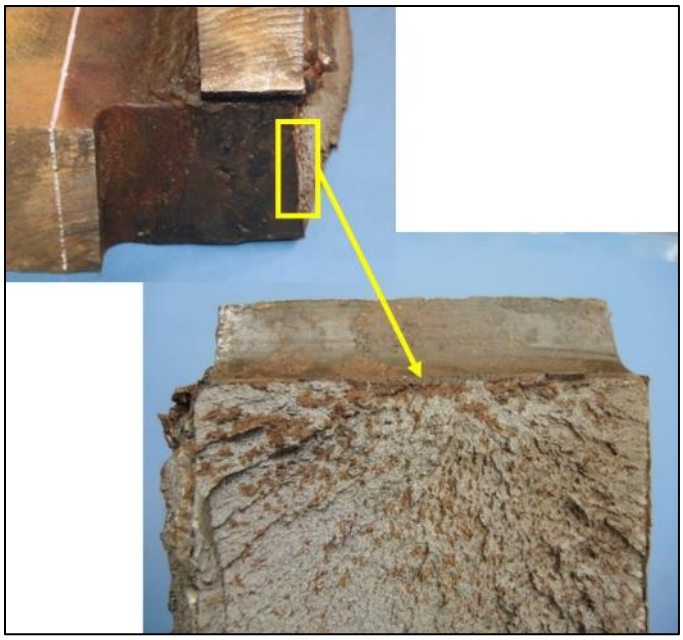

Fig. 14. Dark oxide covered narrow band microcrack fracture origin at the weld access hole (top) of girder sample D.4-SW.

The fractured girder samples D.4-NW, D.4-SW, and E.6-SW were sectioned for further examination at the fracture origins and the adjacent fracture surfaces. Stereomicroscopic examination after sectioning and cleaning with an Alconox detergent solution revealed two distinct regions exhibiting somewhat different fracture morphologies at the fracture origins of samples D.4-NW and E.6-SW. At the edge of the weld access hole, the narrow microcrack band appeared somewhat smoother than the larger elliptical crack origin, as shown in Fig. 15. The microcrack band at the edge of the weld access hole was similar in appearance to the fracture origin of sample D.4-SW, as shown in Fig. 16. In addition, the black oxide layers appeared more tenacious at the edge of the weld access holes and could not be removed or cleaned. This observation indicated that the narrow band microcracks and the elliptical cracks formed at different times.

Again, the dark tenacious oxide layer indicated that the crack surfaces were exposed to elevated temperatures. During fabrication of the girders there were three thermal processes of sufficiently high temperature that would induce such oxides: (1) thermal cutting of the weld access holes, (2) complete joint penetration (CJP) groove welding of the girder flanges, and (3) thermal cutting of the run-off tabs used to complete the flange CJP welds. It can be further concluded, therefore, that the oxide layer on the narrow band microcracks at the weld access hole surfaces developed during thermal cutting of the weld access holes, whereas the larger elliptical cracks formed during CJP groove welding of the flanges. However, oxidation of the pop-in crack surfaces could have occurred during CJP welding of the girder flanges and/or thermal cutting of the run-off tabs. This

sequence of crack formation clearly indicates that the larger elliptical cracks initiated from the microcracks driven by welding-induced residual stresses associated with CJP groove welding of the flange plates. That is, the elliptical cracks “popped-in” from the microcracks during welding and are referred to as such throughout this report.

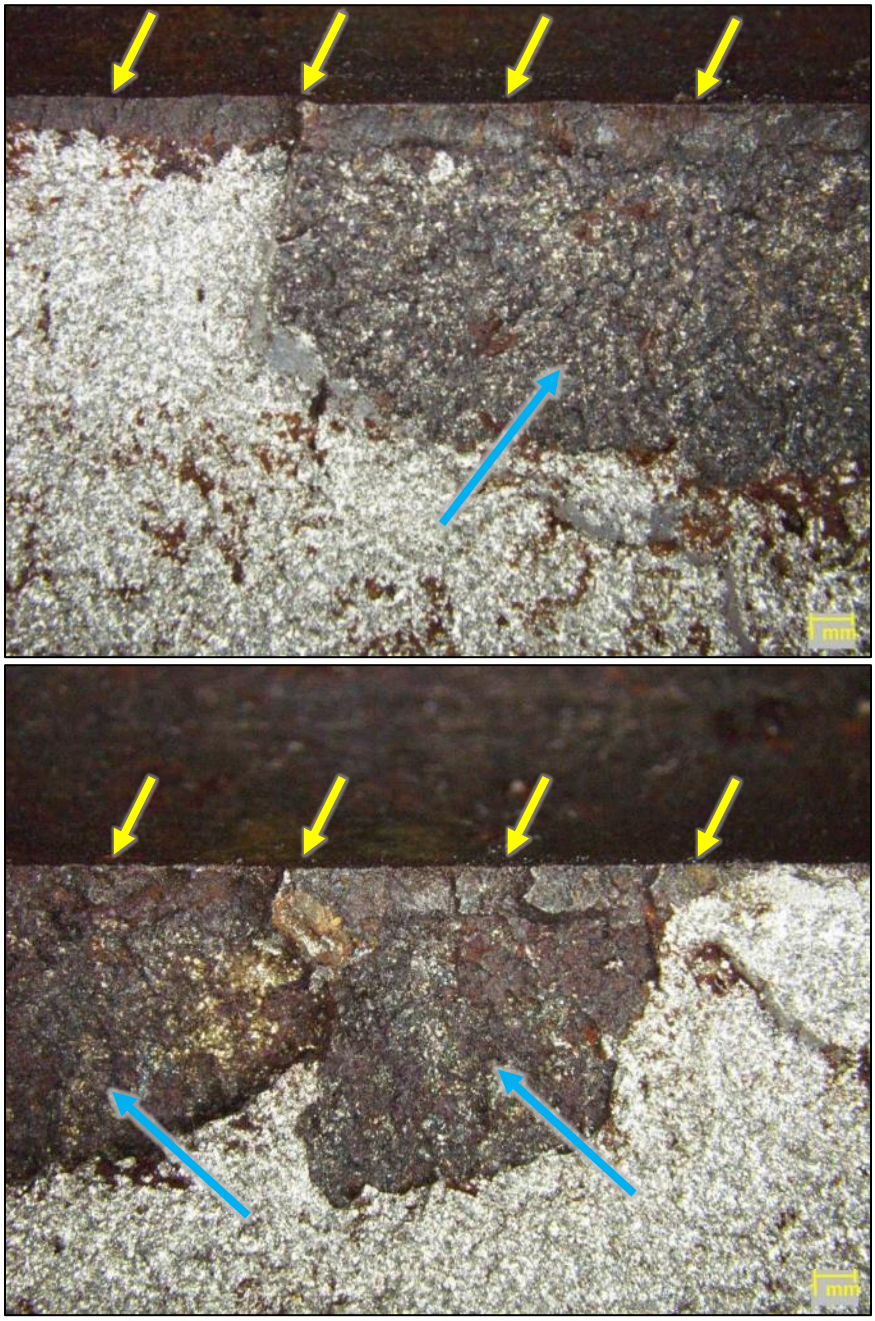

Fig. 15. Origin of D.4-NW exhibited narrow band microcracks (yellow arrows) at the edge to the weld access hole with a tenacious dark oxide layer. The elliptical crack (blue arrows) “popped-in” from the microcracks and exhibited a dark oxide layer that was partially removed after cleaning.

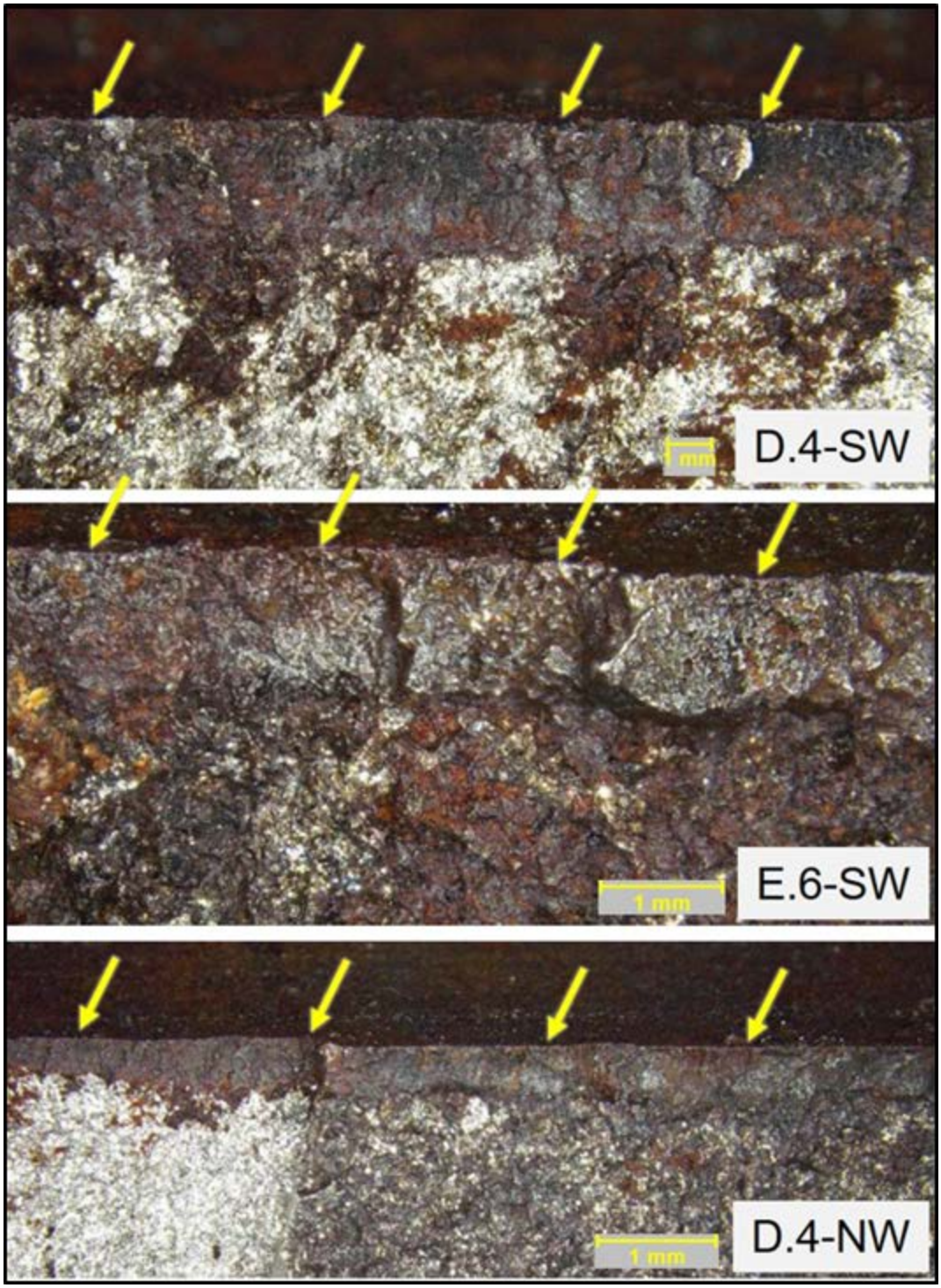

Fig. 16. Fracture origins of samples D.4-SW (top), E.6-SW (center) and D.4-NW (bottom) showing microcracks that initiated during thermal cutting of the access holes.

Visual examination of the fracture surfaces did not reveal any pre-existing mechanical or metallurgical plate deficiencies in the vicinity of the fracture origins or the fracture surfaces which, if present, could have contributed to the subject fractures. Moreover, examination of the fractures did not reveal any evidence of progressive cracking in the nature of fatigue or stress corrosion cracking.

Further visual examination revealed linear ridges typical of thermal cutting on the weld access hole surfaces that were oriented in the through-thickness direction, as shown in Fig. 17.

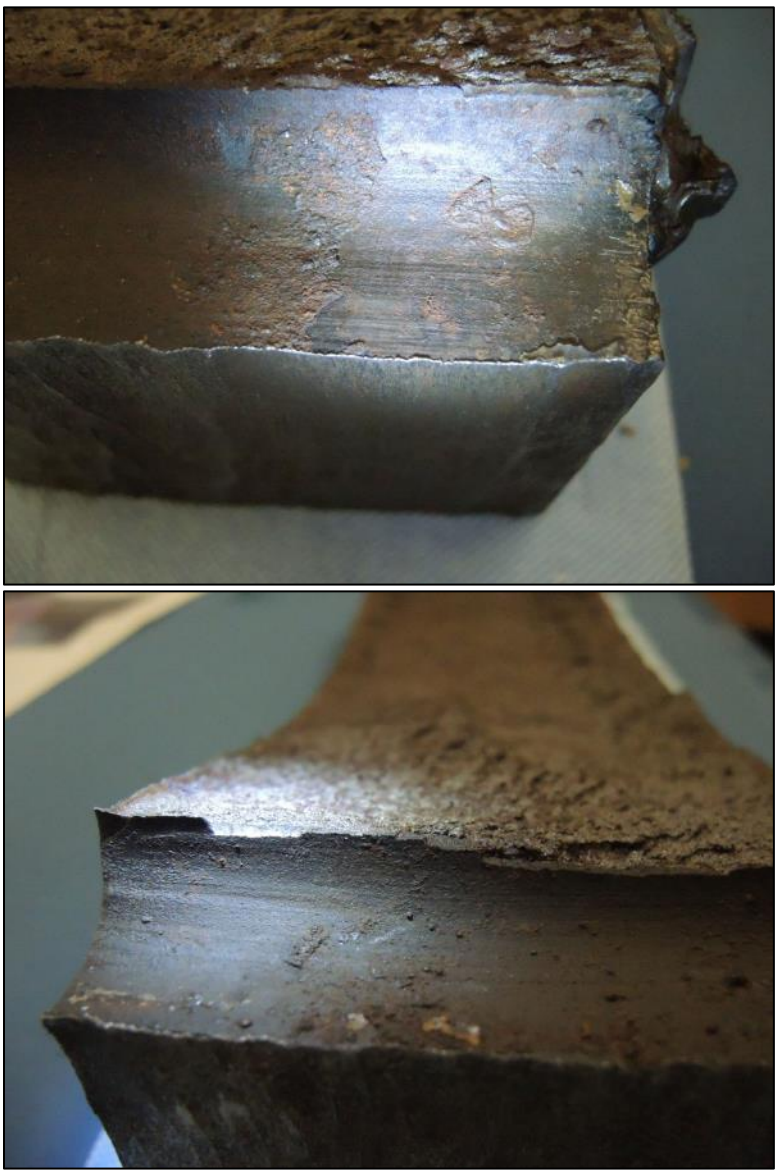

Fig. 17. Weld access hole surfaces in samples D.4-SW (top) and E.6-SW (bottom).

The access hole in intact sample E.6-N measured approximately 4.6 to 5 in. long (parallel to longitudinal girder axis) x 0.68 to 0.86 in. wide (transverse to the girder axis), while the access holes in girder samples D.4-N, D.4-S, and E.6-S measured approximately 4 to 5 in. long x 0.85 to 1 in. wide. It should be noted that these access hole measurements are were made on the as-received samples cut from the Fremont Street girders and, thus, do not reflect the full width of the holes.

3.4.2 Wet Fluorescent Magnetic Particle Testing

Prior to sectioning through the fracture surfaces, fluorescent magnetic particle (FMT) testing of the access hole radii in samples D.4-NW, D.4-SW, and E.6-SW revealed multiple cracks parallel and adjacent to the girder fractures within the thermally cut surfaces, as shown in Fig. 18. Additional FMT images are provided in Appendix C, Fig. 191 through Fig. 193. FMT of the radii in sample E.6-N did not reveal any indications of cracking. These FMT indications are indicative of additional microcracks relative to those observed on the fracture surfaces adjacent to the access hole surfaces. Additionally, FMT did not reveal microcracks in the thermally cut flat (straight) regions adjacent to the thermally cut radii or along the outboard flange edges. The absence of microcracks along straight, thermally cut edges is not unusual and most likely due to lower thermally induced residual stresses.

It is important note that thermal-cutting-induced microcracks will not necessarily be detected by FMT or dye penetrant testing (PT) because of their very small size and the irregular profile of thermally cut surfaces. This deficiency in detectability is one of the reasons why codes such as AWS D1.1 [4] and the AISC Steel Construction Manual [5] require grinding of thermally cut surfaces in thick plates prior to performing MT or PT examinations.

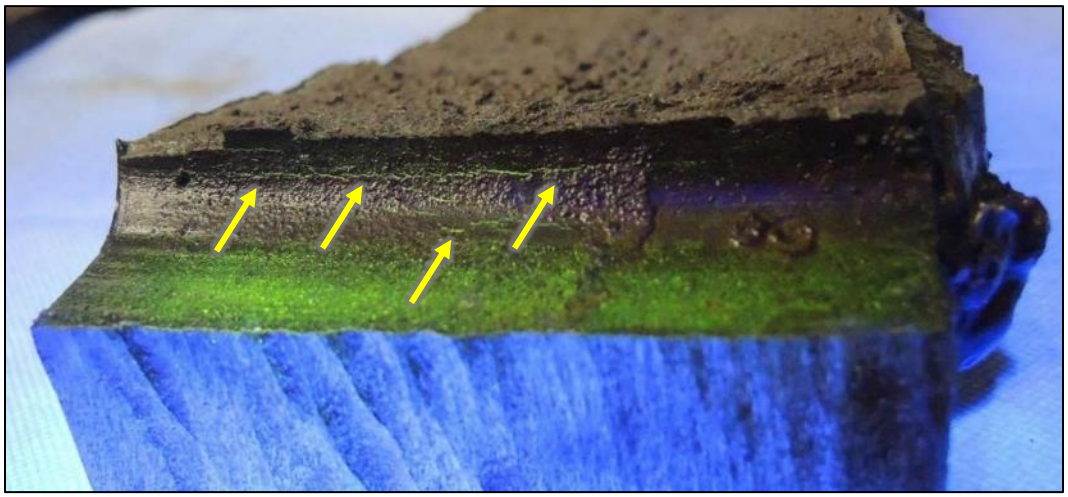

Fig. 18. Cracking in the radius of the thermally cut access hole surface of sample D.4-SW, as identified by fluorescent magnetic particle testing.

3.4.3 Summary of Observed Cracking

Based on the visual and FMT examinations, the locations of the observed microcracks, pop-in cracks, and flange fractures are given in Table 4 and Fig. 19. It is evident from this summary that both the pop-in cracks and flange fractures occurred in the west side access holes relative to the hanger centerline. The sequence of the girder flange fractures and the mechanisms associated with the west-sidedness of the pop-in crack locations is discussed in detail in Section 4.

Table 4 – Summary of Observed Cracking

Location	Microcracks	Pop-in Crack	Flange Fracture
D.4-NW	X	X	X
D.4-NE	X		
D.4-SW	X	X	X
D.4-SE			
E.6-NW	X		
E.6-NE	X		
E.6-SW	X	X	X
E.6-SE	X		

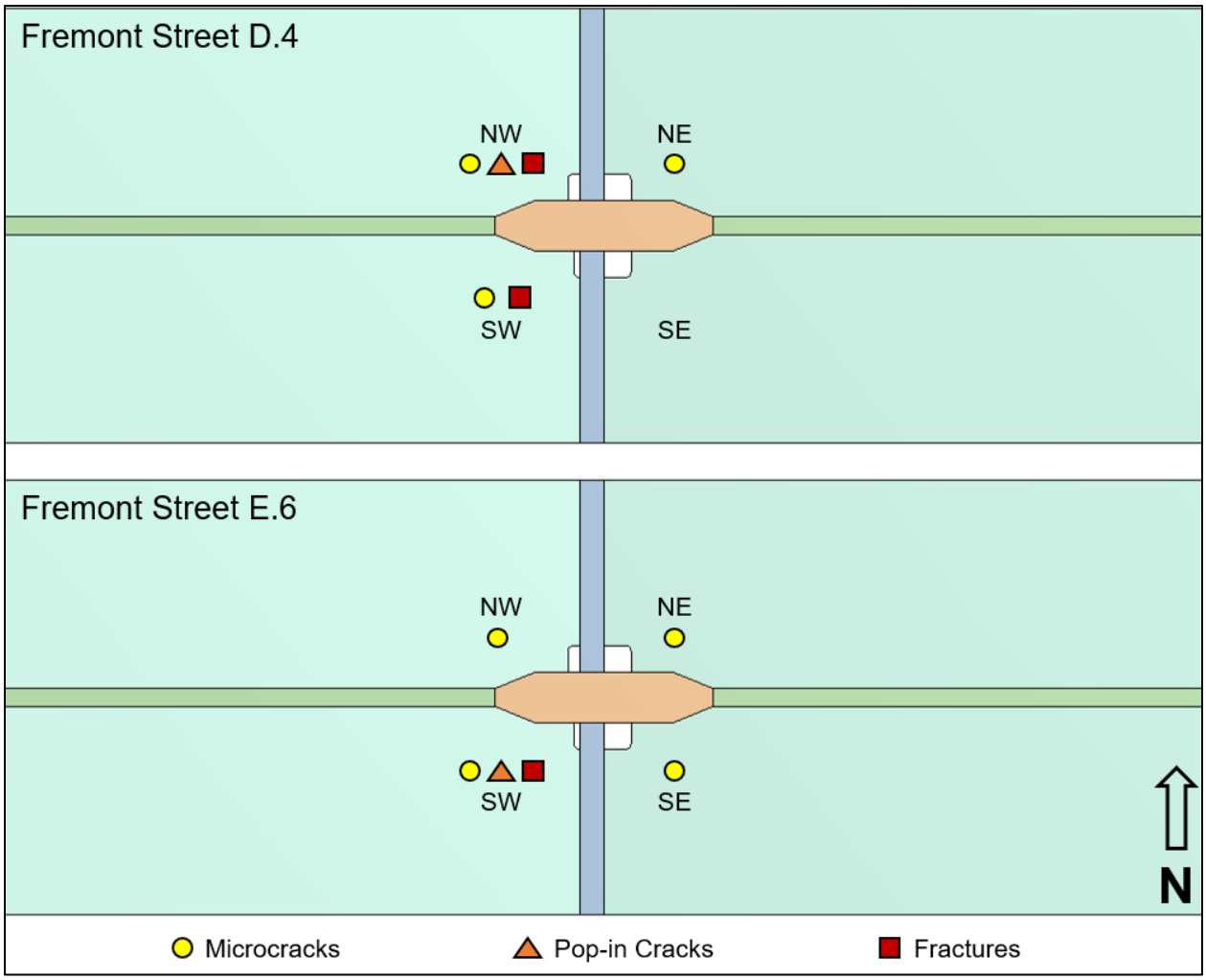

Fig. 19. Summary of observed cracking and fractures. Diagram is generic and not representative of actual weld access hole dimensions. The thin, blue rectangles perpendicular to the orange hangers are the centerline stiffeners.

3.4.4 Scanning Electron Microscopy and Energy Dispersive X-Ray Spectroscopy

Scanning electron microscopy (SEM) was performed to further evaluate the fracture origins and adjacent fracture surfaces at higher magnifications.

SEM examination of samples D.4-NW, D.4-SW, and E.6-SW revealed nearly identical fracture morphologies. The narrow band microcracks adjacent to the weld access hole radii exhibited tenacious oxide-covered fractures even after cleaning with Alconox, as shown in Fig. 20. In contrast, the larger elliptically shaped cracks in samples D.4-SW and E.6-SW exhibited less oxide after cleaning than the microcracks, indicating that the surface oxide on the elliptical cracks was slightly less adherent and tenacious than the

microcracks. As such, it can also be concluded that the elliptical cracks were most likely exposed to lower elevated temperatures than the narrow crack bands. This further confirmed that the elliptical crack surfaces formed after development of the shallower microcracks. That is, the narrow band microcracks formed during thermal cutting of the weld access holes, and the elliptical cracks popped-in during the CJP groove welding of the flange plates.

SEM examination to assess microcrack mode of fracture, as well as the elliptical cracks, revealed nearly identical fracture morphologies consisting almost entirely of low-energy cleavage fracture, as shown in Fig. 21. The flange fracture surfaces, remote from the micro and elliptical crack origins, also exhibited cleavage or quasi-cleavage fracture, as is characteristic of rapid low-energy (brittle) fracture of the flange plates.

Typically, even low-energy cleavage fractures exhibit a small amount of ductile crack initiation in the form of microvoid coalescence along the crack tip front. Additionally, the presence of localized crack tip microvoid coalescence can provide an indication of the level of fracture toughness associated with fracture initiation. In this regard, SEM examination of the leading edges of the elliptical cracks, in fact, revealed a narrow band of microvoid coalescence, shown in Fig. 22. This narrow band of microvoid coalescence indicates that the flange fractures initiated at a toughness level in the lower transition region corresponding to a fracture toughness in the range of approximately 40 to 70 ksi√in. (see Section 3.6.3).

Additional SEM images are provided in Appendix C, Fig. 194 through Fig. 204.

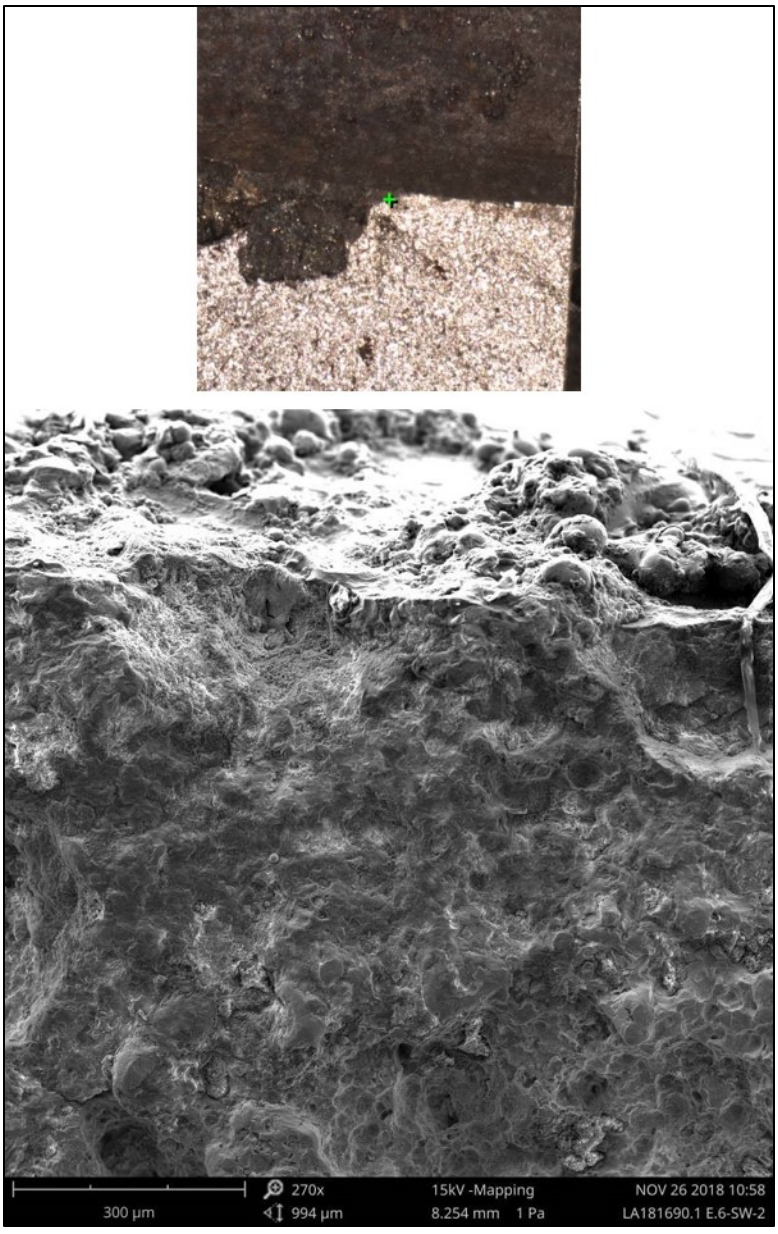

Fig. 20. Oxide covered microcrack fracture origin after cleaning of sample E.6-SW.

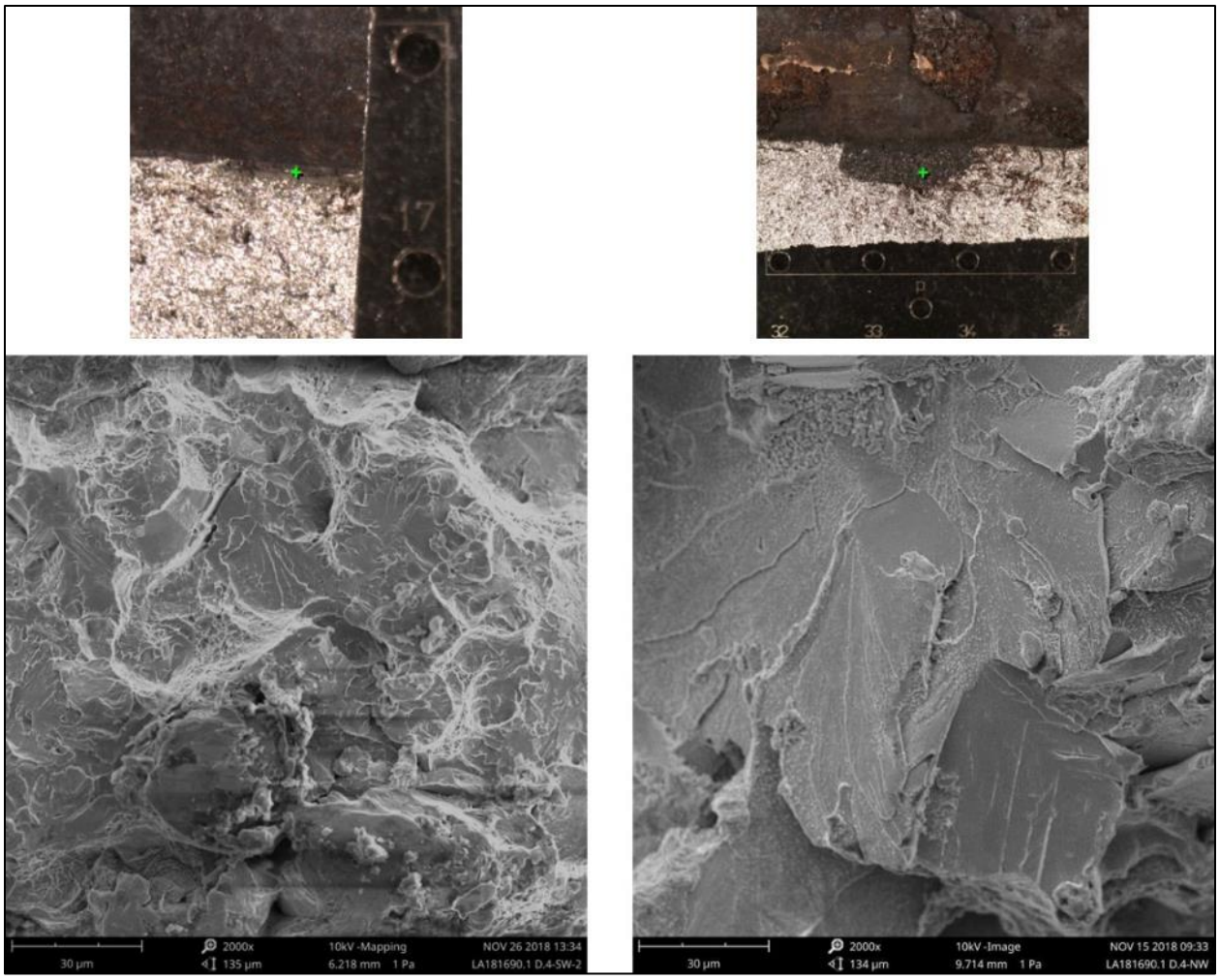

Fig. 21. (Left) Typical SEM image of microcrack fracture after cleaning in sample D.4-SW exhibiting a low-energy cleavage fracture morphology. (Right) Typical SEM image of elliptical pop-in crack fracture in sample D.4-NW exhibiting a low-energy cleavage fracture morphology.

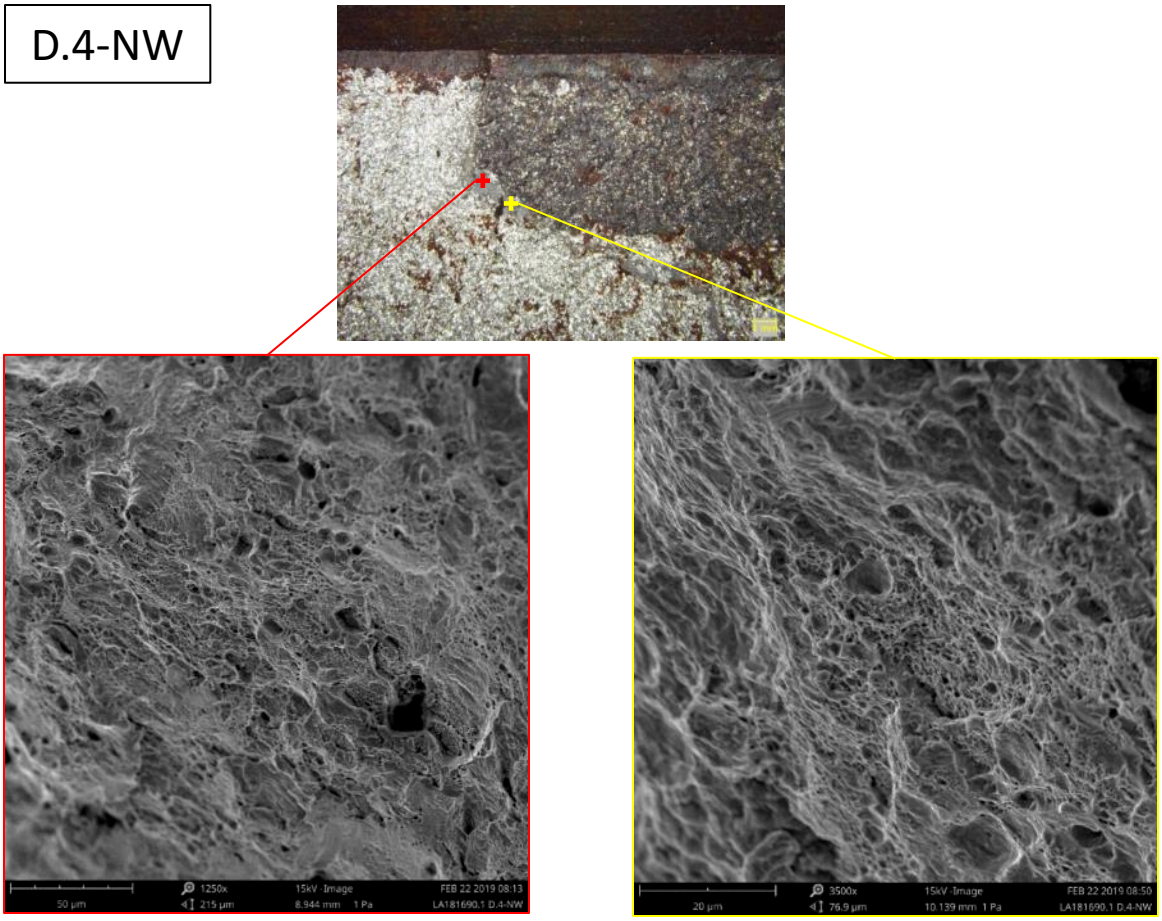

Fig. 22. SEM images at the leading edge of oxidized elliptical crack in girder sample D.4-NW showing a narrow band of microvoid coalescence.

Energy dispersive X-ray spectroscopy (EDS) was utilized to identify the elements present on the fracture surface of sample E.6-SW. EDS utilizes the electron beam of the SEM to excite X-rays from the sample surface. The generated X-rays identify the elements present on the surface and their approximate concentrations.

Results of the EDS analysis, shown in Fig. 23, principally revealed the presence of iron and oxygen, most likely in the form of high temperature iron oxide, as well as iron and manganese from the underlying steel In addition, EDS analysis revealed very minor peaks of calcium, carbon, silicon, manganese, and aluminum. The presence of these later elements is attributed to debris that was deposited on the surface following the fractures during removal of the girder fireproofing material, subsequent NDE, and sample removal and handling. Moreover, no significant quantities of elements associated with fireproofing material (e.g., magnesium) were identified on the fracture surfaces, which indicates that the flange fractures occurred after the fireproofing was applied in August 2016 [26].

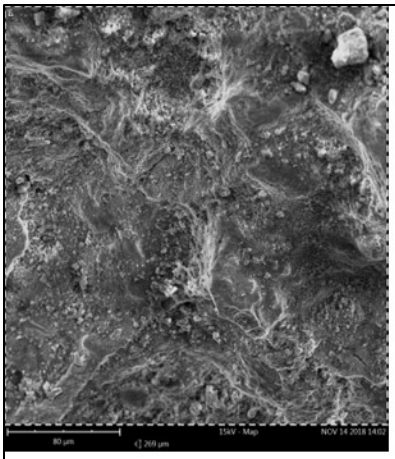

Element Symbol	Element Name	Atomic Conc.	Weight Conc.
O	Oxygen	74.92	48.85
Fe	Iron	20.61	46.91
Ca	Calcium	0.83	1.36
C	Carbon	2.25	1.10
Si	Silicon	0.49	0.56
Mn	Manganese	0.23	0.51
Al	Aluminum	0.42	0.47
Mg	Magnesium	0.24	0.24

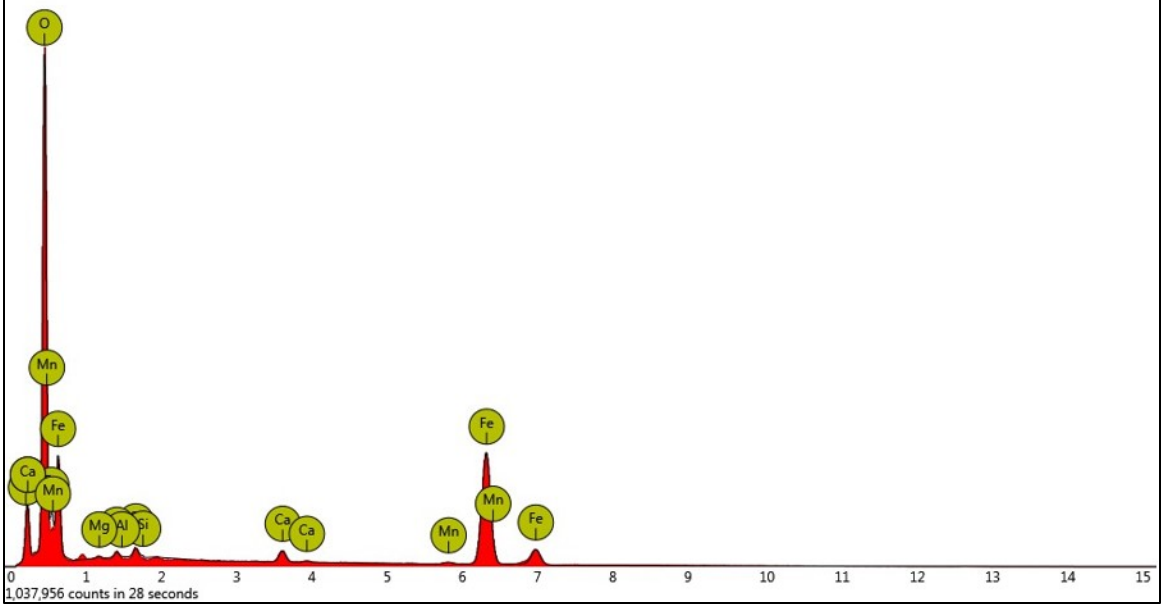

Fig. 23. EDS results from the fracture origin of sample E.6-SW.

3.4.5 Micro- and Macro-Section Examinations

Metallographic micro-specimens, oriented transverse through the microcracks and elliptical pop-in cracks (D.4-SW, D.4-NW, and E.6-SW) and through intact access hole radii from samples E.6-NE, E.6-NW, E.6-SE, and D.4-NE, were prepared using standard metallographic techniques. That is, the specimens were mounted, ground flat, polished, and suitably etched for metallographic examination.

Examination of prepared micro-specimens (except specimen E.6-SW) revealed multiple secondary microcracks in each weld access hole radius, as shown in Fig. 24 and Appendix C, Fig. 205 through Fig. 212. The cracks were filled with dark, high temperature oxide, shown in in Fig. 25 and Appendix C, Fig. 213. Etching of the microspecimens

revealed an untempered martensitic layer at the radii surfaces approximately 0.05 in. (1.25 mm) in depth, which is approximately the same depth as the narrow band, dark oxide covered microcracks, as shown in Fig. 26 and Appendix C, Fig. 214 through Fig. 216.

Martensite is a hard and brittle microstructure that forms when steel is heated above approximately 1340°F (where it transforms to crystalline structure known as austenite) and then rapidly cooled (quenched). The faster the cooling rate, the harder the martensite will be after cooling. During rapid cooling and transformation to martensite, the microstructure undergoes a volume change, which results in locally high stresses that can lead to surface cracks. In this case, the formation of microcracks was due to the overwhelming magnitude and depth of the thermally induced residual stresses relative to very shallow residual stresses induced by the formation of a thin layer of martensite.

These observations clearly indicated that the narrow band microcracks formed in the brittle, high hardness martensitic structure (see Section 3.4.5) during rapid cooling that occurred following thermal cutting of the access holes.

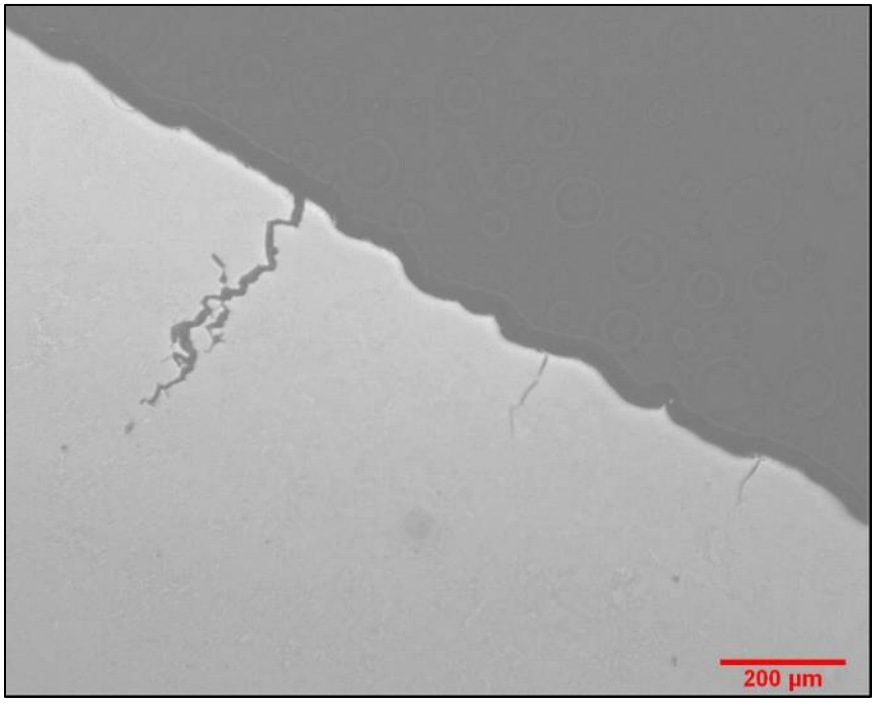

Fig. 24. Multiple secondary, oxide-filled microcracks in the weld access radius of sample D.4-SW.

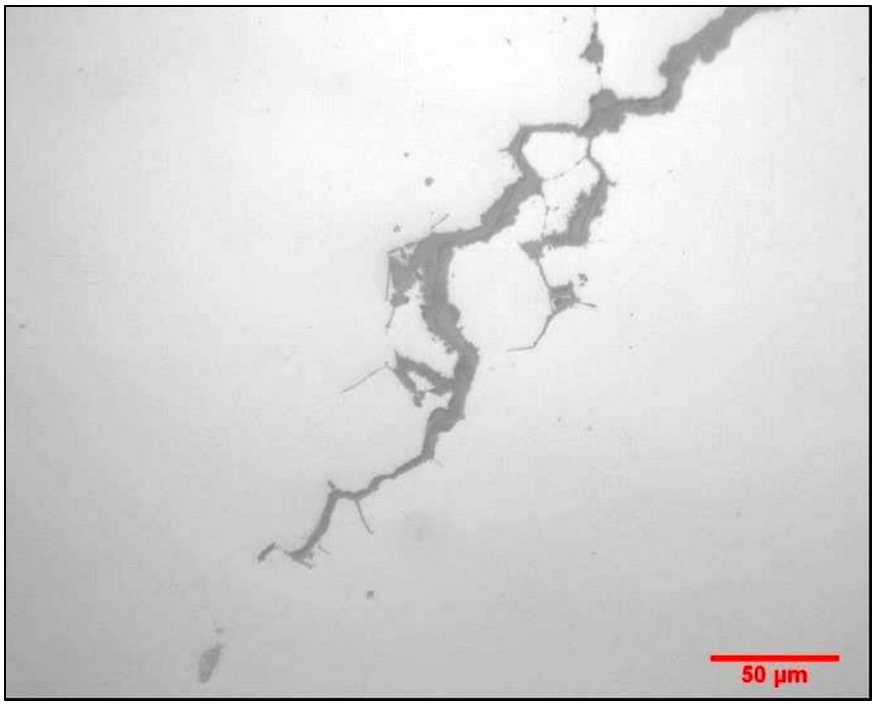

Fig. 25. Microcrack in the weld access hole of sample D.4-SW filled with dark, high temperature oxide.

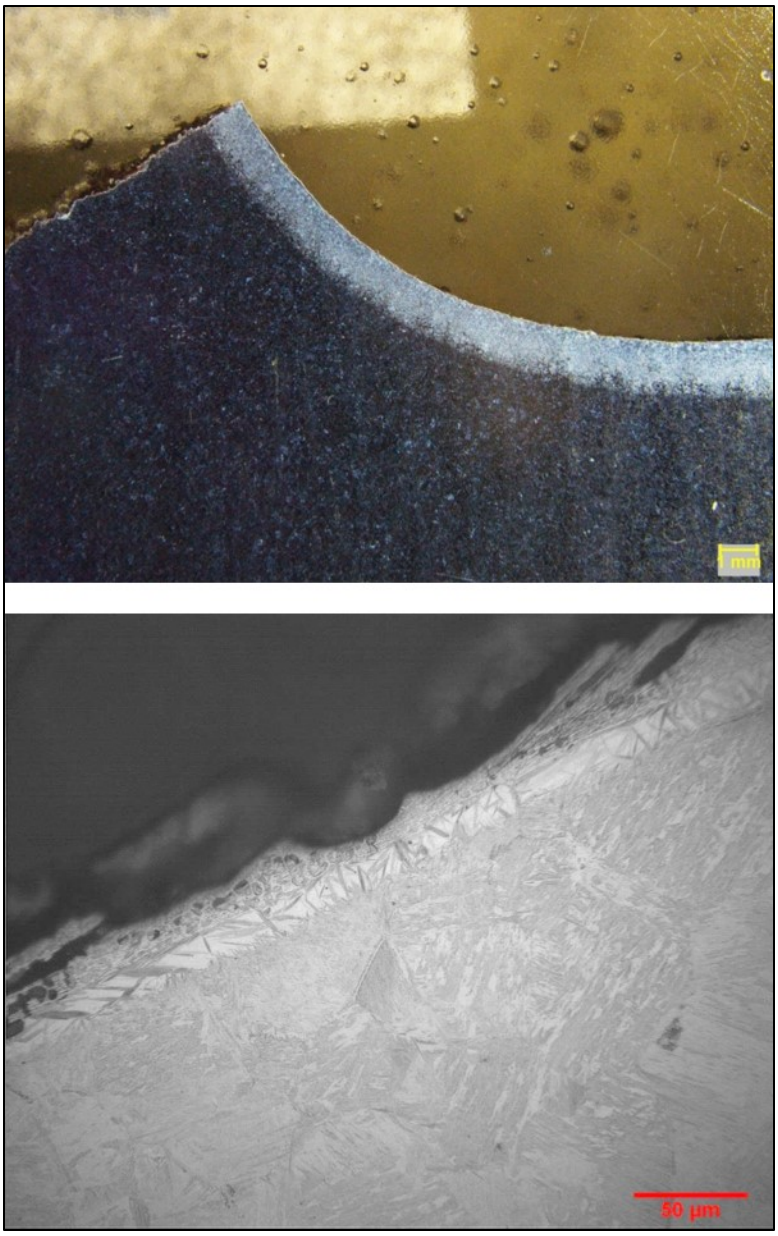

Fig. 26. Martensitic layer at the weld access hole radius of sample E.6-SW (fractured side). The martensitic layer appears as the lighter-etching band in the stereomicroscopic image at the top. The bottom metallographic image shows the martensitic structure within the white band.

The microstructure of the plate material remote from the heat affected surfaces consisted of a fine-grained structure of ferrite and pearlite, shown in Fig. 27 and Appendix C, Fig. 217, as is typical for steel plates utilized for structural applications such as the TTC girders.

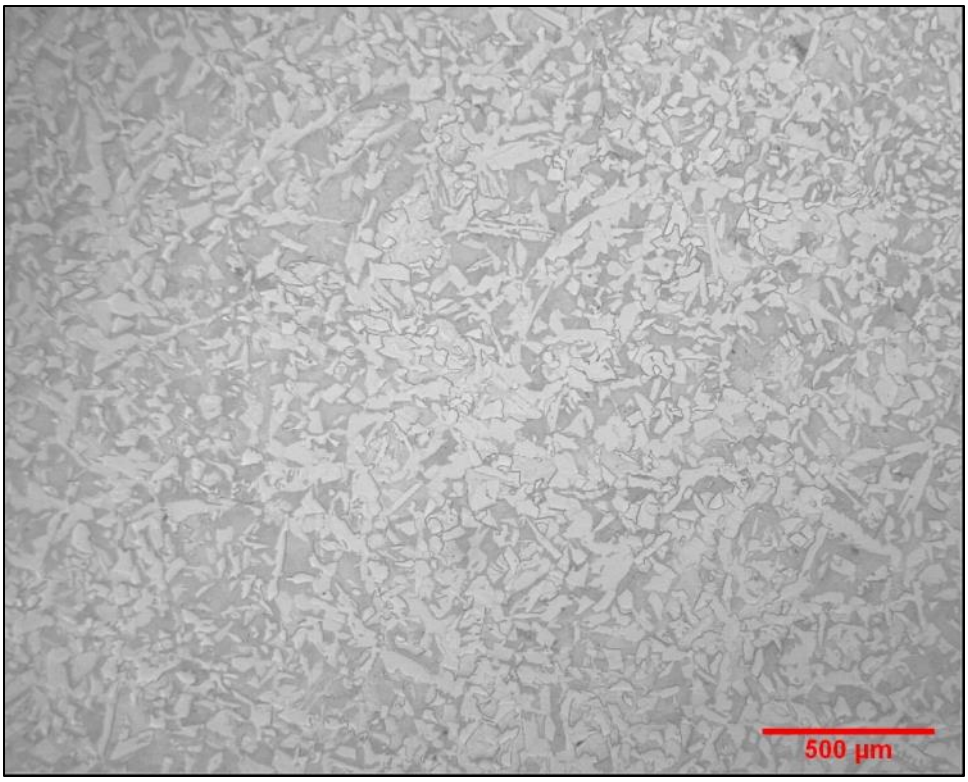

Fig. 27. Fine grained ferrite (bright) and pearlite (dark) grain structure for the flange steel plate of sample D.4-SW.

Macro-sections were also prepared from the flange plates parallel to, and approximately 1 in. below, the fracture surfaces of D.4-SW and E.6-SW, and from the intact plates of E.6-NW in the same relative location and orientation. The macro-sections were etched in accordance with ASTM E340, “Standard Practice for Macroetching Metals and Alloys” [3]. Examination of the macro-sections did not reveal any metallurgical anomalies of the girder flange base metal, as shown in Fig. 28 and Appendix C, Fig. 218.

Fig. 28. Macro-section from girder samples D.4-SW.

3.4.6 Microhardness Testing

Vickers microhardness (HV) testing was performed on the prepared micro-sections from each girder flange. The hardness traverse on each sample was made perpendicular to the weld access hole radius, extending from the hole surface toward the specimen center, as shown in Appendix C, Fig. 219. As expected, results of the HV measurements, given in Appendix D, Table 22 through Table 26, revealed high surface hardness in the heat affected zone from the thermal cutting, with maximum hardness levels of 413 to 526 HV (approximately equivalent to 42 to 51 HRC).

3.5 Fracture Mode Assessment

Initially, shallow surface microcracks developed during thermal cutting of the weld access holes in the highly hardened and brittle martensitic surface layer. These cracks propagated by cleavage to a maximum depth of approximately 0.06 in. from the access hole surface. Thereafter, these surface microcracks served as initiation sites for the larger elliptical cracks that popped-in at two of the four flange sections during CJP groove welding of the flange plates. The two large elliptical cracks (one in each of the two Fremont Street girders) also propagated by cleavage to a maximum depth of 0.38 in. The flange fractures initiated from these pre-existing fabrication-related (i.e., thermal cutting and/or welding) cracks and propagated through the width of the flanges, essentially perpendicular to the flange axes. These flange fracture surfaces, remote from the pre-existing crack origins, exhibited cleavage or quasi-cleavage, as is characteristic of rapid, low-energy (brittle) fracture.

3.6 Girder Steel Properties

3.6.1 Charpy V-Notch Toughness Testing

Charpy V-notch (CVN) impact testing is an efficient indirect assessment of a material's fracture toughness or resistance to brittle, low-energy fracture in the presence of a crack-like flaw such as the observed pop-in cracks in the Fremont Street girder flanges. As such, CVN testing was performed on specimens machined from the A572, Gr. 50 flange surfaces (top and bottom), ¼ and ¾ thicknesses (¼ - ¾ t), and the flange mid-thickness (½ t) for the four girder samples at Fremont Street (D.4-N, D.4-S, E.6-S, and E.6-N). CVN specimens were also machined from the through-thickness 3-in. diameter core samples removed from the girder flanges above First Street, and the girder hangers at both Fremont Street and First Street. For those core samples removed from the girder hangers, the "top" surface location refers to the north facing surface and the "bottom" surface location corresponds to the south facing surface of the hanger plates. Specimen removal locations and orientation are shown in Appendix C, Fig. 220 and Fig. 221.

Standard CVN specimens (10 mm x 10 mm x 55 mm) were machined and tested at various temperatures in accordance with the requirements of ASTM A370 “Standard Test Methods and Definitions for Mechanical Testing of Steel Product” [6] and ASTM E23, “Test Methods for Notched Bar Impact Testing of Metallic Materials” [7]. Results of the CVN toughness testing are shown in Fig. 29, Fig. 30, and Appendix C, Fig. 222 through Fig. 230 and are given in Appendix D, Table 27 through Table 39.

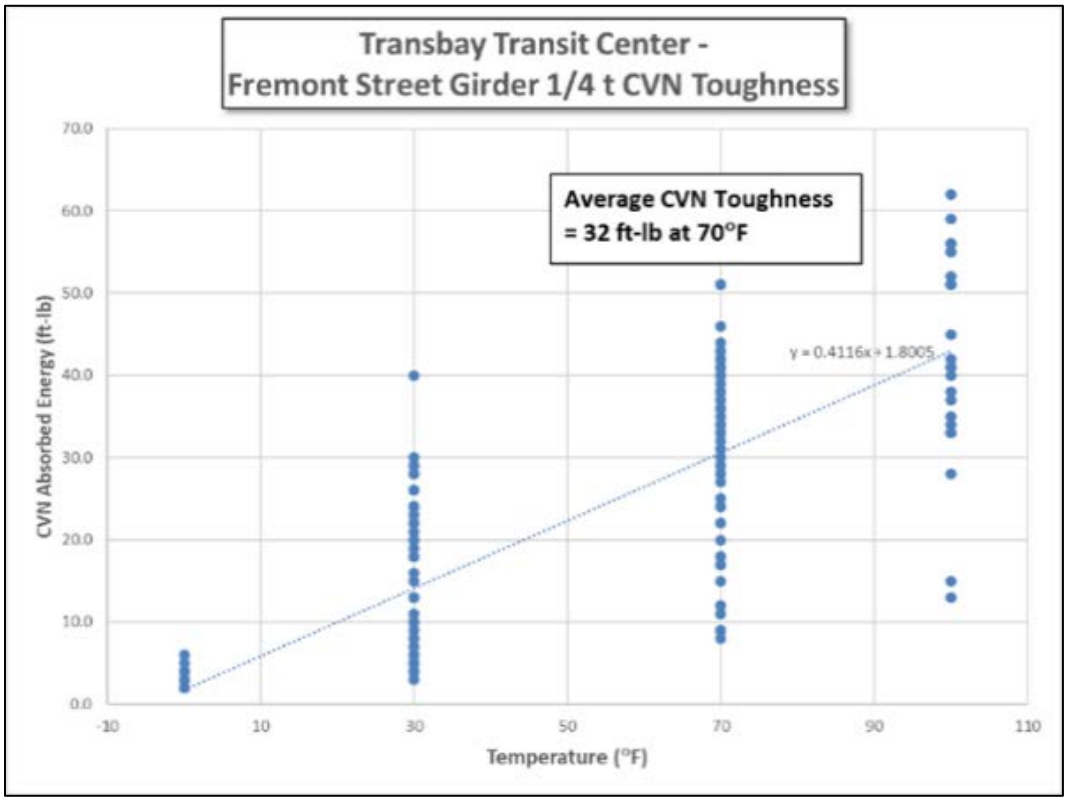

Fig. 29 Fremont Street CVN absorbed energy results for the ¼ - ¾ t location as a function of temperature.

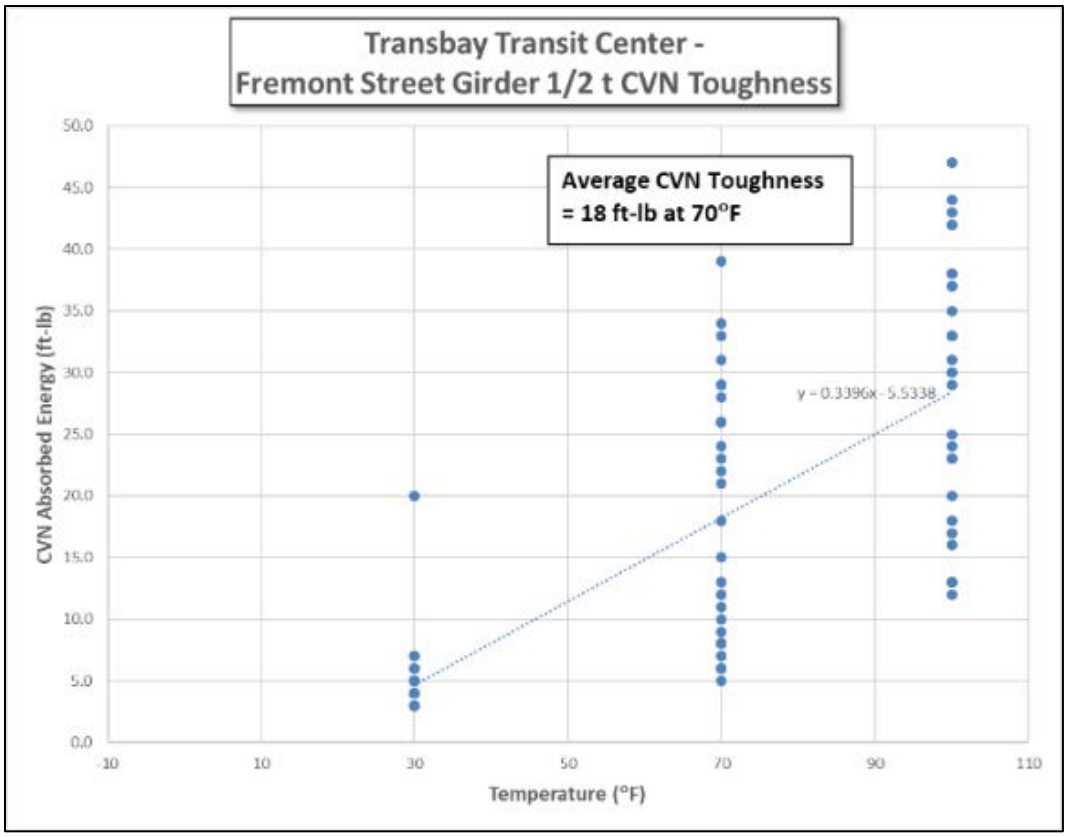

Fig. 30 Fremont Street CVN absorbed energy results for the ½ t location as a function of temperature.

It is evident from the flange CVN results that although the ¼ - ¾ t location absorbed energy levels are close to or exceed the specified requirements of 20 ft-lb at 70°F, the mid-thickness (½ t) levels are very low, indicating unacceptably low fracture toughness from a service perspective in the region of the plates where the oxide covered microcracks and elliptical cracks occurred.

In contrast, CVN results from the girder hanger material (A572, Gr. 50) indicated that all specimen locations significantly exceeded the specification requirements of 20 ft-lb at 70°F and exceed the requirements at 30°F (see Appendix D, Table 36 through Table 39).

A summary of the measured mean CVN toughness levels (Appendix D) for the surface, ¼ - ¾ t, and ½ t locations at 30 and 70ºF is provided in Table 5. These results are consistent with the CVN values reported in the mill certs for melt U1588, the melt from which the TPG3 bottom flange plates were fabricated (see Table 40 in Appendix D).

Table 5 – Mean CVN Toughness – Absorbed Energy (ft-lb)

Thickness Location	Fremont Street	First Street	Hanger Plates
	70°F	**70°F**	**70°F**
Surface	50	45	100
¼ - ¾ t	31	33	84
½ t	18	34	54
	30°F	**30°F**	**30°F**
Surface	28	33	82
¼ - ¾ t	13	7	50
½ t	5	6	26

It is clear from these results that:

- the Fremont Street flange plate ¼ - ¾ t toughness is low and low relative to typical industry levels (see Section 3.6.2),
- the First Street flange plate ¼ - ¾ t toughness is slightly higher than Fremont Street at 70ºF, but is nearly identical to Fremont Street at 30ºF,
- the Fremont Street and First Street flange plate ½ t toughness levels are substantially lower than the ¼ t toughness and unacceptable from a flaw tolerance performance perspective, and
- the 4-in. thick hanger plate material, which is also A572 Gr. 50, exhibits considerably better CVN toughness than the 4-in. thick flange plates, especially at 30 ºF.

Finally, the mean ½ t CVN toughness level at 50ºF (based on interpolation from test data at 30 and 70°F), the temperature close to the temperature at which the fractures occurred, was only 11 ft-lb and the lower bound toughness was less than 5 ft-lb. This level of toughness is considered very low and provides negligible resistance to fracture from pre-existing cracks such as the observed oxidized elliptical cracks.

3.6.2 Structural Steel CVN Toughness Literature Review

To assess the extent to which the TPG3 flange plate CVN toughness levels can be considered unacceptably low, a literature review was performed of CVN test results for structural steel with thicknesses equal to or greater than 2.5 in. In this regard, several large industry studies in 1989 [8] and in 2003 [9] revealed typical mean (average) ¼ t CVN toughness levels for A572, Gr. 50, 4-in. thick plate to be approximately 46 ft-lb (1989) and 52 ft-lb (2003) at 70°F. Additionally, this review revealed that the reduction in ½ t toughness relative to the ¼ t toughness can be as high as 12% (see circled data point in

Fig. 31), when plates were normalized as part of their heat treatment process. However, if plates are not normalized, then the decrease in the ½ t toughness relative to the ¼ t toughness can be substantial as occurred for the Fremont Street girders.

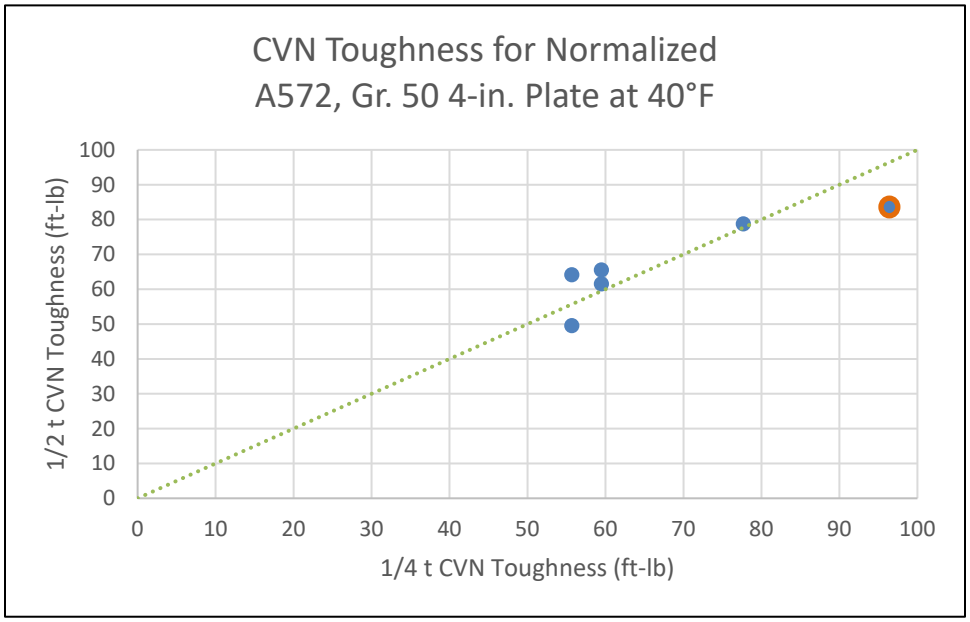

Fig. 31. Relationship between ¼ t and ½ t CVN toughness levels for normalized A572, Gr. 50, structural steel.

3.6.3 Flange Fracture Toughness

Assessment of a structure's crack tolerance requires an estimate of its fracture toughness at a temperature of interest, in this instance, the likely temperature at which the girder flange fractures occurred. Based on discussions with all interested parties, the most likely ambient temperature at the time the girder fractures occurred was about 50ºF. The daily minimum temperatures in San Francisco between January and August 2018 are plotted in Fig. 32 [40], with the black line representing a best-fit fourth-order polynomial regression and the red lines indicating clusters of low-temperature days. The temperature of the steel comprising the TTC trends with the ambient temperatures, but due to its thermal capacity it does not reach the minimum ambient temperature on a given day. For this reason, a steel temperature of 50ºF was agreed upon. Given the dependence of fracture toughness on temperature (i.e., lower temperatures correspond to lower fracture toughness levels), it is most likely that the girder fractures occurred during the clusters of low-temperature days when the flange toughness was lowest.

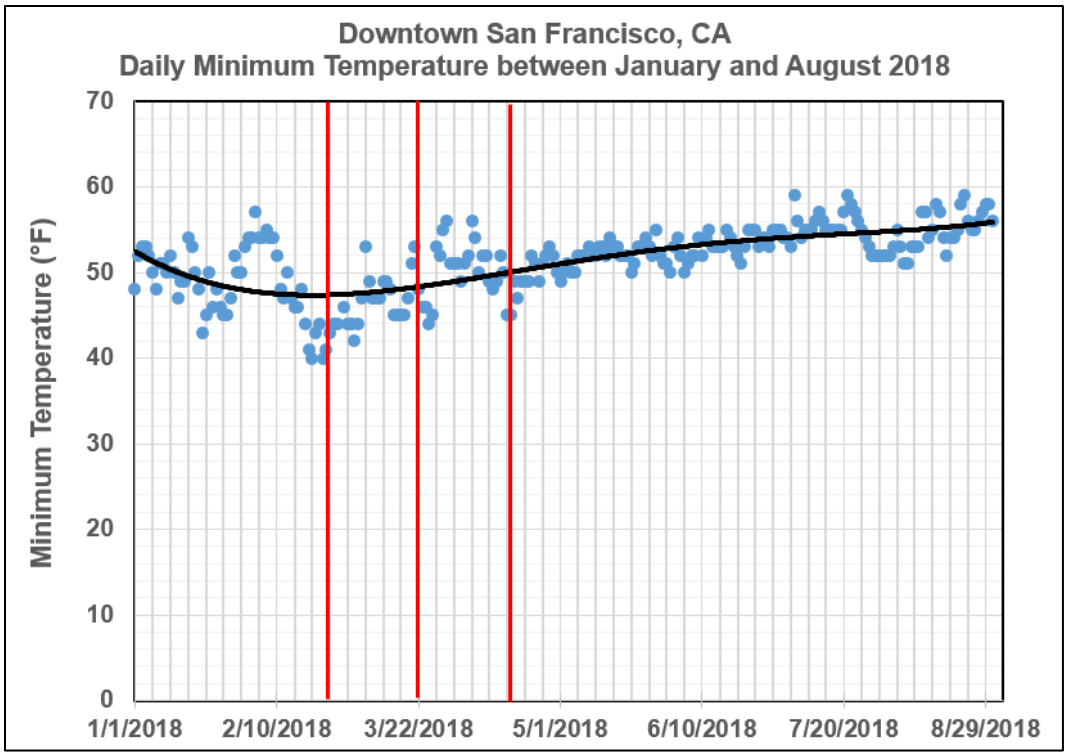

Fig. 32. Daily minimum temperatures in San Francisco, CA, between January and August 2018. A fourth-order polynomial regression is shown with the black line, and the red lines indicate clusters of low-temperature days.

Furthermore, as mentioned above, CVN absorbed energy is an indirect assessment of a material's fracture toughness or resistance to brittle, low-energy fracture in the presence of a crack-like flaw. Accordingly, fracture toughness (K_{1c}), a fracture mechanics parameter and inherent material property that is a function of temperature for structural steel, must be estimated from the CVN test results (see Appendix D).

The girder flange fracture toughness was estimated using the two-stage CVN-K_{1d}-K_{1c} and temperature shift (T_s) correlations [10,11] and the Master Curve [12] approach. In the lower shelf and lower transition regimes, flange material dynamic fracture toughness (K_{1d}) was calculated using the following relationships:

$$K_{1d}^2 = (5)(CVN)(E)$$
$$T_s = 215\text{-}1.5\,\sigma_y \quad (1)$$

where:

CVN = absorbed energy (ft-lb)
E = elastic modulus (psi)
T_s = dynamic-to-static loading rate temperature shift (°F)
σ_y = flange material yield strength (ksi)

Since notch acuity and loading rate do not significantly affect fracture toughness in the upper shelf and upper transition regimes, the following CVN – K_{1c} relationship [10,11] was used to estimate static fracture toughness (K_{1c}):

$$\left[\frac{K_{1c}}{\sigma_y}\right]^2 = 5\left(\frac{CVN}{\sigma_y} - 0.05\right) \quad (2)$$

Applying the Master Curve approach to the CVN-based K_{1d}-K_{1c} results obtained from Eqs. (1) and (2), the girder flange fracture toughness at the ¼ - ¾ t and ½ t locations was calculated as a function of temperature, as shown in Fig. 33 and Fig. 34.

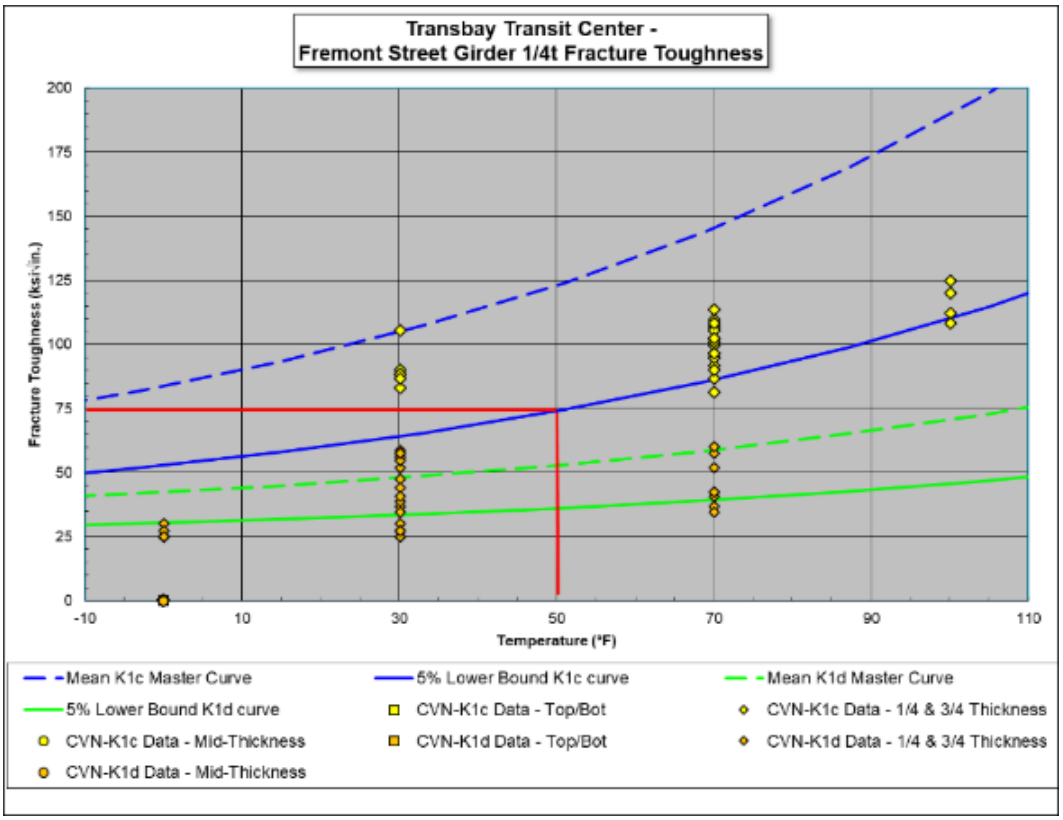

Fig. 33 Flange fracture toughness at the ¼ t location.

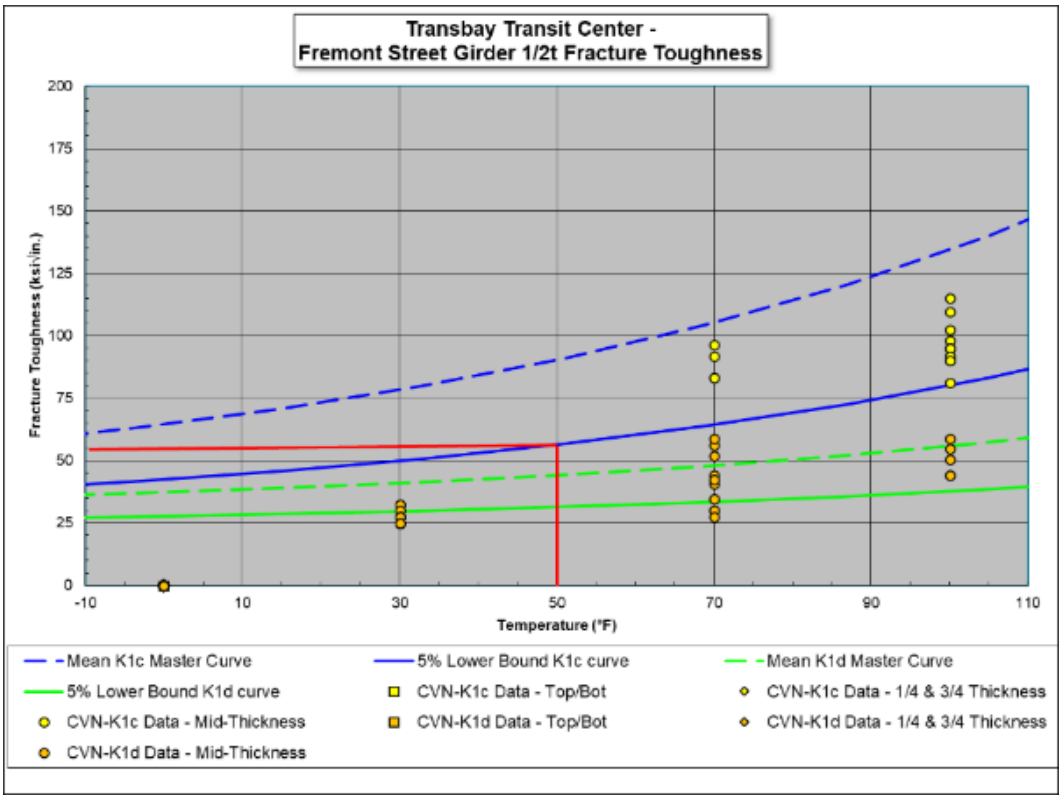

Fig. 34 Flange fracture toughness at the ½ t location.

From these results, the ¼ t and ½ t fracture toughness levels at 50ºF were determined to be approximately 75 and 55 ksi√in., respectively. The ½ t toughness is considered to be very low. Further, it should be noted that the 5% lower bound curve was used to establish toughness rather than the mean curve, because the results of the SEM examination indicated that the governing fracture toughness was in the lower transition regime and low energy fractures, such as those that occurred at the TTC, generally occur at low toughness levels.

3.6.4 Tensile Testing

To assess the flange plate tensile properties, transversely oriented (perpendicular to the flange axis), standard round tensile specimens were machined from the ¼ and ½ t locations. In addition, longitudinally oriented specimens were prepared from the ¼, ½, and ¾ t locations. Specimen removal locations and orientations are shown in Appendix C, Fig. 231 and Fig. 232. Tensile specimens were tested at room temperature in accordance with the requirements of ASTM A370, “Standard Test Methods and Definitions for Mechanical Testing of Steel Product” [6] and ASTM E8, “Test Methods for Tension Testing of Metallic Materials” [13].

Results of the tensile testing are given in Appendix D, Table 41 through Table 47, which show that the flange material conformed to the tensile requirements of ASTM A572, “Standard Specification for High-Strength Low-Alloy Columbium-Vanadium Structural Steel” for Gr. 50, as specified.

3.6.5 Macro-Section Hardness Testing

Rockwell B hardness (HRB) measurements were performed on macro-section specimens prepared from girder samples D.4-S and E.6-N. The cross-sections were ground, polished, and etched to reveal the flange CJP groove weld and fillet weld profiles, as shown in Appendix C, Fig. 233 and Fig. 234. Hardness measurements were performed on the stiffener base material and two flange plates, the weld heat affected zones (HAZ), and the fillet and the flange groove welds. Results of the testing, given in Appendix D, Table 48, revealed hardness levels in the range expected for A572, Gr. 50 structural steel. Additionally, the weld and HAZ hardness levels were considered typical for the application.

3.6.6 Surface Hardness Testing

Rockwell C (HRC) hardness testing was performed on the radii surfaces of the weld access holes and sides of the girder flanges in the as-received condition (i.e., no surface preparation), as shown in Appendix C, Fig. 235 and Fig. 236. Results of the surface hardness testing, given in Appendix D, Table 49 and Table 50, revealed high surface hardness levels, as would be expected for thermally cut surfaces and is consistent with the metallurgical findings, which revealed a martensitic layer at the radii surfaces.

3.6.7 Compositional Analysis

Composition of the eight girder flange sections was determined by Direct Reading Atomic Emissions Spectroscopy. Results of the compositional analyses, provided in Appendix D, Table 51 and Table 52, confirmed that the flange material conformed to the requirements of ASTM A572, “Standard Specification for High-Strength Low-Alloy Columbium-Vanadium Structural Steel” [14] for Grade 50, as specified. In addition, the carbon equivalent (CE) was calculated in accordance with AWS D1.1 [4] for each of the flange sections, as follows:

	D.4-NE	D.4-NW	D.4-SE	D.4-SW	E.6-NE	E.6-NW	E.6-SE	E.6-SW
CE	0.45	0.49	0.42	0.47	0.44	0.43	0.43	0.50

It is evident that flange sections D.4-NW and E.6-SW exhibited the highest CEs of the eight flange sections evaluated. Moreover, it should be noted that flange sections D.4-NW and E.6-SW were also the sections in which the large elliptical cracks developed. In this regard, it is possible that the higher CEs for these two locations contributed to greater

susceptibility to crack formation, as well as the measured lower CVN toughness – both causal factors to the flange fractures.

3.7 Metallurgical Assessment Conclusions

Analyses and testing revealed that the TTC TPG3 girder flange fractures initiated from pre-existing cracks that developed during thermal cutting of the weld access hole radii and subsequent welding of the flange CJP groove welds prior to service, as follows:

- Initially, shallow surface microcracks developed during thermal cutting of the weld access holes in the highly hardened and brittle martensitic surface layer.
- Thereafter, larger pop-in cracks formed in two of the four flanges during CJP groove welding of the flange plates.
- Rapid, low-energy fracture of the flanges initiated from these pre-existing fabrication-induced cracks, as the girder was subjected to service loading in addition to the normal residual stresses due to welded fabrication.
- Dark, tenacious, high temperature oxide present on both the shallow microcracks and the larger pop-in cracks, confirmed that both crack types formed at elevated temperatures, which only occur during fabrication processes.
- Abnormally low fracture toughness (as confirmed by CVN toughness testing) in the mid-thickness region of the flange plates, provided little resistance to the presence of the pre-existing pop-in cracks, which subsequently initiated flange fracture under the combination of typical weld-induced residual and normal service-induced stresses.

4. FREMONT STREET GIRDER FLANGE FRACTURE ASSESSMENT

As discussed in Section 3.1.1, bottom flange fractures were discovered in the TPG3 girders running over Fremont Street. The north girder, located on the D.4 line, had both the northwest and southwest bottom flanges fracture, as shown in Fig. 177 and Fig. 178. The south girder located along the E.6 line, southwest bottom flange also fractured as shown in Fig. 180. Due to the similarity in geometry and loading between the D.4 and E.6 Fremont Street girders, only the D.4 girder is discussed in this section. Therefore, the results of this section are representative for both Fremont Street TPG3 girders and their associated bottom flange fractures. Additionally, the initial flange fracture most likely occurred in the northwest bottom flange of the D.4 girder and, as such, all results discussed below are based on the D.4 fracture.

To perform the bottom flange fracture assessment, each stage of crack initiation over time was analyzed in detail. To this end, the Fremont Street D.4 girder northwest bottom flange fracture sequence was represented as follows:

1. Microcrack to pop-in crack initiation.
2. Pop-in crack arrest.
3. Bottom flange fracture initiation from the pop-in crack.

4.1 Pop-In Crack Initiation from Microcrack

From the fracture mode assessment in Section 3.5, microcracks developed in the weld access hole surface radii during thermal cutting. Based on the metallurgical assessment, the microcrack at the fracture origin had a length of approximately 1.5 in. with a depth varying between 0.02 in. and 0.06 in. Due solely to residual stresses developed during the CJP groove welding of the bottom flanges, an elliptical "pop-in" crack initiated from the microcrack with an arrested size of approximately 0. 38 in. deep (a) x 1.2 in. long (2c). Fig. 35 shows the fracture surface and provides details on the various stages of crack progression, from microcrack to bottom flange low-energy fracture.

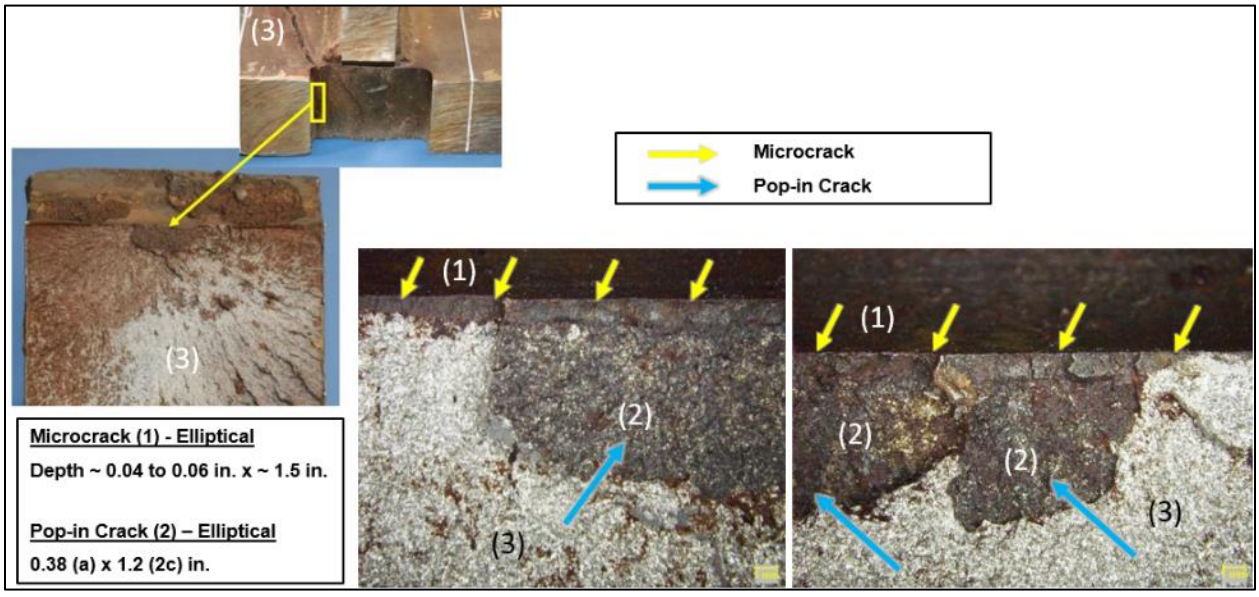

Fig. 35. Fremont Street D.4 girder fracture features: (1) microcracks, (2) pop-in crack, and (3) bottom flange fracture.

The subsequent sections detail the fracture mechanics calculations that describe initiation of the pop-in crack from the microcrack and flange fracture from the pop-in crack.

4.1.1 Microcrack Characteristics

The TTC Fremont Street girder bottom flange weld access holes were thermally cut prior to bottom flange CJP groove welding. During thermal cutting microcracks formed along the radii of the weld access holes, attaining a maximum depth of approximately 0.06 in., as shown in Fig. 36.

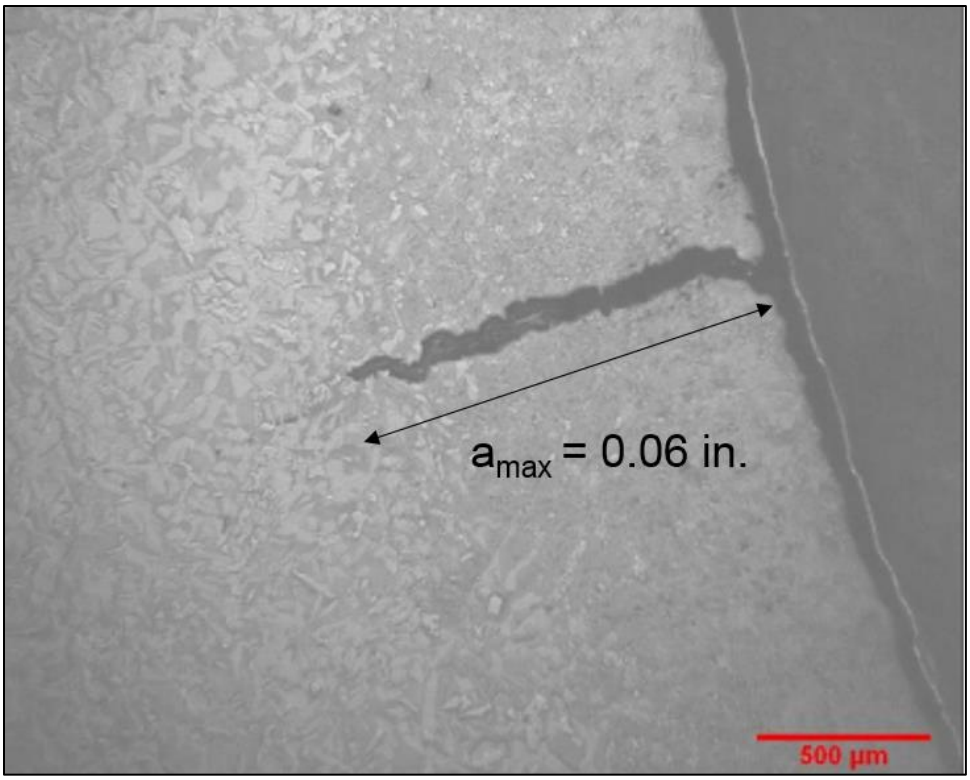

Fig. 36. Cross-sectional view of a weld access hole microcrack with the maximum depth shown for reference.

Based on the metallurgical conclusions described in Section 3.7, the microcracks were located in untempered martensite, thus, the fracture toughness could be at the lower bound for structural steel (~25 to 30 ksi√in. [15]) up to the maximum ½ t toughness of 55 to 60 ksi√in.at 50°F, as shown in Fig. 37 (red lines). The fracture toughness of high-strength, high-hardness materials, such as untempered martensite, is essentially invariant with respect to temperature.

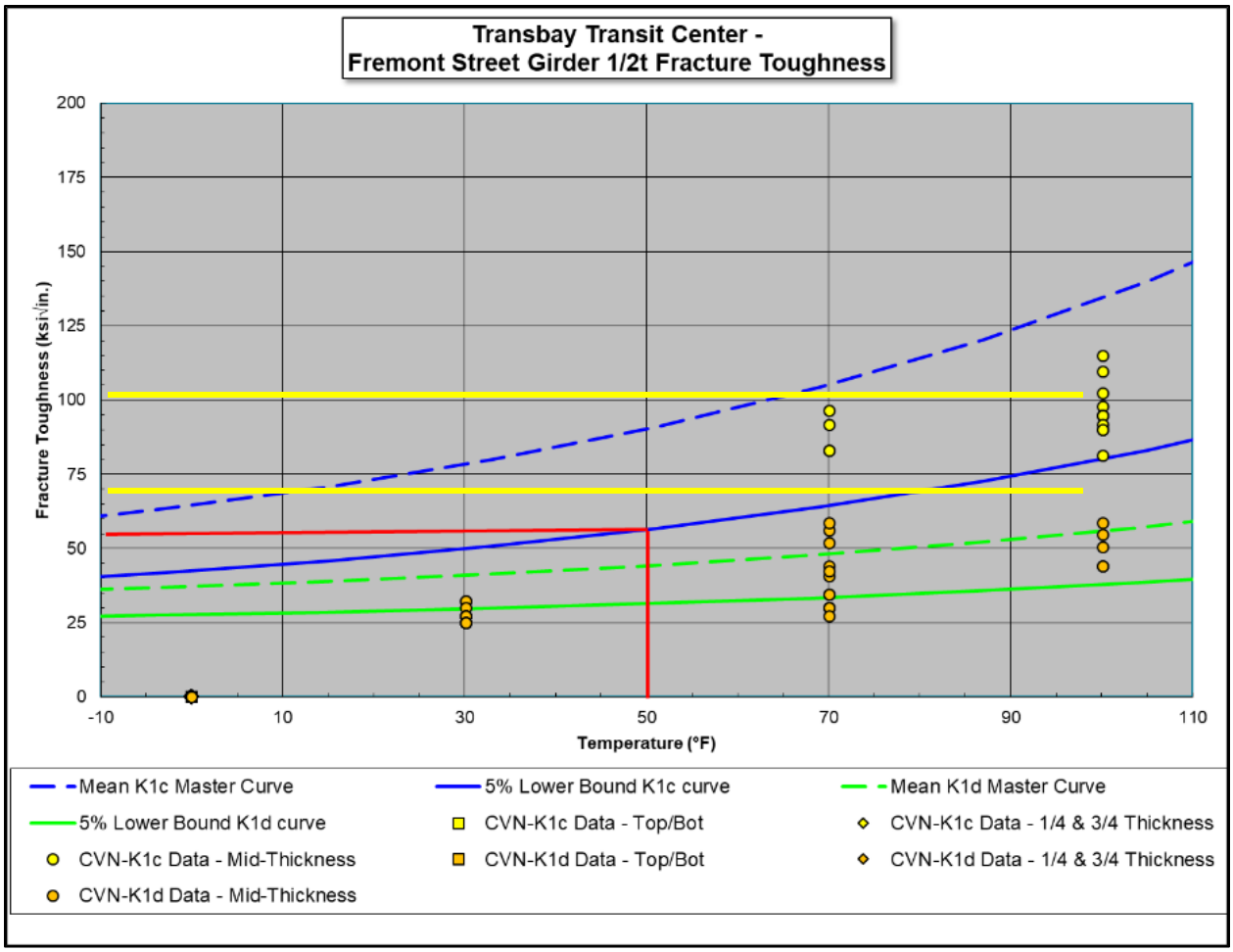

Fig. 37. Fracture toughness data at ½ t. The toughness at 50°F is approximately 55 to 60 ksi√in. (red lines) and the upper shelf fracture toughness is in the range of 70 to 100 ksi√in. (yellow lines).

4.1.2 Pop-In Crack Initiation – Fracture Mechanics Calculations

Currently, the most effective methodology for assessing crack or fracture initiation in a structure or component – such as the TPG3 girder flange – is the fracture mechanics-based Failure Assessment Diagram (FAD) approach [10]. For a known flaw or crack size and applied loading, the FAD methodology calculates the position of a crack assessment point, which is then compared to an allowable failure curve, as illustrated in Fig. 38. The FAD approach assumes the cracked material (e.g., the girder flange) to be linear-elastic, perfectly-plastic and further assumes the extent of plasticity around the crack front to be modestly low.

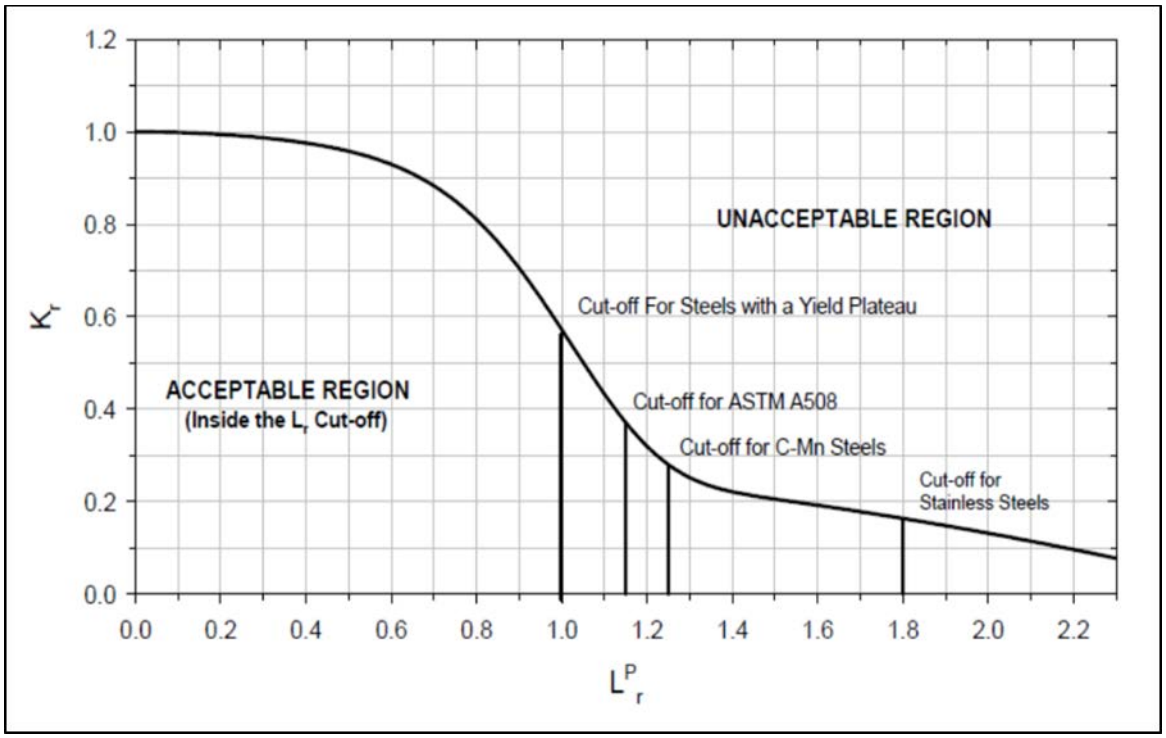

Fig. 38 Failure Assessment Diagram (FAD) from API 579-1/ASME FFS-1 [10]

The FAD is a function of two parameters, Kr and Lr, which are the ordinate and abscissa, respectively. The former is known as the toughness ratio and is a ratio of the stress intensity factor (K_1) to the fracture toughness of the material (K_{1c}). The latter is the load ratio, defined as the ratio of the reference stress (σ_{ref}) to the yield strength (σ_y) of the material. The maximum permitted value of Kr, as a function of Lr, is plotted using the FAD curve, the expression for which is given below in Eq. (3). Fracture instability occurs when the failure assessment point exceeds the FAD curve.

$$K_r = (1 - 0.14(L_r^P)^2)\left(0.3 + 0.7exp(-0.65(L_r^P)^6)\right) \quad (3)$$

API 579-1/ASME FFS-1 [10] provides closed form solutions for K_1 and σ_{ref} for a range of component and crack geometries. Accordingly, the flange microcrack was modelled as an elliptical surface flaw in a plate [10], as illustrated in Fig. 39, where K_1 and σ_{ref} were calculated using Eqs. (4) and (5).

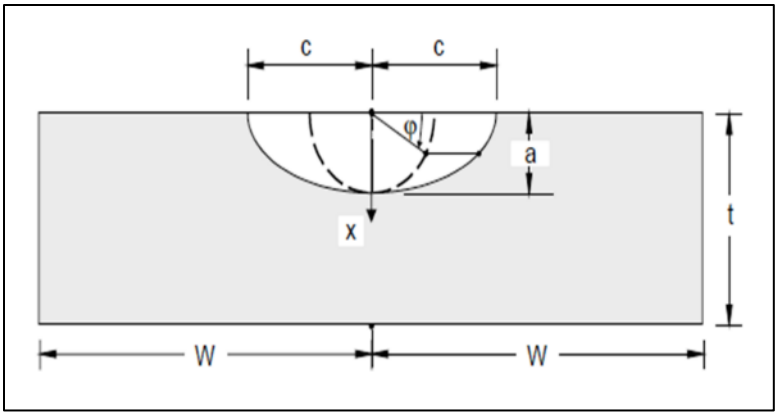

Fig. 39 Geometric representation of a surface-breaking elliptical crack in a plate. In this case, 2W corresponds to the flange thickness and t to the flange width.

$$K_I = \left[G_0\{\sigma_0 + p_c\} + G_1\sigma_1\left(\frac{a}{t}\right) + G_2\sigma_2\left(\frac{a}{t}\right)^2 + G_3\sigma_3\left(\frac{a}{t}\right)^3 + G_4\sigma_4\left(\frac{a}{t}\right)^4 \right] \sqrt{\frac{\pi a}{Q}}\, f_w \qquad (4)$$

$$\sigma_{ref} = \frac{gP_b + [(gP_b)^2 + 9P_m^2(1-\alpha)^2]^{0.5}}{3(1-\alpha)^2} \qquad (5)$$

All variable details in Eqs. (4) and (5) above are provided in [10].

When the pop-in crack initiated, the only stress present was the self-limiting residual stress associated with welding of the bottom flange CJP groove weld. Based on typical CJP groove weld residual stress distributions in thick plates (see [10], [18], and [19]), near-yield strength level residual stresses were necessarily present at the weld access hole surface, which decreased rapidly with distance into the flange width, as illustrated in Fig. 40 (represented as a 4th order polynomial). Namely, Fig. 40 demonstrates that the yield strength level residual stress decreases rapidly with distance away from the weld access hole radius surface into the flange width.

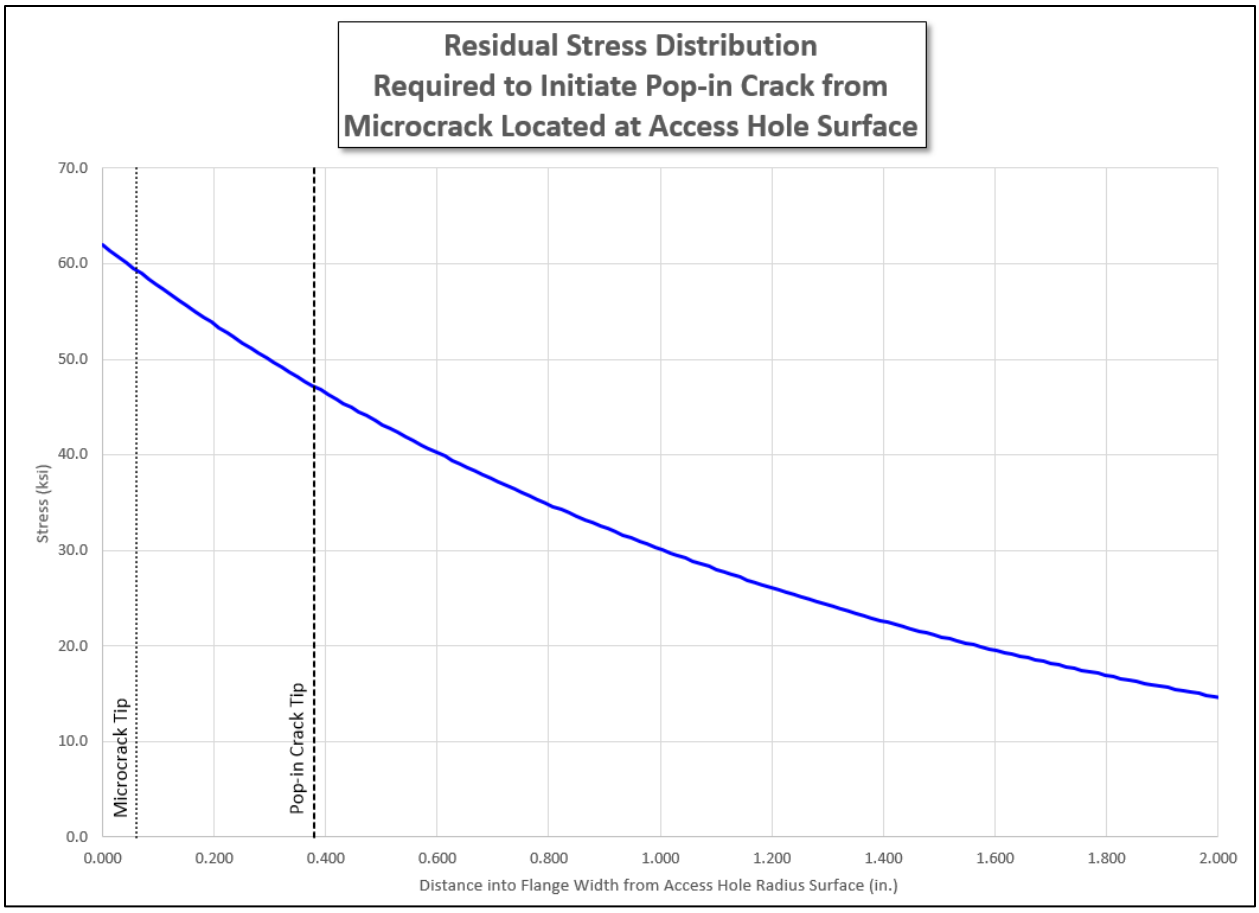

Fig. 40. Approximate residual stress distribution necessary to cause pop-in crack initiation at a fracture toughness of approximately 30 ksi√in.

Thus, for the 0.06 in. deep (a) microcrack described in Section 4.1.1 and plate fracture toughness (K_{1c}) of 30 ksi√in., the yield strength level residual stress at the access hole radius surface (Fig. 40) was incremented until crack initiation was indicated in the FAD, as shown in Fig. 41 (purple circle). That is, pop-in crack initiation from a 0.06 in. deep microcrack at a fracture toughness (K_{1c}) of 30 ksi√in. will occur under the residual stress distribution shown in Fig. 40.

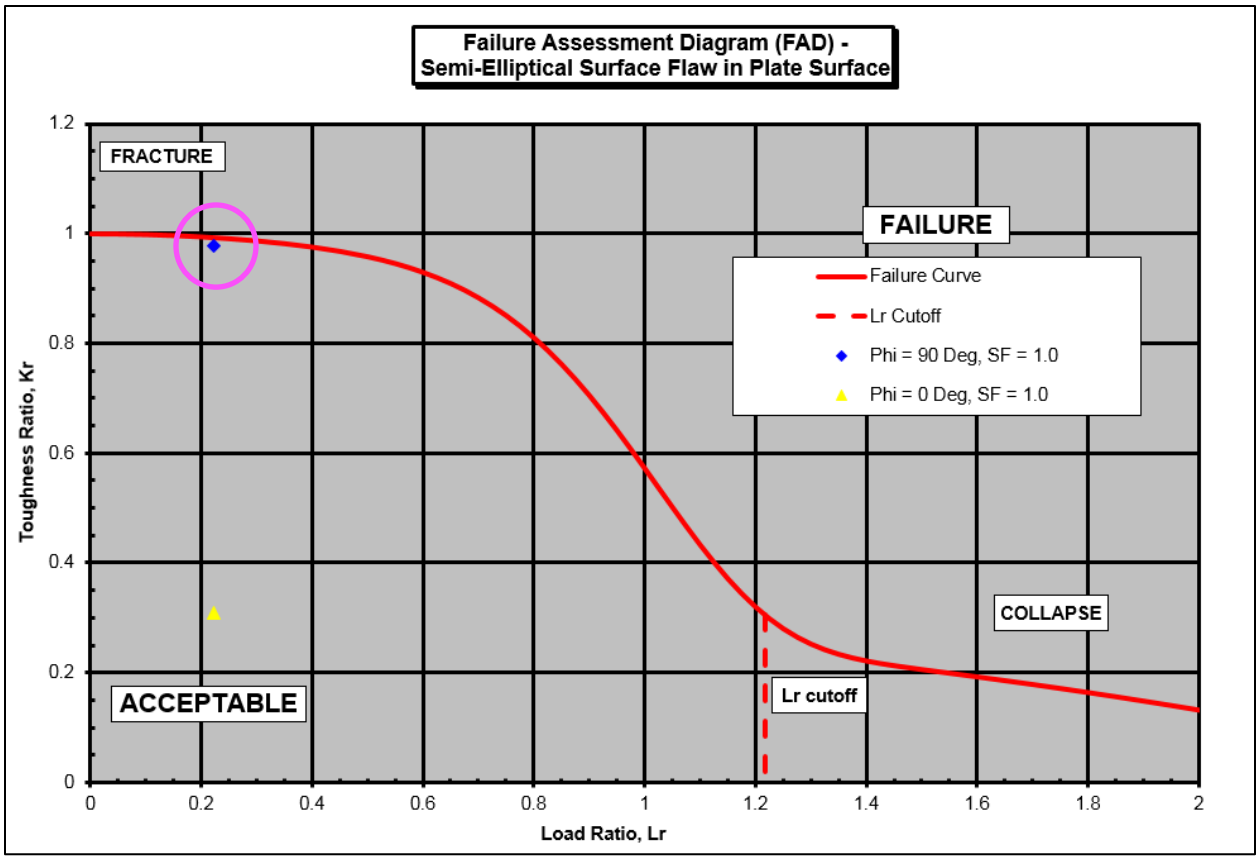

Fig. 41. Failure assessment diagram (FAD) showing pop-in crack initiation at the Fig. 40 residual stresses with a lower bound fracture toughness of approximately 30 ksi√in. See Fig. 39 for definition of Phi (φ). SF = Safety Factor.

Validation of this pop-in initiation analysis was performed by utilizing a closed-form stress intensity factor solution developed by Sneddon [20], Irwin [21], and Kobayashi [22]. The validation calculations, detailed in Appendix E, revealed that pop-in crack initiation from a microcrack will occur at a plate fracture toughness (K_{1c}) of 30 ksi√in. and a near yield strength residual stress of approximately 64 ksi. This validation result is in excellent agreement with the FAD and residual stress analyses given above.

The FAD results shown in Fig. 41 are based on a near surface, untempered martensitic microstructure fracture toughness of 30 ksi√in. If, however, it is assumed that the nominal ½ t plate fracture toughness of approximately 55 to 60 ksi√in. was the governing fracture toughness, then the Fig. 40 residual stress distribution would not be sufficient to initiate the pop-in crack, as shown by the FAD results given in Fig. 42 (green circle).

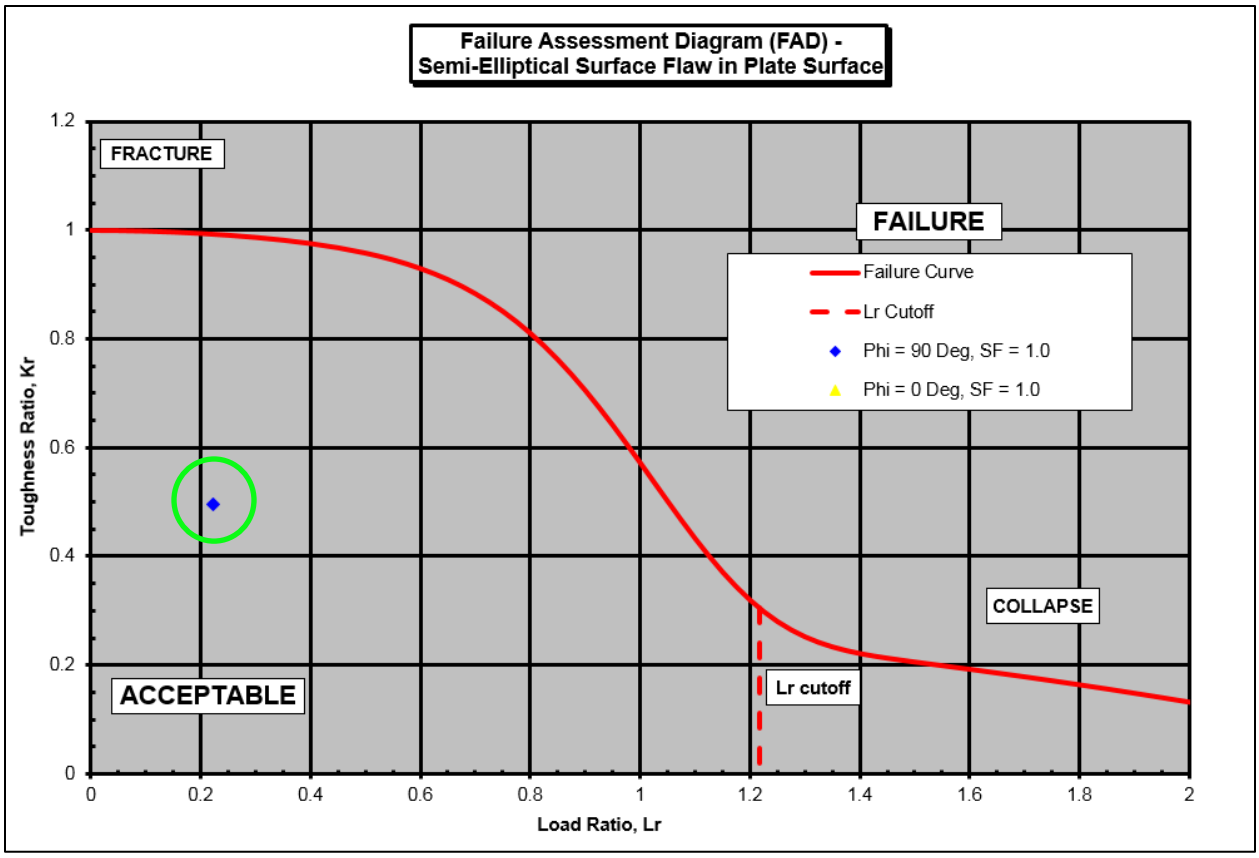

Fig. 42. Failure assessment diagram (FAD) demonstrating that pop-in crack initiation would not have occurred at the Fig. 40 residual stresses with an upper bound fracture toughness of approximately 55 to 60 ksi√in.

If the prevailing fracture toughness at the time of pop-in crack initiation had been the ½ t toughness of 55 to 60 ksi√in., then a significantly different stress distribution would have been required for initiation. Thus, for the 0.06 in. deep microcrack, the full-section (flange width) stress distribution shown in Fig. 43 would have been required for pop-in crack initiation to have occurred, as demonstrated by the FAD results given in Fig. 44 (purple circle).

A summary of the FAD calculations for pop-in crack initiation is given in Table 6.

Table 6 – Pop-in Crack Initiation FAD Summary

Residual Stress Distribution	P_m (ksi)	P_b (ksi)	K_{1C} (ksi√in.)	K_1 (ksi√in.)	FAD Failure (Y/N)
Fig. 40	6.4	15.5	30	29.3	Y
Fig. 40	6.4	15.5	60	29.8	N
Fig. 43	62	0	60	30.4	Y

P_m – membrane stress, P_b – bending stress, K_{1C} – fracture toughness, K_1 – stress intensity factor

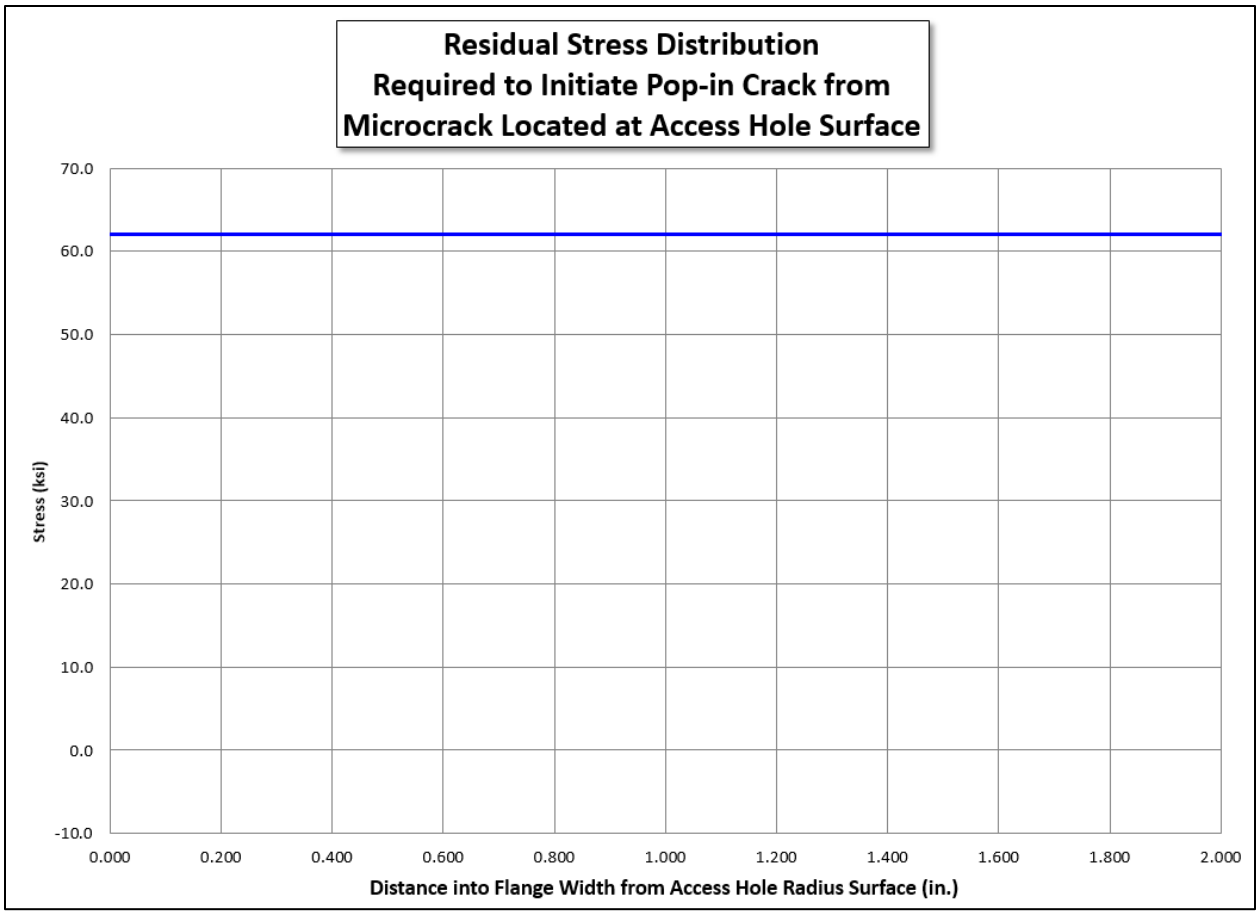

Fig. 43. Residual stress distribution necessary to cause pop-in crack initiation at a fracture toughness of approximately 55 to 60 ksi√in.

Moreover, it is important to note on Fig. 44 that the assessment point intercepts the FAD curve at an Lr ratio greater than 1.0. This region of the FAD corresponds to fracture by plastic collapse and extensive inelastic deformation. However, as previously shown (see Section 3.4), crack initiation and fracture in the girder flanges occurred by low-energy brittle fractures with little, if any, associated plastic deformation. As such, the full-section yield strength level residual stress distribution shown in Fig. 41 could not have been present in the flange during fabrication. Rather, a residual stress distribution similar to the distribution shown Fig. 40 was necessarily present at the time of pop-in crack initiation. Furthermore, the Fig. 40 residual stress distribution could only have occurred during welding of the flange CJP groove weld.

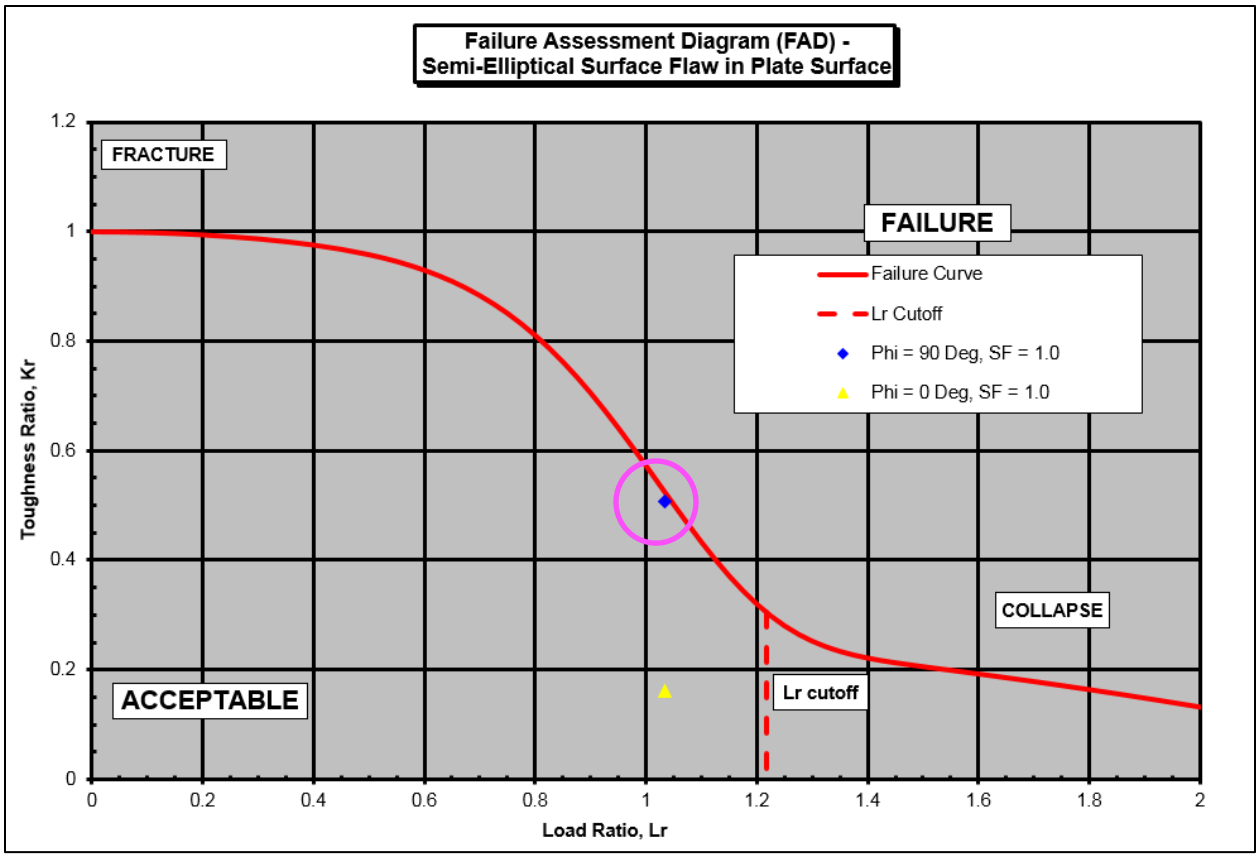

Fig. 44. Failure assessment diagram (FAD) demonstrating that pop-in crack initiation would have been ductile in nature under the Fig. 43 residual stresses with an upper bound fracture toughness of approximately 55 to 60 ksi√in.

4.1.3 Residual Stress Validation – Thermal FE Analysis

Finite element (FE) stress analyses of both the Fremont Street and First Street girders were performed to determine whether stresses due to bottom flange CJP groove weld shrinkage were sufficient to drive crack initiation at the weld access holes. In addition, the analyses assessed whether the fracture mechanics pop-in crack initiation results were consistent with the observed presence of pop-in cracks in the Fremont Street girder flange and the absence of such cracks in the First Street flanges.

The primary region of interest in these analyses was the access hole local to the interface between bottom flange and tapered hanger. Since stresses in this region caused by welding are highly localized, a local FE model was considered suitable for analysis. For both Fremont Street and First Street girders, a segment of bottom flange was extracted from the overall girder solid model (see Section 4.3.1.1), meshed, given proper support conditions at the boundaries cut from the overall model, and loaded at its groove-welded end in a manner consistent with weld shrinkage. Once solved, the models' stresses local

to access hole radii were investigated. These analyses were conducted for both uncracked and cracked versions of both streets' FE models.

Loading arising from weld shrinkage was simulated by applying a temperature drop locally to a group of elements at the groove-welded end of the flange FE models that constitute an idealized weld. A temperature drop approximately equal to the material's stress-relieving temperature was employed [16], since this is a reasonable estimate of the temperature range over which residual stresses can develop in the weld upon cooling.

4.1.3.1 FE Model Details

The model was developed by extracting a suitable segment of the bottom flange from the overall girder solid model (see Section 4.3.1). Fig. 45 shows the Fremont Street girder solid model, with an inset showing a close-up view of the portion of bottom flange local to the tapered hanger. Fig. 46 shows the segment of bottom flange that was selected for modeling, as extracted from the overall girder model. The segment selected was that residing west of the flange-to-flange groove weld and north of the girder web.

The selected segment of bottom flange was brought into ANSYS [17] and meshed with SOLID186 elements. The SOLID186 element is a three-dimensional 20-node solid element that exhibits quadratic displacement behavior. It is particularly suitable for accurately modeling three-dimensional stress states to a degree that would not be possible using structural elements such as beams or shells. With sufficient mesh refinement, it can represent stress fields quite accurately for arbitrary loading, including applied temperatures.

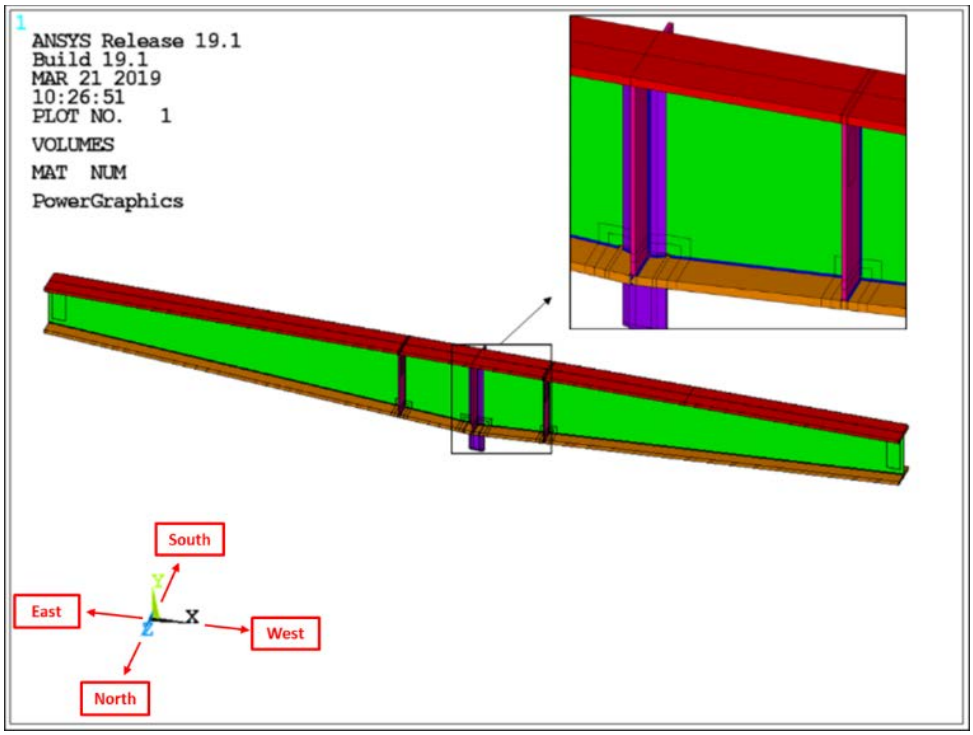

Fig. 45. Fremont Street girder solid model. Different colors distinguish the various components making up the fabricated girder. Inset shows close-up view of bottom-flange, local to tapered hanger. Cardinal directions shown in red relative to cartesian directions.

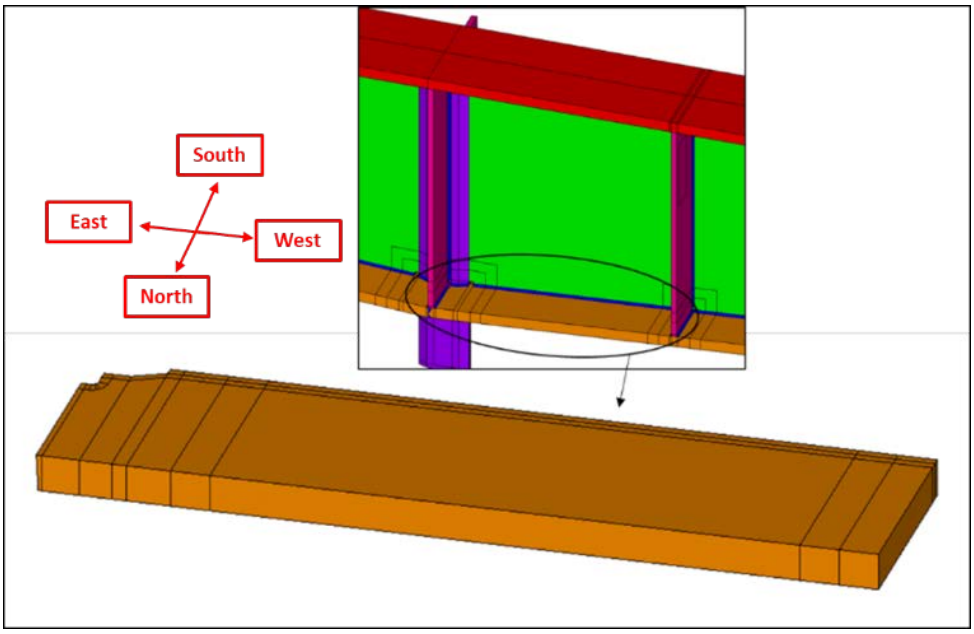

Fig. 46. Section of bottom flange extracted from parent solid model for stress analysis under groove-weld-shrinkage loading.

The meshed FE model is depicted in Fig. 47, which shows increased mesh density at the groove-welded end as compared to the coarser discretization proceeding along the flange length, moving away from the groove-welded end. The top insets show mesh density increased further still, local to the access hole radius, to most accurately calculate the local stresses and their gradients.

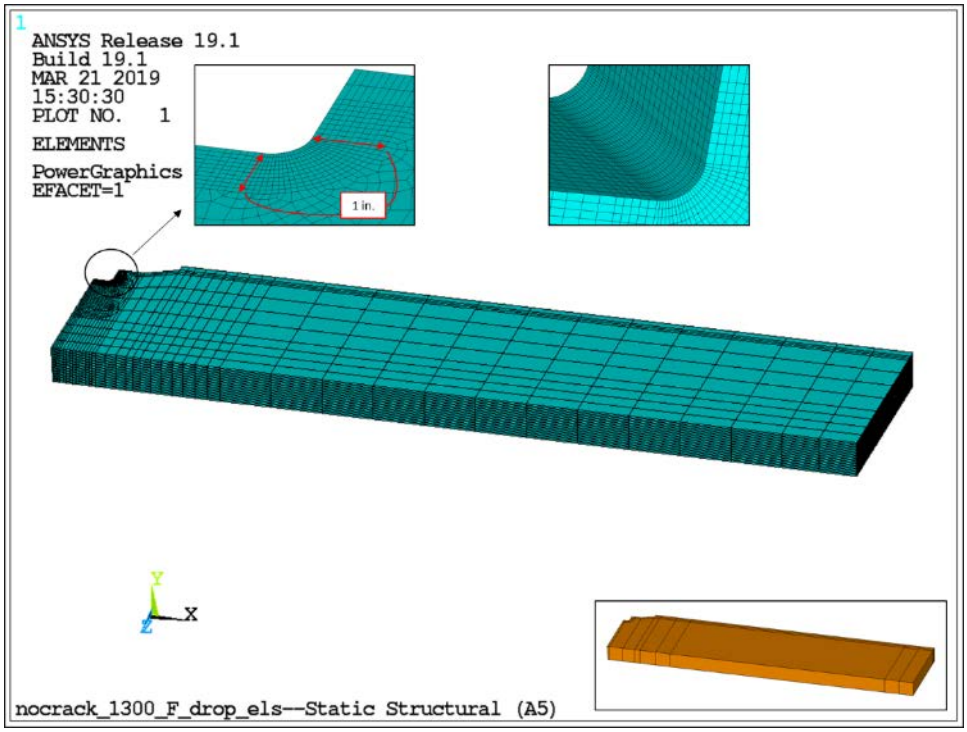

Fig. 47. Finite-element mesh of the bottom flange solid-model segment shown in Fig. 46 (repeated here in lower-right inset). Note increased mesh density local to groove-welded end. Upper insets show the high-density mesh employed local to access hole radius.

According to welding-sequence information provided to LPI [26], several girder welds had not yet been completed at the time the bottom flange was groove-welded together. Fig. 48 depicts the girder solid model in the state it had been in just prior to groove welding of the bottom flanges. Specifically, vertical stiffeners had not yet been welded, and, more significantly insofar as access-hole-radius stress is concerned, the fillet weld between the flange plates and tapered hanger had not yet been made. Not being connected to the tapered hanger permits the flange to pull away from the tapered hanger in response to weld shrinkage.

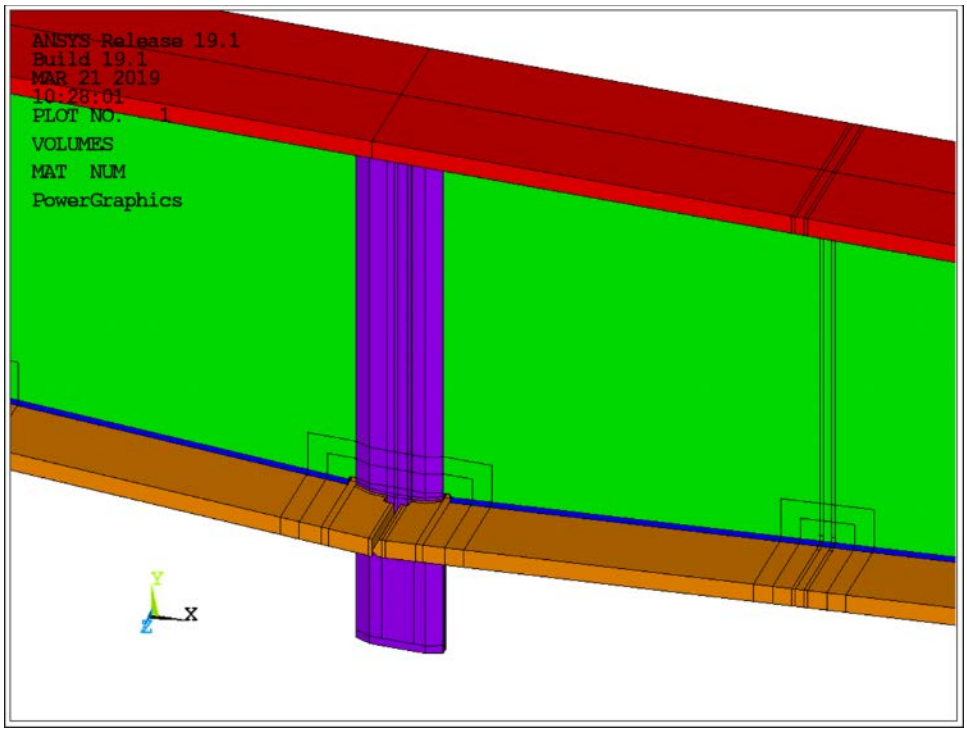

Fig. 48. Girder solid model prior to groove welding the bottom flange plates together. Configuration is based on welding sequence provided to LPI. Note the absence of vertical stiffeners and welds between bottom flange and tapered hanger.

Based on the reported girder weld sequence, appropriate boundary conditions were applied to the model. Fig. 49 shows the associated boundary conditions corresponding to flange support provided by web-to-flange fillet welds, symmetry about the girder web, and symmetry about the groove weld's approximate center line. The groove weld symmetry condition is a reasonable approximation of the response of the two bottom flanges being pulled from both sides of the shrinking weld, especially insofar as stresses away from the groove weld but local to the access hole radii are concerned. Also note the absence of any prescribed constraint at the interface of the bottom flange to the tapered hanger, since a weld did not exist there at the time of groove-welding. Lastly, the cut at the right end of the model has no prescribed constraint. Initial studies indicated that this end was sufficiently removed from the loaded (left) end, and sufficiently supported by the web-to-flange fillet weld, to be of no influence whether left free or fixed.

Elasto-plastic material properties were accounted for in the FE model (see Fig. 77 in Section 4.3.1.3).

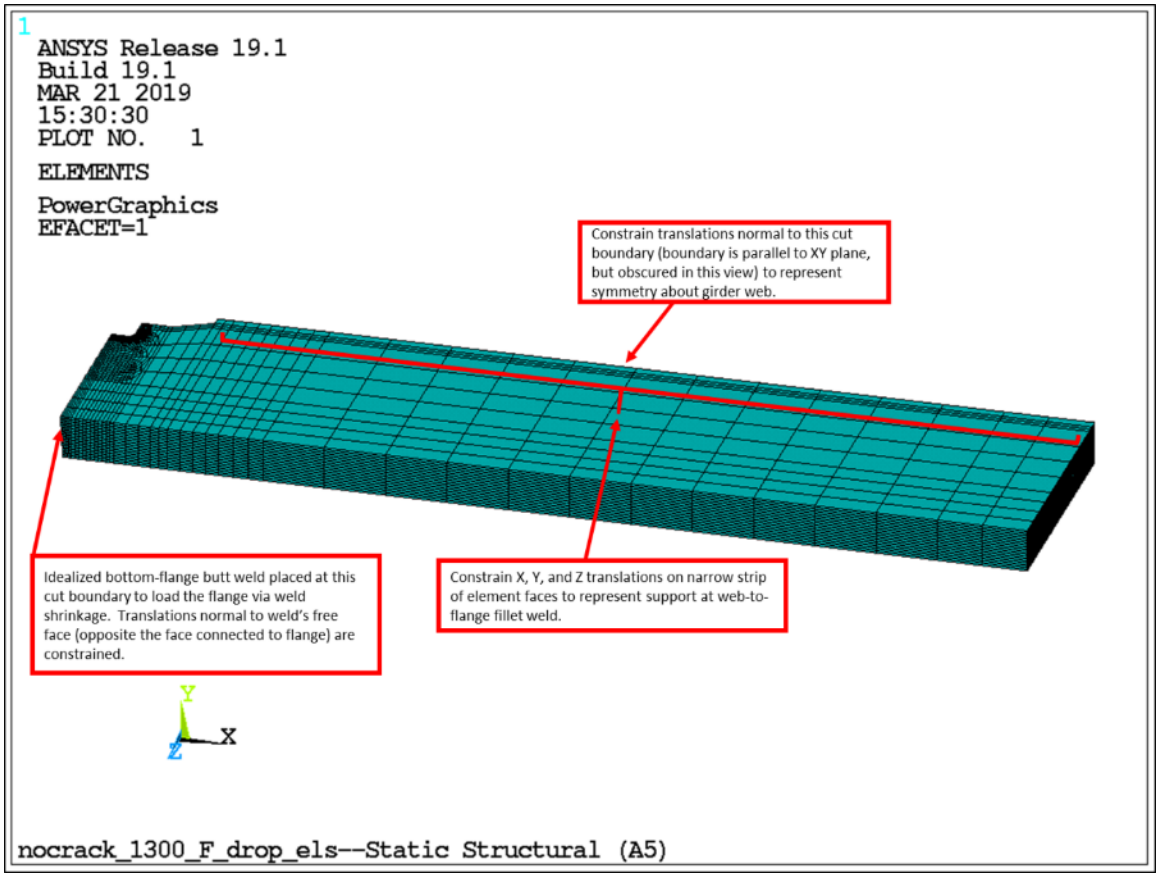

Fig. 49. Boundary conditions for bottom-flange FE model. Boundary conditions represent the effect of support from neighboring structure.

4.1.3.2 Loading

The groove weld between bottom flanges is shown in Fig. 50. (Despite the symmetries exploited in the modeling, the figure shows a zoomed-in view of the *entire* weld, both adjacent flanges north of the girder web, and other neighboring girder components.) When the weld cools and solidifies, it shrinks, pulling neighboring flange material in all three orthogonal directions as it does so.

As an idealization of this effect, and consistent with symmetry considerations discussed previously, elements representing half the volume of the weld were added to the end of the flange FE model (see Fig. 47) and loaded with a temperature drop equal in magnitude to the approximate stress-relieving temperature of the flange material.

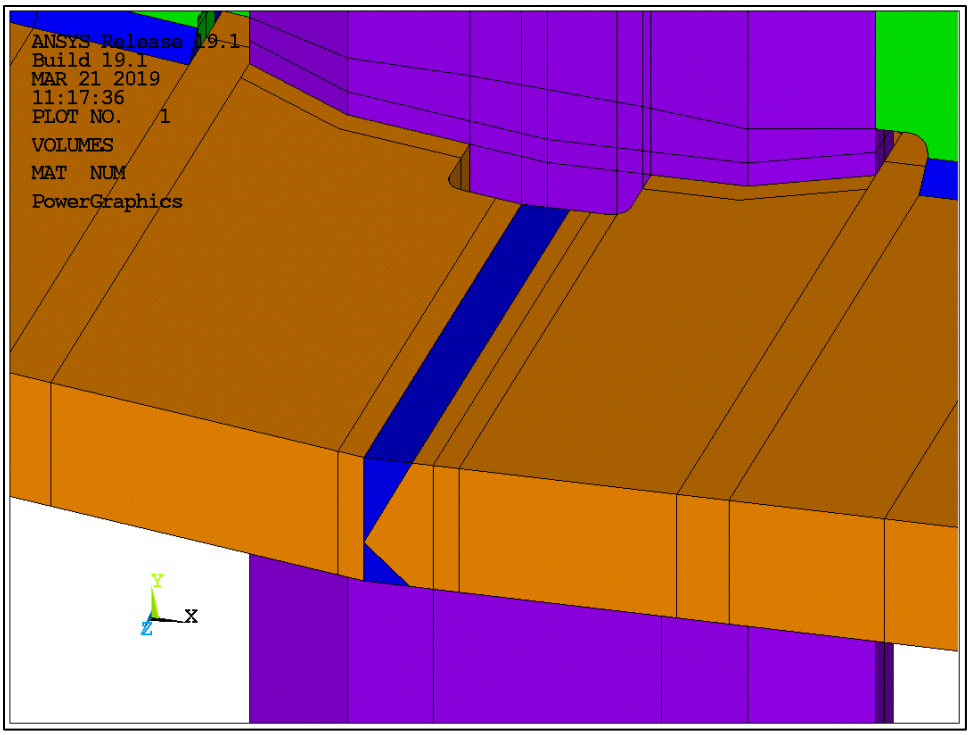

Fig. 50. Groove-weld region of Fremont Street solid model (dark blue), bottom flange.

Fig. 51 shows a contour plot of the applied-temperature distribution: a uniform change of -1300°F. Note that the thermal-strain-free reference temperature in the FE model is set to 0°F. This is of no consequence, since it is the *change* in temperature, here taken as -1300°F, that creates thermal loading. By setting the thermal-strain-free reference temperature equal to zero, the applied temperature and applied temperature *change* become identical.

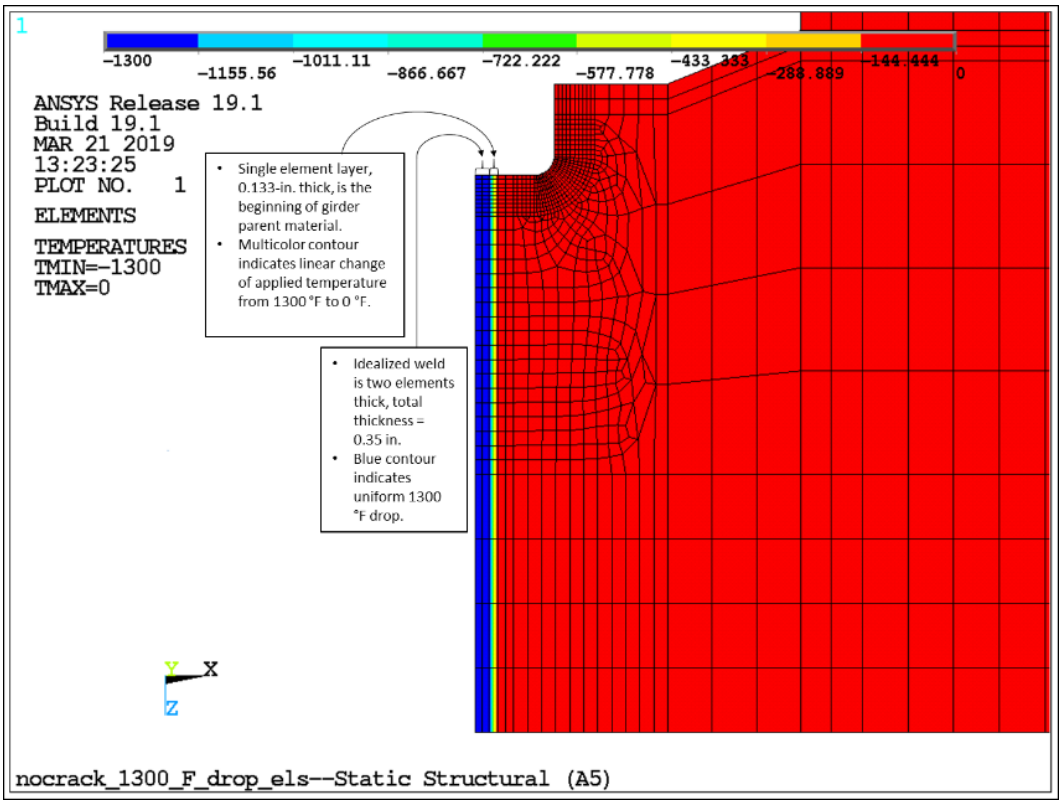

Fig. 51. Uniform temperature distribution of -1300°F in idealized weld region of bottom flange FE model.

4.1.3.3 Results – Uncracked Model

A deformed-shape plot of the FE model in response to the temperature drop is shown in Fig. 52, scaled 15x for visibility. The effect of weld shrinkage is clearly evident on the access hole radius. Though this plot corresponds to the Fremont Street uncracked model, the deformed shape is typical of all models studied for weld-induced residual stress effects.

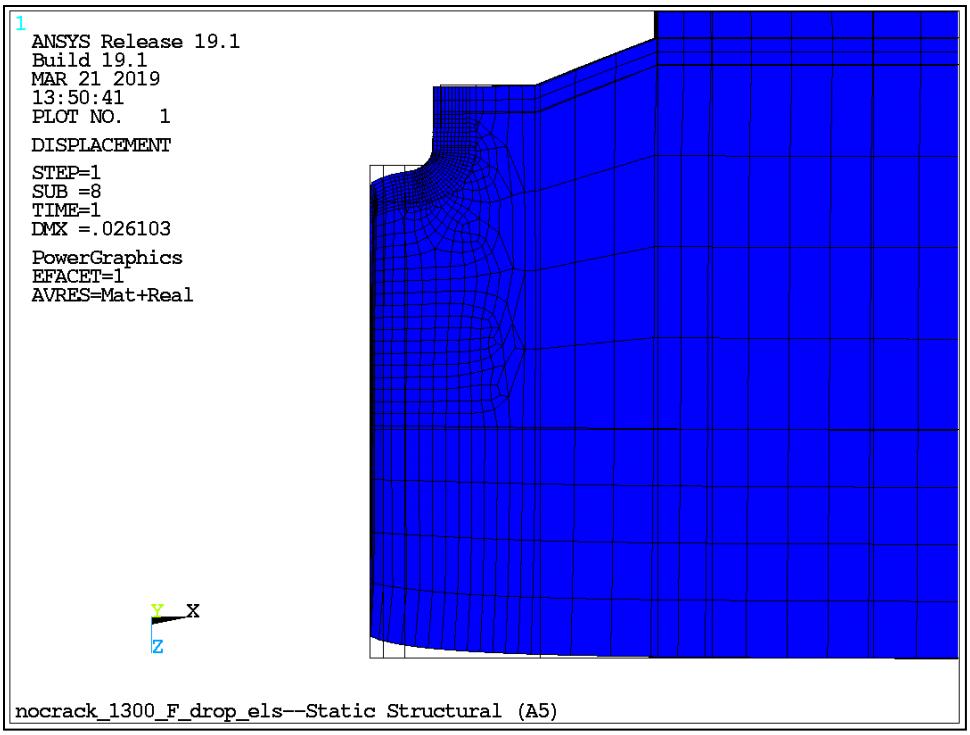

Fig. 52. Deformed shape of Fremont Street FE model due to weld shrinkage (scaled 15x for visibility).

A contour plot of maximum (i.e., first) principal stress local to the access hole radius is shown in Fig. 53. It is important to note that the direction of principal stress is substantially in the radius' circumferential direction. Tensile stresses between 65 and 75 ksi prevail across the entire 4-in. thickness of the bottom flange and approximately halfway along the arc of the radius. The direction and tensile nature of these stresses are consistent with the deformation of the radius exhibited in Fig. 52.

Most importantly, this orientation of maximum principal stress is perpendicular to the axis of the access-hole microcracks and, thus, the driving force for pop-in crack initiation from the pre-existing microcracks.

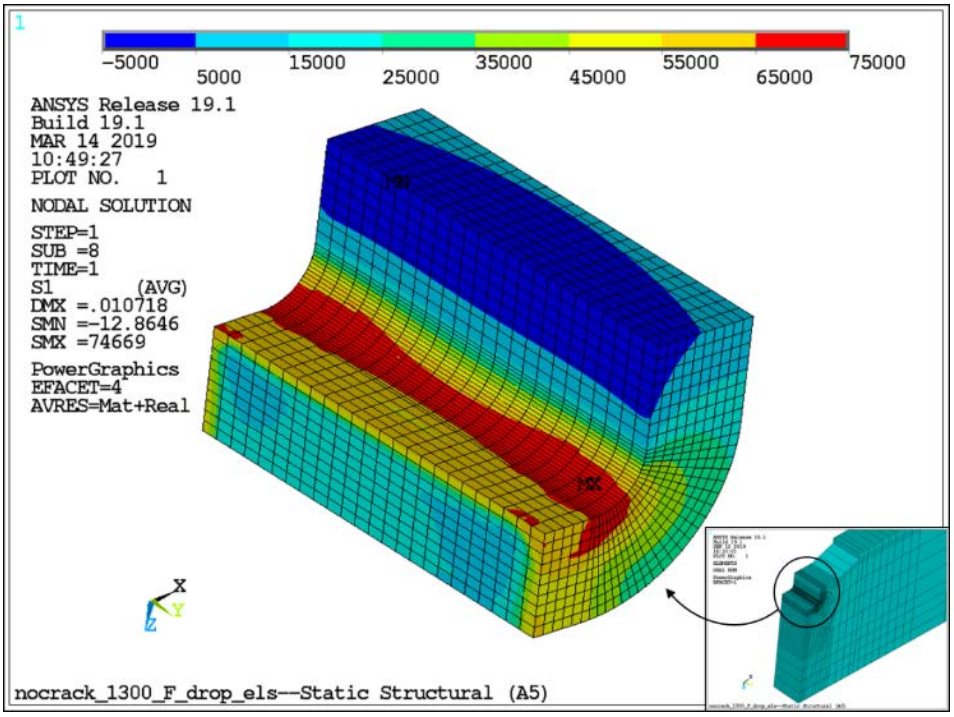

Fig. 53. Distribution of maximum principal stress local to the weld access hole radius the in Fremont Street girder. Stress exceeds 65 ksi across the 4-in. thickness of bottom flange.

At the center of the access hole radius surface the stress peaks at 61.7 ksi, which is slightly lower than described above, and drops off rapidly proceeding into the flange material. Fig. 54, top and bottom, shows the drop off over paths normal to the radius surface and parallel to the flange width, respectively. At 0.38 in. along the paths, stress drops to approximately 30% of the surface peak; at 1 in. along the paths, stress drops to approximately 10% of the surface peak.

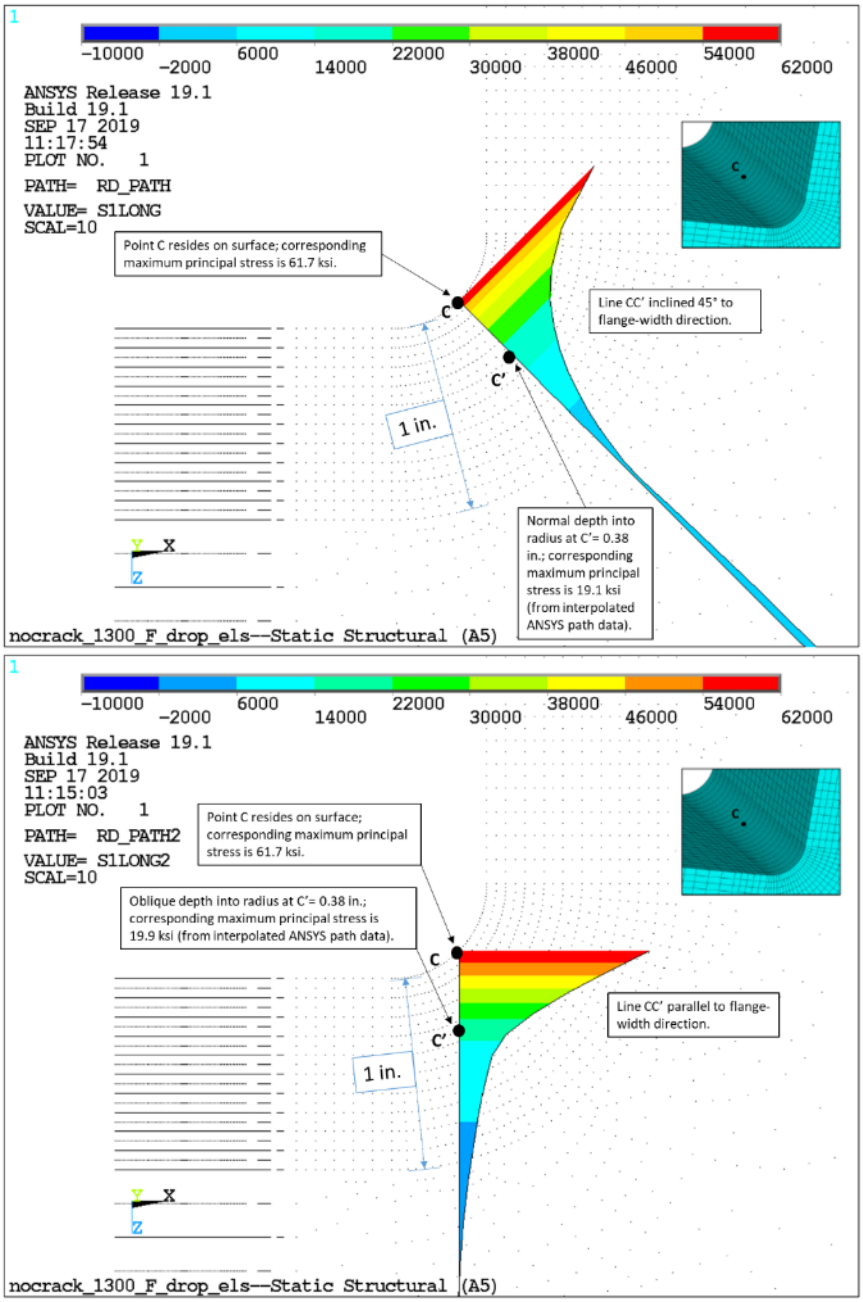

Fig. 54. Distribution of maximum principal stress over indicated paths (normal to radius surface, top, and parallel to flange width, bottom) starting at point C, the mid-thickness of the access hole for the Fremont Street girder (FE model nodes are shown for context).

A numerical plot of the residual stress results from Fig. 54 is provided in Fig. 55. In addition, this plot also shows the initially assumed residual stress distribution used above in Section 4.1.2 (Fig. 40), together with US Army Corp of Engineers' (USACE) research

results [18,19]. The USACE results [18,19] include both FE and experimental residual stress distributions for plates and groove welded wide-flange sections. Although the geometries analyzed [18,19] do not exactly match the TTC girder geometry, they do show the typical behavior exhibited by groove welded joints, which is that residual stresses adjacent to the weld or at the plate surface are high, generally near the plate's yield strength, and decrease rapidly as the distance from the weld or surface increases. It is also evident that the USACE results are in very good agreement with the FE residual stress distribution calculated here (purple curve in Fig. 55), as well as the derived, upper bound residual stress distribution derived here (blue curve in Fig. 55).

Further, the results provided in [19] for groove welding heavy wide-flange sections suggests that the final residual stress state is relatively independent of the number of weld passes used to make or model the groove weld. Therefore, the methodology used herein to estimate the residual stress state in the vicinity of the access holes is considered very reasonable, especially since the only stress present to initiate the pop-in cracks was the stress developed from welding the bottom flange groove weld joint. Specifically, the longitudinal shrinkage associated with that welding, much more so than any transverse phenomena, was the primary contributor to opening the radius and causing the high stress at the access hole. Fig. 52 is illustrative in this regard.

It can be concluded, therefore, that the residual stress distribution derived here and shown in Fig. 55 (blue curve) provides a very reasonable upper bound for the residual stress distribution necessarily present to initiate the pop-in cracks from the microcracks. Moreover, the most likely distribution of residual stress is the purple curve in Fig. 55, since it was calculated for the actual flange and access hole geometries.

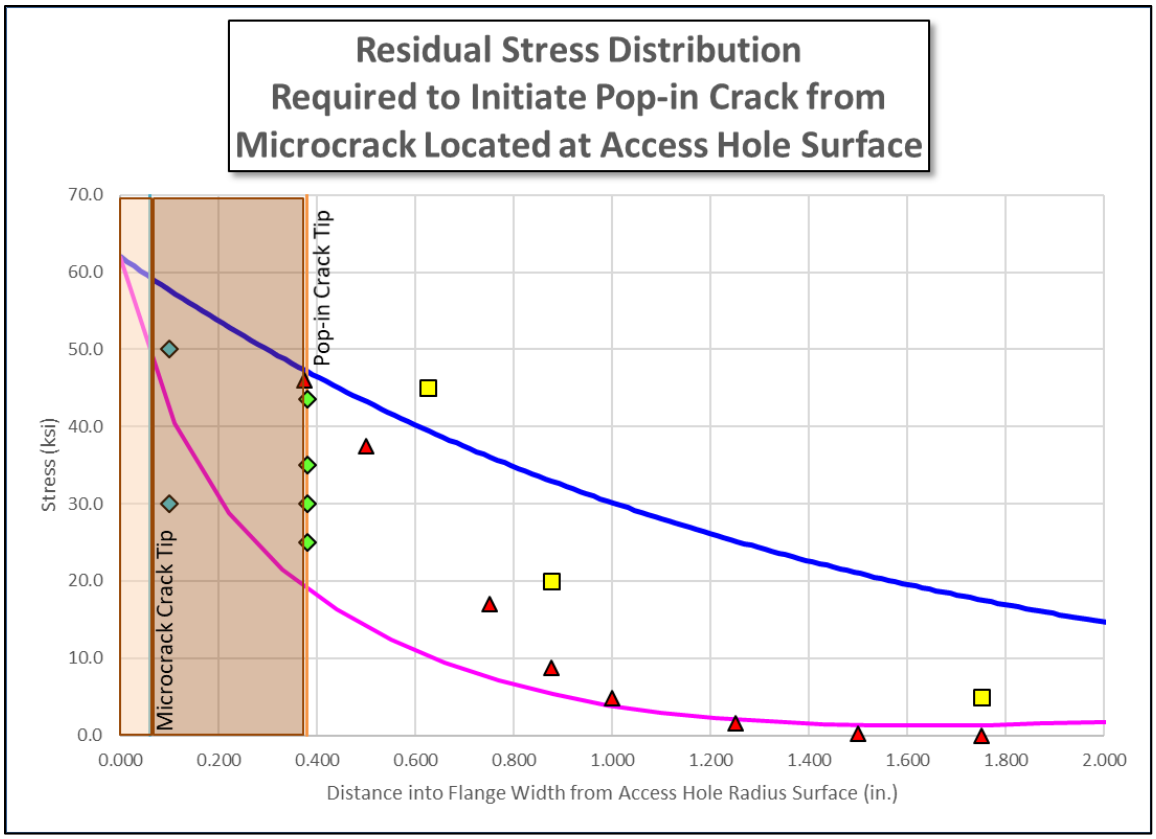

Fig. 55. Residual stress distributions (curves) necessary to initiate pop-in cracking from the pre-existing microcracks. The blue curve is the upper bound, derived distribution and the purple curve is the thermal FE calculated distribution. These curves bound USACE experimental (yellow squares [18] and green diamonds [19]) and FE calculated (red triangles [18] and blue diamonds [19]) residual stress results.

4.1.4 Alternative Residual Stress Analysis

The residual-stress analysis of the Fremont Street girder discussed in Section 4.1.3 was not intended to establish a detailed stress distribution within the groove weld; rather, it was directed at determining the effect of that weld's shrinkage on stress local to the access hole, a region adjacent to the weld. In the present section, an alternative analysis is discussed, one that was directed at determining both a more detailed distribution of stress within the weld and weld-shrinkage effects on the access hole. As was the case for the analyses discussed in Section 4.1.3, the analysis approach discussed herein is an adaptation of that presented in [16], but employs refinements that permit the more detailed description of stress distribution local to the weld.

For clarity, the model/analysis discussed in Section 4.1.3 and the alternative model/analysis will herein be referred to as the "weld-shrinkage" and "weld-stress" model/analysis, respectively.

The following terminology will be helpful:

> *Longitudinal* shall be interpreted as being in the direction of the long dimension of the girder-flange groove weld. This is the direction in which the weld is laid and is parallel to the width of the girder flange.
>
> *Transverse* shall be interpreted as being directed across the girder-flange groove weld in a direction parallel to the length of the girder flange.
>
> *Vertical* shall be interpreted as being directed through the depth of the girder-flange groove weld in a direction through the thickness of the girder flange.

Due to the small slope of the girder flanges, the above orientations will not align perfectly with analogous directions in the global coordinate system in which the analysis was conducted. Nevertheless, the above definitions for longitudinal, transverse, and vertical will be sufficiently clear for identifying directions along, across, and through the girder-flange groove weld, respectively.

4.1.4.1 Model Description

Fig. 56 shows a global view of the “weld-stress” model, along with an inset showing mesh detail local to the access hole. Similar to the weld-shrinkage model, symmetry across the web plane is exploited, and several feet of flange beyond the weld is modeled. The weld-stress model, however, does not assume symmetry across the groove weld, and includes several feet of flange to both sides of it. With this approach, any asymmetric response across the weld can be accounted for. Applied boundary conditions, indicated in Fig. 56 by the aqua-colored symbols, represent both flange-to-web fillet-weld support and symmetry across the web as was the case for the weld-shrinkage model. The color contouring along the flange width local to the access hole represents the temperature loading and is discussed next.

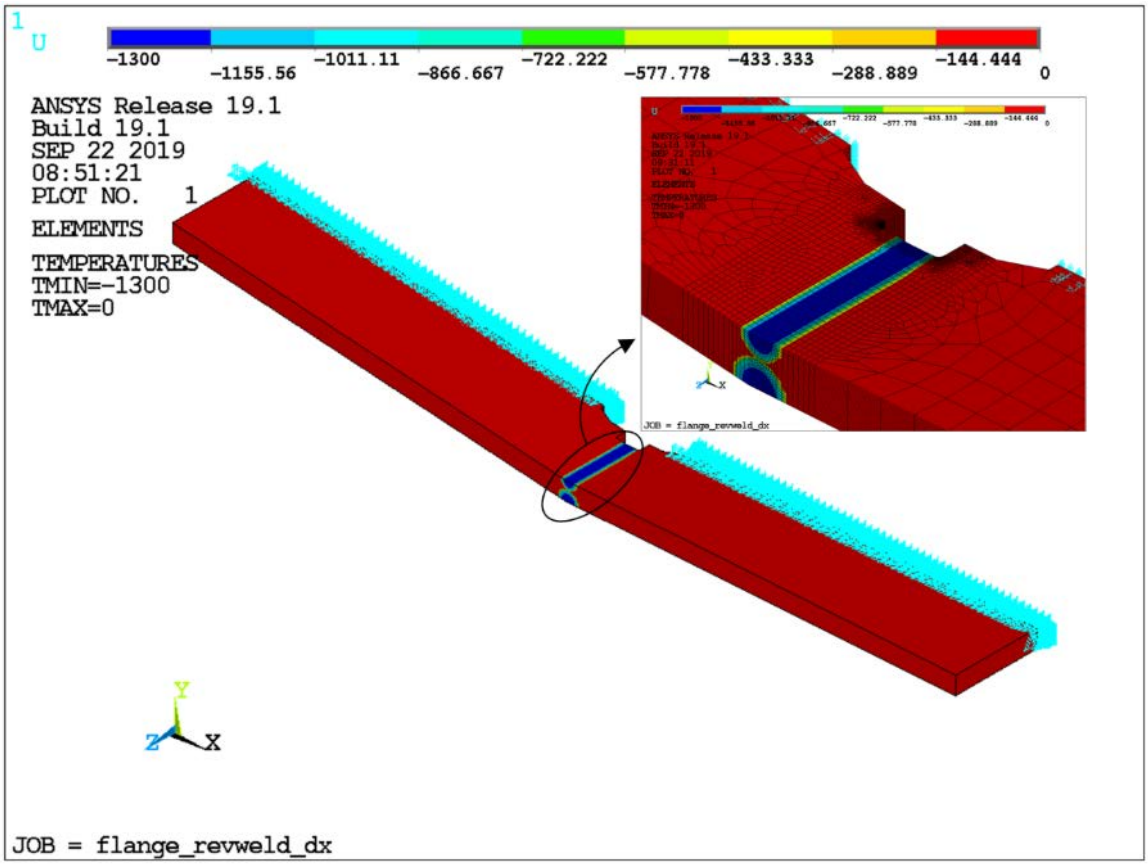

Fig. 56. Local finite-element model of Fremont Street lower flange showing temperature-distribution contour. Boundary conditions are indicated by aqua-colored symbols and are as described in Section 4.1.3.1.

4.1.4.2 Loading

Unlike the uniform temperature drop employed in the weld-shrinkage model, the weld-stress model employed a distribution nonuniform in a transverse plane. Fig. 57 shows a contour plot of the applied temperature field. The applied temperature ranges from -1300 to 0°F, dropping off radially from the center of the weld's surfaces at the flange inner and outer surfaces. The extents of the top and bottom "footprints" are driven by the weld cross section, being roughly in proportion to the top and bottom regions thereof. The loading also extends somewhat past the boundaries of the weld—shown in heavy black outline and based on LPI's observation of actual samples taken from the field—in recognition of the fact that heating associated with actual welding extends beyond the weld itself. The use of a radial drop-off is an adaptation of temperature loading described in [16].

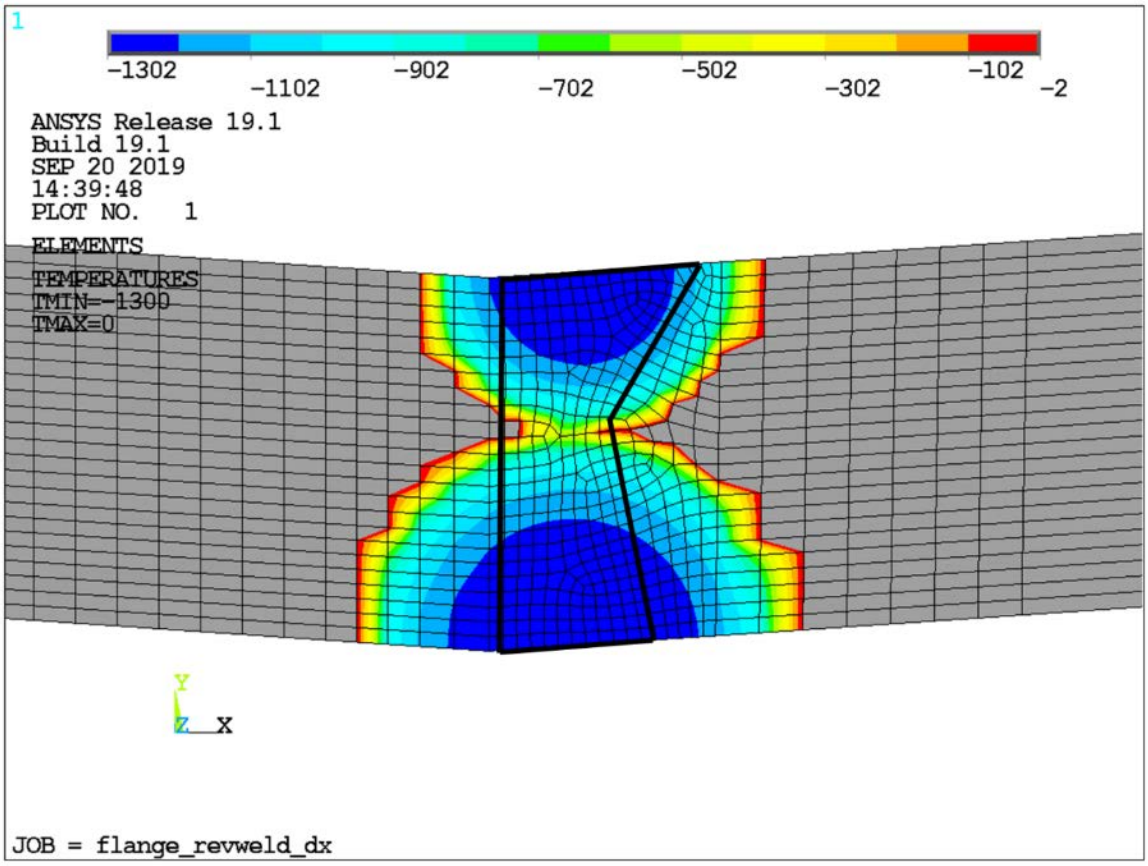

Fig. 57. Applied temperature distribution local to groove weld. Weld region delineated by heavy black line.

4.1.4.3 Results – Local to Groove Weld

Results of the weld-stress analysis are interpreted in light of the plots shown in Fig. 58 [35] and the discussion presented in [36]. It bears noting that the plots shown in Fig. 53 are also shown in [36] in its Figure 7.27; both [35] and [36] discuss work performed by the same researcher. The figure shows through-thickness distributions of longitudinal, transverse, and vertical (labeled “Perp.” in that plot) measured residual stresses for a 1-in.-thick, multi-pass, groove-welded low-carbon-steel plate. Analysis of the weld-stress model made no attempt to match the exact magnitudes of stress shown in the figure. Rather, it sought to match the spatial distributions.

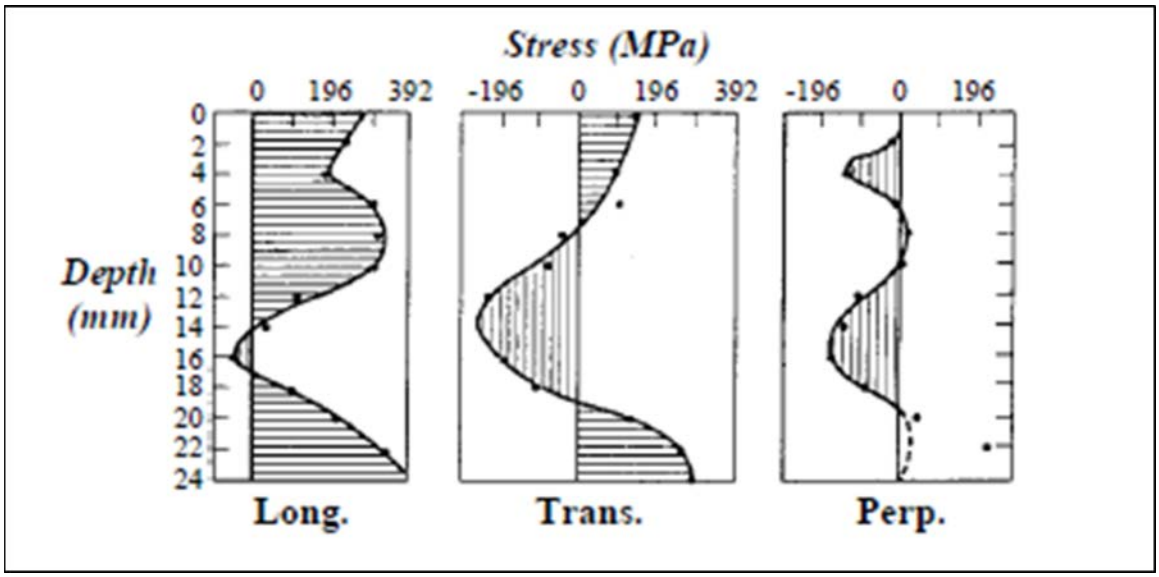

Fig. 58. Through-thickness distribution of three orthogonal components of residual stress in a thick, groove-welded plate, excerpted from [16].

Fig. 59 and Fig. 60 show, respectively, through-thickness distributions of calculated longitudinal and transverse residual stress along a path located approximately through the middle of the weld cross section (depicted by the heavy black outline of Fig. 57) and located midway across the girder-flange width. Shown for context in each figure is a node plot of the finite-element model. Though not identical, these calculated paths plots show a noticeable similarity to the corresponding plots of measured stress shown in Fig. 58. Longitudinal and transverse maxima are, respectively, 90 ksi and 43.5 ksi; that longitudinal is higher than transverse is consistent with Fig. 58, though not by the same ratio. (The legends on color contour plots of this section are in stress units of psi; the textual discussion is in terms of ksi.)

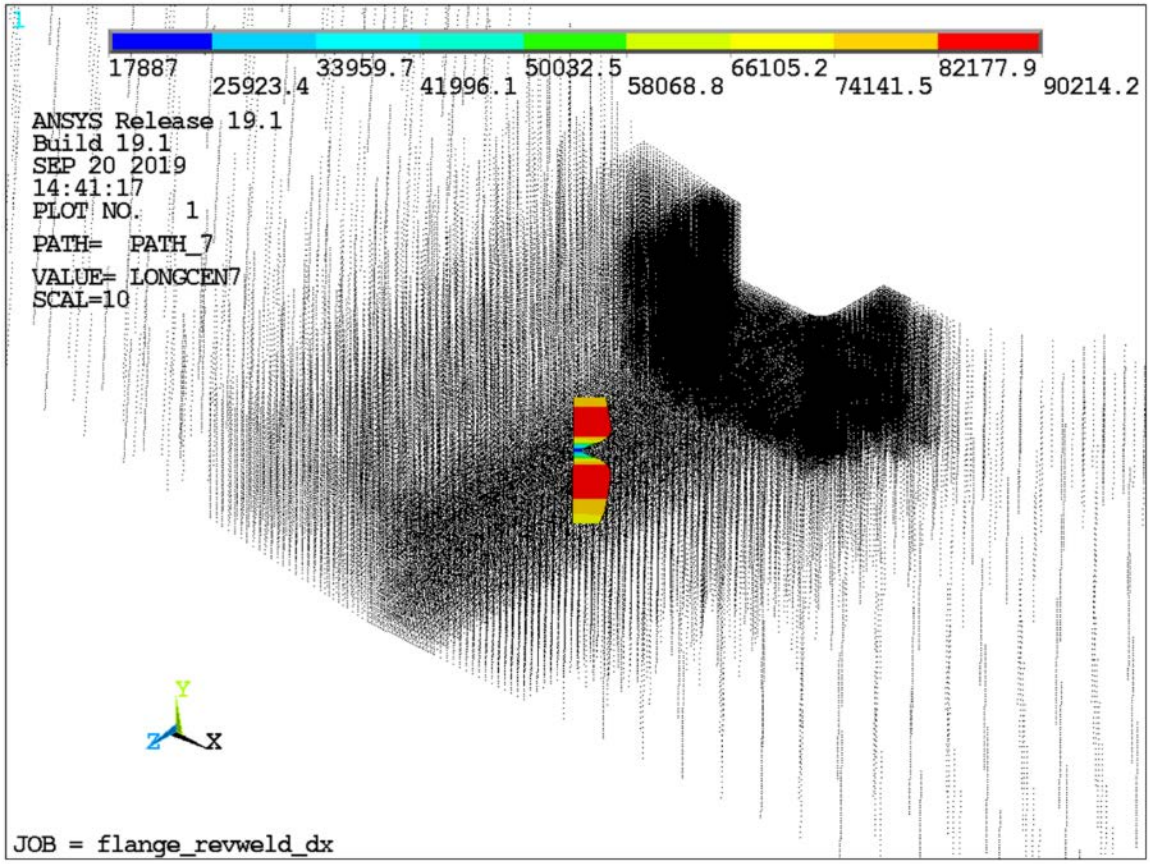

Fig. 59. Through-thickness distribution of calculated longitudinal residual stress at center of flange groove weld. Note similarity of distribution compared to longitudinal-stress plot shown in Fig. 58.

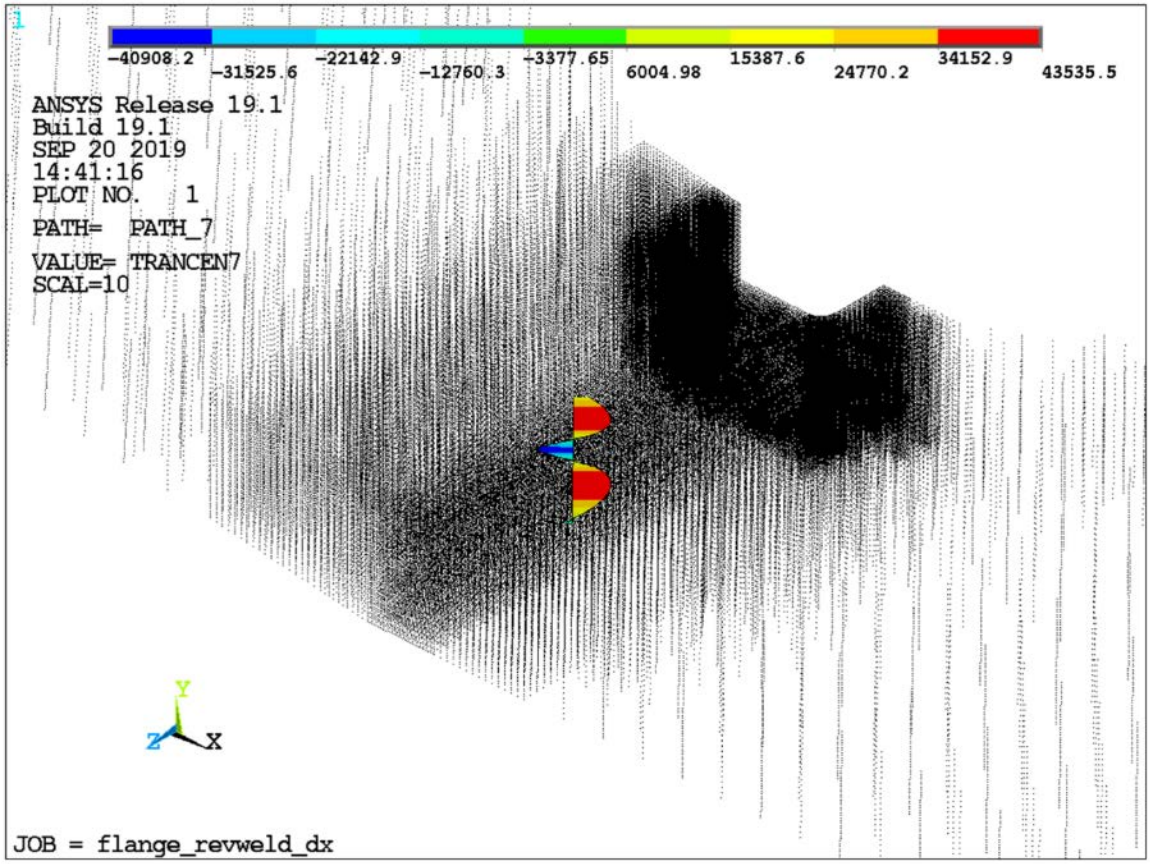

Fig. 60. Through-thickness distribution of calculated transverse residual stress at center of flange groove weld. Note similarity of distribution compared to transverse-stress plot shown in Fig. 58.

Fig. 61 and Fig. 62 show, respectively, plots of calculated longitudinal and transverse residual stress along a path on the inner surface of the girder's bottom flange and parallel to the girder-flange width, located approximately at the middle of the weld cross section. The longitudinal maximum, 80 ksi, is greater than the transverse maximum, 25.5 ksi, as is typical for groove welded plates. Longitudinal stress approaches zero at the ends as is required at the free surfaces. Transverse stress turns compressive near the ends, consistent with the discussion found in [36] (p. 238).

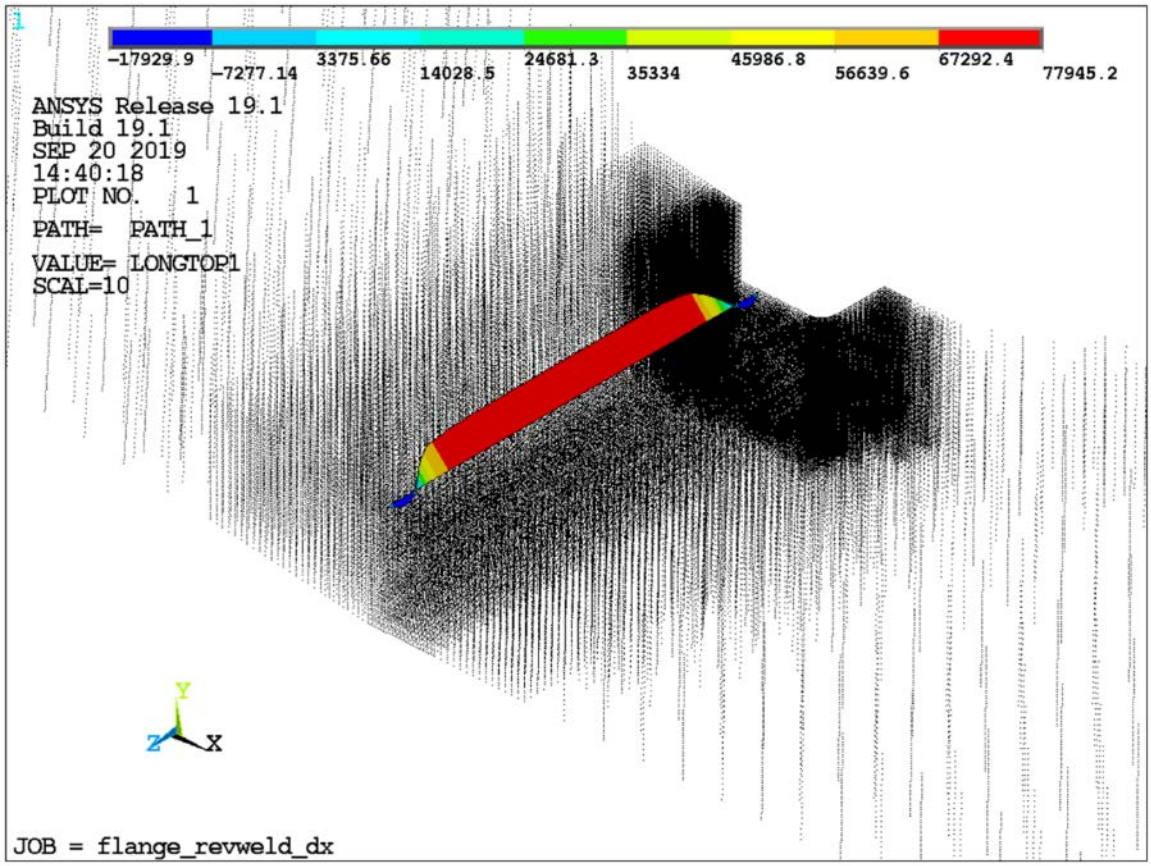

Fig. 61. Longitudinal distribution of longitudinal residual stress, outer surface of Fremont Street lower flange, at groove weld.

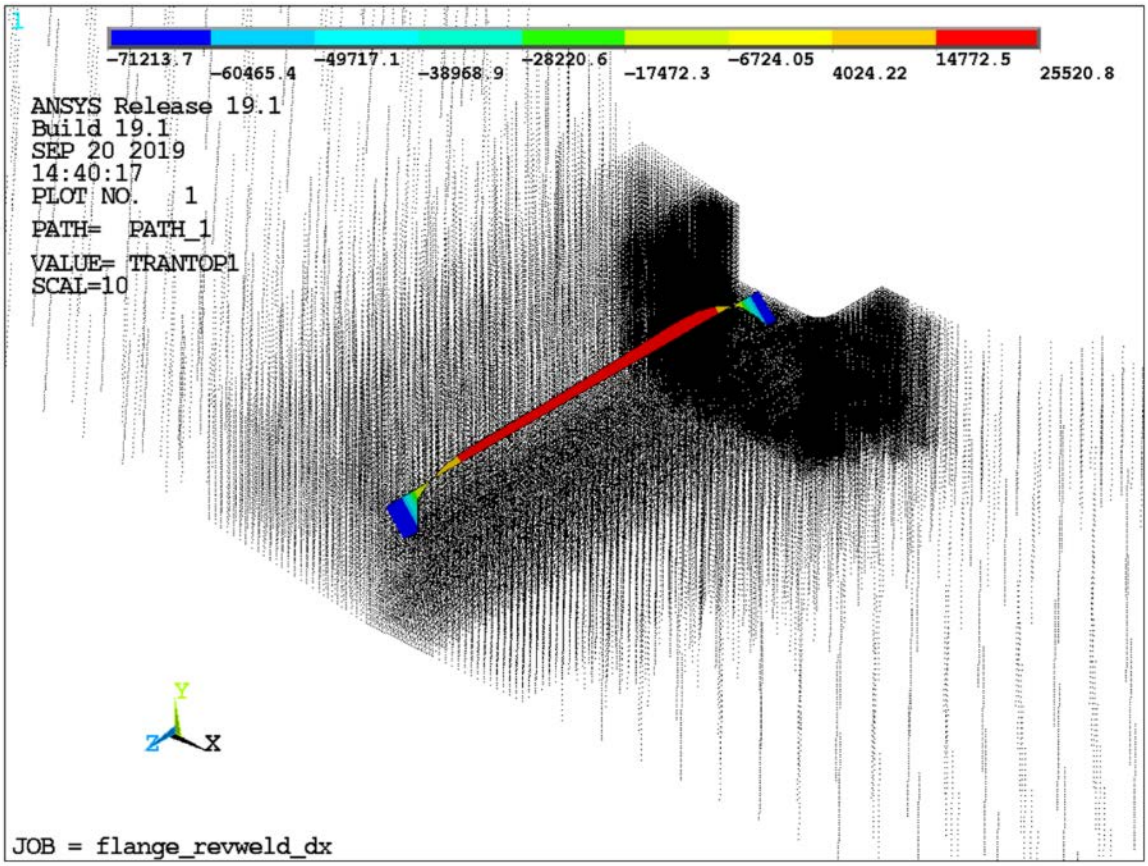

Fig. 62. Longitudinal distribution of transverse residual stress, outer surface of Fremont Street lower flange, at groove weld. Tensile along most of path length, turning compressive near ends. Tensile-stress magnitude lower than longitudinal-stress magnitude (compare to Fig. 61).

A plot of calculated longitudinal residual stress along a path on the outer surface of the girder flange located midway across the flange width is shown in Fig. 63. Consistent with expected behavior for groove welded plates, the stress changes from tensile to compressive, moving away from the weld.

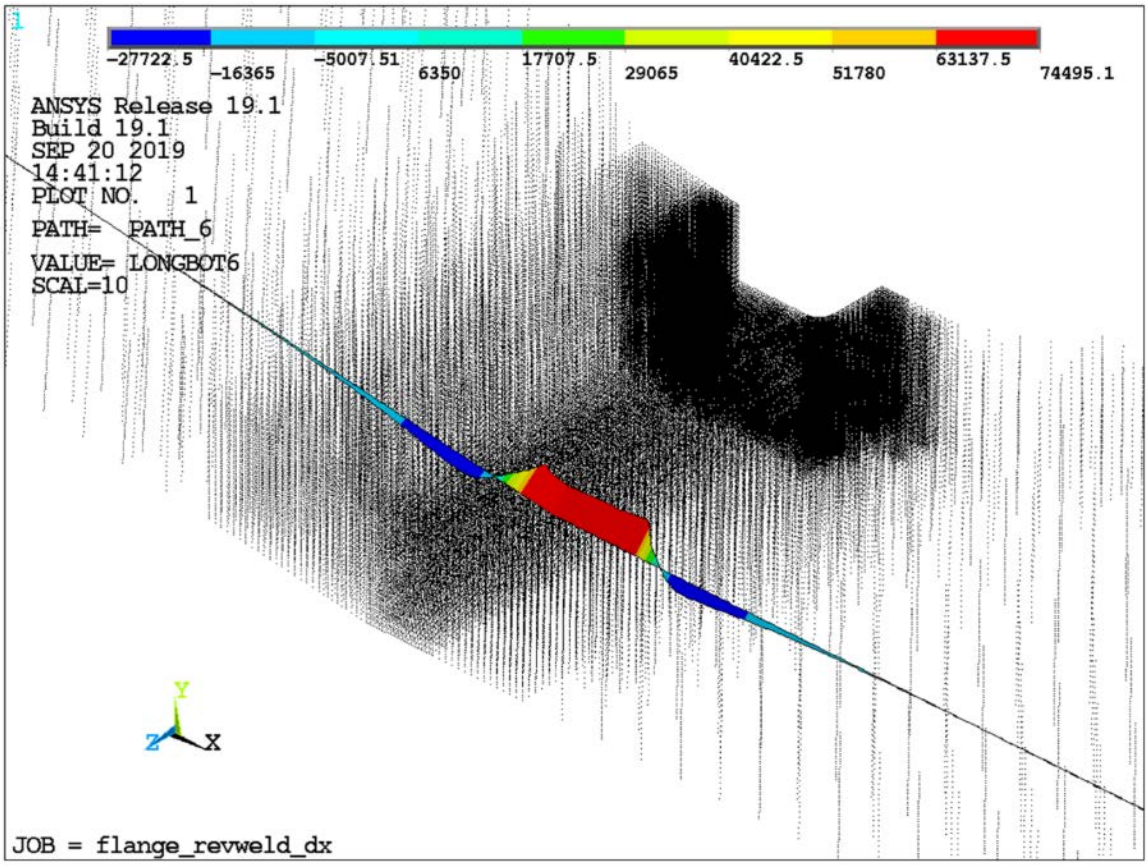

Fig. 63. Transverse distribution of longitudinal residual stress, outer surface of Fremont Street lower flange, along a section through center of groove weld. Note transition from tension to compression outward from weld.

Lastly, Fig. 64 and Fig. 65 show, respectively, through-thickness distributions of calculated longitudinal and transverse residual stress at the access-hole end of the groove weld. As required at a free surface, longitudinal stress is (essentially) zero, notwithstanding some chattering of computed values about zero. Transverse stress runs compressive, again, consistent with [36] (p. 238).

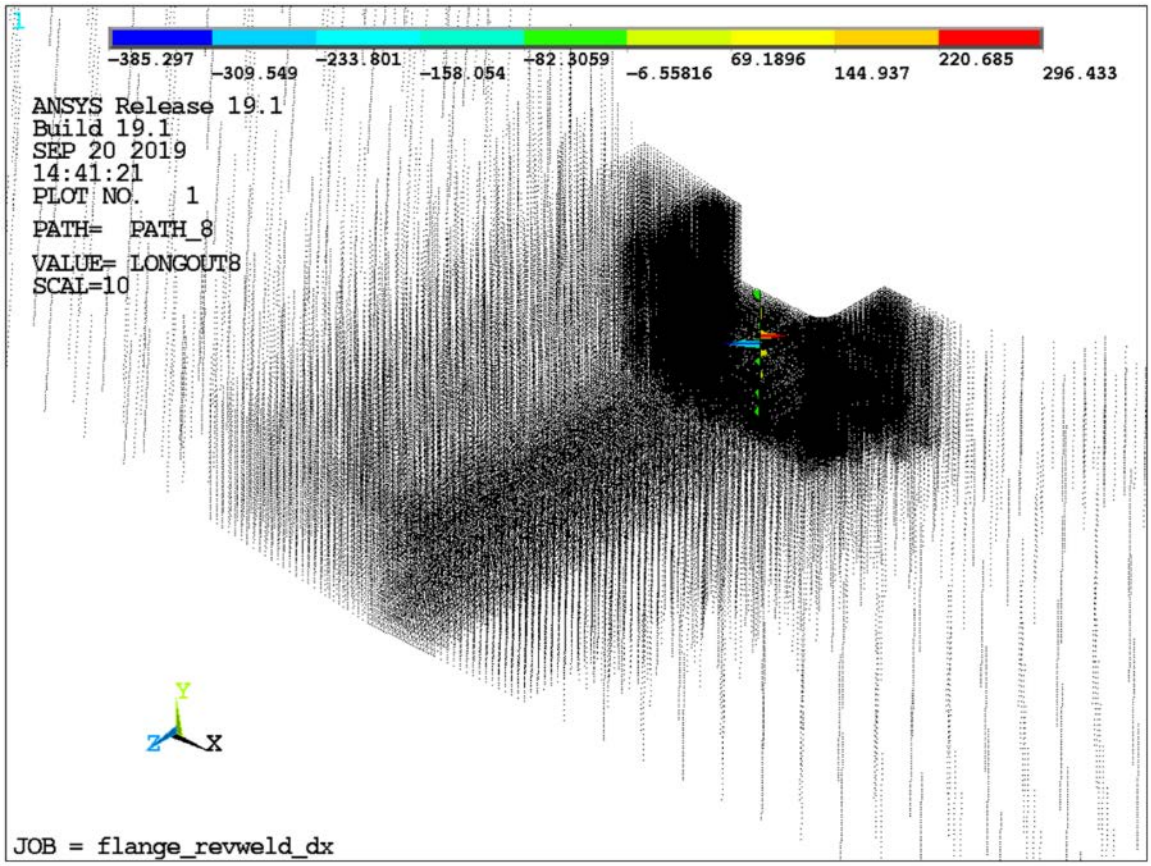

Fig. 64. Through-thickness distribution of longitudinal residual stress at end of groove weld nearest access-hole radii. Near-zero magnitudes consistent with the free-surface condition.

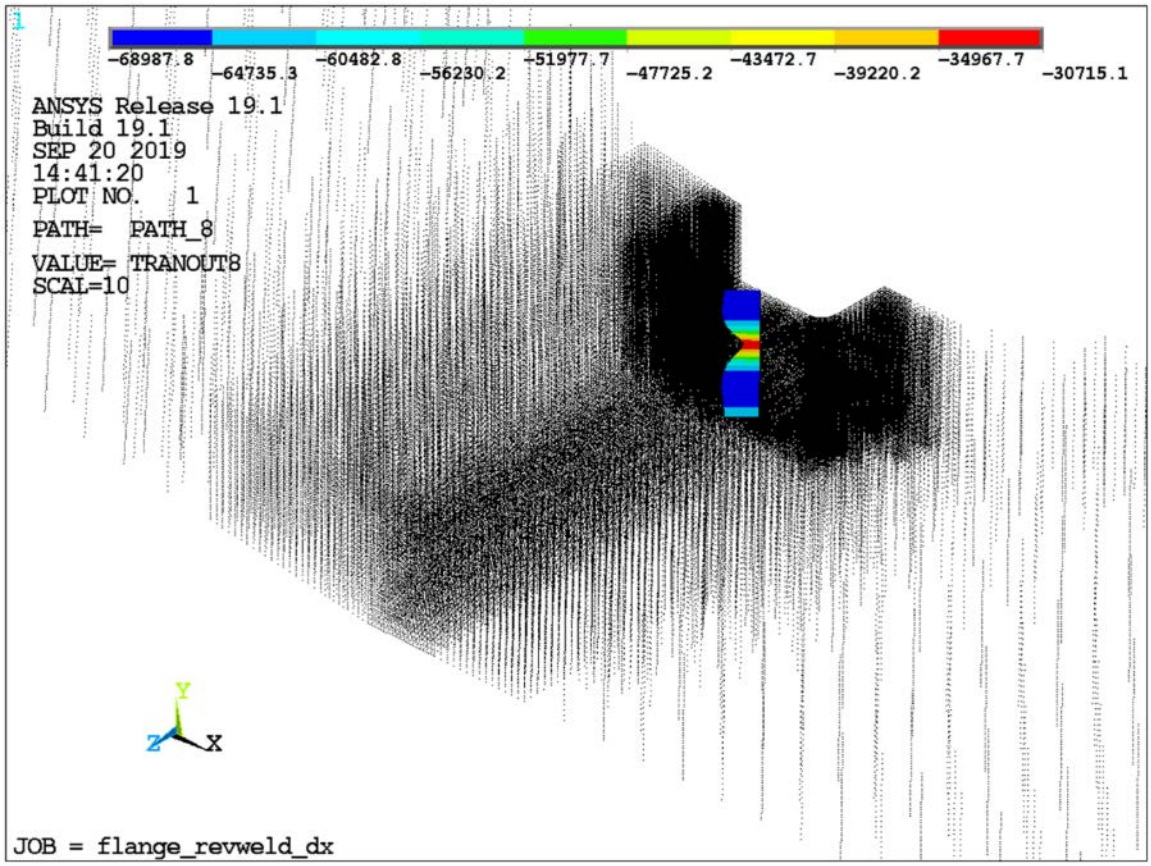

Fig. 65. Through-thickness distribution of transverse residual stress at end of groove weld nearest access-hole radii. Stresses are compressive, though of variable magnitude.

4.1.4.4 Results – Local to Access Hole

Fig. 66 shows a contour plot of maximum principal stress distributed over east and west access-hole radii. Comparison of the contours between the two reveals an overall higher stress state at the surface of the west radius. Further, average values at the radii centers over the entire flange thickness are 74.6 ksi and 84.5 ksi for the east and west radii, respectively.

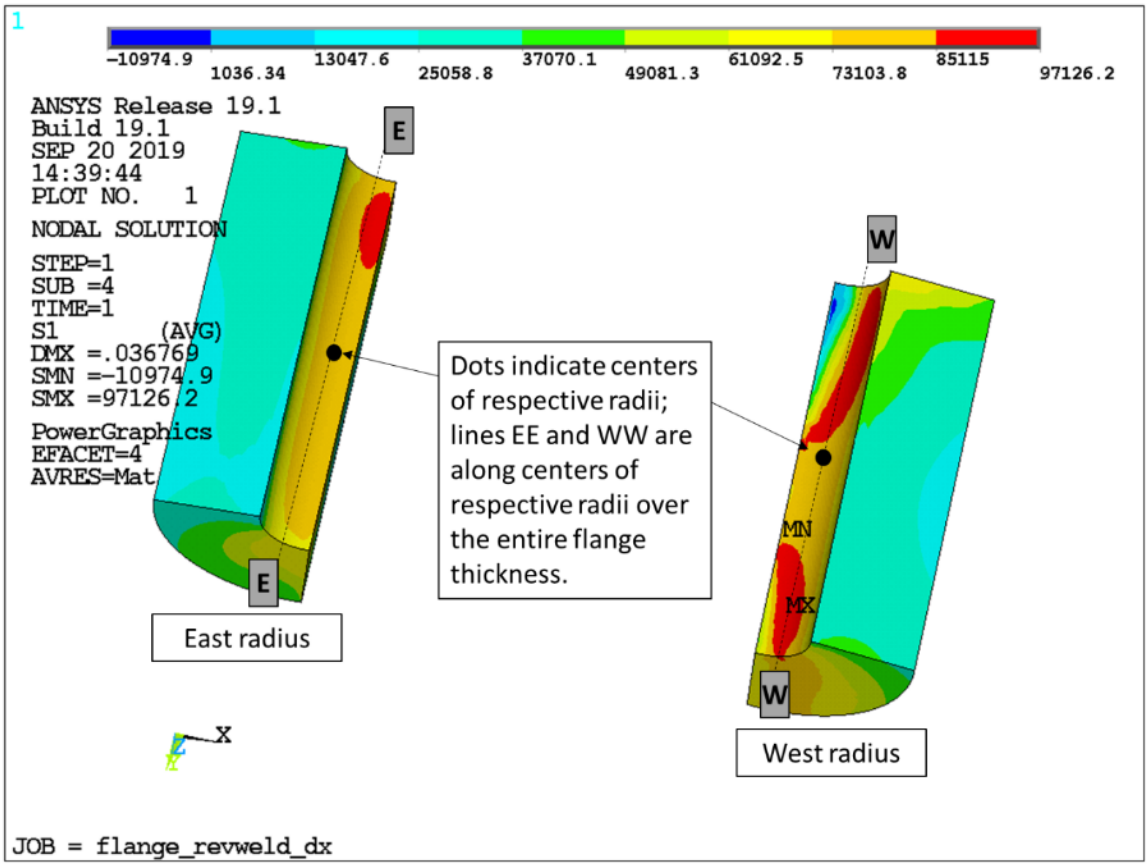

Fig. 66. Contour plot of maximum principal stress in access-hole radii. Generally higher values prevail over west radius compared to east radius. Average values along lines EE and WW are 74.6 and 84.5 ksi, respectively.

Maximum principal stresses at the centers of the east and west radii are presented in Fig. 67. The west value, 78 ksi, is 4% higher than the east value, 75 ksi.

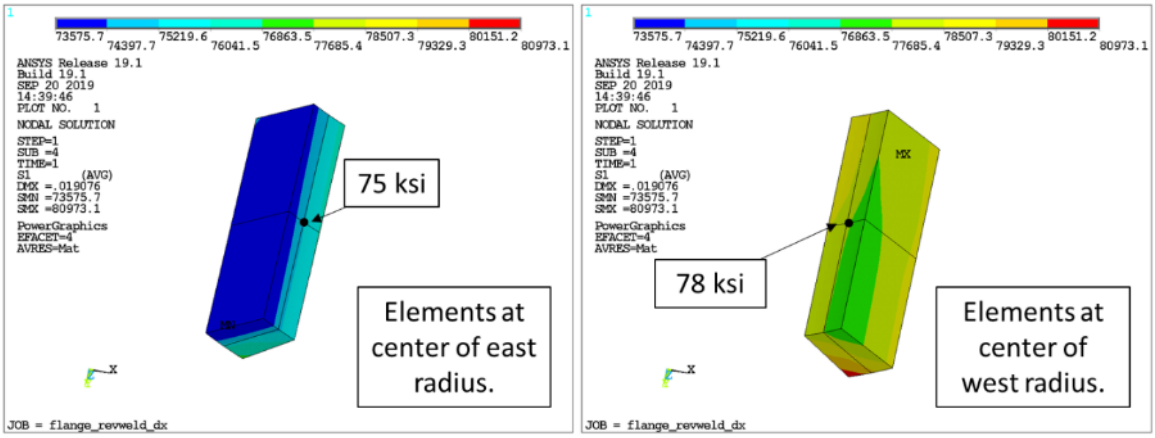

Fig. 67. Contour plots of maximum principal stress local to access-hole-radii centers.

4.1.4.5 Conclusion

Although the computed stresses are rather high in some locations—in excess of 90 ksi—one must keep in mind that in the analysis of the yielding of ductile metals it is the effective stress, often referred to as von Mises stress, that should be compared to material yield strength. Individual stress components, however, can often exceed yield strength by quite a bit. Further, the finite-element stresses presented are true stresses, the magnitudes of which will be approximately 10%-15% higher than the more conventional, and more familiar, engineering stresses. Apart from this issue, however, the fact that a plausible distribution of stress within the weld and HAZ has been obtained provides increased confidence in the access-hole stresses, and their bias toward the west side, in particular.

4.2 Pop-in Crack Arrest

Immediately following pop-in crack initiation, unstable crack propagation occurred due to the self-limiting residual stress from the CJP groove weld. Further crack extension was arrested when the pop-in crack attained a depth (a) of 0.38 in. due to the combination of a local reduction in residual stress and probable increase in fracture toughness.

The pop-in crack was located at the mid-thickness (½ t) of the bottom flange weld access hole radius surface where the static fracture toughness (K_{1C}) was determined to be approximately 55 to 60 ksi√in. at 50°F. However, propagation of an unstable crack is governed by a toughness lower than the static fracture toughness, known as the arrest fracture toughness (K_{1A}). Based on ASME Sec. XI, Fig. A-4200-1 [23], as well as API-579 [19], the crack arrest fracture toughness at 50°F could have been as low as approximately 30 ksi√in.

Depending on the temperature the bottom flange access hole region attained during CJP groove welding, the maximum fracture toughness would have been higher. At the ½-t, the flange exhibited a low upper shelf toughness, with an average CVN absorbed energy of approximately 30 ft-lb, which limits the elevated temperature upper shelf fracture toughness to about 70 to 100 ksi√in., as shown in Fig. 37 (yellow lines) and corroborated in BS7910, Sec. J.5 [24].

The corresponding crack arrest fracture toughness (K_{1A}) based on the upper shelf fracture toughness (K_{1C}) (Fig. 37, yellow lines) is approximately 40-60 ksi√in., depending on the temperature (based on methods described in API-579 [19]). Thus, from 50°F to upper shelf elevated temperature, the crack arrest fracture toughness varies from 30 to 60 ksi√in.

FAD calculations performed using the upper range of crack arrest toughness (55 to 60 ksi√in.) in combination with the Fig. 40 residual stresses indicate that a pop-in crack 0.38-in. deep would arrest, as shown in Fig. 68 (green circle).

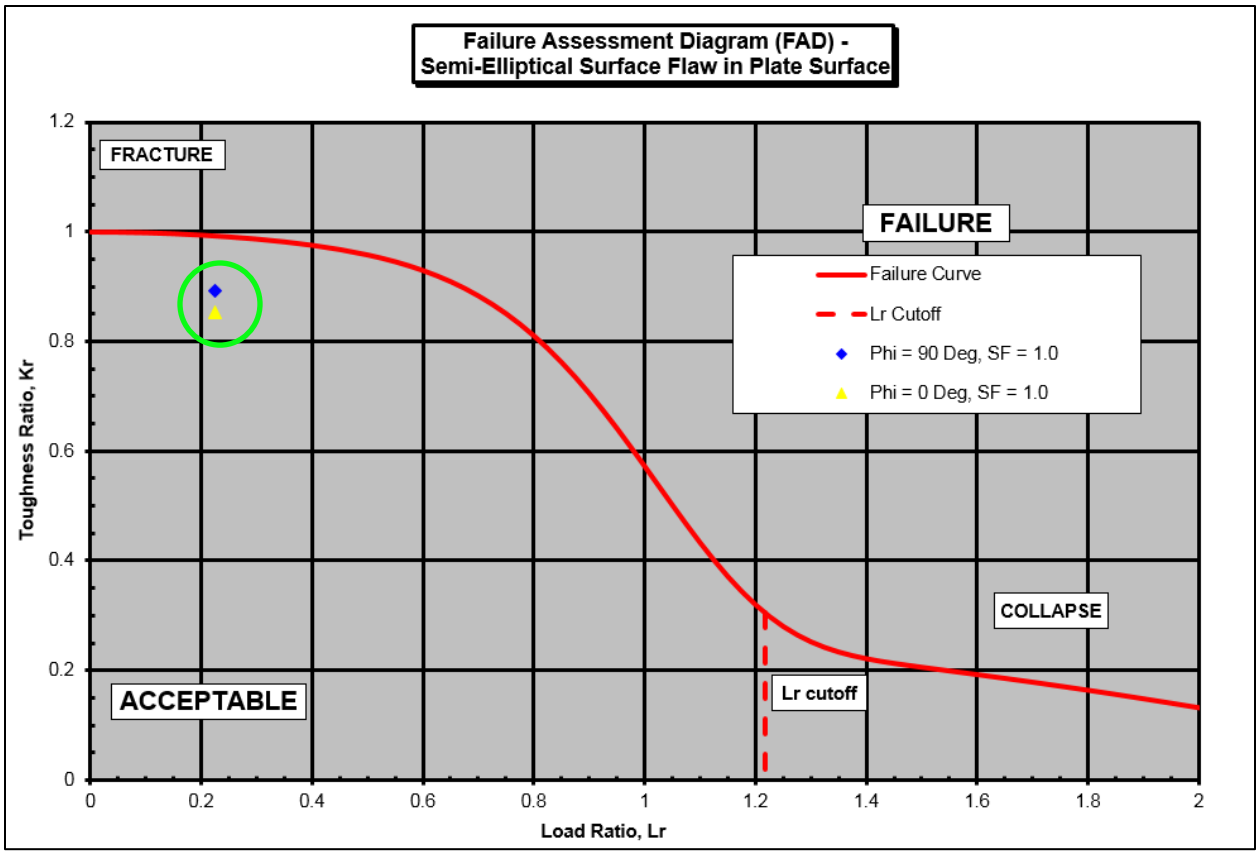

Fig. 68. Failure assessment diagram (FAD) demonstrating that pop-in crack propagation would arrest at a depth of 0.38 in. under the Fig. 40 residual stresses with a crack arrest fracture toughness of approximately 55 to 60 ksi√in.

In contrast, if the crack arrest fracture toughness was below approximately 50 ksi√in. then the pop-in crack would not have arrested at a depth of 0.38 in. and would have continued to propagate, as shown in Fig. 69.

These FAD results indicate that the pop-in crack likely arrested at an elevated temperature associated with CJP groove welding, at the upper shelf crack arrest fracture toughness of approximately 55 to 60 ksi√in.

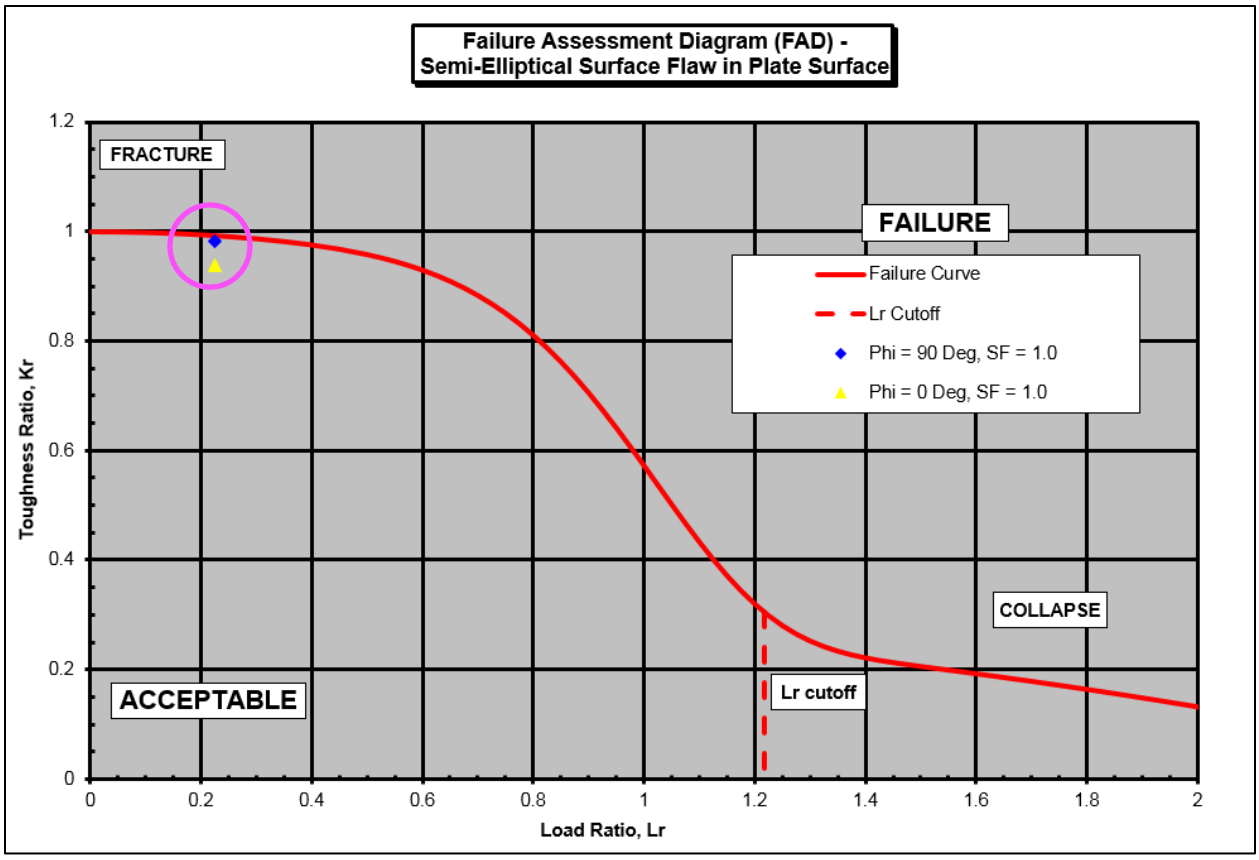

Fig. 69. Failure assessment diagram (FAD) demonstrating that pop-in crack propagation would not arrest at a depth of 0.38 in. under the Fig. 40 residual stresses with a crack arrest fracture toughness lower than approximately 50 ksi√in.

4.3 Bottom Flange Fracture Initiation

Fracture of the Fremont Street D.4 northwest bottom flange initiated from the 1.2 in. long (2c) x 0.38 in. deep (a) pop-in crack located at the mid-thickness of the 4-in. flange plate weld access hole radius surface (see Section 4.1). Low-energy, brittle fracture was driven by a combination of normal service-induced stresses and the residual stresses from the bottom flange CJP groove weld. Details of the service stress determination and the bottom flange fracture initiation calculations are shown in the following subsections.

4.3.1 Service Stress Determination – FE Analysis

To determine the weld access hole service stresses at the time of bottom flange fracture initiation, a finite element (FE) model of the Fremont Street D.4 TPG3 girder was developed using the commercially available FE software ANSYS [17]. Since the Fremont Street D.4 and Fremont Street E.6 TPG3 girders are geometrically similar and the total

load, based on TT analyses [26], is within 5% it was not necessary to perform FE analyses of the E.6 girder.

Based on a review of the TT analyses [26,27], together with input from all interested parties, LPI considers [26,27] to provide a reasonable and appropriate representation of the loads and boundary conditions for the TPG3 girders at the time of the Fremont Street fractures.

4.3.1.1 Solid Geometry

A three-dimensional (3D) solid geometry of the TPG3 girder was created from the shop drawings [25] and as-built photographs and sketches. Fig. 70 shows an isometric view of the modeled TPG3 girder structure.

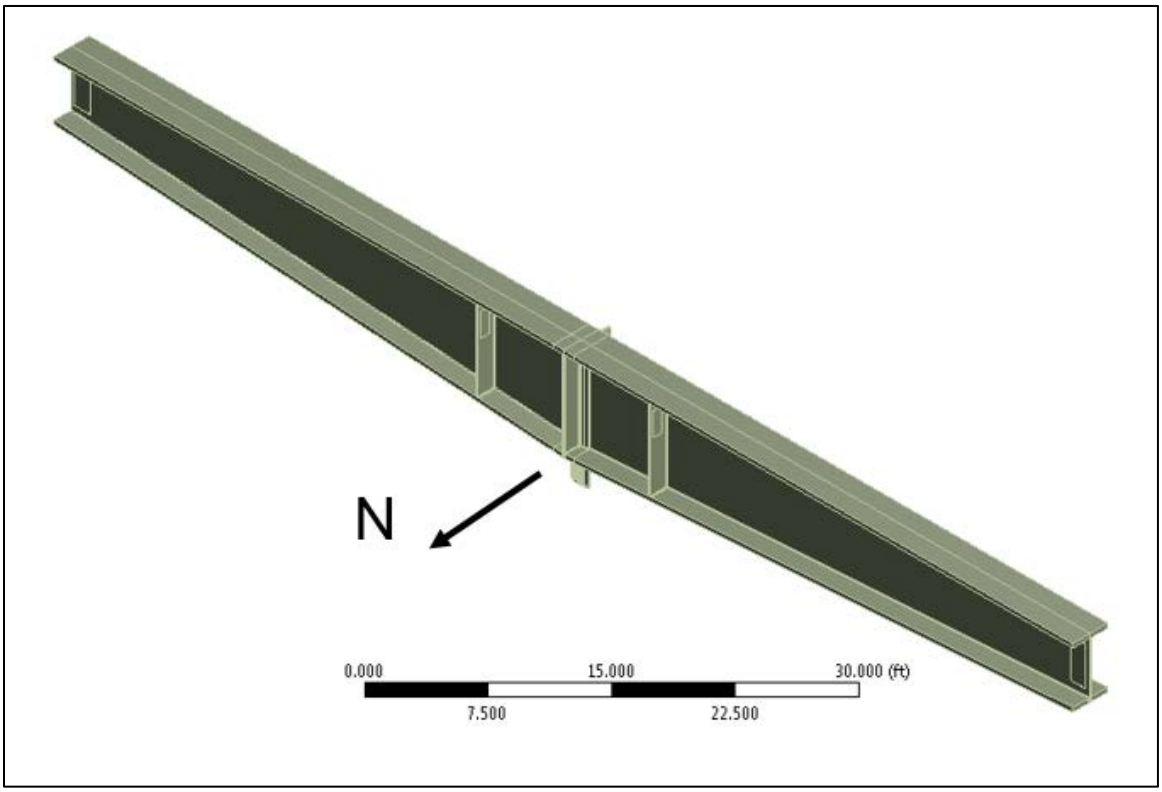

Fig. 70. TPG3 girder geometric model – Fremont Street D.4 line

Additional geometric model images of the overall TPG3 girder dimensions are given in Appendix F.

Composite behavior between the TPG3 girder structural steel and the concrete roof deck was also included, as shown in Fig. 71. Note that the concrete deck dimensions were based on the TT report [27] section detailing their investigation into the increase in TPG3

girder section modulus due to composite action at the time of bottom flange fracture initiation.

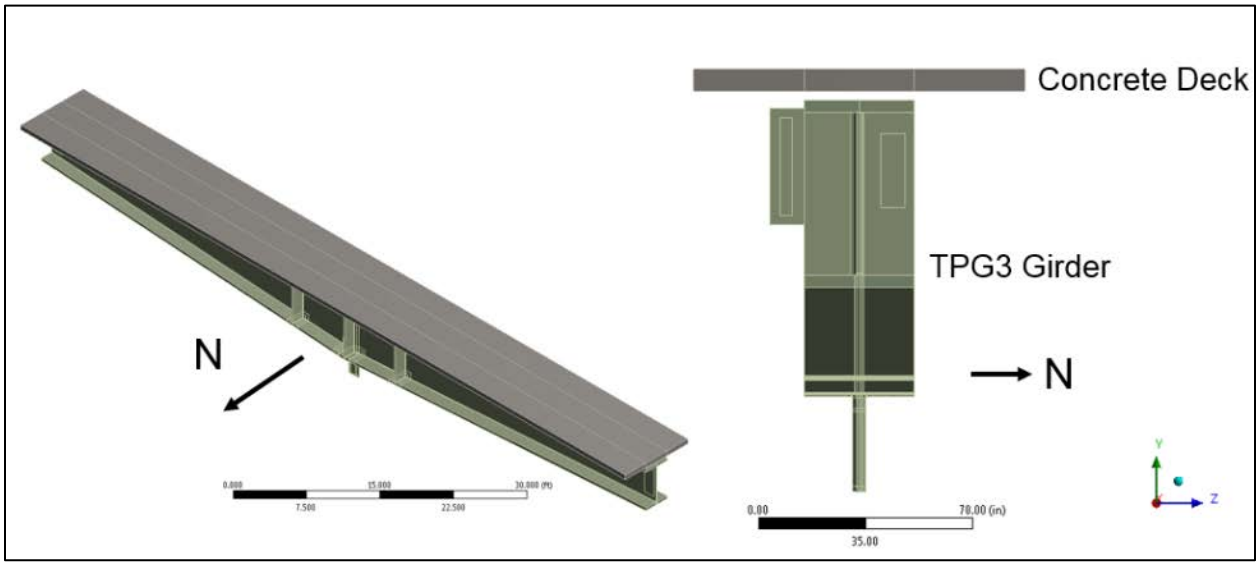

Fig. 71. Composite TPG3 girder geometric model with the concrete deck included – Fremont Street D.4 line

To accurately represent the stress state at the weld access hole fracture origin, local geometric details were represented in the 3D FE model, including explicitly modeled fillet welds in the region of interest, measured weld access hole dimensions, and offset centerline (CL) stiffeners.

All fillet welds near the weld access holes, including bottom flange-to-hanger, bottom flange-to-stiffener, bottom flange-to-web, and stiffener-to-hanger, were modeled assuming a ¾ in. leg length [25], as shown in Fig. 72 below.

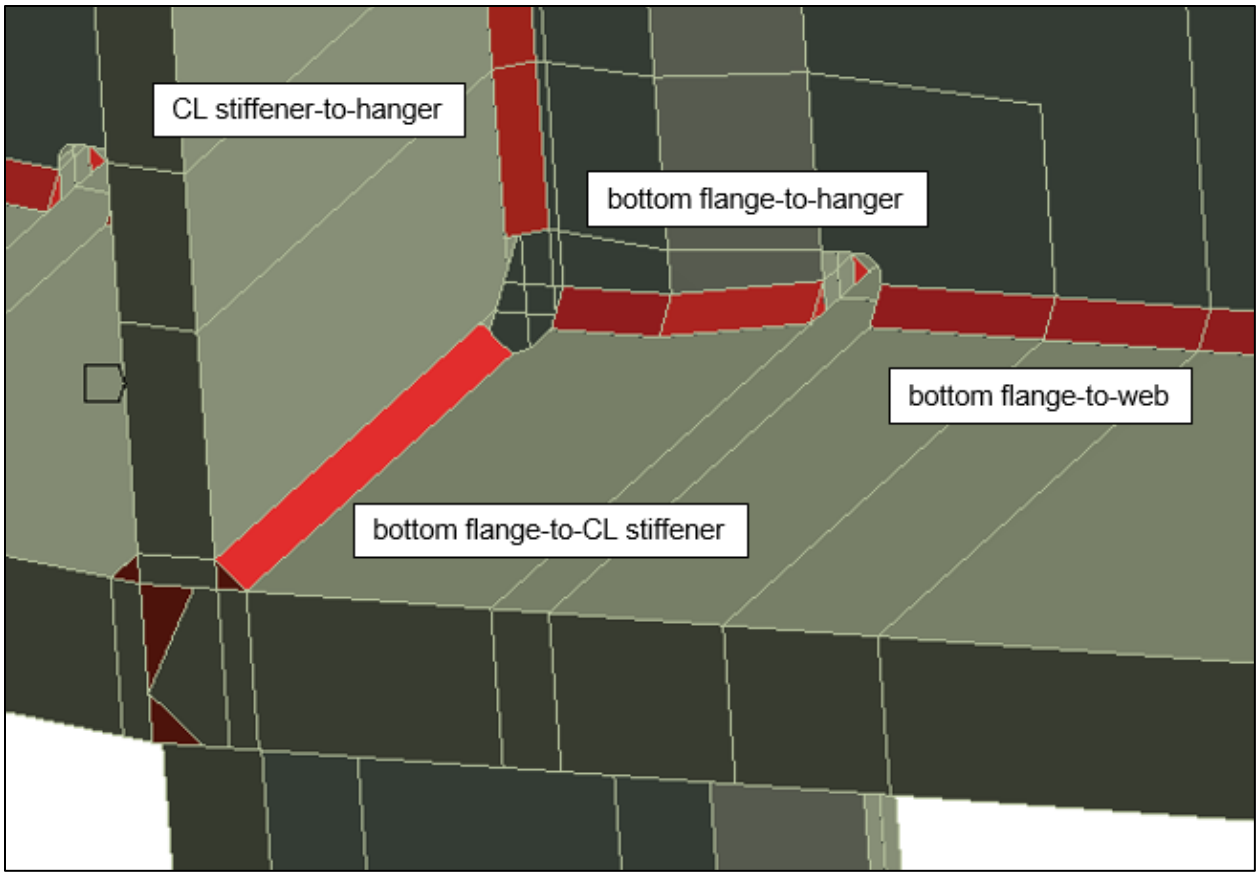

Fig. 72. Fillet welds in the region of interest near the weld access holes (3/4 in. leg length).

For the Fremont Street TPG3 girders the fillet welds were not wrapped around the hanger or the web, as shown in Fig. 73 below.

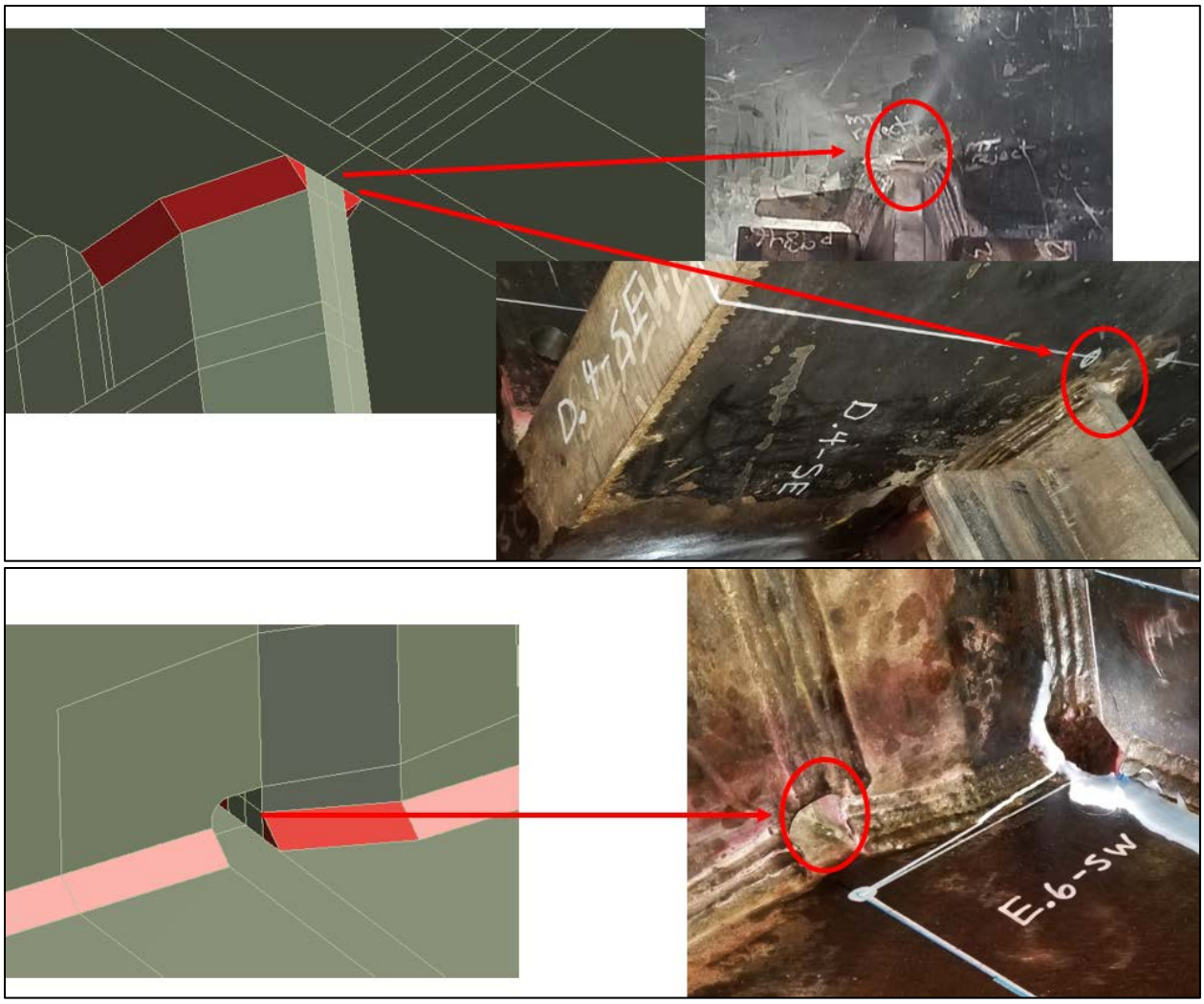

Fig. 73. Unwrapped bottom flange fillet welds of the Fremont Street TPG3 girders.

Additionally, the Fremont Street D.4 TPG3 girder CL stiffeners were offset approximately 1 in. to the west, as shown in Fig. 74 below.

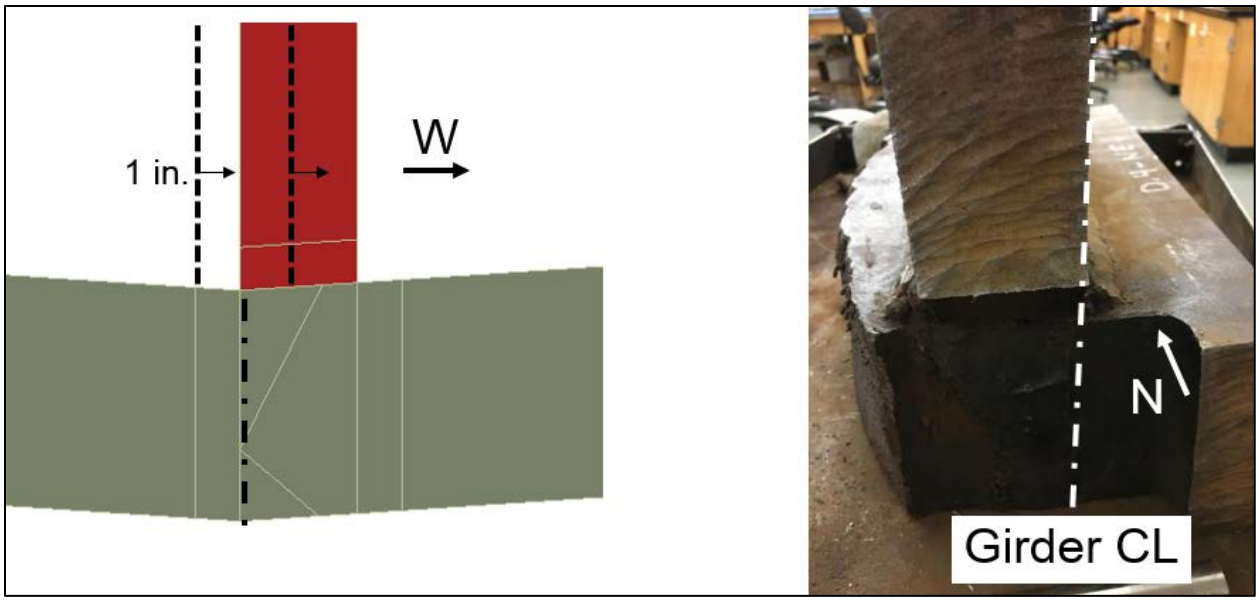

Fig. 74. CL stiffener offset 1 in. to the west of the TPG3 girder CL on the Fremont Street D.4 line

The weld access hole dimensions were measured in relation to the offset CL stiffeners by TT, with Fig. 75 displaying the overall dimensions of the access holes at the fracture origin side.

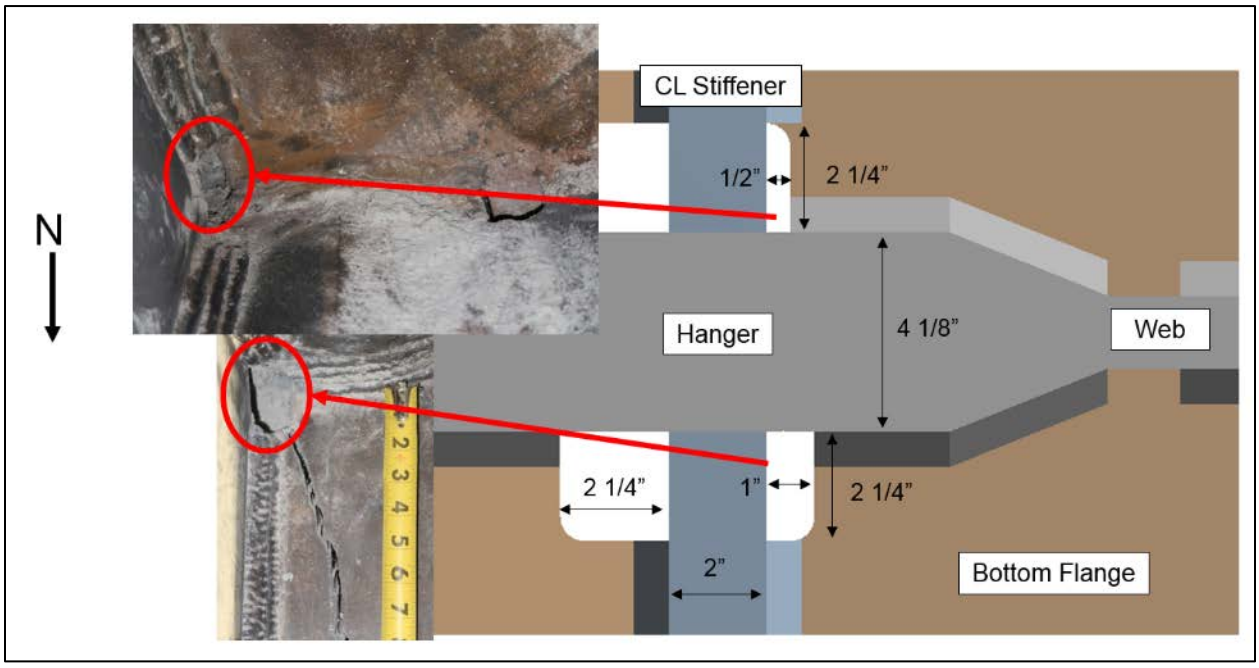

Fig. 75. Weld access hole dimensions for the TPG3 girder on the Fremont Street D.4 line. Note that Appendix D contains all relevant TPG3 girder dimensions.

4.3.1.2 Finite Element Mesh

The 3D geometric model was then discretized using the SOLID186 elements [17] such that a FE mesh could be created. The following is a summary of the meshing parameters utilized:

- Dense mesh in areas of interest
  - 0.25 in. quadratic (20-node) brick elements
  - Applied 4 in. in all directions from details of interest
- Coarser mesh for remainder of model
  - 2 in. quadratic brick elements
- Tetrahedral transition mesh
  - 0.625 in. “soft” sizing for 4 in. transition zone
- Mesh-independent results confirmed (shown in Section 5.3.1.3)
  - 2x refinement (0.125 in.) produced equivalent results

Fig. 76 shows the FE mesh density in the vicinity of the weld access holes.

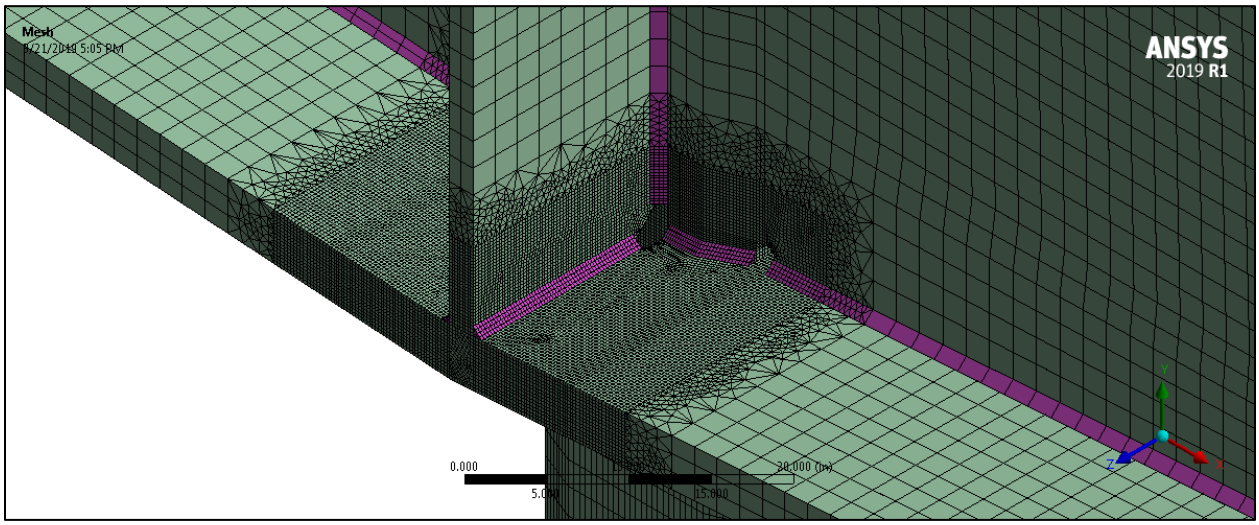

Fig. 76. FE mesh density of the TPG3 girder along the Fremont Street D.4 line.

4.3.1.3 Material Model

To represent the nonlinear material behavior of the TPG3 girder, two multilinear isotropic plasticity [17] curves were developed using the Ramberg-Osgood procedure as described in API-579 [19], one for the ASTM A572 [14] Gr. 50 structural steel plates and a second for the 70 ksi fillet weld filler metal, as shown in Fig. 77

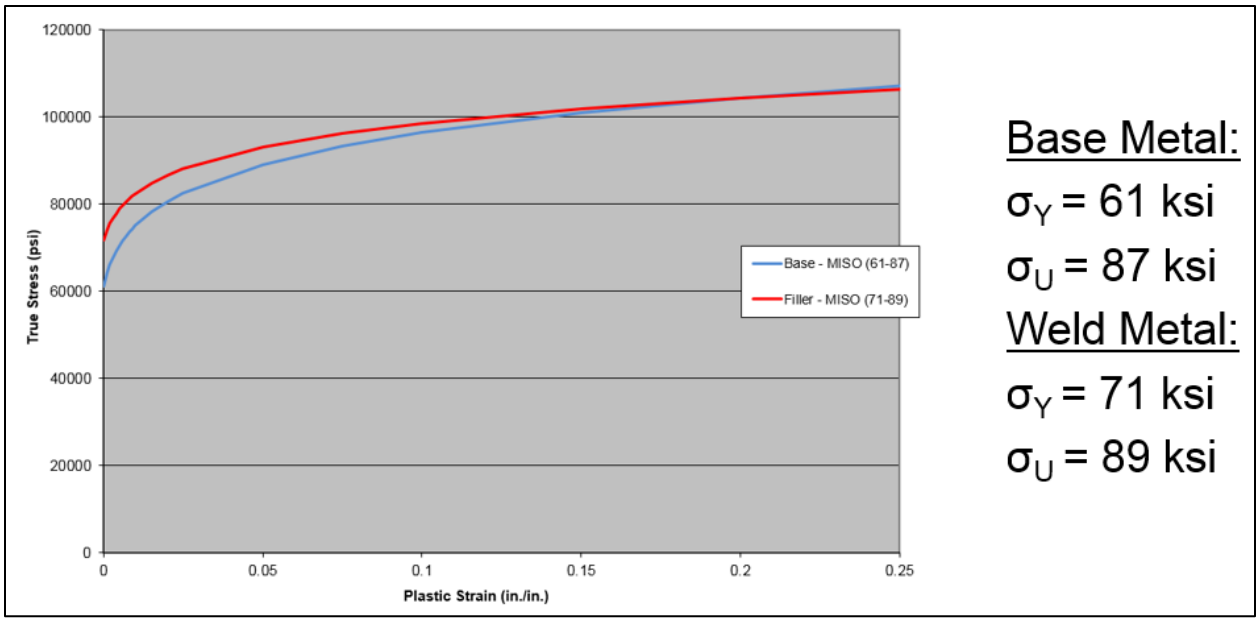

Fig. 77. Multilinear isotropic (MISO) hardening plasticity curves for the base metal and the weld metal.

The plate material curve was based on the average yield strength and ultimate tensile strength (UTS) of the 68 tensile tests performed, as described in Section 3.6.4. Similarly, the filler weld metal UTS was estimated from the 12 Rockwell B Hardness tests performed, as described in Section 3.6.5. The filler weld metal yield strength was based on Lincoln Electric data sheets [28], as specified in the Herrick WPS documents [29].

Since the concrete roof deck was only included to provide composite behavior, the density was set to approximately zero due to the effect of the roof deck weight being included in the external loads described below in Section 4.3.1.6. The concrete stiffness (E = 3604 ksi) was based on information supplied by TT [27].

4.3.1.4 Connectivity and Contact

To obtain accurate stress results in the TPG3 girder region of interest, the real load path through the welds was represented by contiguously meshing the fillet welds with the plates by node merging, as shown in Fig. 78. Bonded contact was used in the transition and coarsely meshed regions.

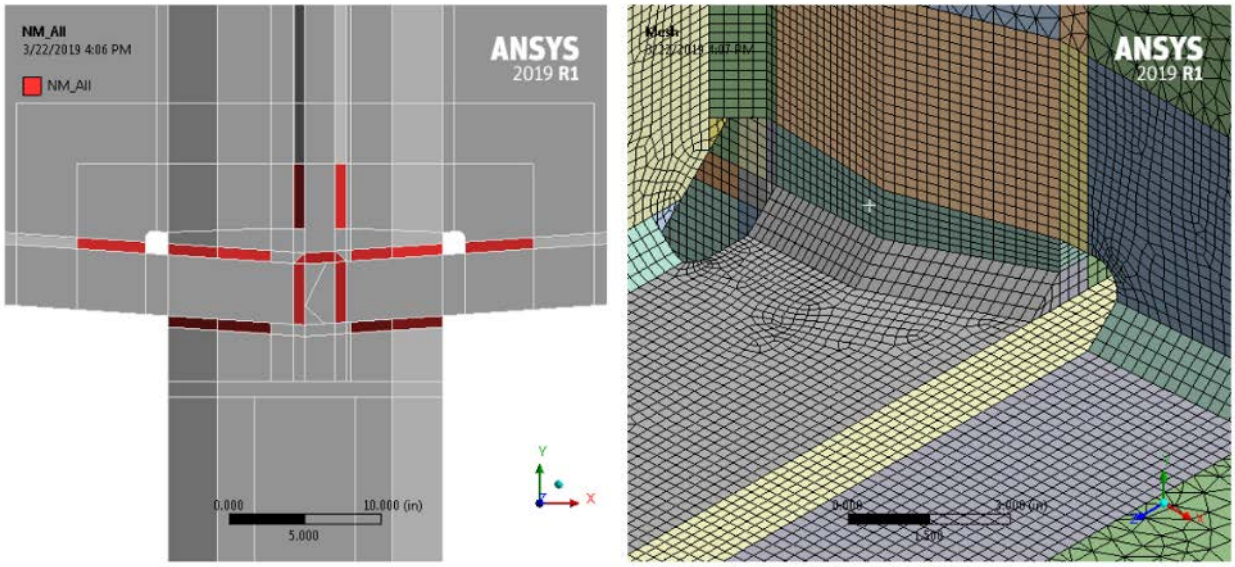

Fig. 78. Left – Weld bodies contiguously meshed via node merge with plate bodies. Right – Mesh detail showing contiguous mesh.

All faying surfaces included frictionless contact such that any bearing contact was represented in the FE model, as shown in Fig. 79.

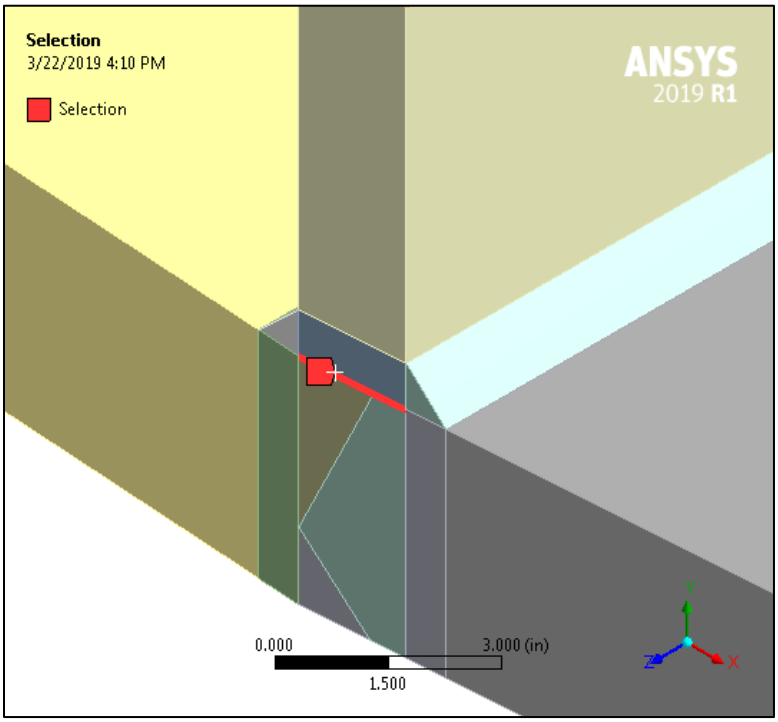

Fig. 79. Instance of frictionless faying contact shown by red-highlighted edge.

4.3.1.5 Boundary Conditions

Interaction of the TPG3 girder and the surrounding steel structure was represented in the FE model by including appropriate boundary conditions (i.e., constraints) at the connection locations. End and lateral constraint are discussed in Sections 4.3.1.5.1 and 4.3.1.5.2, respectively.

4.3.1.5.1 End Constraint

The TPG3 girders are connected to columns at each end using a shear tab with fifty-five 1.5 in. diameter Grade A490 bolts, as shown in Skanska drawing 2964AB [25]. For design, these connections would typically be treated as pinned, providing conservatism in the final stress state of the TPG3 girder. In a root cause investigation, it is necessary to obtain a more accurate representation of the end constraint for input into the FE model. Using an ETABS model, TT performed an end fixity investigation, as described in [27], and provided a calibrated torsional spring stiffness ($k\theta$ = 330,000 kip-ft/rad) for use with the pinned boundary condition at each end of the TPG3 girder FE model. This end constraint boundary condition was applied to the bolt group patch, allowing for rotation about the girder end, as shown in Fig. 80.

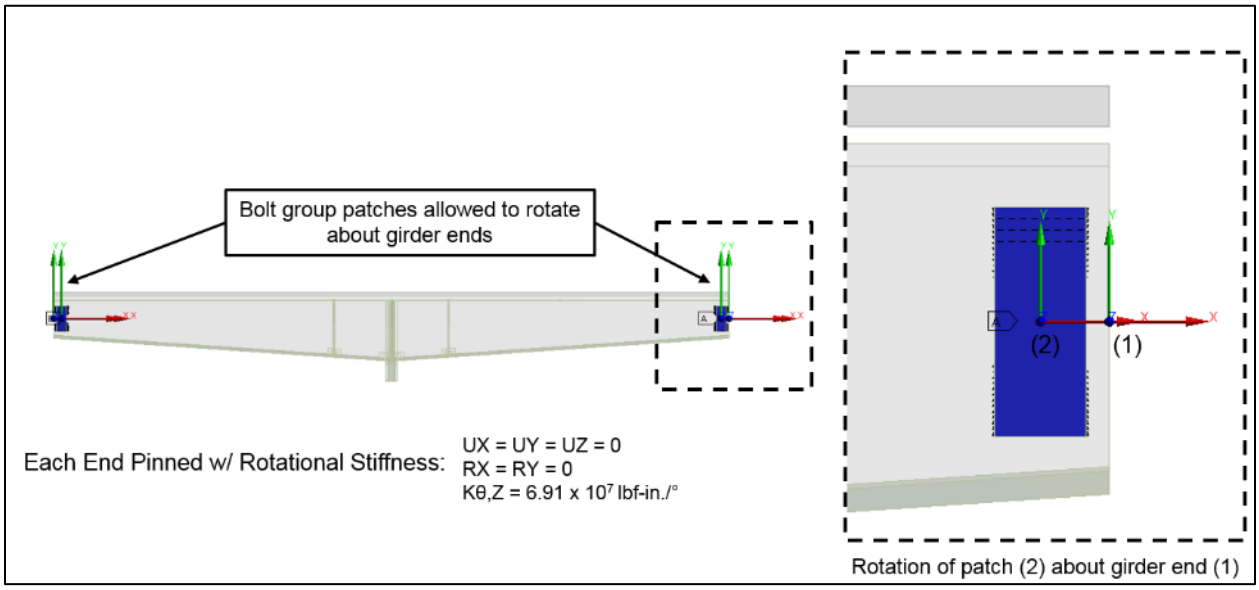

Fig. 80. End boundary conditions showing pinned connections with rotational constraint of the bolt group patches about the girder ends.

4.3.1.5.2 Lateral Constraint

In addition to the end connections, the TPG3 girder has four additional primary structural member connections, as shown in TT drawing S1-2206 [30]: a W44 x 262 steel beam at

the centerline stiffener, a W40 x 431 steel beam and a TPG2 girder at the stiffeners located approximately 7 feet from the centerline, and a W14 x 257 steel column attached to the hanger. Effective axial and bending stiffnesses for these adjoining members were calculated using standard strength-of-materials relationships [31] and are summarized in Table 7 below:

Table 7 – Equivalent Stiffness of Adjoining Structural Members

E (psi) = 29×10^6	Type	L (in.)	I (in.^{4})	A (in.^{2})	K (lb/in.)
Axial (K = AE/L)	W40 x 431	762	34,800	127	4,833,333
	W44 x 262	288	24,100	77.2	7,773,611
Bending ($K = 3EI/L^3$)	W14 x 257	171	1,290	75.6	22,445

E – elastic modulus, A – cross-sectional area,
I – 2nd area moment of inertia, L – length, K – spring stiffness

Note that the effective axial stiffness of the TPG2 girder was assumed equivalent to the W40 x 431 beam. The lateral constraint provided at these connections was included in the FE model by attaching linear springs to the individual bolt group patches, as shown in Fig. 81.

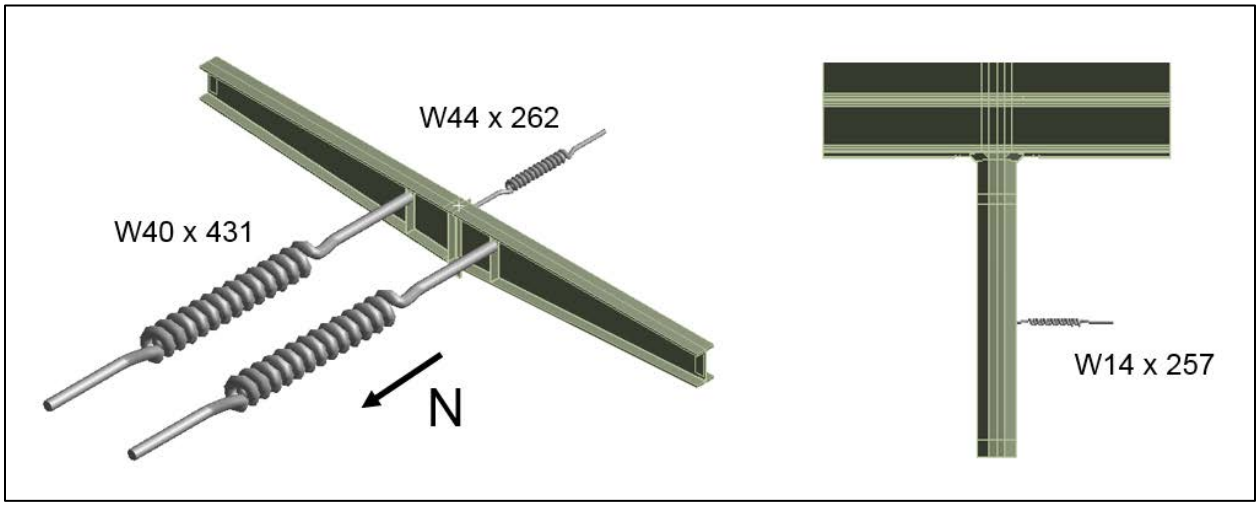

Fig. 81. Lateral constraint boundary conditions. An equivalent linear spring was attached to each respective bolt group patch.

4.3.1.6 Service Loading

Based on the Webcor construction schedule and the TJPA construction cameras, TT developed a construction timeline [26], shown in Fig. 82, such that an accurate loading history could be determined.

Date	Level	Construction Activity
09/25/2015 to 10/16/2015	Roof	TPG3 girders and neighboring frames at the roof level were erected and then covered by a metal deck.
03/25/2016	Bus Deck	A 10" thick slab was placed on the metal deck at the bus deck level. At this point, since the roof slab was not in place yet, all the loads applied to TPG3 girders from the Bus deck level were supported by the bare steel section. These are referred to as “pre-composite” loads.
04/04/2016	Roof	The roof level concrete slab was placed over the metal deck. All the loads applied to TPG3 girders after this point in time are referred to as “post-composite” loads.
04/26/2016	Bus Deck	An additional 4" thick concrete slab was placed at the bus deck level.
05/16/2016	Roof	Interior walls/curbs were placed at the roof level on May 16, 2016.
07/01/2016 to 03/24/2017	Bus Deck	Construction of various parts of the ridge/built-up slab, drive aisle topping slab, interior topping slab and central island topping slab at the bus deck level.
		Spray-on fireproofing was applied at the bus deck level. Fireproofing around TPG3 girders was applied in the first week of August 2016 (see photos at the end of Appendix A1).
	Roof	Pour/strip the roof deck (08/31/2016 to 09/01/2016).
		Spray on fireproofing at roof buildings (07/07/2016 to 09/24/2016).
02/13/2017 to 06/29/2017	Roof	Placement of the roof protection slab (i.e. architectural topping slab).
06/29/2017 to 06/14/2018	Roof	Placement of trees/palms, concrete sub-slabs and completion of grading at roof level.

Fig. 82. Construction timeline per TT report [26]

TT then created a loading summary that included both pre-composite loads (those that occurred prior to the roof deck concrete being poured) and post-composite loads as shown below:

- Weights of construction, pre-composite:
  - Weight of TPG3 girders and other Roof steel framing members
  - Weight of Bus-Deck floor steel framing and hangers
  - Weight of 10-in. slab (7-in. NWC + 3-in. metal deck) at Bus-Deck level
  - Weight of 10-in. slab (7-in. NWC + 3-in. metal deck) at Roof level
- Weights of construction, post-composite:
  - Weight of 4-in. concrete structural topping at Bus-Deck level
  - Weight of Architectural toppings at Bus-Deck level
  - Weight of protection slab and drainage topping at Roof level
  - Weights of soil, tree and other landscape items at Roof level
  - MEP loads at Roof level

- Weight of penthouse structure

From this investigation, TT developed the following load sequence up until Fremont Street girder bottom flange fracture initiation:

1. Pre-composite dead load (DL) only
2. Post-composite superimposed dead load (SDL) + DL
3. Post-composite live load (LL) + SDL + DL

The unfactored loading for each of the three load sequences was supplied by TT, as described in detail in their report [26]. To account for post-composite load sharing with the surrounding structure, a 90% scaling factor was applied to the unfactored SDL and LL [27]. Load application locations are shown in Fig. 83, where the roof deck pressure was applied to the top flange area and the external member forces were applied to each respective bolt group patch. Note that a gravitational load was included to account for the self-weight of the TPG3 girder.

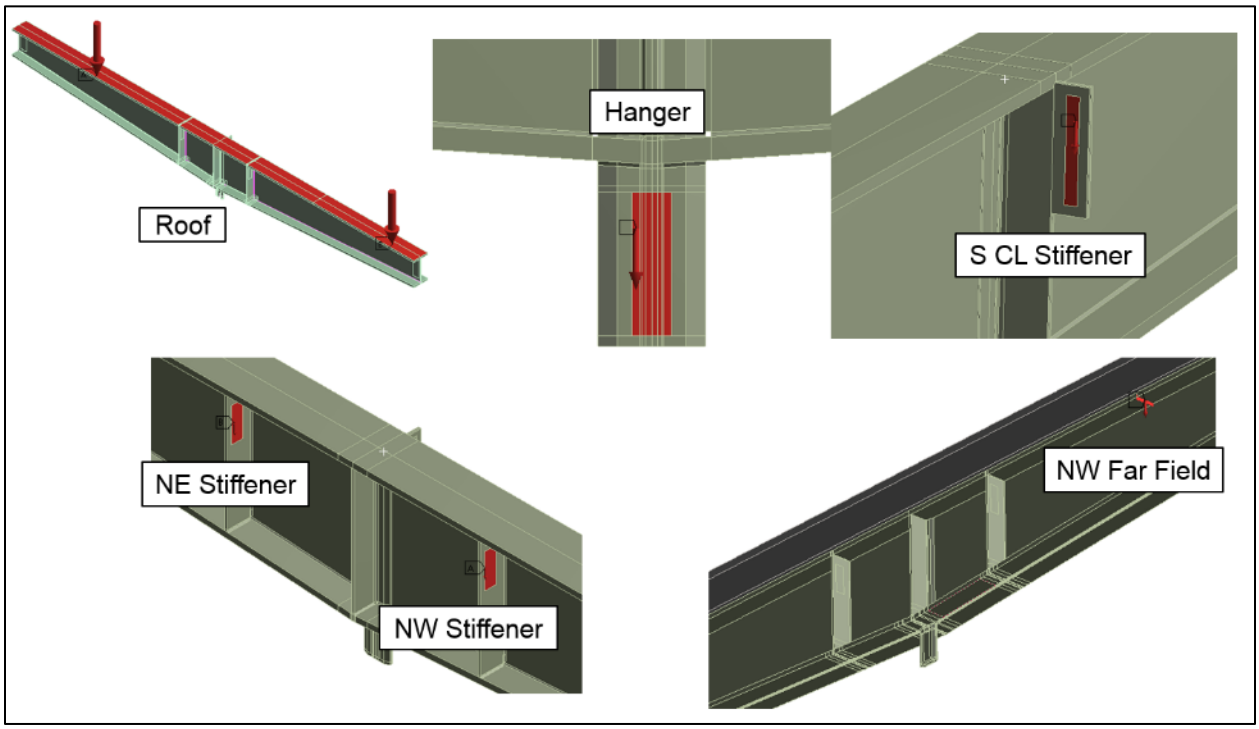

Fig. 83. External loading locations within the FE model. All forces applied through respective bolt group patches (except for NW far field load which was applied directly to the girder top flange). The roof deck pressures were applied to the top flange area.

Table 8 summarizes the total load applied at each detail shown in Fig. 83 for the three load sequences analyzed:

Table 8 – Total Applied Loading at each Load Sequence - Fremont Street D.4 TPG3 Girder

	Pressure (psi)		Forces (lb)				
	Roof - East	Roof - West	Hanger	S CL Stiffener	NW Stiffener	NW Far Field	NE Stiffener
LS 1: DL	1.32	1.32	162,000	76,000	138,000	46,000	106,000
LS 2: DL + SDL	4.30	4.30	411,300	221,800	372,000	52,300	404,800
LS 3: DL + SDL + LL	4.74	4.74	484,200	239,800	402,600	60,400	436,300

4.3.1.7 Solution Settings

All FE simulations performed were nonlinear, including the effects of large deformation using the NLGEOM command within ANSYS, changing contact status as described in Section 4.3.1.4, and material plasticity, as described in Section 4.3.1.3. Also note that the FE simulations included concrete roof deck element birth and death (i.e., adding or removing elements during sequential solutions) such that both pre- and post-composite behavior could be examined using the load sequence described above in Section 4.3.1.6.

4.3.1.8 FE Model Validation – Fracture Face Opening Results

Validation of both the FE model and the external loading at the time of D.4 bottom flange fracture was performed by including both the northwest and southwest fractures in a modified FE model, shown in Fig. 84.

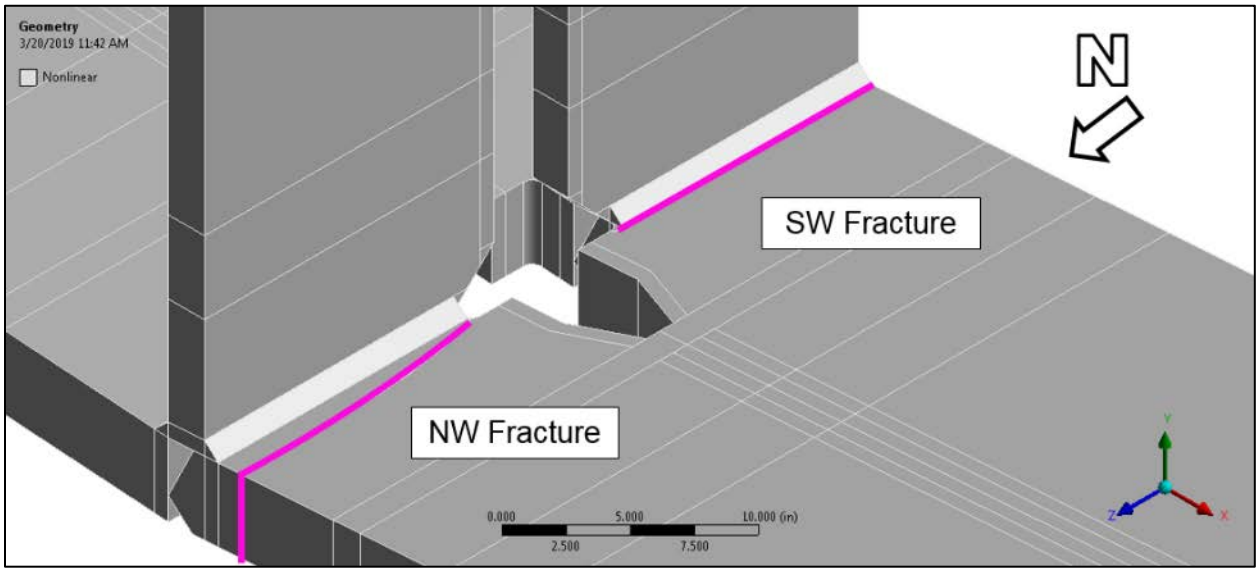

Fig. 84. Fremont Street D.4 FE model with both the NW and SW fractures included (highlighted in purple). Note that only the bottom flange, CL stiffeners, and welds are shown.

The proposed loads present at D.4 bottom flange fracture initiation (load sequence 3 as shown in Table 8) were applied to the FE model such that the calculated fracture face openings could be compared to the measurements made by TT. Fig. 85 below provides a comparison between the measured and calculated northwest fracture opening on the top surface of the bottom flange.

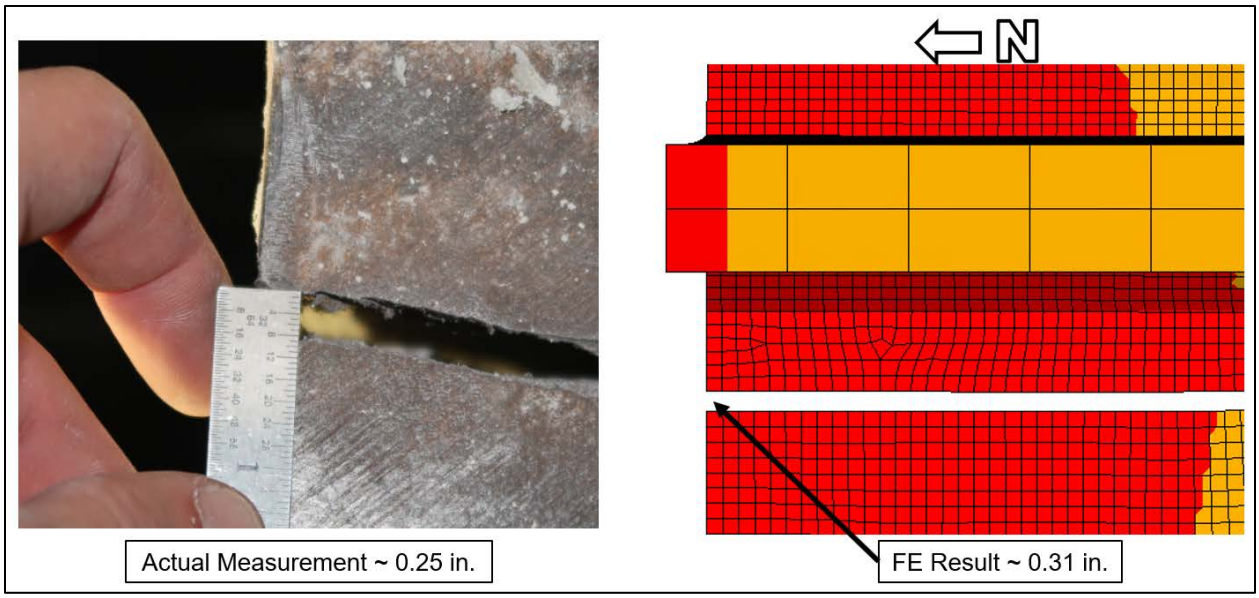

Fig. 85. Fremont Street D.4 crack opening comparison between the measured crack opening and the FE crack opening results – NW fracture at 1.0(DL+SDL) + 1.0(LL).

Similarly, the crack opening of the southwest fracture is compared in Fig. 86 below:

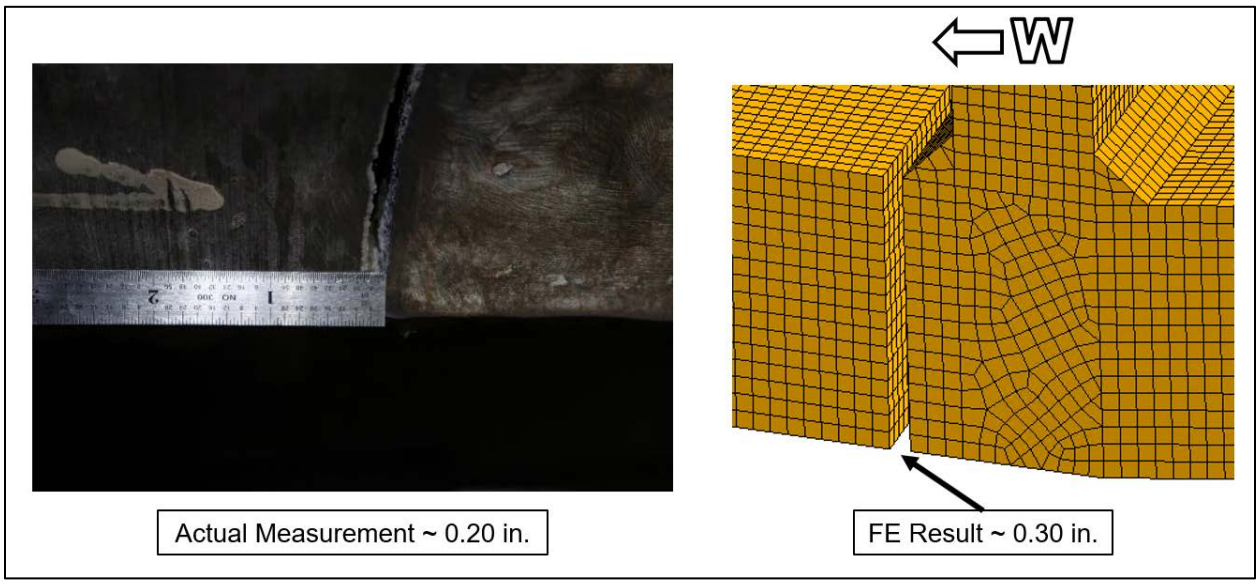

Fig. 86. Fremont Street D.4 crack opening comparison between the measured crack opening and the FE crack opening results – SW fracture at 1.0(DL+SDL) + 1.0(LL).

FE results of the calculated crack openings correlate very well with the crack opening measurements performed by TT, indicating that the external loads described in Section 4.3.1.6, in combination with the FE model built here, accurately represent the stress state at the time of D.4 bottom flange fracture initiation.

To provide further validation, a sensitivity analysis of fracture opening to applied external load was performed using the load cases described in Table 9.

Table 9 − Total Applied Load – Fracture Opening Sensitivity Analyses

Load Case	Description	Total External Load (kips)
1	10% of fracture loads	180
2	Fracture loads (DL + SDL + LL)	1802
3	1.25x fracture loads	2252
4	1.5x fracture loads	2703
5	1.75x fracture loads	3153

Note: TPG3 girder self-weight of 122 kips was included in all cases

Results of the crack opening sensitivity analysis further corroborate the conclusion that the FE analyses performed provide an accurate estimate of the stress state within the TPG3 girder, as the crack opening versus applied load plot in Fig. 87 displays. The

calculated crack openings do not match the measured values for large deviations in the external load applied.

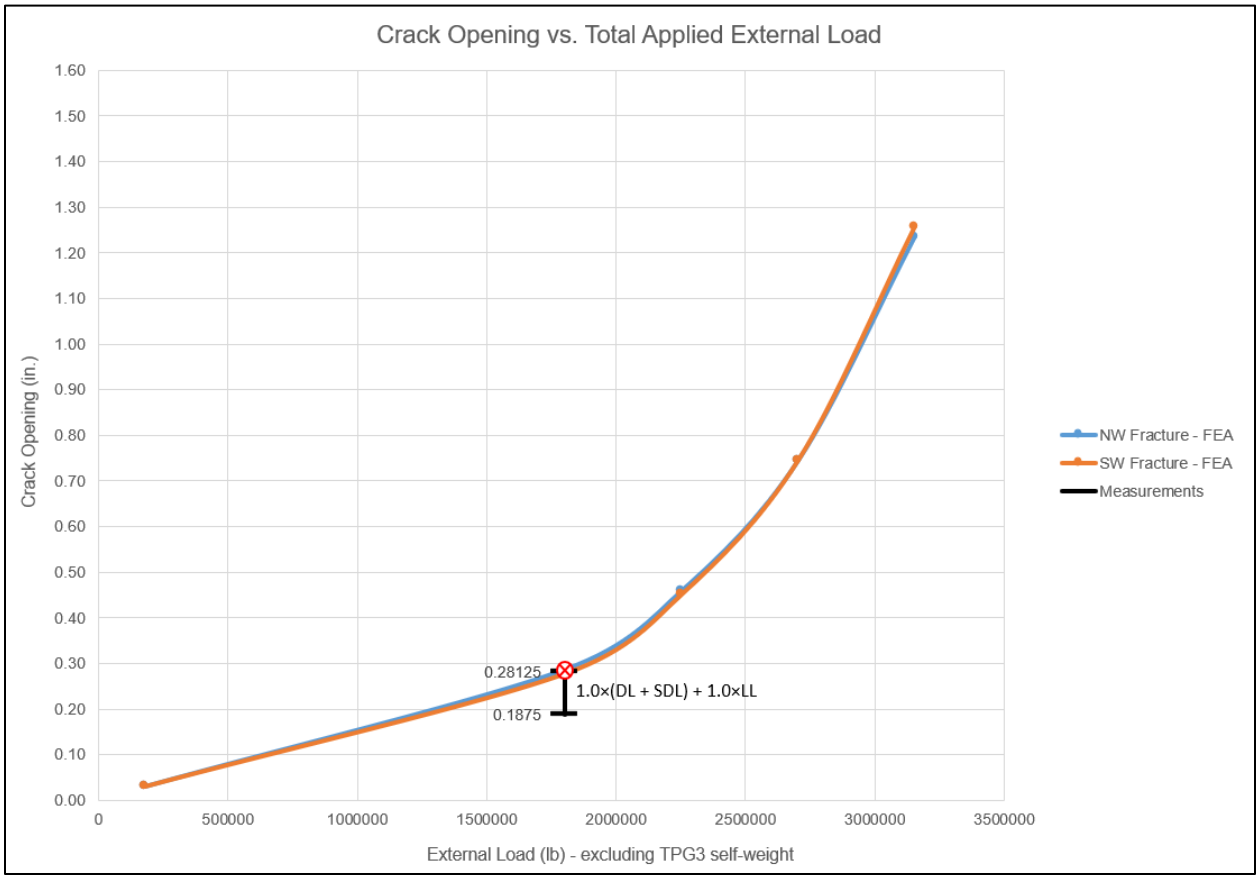

Fig. 87. Fremont Street D.4 crack opening sensitivity to total applied load.

4.3.1.9 FE Results

Bottom flange access hole FE results for the loads at the time of D.4 fracture (load sequence 3 from Table 8) were generated such that through-thickness stress profiles could be developed for input into the fracture mechanics calculations given in Section 4.3.2.

To develop an overall understanding of the TPG3 girder behavior at the time of bottom flange fracture initiation, total strain near the weld access holes was reviewed, as shown in Fig. 88.

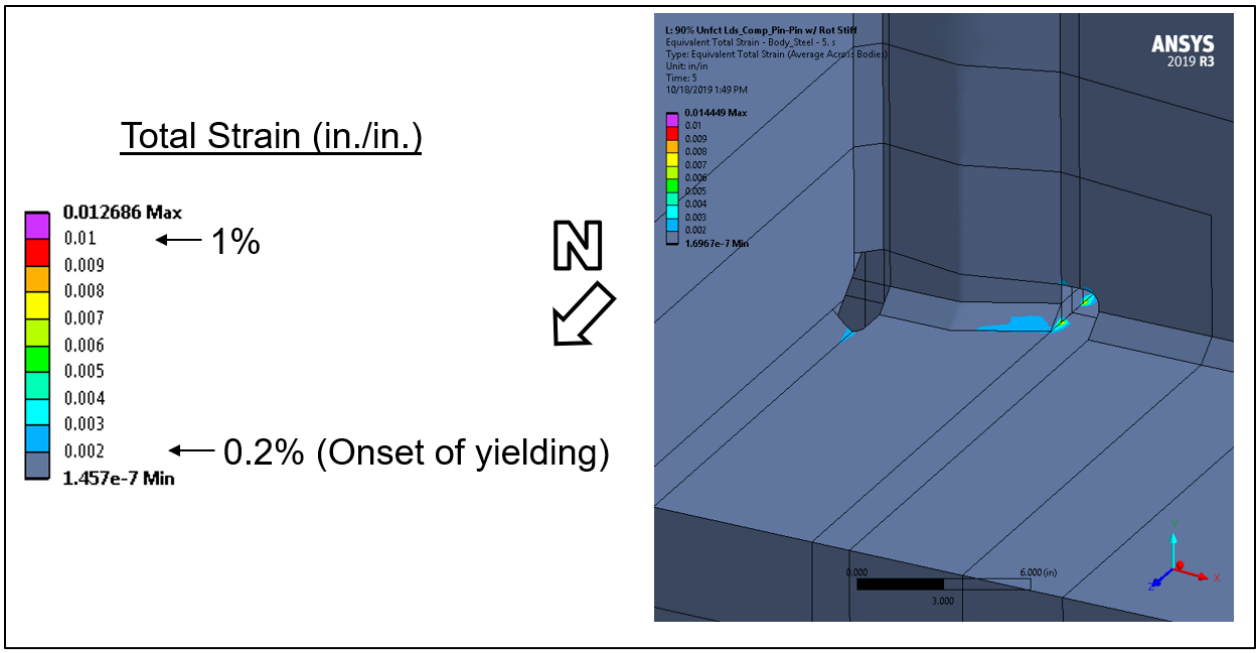

Fig. 88. Total strain (in./in.) near the NW weld access hole indicating only localized areas at fillet weld toes exceeded the material yield strength (grey is below yield) at 1.0(DL+SDL) + 1.0(LL).

As typically occurs in structural steel design, the total strain contour plot (Fig. 88) demonstrates that a majority of the TPG3 girder behaved in an elastic manner, with only minimal localized yielding in regions of higher stress concentration near the fillet weld toes (grey indicates strain in the elastic regime).

Brittle fracture is driven by local tensile stresses; therefore, the most critical component of stress is the maximum principal stress. An overall view of the maximum principal stress in the TPG3 girder hanger region demonstrates only localized areas exhibiting tensile stresses above the material yield strength, as shown in Fig. 89.

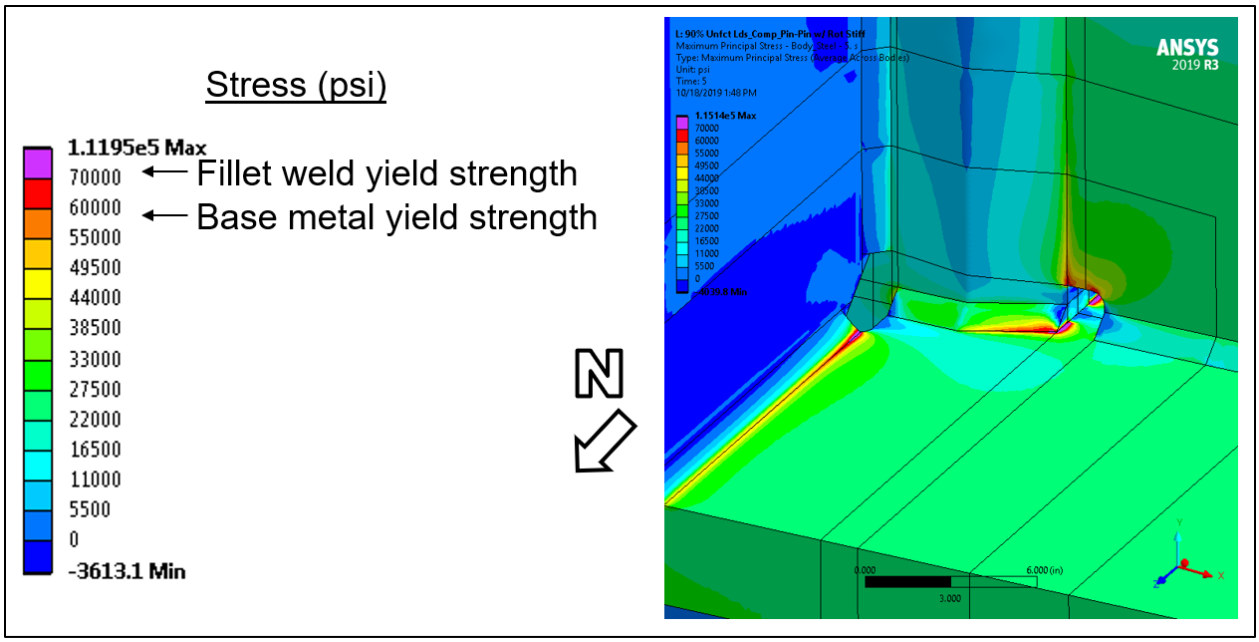

Fig. 89. Maximum principal stress (psi) near the NW weld access hole indicating only localized areas experienced tensile stresses that exceeded the material yield strength at 1.0(DL+SDL) +1.0(LL).

Additional Fremont Street D.4 FE results for all load sequences are given in Appendix G.

4.3.1.9.1 Weld Access Hole Stress and Strain

Since bottom flange fracture initiated at the mid-thickness of the weld access hole radius surface, these regions were further evaluated. Fig. 90 shows total strain in the D.4 north bottom flange weld access hole, which demonstrates minimal localized yielding in the region of fracture initiation.

The corresponding maximum principal stress in the D.4 north bottom flange weld access hole is shown in Fig. 91. As shown, the northwest fracture initiated in a region of elevated stress due to the stress concentrating effect of the weld access hole geometry.

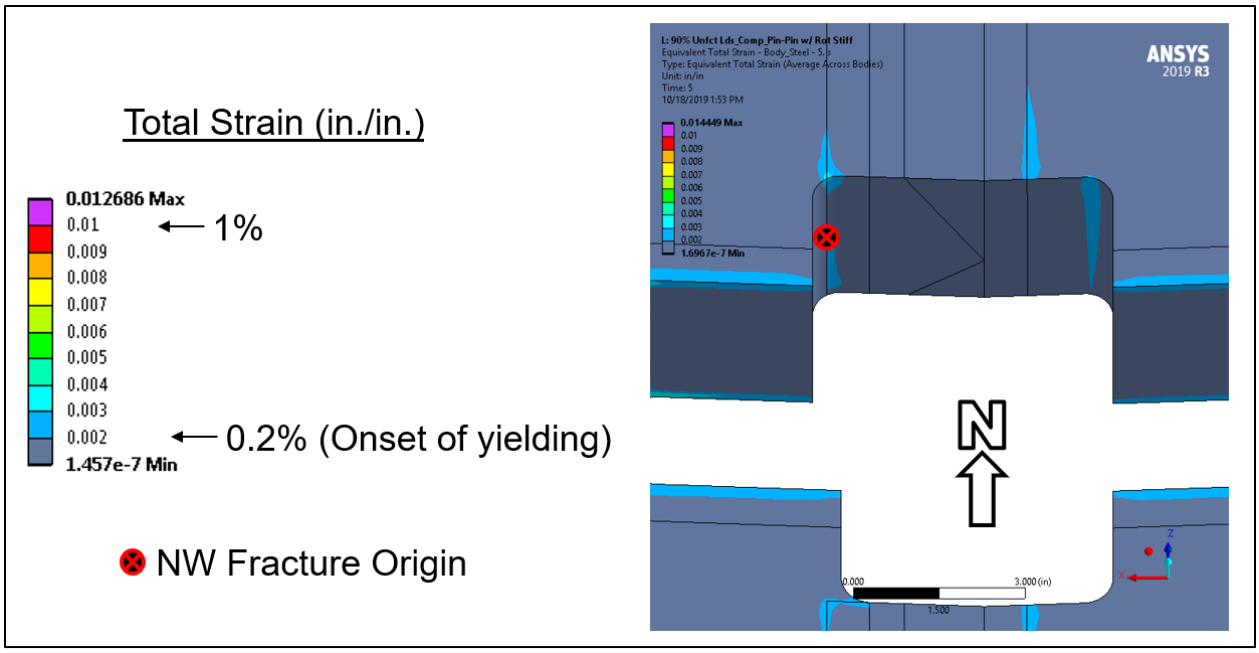

Fig. 90. D.4 north bottom flange weld access hole total strain (in./in.) with the NW fracture origin highlighted (red circle) at loading corresponding to 1.0(DL+SDL) + 1.0(LL). Contour plot is at an angled view looking into the access hole with the hanger removed.

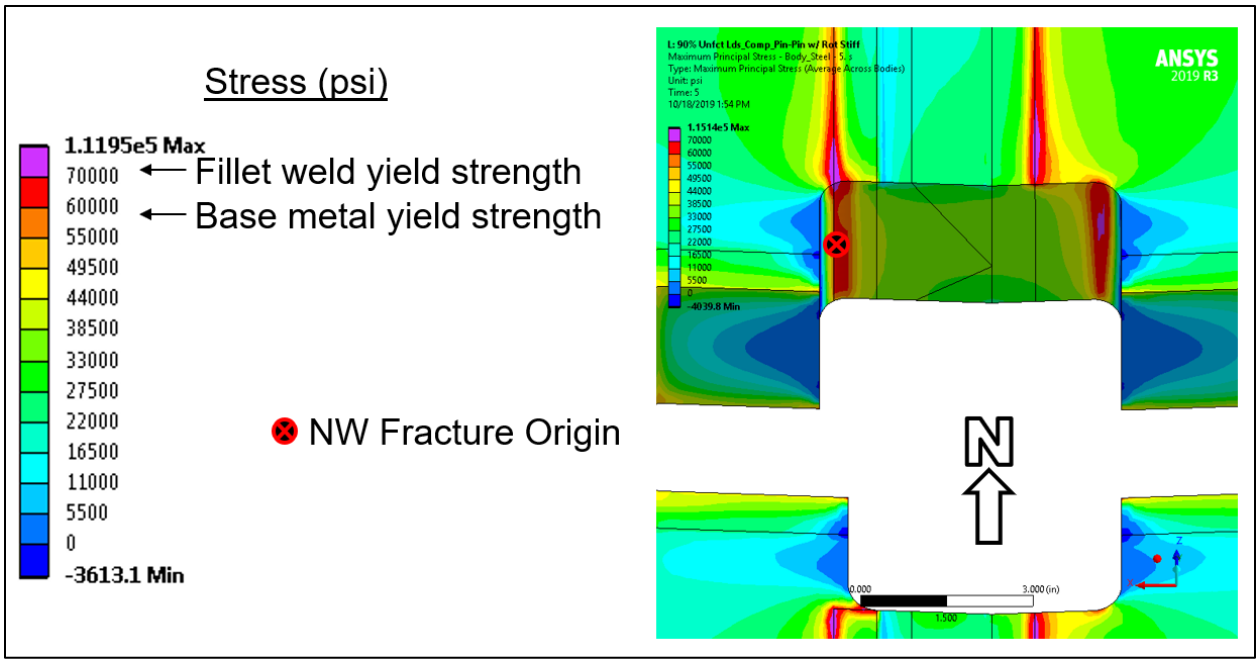

Fig. 91. D.4 north bottom flange weld access hole maximum principal stress (psi) with the NW fracture origin highlighted at 1.0(DL+SDL) + 1.0(LL). Contour plot is at an angled view looking into the access hole with the hanger removed.

Similar to the northwest bottom flange weld access hole, Fig. 92 shows a total strain contour plot of the south bottom flange access hole, looking towards the southwest fracture origin.

As noted for the D.4 north bottom flange weld access hole, the D.4 south bottom flange access hole sustained limited, localized yielding at the time of fracture.

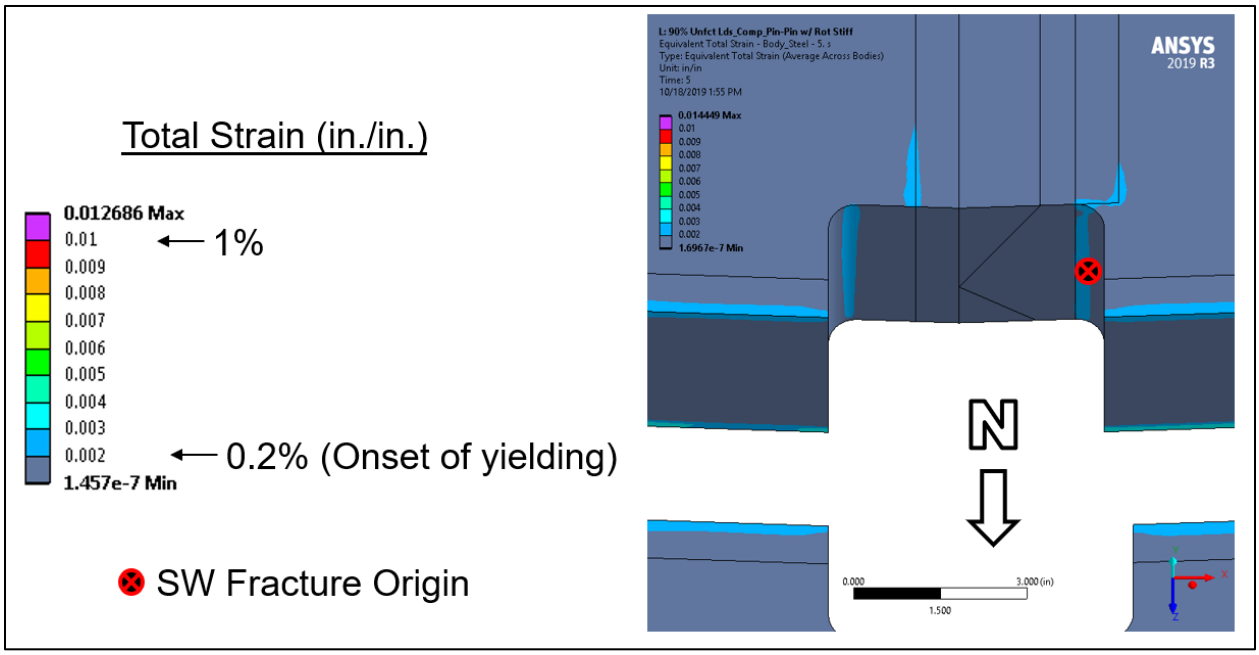

Fig. 92. South bottom flange weld access hole total strain (in./in.) with the SW fracture origin highlighted at 1.0(DL+SDL) + 1.0(LL). Contour plot is at an angled view looking into the access hole with the hanger removed.

The corresponding maximum principal stress for the south bottom flange weld access is shown in Fig. 93 for the same region. Similar to the northwest fracture, the southwest fracture also initiated (red circle, Fig. 93) in a region of stress concentration due to the weld access hole geometry.

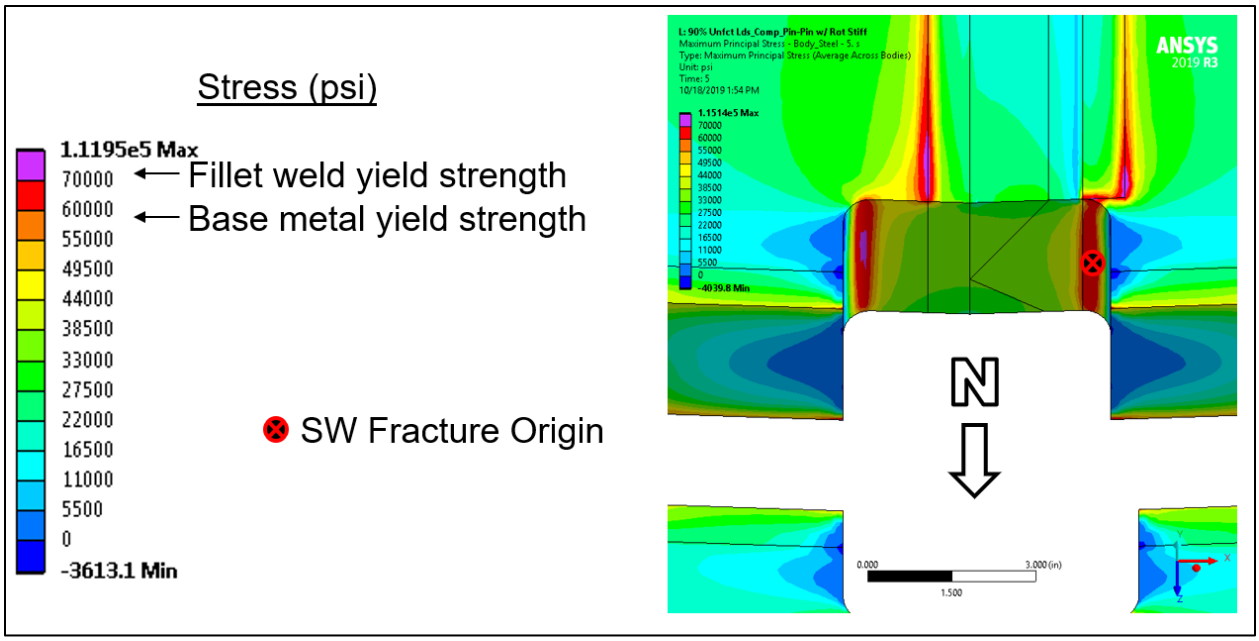

Fig. 93. South bottom flange weld access hole maximum principal stress (psi) with the SW fracture origin highlighted at 1.0(DL+SDL) + 1.0(LL). Contour plot is at an angled view looking into the access hole with the hanger removed.

4.3.1.9.2 Fracture Path Stress Profiles

As shown in Section 4.3.1.9.1, the Fremont Street D.4 TPG3 girder fractures initiated in areas of local stress concentration. However, this local stress elevation at the access holes decreased rapidly to the nominal flange stress a short distance away from the access hole radius.

Therefore, in order to properly characterize the flange fracture stress needed in the fracture mechanics assessment of Section 4.3.2, it was necessary to output the maximum principal stress along a path that originated at the pop-in crack fracture origin and extended to the flange edge (i.e., the fracture path), as shown in Fig. 94, for both the northwest and southwest fractures. The maximum principal stress results along these paths are shown in Fig. 95.

The stresses along the paths attain the nominal flange stress approximately 2 in. from the weld access holes and, as such, the Fig. 95 plot is truncated for clarity near the microcrack and the pop-in crack initiation sites (shown on the plot as dotted vertical lines). As shown, the maximum principal stress at the weld access hole surface is in the range of 45 to 55 ksi, which then rapidly decreases to bottom flange mid-thickness nominal stress of about 30 ksi.

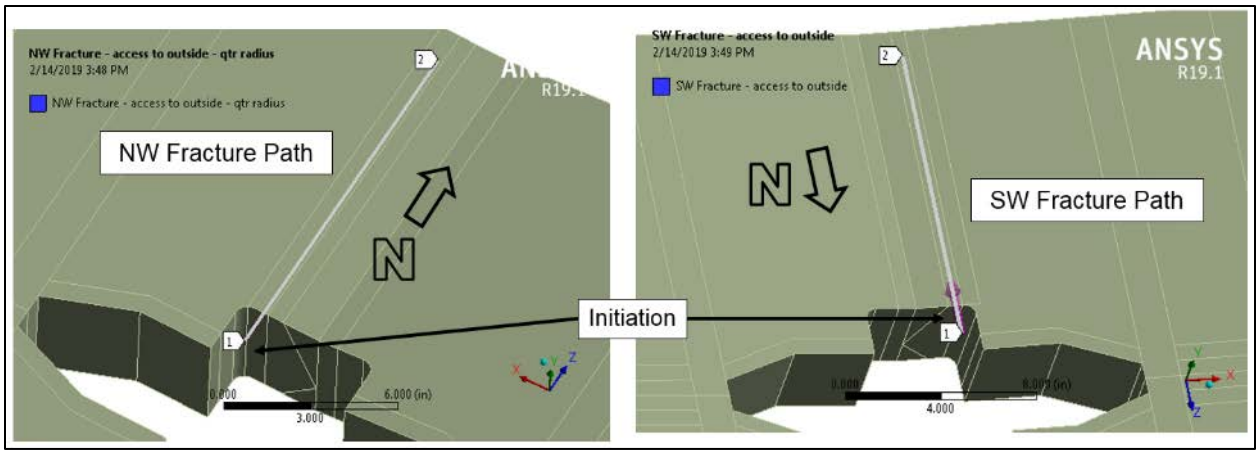

Fig. 94. Stress paths through the mid-thickness of the bottom flange originating at the NW and SW weld access hole fracture initiation sites.

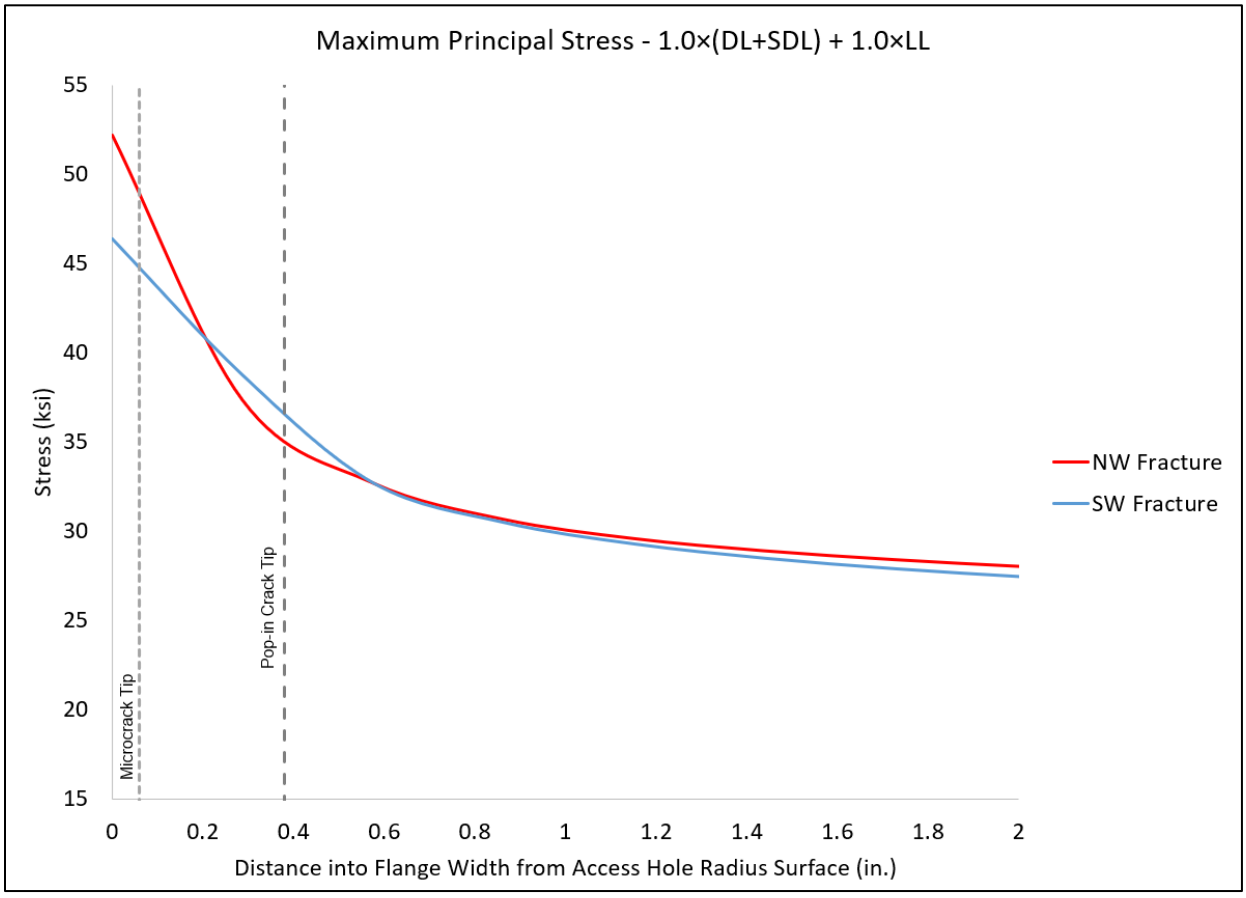

Fig. 95. Maximum principal stress along the NW and SW fracture paths (shown in Fig. 94). The relative locations on the microcrack and pop-in crack tips are identified by dashed vertical lines.

4.3.2 Fracture Mechanics Calculations

As discussed in Section 4.3.1.9, service-induced girder flange stresses were calculated for the regions that contained the fractures using the FE method. To facilitate the fracture mechanics calculations, the stress profiles along the northwest and southwest fracture paths were normalized with respect to the flange width and are given in Fig. 96. Then 4th order polynomials were fit to these profiles for use in the closed-form fracture mechanics calculations using Eq.'s (4) and (5). It should be noted that the 4th order fit is currently the most accurate method for representing the stress distribution imposed on a crack, other than embedding a crack in an FE model and calculating stress intensity factor (K_1) solutions directly from the FE generated stress distribution. However, FE-based solutions for K are time consuming and are generally used to validate complicated closed-form analyses or analyses that involve significant plasticity and require J-integral solutions.

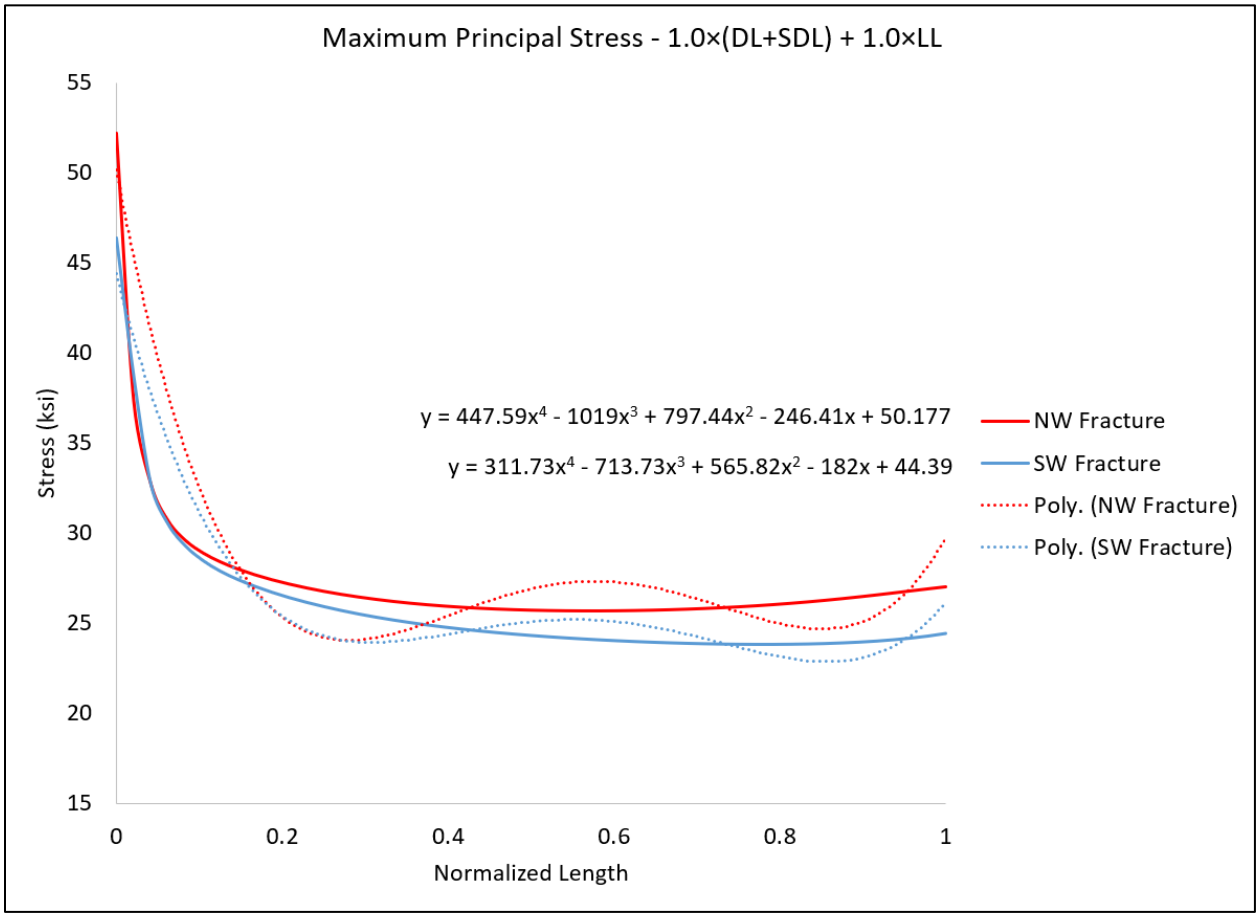

Fig. 96. Flange maximum principal stress along the normalized fracture paths from the weld access holes (0) to the flange edges (1) (see Fig. 94) with the 4th order polynomial fit shown (dashed lines).

At the bottom flange mid-thickness, the static fracture toughness was approximately 55-60 ksivin., per Section 4.1. Initially assuming only service induced stresses given in Fig. 96, that is, no residual stresses were acting at the time of flange fracture on the pre-existing 0.38 in. deep (a) x 1.2 in. long (2c) pop-in crack, gives the FAD results shown in Fig. 97.

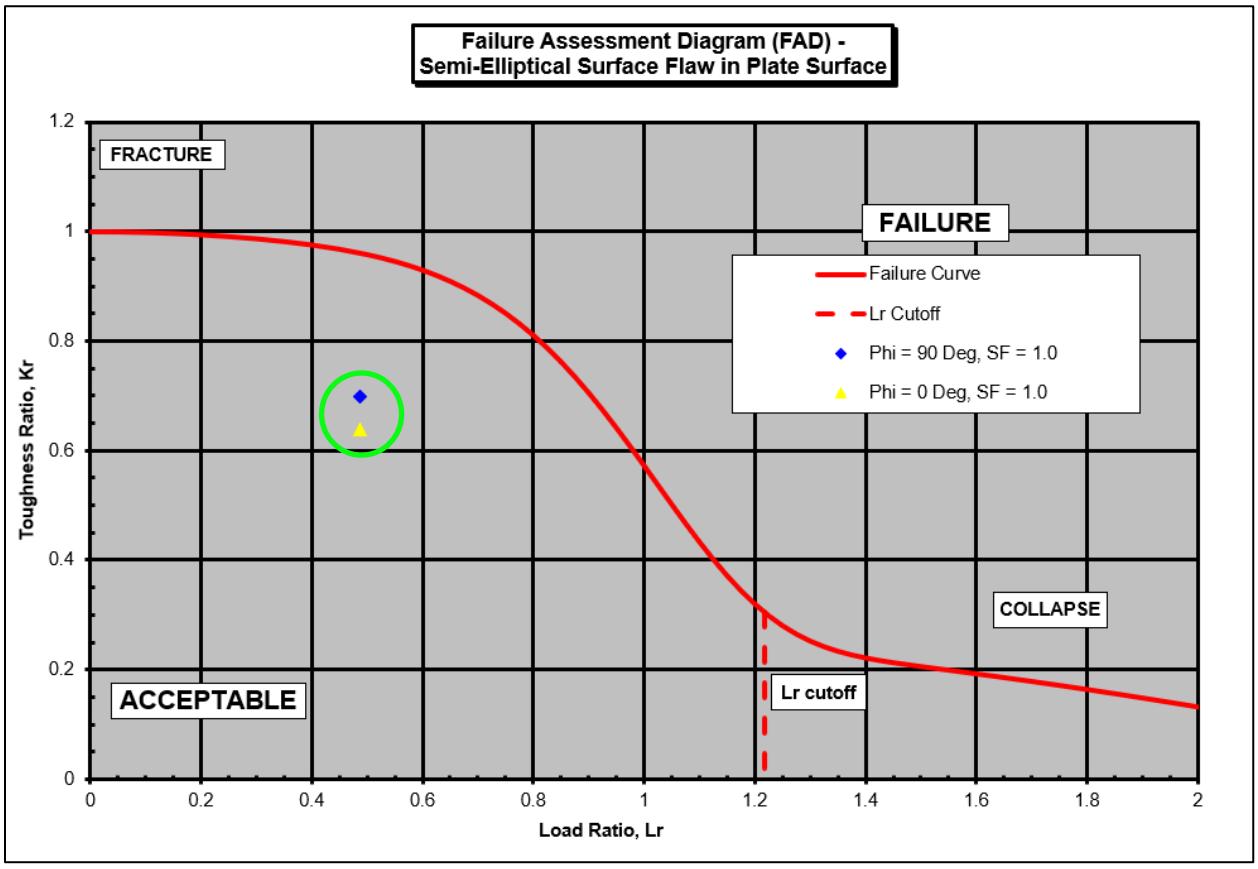

Fig. 97. FAD assessment points, circled in green, due to service stresses only at a fracture toughness of approximately 55 to 60 ksivin.

It is clear from these FAD calculations (green circle), that the D.4 bottom flange fracture would not have initiated from the pop-in crack under service stresses alone. As such, a stress intensity factor (K_1) contribution due to the CJP groove weld-induced residual stresses was required to initiate the bottom flange fractures. The residual stress contribution necessary to initiate the fracture can be determined by incrementally increasing the residual stress K_1 component of the FAD analysis until fracture is indicated by an assessment point landing on the FAD curve shown in Fig. 97. Accordingly, the minimum additional residual stress-induced K_1 necessary to initiate the D.4 bottom flange fracture was in the range of approximately 19 to 22 ksivin., as shown in Fig. 98 (purple circle), which includes both service and residual stresses contributions to K_1.

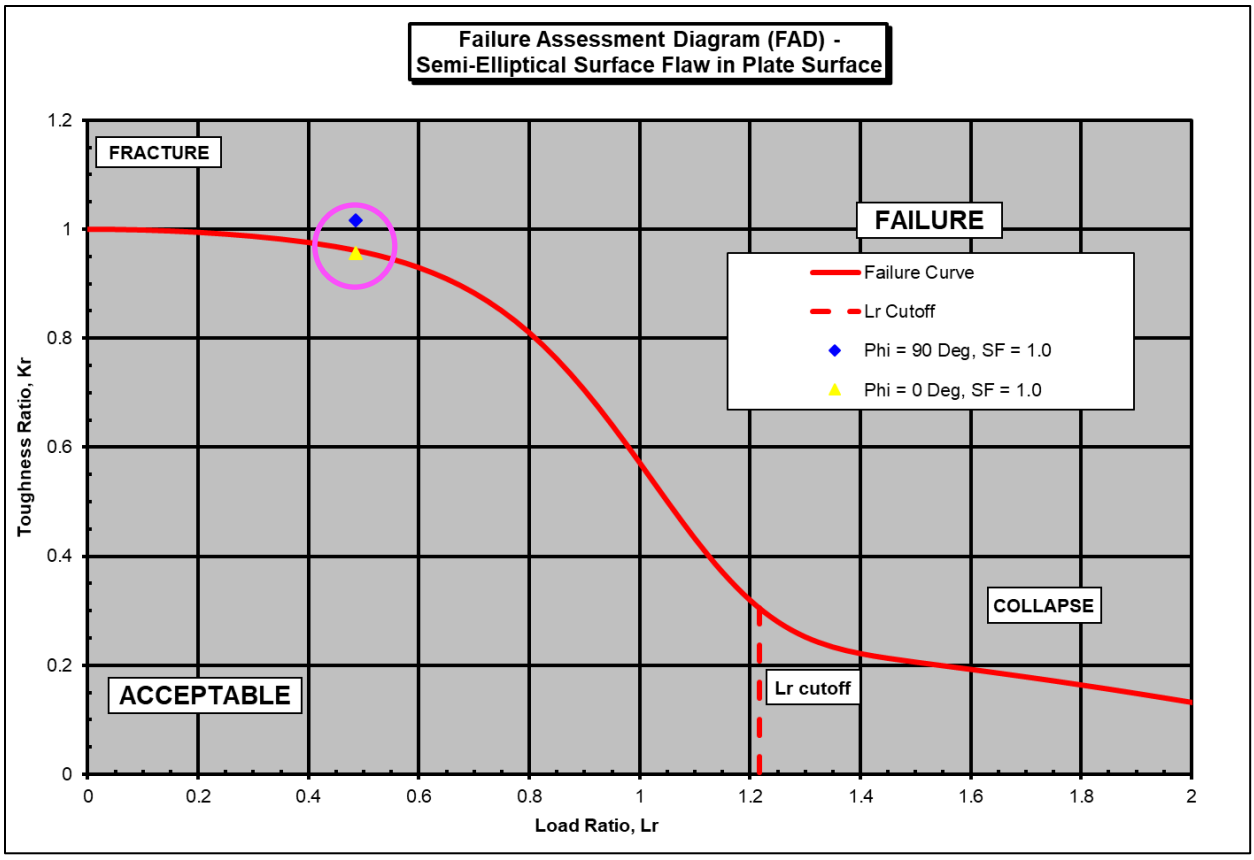

Fig. 98. FAD assessment points, circled in purple, due to service stresses and an additional stress intensity factor due to residual stresses at a fracture toughness of approximately 55 to 60 ksi√in.

A summary of the FAD results is given in Table 10.

Table 10 – Bottom Flange Fracture Initiation FAD Summary

	Peak Stress (ksi)	K_1 (ksi√in.)	K_{1C} (ksi√in.)	FAD Failure (Y/N)
Service Stress Only	50.2	42.0	60	N
Residual Stress Only	25.0	19.0		N
Combined Stresses	75.2	61.0		Y

K_{1C} – fracture toughness, K_1 – stress intensity factor

To assess the effect of applied LL on the service load K_1 and the subsequent residual stress necessary to cause fracture, a sensitivity analysis was performed using the load cases described in Table 11.

Table 11 – LL Applied – Stress Intensity Factor Sensitivity Analysis

Load Case	Description	Live Load (kips)
1	0.0xLL	0
2	1.0xLL	178
3	2.0xLL	355
4	3.0xLL	533
5	4.0xLL	710

Note: DL + SDL = 1624 kips, TPG3 girder self-weight = 122 kips

From these FE analyses the stress profiles along the northwest fracture were output, as shown in Fig. 99, and were used in subsequent fracture mechanics calculations.

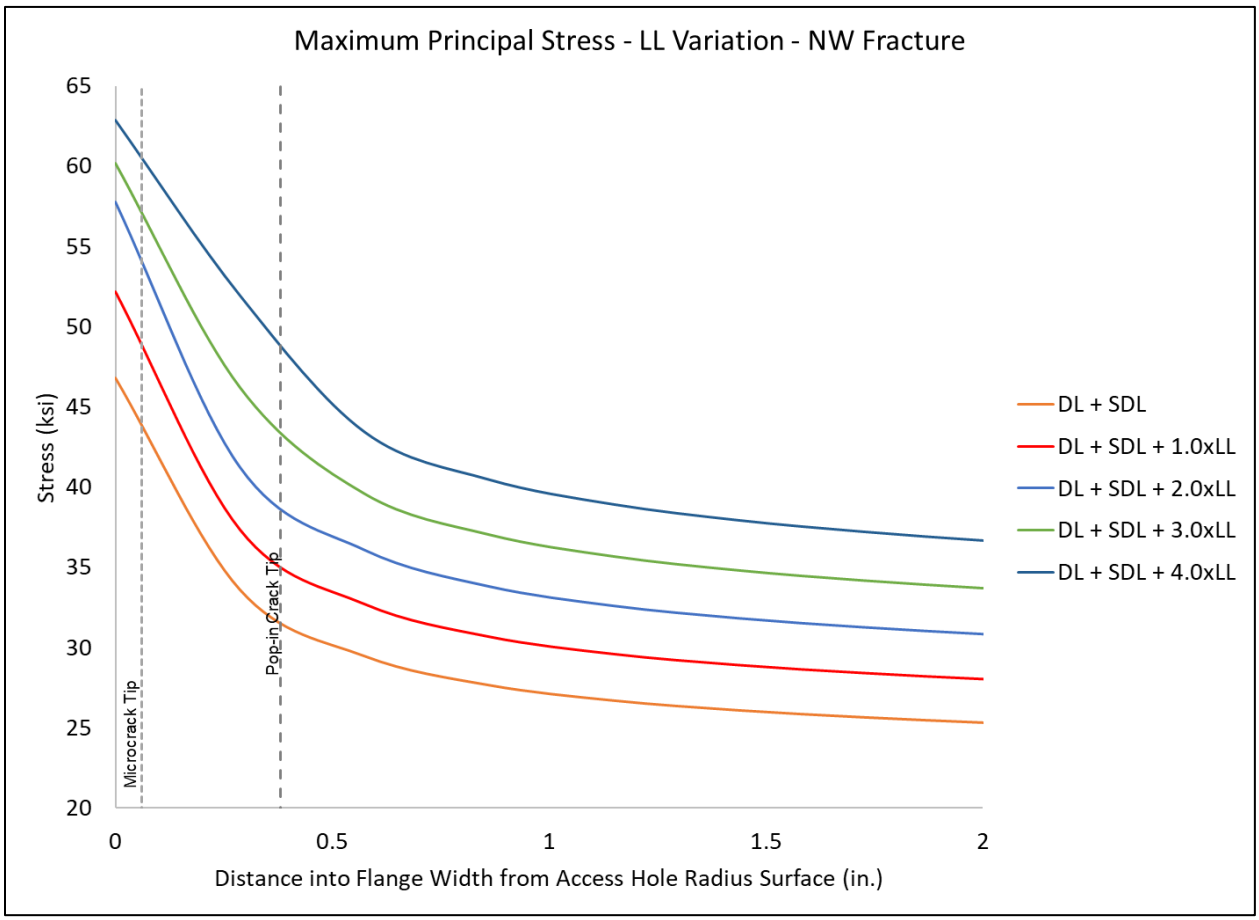

Fig. 99. Maximum principal stress along the NW fracture path for various applied LL. The relative locations on the microcrack and pop-in crack tips are identified by dashed vertical lines.

Using the approach described previously in this section, K_1 for each LL case was calculated and is summarized in Table 12.

Table 12 – Stress Intensity Factors – LL Sensitivity Analysis

Load Case	Peak Stress	K1
	(ksi)	(ksi√in.)
0.0xLL	44.8	37.5
1.0xLL	50.2	42.0
2.0xLL	55.8	46.6
3.0xLL	58.2	48.9
4.0xLL	60.9	51.5

K_1 – stress intensity factor

An increase in the LL magnitude will cause a corresponding increase in K_1 but, as Table 12 demonstrates, K_1 does not exceed the static fracture toughness of approximately 55-60 ksi√in., even at 4.0 times the LL.

To provide a full assessment of the effect of LL magnitude on fracture, FAD calculations were performed and are summarized in Fig. 100.

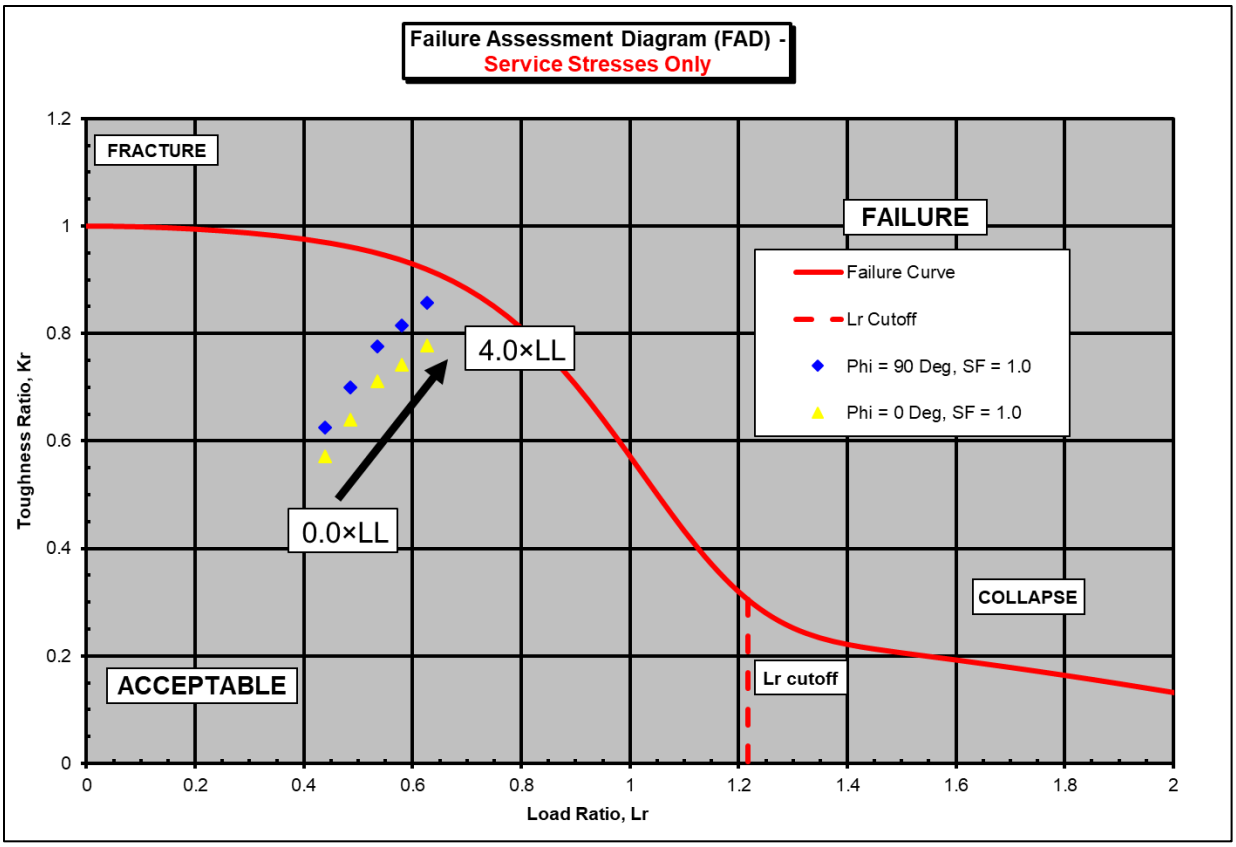

Fig. 100. FAD assessment points due to service stresses only at a fracture toughness of approximately 55 to 60 ksi√in. – LL sensitivity analyses

Fig. 100 indicates that for a LL factor up to 4.0 residual stresses would have been needed to cause fracture. To determine the residual stress contribution necessary to cause fracture the residual stress K_1 was incrementally increased such that all assessment points in Fig. 100 were shifted to the FAD curve, as shown in Fig. 101.

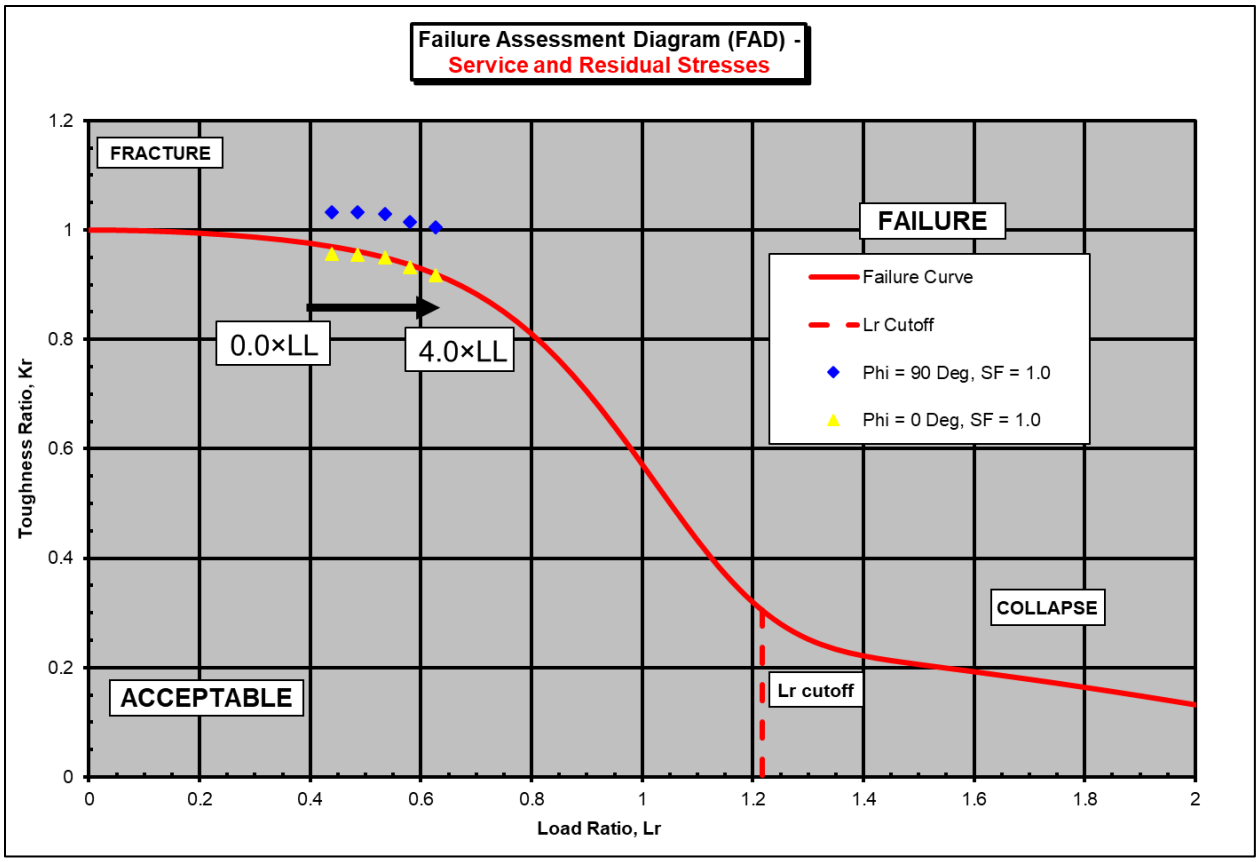

Fig. 101. FAD assessment points due to service stresses and an additional stress intensity factor due to residual stresses at a fracture toughness of approximately 55 to 60 ksi√in. – LL sensitivity analyses

A summary of the residual stress K_1 necessary to cause fracture is provided in Fig. 102 for each LL factor.

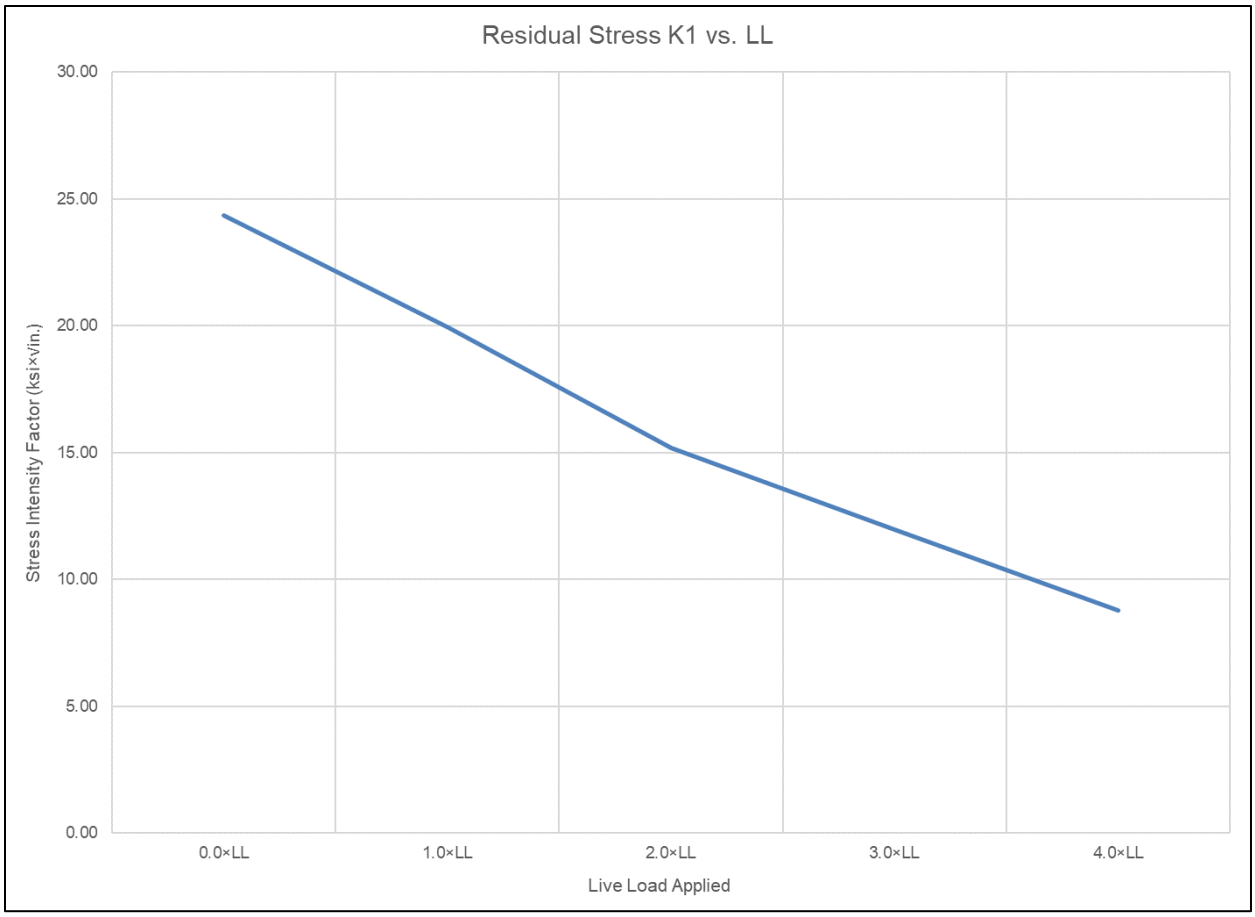

Fig. 102. Residual stress K_1 necessary to cause fracture of the Fig. 100 assessment points, as shown in Fig. 101, at a fracture toughness of approximately 55 to 60 ksi√in. – LL sensitivity analyses

The LL sensitivity analysis performed clearly shows that residual stress was a contributing factor to the Fremont Street TPG3 girder fractures, even accounting for the uncertainty in LL present.

4.3.2.1.1 Stress Intensity Factor Validation – Service Stresses

To validate the service induced stress intensity factor calculated using closed-form fracture mechanics solutions, as given shown in Table 10, the girder FE model was modified to include the pop-in crack, as shown in Fig. 103.

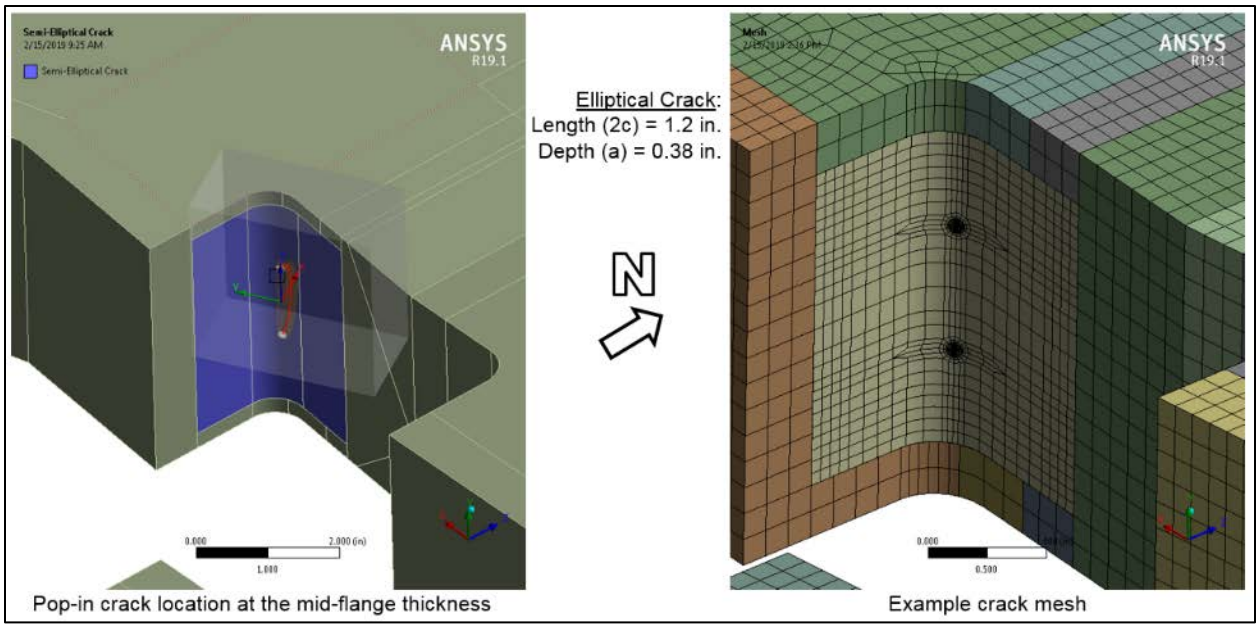

Fig. 103. FE model and mesh with the pop-in crack included.

The loading described in Section 4.3.1.6 was applied to the FE model and the stress intensity factor along the crack front was calculated for comparison with the previously calculated closed-form K_1 solutions, which determined K_1 to be approximately 38.4 to 42.0 ksi√in.

Results of the crack FE analyses, shown in Fig. 104, revealed calculated stress intensity factor values across the crack front that varied from 28 to 31 ksi√in. It should be noted that two methods were used to develop the crack tip FE mesh that were embedded in the girder FE model. Both methods provided similar stress intensity factor results and are shown in Fig. 104.

As expected, the FAD calculated stress intensity values are slightly higher due to the 4th order polynomial approximation of the through-thickness stress distribution. In contrast, the FE calculated stress intensity is based on the exact stress field imposed on the crack and is calculated explicitly using the domain integral method [17].

It is also important to note that the 4th order approximation will provide more accurate results than assuming a uniform membrane and/or bending stress across the crack front and flange, as these simplified stress distributions will significantly overestimate the crack tip driving force. However, the more simplified uniform membrane and/or bending stress distributions are better suited when used during design as they are inherently conservative.

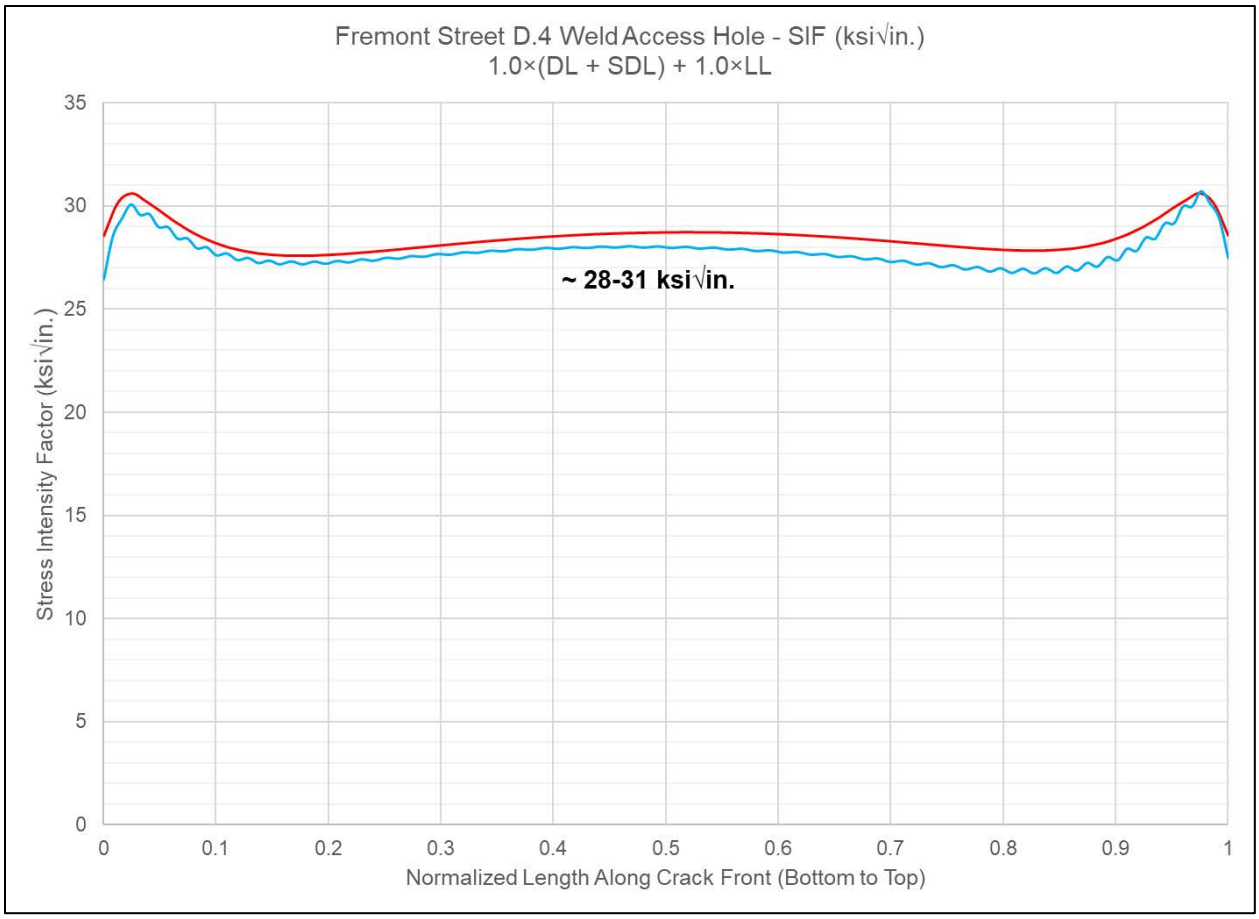

Fig. 104. FE stress intensity factor along the pop-in crack front due to service loading.

4.3.2.1.2 Stress Intensity Factor Validation – Residual Stresses

The uncracked FE model described in Section 4.1.3.3 was subsequently modified to include the 0.06 in. deep (a) x 1.2 in. wide (2c) microcrack in order to calculate the stress intensity factor at multiple points along the crack front with the FE model subjected to weld-shrinkage induced loading described in Section 4.1.3.

Fig. 105 shows a close-up view showing the crack tip mesh. The regularity of the crack mesh is clearly seen in the inset of Fig. 105. The spider-web-like portion of the mesh shown at the end of the crack free surface (shown as a yellow line in the figure) exists at multiple locations along the arc length of the crack front, and is configured this way to permit corresponding stress intensity factor contour integrations to be calculated along the circular arcs. There exists a roughly one-to-one correspondence between number of contour-integration paths and number of circular element-edge paths of a particular radius in the crack mesh. Accuracy of the calculated K_1 values increases with increasing radius along which integration is performed. A wireframe view of the FE model local to the crack is provided in Fig. 106 and shows the crack front below the access hole radius surface.

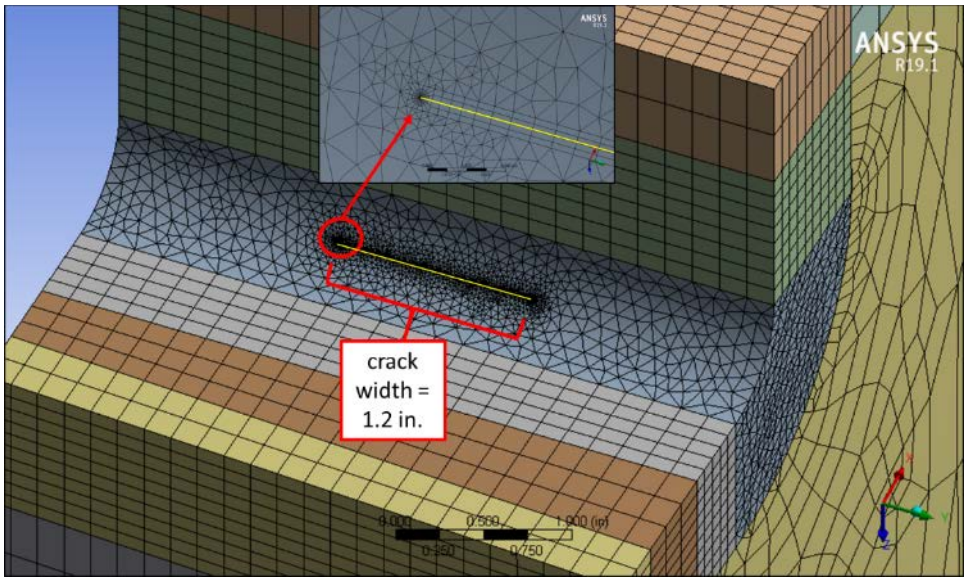

Fig. 105. Fremont Street crack mesh for the 0.06 in. deep x 1.2 in. long pre-existing microcrack prior to pop-in crack formation. Free surface of microcrack is shown in yellow.

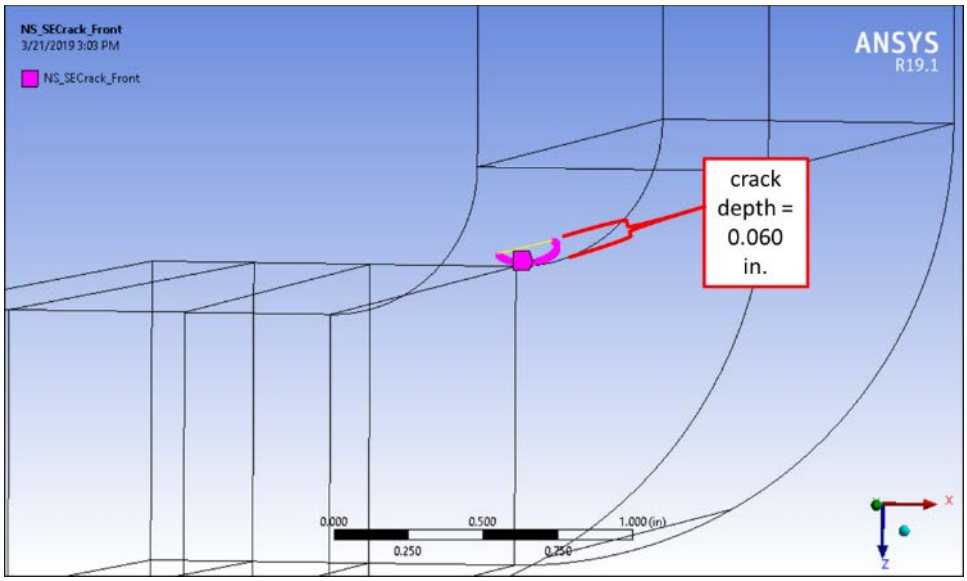

Fig. 106. Wireframe view showing depth of the microcrack of Fremont Street FE model. The purple line indicates the crack front.

A plot of K_1 along the crack front is shown in Fig. 107. The maximum value of K_1 was calculated to be approximately 27 ksi√in. and exists at the deepest location of the crack front. It is important to note that the plot represents, at each point along the arc length of the crack front, the stress intensity factor calculated using the last (i.e., largest radius) circular contour and, therefore, represents the most accurate calculation at that point.

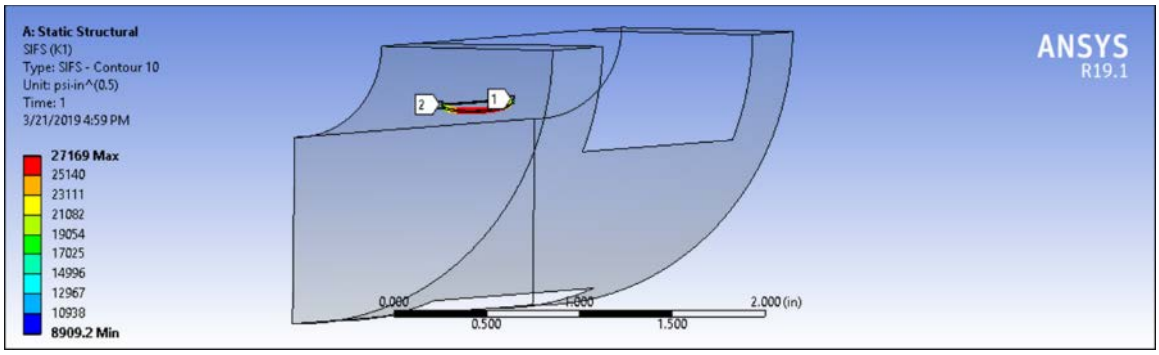

Fig. 107. Microcrack stress intensity factor plot the Fremont Street FE model subject to weld-shrinkage loading. Plot corresponds to outermost contour around the crack front, with a peak K_1 of approximately 27 ksi√in.

Alternatively, FE-based K_1 calculations can be viewed in terms of the FE mesh contour path, given in Fig. 108, which shows K_1 versus arc-length position along the crack front. There is one curve for each of several contour-integration paths used. Although ten integration paths (see Fig. 105 inset) were specified in building the FE model, only paths 6 through 10 are shown in the figure, since, as is often the case in FE-based fracture mechanics calculations, the first few path results are less accurate. The higher number paths (6-10) generally exhibit significantly improved convergence and, thus, more accurate K_1 values. In Fig. 108, it is evident that in progressing from path 6 (the topmost curve) to path 10 (the bottommost curve) the distance between curves becomes progressively smaller, indicating convergence to a final value for K_1 of approximately 27 ksi√in.

Similar to the 0.060 in. deep microcrack, the 0.38-in. deep pop-in crack was incorporated into the girder FE model. The resulting FE crack model was also evaluated for weld-shrinkage loading. All of the general concepts discussed previously in connection with the microcrack apply in this case as well.

Fig. 109 shows the crack mesh, with the regular, structured mesh for the crack clearly visible, while the wireframe view of Fig. 110 shows the depth of the pop-in crack front.

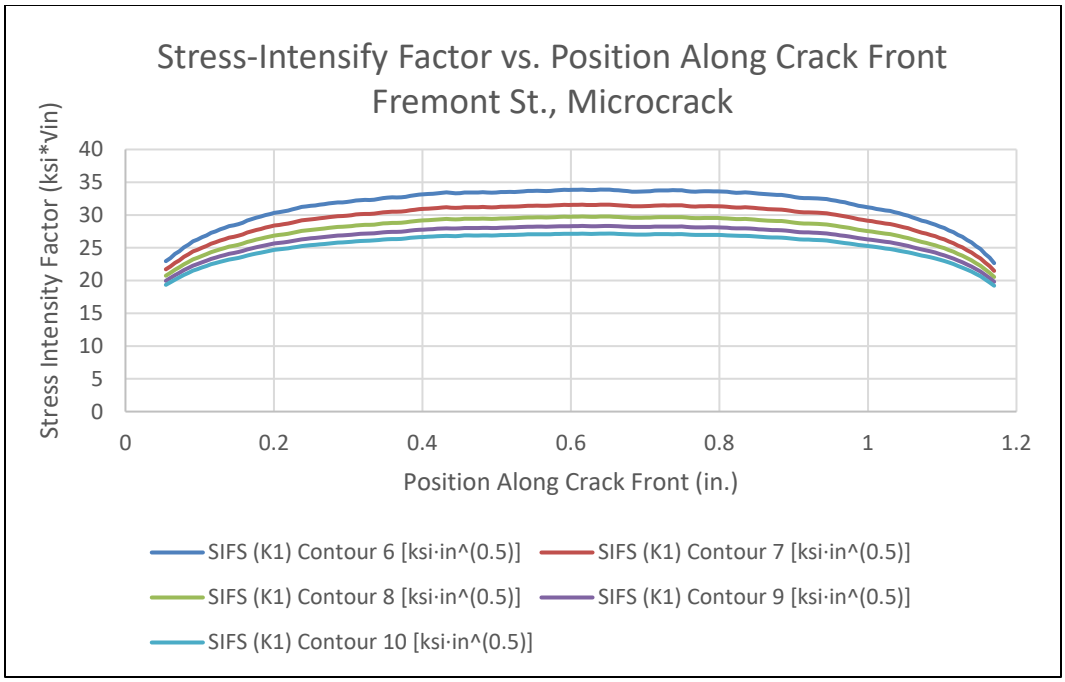

Fig. 108. Stress intensity factor (K_1) versus position along crack front for the microcrack in the Fremont Street FE model under groove-weld-shrinkage loading. Contours 6 through 10 show a converging trend (from top curve to bottom curve) toward a K_1 of approximately 27 ksi√in.

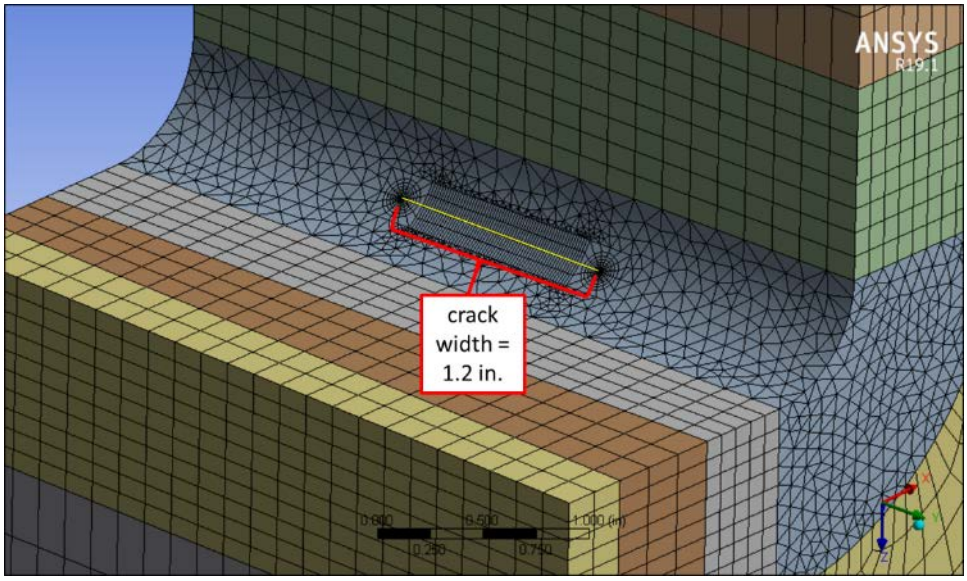

Fig. 109. Fremont Street crack mesh for the 0.38 in. deep x 1.2 long pre-existing pop-in crack. The free surface of crack is shown in yellow.

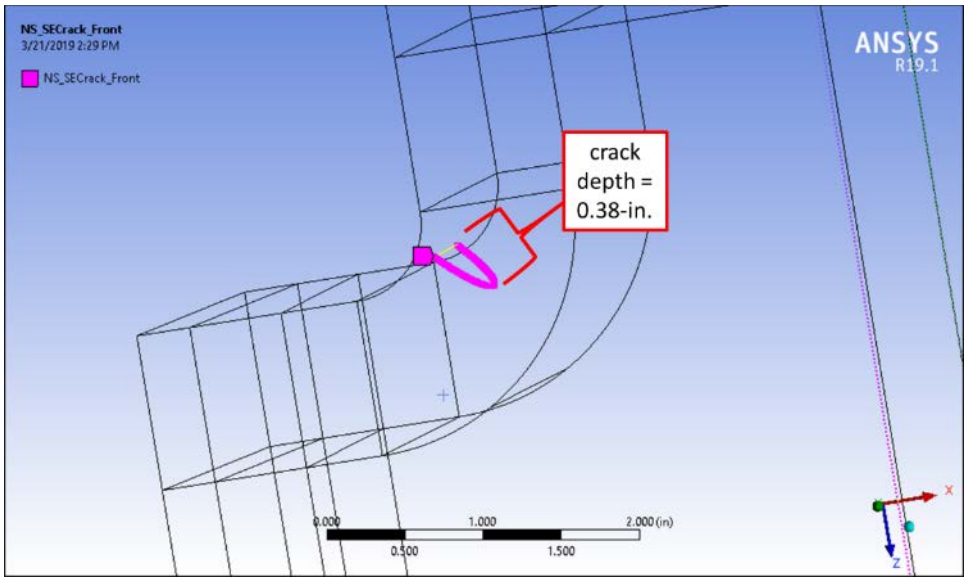

Fig. 110. Wireframe view showing the depth of the Fremont Street pop-in crack. The purple line indicates the crack front.

A plot of stress intensity factor along the crack front is shown in Fig. 111. Ignoring the spurious results where the crack intersects the free surface, which occurs for FE calculated K_1 values due to a combination of mesh-discretization and orientation of the tangential path upon which the stress intensity factor is calculated, the maximum K_1 was calculated to be approximately 21 ksi$\sqrt{}$in. at the deepest point. It is not surprising that the pop-in crack K_1 is lower than K_1 calculated for the microcrack, since the stress intensity factor is directly proportional to the prevailing stress level which, in this case, is the self-equilibrating residual stresses and is lower at the pop-in crack tip than at the microcrack tip.

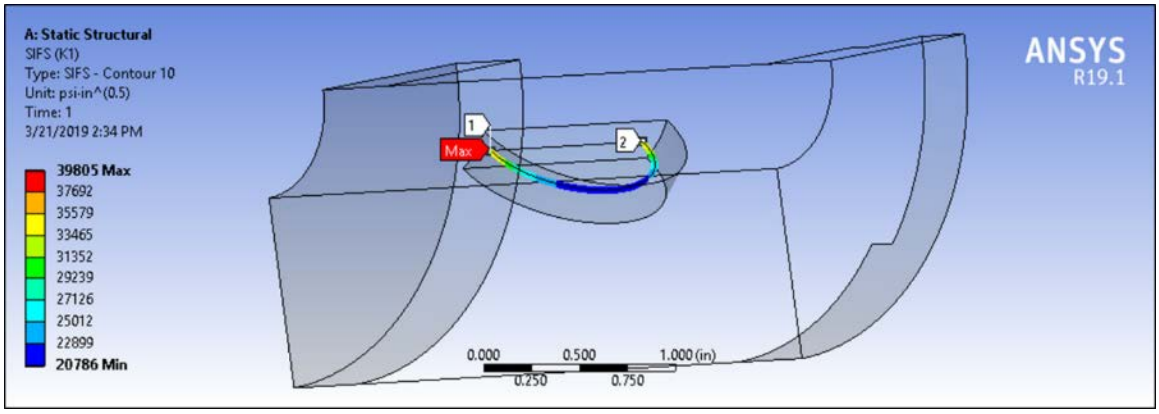

Fig. 111. Stress intensity factor across the crack front of the Fremont Street pop-in crack due to weld-shrinkage loading.

Similar to Fig. 108, Fig. 112 shows contour paths 6 through 10. Convergence is much faster in this case, as demonstrated by the near coincidence of the curves at maximum crack depth. As previously discussed for Fig. 108 the spurious results at the curve endpoints in Fig. 111 can be disregarded.

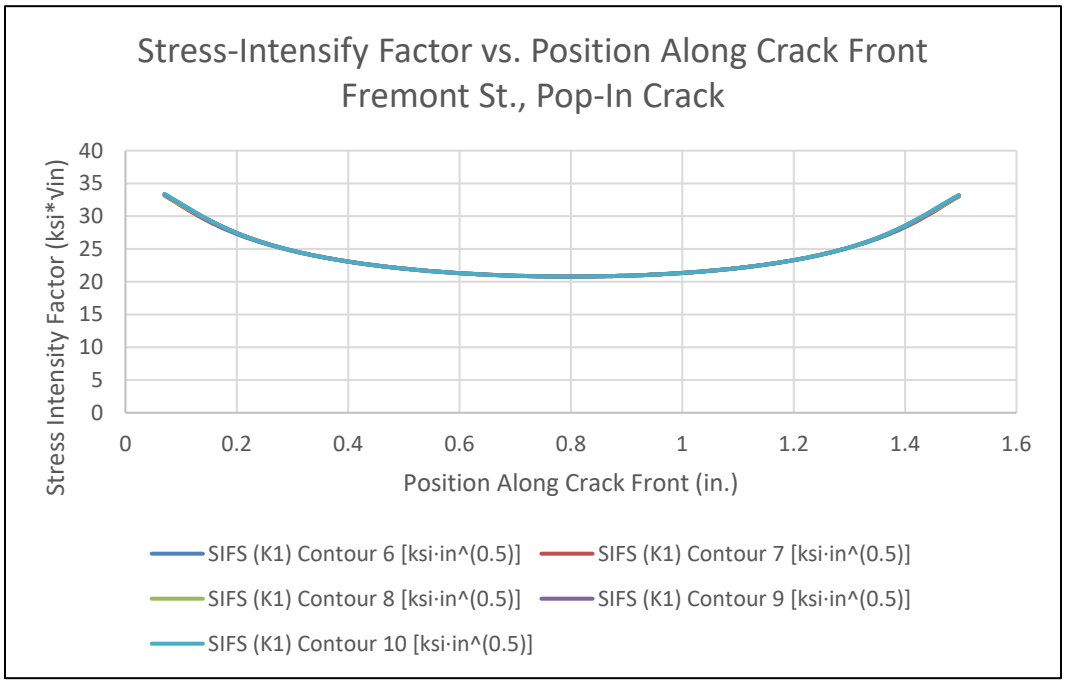

Fig. 112. Stress intensity factor (K_1) versus position along crack front for the pop-in crack in the Fremont Street FE model under groove-weld-shrinkage loading. Contours 6 through 10 show a converging trend (from top curve to bottom curve) toward a K_1 of approximately 21 ksi√in.

Thus, based on the thermal FE analysis results for the 0.38 in. deep pop-in crack, the stress intensity factor across the crack was determined to vary from 19 to 28 ksi√in. with an average value of 22 ksi√in., as shown in Fig. 113.

It is evident that the thermal FE calculated stress intensity factor results under weld-shrinkage residual stress are in excellent agreement with the previously estimated residual stress K_1 results (Section 4.3.2) of 20 to 22 ksi√in.

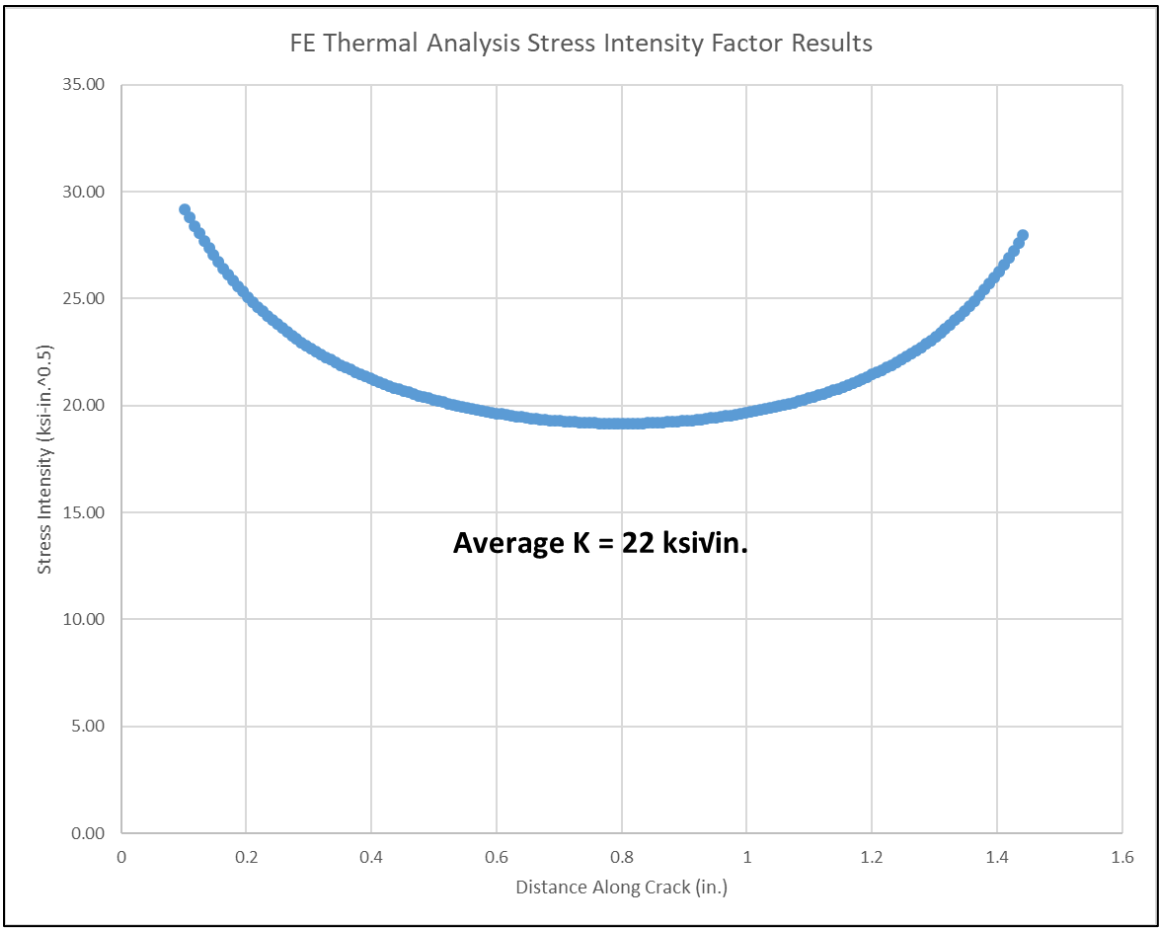

Fig. 113. FE stress intensity factor along the pop-in crack front due to weld-shrinkage thermal loading (residual stresses).

4.4 Fremont Street Fracture Timing

The Fremont Street girder bottom flange fractures (at D.4 and E.6) were determined to be low-energy, brittle fractures that initiated from pre-existing cracks approximately 1-1/4 in. long x 3/8 in. deep located at the mid-thickness of the 4-in. flange plate weld access hole radii. Fractures of this nature are governed by three driving force parameters: (1) the presence of a crack or other linear-like flaw, (2) tensile stresses due to service loading (gravity, seismic, wind, etc.) and/or residual stresses such as those induced by welding, and (3) low material fracture toughness. Moreover, all three elements are required and must act concurrently for brittle fracture to occur. Given this concurrency requirement and that each driving force parameter can be associated with a particular time frame, the most likely time for when the fractures occurred can be established.

A description of each of the three driving force parameters and their timing is as follows:

1. As indicated above, examination of the girder fracture surfaces revealed semi-elliptical cracks that were covered with dark, tenacious oxides. The dark tenacious oxide layer indicated that the crack surfaces were exposed to elevated temperatures. During fabrication of the girders there were three thermal processes of sufficiently high temperature that would induce such oxides: (a) thermal cutting of the weld access holes, (b) CJP groove welding of the girder flanges, and (c) thermal cutting of the run-off tabs used to complete the flange CJP welds. All fabrication activities were performed prior to the application of the girder fireproofing, which was completed by September 2016 [26]. In addition, there was no evidence of fireproofing on the fracture surfaces, which further confirms that the fractures could not have occurred prior to September 2016.

   It is important to note, that most of the fracture surfaces, however, were clean and relatively free of oxidation (rust), only exhibiting minimal flash rusting or light oxidation. The absence of long-term oxidation (rusting) in the TTC open-air bus deck environment suggests that the fractures were less than 12 months old, and most likely 6 to 12 months old. Since the girder fractures were discovered on September 25, 2018, the fractures could not have initiated prior to about January 2018.

2. Stresses due to service loading and/or fabrication-induced residual stresses developed and attained peak levels at different times. Residual stresses occurred during fabrication, which was completed prior to September 2016. In contrast, service stresses developed over several years, as shown in Fig. 82 [26].

   From this figure, it is evident that the majority of service-induced loading was in-place no later than June 2018, with nearly all of this loading in-place by June 2017. Therefore, the girder fractures most likely occurred between June 2017 and June 2018.

3. Low-energy, brittle fracture in the presence of cracks or linear-like flaws is principally dependent on the material's fracture toughness. Essentially, fracture toughness is a measure of a material's resistance, when cracked, to brittle fracture. When fracture toughness is high, brittle fracture generally does not occur and fracture occurs by ductile tearing and is associated with significant inelastic (permanent) deformation. Conversely, when the fracture toughness is low, as was the case for the Fremont Street girder flanges, brittle fracture in the presence of cracks, is very likely to occur. Furthermore, fracture toughness for steels is strongly dependent on temperature. That is, fracture toughness decreases with decreasing material temperature, as shown in Fig. 34. As such, brittle fracture is most likely to occur at colder temperatures rather than warmer temperatures.

That being the case, LPI evaluated the daily minimum temperatures in San Francisco between January and August 2018, as shown in Fig. 32. The black line represents a best-fit fourth-order polynomial regression and the red lines indicate clusters of low-temperature days. The temperature of the steel comprising the TTC bus deck trends with the ambient temperatures, but due to its thermal capacity it does not necessarily attain the minimum ambient temperature on a given day. Given the dependence of fracture toughness on temperature (i.e., lower temperatures correspond to lower fracture toughness levels), it is most likely that the girder fractures occurred during one of the clusters of low-temperature days when the flange toughness was lowest.

Based on when these low temperature cluster days happened, the girder fractures necessarily occurred between the end of February 2018 and the end of April 2018.

From LPI's review of the three driving force parameters that dictated the occurrence of low-energy, brittle fractures in the TTC Fremont Street girders, it can be concluded that the fractures occurred between the end of February 2018 and the end of April 2018. The most likely time of occurrence is the end of February 2018 when the ambient temperature was the lowest (~ 40ºF) and was less than 50ºF for many consecutive days and even weeks.

4.5 Fremont Street Bottom Flange Fracture Conclusions

Based on the analyses described in Section 4 regarding fracture of the Fremont Street girder bottom flanges, the following can be concluded:

- Yield strength level residual stresses at the weld access hole radius surface, induced by CJP groove welding, were required to initiate the pop-in crack from the 0.06 in. deep microcracks.
- These weld-induced residual stresses decreased rapidly as the distance into the bottom flange from the weld access hole radius surface increased.
- Service induced stresses corresponding to 1.0(DL+SDL) + 1.0(LL), described in Section 4.3.1.9, were not sufficient to initiate the bottom flange fracture from the pre-existing 0.38 in. deep x 1.2 in. long pop-in crack located at the weld access hole radius surface, in the mid-thickness of the 4-in. thick bottom flange, where the fracture toughness (K_{1C}) was approximately 55 to 60 ksivin. at 50°F.
- Fremont Street D.4 girder bottom flange fracture initiated under the combination of normal service induced stresses and residual stresses associated with CJP groove welding.
- Once Fremont Street D.4-NW fractured, the stresses at D.4-SW increased significantly with a corresponding high loading rate, which resulted in an apparent

lower fracture toughness at D.4-SW. The combination of higher stress and lower toughness induced fracture of D.4-SW from a significantly smaller microcrack.

- After Fremont Street D.4 completely fractured, the imposed loads were shed throughout the adjacent structure. This redistribution increased stresses in the E.6 girder sufficiently to initiate fracture from a relatively large pop-in crack in the E.6-SW bottom flange. However, there was insufficient driving force remaining after load shedding to initiate fracture from the small microcrack in E.6-NW.

Note that the bottom flange fracture of the Fremont Street E.6 girder is also represented by the above conclusions, as the initial fracture on the north side of D.4 was identical to that on the south side of E.6.

5. FIRST STREET TPG3 ASSESSMENT

Above First Street are two tapered plate girders that are nearly identical to those above Fremont Street, neither of which had fractured. Identified as “D” on the north side and “F” on the south, these girders were assessed to determine why they did not crack and what the stress levels are in fracture-critical areas when subjected to factored design loads. Included in the assessment was a metallurgical evaluation of weld access hole core samples removed from the bottom flanges, as well as an analysis of the proposed reinforcement retrofit.

5.1 Metallurgical Evaluation

Core samples obtained during the installation of the reinforcement retrofit (see Section 5.4) were extracted and a metallurgical evaluation was performed, including magnetic particle testing. The retrofit plate material was also evaluated.

5.1.1 Girder Flange and Web Core Samples

Sixteen core samples were submitted, as described in Table 13 and Table 14. A total of eight 2-in. core samples were removed from girder flange weld access holes on the north and south girders above First Street (Girders D and F, respectively). In addition, eight 4-in. core samples were removed from girder web stress relief holes on the north and south girders above First Street (Girders D and F, respectively) and above Fremont Street (Girders D.4 and E.6, respectively). A representative image of the core sample removal locations is shown in Fig. 114.

Table 13 – First Street Core Sample Identification

Sample Location	Sample Identification	Sample Description
First Street North Side Girder	D-NE	2 in. core, Girder weld access hole
	D-NW	2 in. core, Girder weld access hole
	D-SE	2 in. core, Girder weld access hole
	D-SW	2 in. core, Girder weld access hole
	D-E	4 in. core, Web stress relief hole
	D-W	4 in. core, Web stress relief hole
First Street South Side Girder	F-NE	2 in. core, Girder weld access hole
	F-NW	2 in. core, Girder weld access hole
	F-SE	2 in. core, Girder weld access hole
	F-SW	2 in. core, Girder weld access hole
	F-E	4 in. core, Web stress relief hole
	F-W	4 in. core, Web stress relief hole

Table 14 – Fremont Street Core Sample Identification

Sample Location	Sample Identification	Sample Description
Fremont Street North Side Girder	D.4-E	4 in. core, Web stress relief hole
	D.4-W	4 in. core, Web stress relief hole
Fremont Street South Side Girder	E.6-E	4 in. core, Web stress relief hole
	E.6-W	4 in. core, Web stress relief hole

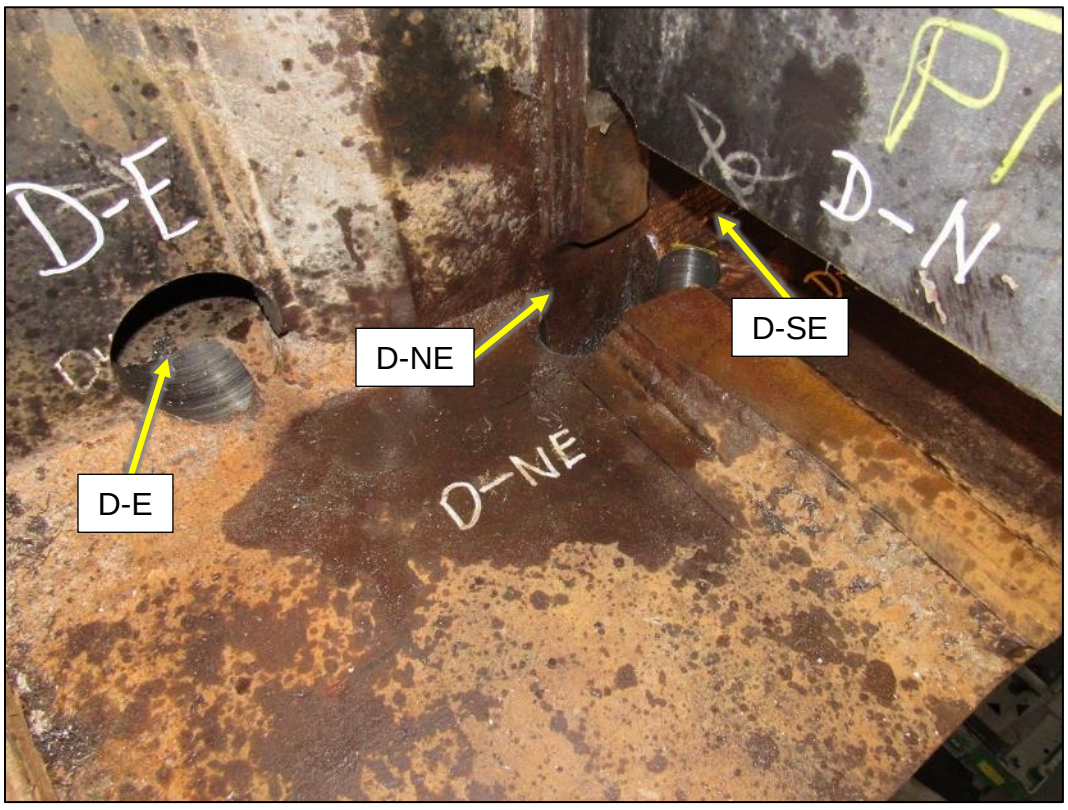

Fig. 114. North girder above First Street after core sample removal.

The submitted girder flange weld access hole core samples are shown in Fig. 115 and Fig. 116 in the as-received condition. The submitted girder web stress relief hole core samples are shown in Fig. 117 and Fig. 118 in the as-received condition. Wet fluorescent magnetic particle testing (FMT) of the weld access hole and stress relief hole surfaces of the core samples was performed. Crack-like indications were observed on core samples D-NE, D-NW, D-SE, and F-W. A representative image is shown in Fig. 119. Additional images are provided in Appendix H.

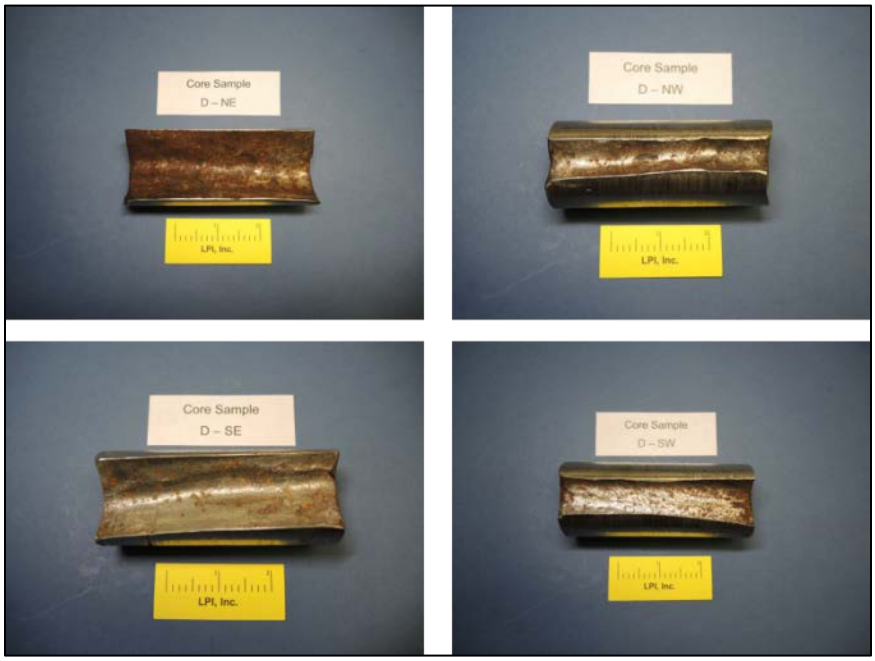

Fig. 115. Flange core samples from the north girder above First Street (Girder D) in the as-received condition.

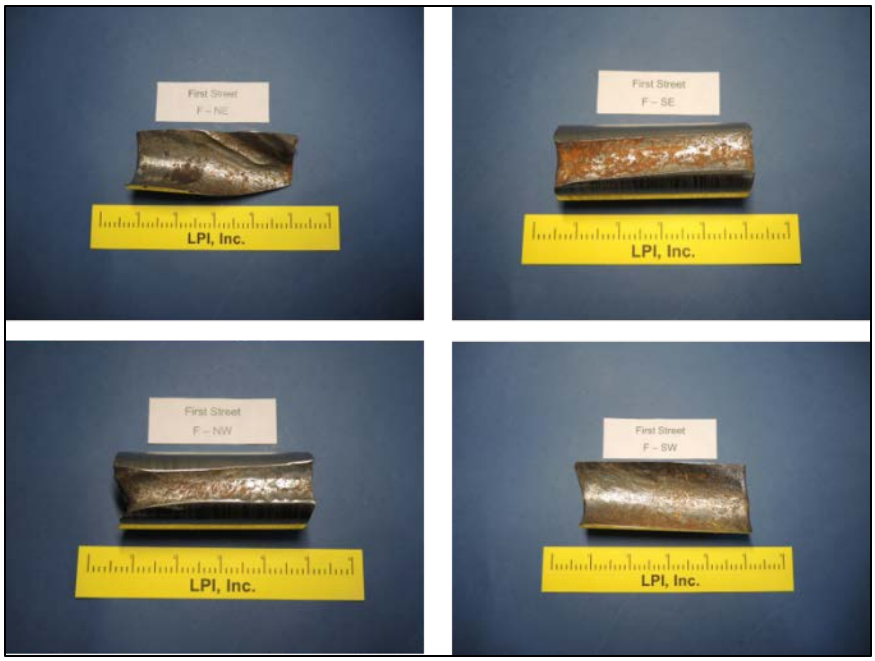

Fig. 116. Flange core samples from the south girder above First Street (Girder F) in the as-received condition.

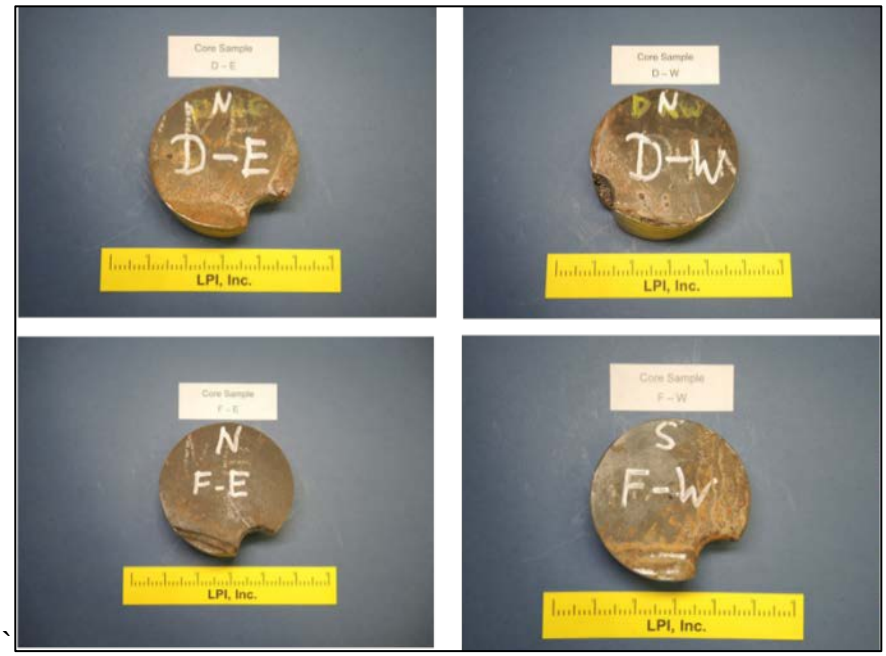

Fig. 117. Web core samples from the girders above First Street (Girders D and F) in the as-received condition.

Fig. 118. Web core samples from the girders above Fremont Street (Girders D.4 and E.6) in the as-received condition.

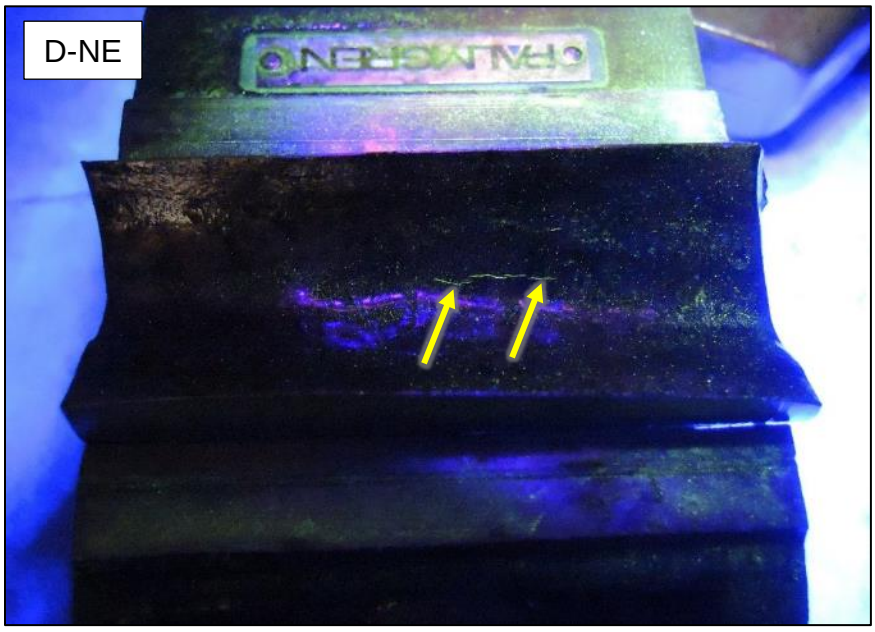

Fig. 119. Representative image of the flange weld access hole surface of core sample D-NE following wet fluorescent magnetic particle testing showing cracks (arrows).

Following FMT, transverse metallographic cross-sections were prepared through the core samples in order to evaluate the weld access hole surfaces and identified cracks. For those samples that did not exhibit MT indications, the cross-section specimens were taken from the sample mid-thickness. For those samples that did exhibit FMT indications, the cross-section specimens were prepared transversely through the FMT indications.

As shown in Fig. 120 and Appendix H, metallographic examination confirmed that samples D-NE, D-NW, D-SE, and F-W exhibited microcracks initiating from the weld access hole surface, identical to those identified in the Fremont Street girder flanges. Cracks were not evident in the metallographic specimens sectioned from the remaining samples.

Etching of the D-NE, D-NW, D-SE, and F-W specimens revealed areas of untempered martensite (“white layer”) and a narrow martensitic band along the weld access hole surface approximately 0.02 to 0.03 in. (0.51 to 0.76 mm) in depth. The observed cracks initiated within these brittle, high hardness martensitic layers, which formed during the rapid cooling following thermal cutting of the access holes. A martensitic layer was not observed on the remaining samples.

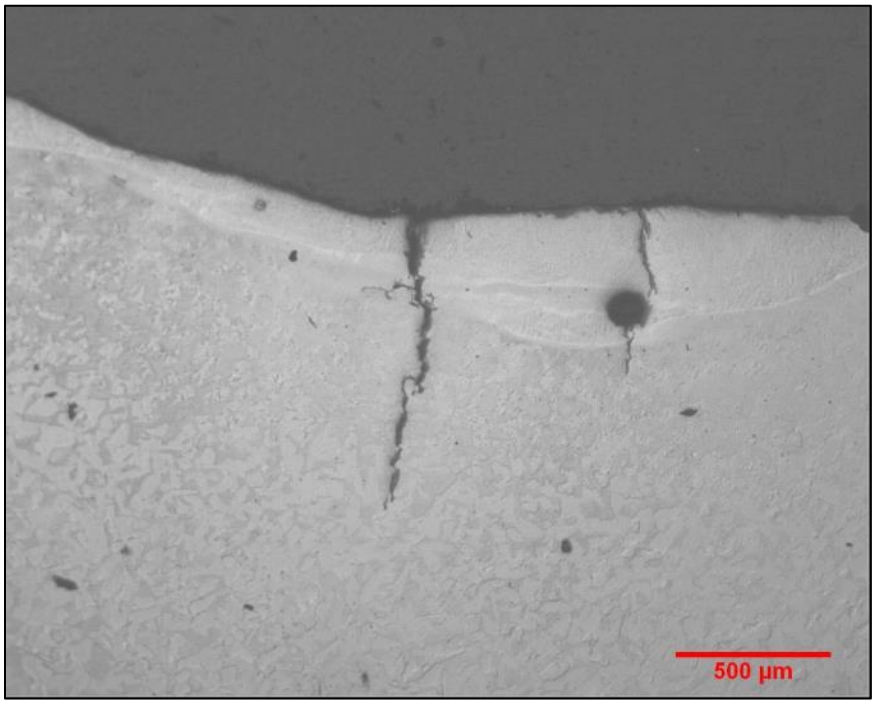

Fig. 120. Representative metallographic image of the flange weld access hole surface of core sample D-NW revealing cracks in the martensitic surface layer.

Results of the testing indicated that the core samples D-NE, D-NW, D-SE, and F-W, which were removed from the north and south girders above First Street, exhibited cracking in

the weld access and stress relief holes. The cracking was due to martensite formation at the hole surfaces following rapid cooling during thermal cutting operations of the holes.

Based on the results of the First Street core samples, it is clear that the grinding performed following the Fremont Street girder fractures was neither uniform nor did it produce a bright metal finish. Had a uniform bright metal finish been achieved, it would have removed the untempered martensite layer and microcracks.

5.1.2 Reinforcement Plate Sample

A sample repair plate of A709 HPS, Gr. 70W, was cold-bent to the appropriate angle and sent to LPI for evaluation. The subject sample repair plate is shown in Fig. 121 in the as-received condition. The plate exhibited markings of “1190011A-1”, “Sample Bent Pl.”, and “O.S.V. Press”. Tensile and CVN specimens were sectioned from both the bent area and one end of the plate, as shown in Fig. 122. It should be noted that the test plate, though not from the same heat as the actual reinforcement plates, exhibited compositional and mechanical properties that were very similar to those reported in the reinforcement plate mill certs [37].

Fig. 121. Sample repair plate in the as-received condition.

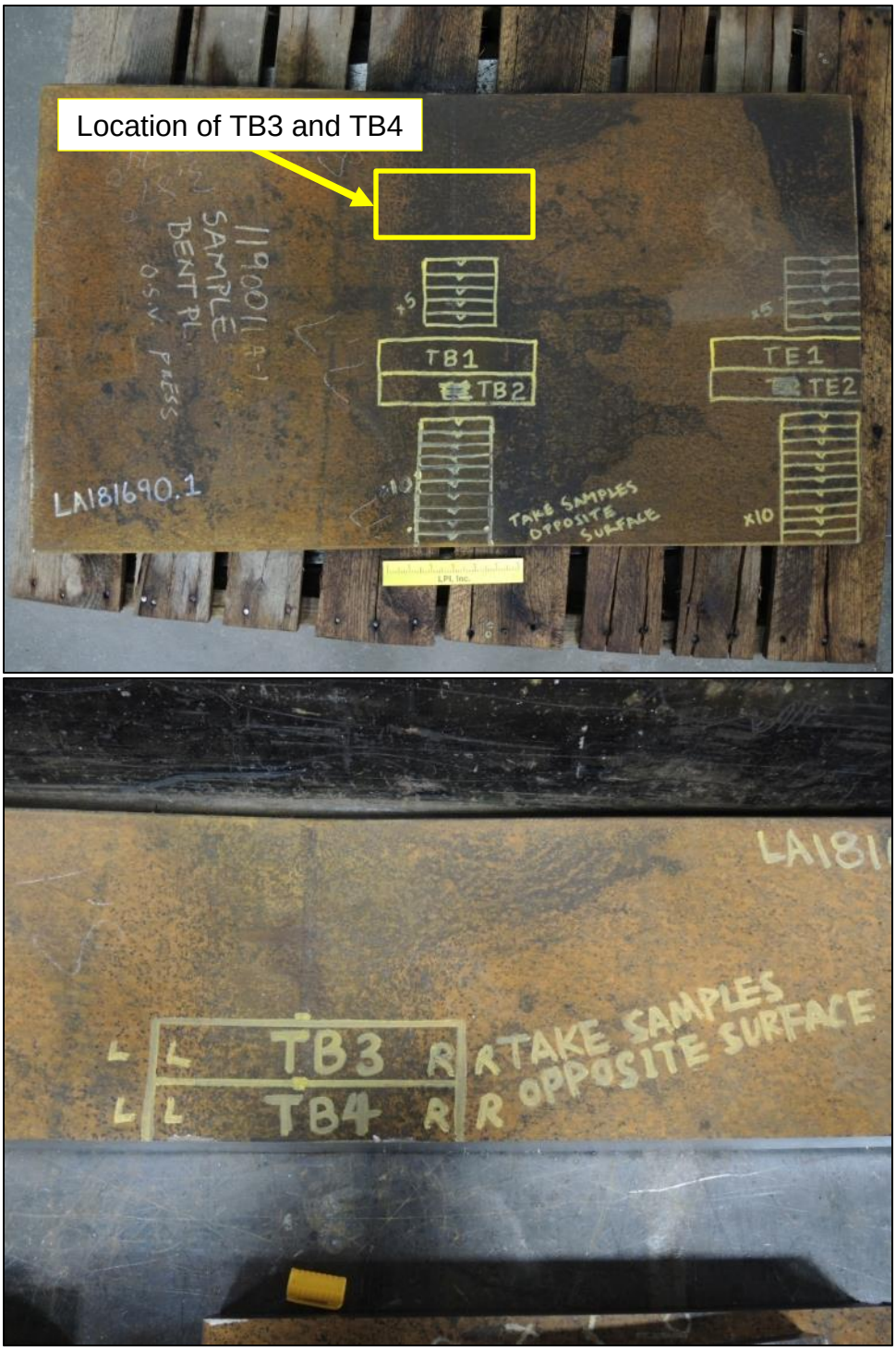

Fig. 122. Tensile and CVN specimen location mark-up prior to sectioning.

5.1.2.1 Tensile Testing

Standard round tensile specimens were machined from the convex surface of the repair plate, oriented perpendicular to the bend direction (longitudinal direction of the plate). Specimens TB1 through TB4 were centered at the bend, while specimens TE1 and TE2 were located at one of the plate ends.

Results of the testing, provided in Table 15, indicated that specimens TB3, TB4, TE1, and TE2 met the tensile requirements of ASTM A709 Grade HPS 70W [32]. Specimens TB1 and TB2 met the ultimate tensile strength and yield strength requirements, but fractured outside of the designated gauge length area. As such, the percent elongation was not valid.

As expected, plate properties in the cold-bend exhibited slightly higher ultimate tensile and yield strengths, and lower percent elongation than the properties of the material at the end of the sample repair plate. This difference is expected for cold-worked versus non-cold-worked structural steel, but will not impact the capabilities of the repair plate for its intended function.

Table 15 – Sample Reinforcement Plate Tensile Test Results

Specimen ID	Ultimate Tensile Strength (ksi)	Yield Strength (ksi)	Elongation (%)
TB1	95.4	90.0	9*
TB2	95.1	90.4	10*
TB3	95.1	89.7	22
TB4	95.9	90.2	22
TE1	91.7	78.4	32
TE2	91.9	78.9	28
Per ASTM A709, Grade HPS 70W	85-110	70, min.	19, min.

* Test results not valid due to specimens fracturing outside of the designated gauge length.

5.1.2.2 Charpy V-Notch Toughness Testing

Charpy V-notch (CVN) impact toughness testing was performed on specimens machined from the convex surface of the cold-bent repair plate, oriented perpendicular to the bend direction (longitudinal direction of the plate). The notch was oriented in the transverse direction of the plate, parallel to the bend. The specimens were tested over a temperature range of -40°F to 70°F. Specimens B1 through B12 were centered at the bend and specimens E1 through E12 were located at the plate end.

Results of the testing, provided in Table 16, indicated that the absorbed energy (toughness) for each group of specimens was relatively uniform across all temperatures, and the specimens from the end exhibited slightly higher toughness levels than those

sectioned from the bend. However, the variation in toughness between the two locations is expected for cold-worked versus non-cold-worked structural steel. Moreover, the bend region CVN toughness is considered very good and, as such, bending of the repair plates will not adversely affect their performance with regard to the flange reinforcement at First Street or repair of the Fremont Street flange.

Table 16 – Sample Reinforcement Plate CVN Test Results

Specimen ID	Test Temperature (°F)	Absorbed Energy (ft-lb)	Average Absorbed Energy (ft-lb)	Lateral Expansion (in.)	Percent Shear
B-1	70	179	182	0.102	100
B-2	70	197		0.100	100
B-3	70	170		0.102	100
B-4	30	193	195	0.099	100
B-5	30	197		0.098	100
B-6	30	196		0.099	100
B-7	0	197	199	0.099	100
B-8	0	202		0.099	100
B-9	0	198		0.102	100
B-10	-40	133	167	0.097	70
B-11	-40	188		0.101	100
B-12	-40	179		0.096	100
E-1	70	211	205	0.087	100
E-2	70	208		0.097	100
E-3	70	195		0.101	100
E-4	30	207	210	0.087	100
E-5	30	225		0.080	100
E-6	30	198		0.096	100
E-7	0	195	203	0.095	100
E-8	0	199		0.095	100
E-9	0	214		0.089	100
E-10	-40	182	183	0.097	100
E-11	-40	201		0.098	100
E-12	-40	167		0.094	80

5.1.2.3 Simulated Bolt Hole Testing

In order to evaluate the plate with respect to the anticipated drilling of bolt holes required for repair of the girders, two 1-1/4 in. holes were drilled into non-cold-worked areas of the sample repair plate, as shown in Fig. 123. Visual and magnetic particle examinations of the edges of each hole (coincident with the top and bottom surfaces of the plate) and each hole inner diameter surface were performed. Examination did not reveal any evidence of disturbance of the adherent mill scale surface at the hole edges and no indications of cracking at the hole edges or on the hole inner diameter surfaces.

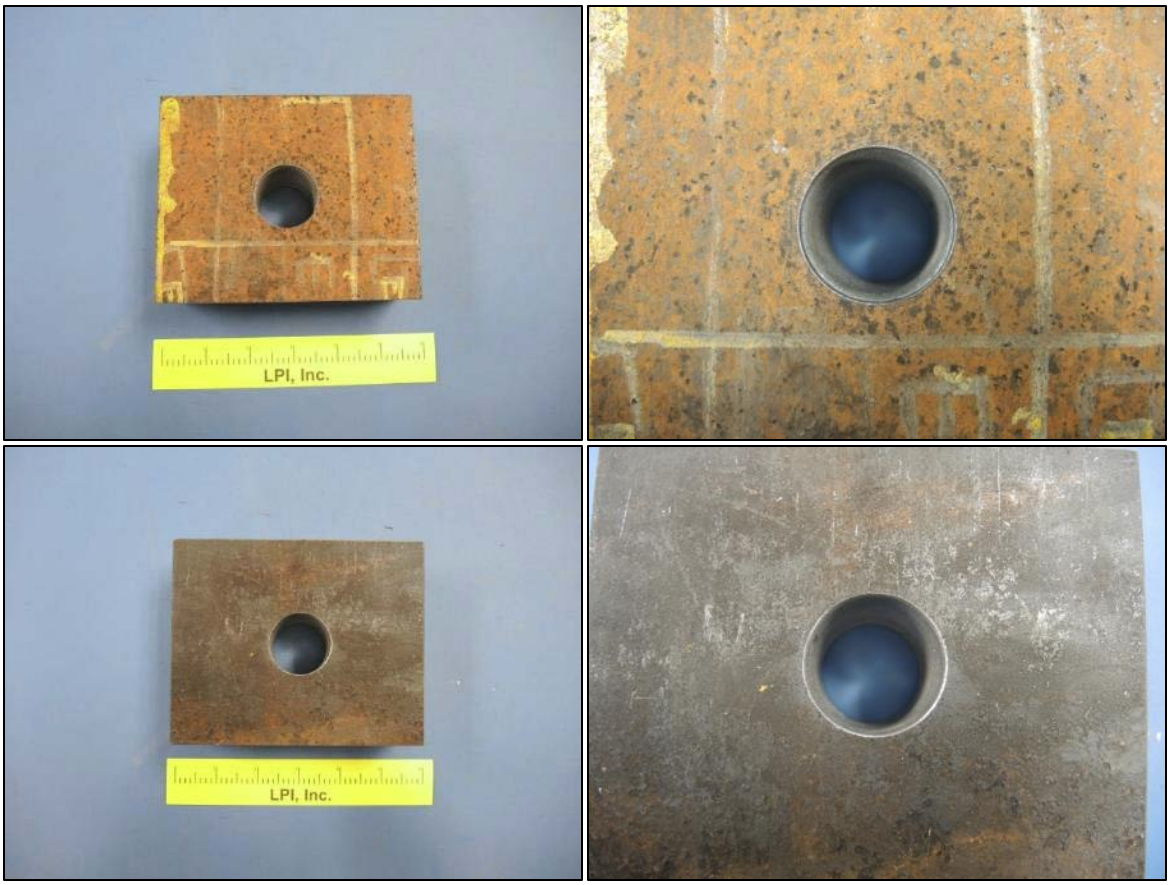

Fig. 123. Overall and close-up images of the two bolt holes drilled in the sample repair plate.

5.2 Weld-Induced Residual Stress

Weld-induced residual stresses in the First Street girders were evaluated in the same manner as those for Fremont Street (see Section 4.1.3).

However, since the weld-access holes at First Street were cut after CJP groove welding the bottom flanges (the Fremont Street access holes were cut prior to CJP groove welding), the Fremont Street FE modelling approach was modified to account for the presence of flange material prior to its removal by cutting after the CJP groove welding was completed.

5.2.1 Model Details

The First Street FE models without and with an access hole are shown in Fig. 124 (a) and (b), respectively. These FE models were adapted from the Fremont Street model by filling in that model's weld-access-hole cutout, resulting in the geometry shown in Fig. 124 (a). By then removing this filled-in region, Fig. 124 (b) is arrived at, which is identical to the

Fremont Street model. Although the First Street cutout is not the exact same geometry as that of Fremont Street, it is sufficiently accurate for the purpose of comparing the weld access hole radius stresses arising from cutting the access hole before or after CJP groove welding of the bottom flanges.

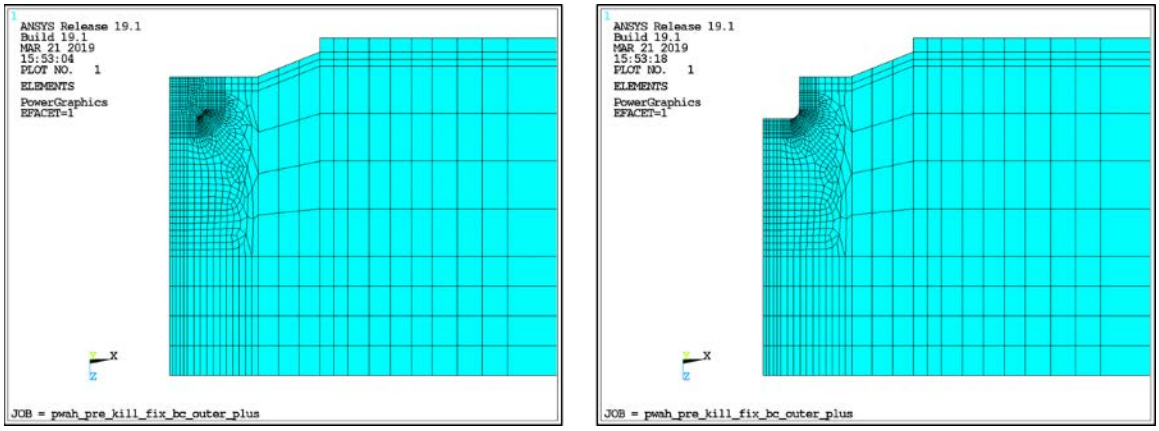

(a) **(b)**

Fig. 124. First Street FE model showing the flange without (a) and with (b) the weld access hole in the model.

Unlike the Fremont Street analysis that consisted of a single step – that of loading the model with applied temperature to induce weld-induced residual stresses – the First Street analysis required two steps. The first load step applied the temperature as in the Fremont case, and the second step was solved for after removing the elements at the access hole. Analysis consisting of removing or adding elements during sequential solutions is known as “birth and death” analysis in finite-element idiom. In the present case, no elements were added so there is no element birth to speak of. Only element removal took place, via “killing” the appropriate elements.

For this analysis, the elements residing in the access-hole location were killed in one step. Several alternate analyses were also conducted in which the killing was done over several steps. During each of these analyses, only a subset of the entire set of access-hole-filling elements were killed, in order to investigate the effect of more gradual material removal. Those analyses will not be discussed here, as results of interest, namely, radius stress remaining after access-hole cutting, were little different from those presented herein. Specifically, maximum principal stress at the center of the radius (point C of Fig. 130) varied from 34.2 to 37.8 ksi over all analyses. The value for the single-kill-step analysis presented herein was found to be 37.2 ksi and is, therefore, deemed to be sufficiently representative of all the various analyses.

5.2.2 Loading

Inasmuch as the weld access hole at First Street was cut after the flange had been welded up to the hanger plate, weld shrinkage would necessarily have loaded the flange along the same width. To simulate this effect in the FE model, a temperature drop of the same magnitude used for Fremont Street was used, only now applied over the correspondingly slightly longer flange width for First Street. Fig. 125 shows the temperature distribution (compare to Fig. 51).

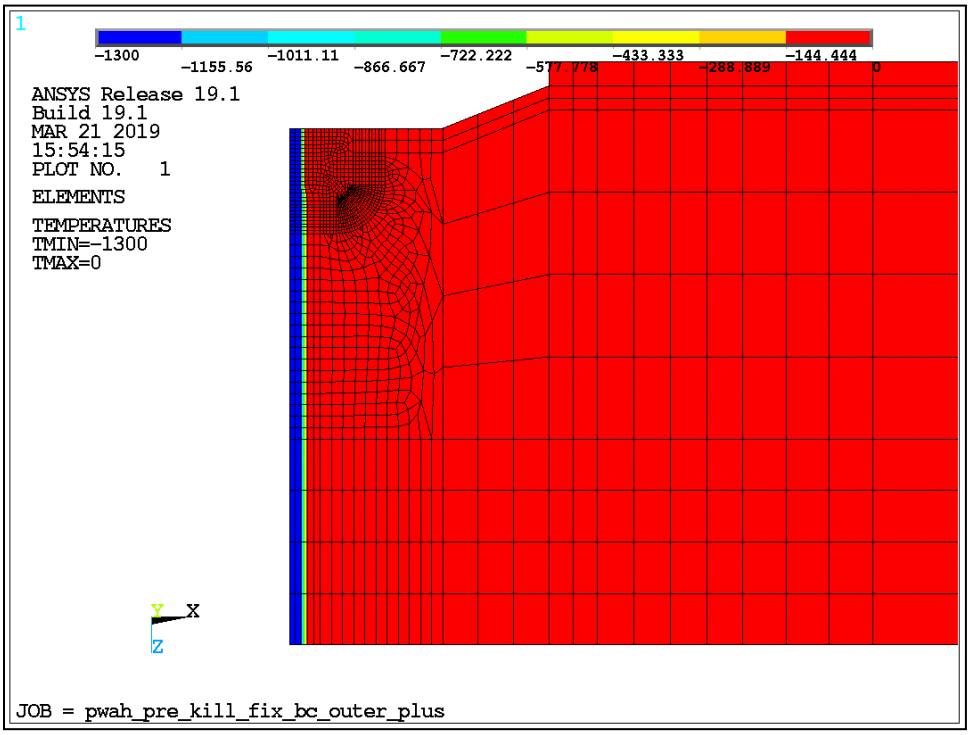

Fig. 125. Uniform temperature distribution of -1300°F in idealized weld region of First Street FE model.

Simulation of weld-induced residual stress via temperature drop in a weld is a reasonable approach given the knowledge that welds do, in fact, shrink and load neighboring structure. Additionally, and perhaps equally important, the magnitude of the temperature drop is related to realistic stress-relieving temperatures for the material. This method is most frequently used in one-step analyses like those for the Fremont Street FE model, however, the temperature-drop approach was modified for analyzing the First Street FE model due to multiple steps required to account for material removal following welding.

The temperature drop was still applied initially, as shown in Fig. 125, but rather than maintain it through the element-killing step, it was deleted and its effect replaced by locking in the resultant displacements on a transverse plane through the flange just beyond the weld zone. Displacements arising from initial application of the temperature

loading were identified midway during solution and subsequently applied before the element-killing step was executed. Fig. 126 shows a dotted line where displacements were fixed and Fig. 127 shows the model after the temperature deletion and element killing.

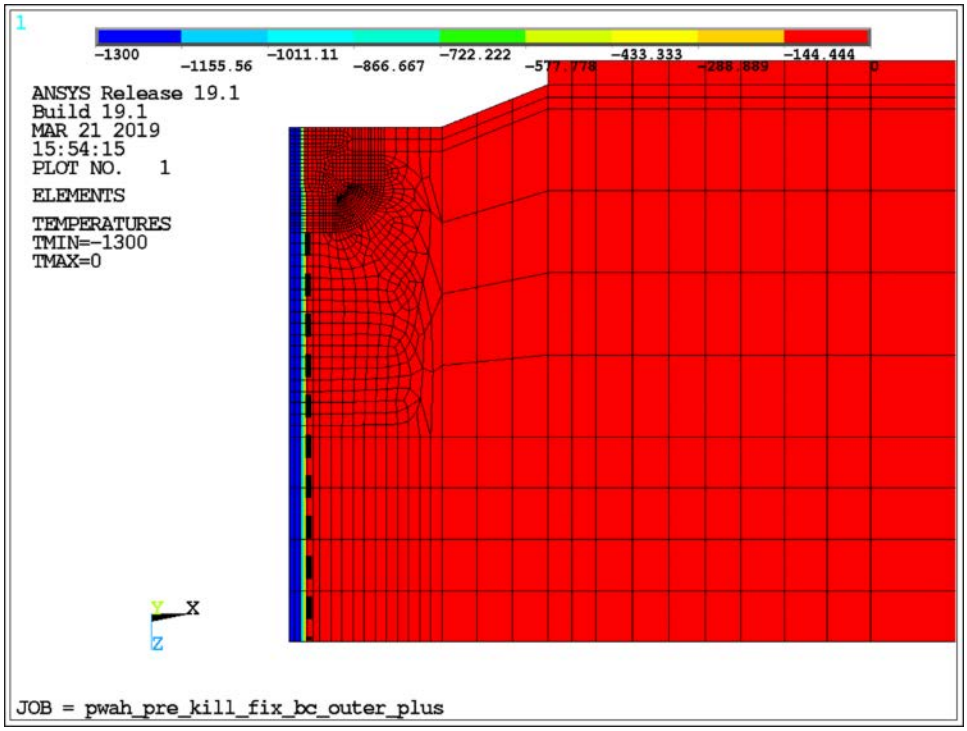

Fig. 126. Dashed line indicates section through First Street FE model on which displacements are fixed after temperature load is first applied, but before their deletion during the simulation of access-hole cutting.

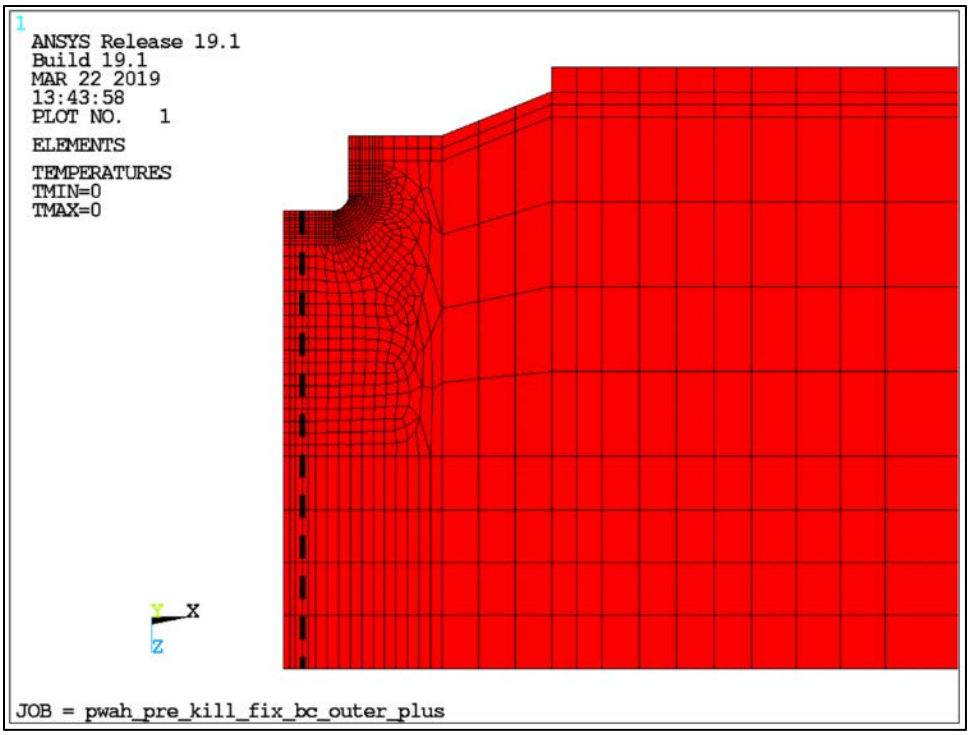

Fig. 127. First Street FE model after the access hole was created and temperature loading removed. Dotted line indicates section on which displacements caused by initial temperature loading are fixed, thereby locking in the shrinkage effect of the weld.

Since the locked-in displacements are directly related to the initial loading, their inclusion to maintain the thermal loading was determined to be a reasonable representation of the local structural response. Nonetheless, before actually employing the method for the First Street FE model, the approach was tested on a simpler Fremont Street FE model. In Fig. 128 (a) the result shown in Fig. 53 is repeated. That result arises from applying and maintaining the temperature load. Fig. 128 (b), on the other hand, shows the results of fixing the temperature-induced displacements in the aforementioned manner, followed by deletion of the applied temperature load. Since the stress distributions are nearly identical, the method was judged sufficiently accurate for use in the First Street analysis.

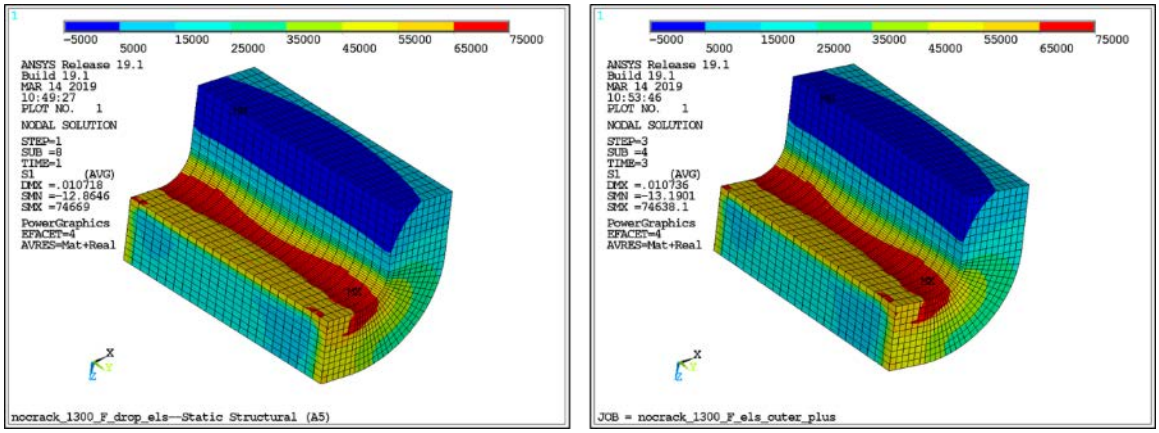

(a) **(b)**

Fig. 128. Results of applying First Street FE model's displacement-locking method to Fremont Street FE model for verification. Fig. 53 results are repeated here in (a) for comparison to results using displacement-locking followed by deleted temperature loads, (b). It is clear that the calculated stress distributions are nearly identical.

All results discussed below for First Street correspond to the element-killed state and, therefore, represent an approximation of the stress state prevailing after cutting of the post-welded access hole.

5.2.3 Results – Uncracked Model

Fig. 129 shows a contour plot of maximum principal stress local to the First Street access hole radius. Notwithstanding stress peaks at the ends (which are top and bottom surfaces of the flange), the stress across the access hole, particularly within the low fracture toughness mid-thickness region, is much lower than the Fremont Street case (see Fig. 53). Further, as shown in the through-width distribution of Fig. 130, peak stress at the center of the radius is approximately 37 ksi, which is significantly lower than the Fremont Street peak of about 62 ksi (see Fig. 54). Similar to Fremont Street, the residual stress is greatly reduced 1 in. into the flange width.

A comparison of Fremont Street and First Street showing the significant difference in the peak residual stress is presented in Fig. 131. It is clear from these results that the sequence in which the access holes were cut during fabrication had a significant effect on the peak residual stress level that initiated the pop-in crack at Fremont Street and was not sufficient to initiate a pop-in crack at First Street.

That the First Street stress is lower than that of Fremont Street is not surprising, given the primacy of longitudinal shrinkage of the flange groove weld in loading the access holes. Much more so than transverse shrinkage, the longitudinal shrinkage causes the access-hole radius to open, resulting in tensile stress in the access-hole circumferential direction. In the First Street case, the material that exists before the hole is cut shields the material in that region from the loading created by longitudinal groove-weld shrinkage.

Although pop-in cracks were not identified in the First Street access hole radii, analyses were performed to assess the stress intensity factor for microcracks and the corresponding likelihood of pop-in crack initiation.

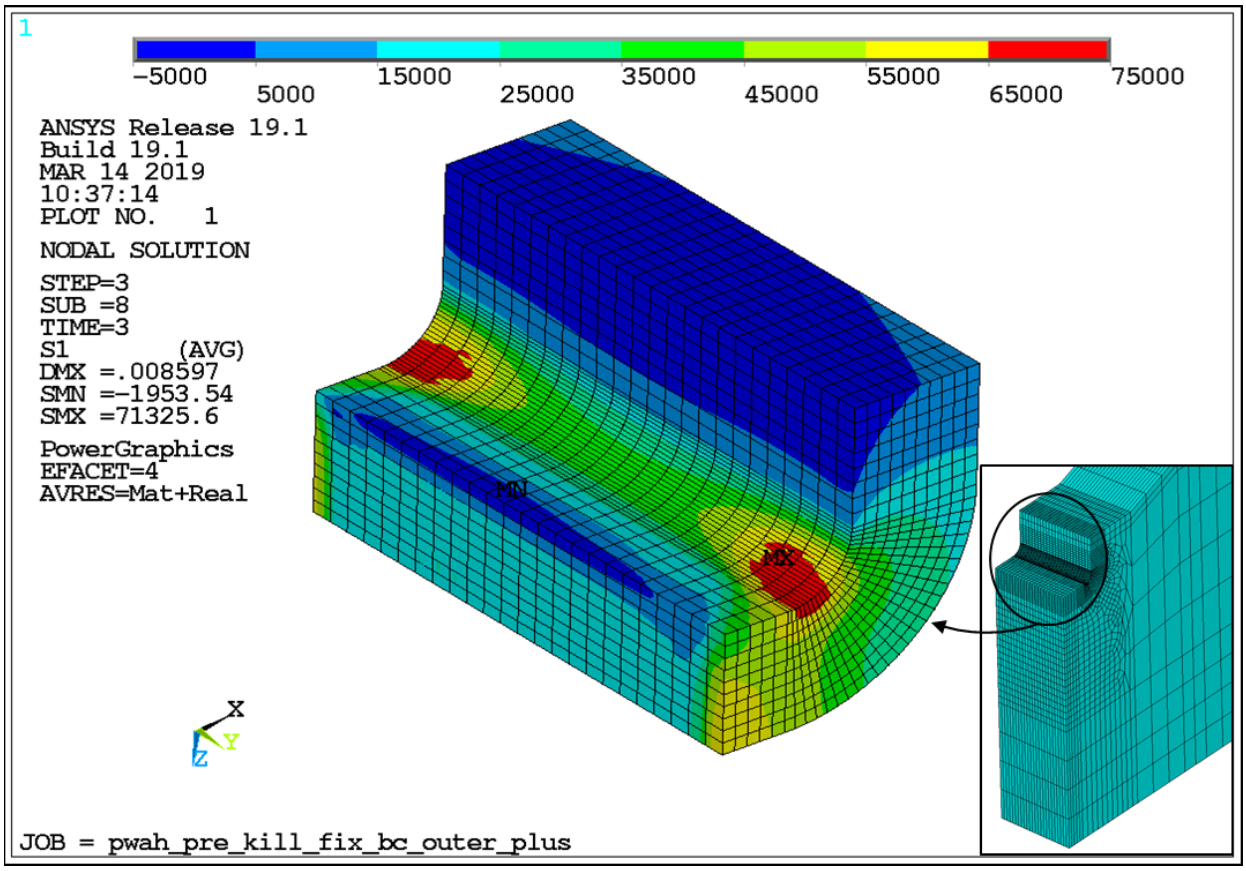

Fig. 129. Distribution of maximum principal stress local to access hole radius following cutting of the access hole in the First Street FE model. Except for the peak stress at the surfaces, the mid-thickness stresses are much lower than Fremont Street.

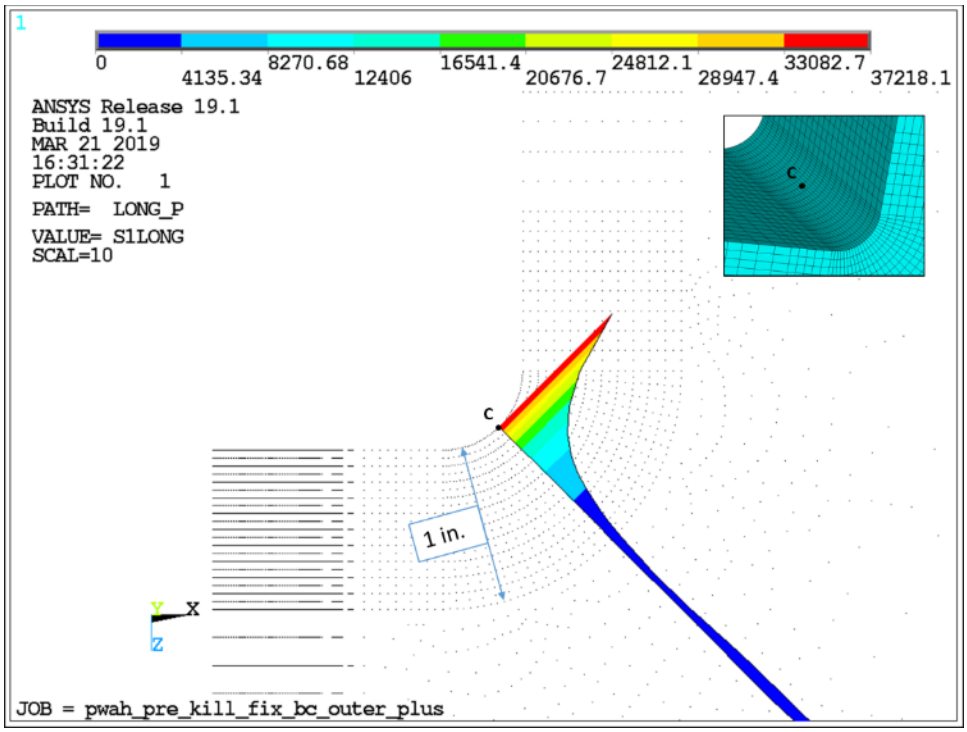

Fig. 130. Distribution of maximum principal stress, taken a point C, the center of the fillet radius of the First Street girder, in the flange width direction. At a depth of 1 in., stress is reduced to approximately 10% of the 37.2 ksi peak.

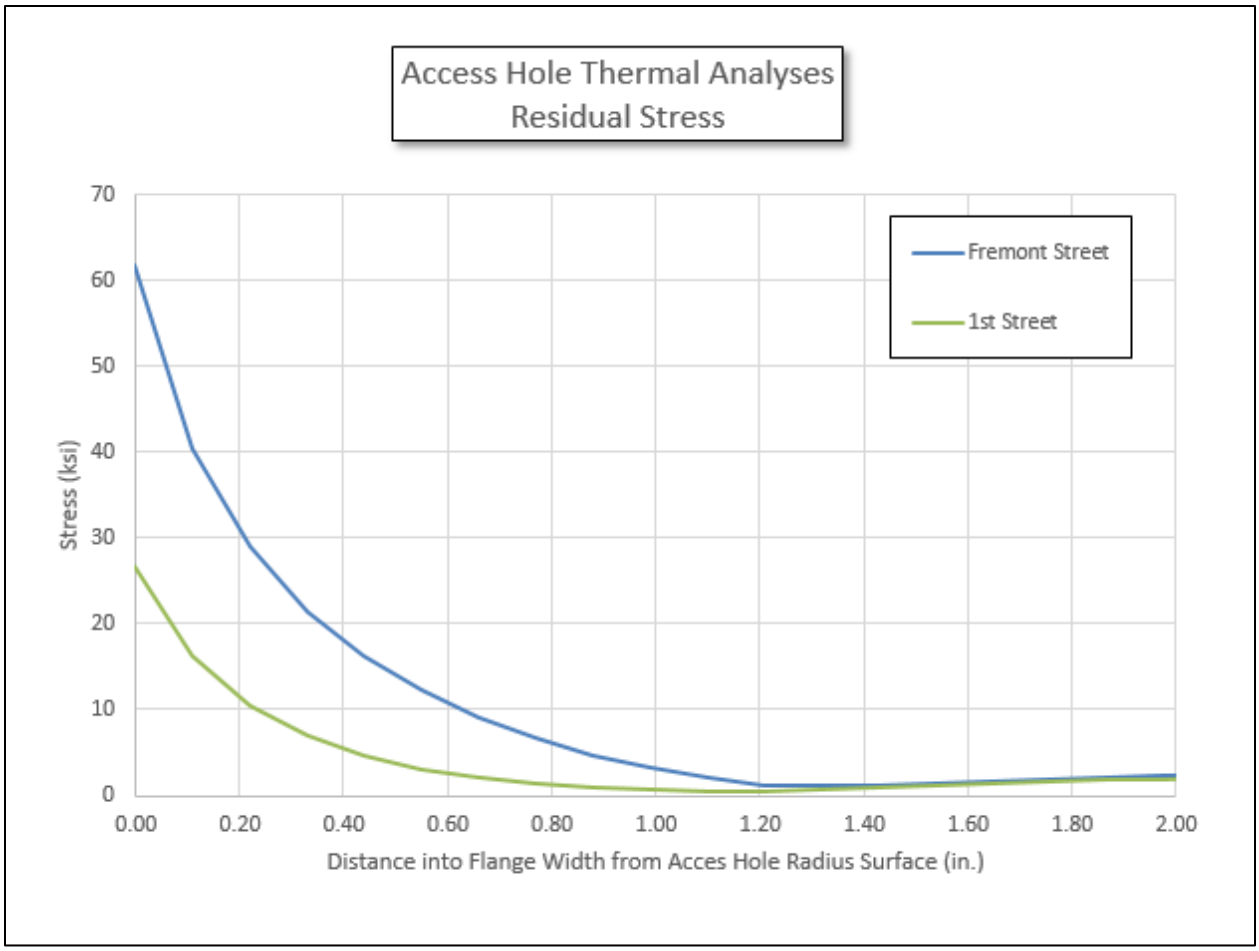

Fig. 131. A comparison of the thermal FE residual stress distributions between Fremont Street and First Street.

5.2.4 Results – Microcrack Model

Similar to the analyses for Fremont Street, a microcrack was inserted into the flange model and analyzed. Fig. 132 shows the mesh, while Fig. 133 shows the extent of crack depth.

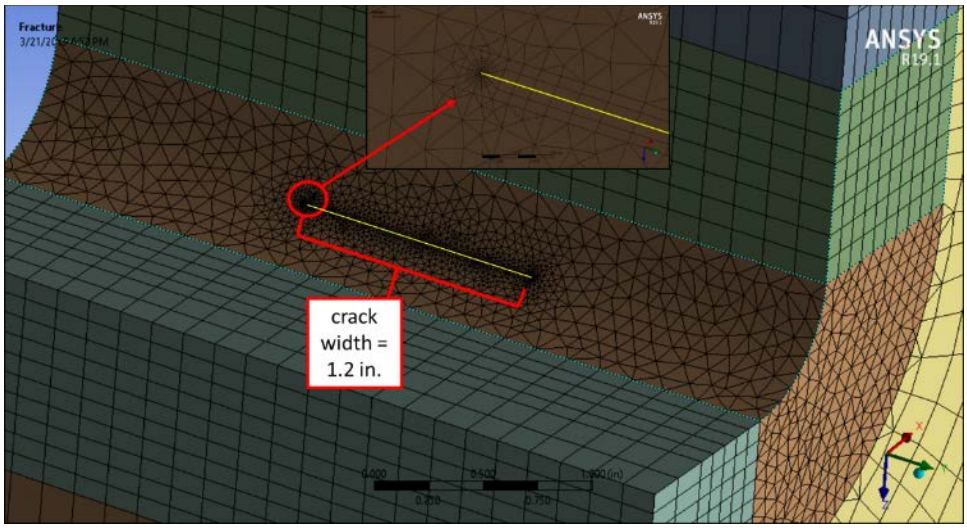

Fig. 132. Crack mesh of First Street FE model. Crack is semi-elliptical, 0.06 in. deep x 1.2-in. long, representing microcracks existing before pop-in crack initiation. Free surface of crack shown in yellow; inset shows close-up view of the structured character of the specialized mesh employed.

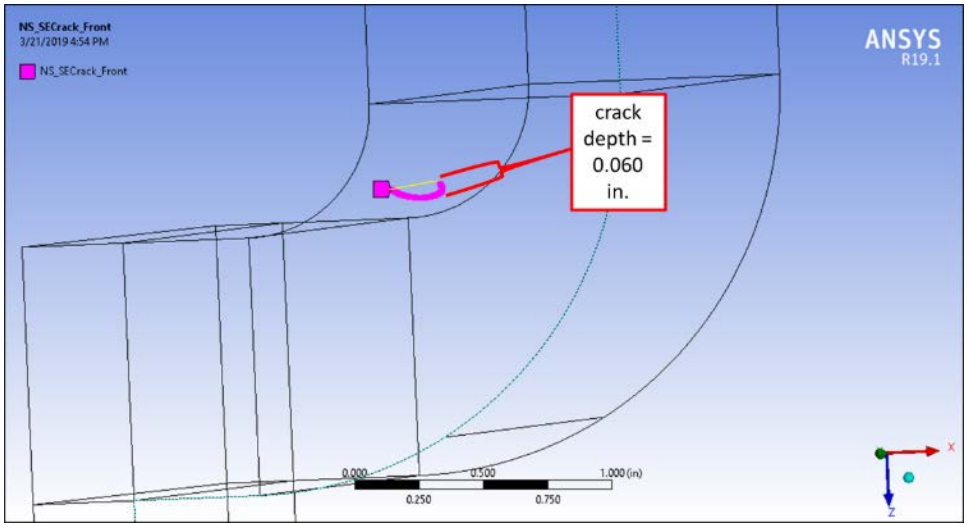

Fig. 133. Wireframe view showing depth of the microcrack of First Street FEM. Purple line shows the crack front.

Fig. 134 and Fig. 135 show plots of stress intensity factor similar to those determined for Fremont Street shown in Fig. 107 and Fig. 108. As shown, K_1 for First Street was determined to be 14.2 ksi√in., which is significantly lower than the 27 ksi√in. calculated for Fremont Street. Therefore, pop-in crack initiation is not predicted to occur at First Street, which is consistent with the absence of pop-in cracks in the First Street flange access holes.

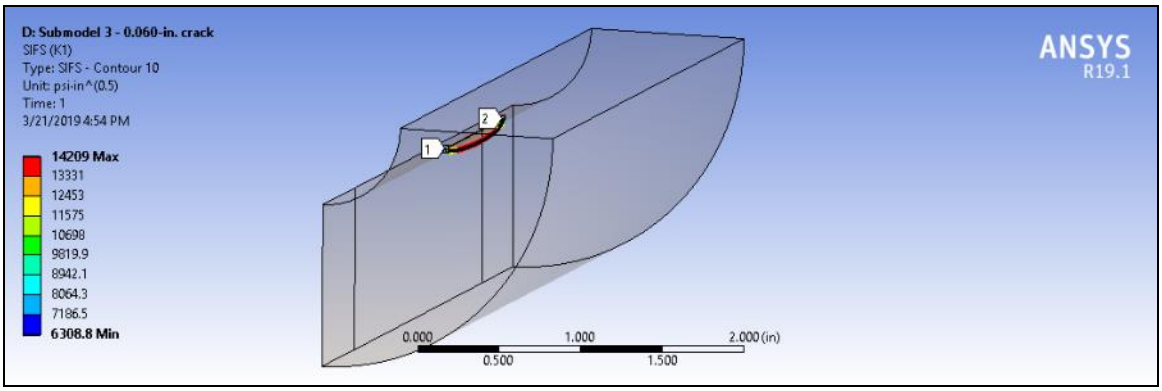

Fig. 134. Microcrack stress intensity factor for the First Street FE model subject to weld-shrinkage loading. Plot corresponds to the outermost contour around the crack front, with a peak K_1 of approximately 14 ksi√in.

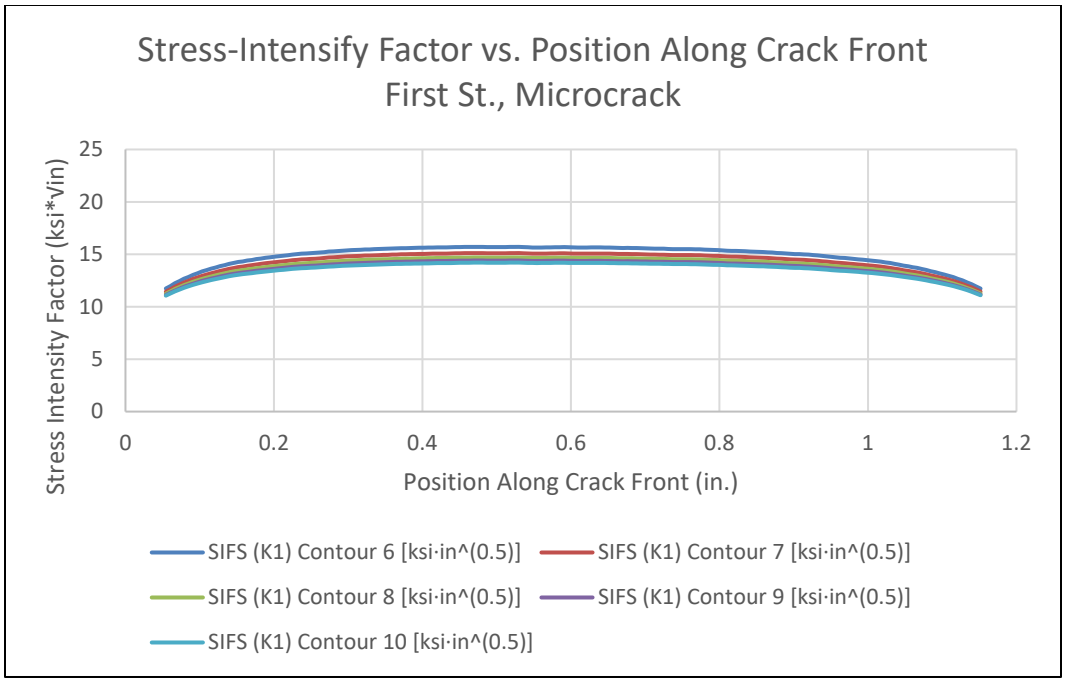

Fig. 135. Stress intensity factor (K_1) versus position along crack front for the microcrack in the First Street FE model under groove-weld-shrinkage loading. Contours 6 through 10 show a converging trend (from top curve to bottom curve) toward a K_1 of approximately 14 ksi√in.

5.2.5 Results – Pop-in Crack Model

Again, similar to what was done for Fremont Street, a pop-in crack was inserted into the model and analyzed. Fig. 136 shows the mesh, while Fig. 137 shows the extent of crack depth.

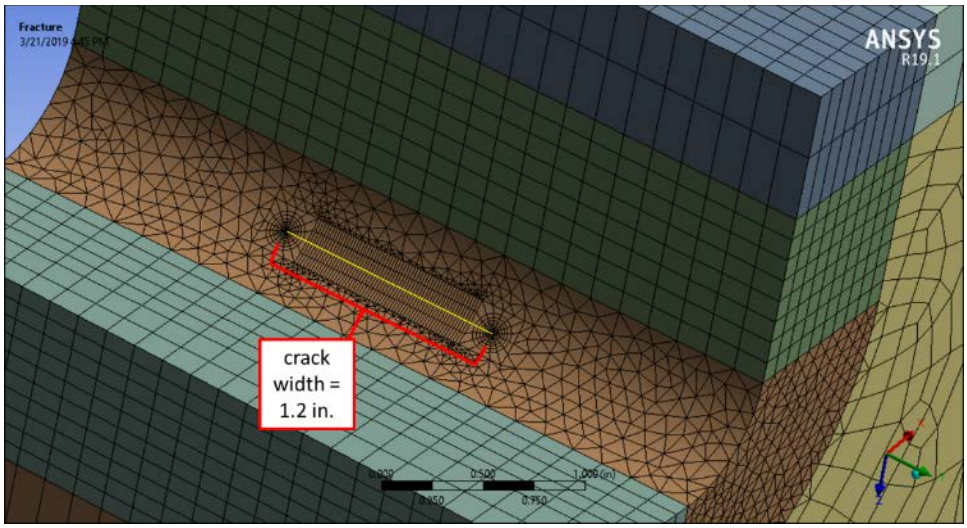

Fig. 136. Crack mesh of First Street FE model. Crack is semi-elliptical, 0.38 in. deep x 1.2-in. wide, 0.38-in. representing the pop-in crack. Free surface of crack shown in yellow. Structured character of specialized mesh local to crack is evident.

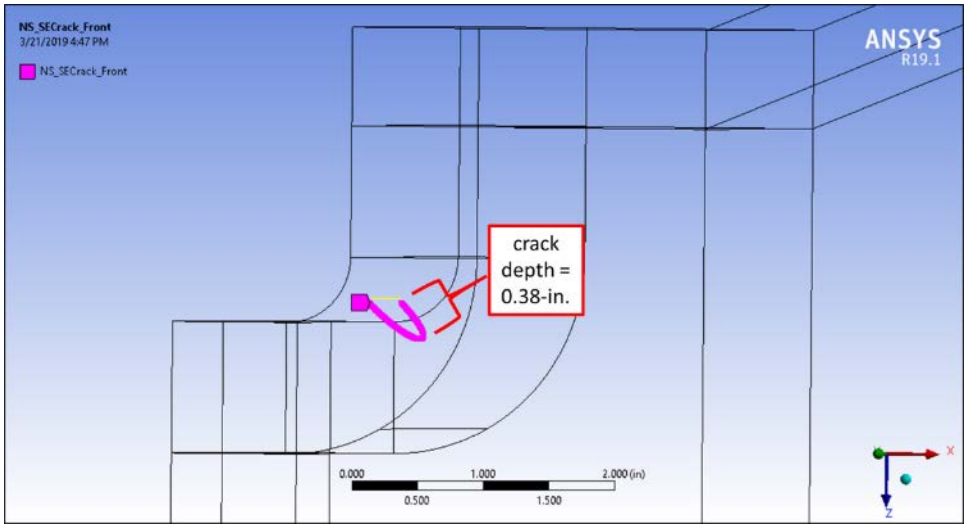

Fig. 137. Wireframe view showing depth of the pop-in crack of First Street FEM. Purple line shows the crack front.

Fig. 138 and Fig. 139 show plots of stress intensity factor analogous to those for Fremont Street shown in Fig. 111 and Fig. 112. As shown, the peak K_1 of 12 ksi$\sqrt{}$in. for First Street is significantly lower than the peak K_1 of 21 ksi$\sqrt{}$in. calculated for Fremont Street. A residual stress K_1 of only 12 ksi$\sqrt{}$in. for First Street significantly reduces the total K_1 for the flange, thereby also significantly reducing the likelihood of flange fracture from a pop-in crack assuming such a crack was present at First Street.

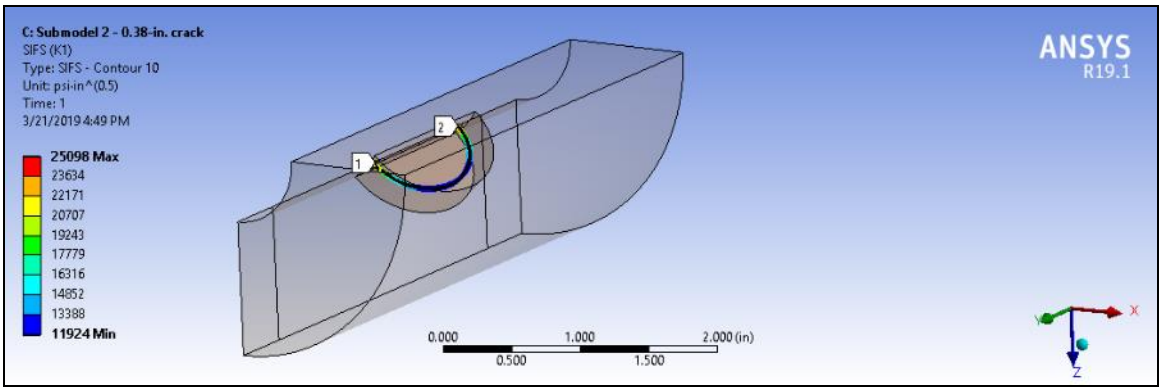

Fig. 138. Pop-in crack stress intensity factor for the First Street FE model subject to weld-shrinkage loading. Plot corresponds to the outermost contour around the crack front, with a peak K_1 of approximately 12 ksi√in. (blue) stress-intensity-factor (SIF) plot for First Street FEM under groove-weld-shrinkage loading.

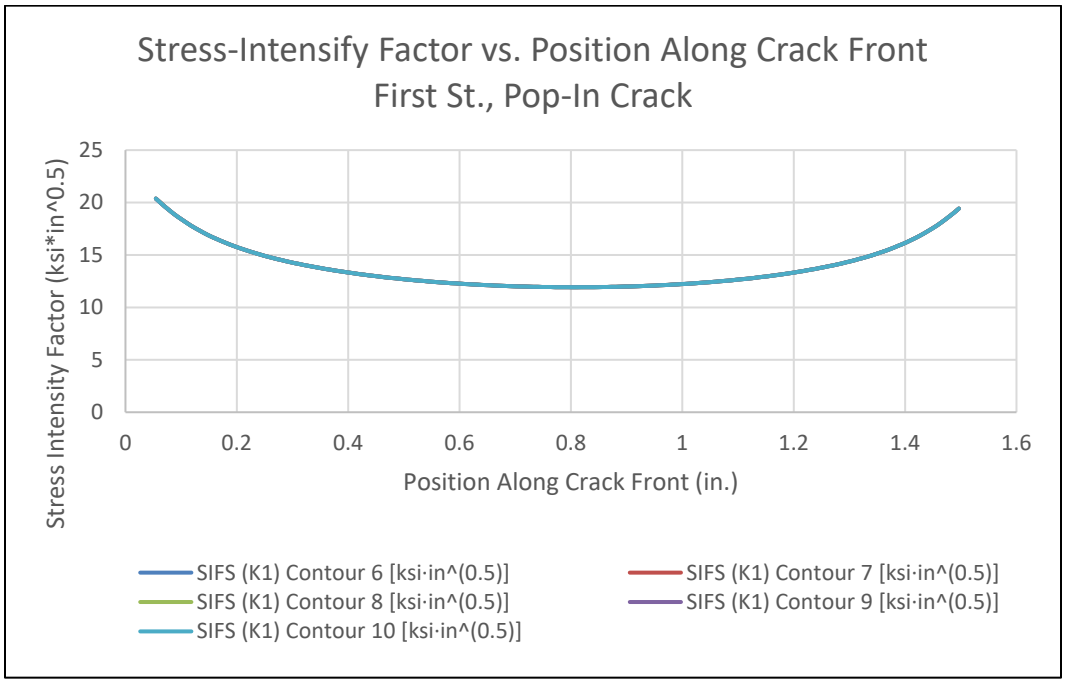

Fig. 139. Stress intensity factor (K_1) versus position along crack front for the microcrack in the First Street FE model under groove-weld-shrinkage loading. Contours 6 through 10 show a converging trend (from top curve to bottom curve) toward a K_1 of approximately 12 ksi√in.

5.3 As-Built Stress Analysis

Stress analysis of the First Street girders was performed using the finite element method to assess the suitability of as-built configuration for its intended service. Model details and analysis results are presented in the following subsections.

5.3.1 Finite Element Model

As part of the design and repair review performed here, stress analyses were performed on the as-fabricated condition of the First Street girder flanges when subjected to factored design loads. Of particular interest were the bottom-flange-to-hanger fillet welds, which are fully wrapped around the First Street hangers. To this end, finite element analysis of the First Street girders was performed using the same model and methodology as the Fremont Street analyses (see Section 4.3.1), except for the items detailed in the following subsections.

5.3.1.1 Geometric Details

The First Street tapered plate girders are nearly identical to those above Fremont Street, with only minor geometric differences. Unless otherwise noted, all geometric details modeled for First Street are the same as those modeled for Fremont Street (see Section 4.3.1).

Weld access holes in the First Street bottom flanges were flame-cut in-situ after fabrication of the CJP groove welds and vary in shape compared to the shop-cut holes of Fremont Street. The holes in the south (“F”) girder are generally larger than those in the north (“D”) girder, and the largest of all the holes exists in the northeast quadrant of the south (“F”) girder, as shown in Fig. 140. Given the observed shapes and sizes of the First Street access holes, the south (“F”) girder was chosen for modeling and analysis. The First Street South (“F”) access holes were modeled according to direct measurements and photographs, as shown in Fig. 141 through Fig. 142.

The ¾-in. fillet welds between the bottom flange and hanger of the First Street girders are fully wrapped around the east and west ends of the hanger, whereas the Fremont Street fillet welds are not. The wrapped fillet welds on the top and bottom sides of the bottom flange are shown in Fig. 143 and Fig. 144, respectively.

During fabrication, the vertical stiffeners at the girder centerline were offset by approximately 1 in. (i.e., half the stiffener thickness) to achieve good fit-up. The north-side stiffener was offset to the west, as shown in Fig. 145, and the south-side stiffener was offset to the east, as shown in Fig. 146.

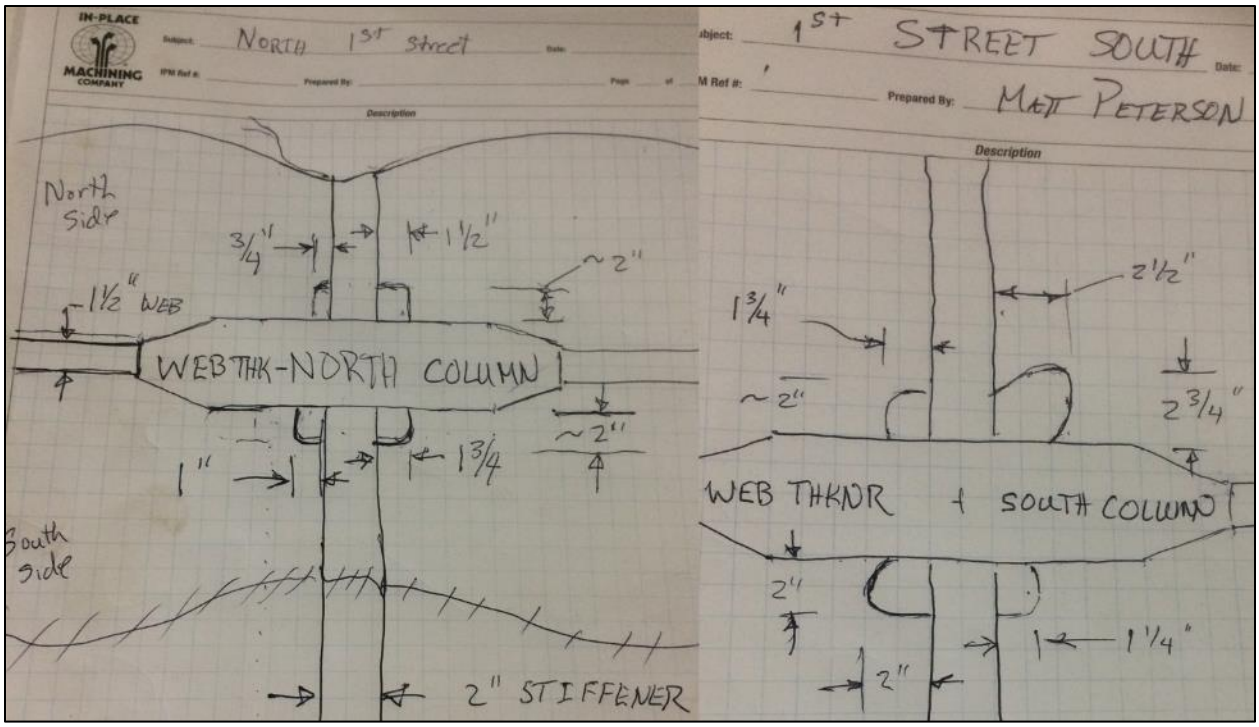

Fig. 140. First Street weld access hole dimensions, measured by In-Place Machining on October 28, 2018.

Fig. 141. Plan views of access holes on First Street South ("F") girder. North is towards the top of the page.

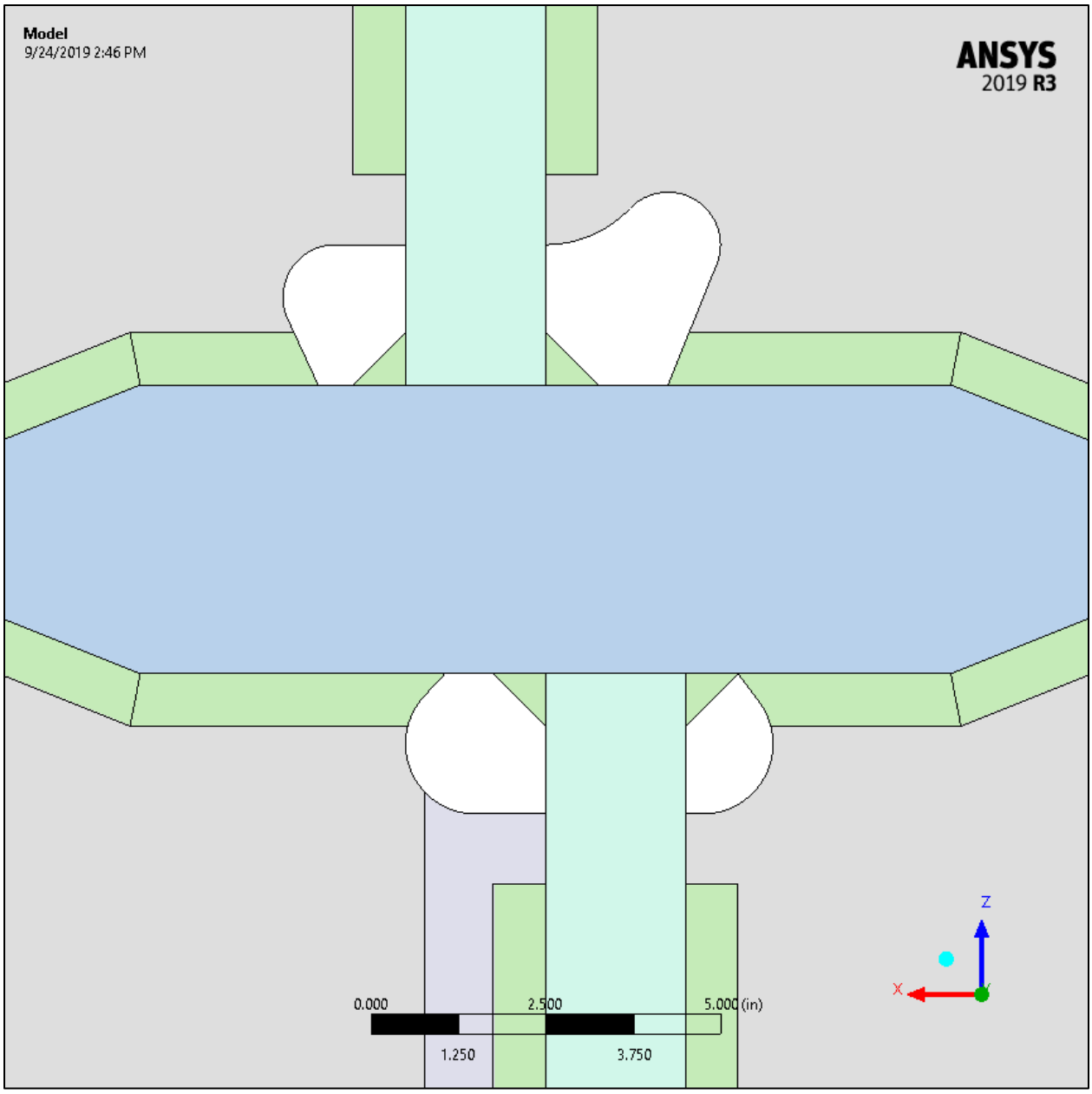

Fig. 142. Plan view of modeled access holes on First Street South ("F") girder. North is towards the top of the page.

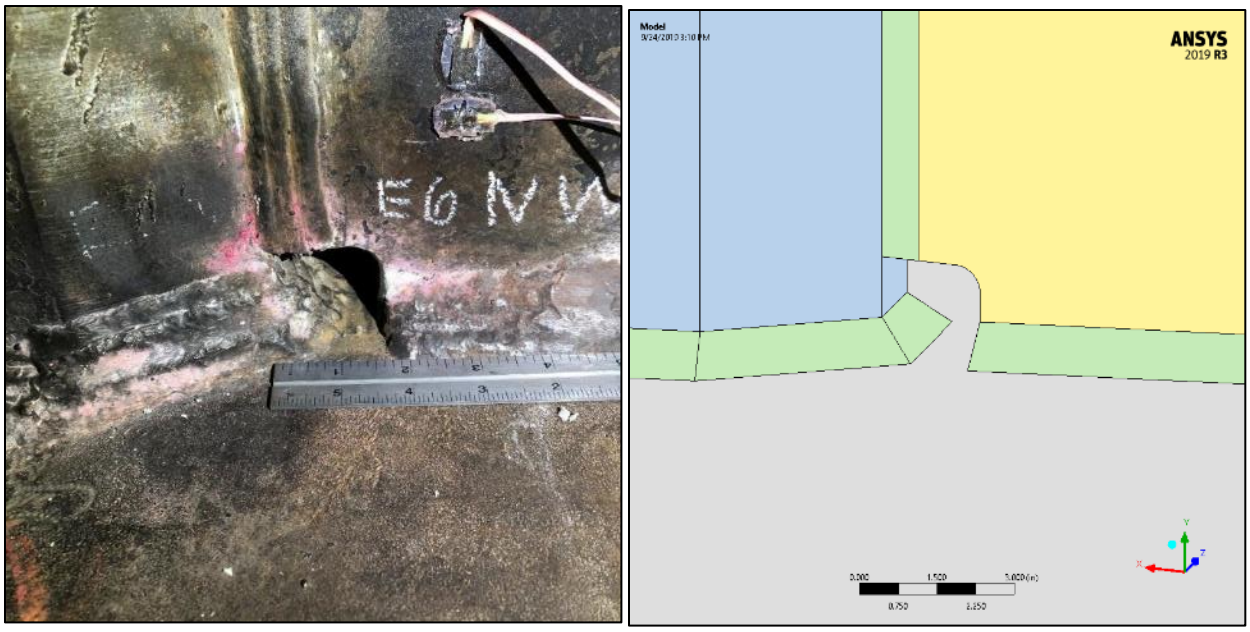

Fig. 143. First Street South (“F”) wrapped fillet welds between bottom flange and hanger (top side of bottom flange).

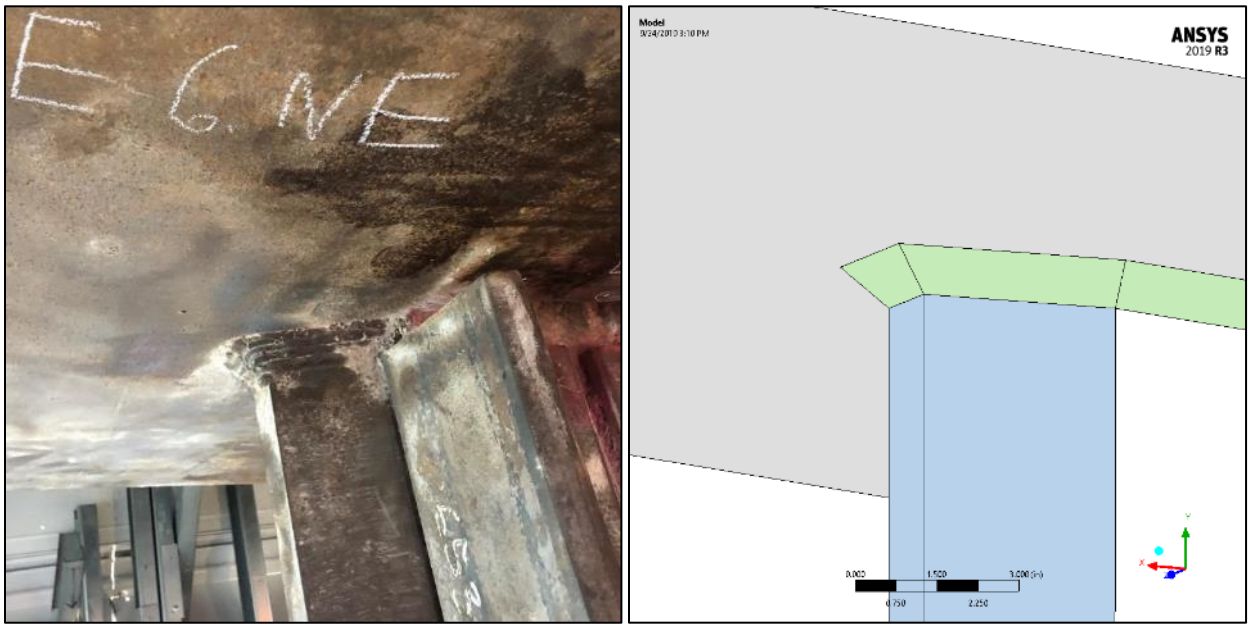

Fig. 144. First Street South (“F”) wrapped fillet welds between bottom flange and hanger (bottom side of bottom flange).

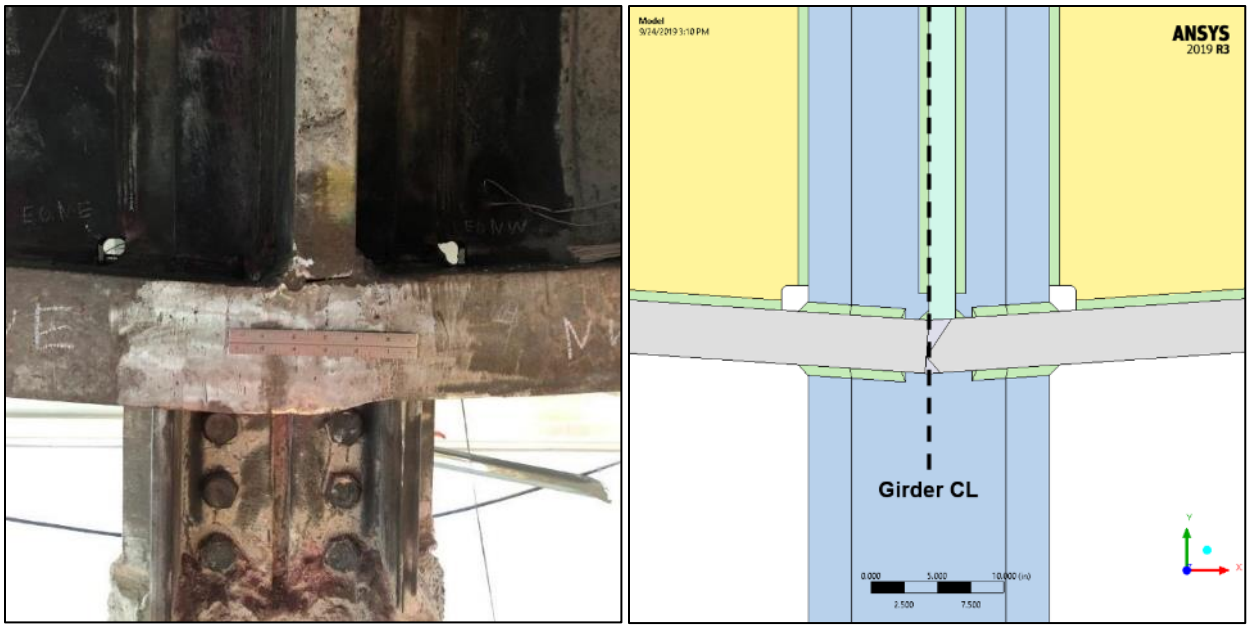

Fig. 145. First Street South (“F”) north-side stiffener offset to the west.

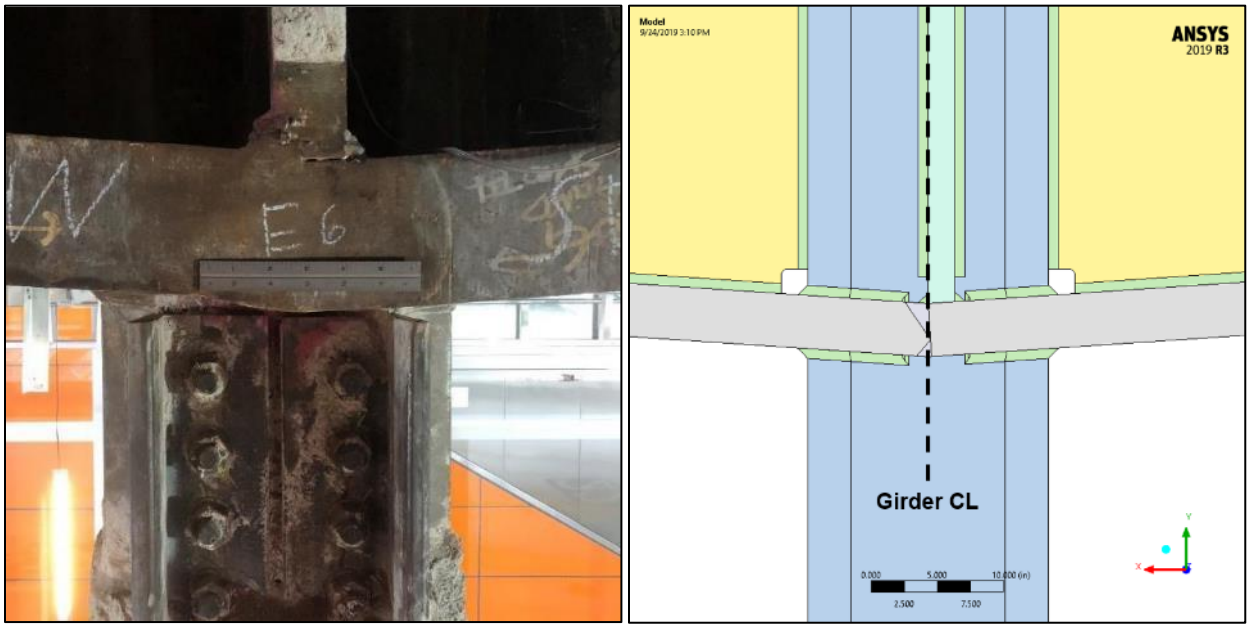

Fig. 146. First Street South (“F”) South-side stiffener offset to the east.

5.3.1.2 Loads

Factored design loads were considered in the analysis of the First Street South (“F”) girder in accordance with the load combination given in Eq. (6). A 90% scaling factor was applied to the SDL and LL magnitudes given in [26] to account for post-composite load

sharing per [27]. The factored loads, as applied to the model, are given in Table 17. The 1.2 factor on DL was also applied to the inertial loading (i.e., gravitational acceleration) to account for the factored self-weight of the tapered plate girder.

$$1.2(DL + SDL) + 1.6(LL) \quad (6)$$

Table 17 – Factored Design Loads Applied to First Street South ("F") Model

Load Case	Forces (lb)			Pressure (psi)
	Hanger	West Stiffener	East Stiffener	Deck
1.2(DL)	336,000	138,000	132,000	2.78
1.2(DL+SDL)	643,800	423,120	475,440	10.75
1.2(DL+SDL) + 1.6(LL)	933,240	528,240	577,680	13.69

5.3.1.3 Verification of Mesh-Independent Results

Areas of the model for which detailed stress distributions were desired were meshed with a nominal element size of 0.25 in. To verify the resulting stresses were independent of mesh size, the mesh in the vicinity of one of the "7-ft" stiffeners (i.e., located approximately 7 ft from the girder centerline) was doubled in density (i.e., 0.125-in. mesh size) and the model was rerun. A comparison of the mesh densities and resulting stresses are given in Fig. 147 and Fig. 148, respectively. It is evident from the stress plots that both meshes provide practically identical results and, therefore, the nominal 0.25-in. mesh size is sufficiently dense to produce mesh-independent results.

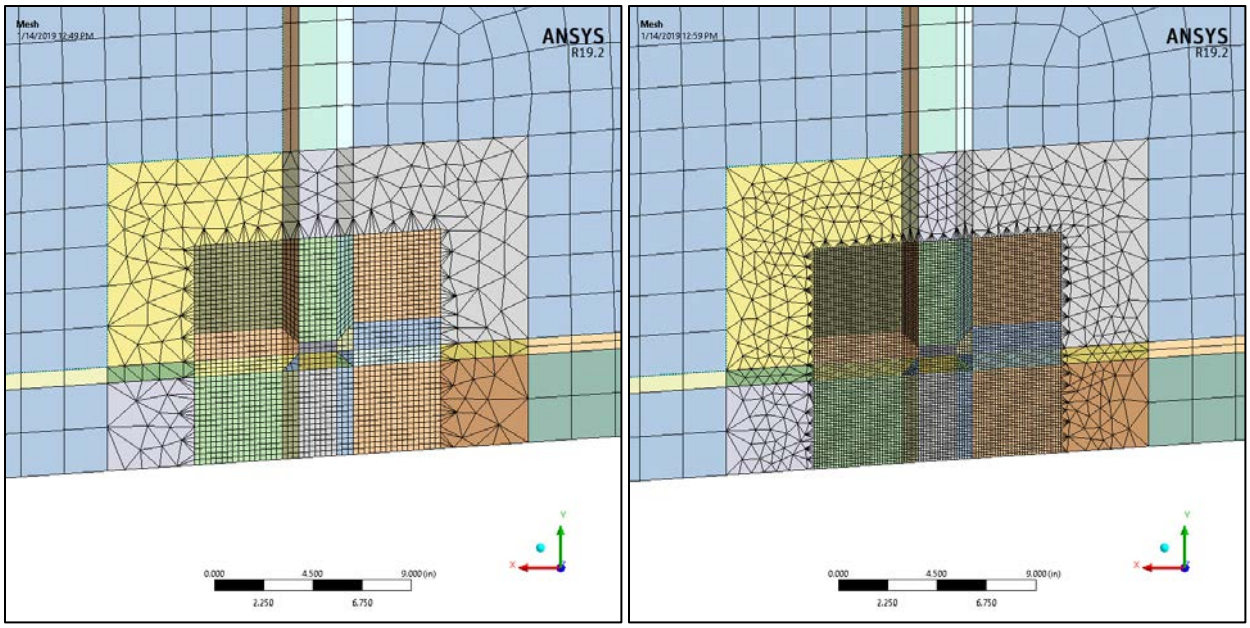

Fig. 147. Views of nominal mesh (left) and refined mesh (right).

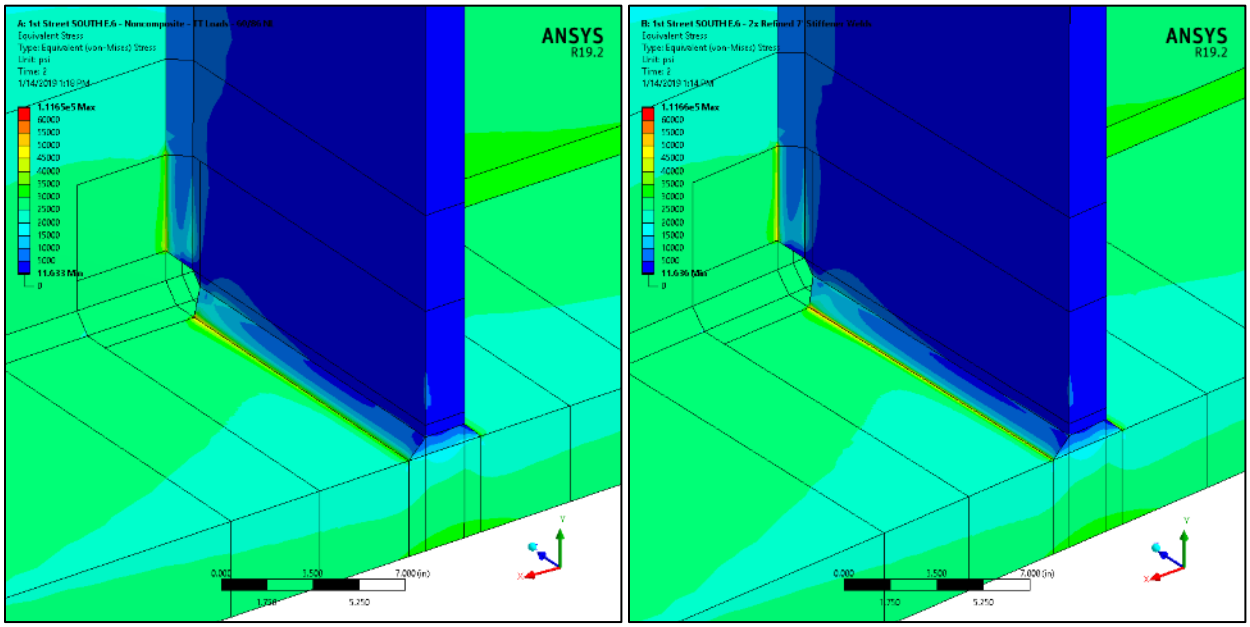

Fig. 148. Von Mises stress results for nominal mesh density (left) and refined mesh (right).

5.3.2 Factored Loading Results

Isometric views of equivalent (von Mises) stress plots are shown in Fig. 149. As is expected for the factored design loads, stresses in the bottom-flange-to-hanger fillet

welds exceed their 70-ksi yield strength. Minor yielding of the web access hole surface is evident, as expected.

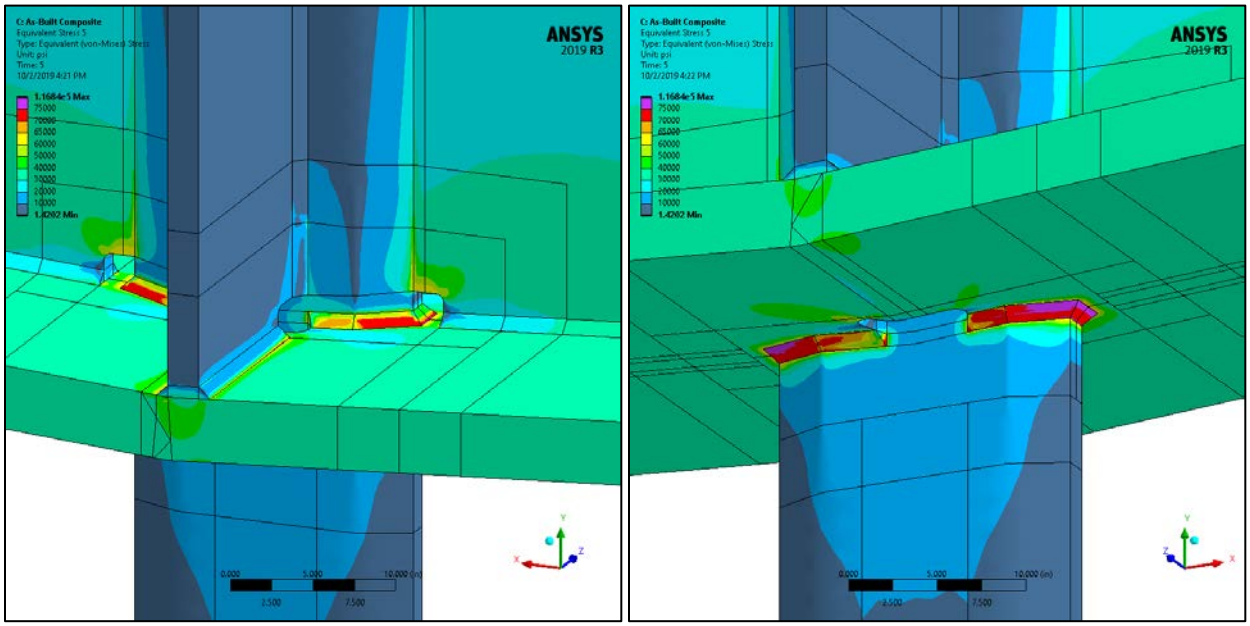

Fig. 149. Equivalent (von Mises) stress plots, view from Southeast looking Northwest.

Maximum (i.e., first) principal stresses on the bottom flange weld access hole surfaces are shown in Fig. 150. All access hole "corners" exhibit surface stresses above yield, with the largest (i.e., northeast) hole having the highest stress. This is typical of weld access holes and is expected for the factored design condition.

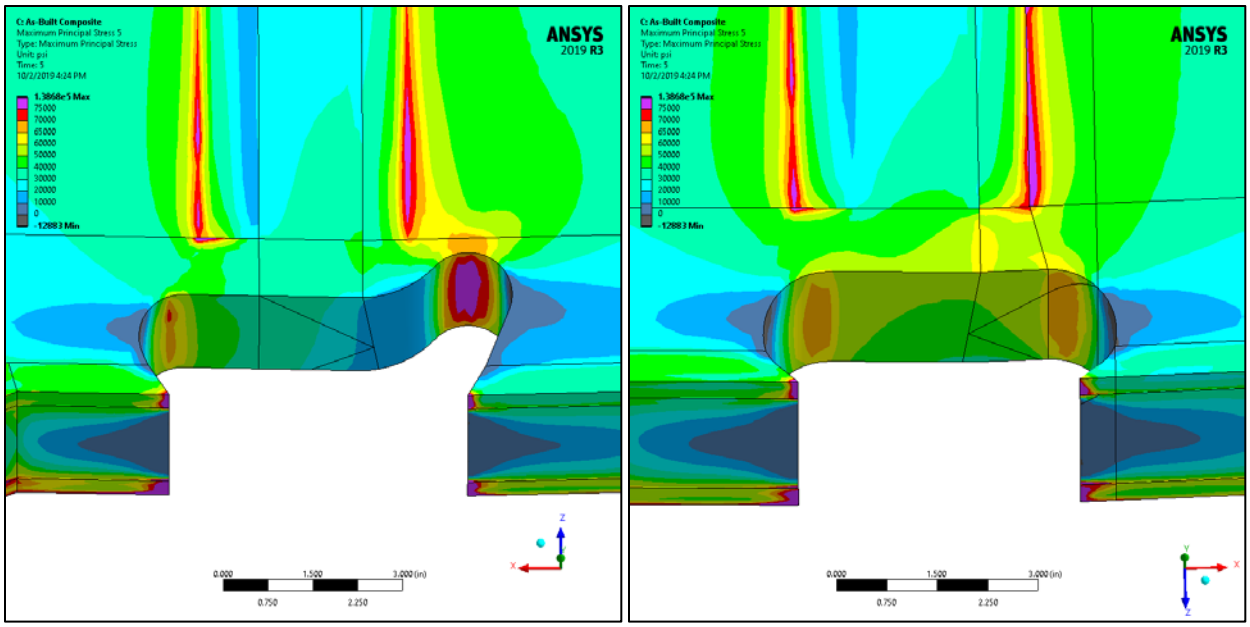

Fig. 150. Maximum principal stress plots of north-side (left) and south-side (right) weld access holes.

Maximum principal stresses on the bottom flange hanger slot surfaces and in the vicinity of the web access hole are shown in Fig. 151. While stresses in the bottom-flange-to-hanger fillet welds are high, the stresses in the bottom flange drop rapidly with distance from the welds, resulting in mid-thickness stresses in the 30 ksi range. The end of the slot has near-zero stress, which is expected of a free surface that is normal to the principal stress direction.

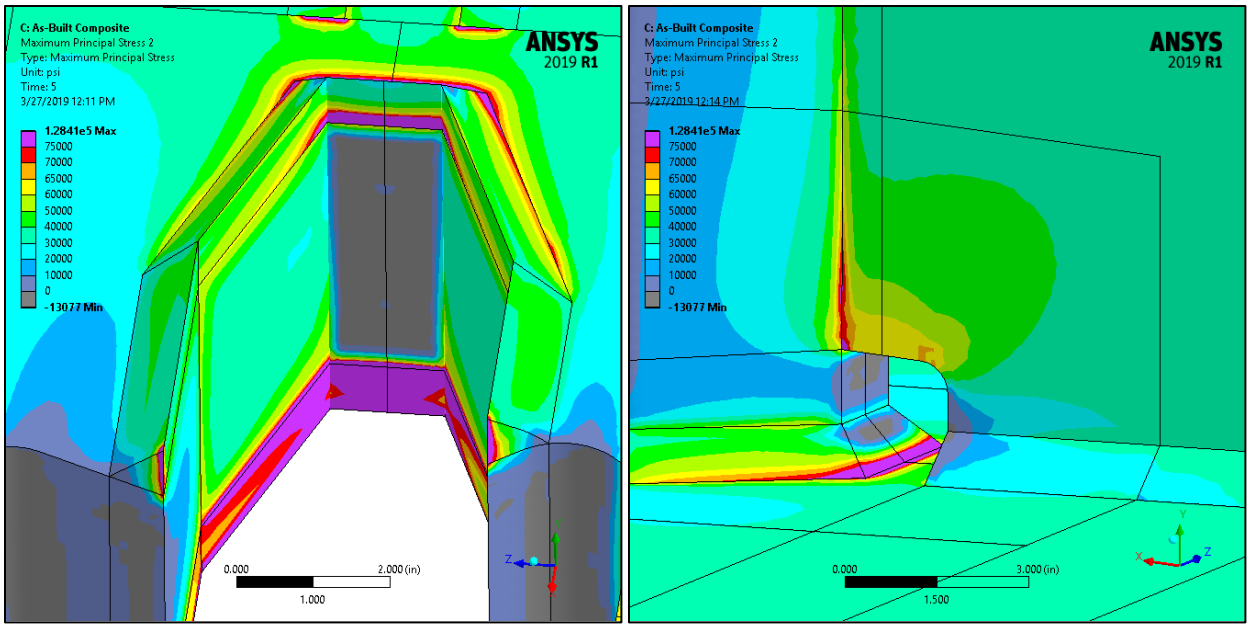

Fig. 151. Maximum principal stress plots of bottom flange hanger slot (left) and web access hole (right).

A section plane was inserted at the mid-thickness of the web to plot internal stresses. Fig. 152 shows both maximum principal stress and the vertical stress component on the mid-thickness plane in the vicinity of the web access hole. While the principal stresses exceed yield local to the welds, the vertical stresses (i.e., the component that would initiate cracking in the hanger) are very low (see Section 5.3.3).

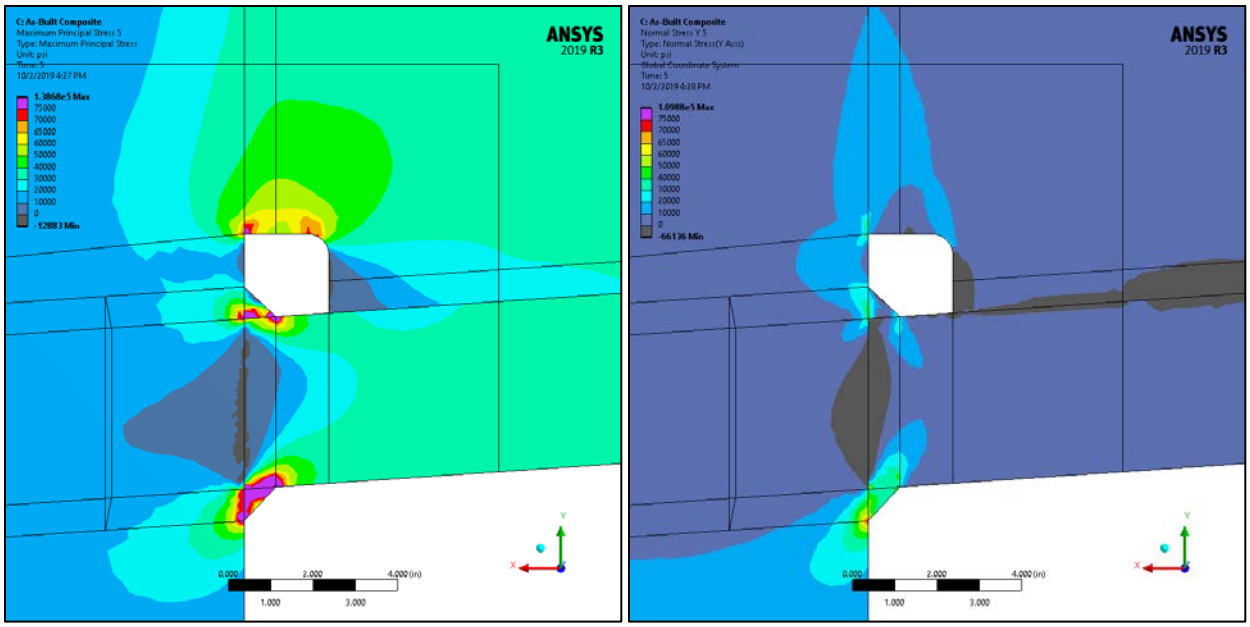

Fig. 152. Web access hole centerline section view of maximum principal stress (left) and vertical stress component (right).

From a stress perspective, the tapered girders are adequately designed for the factored design load case. This does not imply that a code review was performed.

5.3.3 Hanger Assessment

The hanger was assessed for both fracture due to factored design loads and fatigue due to expected cyclic loading, the details of which are provided in the following subsections.

5.3.3.1 Hanger Fracture

To assess the resistance of the hangers to fracture, their fracture toughness must first be quantified. To this end, four 3-in. diameter cores were removed from the hanger plate material. Twenty CVN specimens were machined from each core sample, with four each from the top surface, quarter-thickness, mid-thickness, three-quarter-thickness, and bottom surface locations, totaling eighty specimens. The specimens from each sample-location combination were tested at 30 and 70°F. For further information on CVN testing and conversion to fracture toughness, see Sections 3.6.1 and 3.6.3. CVN test data is given in Table 36 through Table 39 (see Appendix D). The fracture toughness values resulting from the conversion of CVN test data are given in Fig. 153. At the assessment temperature of 50°F, the 5% lower-bound fracture toughness is approximately 110 ksi$\sqrt{\text{in}}$.

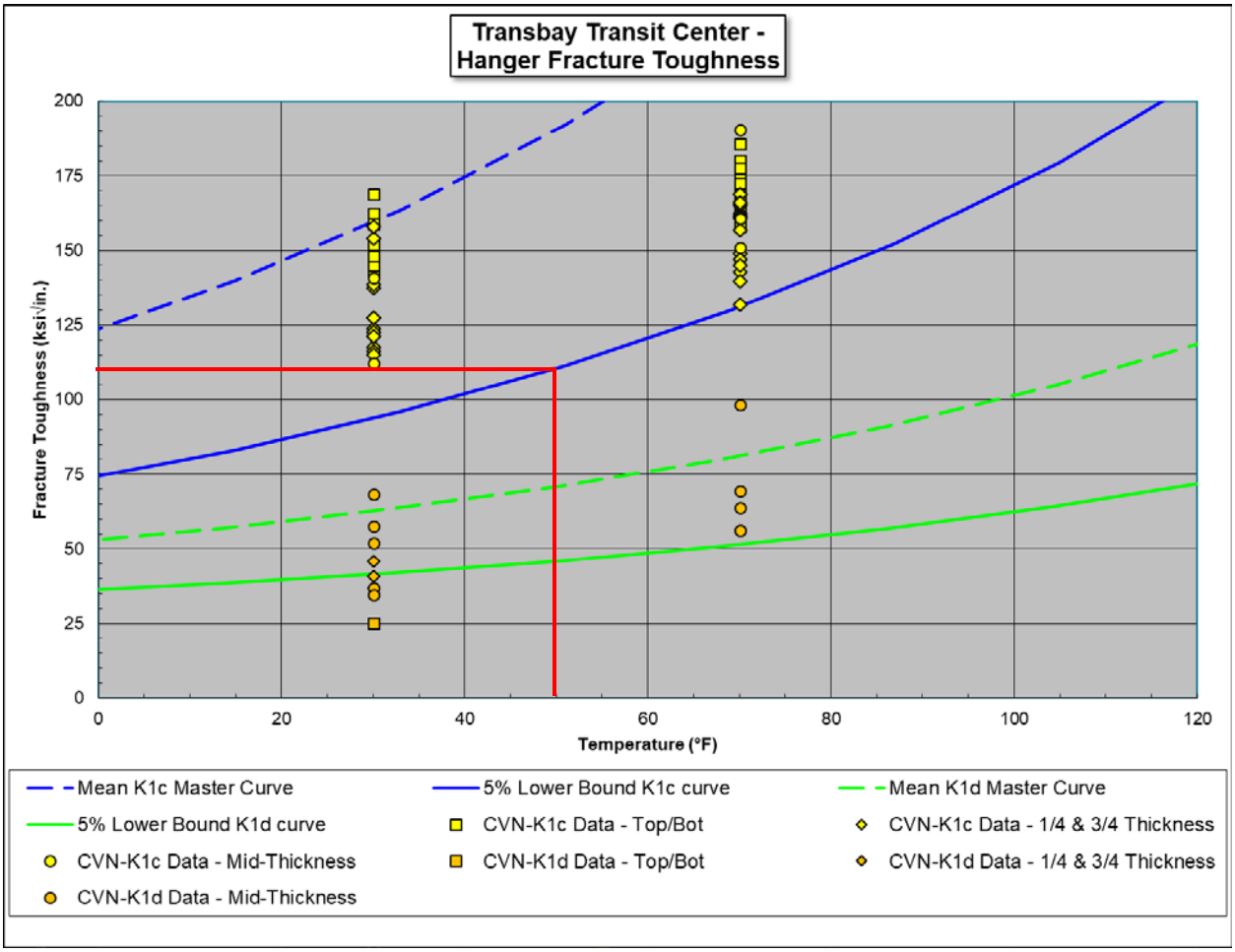

Fig. 153. Hanger fracture toughness data.

The hanger is loaded vertically by the column below, so vertical stresses were examined at three locations: the lower hanger fillet welds, the upper hanger fillet welds, and the reentrant corner of the web access hole. A path for stress output was defined at each of these locations, and are referred to as “lower”, “upper”, and “web”, respectively. The paths begin at mid-thickness of the hanger at its free surface and end at the centerline of the hanger, as shown in Fig. 154. The vertical stress component due to the factored design loads was output along these paths for use in fracture mechanics calculations, as shown in Fig. 155. The results are given for the east side of the hanger, but the stresses on the west side are within 0.5 ksi.

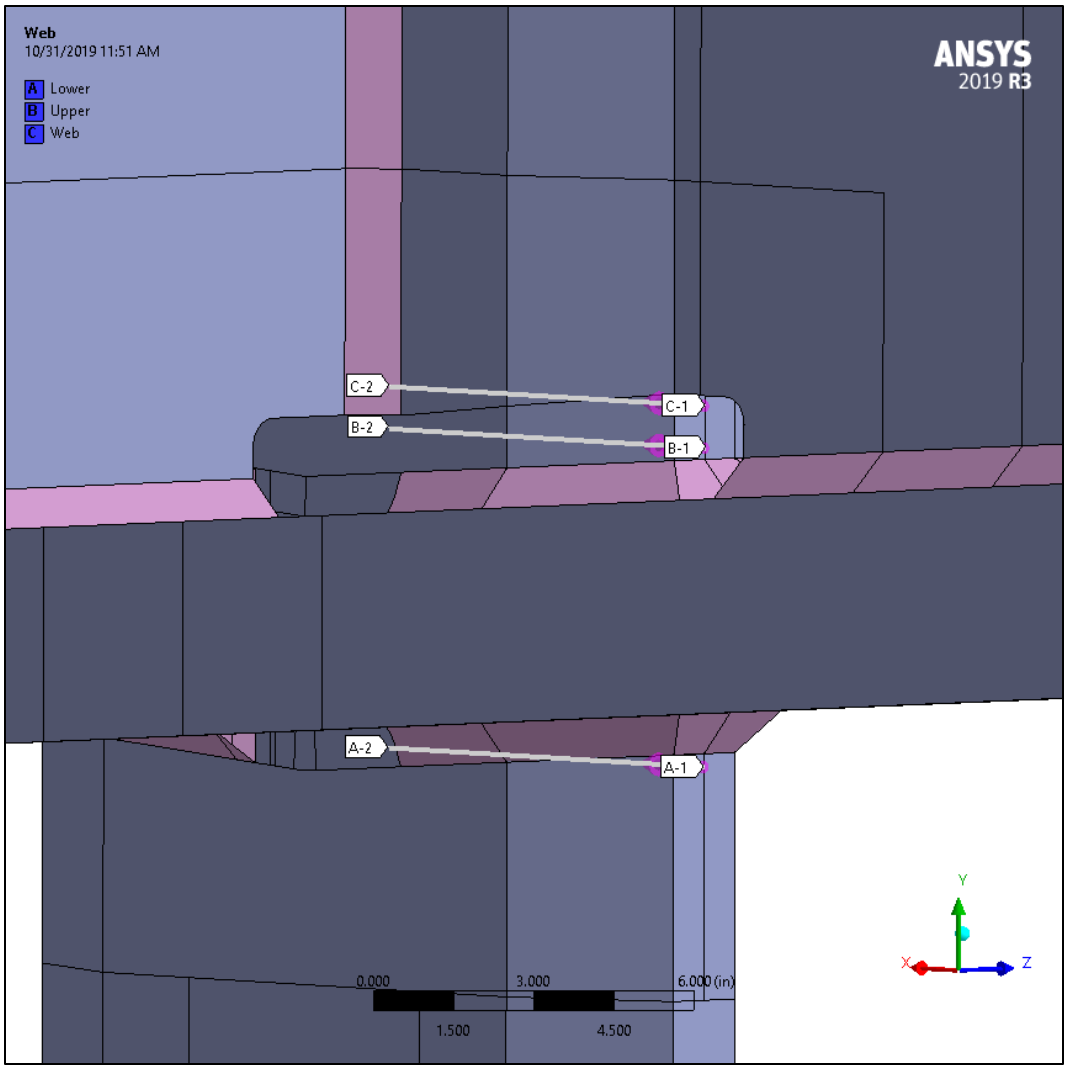

Fig. 154. Paths for hanger stress output.

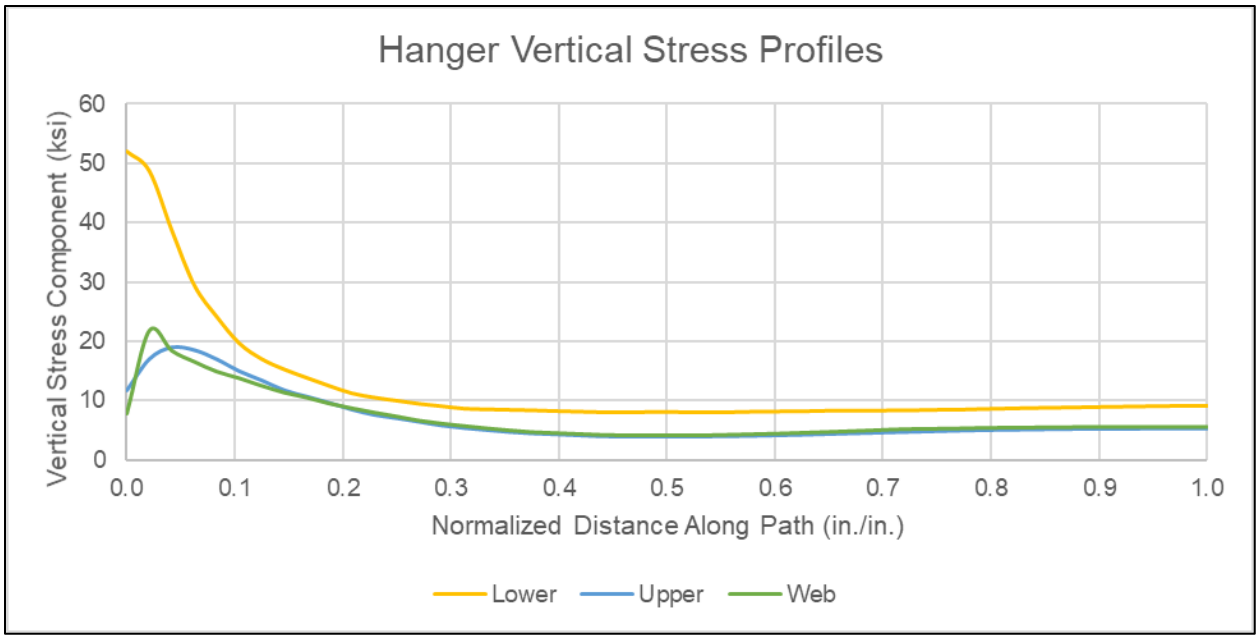

Fig. 155. Vertical stress component profiles in the hanger when subjected to the factored design loads.

FAD calculations were performed to determine the susceptibility of the hanger to fracture. A 1.2 × 0.125-in. semi-elliptical surface flaw was assumed to exist on the hanger, and the "lower" stress profile in Fig. 155 was used. Both FAD assessment points fall well below the failure curve, as shown in **Fig.** 156. The critical crack depth for this stress profile was determined to be 0.596 in. The as-built hanger is, therefore, not susceptible to fracture in the presence of the assumed flaw when subjected to the factored design loads.

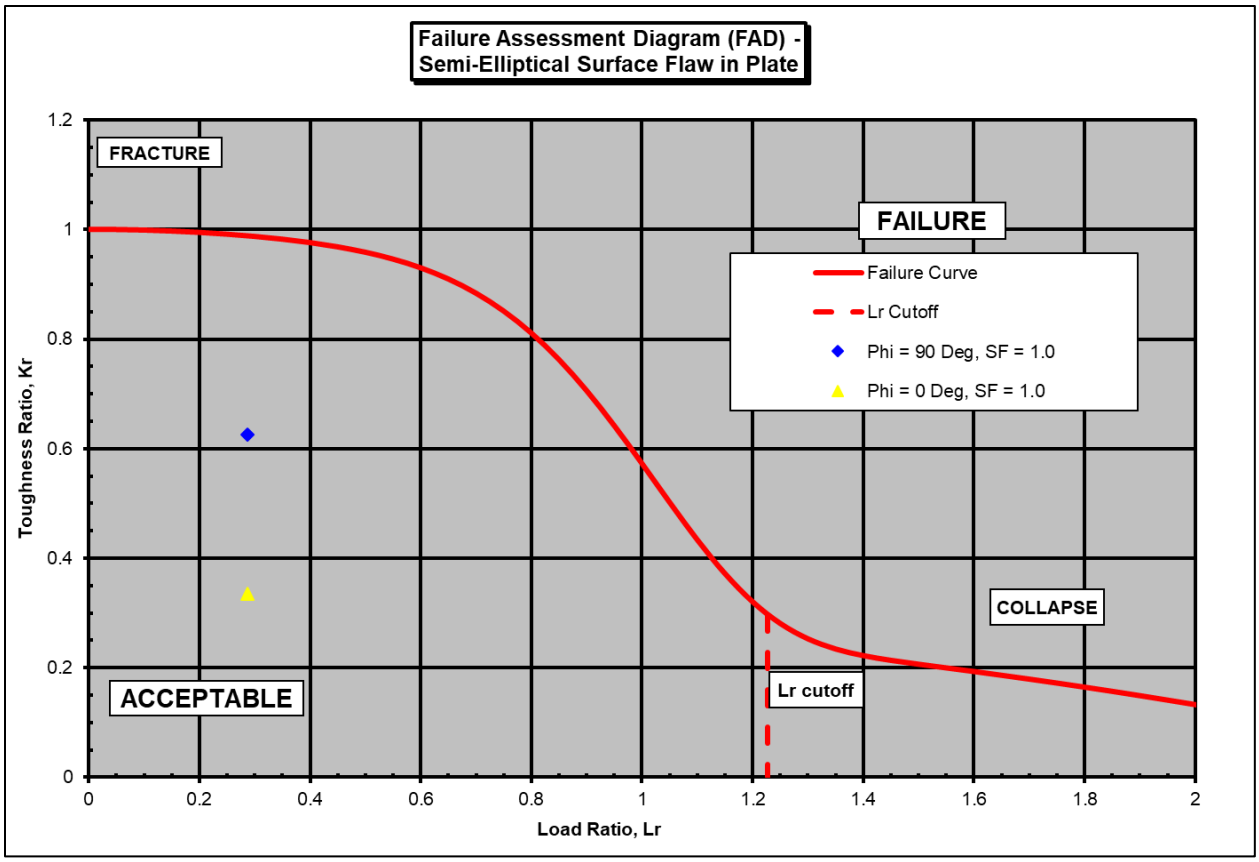

Fig. 156. FAD calculation results for an assumed 1.2 × 0.125-in. semi-elliptical surface flaw on the hanger in the as-built condition when subjected to the factored design loads.

5.3.3.2 Hanger Fatigue

Cyclic stresses due to expected bus traffic were investigated to determine the susceptibility of the hanger to fatigue crack initiation. Per TT [38], the cyclic hanger load associated with a 72-kip AASHTO Design Truck parked as close to the hanger as possible is 9.7 kips. The 1100 buses per day that will service the TTC are lighter than the Design Truck, as shown in Table 18 [39]. Also shown in the table is the calculation of the 43,668-lb effective bus weight, a cubic weighted average that is representative of the entire fleet and used for fatigue life calculations. Scaling the cyclic hanger load associated with the Design Truck indicates that the cyclic hanger load is 5.9 kips for the 43.7-kip effective bus weight.

Table 18 – Transbay Bus Matrix and Effective Weight Calculation

Make	Year	Length (ft)	GVWR (lb)	Series	Qty		γ	γ × GVWR^3
Eldorado	2014	26	14,500	3500	10		0.0157	4.79E+10
Van Hool	2006	30	33,100	5000	51		0.0801	2.90E+12
Van Hool	2009	30	32,600	5100	39		0.0612	2.12E+12
Van Hool	2003	40	40,800	1000	85		0.1334	9.06E+12
Van Hool	2008	40	39,650	1200	27		0.0424	2.64E+12
Gillig	2012	40	39,600	1300	65		0.1020	6.34E+12
Gillig	2014	40	39,600	1400	68		0.1068	6.63E+12
Gillig	2016	40	39,600	1500	55		0.0863	5.36E+12
Gillig	2016	40	39,600	1550	25		0.0392	2.44E+12
Gillig	2017	40	39,600	1580	10		0.0157	9.75E+11
Gillig	2013	40	39,600	6100	54		0.0848	5.26E+12
Van Hool	2010	40	39,650	FC	13		0.0204	1.27E+12
MCI	2000	45	48,000	6000	4		0.0063	6.94E+11
MCI	2002	45	48,000	6050	37		0.0581	6.42E+12
Alexander Dennis	2018	42	57,541	6200	10		0.0157	2.99E+12
Van Hool	2017	60	61,476	2220	29		0.0455	1.06E+13
Van Hool	2006	60	56,650	2100	10		0.0157	2.85E+12
Van Hool	2006	60	56,650	2150	13		0.0204	3.71E+12
Van Hool	2009	60	56,700	2190	9		0.0141	2.58E+12
New Flyer	2013	60	61,476	2200	23		0.0361	8.39E+12
				Total =	637		1.0000	8.33E+13
							$GVWR_{eff}$ =	**43668 lb**

The as-built FE model (see Section 5.3.1) was rerun to determine the cyclic stresses due to the 5.9- and 9.7-kip cyclic loads. For this analysis, unfactored dead and superimposed dead loads were applied, as shown in **Table** 19.

Table 19 – Unfactored Loads for Cyclic Stress Determination

Load Case	Forces (lb)			Pressure (psi)
	Hanger	West Stiffener	East Stiffener	Deck
1.0(DL)	280,000	115,000	110,000	2.31
1.0(DL+SDL)	536,500	352,600	396,200	8.96
1.0(DL+SDL) + 5900	**542,400**	352,600	393,200	8.96
1.0(DL+SDL) + 9700	**546,200**	352,600	393,200	8.96

Vertical stresses were output along the profiles shown in Fig. 154 for the baseline (DL+SDL) and fatigue load cases. Cyclic stresses were determined by subtracting the baseline stress profiles from the fatigue profiles and are given in **Table** 20.

Table 20 – As-Built Cyclic Stresses

Profile	Cyclic Stress (ksi)	
	5.9-kip Load	9.7-kip Load
Lower	0.219	0.362
Upper	0.089	0.146
Web	0.137	0.225

Fatigue crack growth calculations were performed to determine the expected life of the hanger. The TTC is expected to service 1,100 buses per day, for a total of 401,500 cycles per year. For an assumed initial flaw size of 1.2 × 0.125 in. and a critical flaw depth of 0.596 in. (see Section 5.3.3.1), the worst-case cyclic stress range of 0.362 ksi results in a fatigue life well in excess of 10,000 years.

5.3.4 Bottom Flange Focused Crack Mesh Analyses

Sensitivity of the bottom flange to fracture was investigated in the hanger slot by introducing focused crack meshes into the girder FE model. Two crack locations were considered, one in the slot “end corner” and one in the slot “transition corner”, as shown in Fig. 157. It was assumed that a pre-existing 0.38 in. deep x 1.2 in. long semi-elliptical crack was located at the mid-thickness of the bottom flange in the same manner as the pop-in crack from Fremont Street North (“D.4”) (see Section 4.1).

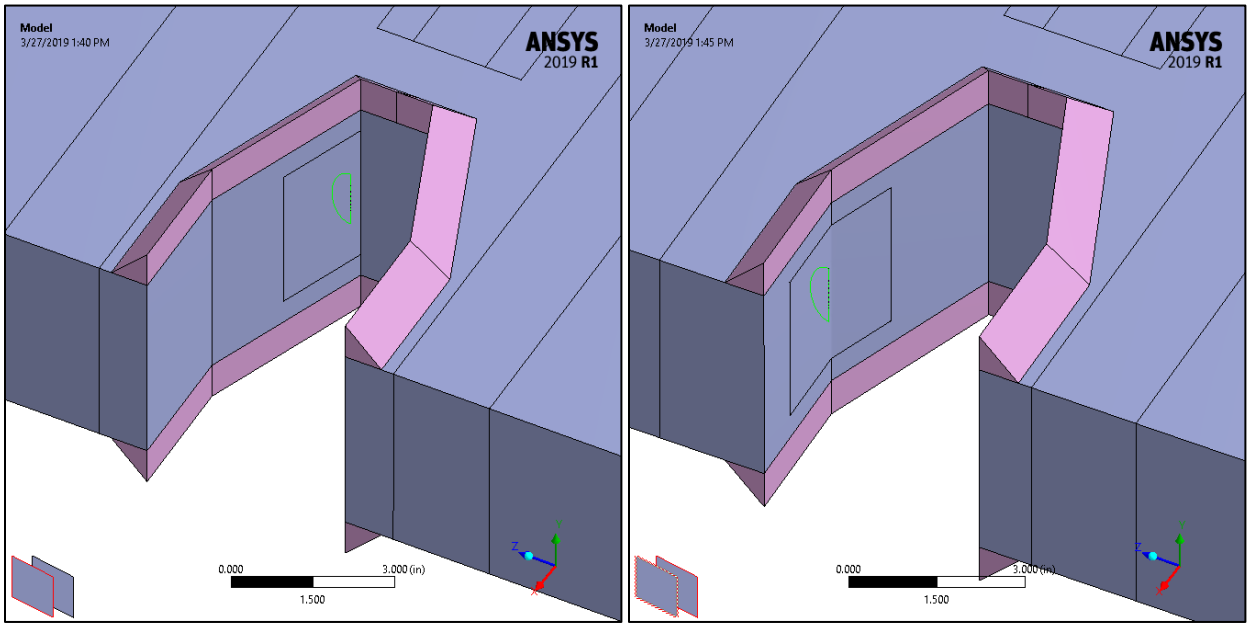

Fig. 157. Bottom flange hanger slot end corner crack (left) and transition corner crack (right). Hanger, stiffener, and web plates are hidden from view.

The full First Street South (“F”) model was reduced to a submodel for these analyses by slicing out a portion of the geometry. Loading was achieved by applying the resulting displacements from the full model to the cut boundaries of the submodel using displacement constraints, thereby recreating the loaded, displaced condition of the full model. The submodel and boundary conditions are shown in Fig. 158.

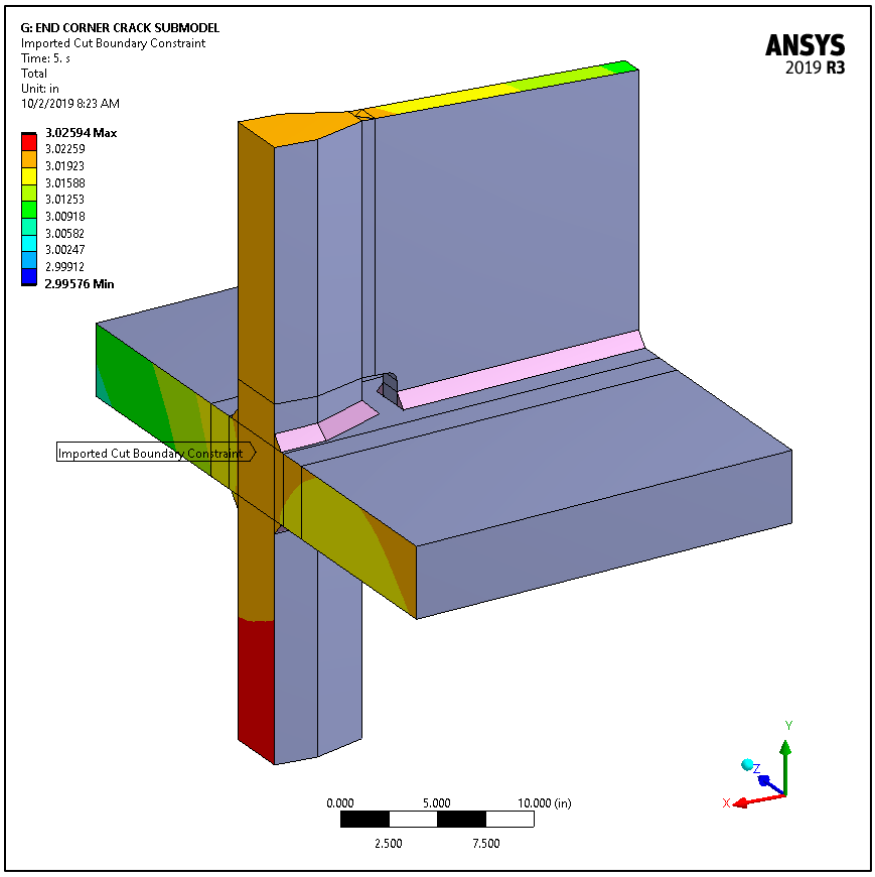

Fig. 158. Submodel with representative cut boundary displacement constraints.

Stress intensity factors resulting from the focused crack mesh analyses are shown in Fig. 159. The bottom flange slot end corner and slot transition corner cracks result in mid-thickness stress intensities of approximately 21 and 29 ksi√in., respectively, both of which are significantly lower than the 55-60 ksi√in. fracture toughness at the mid-thickness of the bottom flange. The bottom flange hanger slot is, therefore, not susceptible to fracture in the presence of an assumed 0.38 in. deep x 1.2 in. long semi-elliptical crack, even when subjected to the factored design loads.

Specific residual stresses associated with the slot were not calculated. However, given the distance the flange slot end is from the flange CJP groove weld, slot residual stresses

will be considerably lower than those developed in the flange weld access holes. The largest contributor of residual stresses for the slot are residual stresses associated with thermal cutting of the flange plate. As previously shown, such stresses, although high at the surface, drop off very rapidly with increasing distance into the flange width. Fracture mechanics calculations using the residual stress distribution shown in Fig. 55 and the factored design stress intensities discussed above (Fig. 159) yields FAD assessment points that fall significantly below the FAD failure curve, similar to the results shown in Fig. 156. As such, fracture from a flaw comparable in size to the weld access hole pop-in cracks will not occur.

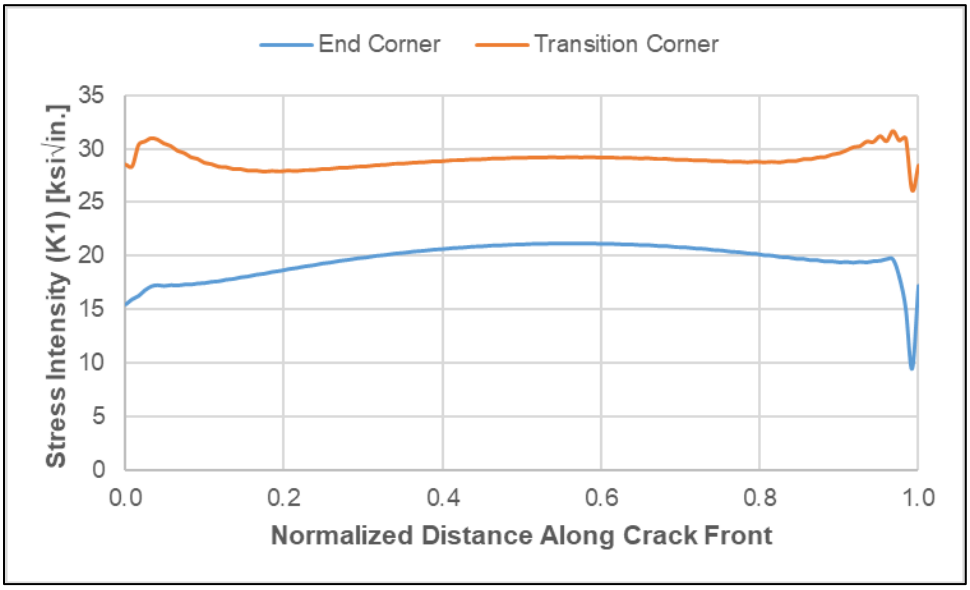

Fig. 159. Stress intensity factors along the end corner and transition corner semi-elliptical crack fronts.

5.3.5 Structural Improvement Considerations

Two modifications to structural details were proposed to improve the stress distributions in those areas and reduce the likelihood of cracking. Stress analysis was performed to consider each of the modifications individually and also in conjunction with one another.

5.3.5.1 Drilled Web Access Holes

One proposed modification was to drill the web access holes to a diameter of 4-in. such that the hole is tangent to both the hanger and the bottom flange. A submodel was created from the full First Street South (“F”) finite element model (in the same manner discussed in Section 5.3.4) and the web access hole enlarged, as shown in Fig. 160.

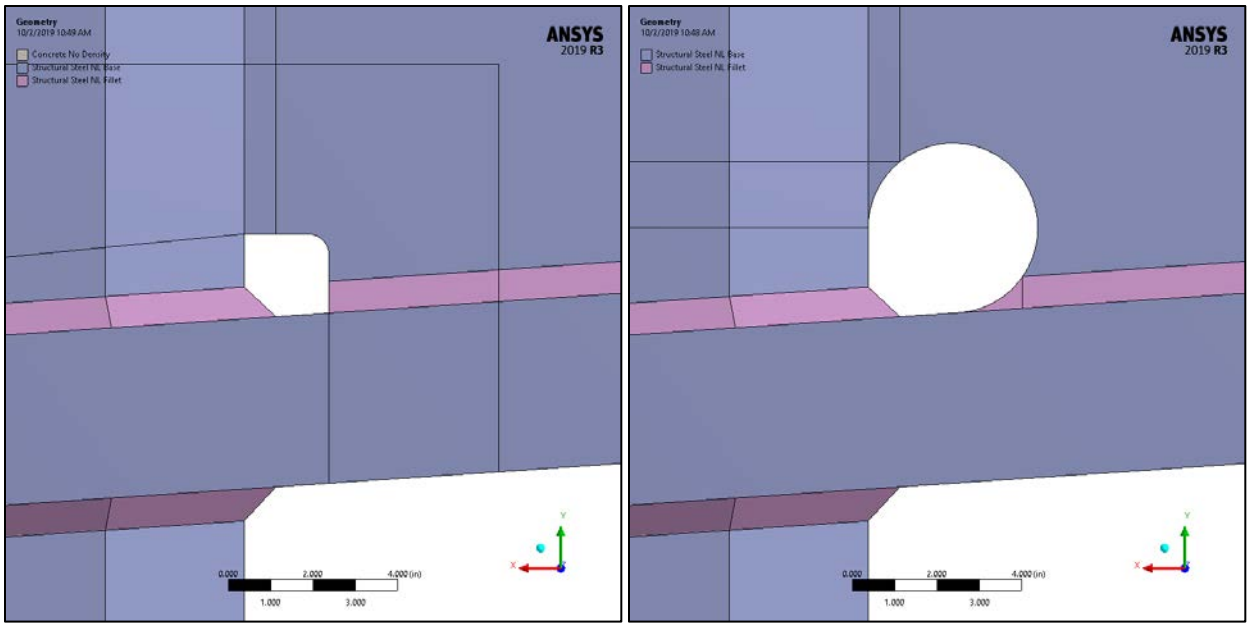

Fig. 160. As-built geometry (left) and drilled web access hole (right).

The model was subjected to the factored design loads via cut-boundary displacement constraints and a section plane was inserted at the mid-thickness of the web to plot internal stresses. Maximum principal stress and the vertical stress component in the drilled configuration are compared to the as-built configuration in Fig. 161 and Fig. 162, respectively. The peak maximum principal stress value is reduced by the drilling, and the location of the peak moves from the CJP web-to-hanger weld to the apex of the drilled hole. The vertical component of stress is not significantly affected by the enlargement of the web access hole.

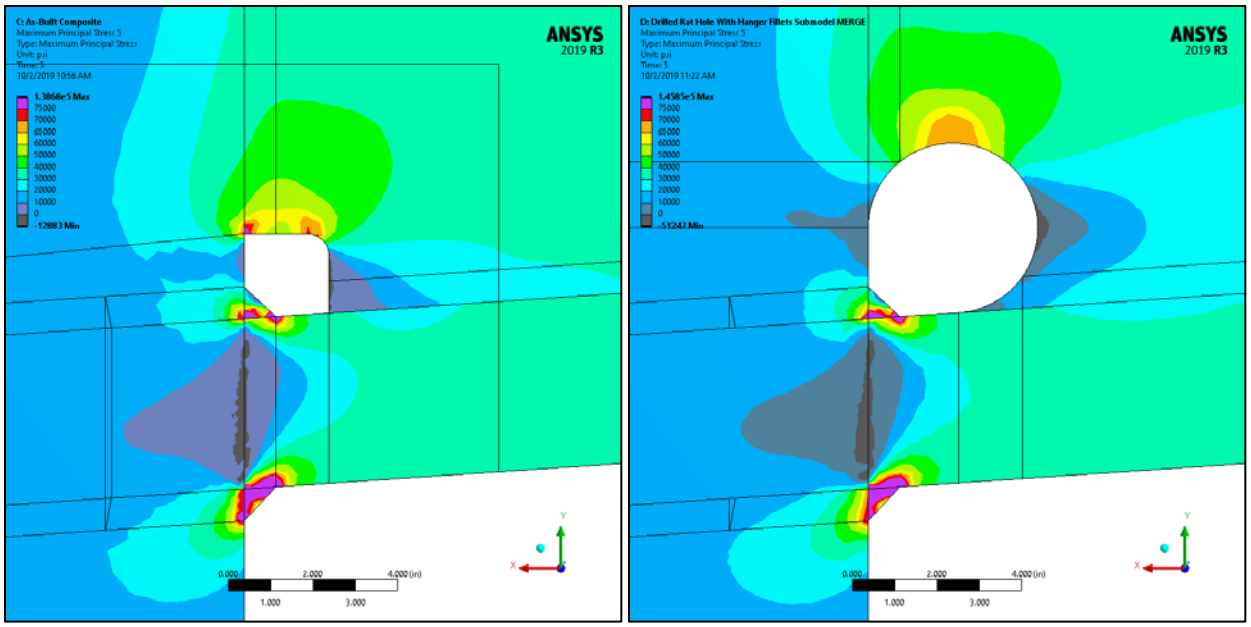

Fig. 161. Centerline section maximum principal stress plots of the as-built (left) and drilled (right) configurations.

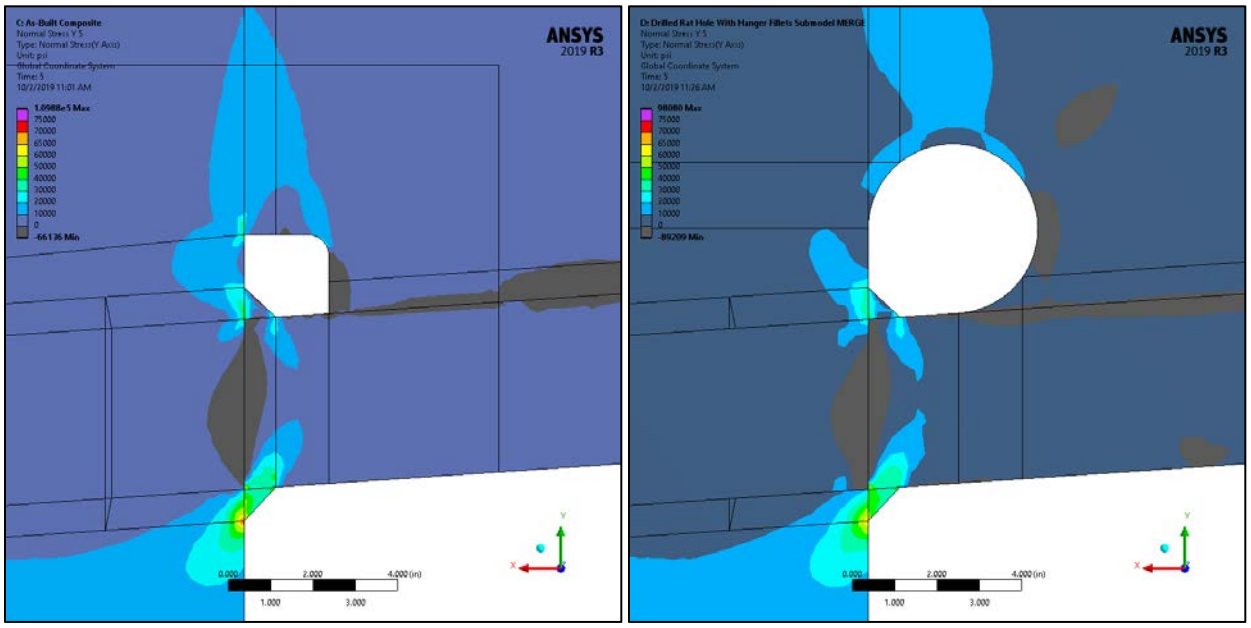

Fig. 162. Centerline section vertical stress component plots of the as-built (left) and drilled (right) configurations.

5.3.5.2 Removed Bottom-Flange-to-Hanger Fillet Welds

The other proposed modification was to completely remove the fillet welds connecting the bottom flange to the hanger from both sides of bottom flange. The full First Street South ("F") finite element model was modified to remove these fillet welds, as shown in Fig. 163. The submodeling method was not employed for this analysis (i.e., the full girder model was used).

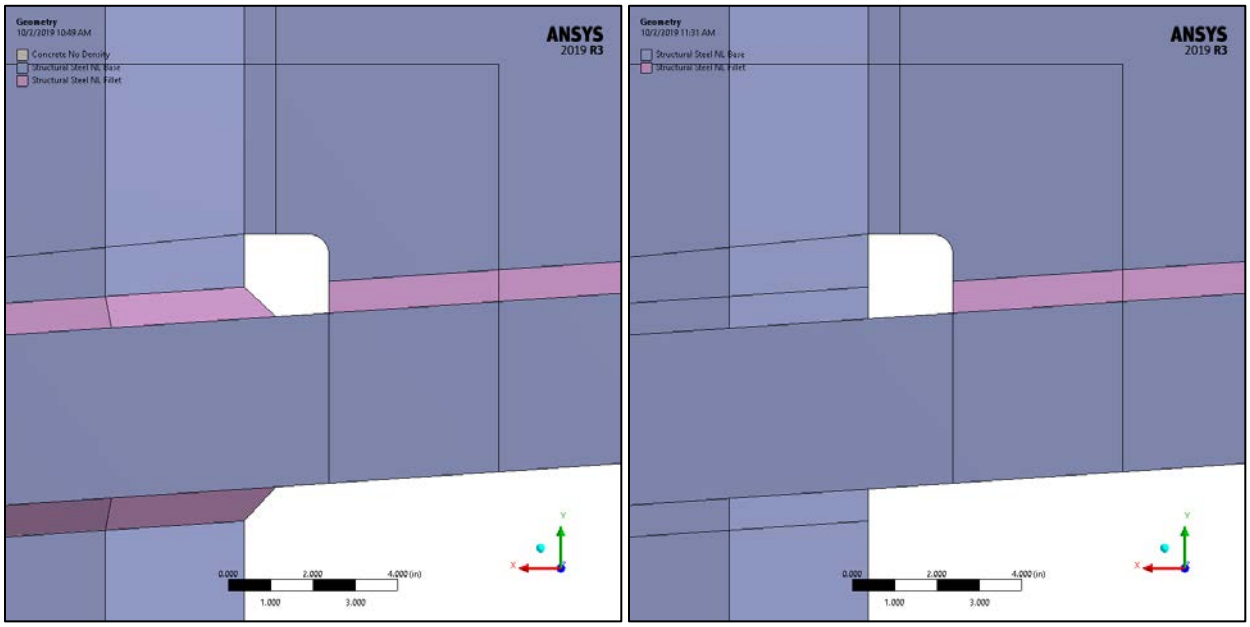

Fig. 163. As-built geometry (left) and removed fillet welds (right).

The full model was subjected to the factored design loads and a section plane was inserted at the mid-thickness of the web to plot internal stresses. Maximum principal stresses in the bottom flange hanger slot are compared between the as-built and modified configurations are shown in Fig. 164. It is evident that removal of the fillet welds significantly reduces flange surface stresses where the fillet welds had been. However, centerline section plots of maximum principal stress in the vicinity of the web access hole are compared in Fig. 165, where it can be seen that the absence of the fillet welds significantly increases stresses at the web-to-hanger CJP welds. In fact, significant yielding is evident in both the web and hanger plates.

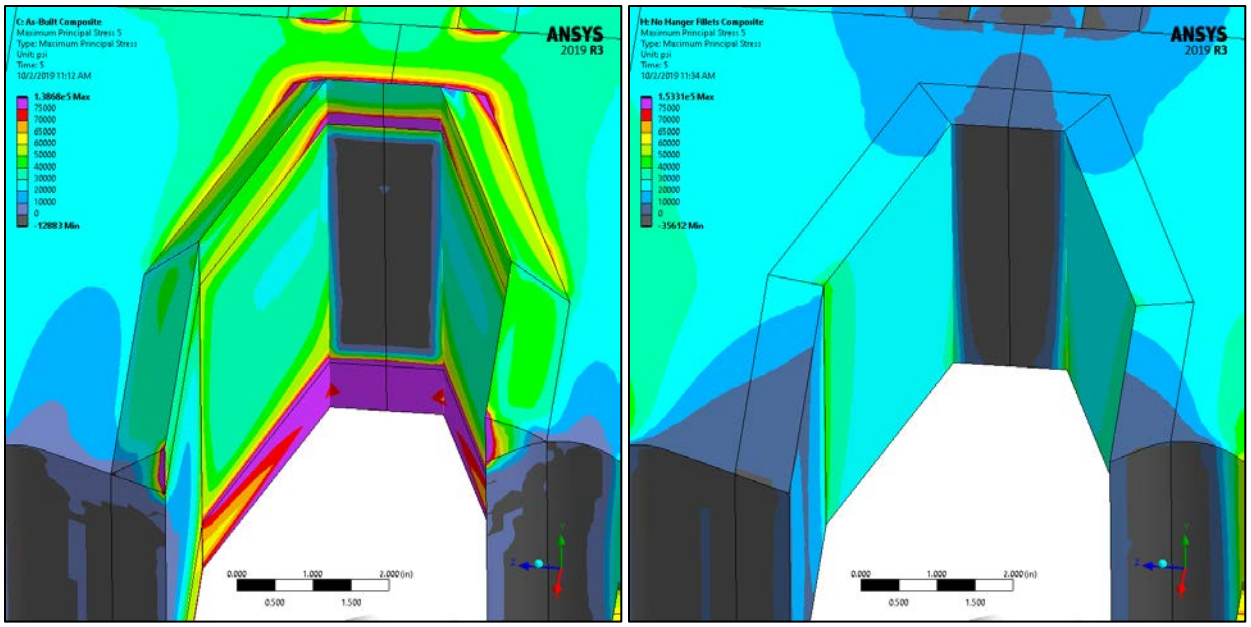

Fig. 164. Maximum principal stress plots of the as-built (left) and removed fillet weld (right) configurations.

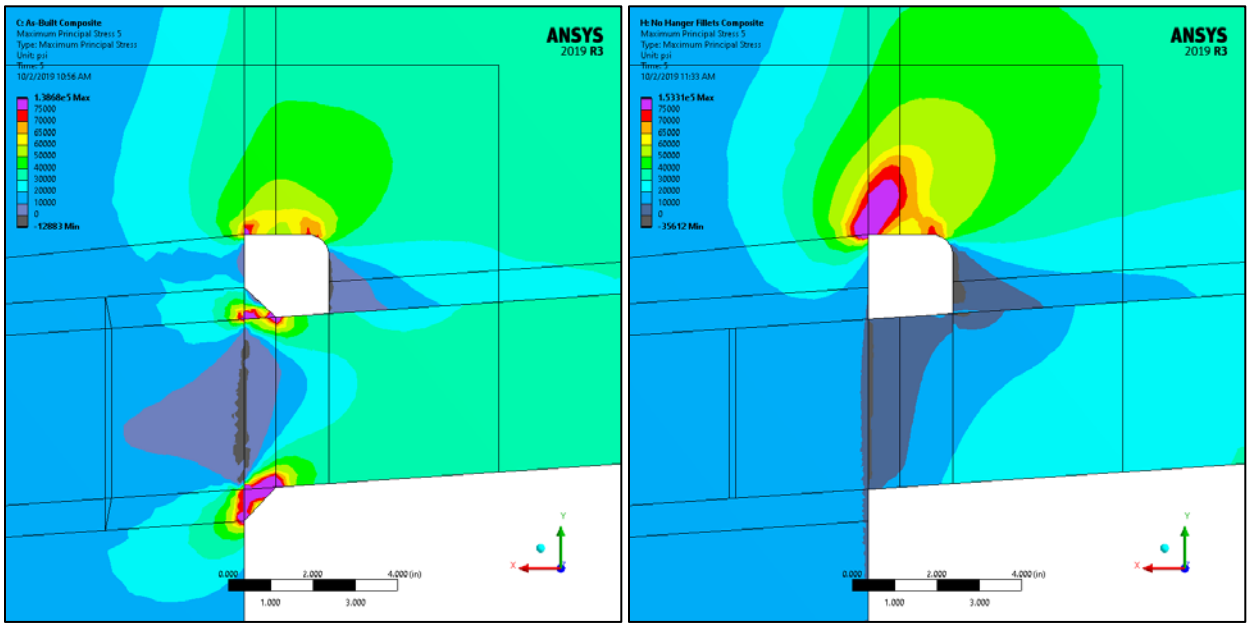

Fig. 165. Centerline section maximum principal stress plots of the as-built (left) and removed fillet weld (right) configurations.

5.3.5.3 Drilled Web Access Holes and Removed Fillet Welds

Additional FE stress analyses were performed considering both proposed modifications acting together, as such a submodel was created from the full model in Section 5.3.5.2 by enlarging the web access hole as was done in Section 5.3.5.1. The modified geometry is compared to the as-built geometry in Fig. 166.

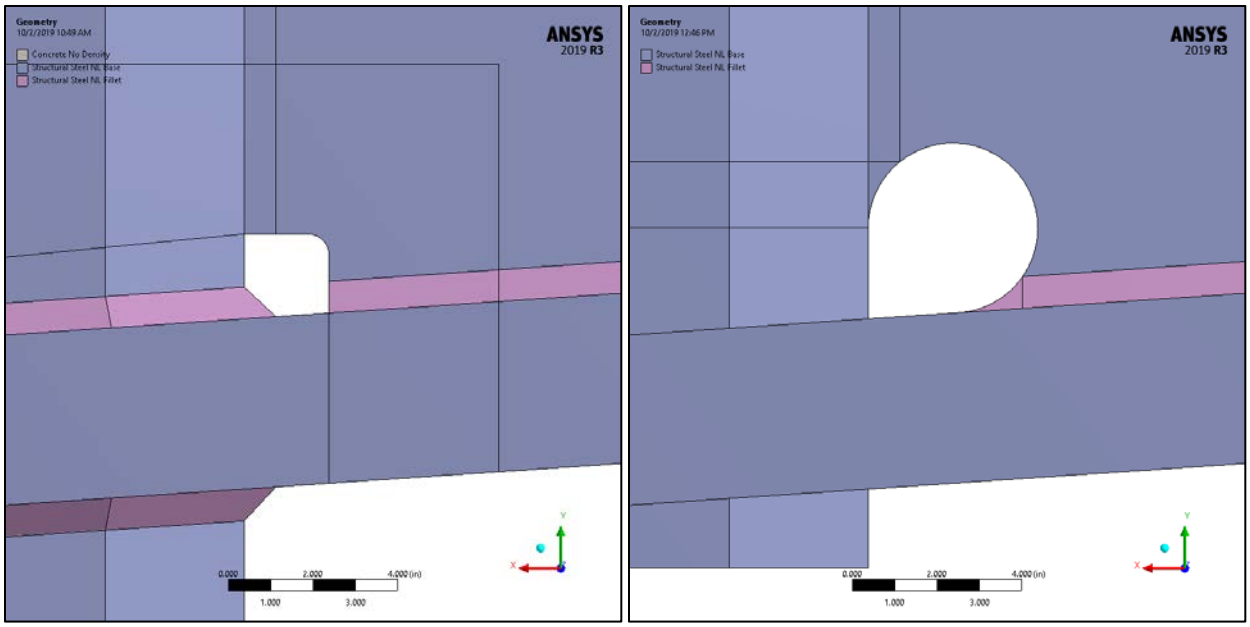

Fig. 166. As-built geometry (left) and modified geometry with drilled web access holes and removed fillet welds (right).

The model was subjected to the factored design loads via cut-boundary displacement constraints and a section plane was inserted at the mid-thickness of the web to plot internal stresses. Maximum principal stresses in the bottom flange hanger slot are compared between the as-built and modified configurations are shown in Fig. 167. It is evident that removal of the fillet welds significantly reduces flange surface stresses in the vicinity of where the fillet welds had been. Centerline section plots of maximum principal stress in the vicinity of the web access hole are compared in Fig. 168, where it can be seen that the absence of the fillet welds increases stresses in the web access hole. This stress state in the access hole is less severe than that of the undrilled hole with removed fillet welds.

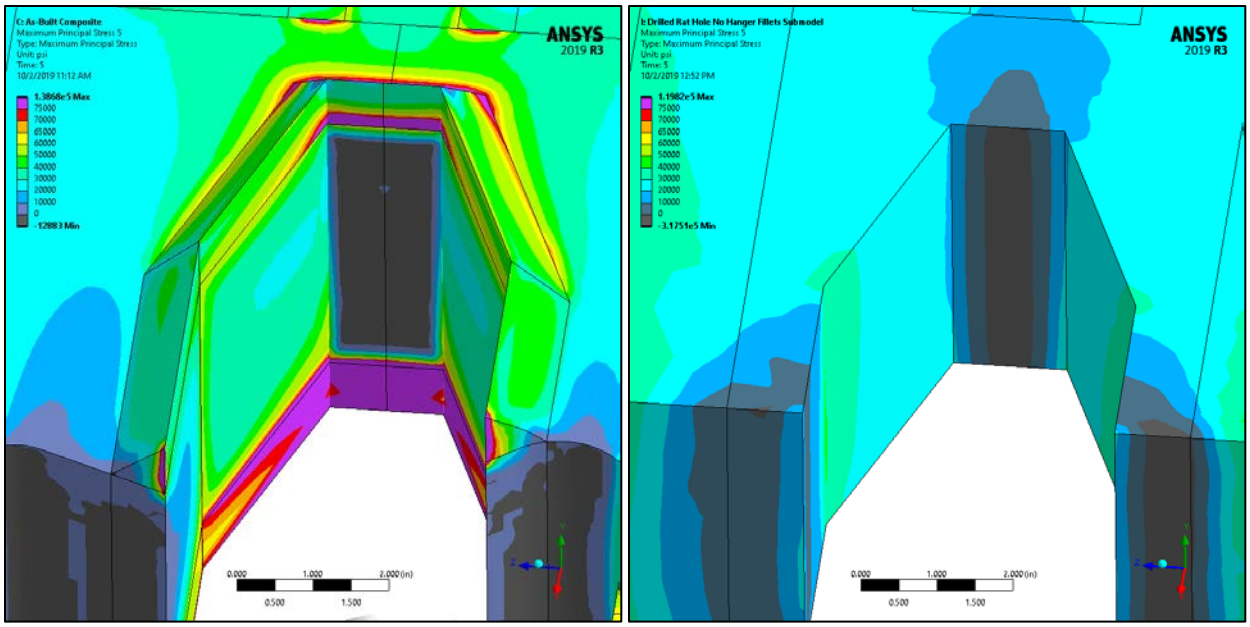

Fig. 167. Maximum principal stress plots of the as-built (left) and drilled web access hole with removed fillet weld (right) configurations.

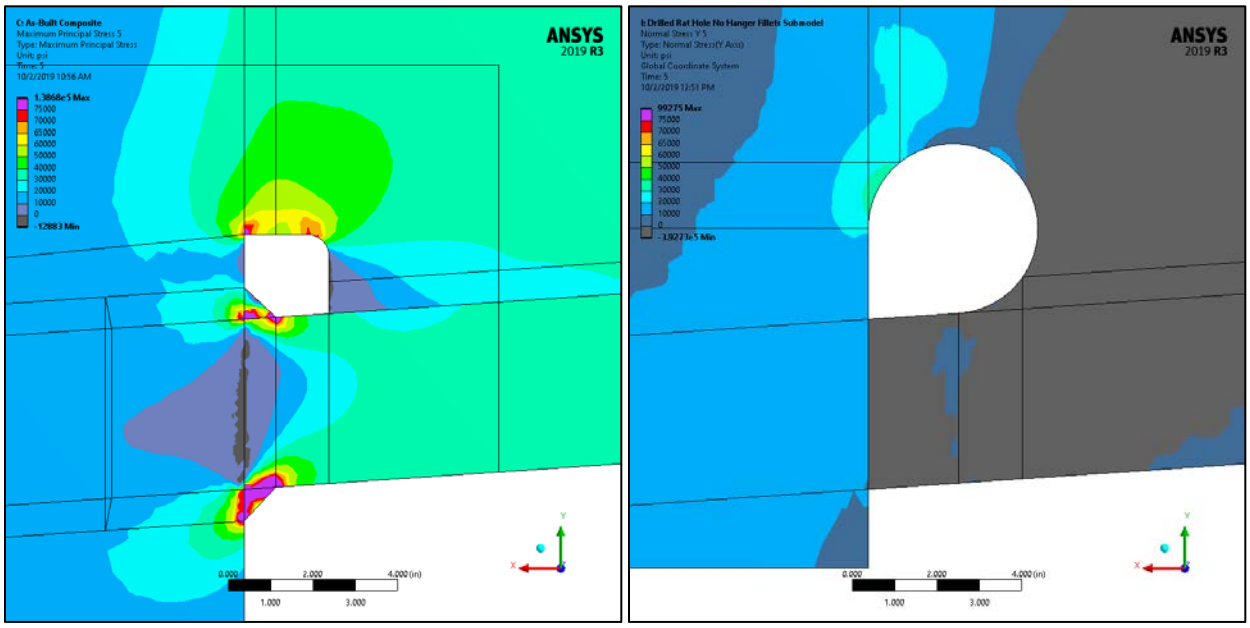

Fig. 168. Centerline section maximum principal stress plots of the as-built (left) and drilled web access hole with removed fillet weld (right) configurations.

5.4 Reinforcement Retrofit Stress Analysis

Based on the results from the analyses considering structural modifications (see Section 5.3.5), a reinforcement retrofit was designed [33]. The retrofit calls for drilling the web access holes but leaves the bottom-flange-to-hanger fillet welds intact. The vertical centerline stiffeners are cut to facilitate the installation of four reinforcing sandwich plates (ASTM A709 HPS, Gr. 70W), which are clamped to the bottom flange with 224 bolts per girder. The retrofit is completed by the addition of four bearing plates that reestablish the compressive load path from the centerline stiffeners to the reinforced bottom flange.

5.4.1 Finite Element Model

Stress analysis was performed to determine the effectiveness of the reinforcement retrofit. The multi-step simulation considered the entire load history of the tapered girder from erection to removal of the temporary jacking load, followed by the full live load and the factored design loads. The load steps were as follows:

1. Coupling of the reinforcement material to the girder, and application of a 10-lb bolt pre-tension.
2. Deactivation of the reinforcement material and the concrete deck, and application of the pre-composite dead loads [1×DL].
3. Activation of the concrete deck, and application of the post-composite dead loads [1×(DL+SDL)].
4. Application of 1,000-kip upward jacking of the hanger.
5. Activation of the reinforcement material.*
6. Deactivation of the material removed during reinforcement retrofitting.*
7. Partial (1,000-lb) pre-tensioning of the bolts.
8. Deletion of the reinforcement material coupling.
9. Locking of the 1,000-lb partial pre-tension.
10. Full (80,000-lb) bolt pre-tensioning.
11. Locking of the 80,000-lb bolt pre-tension.
12. Removal of the jacking load to return to 1×(DL+SDL)
13. 1×(DL+SDL) + 1×LL
14. 1.2×(DL+SDL) + 1.6×LL

* Load steps 5 and 6 are reversed relative to the actual construction sequence. This was necessary to achieve solution convergence and considered to be insignificant to the resulting stress state.

5.4.1.1 Geometry

Using the First Street South (“F”) finite element model as a starting point (see Section 5.3), the reinforcement retrofit [33] geometry was created and added to the FE model. Drilling of the bottom flange weld access, web access, and bolt holes was represented in the model, along with the cutting and drilling of the centerline vertical stiffeners. An overview of the model in the reinforced state is shown in Fig. 169.

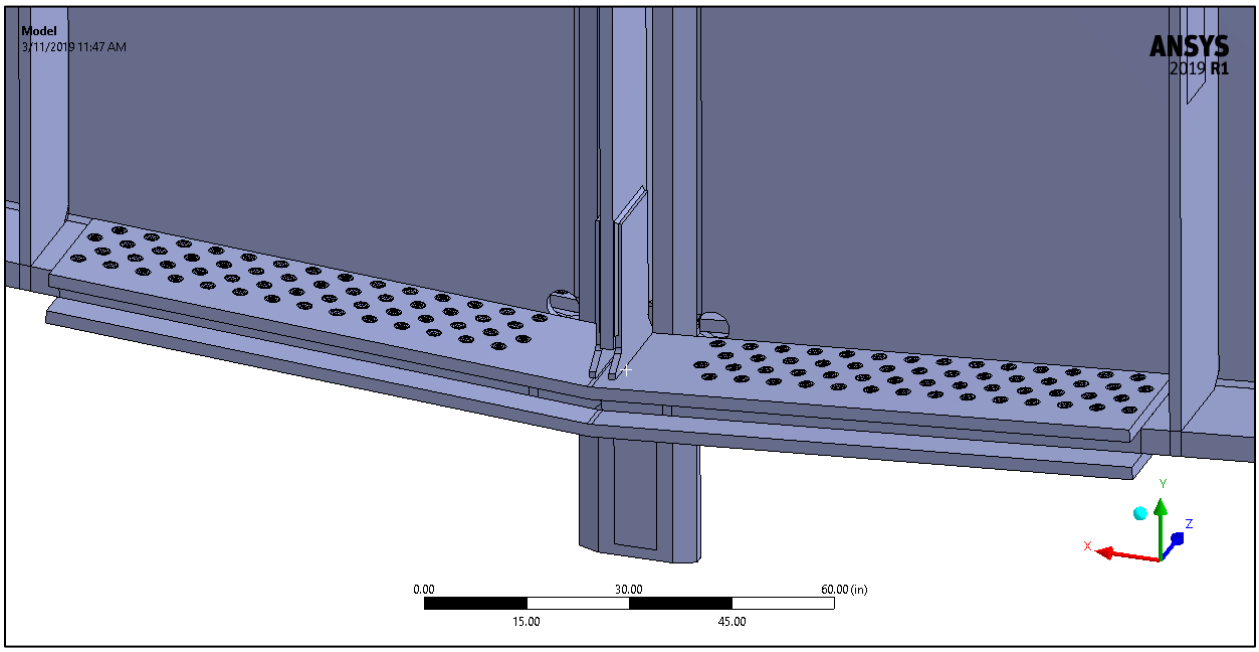

Fig. 169. First Street South (“F”) reinforcement retrofit geometry.

The bolt shanks were modeled with beam elements of appropriate cross-section, and the bolt heads, nuts, and washers were represented by shell elements. A detailed view of the meshed bolts and sandwich plates is shown in Fig. 170.

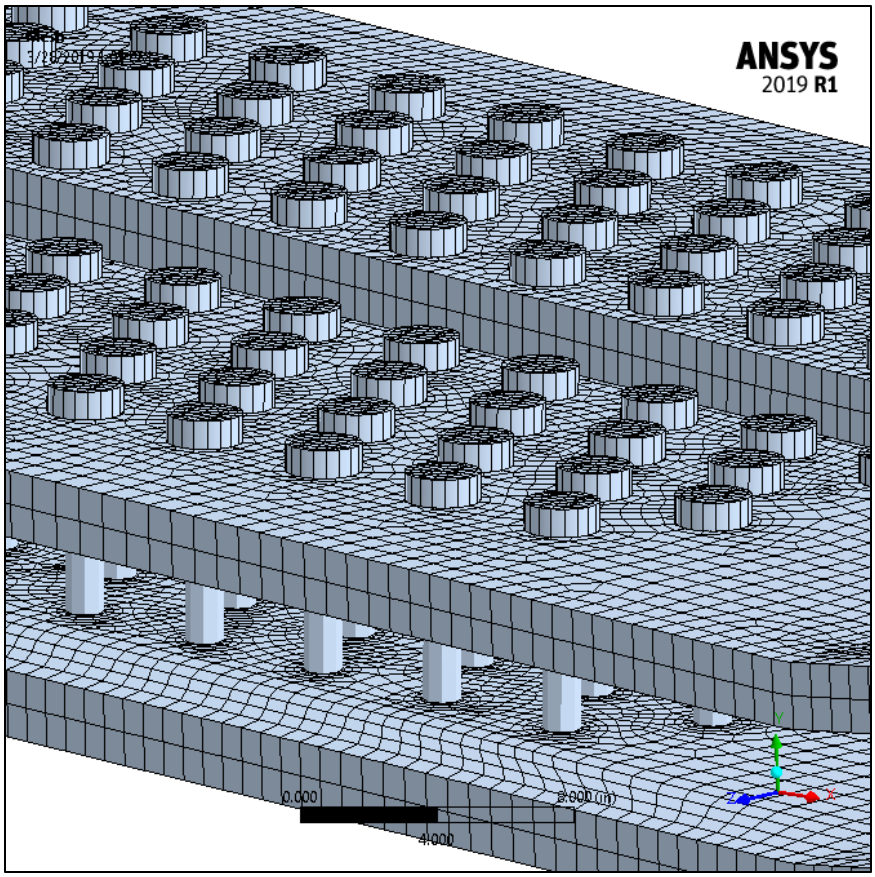

Fig. 170. Detail view of meshed sandwich plates and bolts.

5.4.1.2 Connectivity and Contact

The sandwich plates and bolts are constrained entirely by frictional contact and were prescribed a coefficient of static friction of μ = 0.5. Frictional contact was also defined between all new faying surface pairs from the introduction of the centerline stiffener bearing plates. Bonded contact was employed for all fillet welds in the reinforced structure.

5.4.2 Factored Loading Results

Longitudinal (X-axis) stresses in the reinforcement plates following the removal of the 1,000-lb jacking force are approximately 14 ksi (see Fig. 171) and increase to approximately 22 ksi under the factored design loading. Vertical deflection at the bottom of the hanger is approximately 2.66 in. for the reinforced girder when subjected to the factored design loads, as compared to a deflection of 3.03 in. for the as-designed girder. The plates are, therefore, effective at reinforcing the girder.

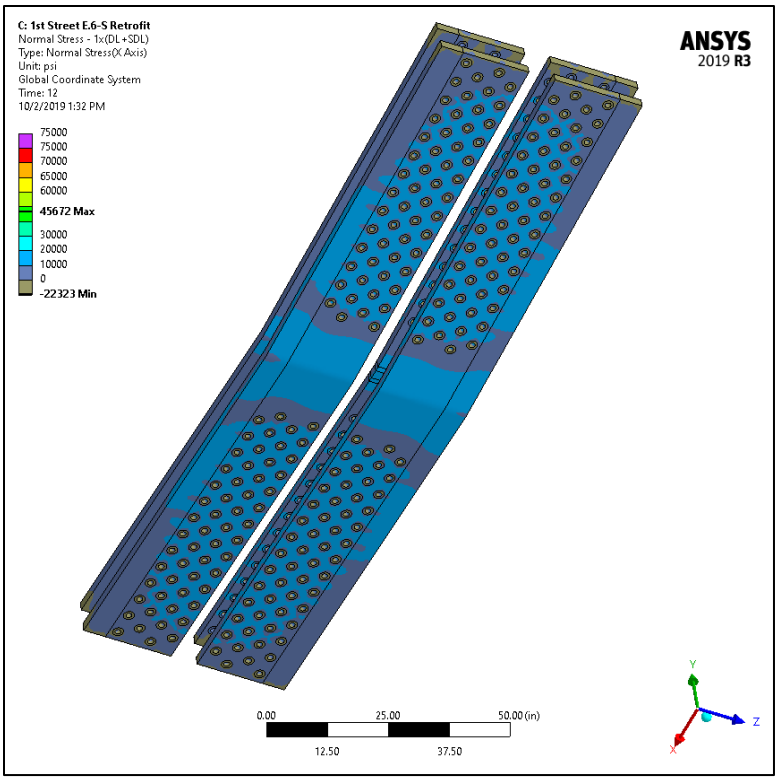

Fig. 171. Bottom view of the reinforcement plates after removal of 1,000-lb jacking force [1×(DL+SDL)].

Stresses in the vicinity of the hanger-to-bottom-flange interface are reduced by the reinforcement, as shown in Fig. 172, further demonstrating the effectiveness of the reinforcement plates.

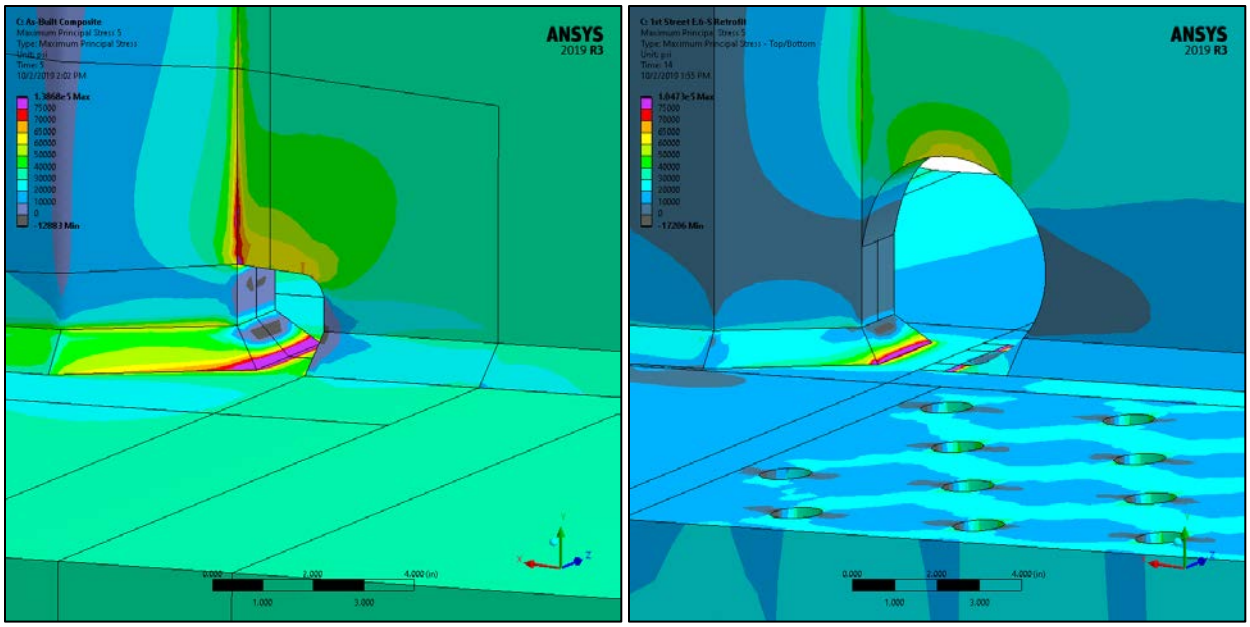

Fig. 172. Maximum principal stress plots for the as-built (left) and reinforced (right, reinforcement plates hidden) configurations subjected to the factored design loads.

5.4.3 Hanger Assessment

The hanger was assessed in the reinforced condition for both fracture due to factored design loads and fatigue due to expected cyclic loading, the details of which are provided in the following subsections.

5.4.3.1 Hanger Fracture

The retrofit model was analyzed for the fully factored load case to assess the effectiveness of the reinforcement as regards the susceptibility of the hanger to fracture. Vertical stress components were output along the paths defined in Fig. 154, and are compared to the as-built results in Fig. 173. It is clear from the results that the reinforcement is effective at reducing hanger stresses.

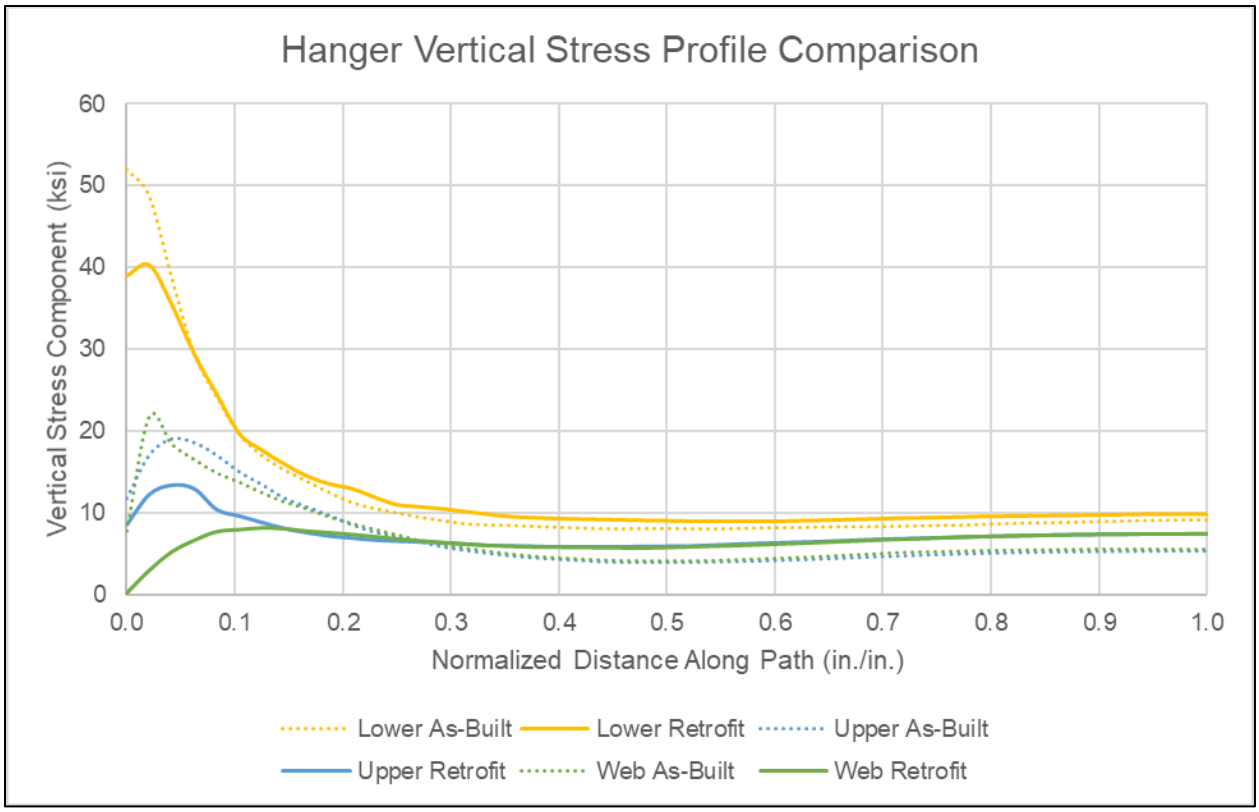

Fig. 173. Comparison of hanger vertical stress profiles.

FAD calculations were performed to determine the susceptibility of the reinforced hanger to fracture. A 1.2 × 0.125-in. semi-elliptical surface flaw was assumed to exist on the hanger, and the "lower" stress profile in Fig. 173 was used. Both FAD assessment points fall well below the failure curve, as shown in Fig. 174. The critical crack depth for this stress profile was determined to be 0.634 in. The reinforced hanger is, therefore, not susceptible to fracture in the presence of the assumed flaw when subjected to the factored design loads.

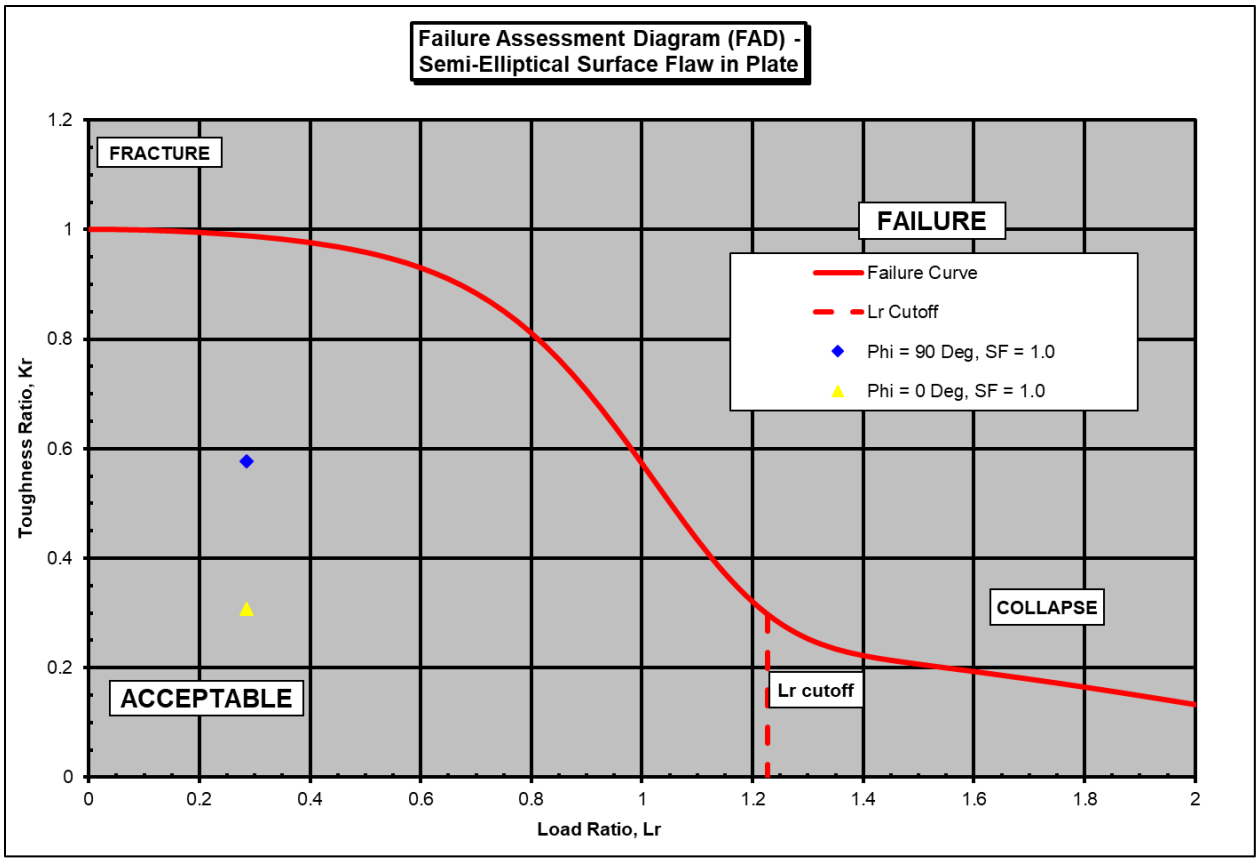

Fig. 174. FAD calculation results for an assumed 1.2 × 0.125-in. semi-elliptical surface flaw on the hanger in the as-built condition when subjected to the factored design loads.

5.4.3.2 Hanger Fatigue

The retrofit model was analyzed for the same 5.9- and 9.7-kip cyclic hanger loads as the as-built model (see Section 5.3.3.2) to assess the effectiveness of the reinforcement at improving the fatigue life of the hanger. Vertical stresses were output along the paths shown in Fig. 154 for the baseline (DL+SDL) and fatigue load cases. Cyclic stresses were determined by subtracting the baseline stress profiles from the fatigue profiles and are compared to the results from the as-built configuration in **Table** 21.

Table 21 – Cyclic Stress Comparison

Profile	Cyclic Stress (ksi)			
	5.9-kip Load		9.7-kip Load	
	As-Built	Retrofit	As-Built	Retrofit
Lower	0.219	0.242	0.362	0.375
Upper	0.089	0.061	0.146	0.097
Rathole	0.137	0.060	0.225	0.096

Cyclic stress ranges are reduced by the retrofit reinforcement for the “Upper” and “Web” locations. The “Lower” location, however, sees a slight increase in cyclic stress due to the reinforcement.

Fatigue crack growth calculations were performed to determine the expected life of the reinforced hanger. The TTC is expected to service 1,100 buses per day, for a total of 401,500 cycles per year. For an assumed initial flaw size of 1.2 × 0.125 in. and a critical flaw depth of 0.634 in. (see Section 5.4.3.1), the worst-case cyclic stress range of 0.375 ksi results in a fatigue life well in excess of 10,000 years.

5.4.4 Focused Crack Mesh Analyses

The focused crack meshes analyzed for the as-built configuration (see Section 5.3.4) were also considered for the retrofit condition to assess the effectiveness of the reinforcement. A submodel was created from the retrofit model (see Section 5.4.1) as shown in Fig. 175, and loaded with cut-boundary displacements from the retrofit model associated with the factored design load case.

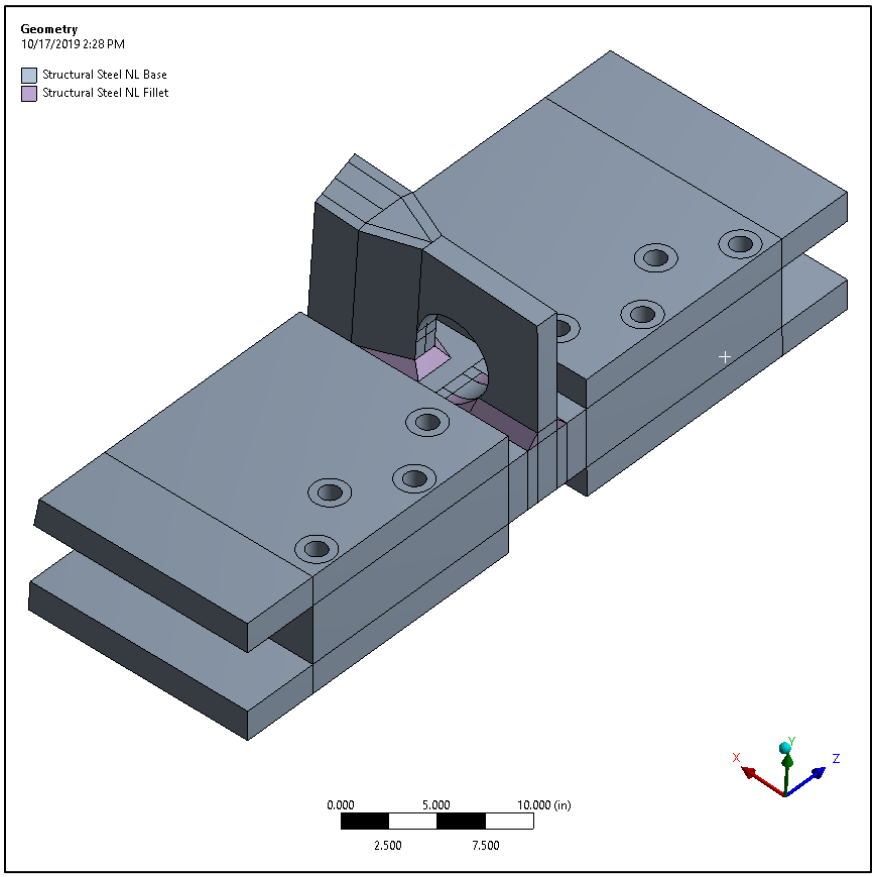

Fig. 175. Retrofit reinforcement submodel.

Stress intensities resulting from the retrofit focused crack mesh analyses are compared to the as-built results in Fig. 176. The bottom flange slot end corner and slot transition corner cracks result in mid-thickness stress intensities of approximately 14 and 15 ksi√in., respectively, which are significantly lower than the stress intensities resulting from the as-built analyses. The retrofit reinforcement is, therefore, effective at reducing the likelihood of flange fracture.

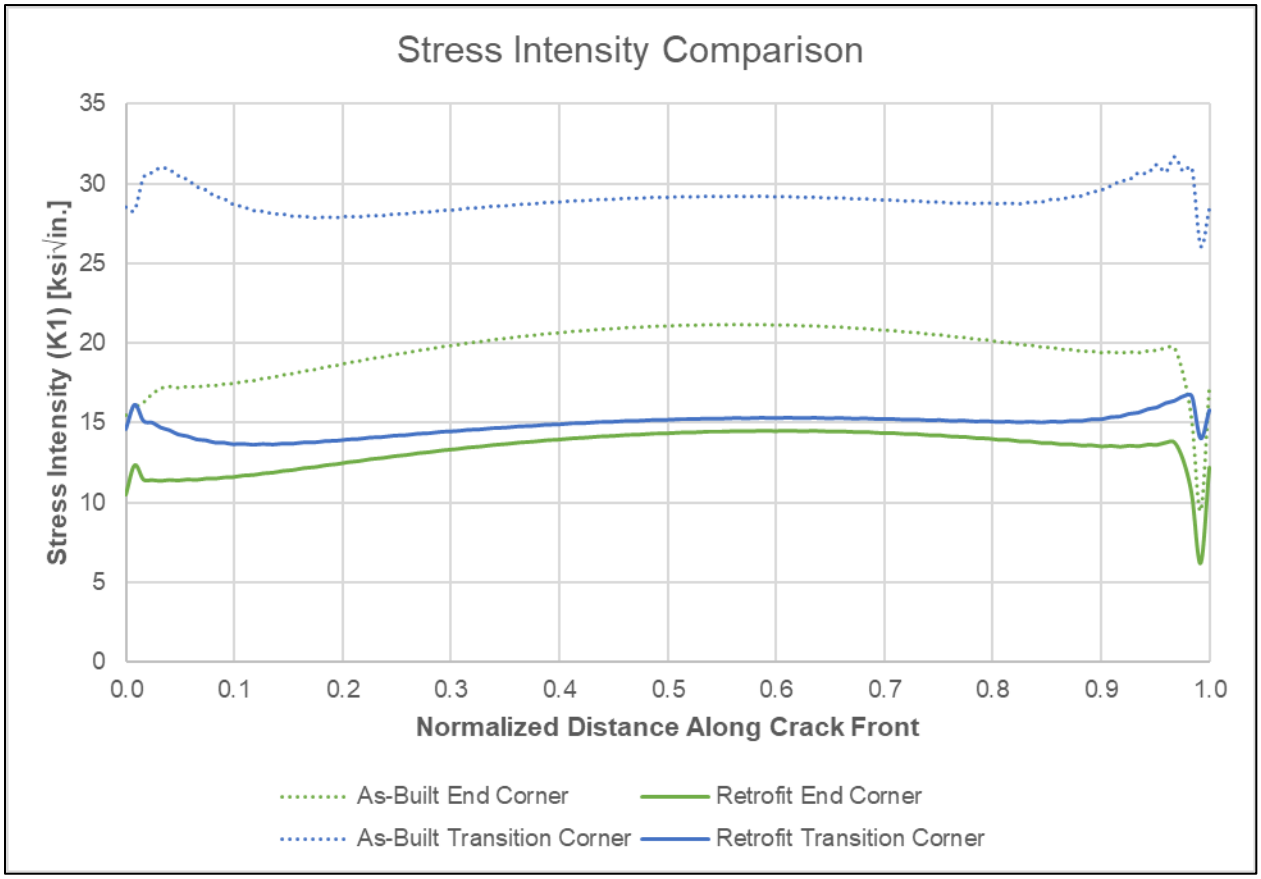

Fig. 176. Comparison of stress intensities between the retrofit and as-built configurations.

5.5 First Street Conclusions

Based on the analyses described in Section 5 concerning the FFS assessment of the First Street TPG3 girders, the following can be concluded:

- The First Street and Fremont Street TPG3 girder weld access hole stress state due to service loading is approximately the same.
- The First Street and Fremont Street TPG3 girders are adequately designed for the factored design load case from a stress perspective.

- Thermal cutting of the weld access holes after CJP groove welding of the bottom flange plates relieved a notable fraction of the CJP groove weld-induced residual stresses, as comparison of Fig. 53 and Fig. 129 clearly shows.
- Fracture of the First Street TPG3 girders did not occur due to the reduced residual stress and the absence of pop-in cracks in the weld access hole radii.
- Based on factored loading the reinforcement is suitable for the intended service at both Fremont and First Streets.
- The bottom flange hanger slots are not susceptible to fracture in the presence of an assumed 0.38 x 1.2 in. pop-in crack when subjected to the factored design loads.
- The hanger is not susceptible to fatigue crack propagation due to expected cyclic loading from bus traffic.

6. CONCLUSIONS

Based on the results of this assessment performed the TTC Fremont Street TPG3 girder flange fractures were caused by the formation of cracks in the weld access hole radii prior to service:

- Initially, microcracks developed during thermal cutting of the weld access holes in the highly hardened and brittle martensitic surface layer.
- Thereafter, larger pop-in cracks formed in two of the four flanges during CJP groove welding of the bottom flange plates.
- Yield strength level residual stresses at the weld access hole surfaces were required for pop-in crack initiation to occur.
- Dark, tenacious, high-temperature oxide was present on both the shallow surface microcracks and the larger pop-in cracks, confirming that both crack types formed at elevated temperatures, which could only have been present during fabrication – that is, CJP groove welding and thermal cutting of the access holes and runoff tabs.
- CVN testing was performed on all flange samples at the top and bottom surfaces, ¼ and ¾ thicknesses, and the ½ thickness (mid-thickness). Although the ¼ thickness CVN results were found to be consistent with the project specification and girder plate mill certifications, the mid-thickness toughness levels were substantially lower than the ¼ thickness toughness and unacceptable from a performance perspective.
- The fracture origins were located in the mid-thickness of the flange where the fracture toughness was exceptionally low. That is, the mean ½ thickness CVN toughness level at 50ºF, the approximate temperature at which the fractures occurred, was only 11 ft-lb and the lower bound toughness was less than 5 ft-lb.

This level of toughness provides negligible resistance to fracture from pre-existing cracks such as the observed microcracks and pop-in cracks.

- Normal service induced stresses were not sufficient to initiate bottom flange fracture.
- Rapid, low-energy fracture of the bottom flanges occurred as the girder was subjected to normal service loading in addition to residual stresses typical of weld access holes, which were already present due to CJP groove welding.

Additionally, the FFS assessment of the First Street TPG3 concluded that:

- The First Street and Fremont Street TPG3 girder weld access hole stress states due to service loading are approximately the same.
- The First Street and Fremont Street TPG3 girders are adequately designed for the factored design load case from a stress perspective.
- Thermally cutting the weld access holes after CJP groove welding of the bottom flange plates relieved a notable fraction of the CJP groove weld-induced residual stresses.
- Fracture of the First Street TPG3 girders did not occur because of lower CJP groove weld-induced residual stress magnitude and the absence of pop-in cracks in the weld access hole radii.
- Based on factored loading the reinforcement will be fit for the intended service at both Fremont and First Streets.
- The bottom flange hanger slots are not susceptible to fracture in the presence of an assumed 0.38 x 1.2 in. pop-in crack when subjected to the factored design loads.
- The hanger is not susceptible to fatigue crack propagation due to expected cyclic loading from bus traffic.

7. REFERENCES

1. Webcor RFI T-2003, SSS – TPG3 Approval Comment Clarification at Weld Termination GL 25-27.pdf
2. McAdam, D. J., and Geil, G. W., “Rate of Oxidation of Steels as Determined from Interference Colors of Oxide Films”, J. of Research of the National Bureau of Standards, Volume 23, July 1939.
3. ASTM E340, “Standard Specification for Macroetching Metals and Alloys”, ASTM International, 2015.
4. AWS D1.1/D1.1M:2015, “Structural Welding Code – Steel”, American Welding Society, 2015.
5. Steel Construction Manual, 15th Edition, American Institute of Steel Construction, 2017.
6. ASTM A370, “Standard Test Methods and Definitions for Mechanical Testing of Steel Products”, ASTM International, 2018.
7. ASTM E23, “Standard Test Methods for Notched Bar Impact Testing of Metallic Materials”, ASTM International, 2018.
8. American Iron and Steel Institute (AISI), “The Variations of Charpy V-Notch Impact Test Properties in Steel Plates”, Contributions to Metallurgy of Steel, July 1989.
9. Somchat, S., Manual, L., and Frank, K. H., Statistical Analysis of Structural Plate Properties”, American Iron and Steel Institute, January 2003.
10. API 579-1/ASME FFS-1, “Fitness-for-Service”, American Society of Mechanical Engineers, American Petroleum Institute, 2016.
11. Barsom, J. and Rolfe, S., “Fracture and Fatigue Control in Structures”, 2nd Ed., Prentice-Hall, Englewood Cliffs, NJ, 1987.
12. Yoon, K. K. and Van Der Sluys, W. A., “Fracture Toughness of Ferritic Steels and Reference Temperature (T_0) of ASTM”, 1998 ASME PVP Conf. Proc., San Diego, CA, July 1998.
13. ASTM E8/E8M, “Standard Test Methods for Tension Testing of Metallic Materials”, ASTM International, 2016.
14. ASTM A572/A572M, “Standard Specification for High-Strength Low-Alloy Columbium-Vanadium Structural Steel”, ASTM International, 2018
15. LPI in-house test-based experience.
16. Bushnell, David, “Computerized Buckling Analysis of Shells”, Wright-Patterson Air Force Base, Report AFWAL-TR-81-3049, pp.165-183.
17. ANSYS Workbench 2019R1, ANSYS Inc., Canonsburg, PA.

18. Chon, T. L., Kim, D. S, Shim, Y. L., Jaeger, J. “Determination of Residual Stress and Effects in Thick-Section Weldments for Hydraulic Structures”, US Army Corps of Engineers Technical Report ITL-92-8, September 1992

19. Jaeger, J., Feng, Z., Kim, D. S, Lee, S. G., Papritan, J. C., Shim, Y. L, and Chon, T. L., “Finite Element Modeling of Welded Thick Plates for Bonneville Navigation Lock”, US Army Corps of Engineers Technical Report ITL-92-2, May 1992.

20. Sneddon, I. N., “The Distribution of Stress in the Neighborhood of a Crack in an Elastic Solid”, Proc. Roy. Soc. London A 187, 1946, pp. 229-260

21. Irwin, G. R., “The Crack Extension Force for a Part-Through Crack in a Plate”, ASME J. Appl. Mech., 1962, pp. 651-654.

22. Kobayashi, A. S., Zii, M. and Hall, L. R., “Approximate Stress Intensity Factor for an Embedded Elliptical Crack Near to Parallel Free Surfaces”, Int. J. Fracture Mech., 1, 1965, pp. 81-95.

23. “Rules for Inservice Inspection of Nuclear Power Plant Components”, ASME Boiler and Pressure Vessel Code Section XI, The American Society of Mechanical Engineers, New York, 2004.

24. “Guide to methods for assessing the acceptability of flaws in metallic structures”, BS 7910, British Standards Institute, London, 2013.

25. Herrick shop drawings from *Herrick MTR’s and Shop Dwgs Builtup Beams.pdf*

26. “Interim Report 4: Study of TPG3 Loads”, Thornton Tomasetti Report, September 17, 2019.

27. Thornton Tomasetti Boundary Conditions Report (not yet furnished).

28. Lincoln Electric Data Sheets (Lincolnweld L-56 and Outershield XLH-70)

29. Herrick Welding Procedure Specifications THC-F1, THC-F2, THC-F3, and THC-F10

30. Thornton Tomasetti layout drawings from *20180925 Fremont Street Drawings Transbay Terminal.pdf*

31. Lindeburg, M. R., “Mechanical Engineering Reference Manual for the PE Exam”, 12th Edition, Professional Publications, Inc., 2006.

32. ASTM A709/A709M-18, “Standard Specification for Structural Steel for Bridges”, ASTM International, 2018.

33. “First Street TPG3 Girders Repairs and Details”, Thornton Tomasetti Drawing S1-8404, Feb. 20, 2019.

34. Mill Cert data from *First Street TPG3 Girders_Drawing_Mill_Certs TPG3.pdf*

35. Hill, Michael R., and Nelson, Drew V., “Determining Residual Stress Through the Thickness of a Welded Plate,” Mechanical Engineering Department, Stanford University, Stanford, California, ASME Publications, PVP 327, 1996.

36. American Welding Society, “Welding Handbook,” 8th edition—Chapter 7, “Residual Stresses and Distortion.”

37. Mill Cert data from *PO 989-1 MTRs.pdf* and *PO 989-2 MTRs.pdf*.

38. “TPG3 Roof Girder Fatigue Investigation”, Thornton Tomasetti Document, October 17, 2018, *20181017 Roof TPG3 Girders Fatigue Investigation_R5.pdf*.

39. “Interim Report 8 (Draft): Fatigue Review of Bus Deck”, Thornton Tomasetti Report, October 11, 2019.

40. National Centers for Environmental Information, National Oceanic and Atmospheric Administration, *www.ncdc.noaa.gov*.

APPENDIX A. ULTRASONIC INSPECTION OF GROOVE WELDS

AWS (2015 EDITION) ULTRASONIC INSPECTION (SHEET 1)

Inspection Instruction

1. Ensure you are qualified to perform this inspection. Verify qualifications at www.lpicert.com.
2. Ensure you have read and understand any project specific Procedure(s) and/or Instruction(s) that may apply to this inspection.
3. Locate, read and understand inspection protocol as specified in industry Test Standard(s) applicable for this test (for example ASTM or NA), identify in Test Standard Box.
4. Ensure ALL Test & Measuring Equipment (T&ME) used for this test is calibrated. Record ALL T&ME serial numbers and calibration information on this form. Identify if calibration is per use.
5. If test temperature is other than room temperature, identify in Notes section.

Check Box ✓ when complete ☒

Project No:	LA181690	Client/Facility:	THORNTON TOMASETTI
Project:	Cracked Girders Trans Bay Center, San Francisco. CA	Test/Exam Standard(s) / Procedure(s) :	FULL PEN WELDS IIW BLOCK LPI UT-2 REV 5 ☒

Weld Diagram :

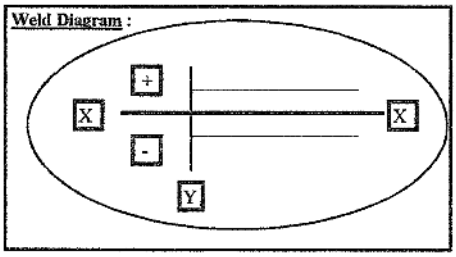

STRUCTURE / DRAWING:	E.6 & D.4 GIRDERS
WELD JOINT AWS:	NOT AVAILABLE
WELDING PROCESS:	NOT AVAILABLE
CALIBRATION BLOCK:	IIW

FLAW DETECTOR DAILY CALIBRATION	PROCEDURES (TEST BLOCK)	INITIALS
	6.22.3 Resolution (RC)-	JM
	6.24.5 Angle Beam (IIW) -	JM
	6.27.2.1 Index Point – (IIW)	JM
	6.27.2.2 Angle Sound Path –(IIW)	JM
	6.27.2.3 Distance Calibration –	JM
	6.27.2.4 Amplitude/Sensitivity–	JM
	6.27.2.5 Resolution (RC)	JM
	6.27.2.6 Approach Distance (IIW)	JM

☒

TEST INFORMATION						DECIBELS				DISCONTINUITY					EVALUATION		
WELD IDENTIFICATION	INDICATION NUMBER	TRANSDUCER ANGLE (deg)	THICKNESS (in)	TESTED FROM FACE	LEG NUMBER	REFERENCE LEVEL (db)	INDICATION LEVEL (db)	ATTENUATION (db)	INDICATION RATING (db)	LENGTH (in)	ANGULAR DISTANCE (in)	DEPTH FROM FACE (in)	DISTANCE FROM 'X' (in)	DISTANCE FROM 'Y' (in)	DEFECT CLASS	ACCEPT	REJECT
D.4 20' E Fremont		70	4.1	B	1&2	46	60	8	+6	1.25	5.4	2.0	0	0.25	D[1]	X	
D.4 20' E Fremont		60 /70	4.1	A	1&2											X	
D.4 20' W Fremont		60 /70	4.1	AB	1&2											X	

Notes: [1] - < than 1/16 in height located in the mid thickness of the weld (root pass of double weld) ☒

TEST EQUIPMENT DOCUMENTATION & CERTIFICATION

Instrument Used:	Inst. Serial No.	Cal. Due Date
GE USMGO +	GOPLS16060061	8/22/19 ☒

Ensure all instructions have been met, form complete, T&ME information entered, Complete Check Boxes

Performed By:	Date:	Reviewed By:	Date:
JOHN MILLER	12/10-14/18	ROBERT S. VECCHIO	12/17/18

Verify Latest Form Revision: www.lpicert.com → →→ *Form: LPI-13.3-Rev-0-Utrasonic-AWS-Sht-1*

AWS (2015 EDITION) ULTRASONIC INSPECTION (SHEET 2)

Inspection Instruction

6. Ensure you are qualified to perform this inspection. Verify qualifications at www.lpicert.com.
7. Ensure you have read and understand any project specific Procedure(s) and/or Instruction(s) that may apply to this inspection.
8. Locate, read and understand inspection protocol as specified in industry Test Standard(s) applicable for this test (for example ASTM or NA), identify in Test Standard Box.
9. Ensure ALL Test & Measuring Equipment (T&ME) used for this test is calibrated. Record ALL T&ME serial numbers and calibration information on this form. Identify if calibration is per use.
10. If test temperature is other than room temperature, identify in Notes section.

Check Box ✔ when complete ☒

Project No:	LA181690	Client/Facility:	THORNTON TOMASETTI
Project:	Cracked Girders Trans Bay Center, San Francisco, CA	Test/Exam Standard(s) / Procedure(s) :	FULL PEN WELDS IIW LPI UT-2 REV 5 ☒

TEST INFORMATION						DECIBELS		DISCONTINUITY						EVALUATION		
WELD IDENTIFICATION	INDICATION NUMBER	TRANSDUCER ANGLE (deg)	THICKNESS (in)	TESTED FROM FACE	LEG NUMBER	REFERENCE LEVEL (db)	INDICATION LEVEL (db)	ATTENUATION (db)	INDICATION RATING (db)	LENGTH (in)	ANGULAR DISTANCE (in)	DEPTH FROM FACE (in)	DISTANCE FROM X (in)	DISTANCE FROM Y (in)	DEFECT CLASS	ACCEPT	REJECT
E.6 20'E Fremont		60/70	4.1	A/B	1-2											X	
D.4 20' E First St		60/70	4.1	A/B	1-2											X	
D.4 20' W First St		60/70	4.1	A/B	1-2											X	
E.6 20' E First St		60/70	4.1	A/B	1-2											X	
E.6 20' First St		60/70	4.1	A/B	1-2											X	

Notes: ☒

TEST EQUIPMENT DOCUMENTATION & CERTIFICATION

Instrument Used:	Inst. Serial No.	Cal. Due Date
SEE PAGE 1		
		☒

Ensure all instructions have been met, form complete, T&ME information entered, Complete Check Boxes

Performed By:	Date:	Reviewed By:	Date:
JOHN MILLER	12/10-14/18	ROBERT S. VECCHIO	12/17/18

Verify Latest Form Revision: www.lpicert.com → →→ *Form: LPI-13.3-Rev-0-Utrasonic-AWS-Sht-2*

APPENDIX B. ULTRASONIC INSPECTION OF BOLTS

ULTRASONIC INSPECTION (SHEET 1)

Inspection Instruction

1. Ensure you are qualified to perform this inspection. Verify qualifications at www.lpicert.com.
2. Ensure you have read and understand any project specific Procedure(s) and/or Instruction(s) that may apply to this inspection.
3. Locate, read and understand test protocol as specified in industry Test Standard(s) applicable for this test (for example ASTM or NA), identify in Test Standard Box.
4. Ensure ALL Test & Measuring Equipment (T&ME) used for this inspection is calibrated. Record ALL T&ME serial numbers and calibration information on this form. Identify if calibration is per use.
5. If test temperature is other than room temperature, identify in Notes section.

Check Box ✔ when complete ☒

Project No:	LA181690	Client/Facility:	Thornton Tomasetti
Project:	Cracked Girders Transbay Transit Center, SF	Test/Exam Standard(s) :	IIW BLOCK & Manufactured Bolt Standards

☒

DESCRIPTION:	UTN OF BOLTS AT BOLTED CONNECTIONS						
MATERIAL TYPE:	STEEL			MATERIAL THICKNESS:	SEE BELOW		
INSPECTION METHOD:	CONTACT						
UNIT:	*GE*			MODEL #:	USMGO+		
TRANSDUCER ANGLE:	0º	FREQUENCY:	5MHZ	DIAMETER:	½"	COUPLANT:	GREASE
ADDITIONAL INFORMATION:	TESTED FROM THREAD END ONLY						

☒

IDENTIFICATION	QTY	DIAMETER	LENGTH	ACCEPT	REJECT	LENGTH	DEPTH	SLAG	POROSITY	LACK OF FUSION	LACK OF PENETRATION	CRACK	UNDERCUT	SURFACE	LAMINATIONS	INDICATION LEVEL A	REFERENCE LEVEL B	ATTENUATION FACTOR C	INDICATION RATING D
D.4 EAST Fremont	50	1 1/4	7.9	X															
"	5	1 1/2	8.9	X															
E.6 WEST Fremont	55	1 1/4	7.9	X															
E.6 EAST	55	1 1/4	7.9	X															

Notes:

☒

TEST EQUIPMENT DOCUMENTATION & CERTIFICATION

Instrument Used:	Inst. Serial No.	Cal. Due Date
GE USMGO+	GOPLS16060061	8/22/2019

☒

Ensure all instructions have been met, form complete, T&ME information entered, Complete Check Boxes

Performed By:	Date:	Reviewed By:	Date:
JOHN MILLER	12/10-14/18	ROBERT S. VECCHIO	12/17/18

Verify Latest Form Revision: www.lpicert.com → →→ *Form: LPI-13.3-Rev-0-Utrasonic-Sht-1*

APPENDIX C. METALLURGICAL EVALUATION SUPPLEMENTARY FIGURES

Fig. 177. Girder sample D.4-N following removal by IPM.

Fig. 178. Girder sample D.4-S following removal by IPM.

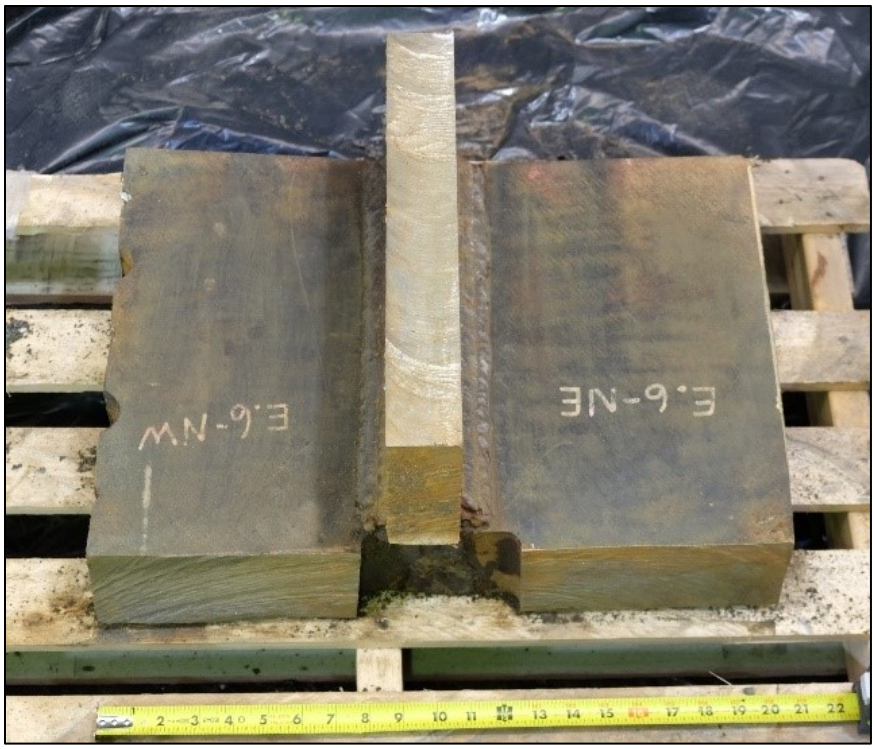

Fig. 179. Girder sample E.6-N following removal by IPM.

Fig. 180. Girder sample E.6-S following removal by IPM.

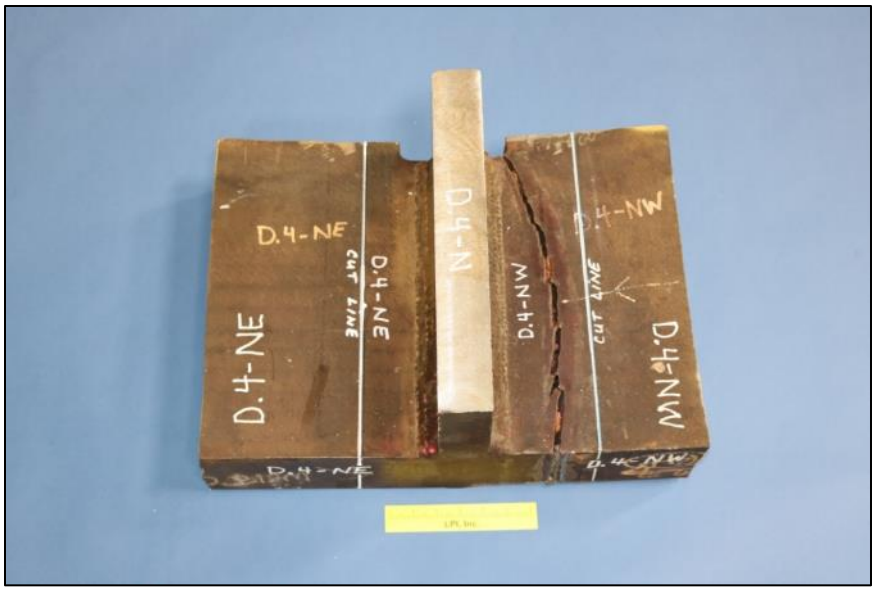

Fig. 181. Girder sample D.4-N in as-received condition upon receipt at LPI.

Fig. 182. Girder sample D.4-S in as-received condition upon receipt at LPI.

Fig. 183. Girder sample E.6-N in as-received condition upon receipt at LPI.

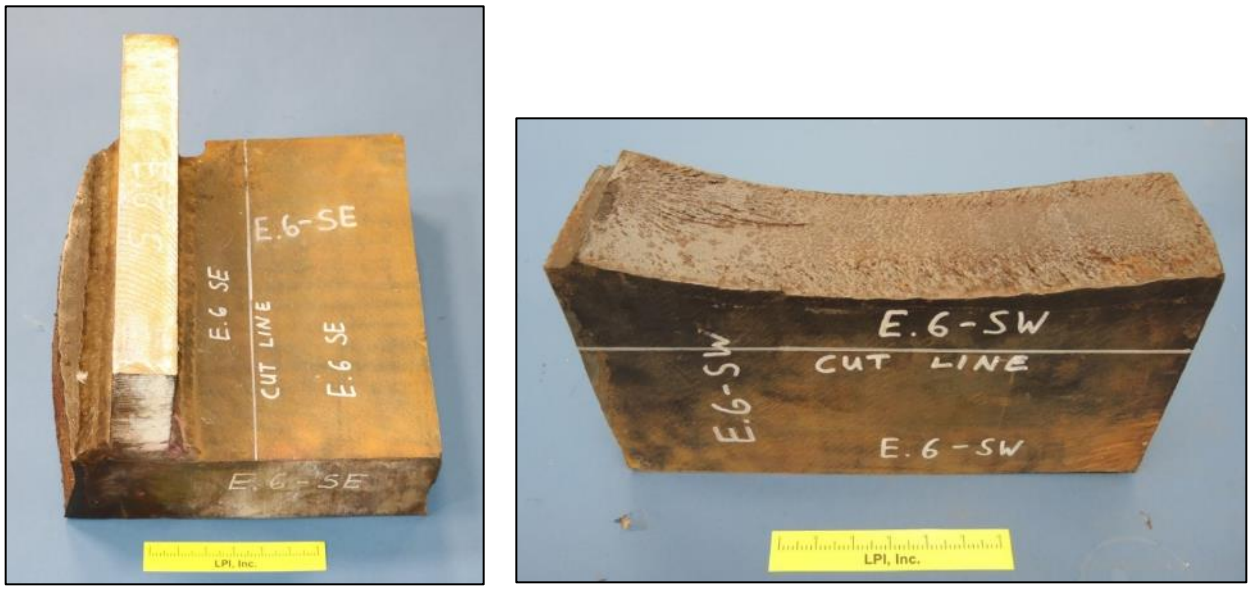

Fig. 184. Girder sample E.6-S in as-received condition upon receipt at LPI.

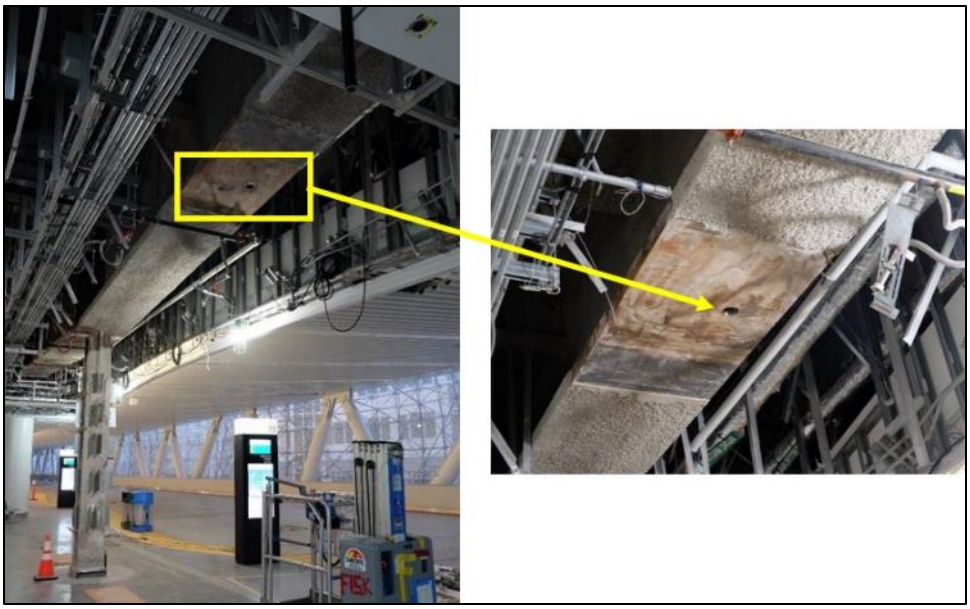

Fig. 185. Typical removal location for the 3-in. diameter core samples removed from girder flanges above First Street.

Fig. 186. 3-in. diameter core samples removed from girder flanges above First Street.

Fig. 187. 3-in. diameter core samples removed from girder flanges above First Street in the as-received condition upon receipt by LPI.

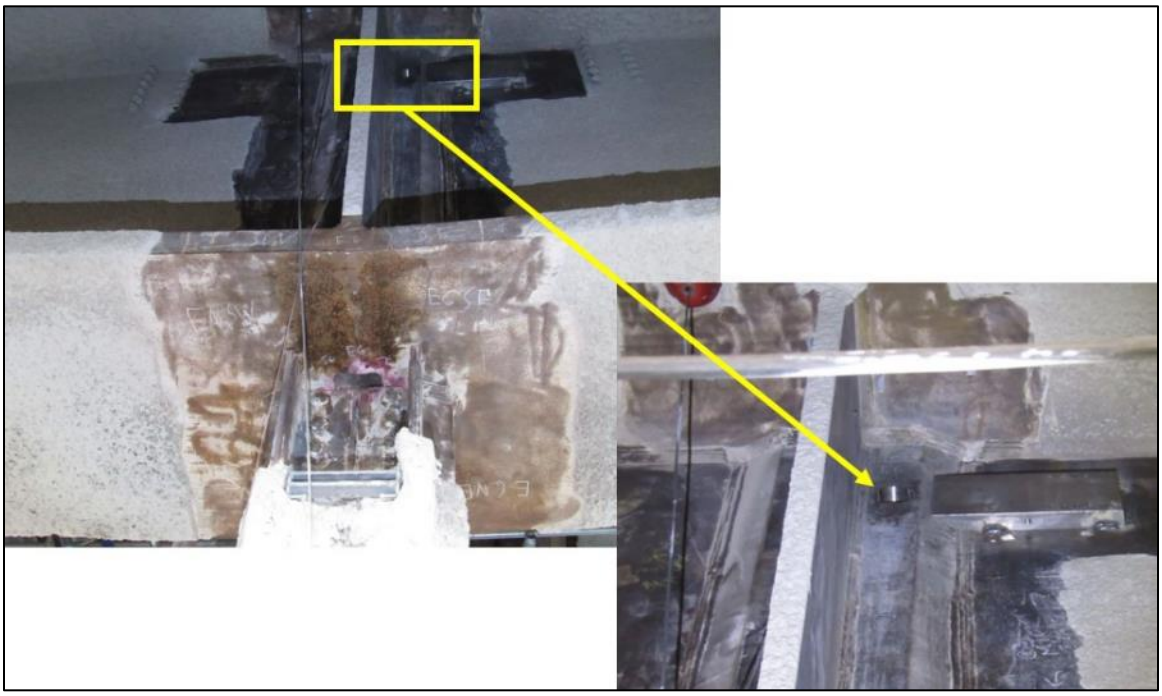

Fig. 188. Typical removal location for the 3-in. diameter core samples removed from girder hangers above Fremont Street and First Street.

Fig. 189. 3-in. diameter core samples removed from girder hangers above Fremont Street and First Street.

Fig. 190. 3-in. diameter core samples removed from girder hangers above Fremont Street and First Street in the as-received condition upon receipt by LPI.

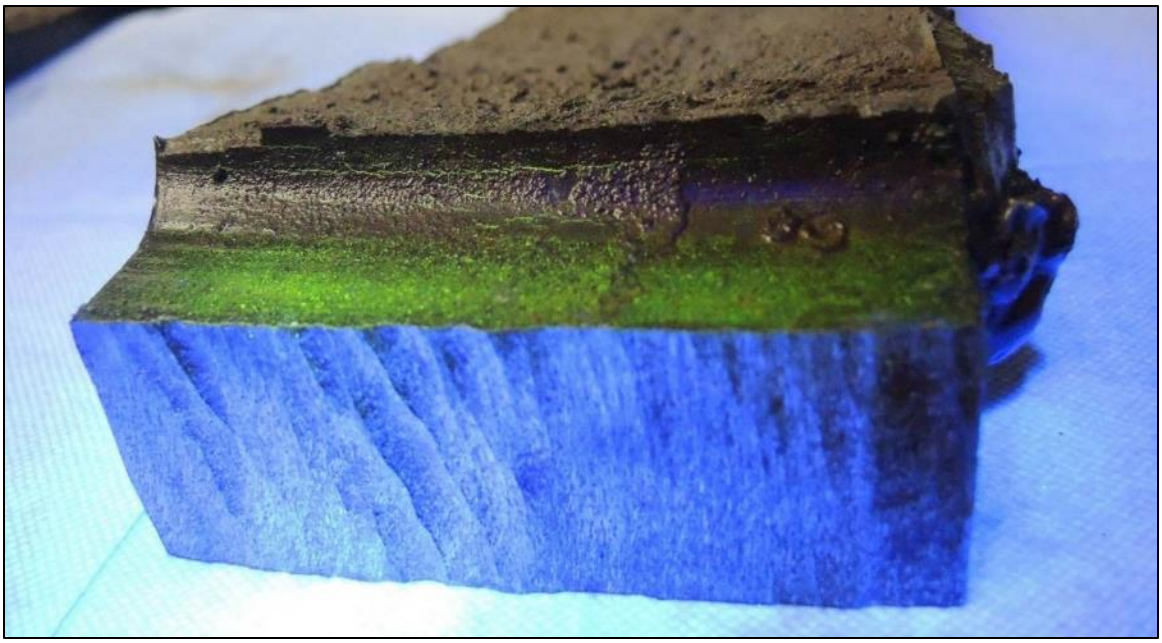

Fig. 191. Secondary cracking in the radius of the weld access hole of sample D.4-SW as identified by fluorescent magnetic particle testing.

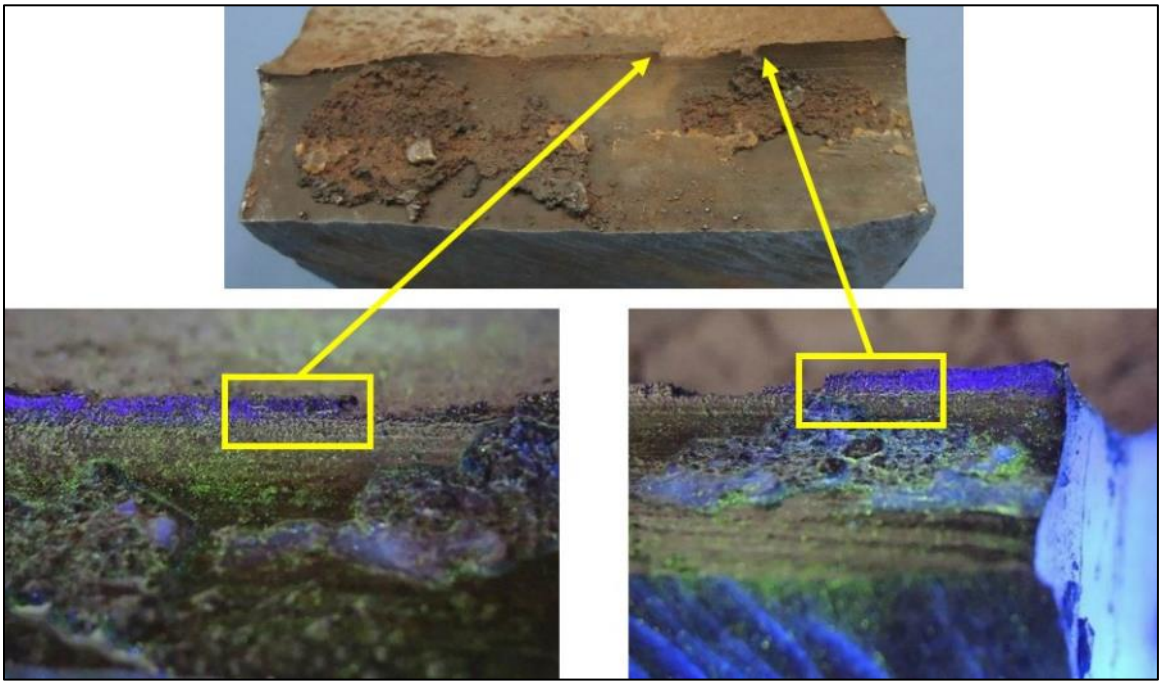

Fig. 192. Secondary cracking in the radius of the weld access hole of sample D.4-NW as identified by fluorescent magnetic particle testing.

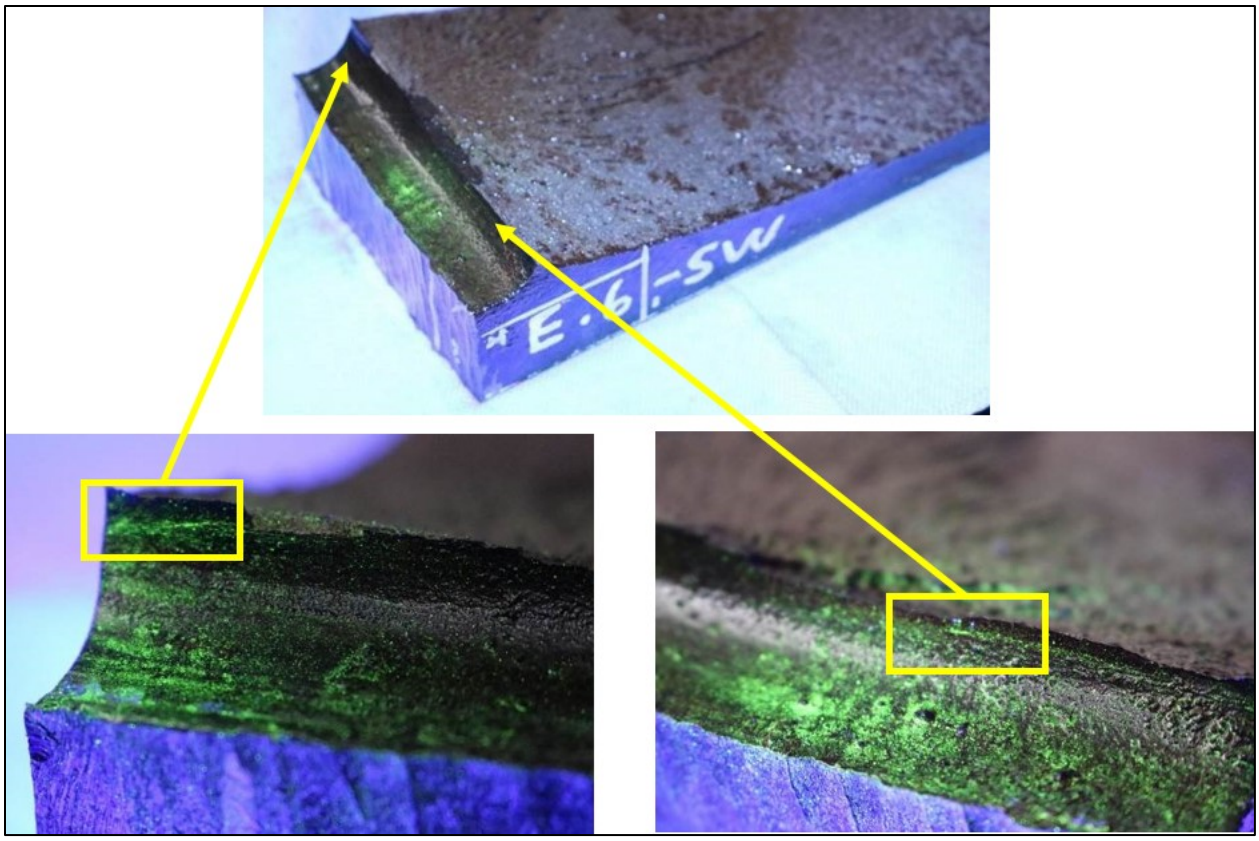

Fig. 193. Secondary cracking in the radius of the weld access hole of sample E.6-SW as identified by fluorescent magnetic particle testing.

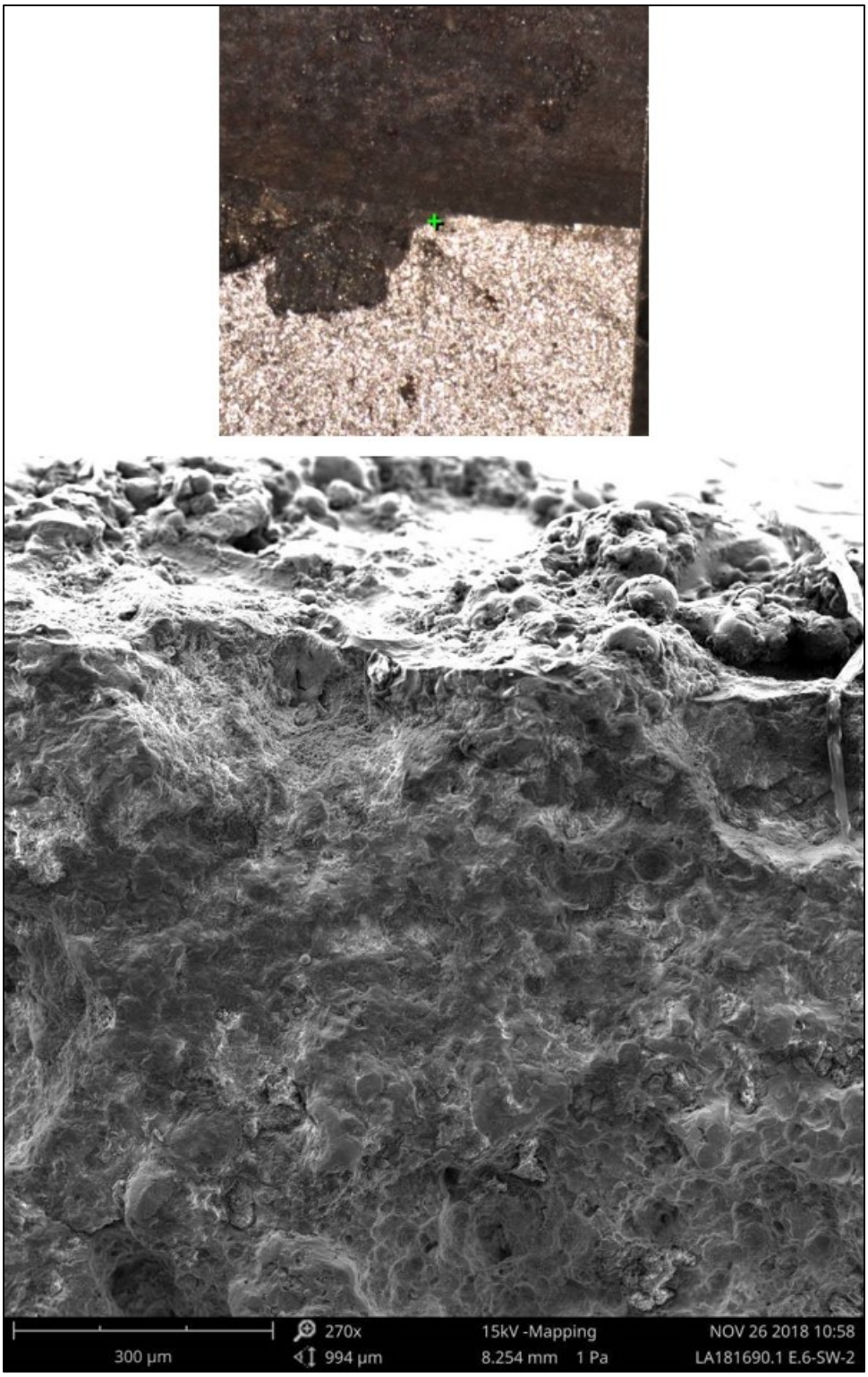

Fig. 194. SEM of oxide covered fracture origin after cleaning of sample E.6-SW.

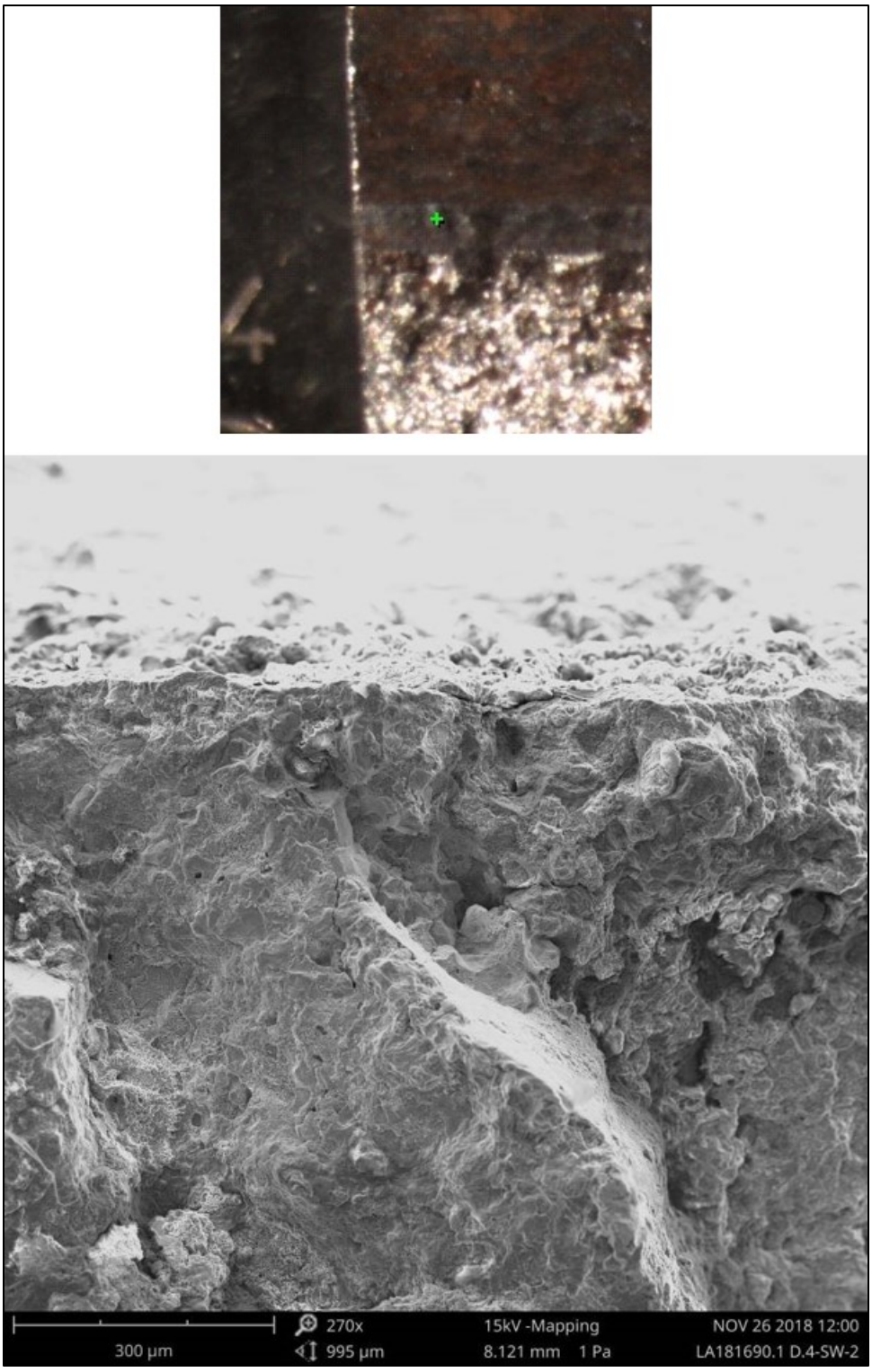

Fig. 195. SEM of oxide covered microcrack fracture origin after cleaning of sample D.4-SW.

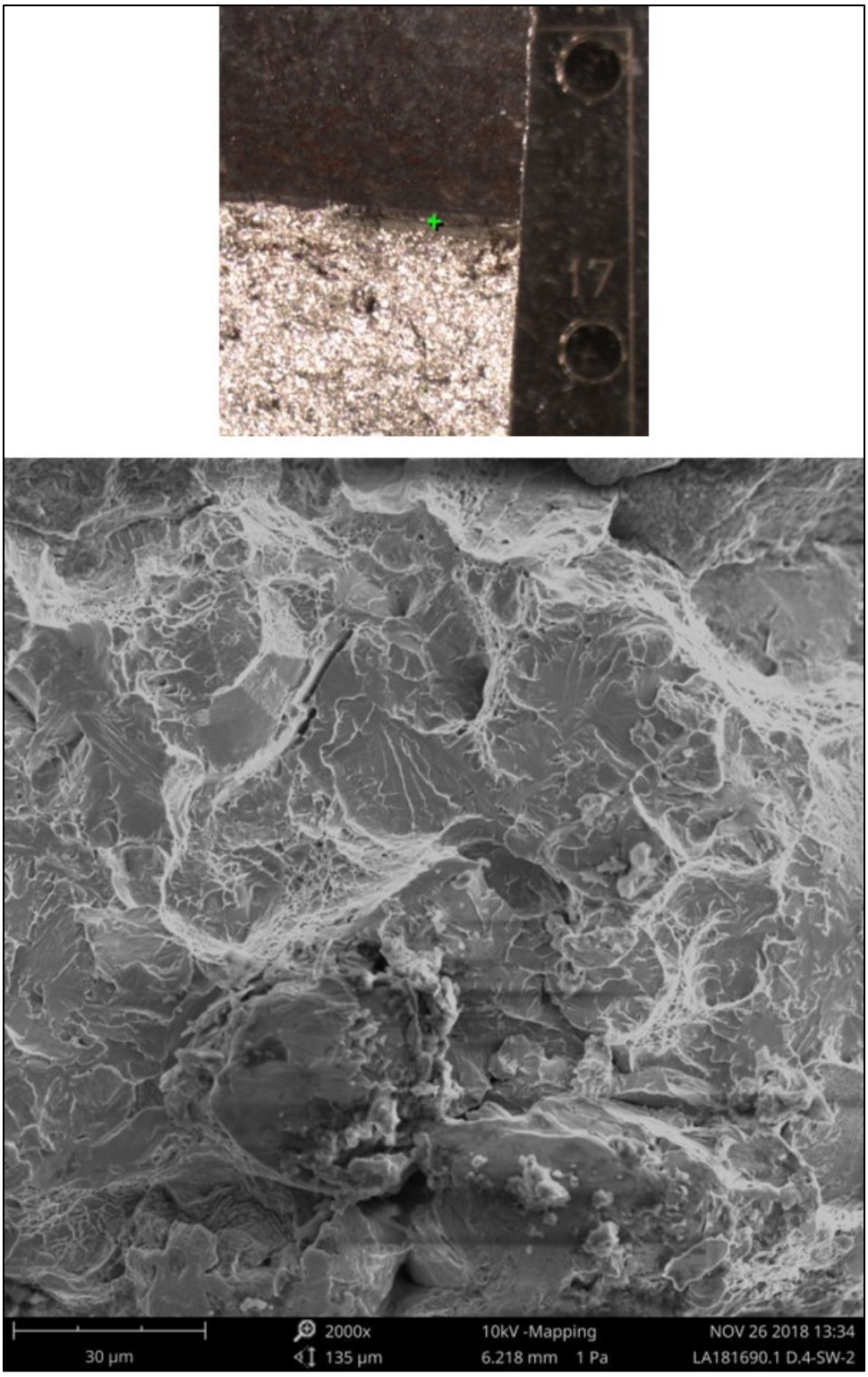

Fig. 196. SEM of microcrack origin showing low-energy (brittle) cleavage fracture morphology in sample D.4-SW.

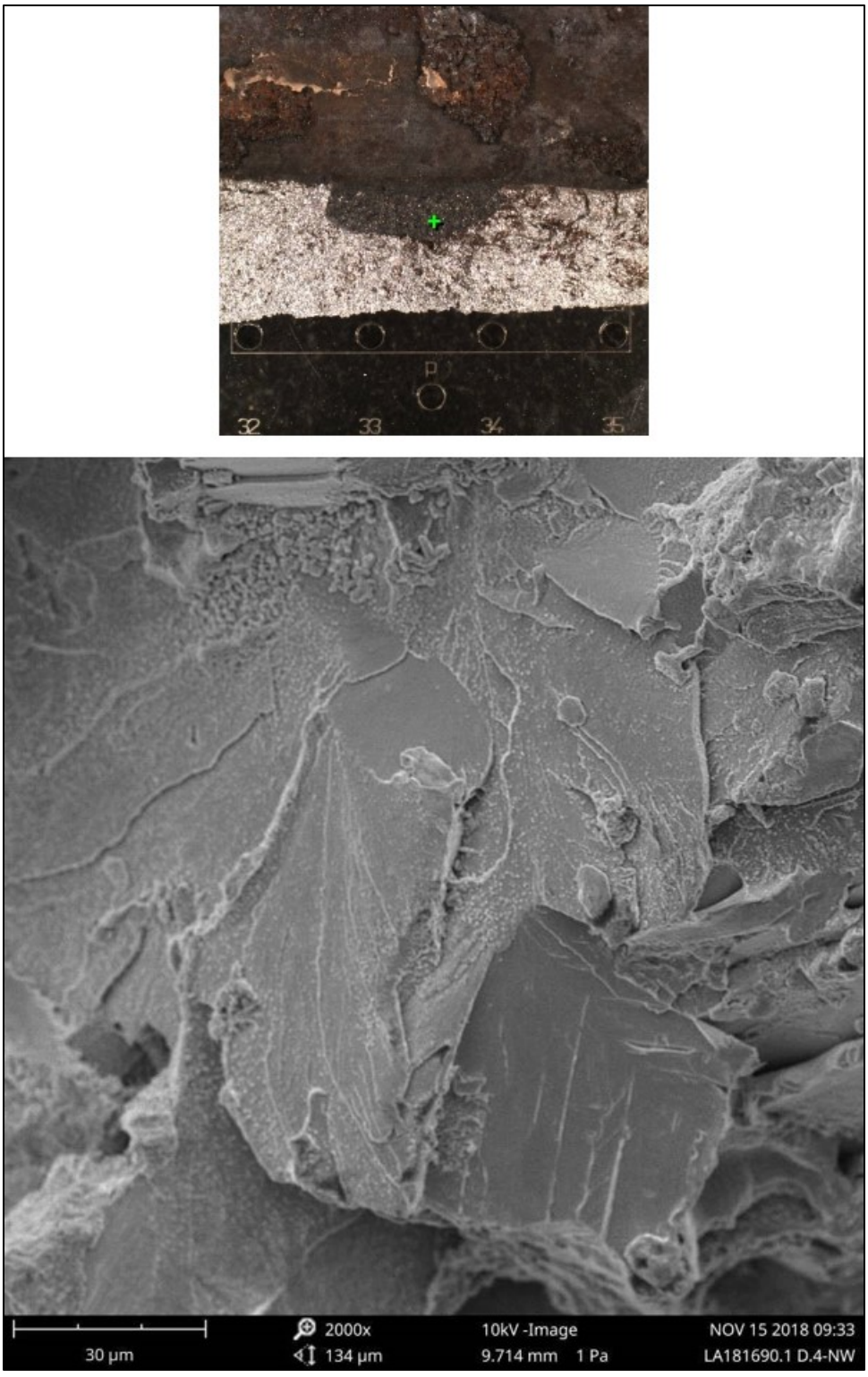

Fig. 197. SEM of elliptical pop-in crack origin showing low-energy (brittle) cleavage fracture morphology in sample D.4-NW.

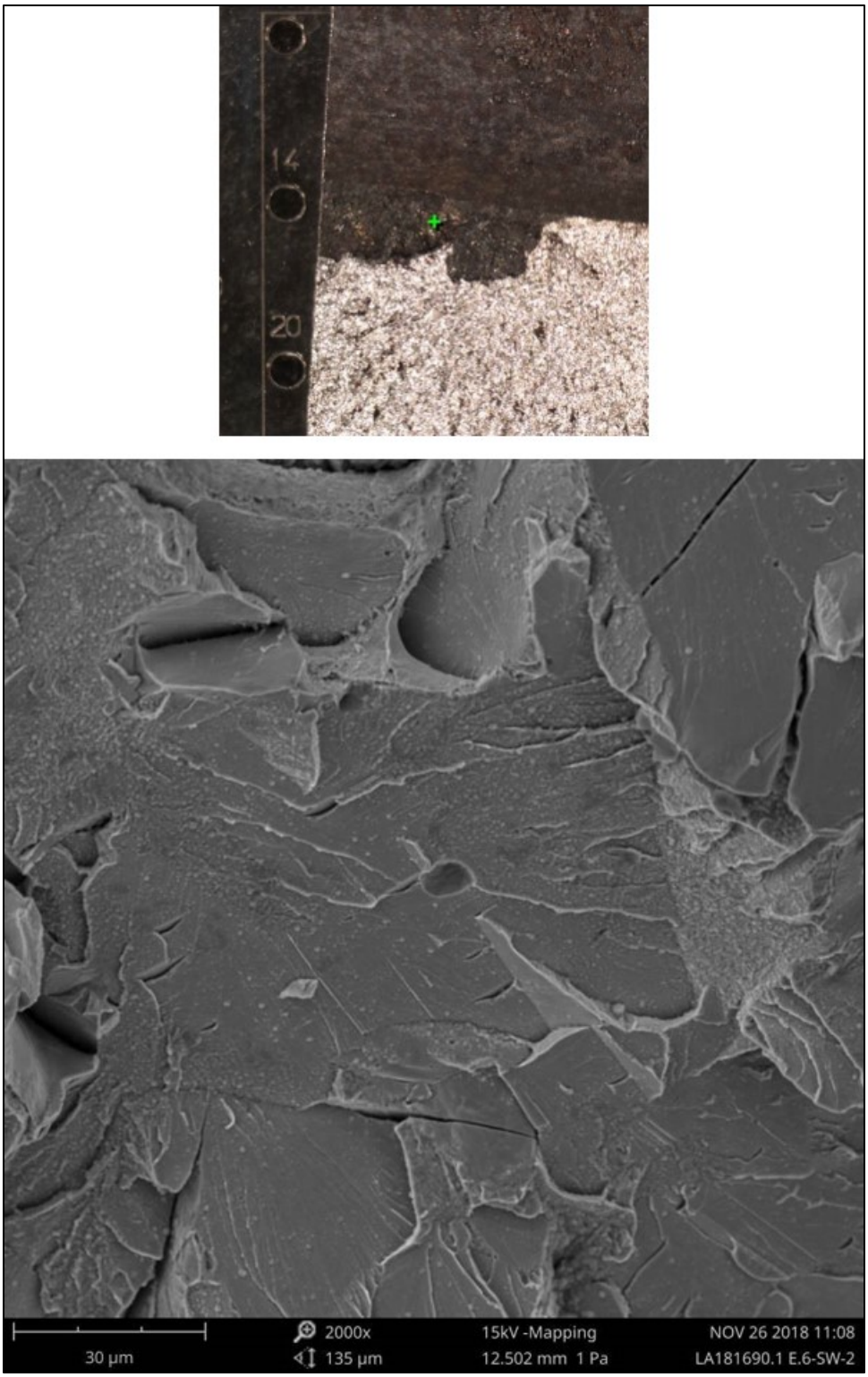

Fig. 198. SEM of elliptical pop-in crack origin showing low-energy (brittle) cleavage fracture morphology in Sample E.6-SW.

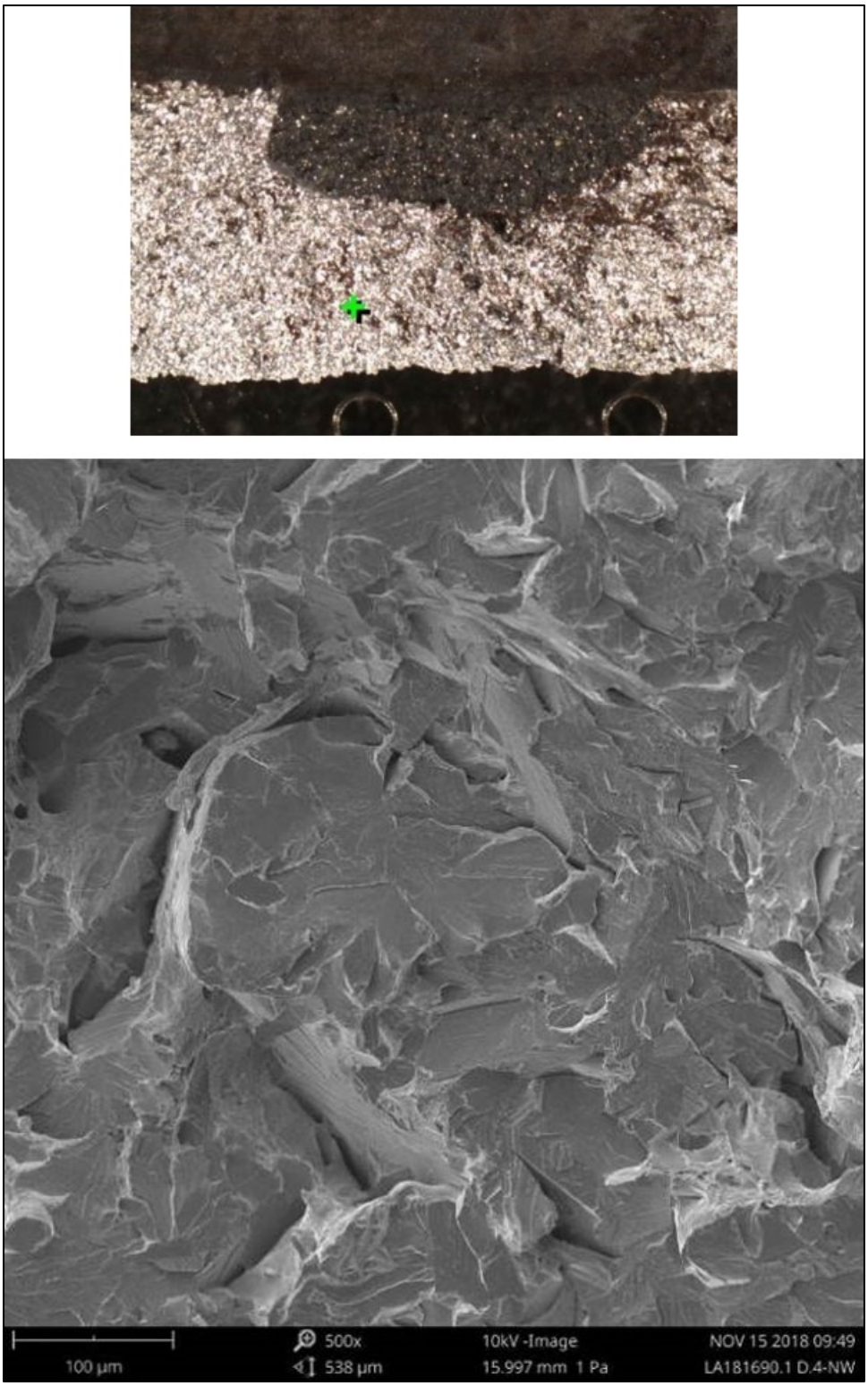

Fig. 199. SEM of sample D.4-NW showing low-energy (brittle) cleavage fracture morphology remote from the origin.

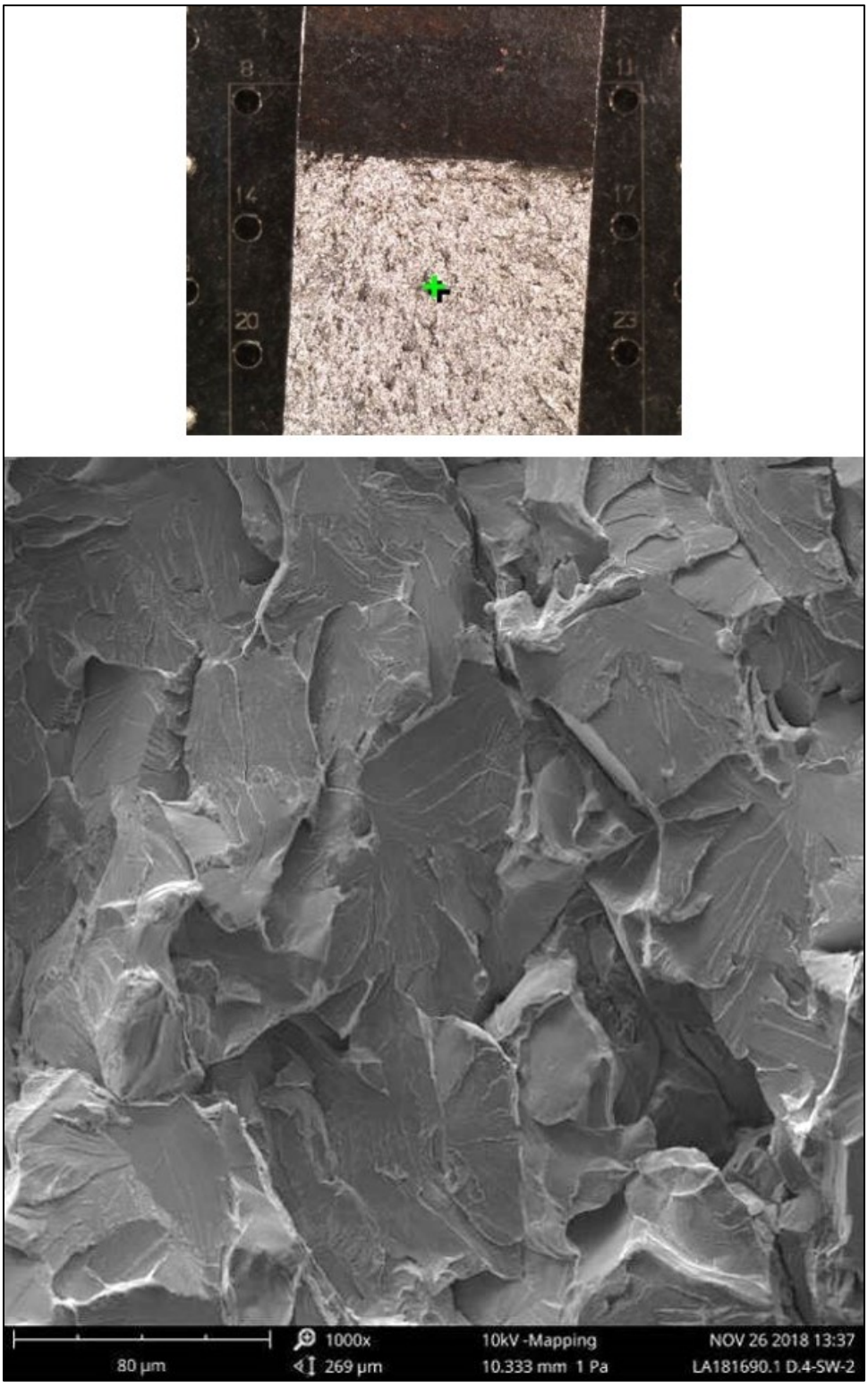

Fig. 200. SEM of sample D.4-SW showing low-energy (brittle) cleavage fracture morphology remote from the origin.

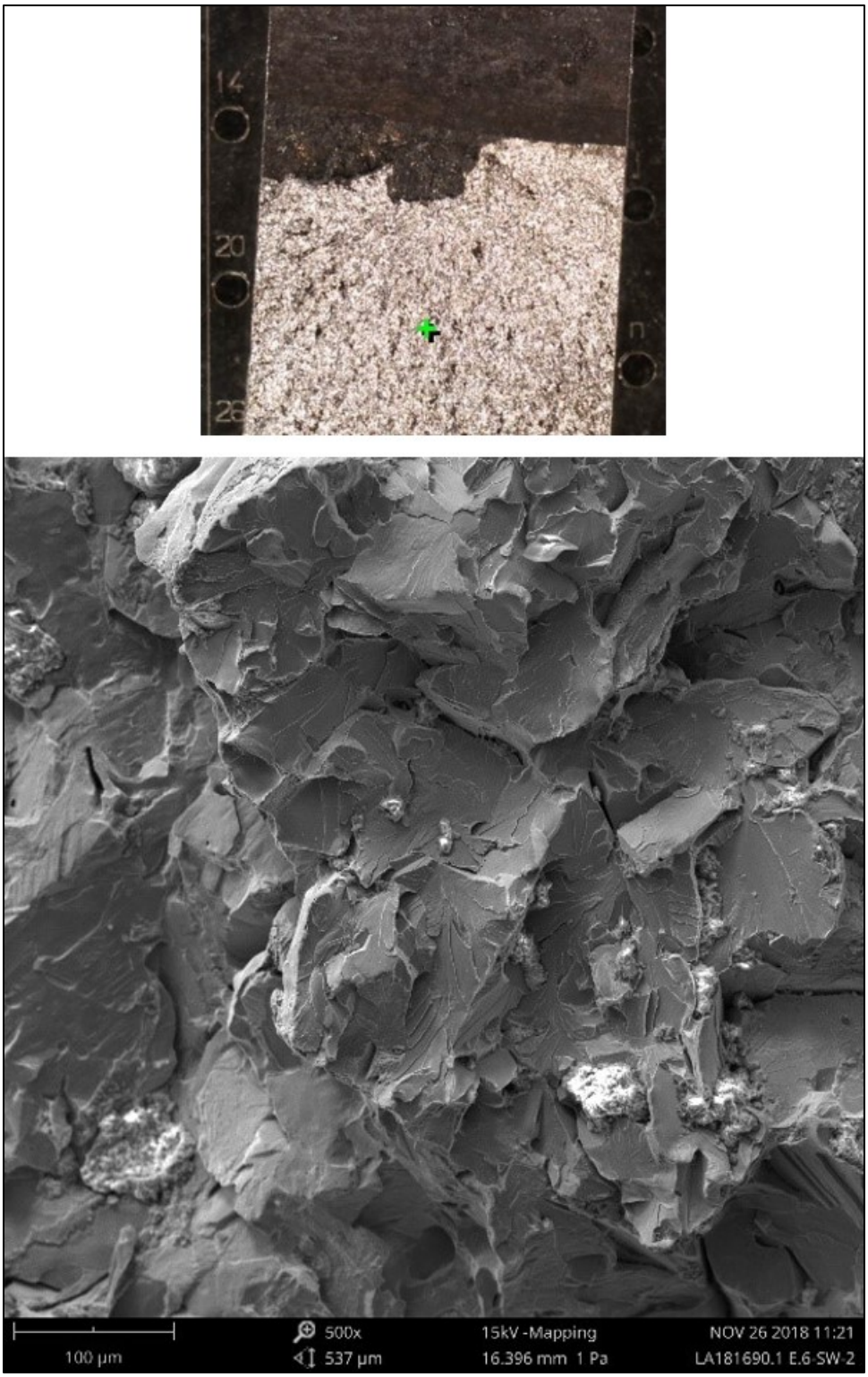

Fig. 201. SEM of sample E.6-SW showing low-energy (brittle) cleavage fracture morphology remote from the origin.

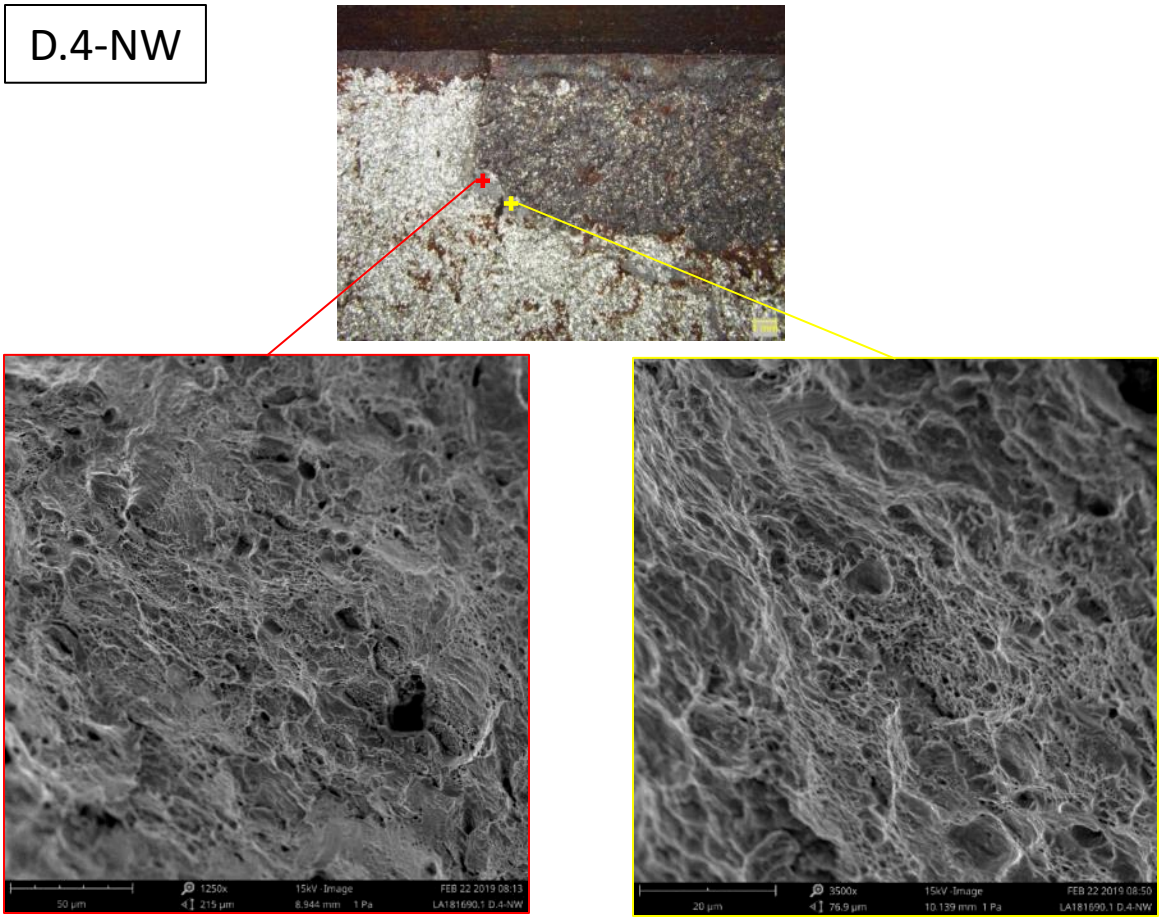

Fig. 202. Representative SEM images of the narrow band of microvoid coalescence between the oxidized elliptical pop-in crack and final fracture on girder sample D.4-NW.

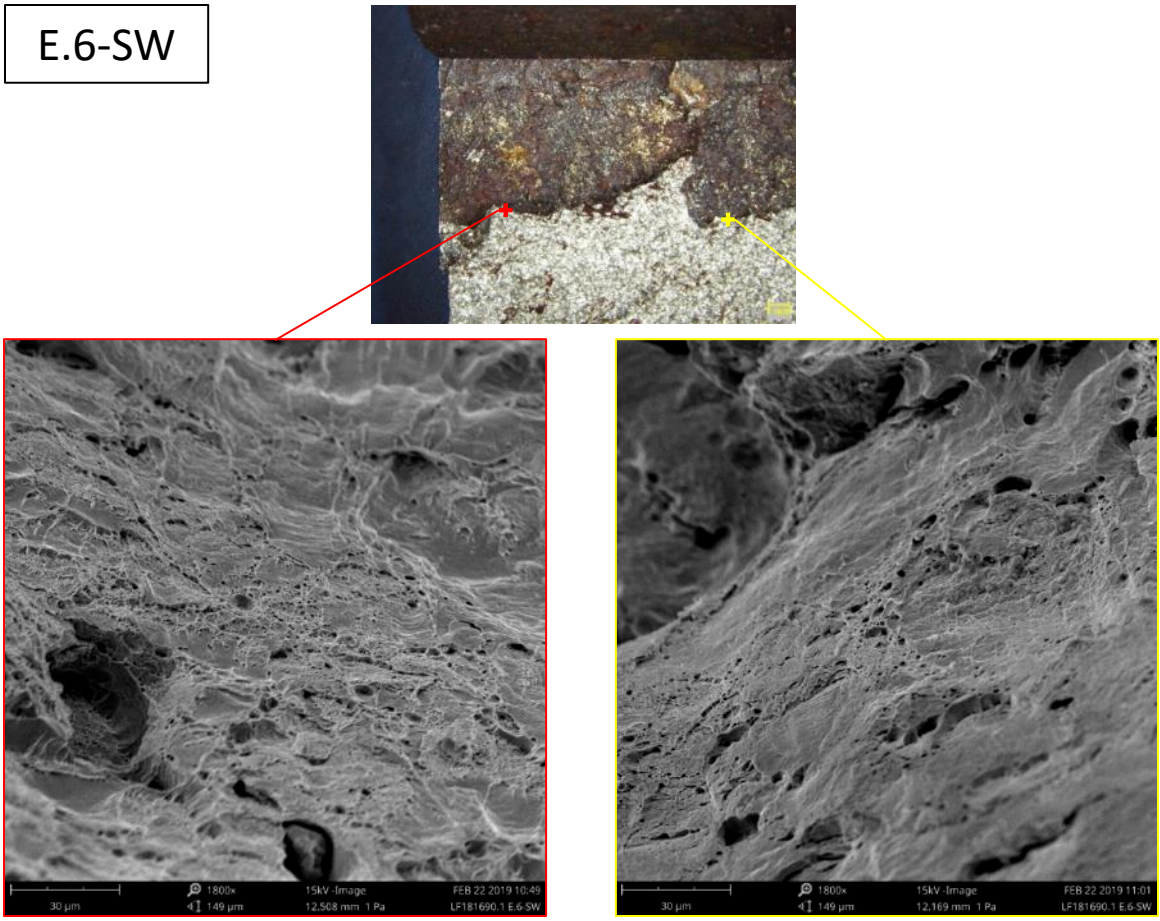

Fig. 203. Representative SEM images of the narrow band of microvoid coalescence between the oxidized elliptical pop-in crack and final fracture on girder sample E.6-SW.

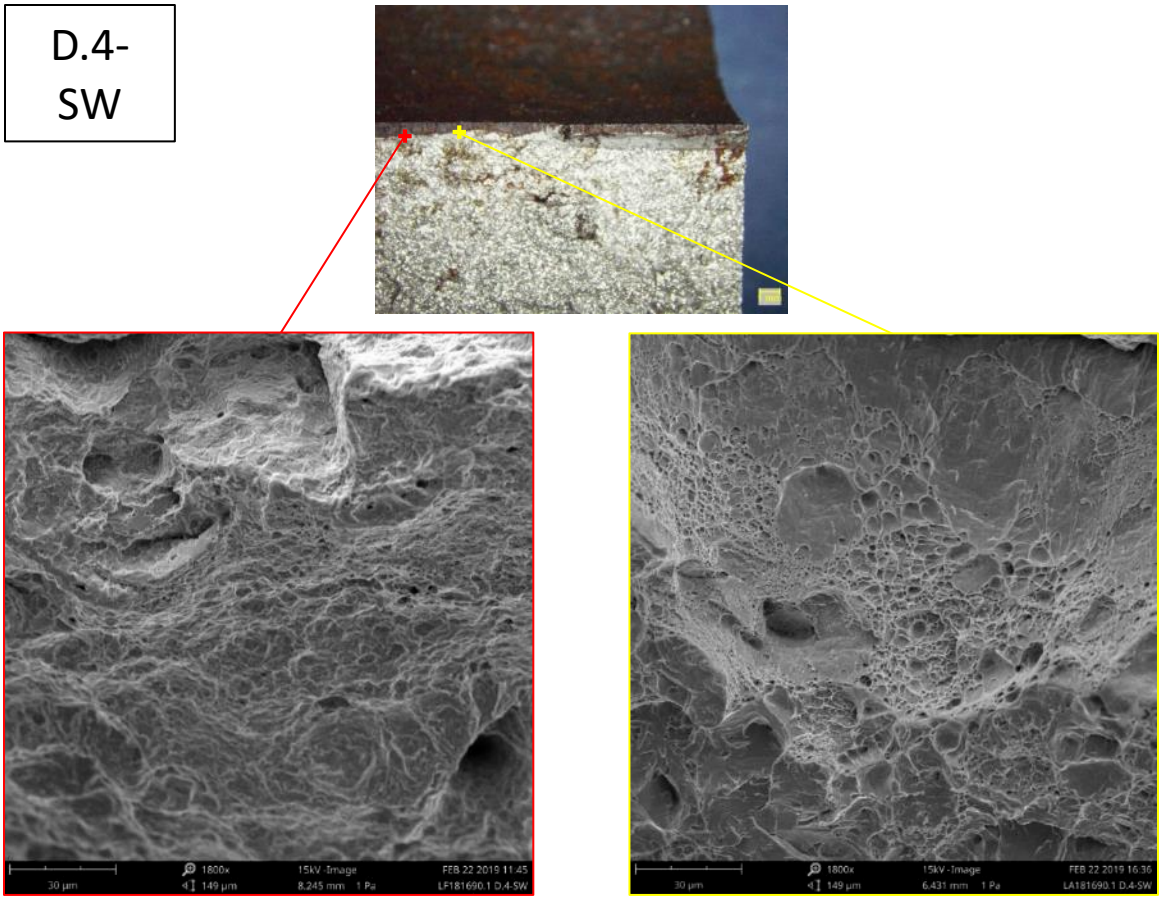

Fig. 204. Representative SEM images of the narrow band of microvoid coalescence between the oxidized microcrack region and final fracture on girder sample D.4-SW.

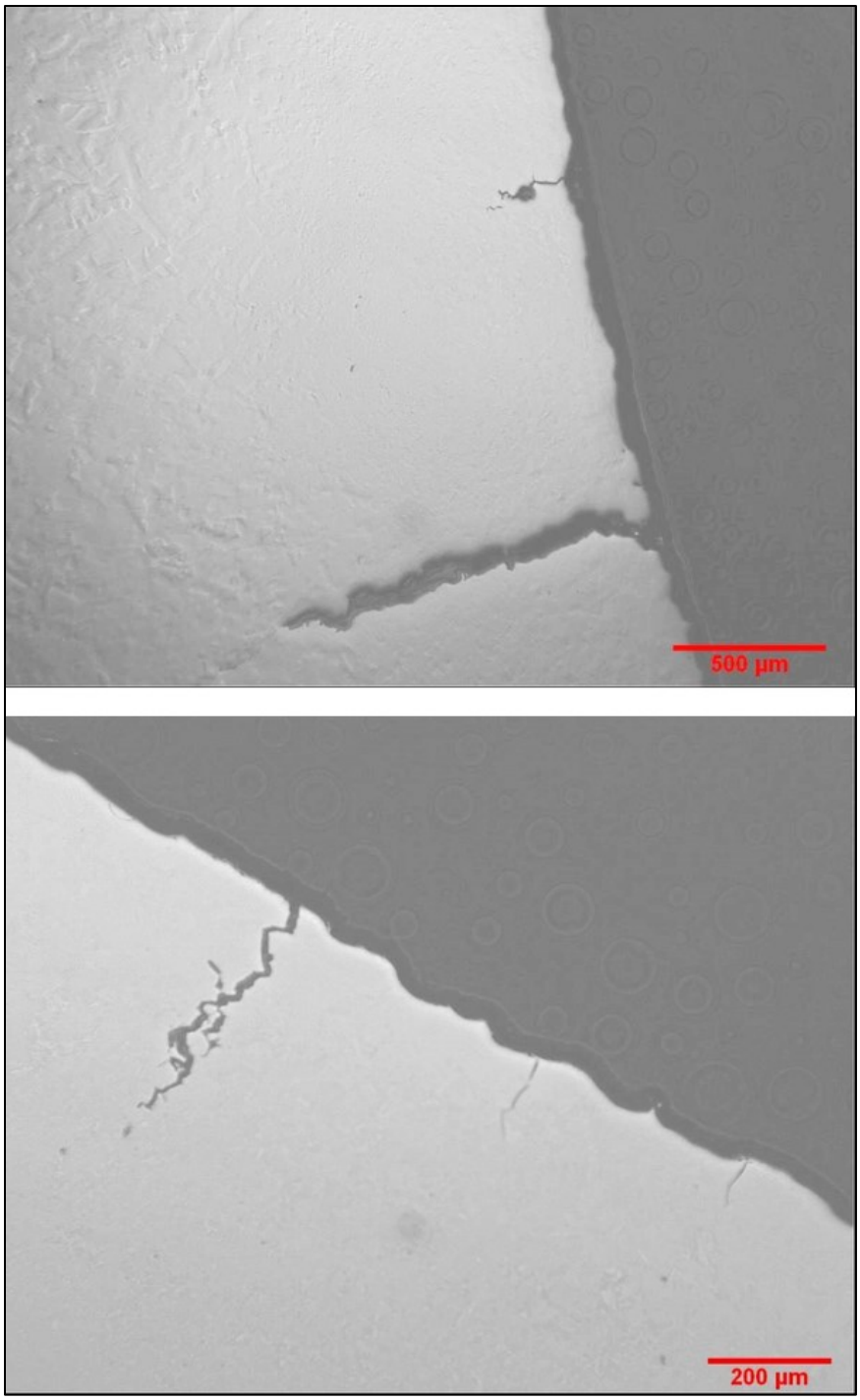

Fig. 205. Multiple secondary cracks in the weld access radius of sample D.4-SW.

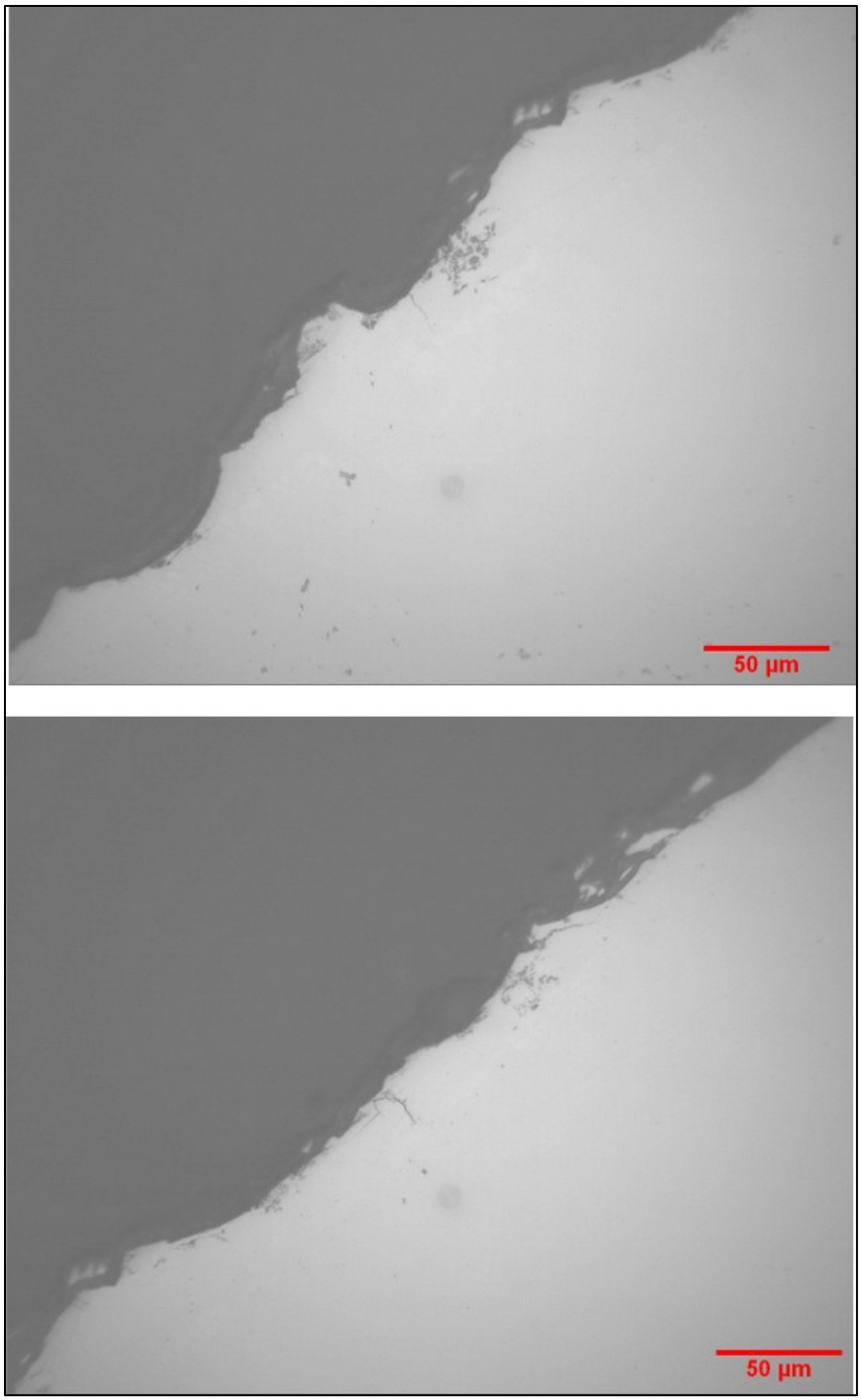

Fig. 206. Multiple secondary cracks in the weld access radius of sample D.4-NW.

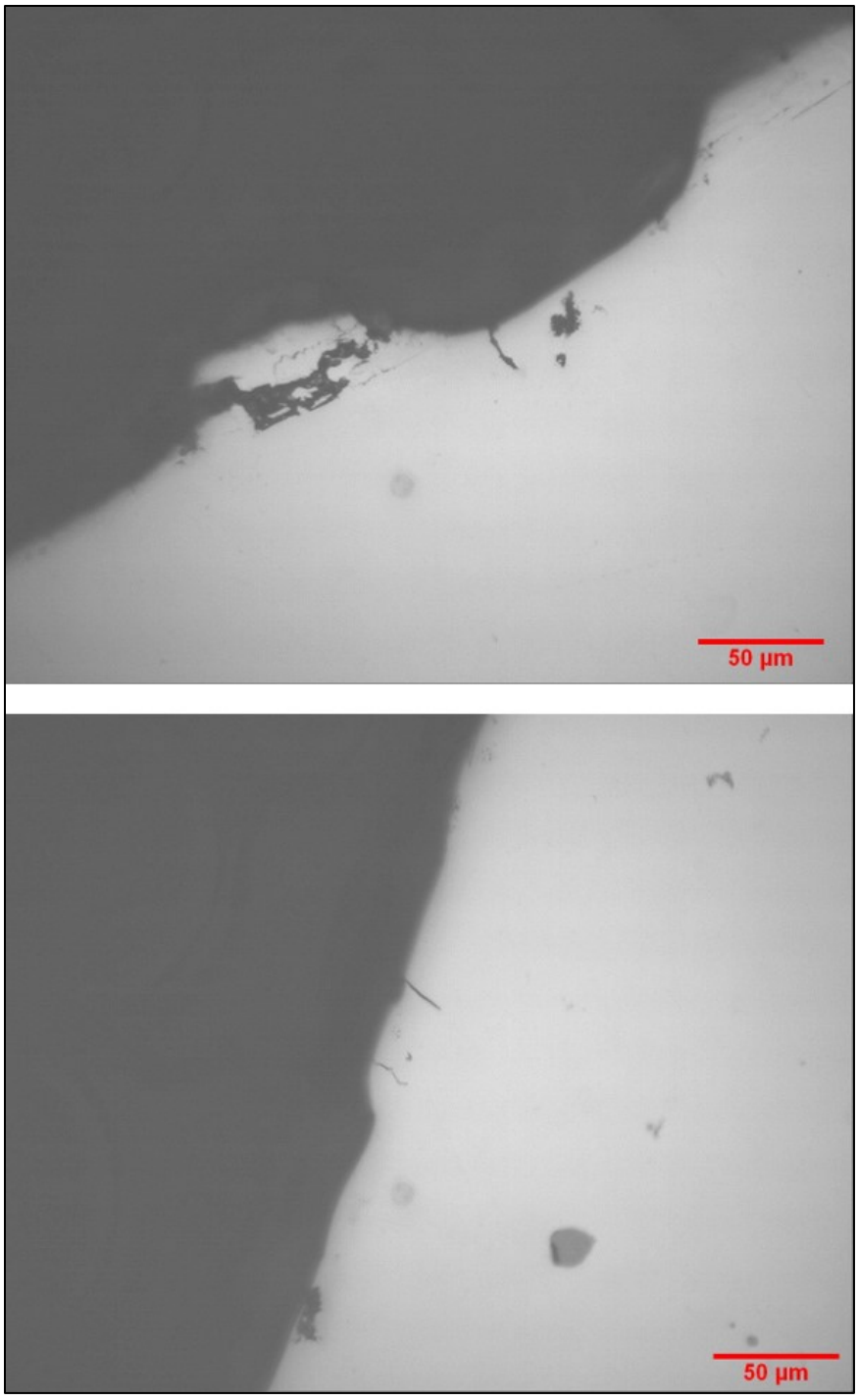

Fig. 207. Multiple secondary cracks in the weld access radius of sample E.6-NE.

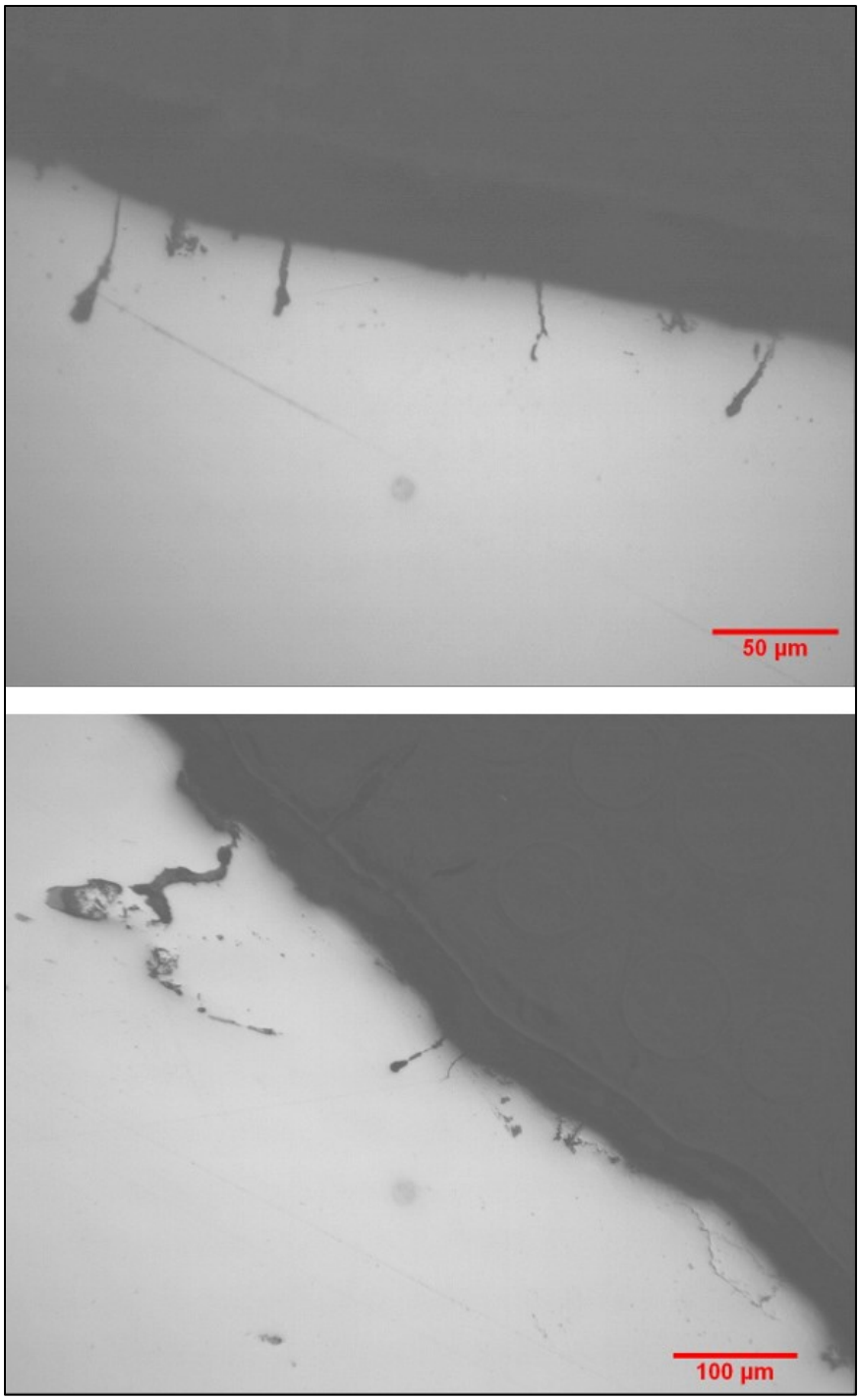

Fig. 208. Multiple secondary cracks in the weld access radius of sample E.6-NW.

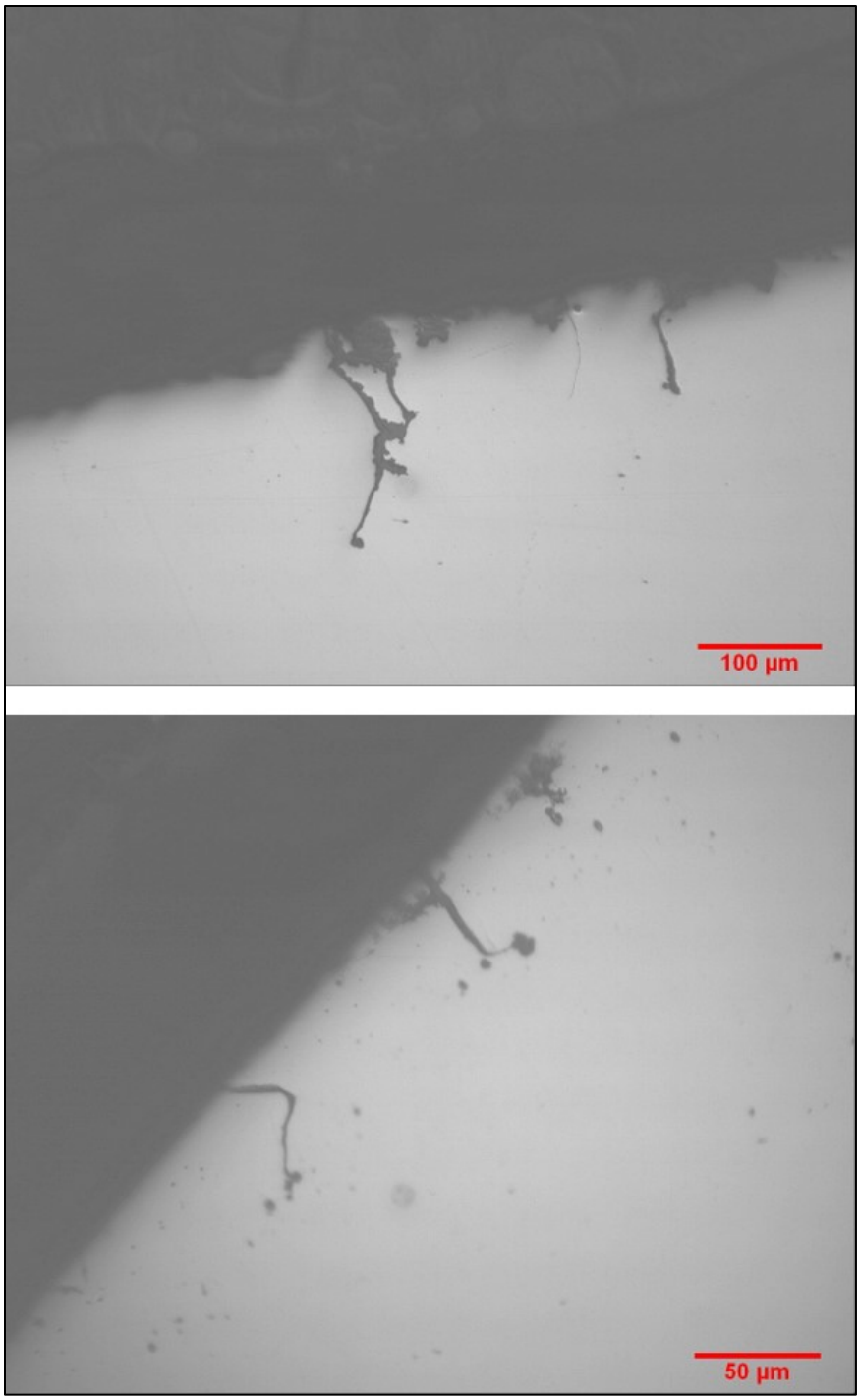

Fig. 209. Multiple secondary cracks in the weld access radius at the top surface of sample E.6-SE.

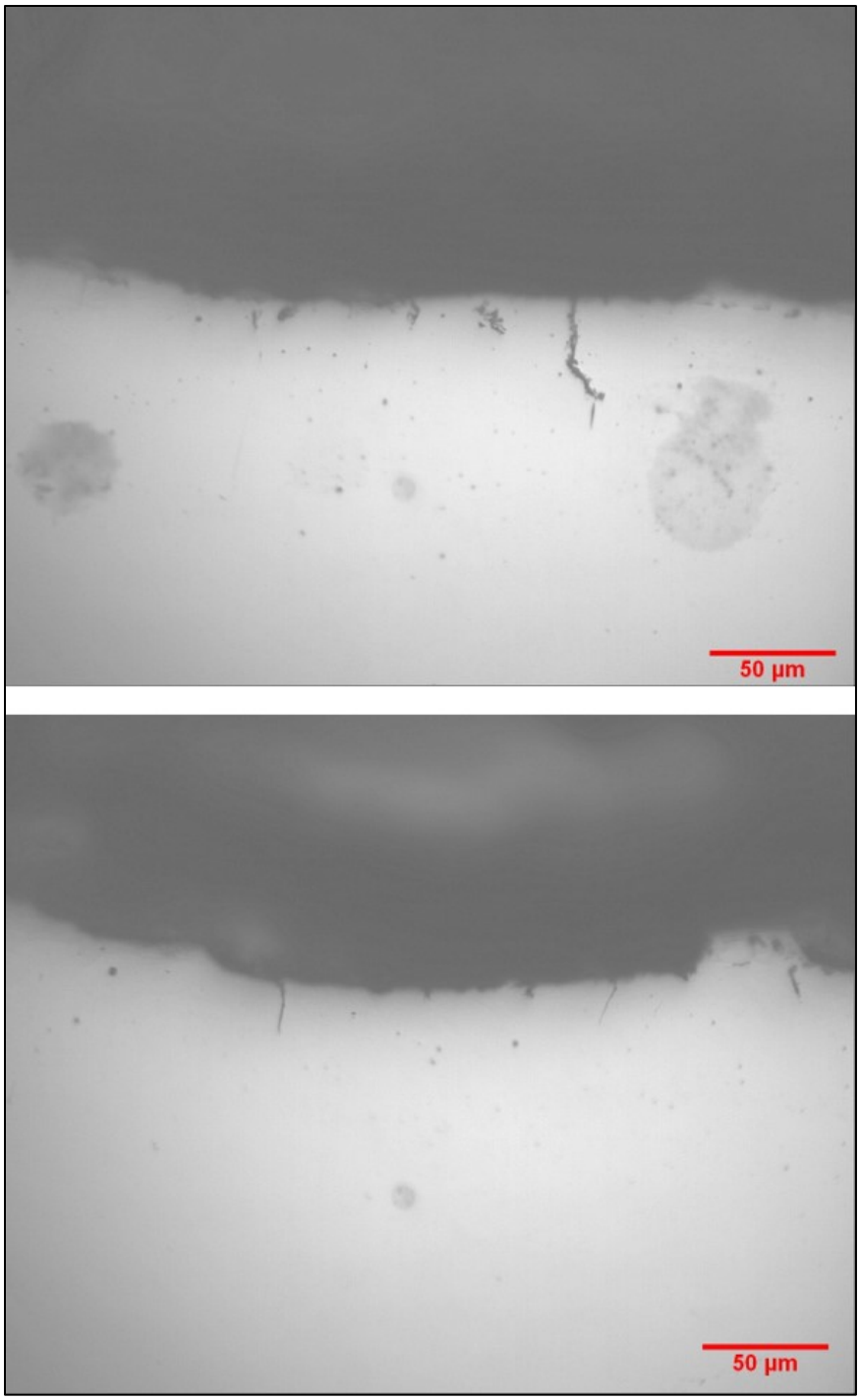

Fig. 210. Multiple secondary cracks in the weld access radius at mid-thickness of sample E.6-SE.

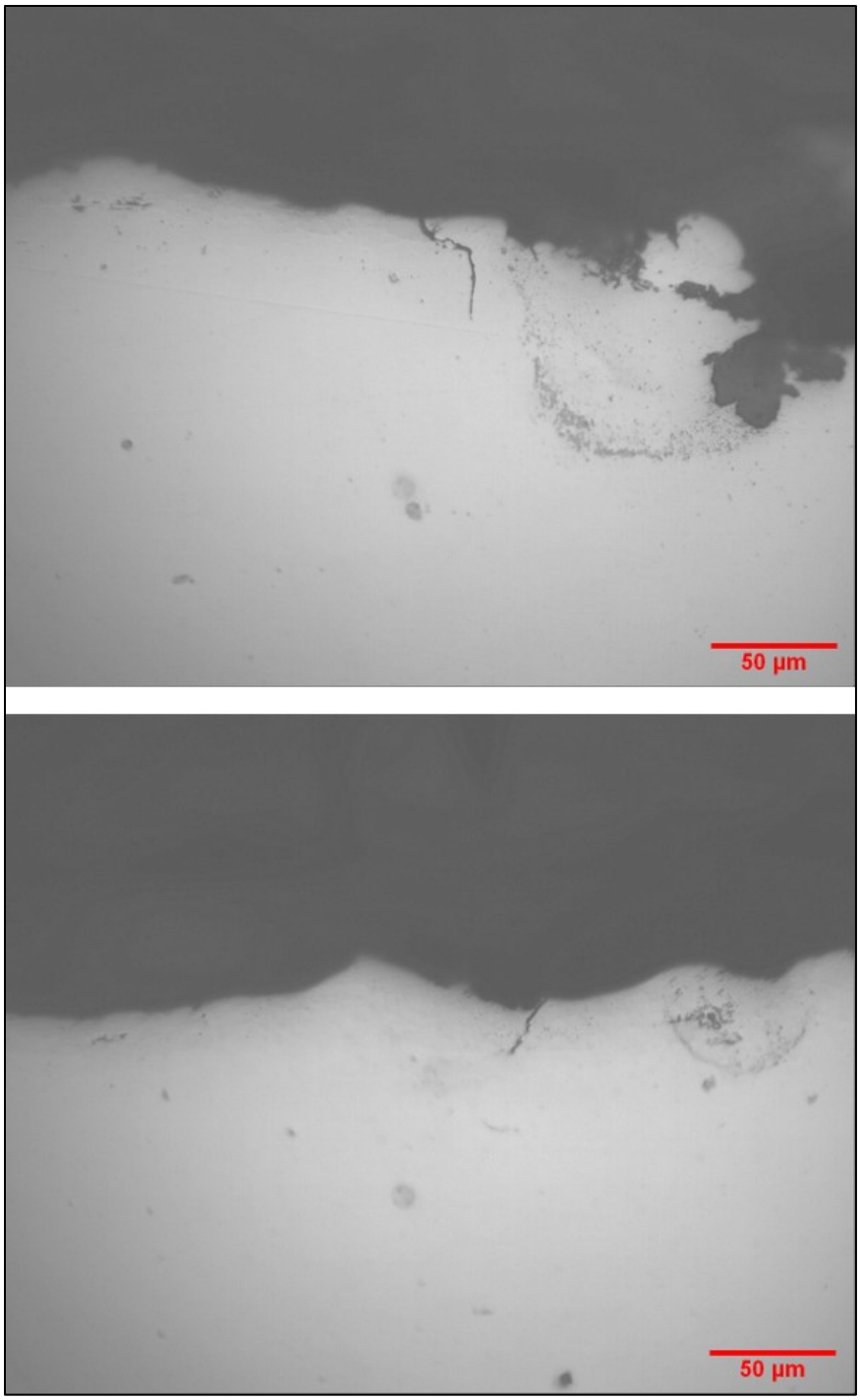

Fig. 211. Multiple secondary cracks in the weld access radius at the top surface of sample D.4-NE.

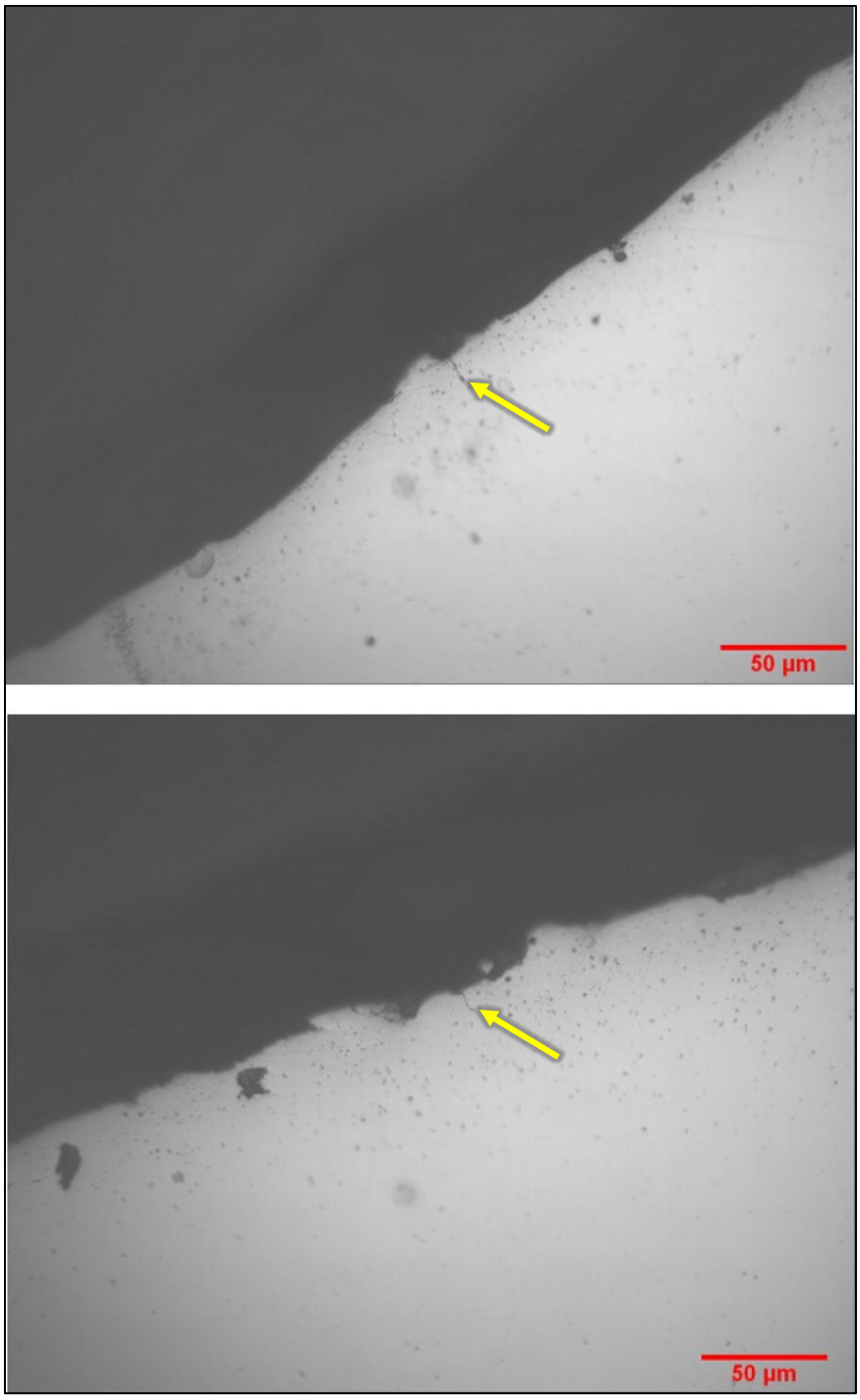

Fig. 212. Multiple secondary cracks in the weld access radius at mid-thickness of sample D.4-NE.

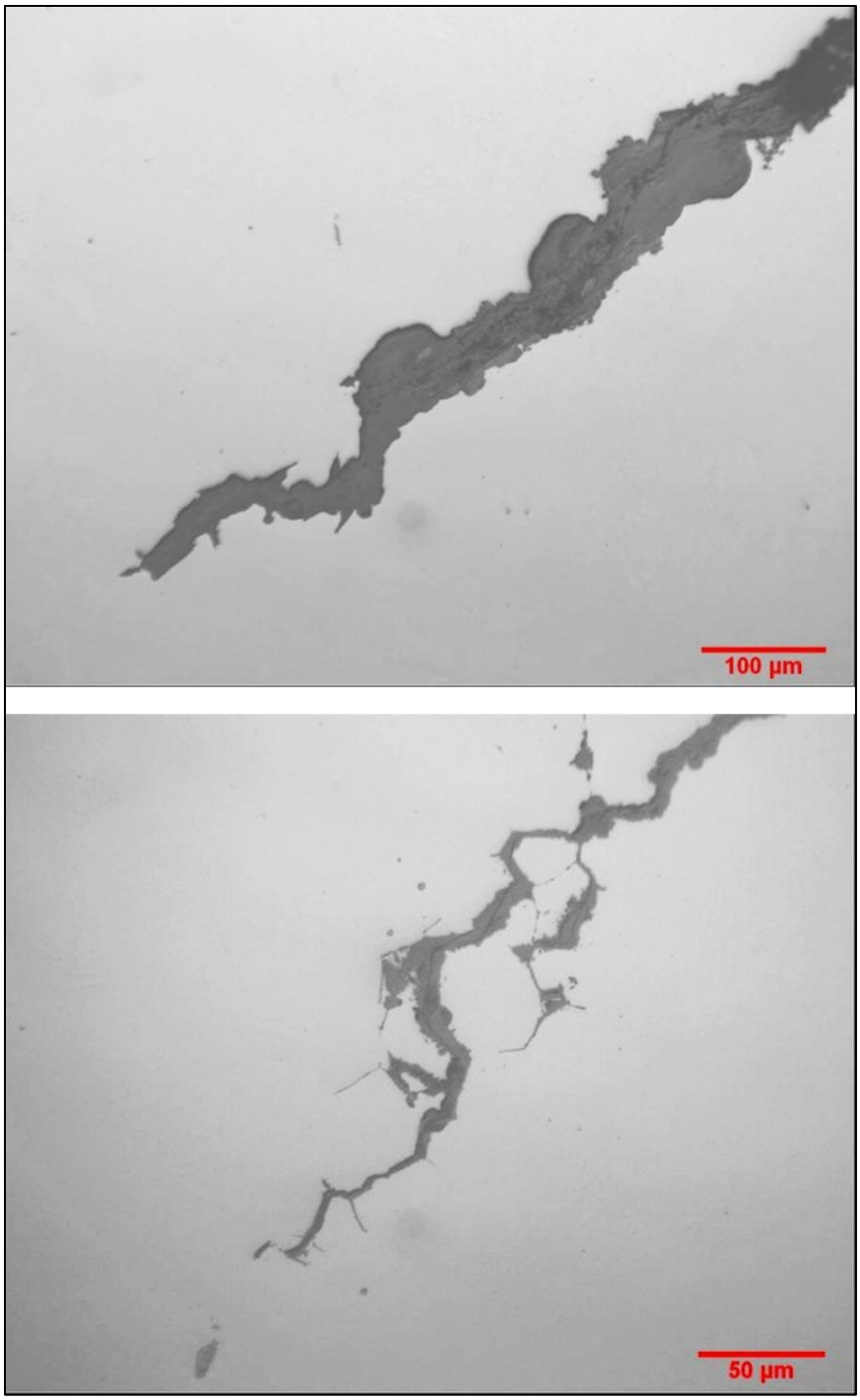

Fig. 213. Cracks filled with dark, high temperature oxide in the weld access hole of sample D.4-SW.

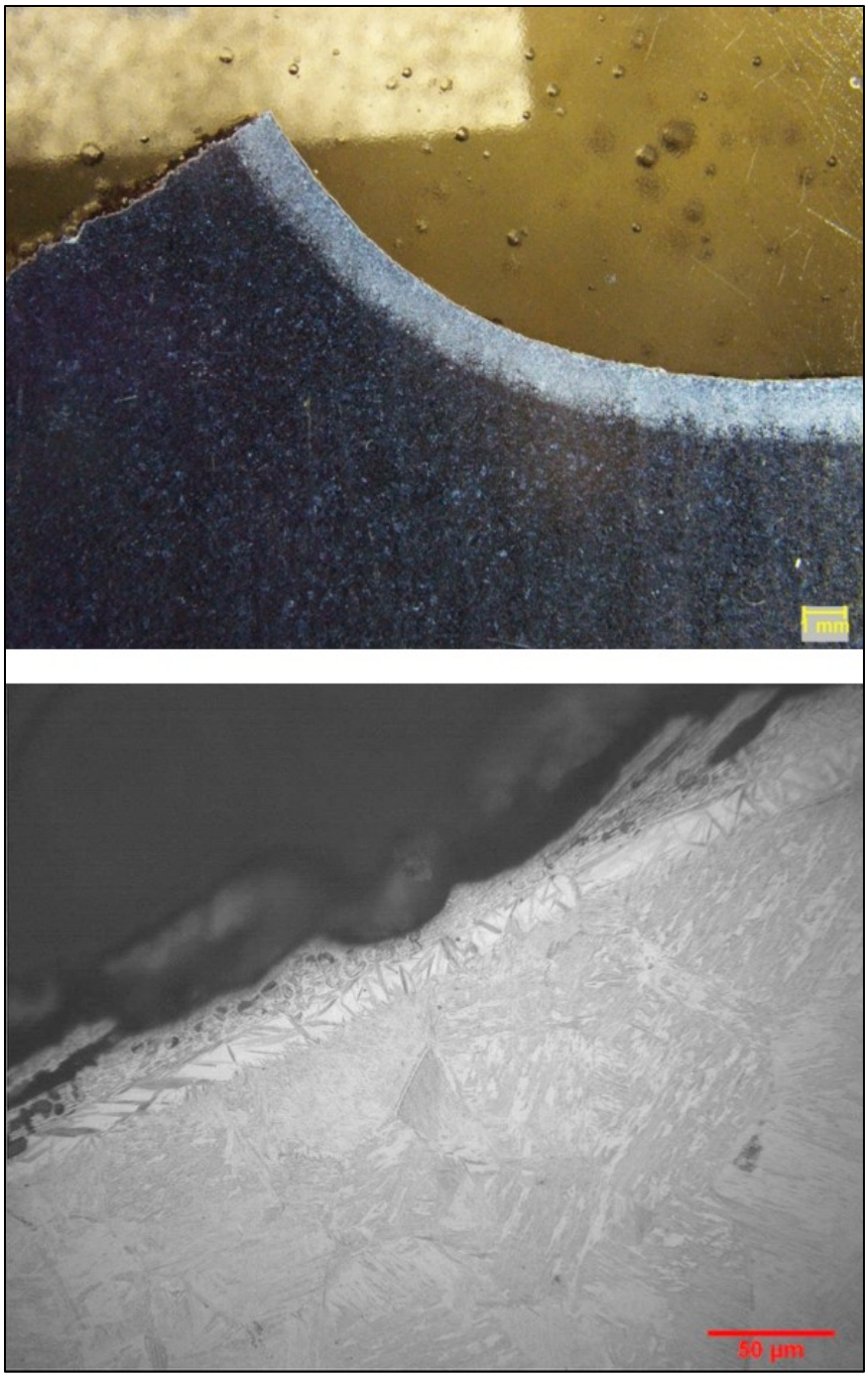

Fig. 214. Martensitic surface structure at the weld access hole radius of sample E.6-SW (fractured side). The martensitic layer appears as the lighter-etching band in the stereomicroscopic image at top. The bottom metallographic image shows the martensitic structure within the band.

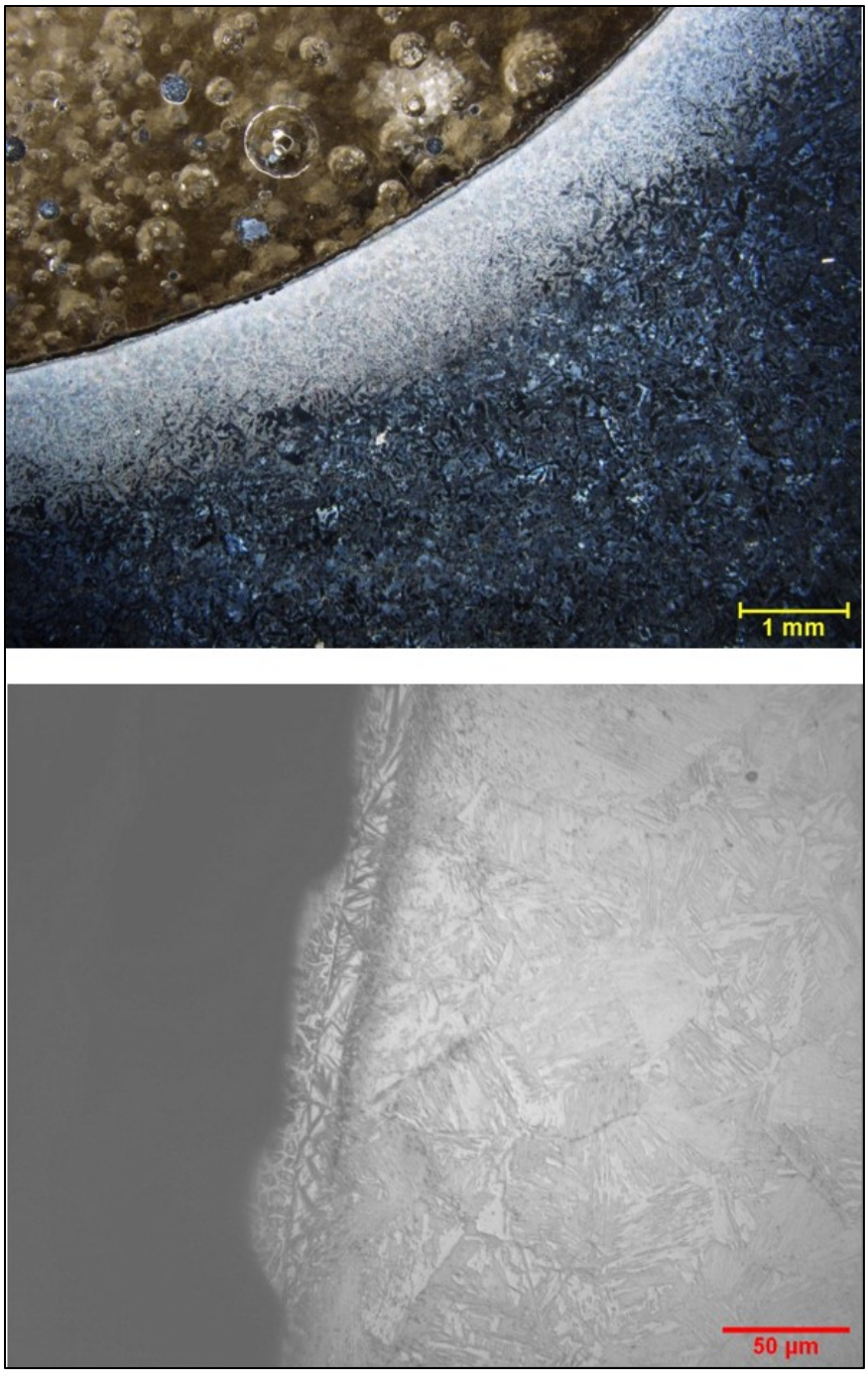

Fig. 215. Martensitic surface structure at the weld access hole radius of sample E.6-SE (intact side). The martensitic layer appears as the lighter-etching band in the stereomicroscopic image at top. The bottom metallographic image shows the martensitic structure within the band.

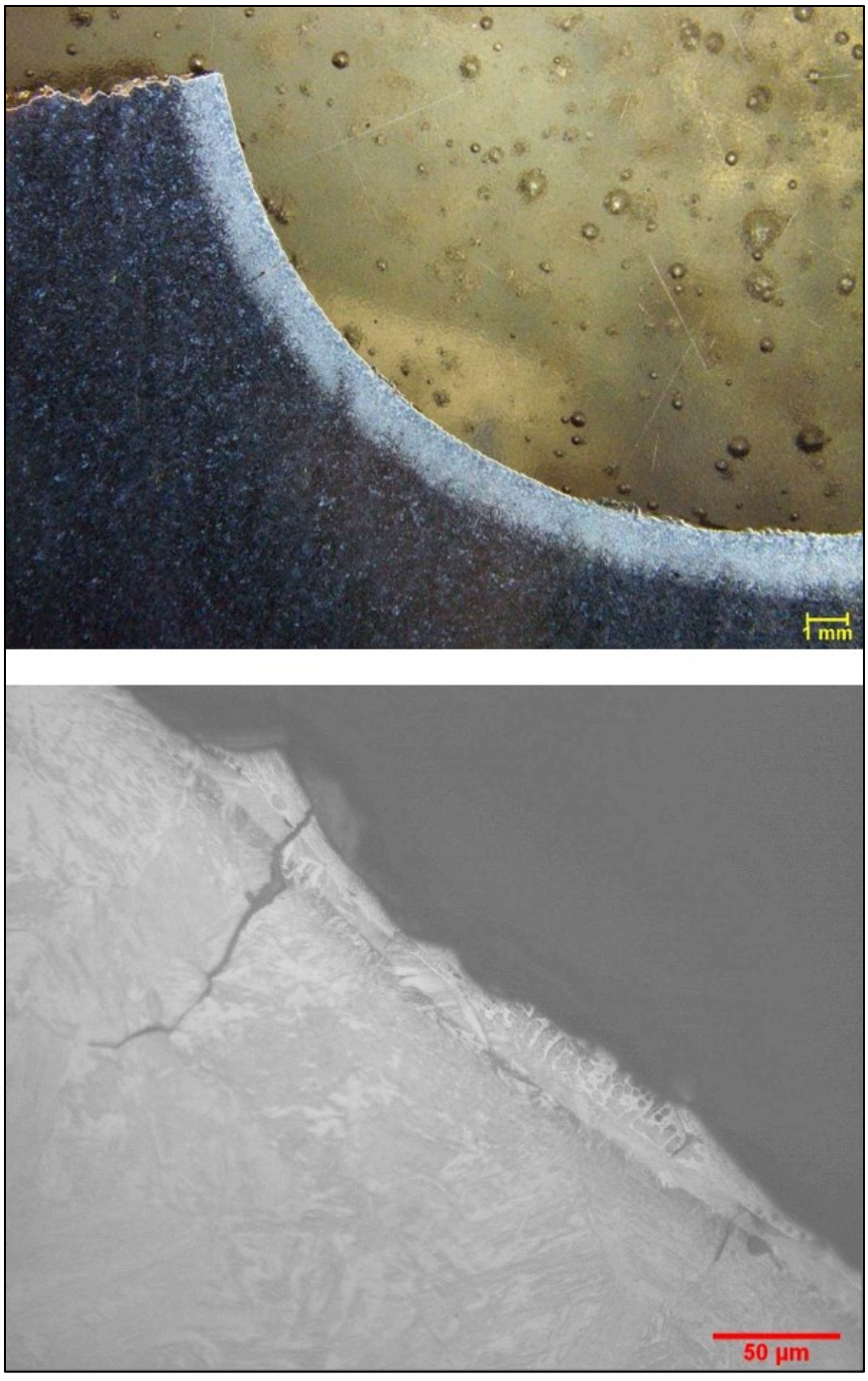

Fig. 216. Martensitic surface structure at the weld access hole radius of sample D.4-NW. The martensitic layer appears as the lighter-etching band in the stereomicroscopic image at top. The bottom metallographic image shows the martensitic structure within the band.

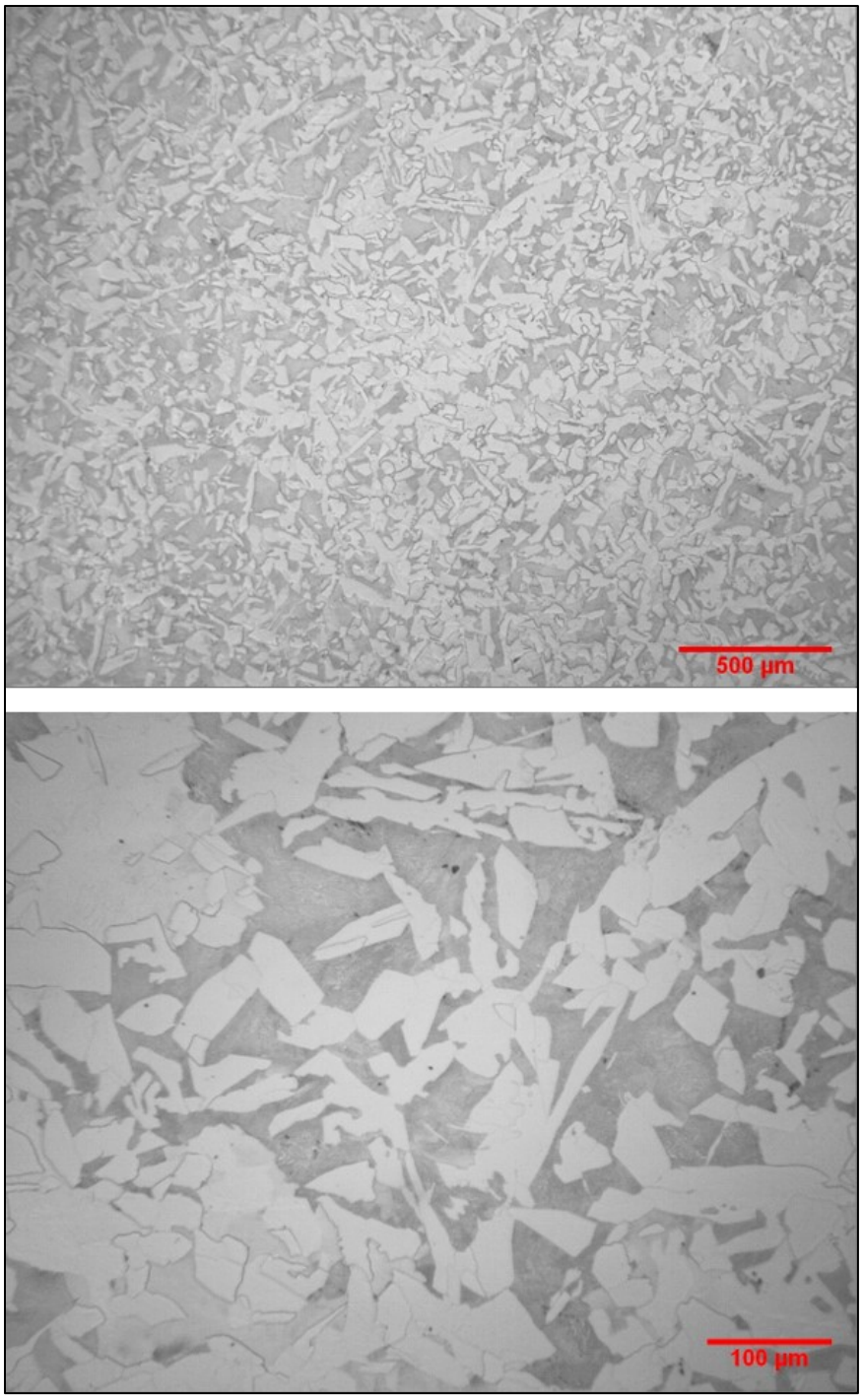

Fig. 217. Fine grained ferrite (bright) and pearlite (dark) grain structure of the flange steel plate of sample D.4-SW.

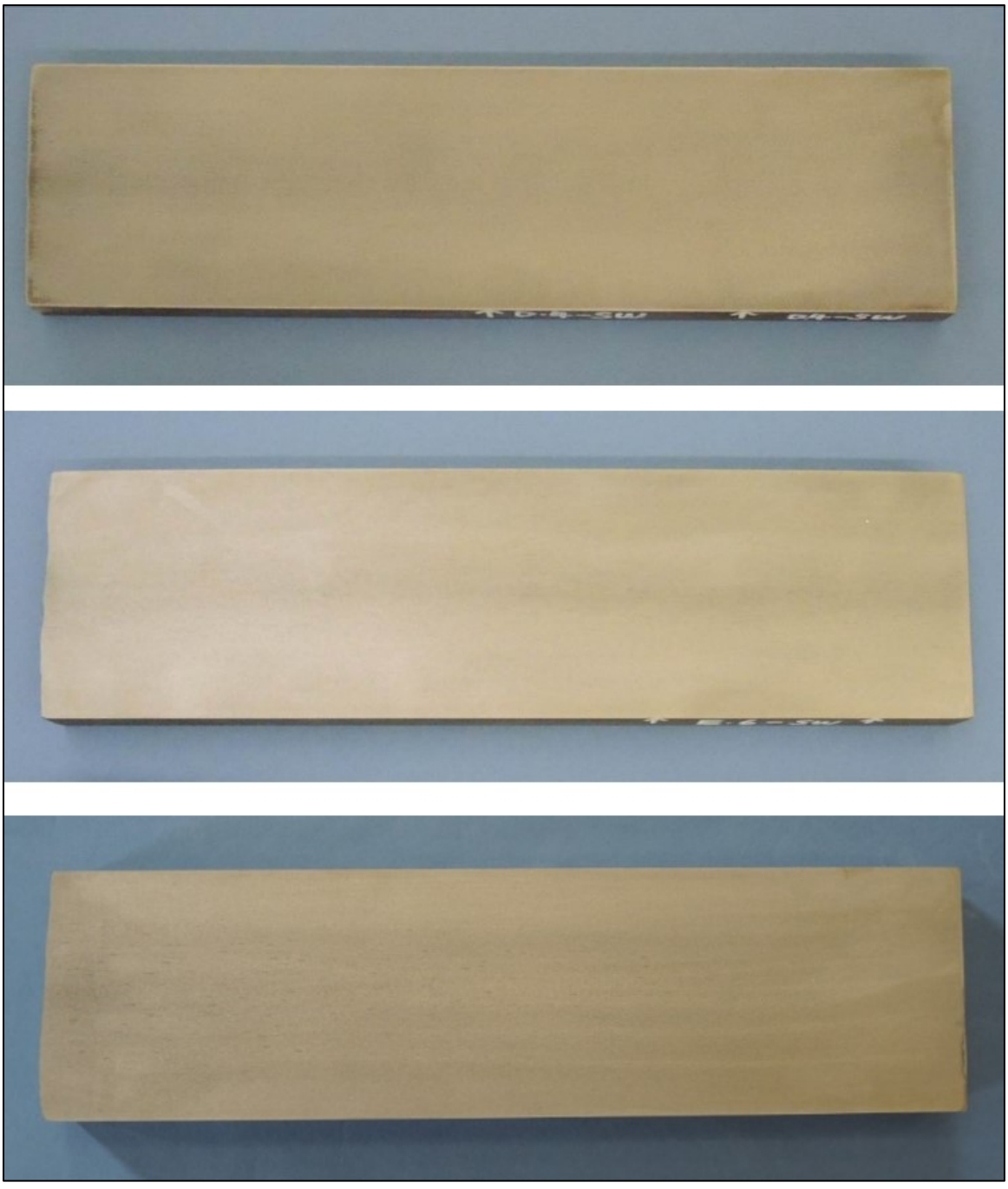

Fig. 218. Macro-sections from girder samples D.4-SW (top), E.6-SW (middle), and E.6-NW (bottom).

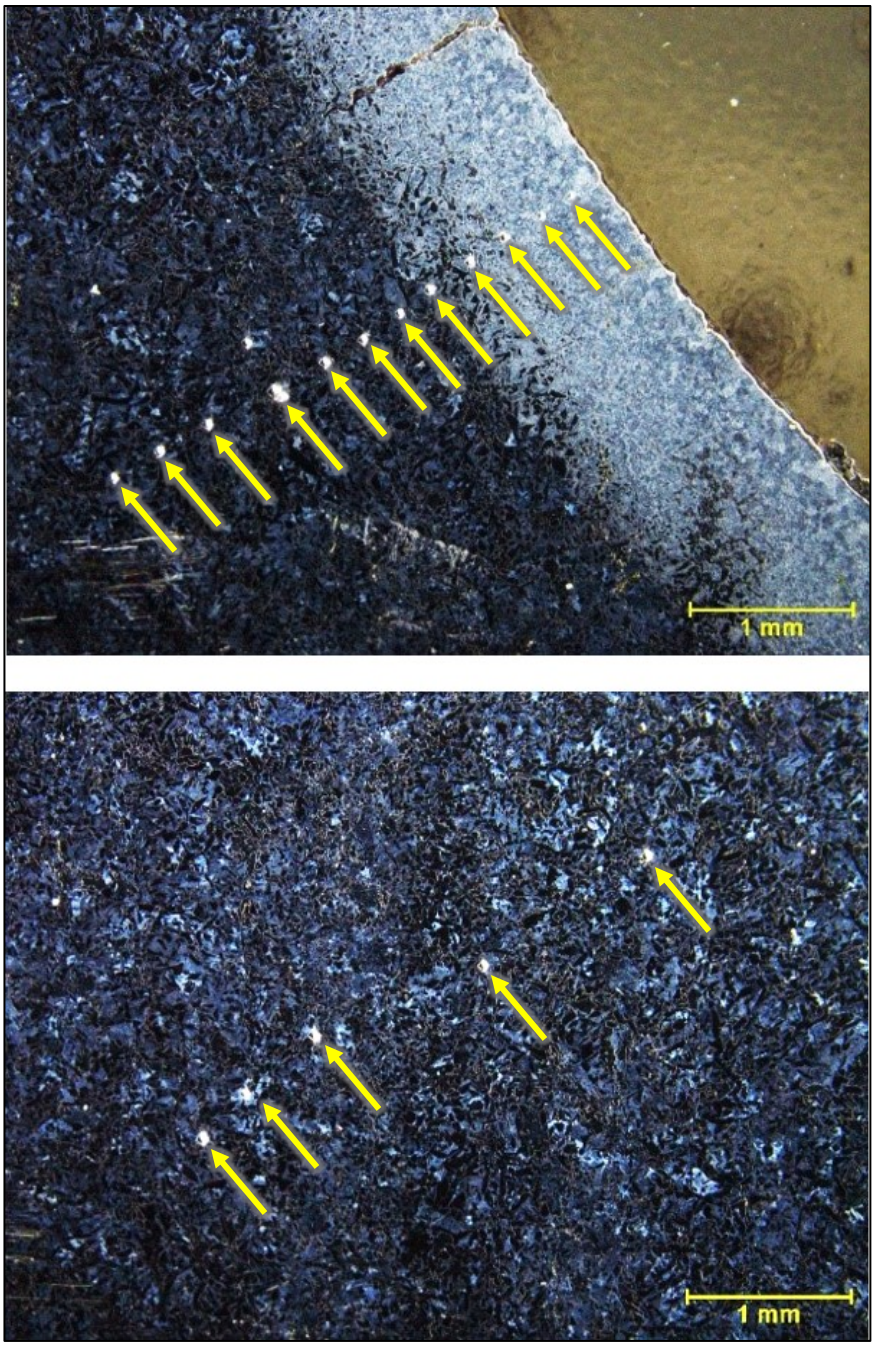

Fig. 219. Vickers microhardness measurement locations on specimen D.4-SW. Hardness traverse from the surface at the weld access hole radius to the center (top) and hardness measurements of the base material remote from the heat affected surface (bottom).

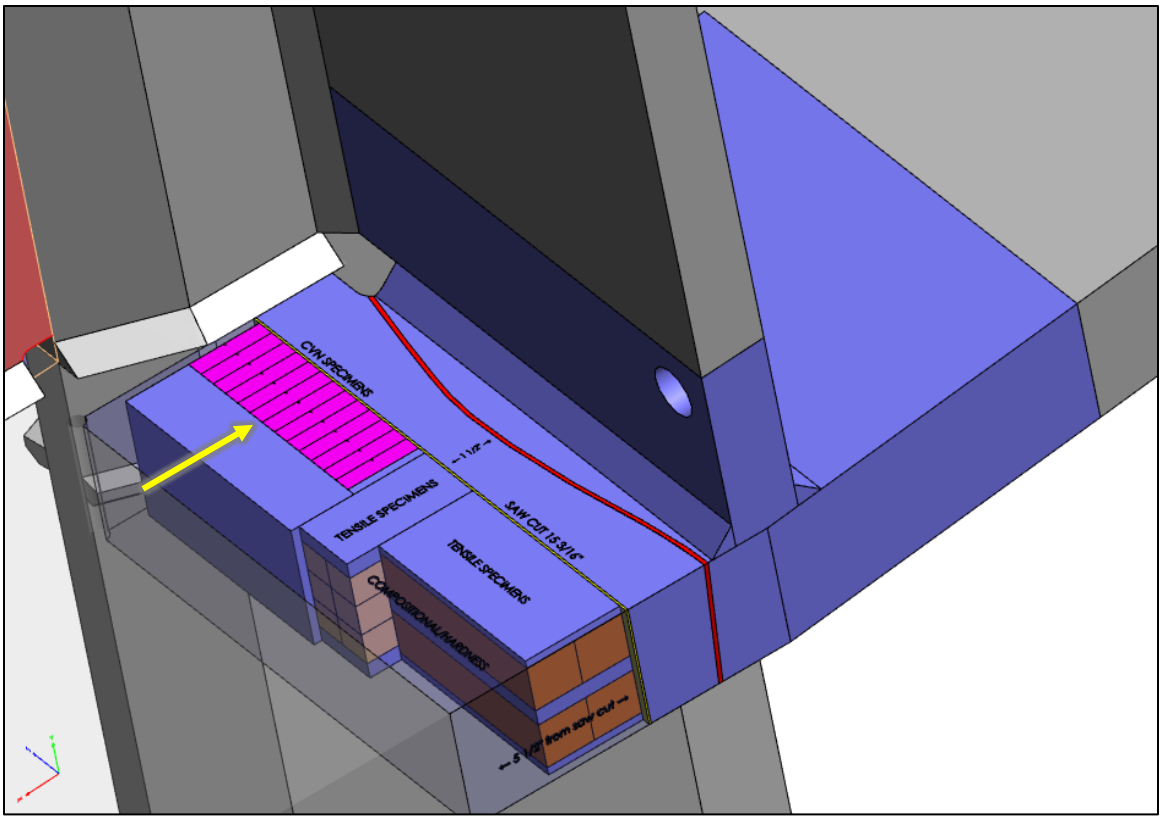

Fig. 220. CVN specimen removal location from the Fremont Street girder samples.

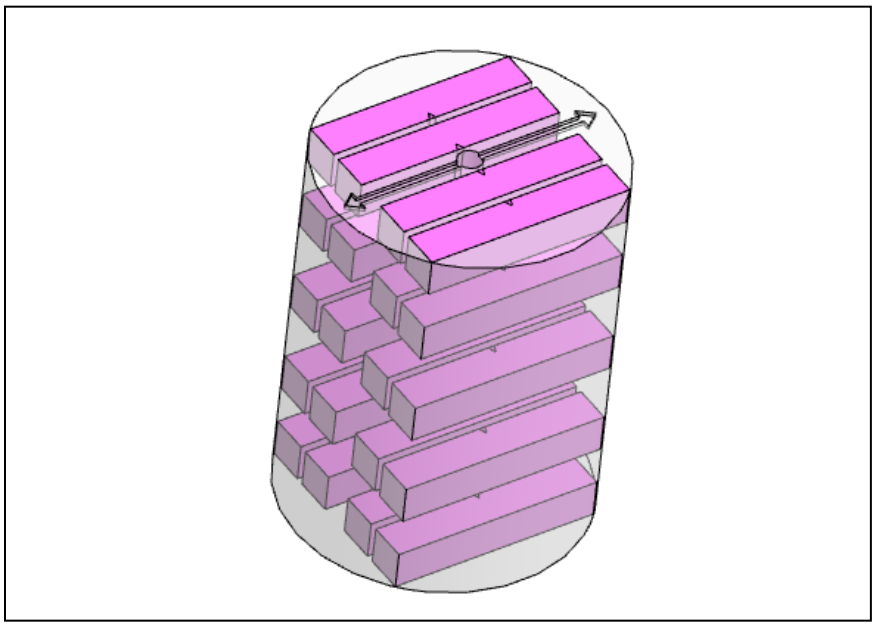

Fig. 221. CVN specimen removal location and orientation for the First Street core samples.

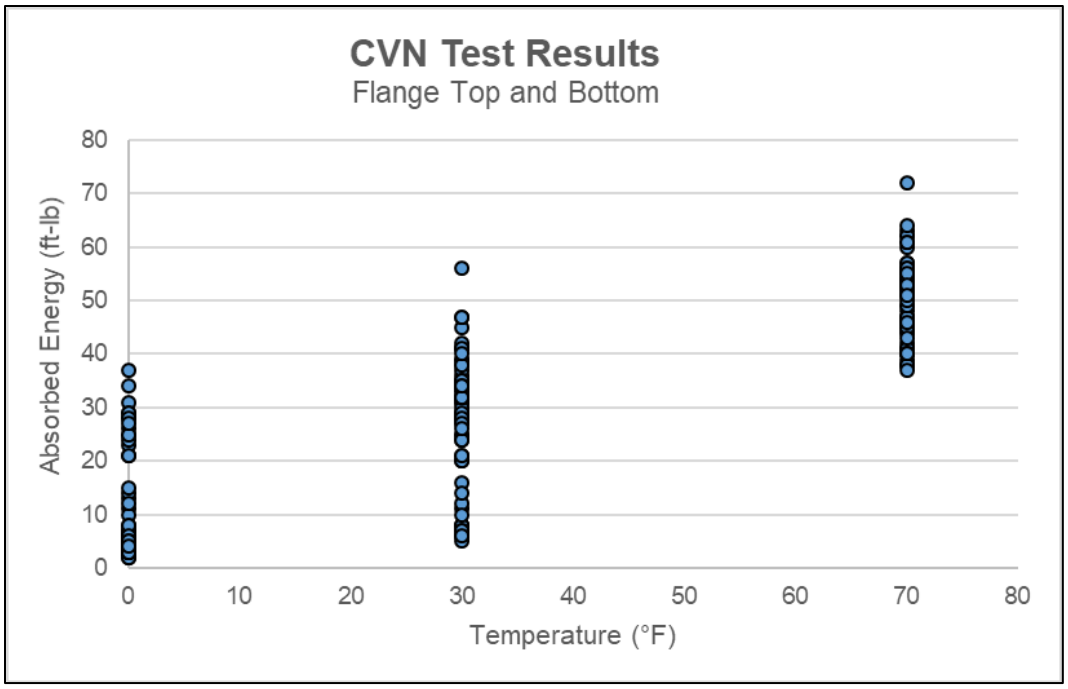

Fig. 222. Fremont street CVN test results from the flange surfaces (tops and bottoms).

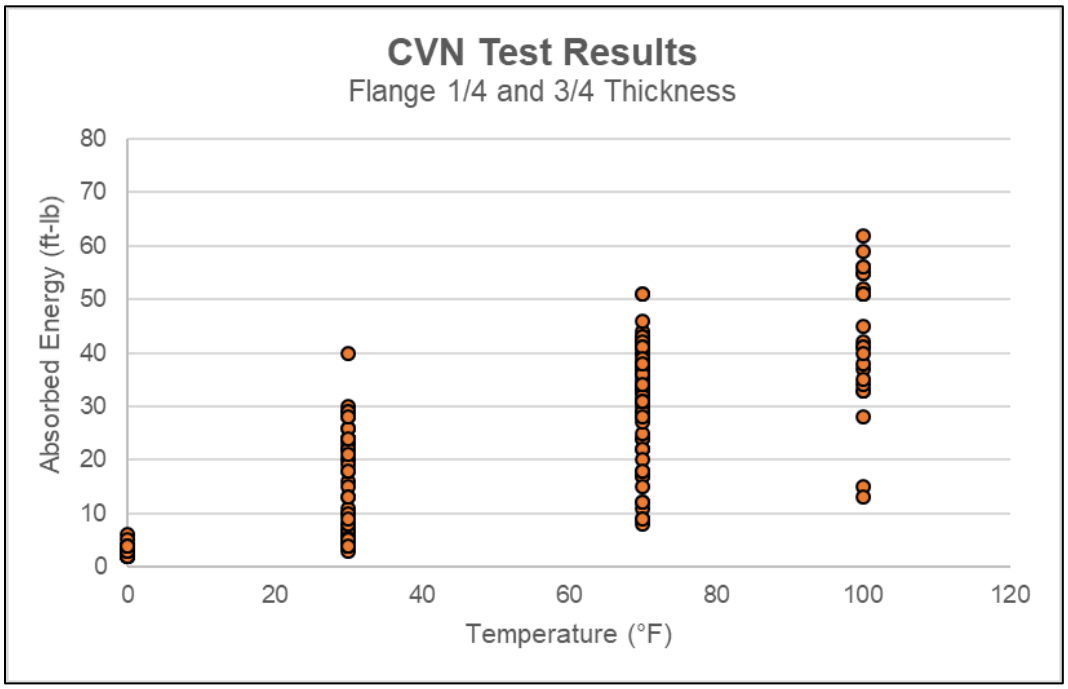

Fig. 223. Fremont street CVN test results from the flange 1/4 and 3/4 thicknesses.

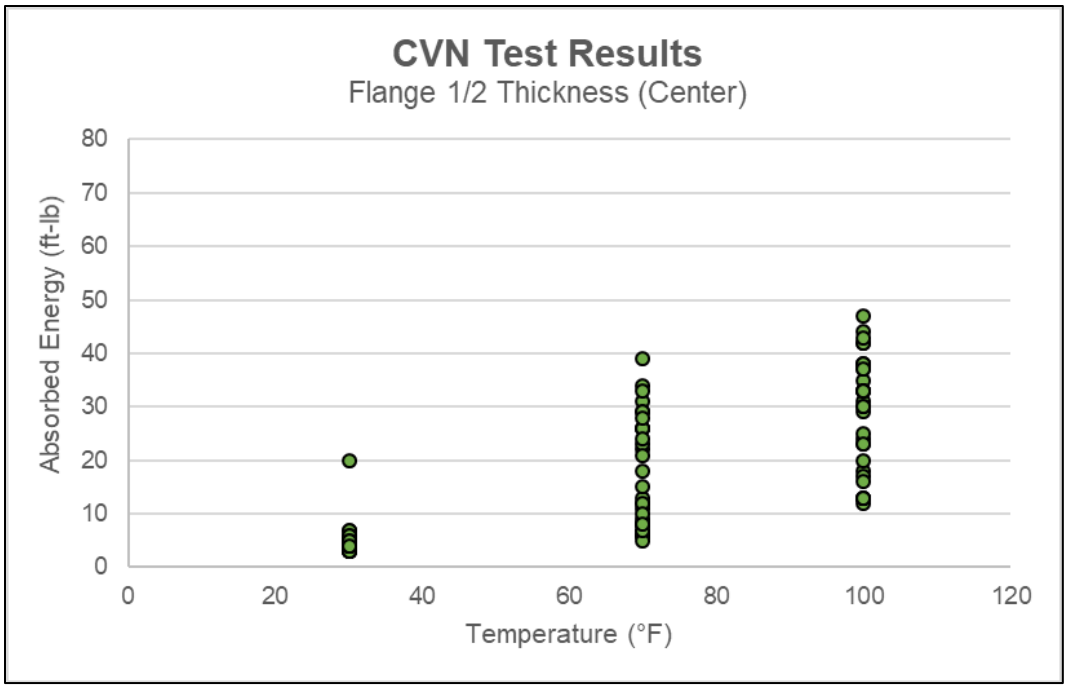

Fig. 224. Fremont street CVN test results from the flange mid-thickness (1/2 thicknesses).

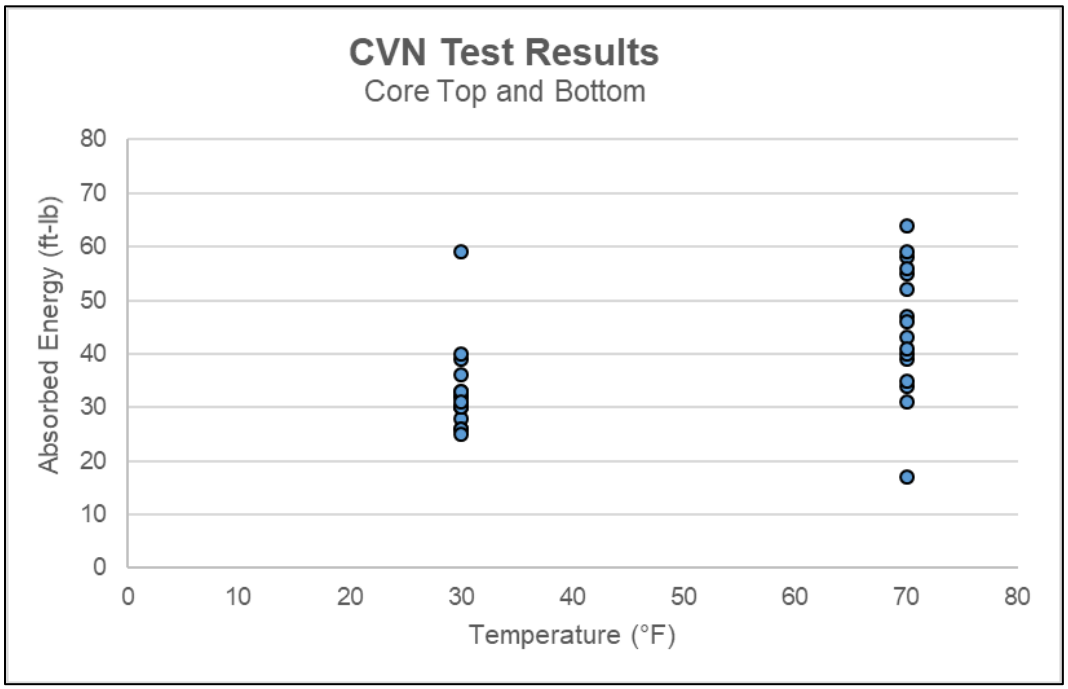

Fig. 225. CVN test results from the NE-18, NW-18, SE-18, and SW-18 core surfaces (tops and bottoms).

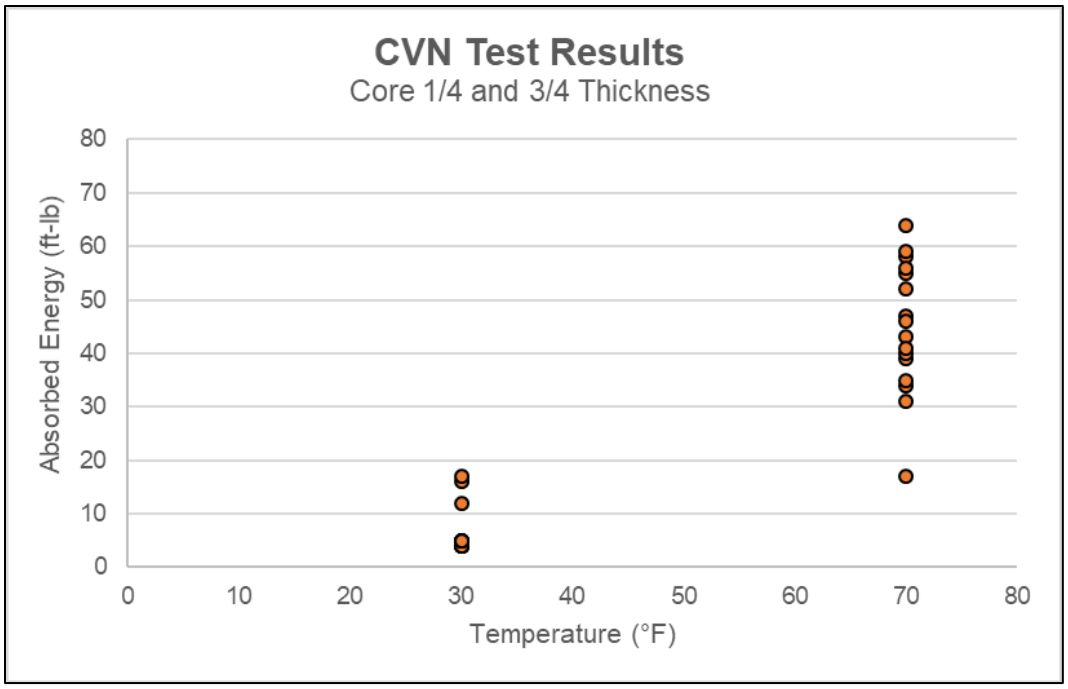

Fig. 226. CVN test results from the NE-18, NW-18, SE-18, SW-18 core sample 1/4 and 3/4 thicknesses.

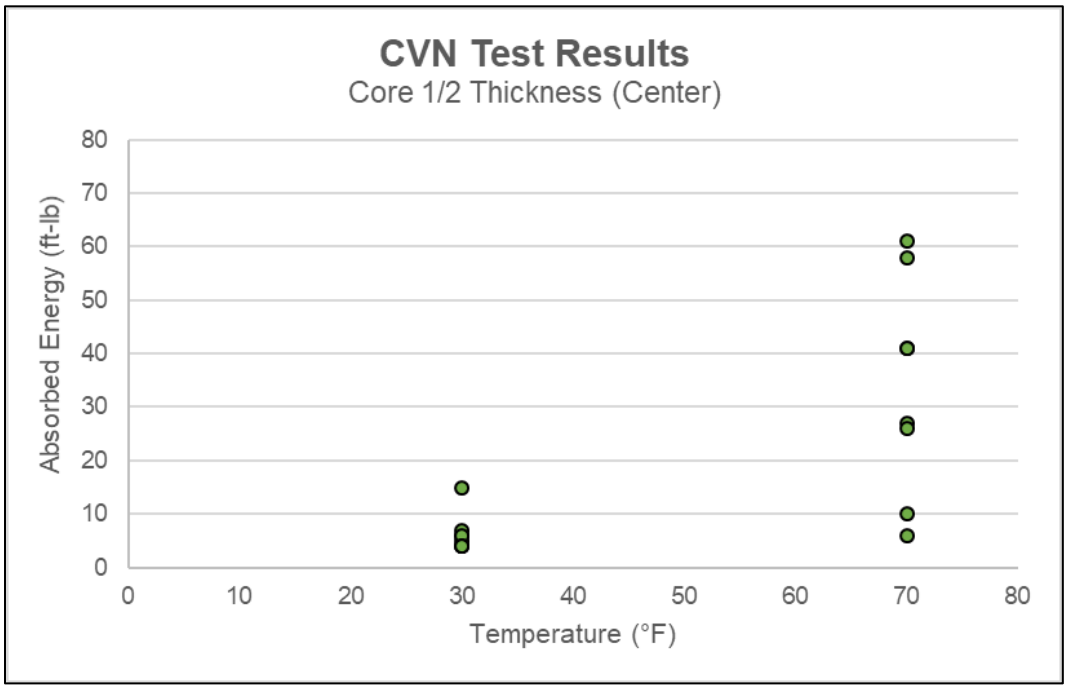

Fig. 227. CVN test results from the NE-18, NW-18, SE-18, SW-18 core sample mid-thickness (1/2 thickness).

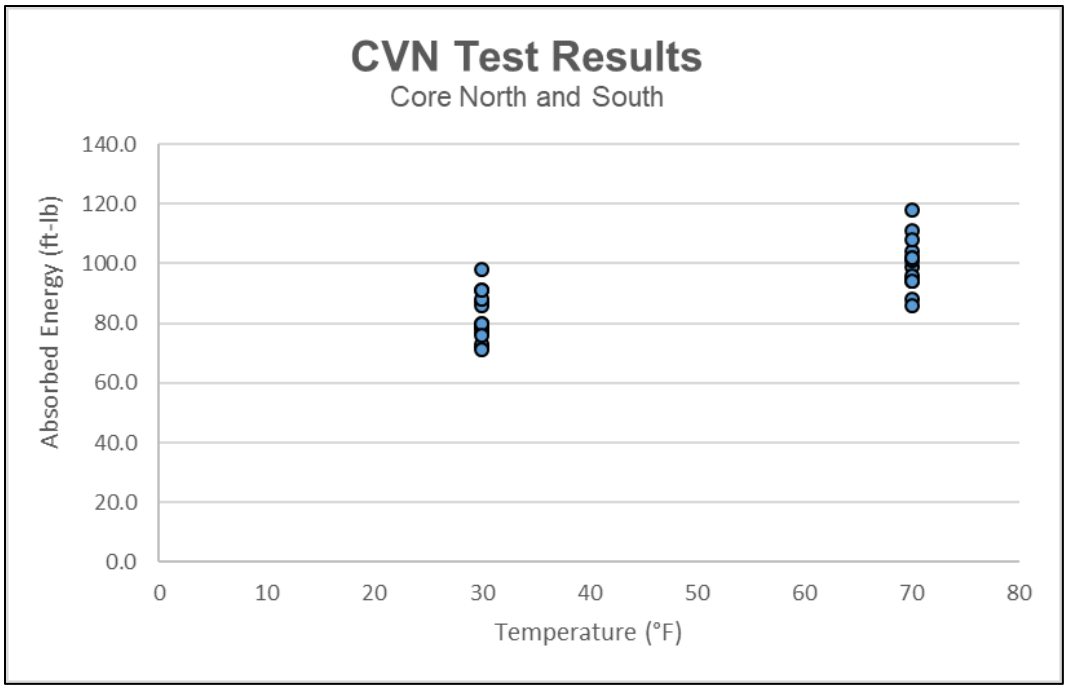

Fig. 228. CVN test results from the N-26, S-26, N-18, S-18 core surfaces (north-facing and south-facing surfaces).

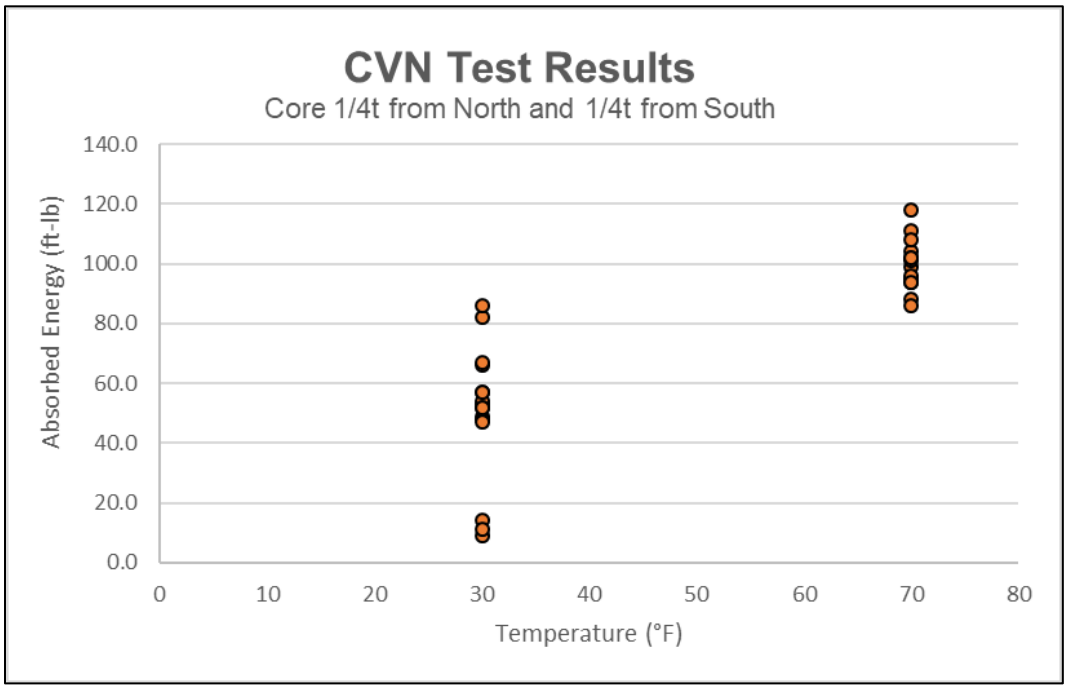

Fig. 229. CVN test results from the N-26, S-26, N-18, S-18 core sample 1/4 and 3/4 thicknesses.

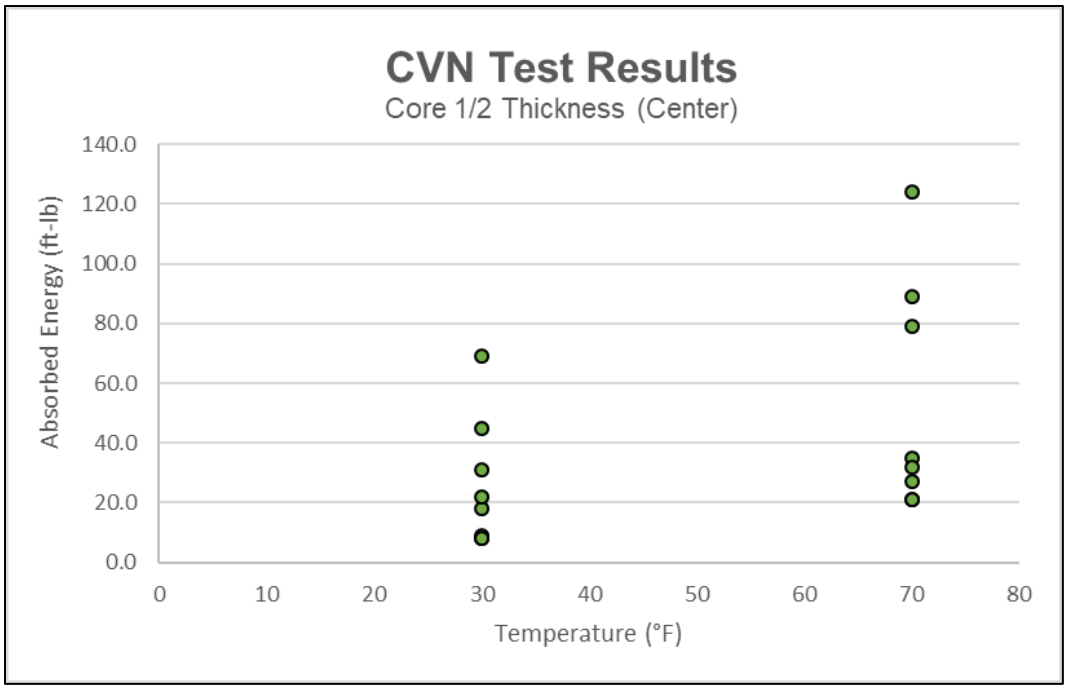

Fig. 230. CVN test results from the N-26, S-26, N-18, S-18 core sample mid-thickness (1/2 thickness).

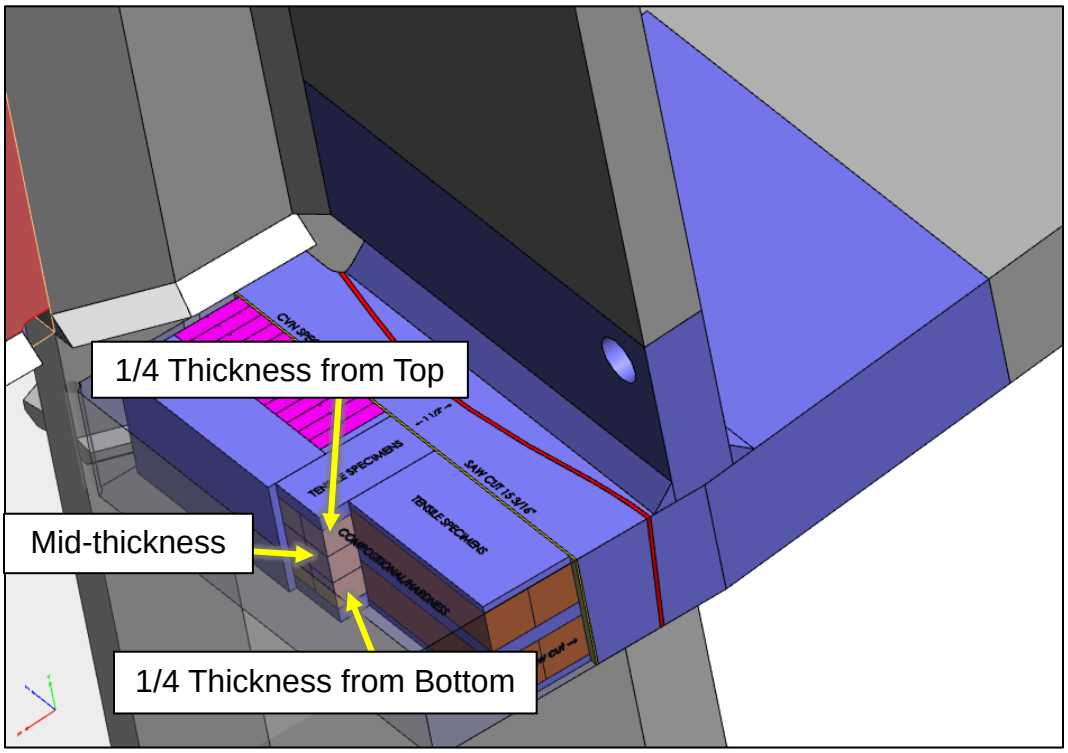

Fig. 231. Longitudinal tensile specimen removal location.

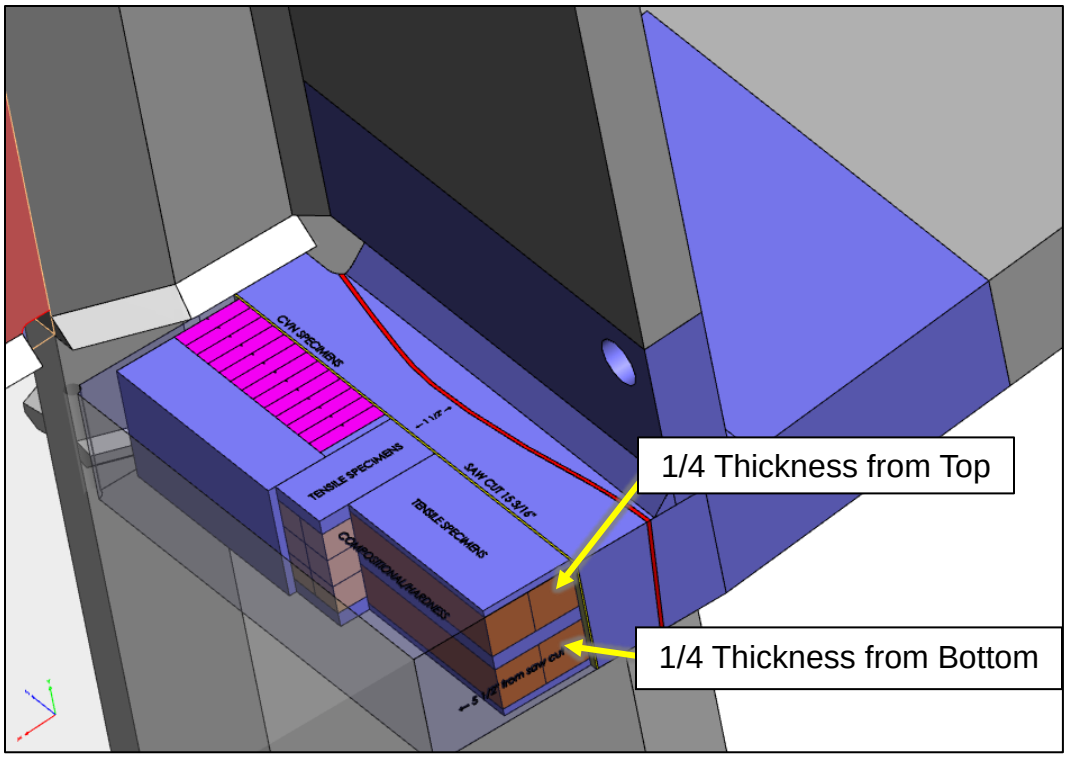

Fig. 232. Transverse tensile specimen removal location.

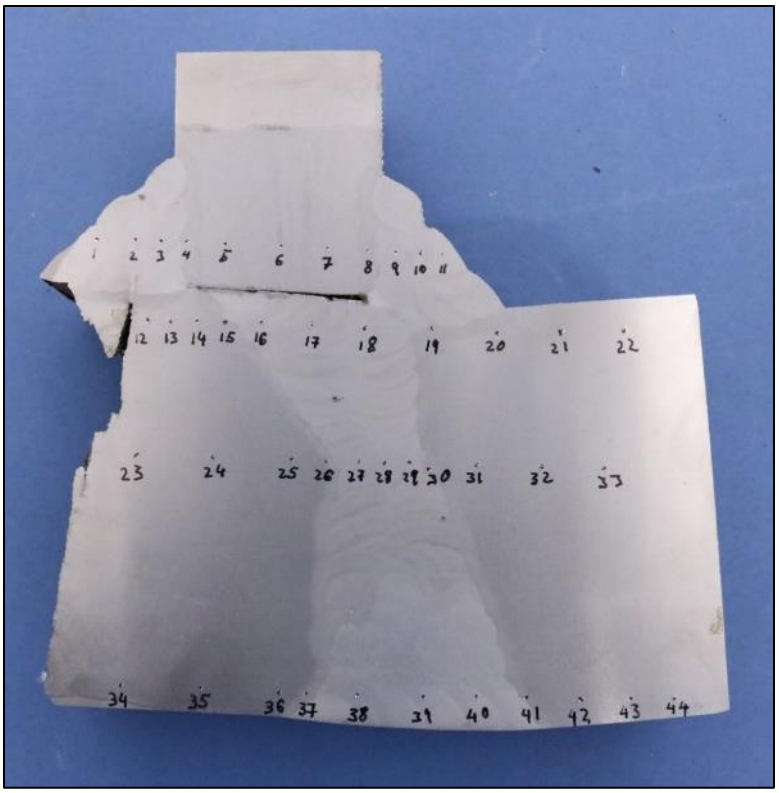

Fig. 233. Cross-section specimen from girder sample D.4-S showing the etched weld profiles and Rockwell B hardness measurement locations.

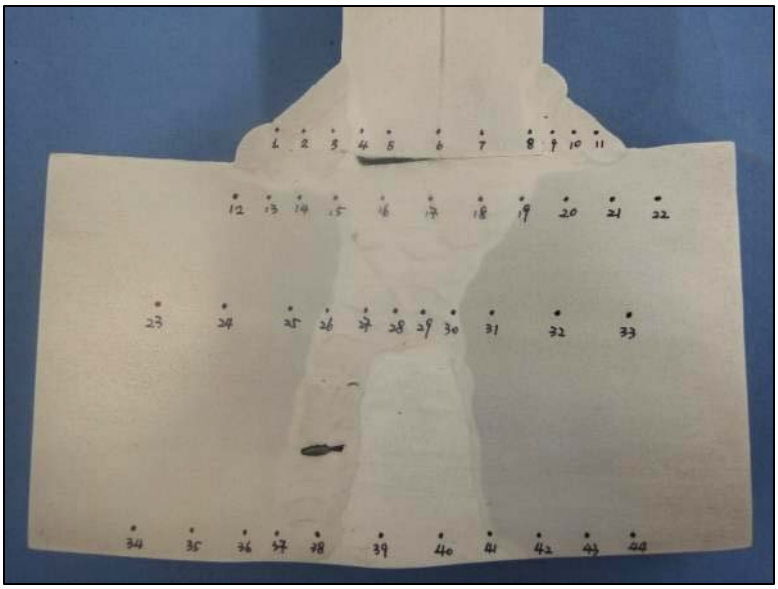

Fig. 234. Cross-section specimen from girder section E.6-N showing etched weld profiles and Rockwell B hardness measurement locations.

Fig. 235. Approximate surface hardness measurement cluster locations in the radii of the weld access holes.

Fig. 236. Approximate surface hardness measurement cluster locations on the flange sides.

APPENDIX D. METALLURGICAL EVALUATION SUPPLEMENTARY TABLES

Table 22 – Vickers Microhardness Measurements

ID	D.4 – NW (HV)	Distance of Indentations to the surface (mm)	D. 4 – SW (HV)	Distance of Indentations to the surface (mm)
1	456	0.14	406	0.24
2	493	0.31	413	0.46
3	339	0.48	306	0.73
4	390	0.66	235	0.98
5	351	0.87	260	1.27
6	285	1.04	280	1.50
7	244	1.28	235	1.79
8	173	1.48	189	2.05
9	231	1.67	216	2.40
10	221	1.88	215	2.89
11	221	2.12	220	3.23
12	221	2.42	213	3.55
13	194	9.45	176	13.13
14	214	9.75	183	14.33
15	191	9.97	164	15.45
16	216	10.30	149	16.01
17	206	10.63	167	16.41

Table 23 – Vickers Microhardness Measurements

ID	D.4 – NE Top[1] (HV)	Distance of Indentations to the surface (mm)	D.4 – NE Mid-thickness[2] (HV)	Distance of Indentations to the surface (mm)
1	413	0.08	394	0.07
2	412	0.27	468	0.30
3	284	0.41	352	0.51
4	301	0.58	331	0.80
5	253	0.76	235	1.06
6	278	0.94	211	1.36
7	334	1.11	197	1.63
8	246	1.29	203	1.95
9	221	1.46	194	2.25
10	209	1.60	200	2.54
11	192	1.75	206	2.85
12	194	1.98	188	3.16
13	186	13.76	185	13.90
14	169	14.02	193	14.21
15	167	14.14	210	14.54
16	174	14.40	213	14.83
17	204	14.74	183	15.18

1. The micro-section was prepared at the top surface of the girder sample.
2. The micro-section was prepared at the 1/2t (mid-thickness) of the girder sample.

Table 24 – Vickers Microhardness Measurements

ID	E.6 – SW Sample 1 (HV)	Distance of Indentations to the surface (mm)	E.6 – SW Sample 2 (HV)	Distance of Indentations to the surface (mm)
1	443	0.13	458	0.06
2	356	0.34	400	0.31
3	280	0.59	392	0.43
4	266	0.78	250	0.75
5	338	1.04	278	1.06
6	253	1.30	220	1.38
7	238	1.58	203	1.69
8	232	1.85	212	2.00
9	202	2.14	201	2.30
10	200	2.43	220	2.58
11	198	2.51	215	2.95
12	200	2.81	202	3.25
13	200	17.59	179	11.03
14	168	18.32	197	11.37
15	189	18.67	178	11.96
16	210	18.98	185	12.36
17	219	19.33	187	12.79

Table 25 – Vickers Microhardness Measurements

ID	E.6 – SE Top[1] (HV)	Distance of Indentations to the surface (mm)	E.6 – SE Mid-thickness[2] (HV)	Distance of Indentations to the surface (mm)
1	439	0.08	468	0.14
2	355	0.29	428	0.35
3	337	0.48	360	0.52
4	320	0.74	397	0.71
5	239	0.97	305	0.91
6	228	1.25	273	1.15
7	265	1.50	222	1.43
8	235	1.75	205	1.73
9	212	2.07	186	2.03
10	229	2.37	211	2.34
11	206	2.67	212	2.64
12	212	2.99	180	2.93
13	177	11.75	188	13.72
14	172	12.09	176	14.02
15	195	12.36	190	14.29
16	184	12.59	177	14.58
17	178	12.93	189	14.90

1. The micro-section was prepared at the top surface of the girder sample
2. The micro-section was prepared at the 1/2t (mid-thickness) of the girder sample.

Table 26 – Vickers Microhardness Measurements

ID	E.6 – NW (HV)	Distance of Indentations to the surface (mm)	E. 6 – NE (HV)	Distance of Indentations to the surface (mm)
1	421	0.14	473	0.11
2	526	0.37	395	0.26
3	425	0.60	389	0.39
4	325	0.84	318	0.61
5	384	1.15	304	0.88
6	248	1.41	294	1.08
7	244	1.72	261	1.33
8	235	2.05	242	1.55
9	219	2.39	237	1.86
10	220	2.74	214	2.12
11	206	3.11	205	2.44
12	206	3.52	241	2.77
13	216	16.21	182	12.15
14	206	16.60	198	12.48
15	245	16.97	193	12.75
16	215	17.25	230	13.09
17	208	17.59	219	13.39

Table 27 – CVN Test Results, Sample D.4-NW

Sample ID	Test Temperature (°F)	Absorbed Energy (ft-lb)	Lateral Expansion (in.)	Percent Shear
D41-Top-1	70	54.0	0.046	40
D41-Top-2	70	53.0	0.043	35
D41-Top-3	70	55.0	0.046	40
D41-Top-4	70	46.0	0.039	30
D41-Top-5	30	41.0	0.035	25
D41-Top-6	30	45.0	0.037	25
D41-Top-7	30	33.0	0.028	20
D41-Top-8	30	31.0	0.026	15
D41-Top-9	0	26.0	0.022	10
D41-Top-10	0	31.0	0.026	15
D41-Top-11	0	5.0	0.003	3
D41-Top-12	0	34.0	0.028	20
D43-1/4t-1	70	37.0	0.032	25
D43-1/4t-2	70	44.0	0.037	30
D43-1/4t-3	70	41.0	0.035	30
D43-1/4t-4	70	42.0	0.036	30
D43-1/4t-5	30	10.0	0.009	5
D43-1/4t-6	30	24.0	0.020	10
D43-1/4t-7	30	6.0	0.006	5
D43-1/4t-8	30	26.0	0.022	10
D43-1/4t-9	0	3.0	0.002	3
D43-1/4t-10	0	3.0	0.001	3
D43-1/4t-11	0	3.0	0.001	3
D43-1/4t-12	0	4.0	0.002	3
D45-1/2t-1	70	12.0	0.012	10
D45-1/2t-2	70	9.0	0.008	10
D45-1/2t-3	70	7.0	0.006	10
D45-1/2t-4	70	8.0	0.007	10
D45-1/2t-5	30	3.0	0.001	3
D45-1/2t-6	30	4.0	0.002	3
D45-1/2t-7	30	4.0	0.004	5
D45-1/2t-8	30	4.0	0.002	3
D45-1/2t-9	100	24.0	0.021	20
D45-1/2t-10	100	29.0	0.024	20
D45-1/2t-11	100	12.0	0.013	15
D45-1/2t-12	100	18.0	0.018	15

Table 27 Continued – CVN Test Results, Sample D.4-NW

Sample ID	Test Temperature (°F)	Absorbed Energy (ft-lb)	Lateral Expansion (in.)	Percent Shear
D47-3/4t-1	70	36	0.031	25
D47-3/4t-2	70	51	0.044	40
D47-3/4t-3	70	28	0.025	20
D47-3/4t-4	70	36	0.031	25
D47-3/4t-5	30	4	0.002	5
D47-3/4t-6	30	5	0.004	5
D47-3/4t-7	30	16	0.014	10
D47-3/4t-8	30	7	0.007	5
D47-3/4t-9	100	56	0.046	40
D47-3/4t-10	100	55	0.046	40
D47-3/4t-11	100	52	0.043	35
D47-3/4t-12	100	51	0.042	35
D49-Bot-1	70	42.0	0.035	25
D49-Bot-2	70	46.0	0.038	30
D49-Bot-3	70	55.0	0.047	40
D49-Bot-4	70	45.0	0.037	30
D49-Bot-5	30	39.0	0.032	20
D49-Bot-6	30	36.0	0.031	20
D49-Bot-7	30	32.0	0.027	15
D49-Bot-8	30	8.0	0.009	5
D49-Bot-9	0	13.0	0.012	5
D49-Bot-10	0	5.0	0.004	3
D49-Bot-11	0	5.0	0.007	3
D49-Bot-12	0	29.0	0.024	15

Table 28 – CVN Test Results, Sample D.4-NE

Sample ID	Test Temperature (°F)	Absorbed Energy (ft-lb)	Lateral Expansion (in.)	Percent Shear
D41-Top-1	70	62.0	0.051	40
D41-Top-2	70	51.0	0.041	30
D41-Top-3	70	63.0	0.051	40
D41-Top-4	70	72.0	0.056	50
D41-Top-5	30	29.0	0.024	15
D41-Top-6	30	27.0	0.023	15
D41-Top-7	30	47.0	0.040	25
D41-Top-8	30	38.0	0.032	20
D41-Top-9	0	5.0	0.005	3
D41-Top-10	0	6.0	0.005	5
D41-Top-11	0	5.0	0.004	3
D41-Top-12	0	5.0	0.004	3
D43-1/4t-1	70	24.0	0.021	20
D43-1/4t-2	70	34.0	0.029	25
D43-1/4t-3	70	11.0	0.013	15
D43-1/4t-4	70	33.0	0.028	20
D43-1/4t-5	30	5.0	0.004	5
D43-1/4t-6	30	18.0	0.016	10
D43-1/4t-7	30	23.0	0.019	10
D43-1/4t-8	30	4.0	0.002	5
D43-1/4t-9	0	3.0	0.002	3
D43-1/4t-10	0	3.0	0.002	3
D43-1/4t-11	0	2.0	0.001	3
D43-1/4t-12	0	4.0	0.003	3
D45-1/2t-1	70	11.0	0.011	15
D45-1/2t-2	70	31.0	0.026	20
D45-1/2t-3	70	6.0	0.007	10
D45-1/2t-4	70	26.0	0.021	20
D45-1/2t-5	30	7.0	0.006	5
D45-1/2t-6	30	7.0	0.007	5
D45-1/2t-7	30	6.0	0.005	5
D45-1/2t-8	30	5.0	0.004	5
D45-1/2t-9	100	35.0	0.031	25
D45-1/2t-10	100	33.0	0.030	25
D45-1/2t-11	100	38.0	0.033	30
D45-1/2t-12	100	47.0	0.041	40

Table 28 Continued – CVN Test Results, Sample D.4-NE

Sample ID	Test Temperature (°F)	Absorbed Energy (ft-lb)	Lateral Expansion (in.)	Percent Shear
D47-3/4t-1	70	9.0	0.009	5
D47-3/4t-2	70	43.0	0.038	25
D47-3/4t-3	70	38.0	0.033	25
D47-3/4t-4	70	34.0	0.029	20
D47-3/4t-5	30	4.0	0.003	5
D47-3/4t-6	30	20.0	0.017	10
D47-3/4t-7	30	4.0	0.003	5
D47-3/4t-8	30	30.0	0.026	15
D47-3/4t-9	0	3.0	0.002	0
D47-3/4t-10	0	4.0	0.003	3
D47-3/4t-11	0	3.0	0.002	3
D47-3/4t-12	0	4.0	0.003	3
D49-Bot-1	70	44.0	0.038	30
D49-Bot-2	70	39.0	0.034	25
D49-Bot-3	70	38.0	0.033	25
D49-Bot-4	70	51.0	0.043	35
D49-Bot-5	30	39.0	0.033	20
D49-Bot-6	30	40.0	0.035	20
D49-Bot-7	30	28.0	0.024	15
D49-Bot-8	30	6.0	0.006	5
D49-Bot-9	0	25.0	0.021	10
D49-Bot-10	0	6.0	0.005	3
D49-Bot-11	0	6.0	0.005	3
D49-Bot-12	0	21.0	0.019	10

Table 29 – CVN Test Results, Sample D.4-SW

Sample ID	Test Temperature (°F)	Absorbed Energy (ft-lb)	Lateral Expansion (in.)	Percent Shear
D41-Top-1	70	53.0	0.043	40
D41-Top-2	70	53.0	0.044	40
D41-Top-3	70	47.0	0.039	35
D41-Top-4	70	56.0	0.045	50
D41-Top-5	30	37.0	0.030	30
D41-Top-6	30	56.0	0.045	35
D41-Top-7	30	35.0	0.028	25
D41-Top-8	30	33.0	0.028	25
D41-Top-9	0	23.0	0.019	10
D41-Top-10	0	28.0	0.023	25
D41-Top-11	0	4.0	0.004	3
D41-Top-12	0	11.0	0.010	10
D43-1/4t-1	70	33.0	0.027	20
D43-1/4t-2	70	40.0	0.034	25
D43-1/4t-3	70	37.0	0.030	20
D43-1/4t-4	70	42.0	0.034	25
D43-1/4t-5	30	15.0	0.013	5
D43-1/4t-6	30	4.0	0.002	5
D43-1/4t-7	30	5.0	0.003	5
D43-1/4t-8	30	5.0	0.003	5
D43-1/4t-9	100	45.0	0.034	35
D43-1/4t-10	100	42.0	0.033	30
D43-1/4t-11	100	55.0	0.043	40
D43-1/4t-12	100	51.0	0.040	40
D45-1/2t-1	70	13.0	0.010	10
D45-1/2t-2	70	12.0	0.010	10
D45-1/2t-3	70	8.0	0.007	15
D45-1/2t-4	70	26.0	0.020	25
D45-1/2t-5	30	5.0	0.003	10
D45-1/2t-6	30	4.0	0.003	5
D45-1/2t-7	30	3.0	0.001	3
D45-1/2t-8	30	3.0	0.001	3
D45-1/2t-9	100	13.0	0.012	15
D45-1/2t-10	100	23.0	0.020	25
D45-1/2t-11	100	20.0	0.016	25
D45-1/2t-12	100	17.0	0.015	20

Table 29 Continued – CVN Test Results, Sample D.4-SW

Sample ID	Test Temperature (°F)	Absorbed Energy (ft-lb)	Lateral Expansion (in.)	Percent Shear
D47-3/4t-1	70	33.0	0.028	25
D47-3/4t-2	70	46.0	0.037	35
D47-3/4t-3	70	22.0	0.018	15
D47-3/4t-4	70	34.0	0.027	25
D47-3/4t-5	30	10.0	0.008	10
D47-3/4t-6	30	6.0	0.004	10
D47-3/4t-7	30	20.0	0.016	15
D47-3/4t-8	30	22.0	0.018	15
D47-3/4t-9	0	3.0	0.000	3
D47-3/4t-10	0	3.0	0.001	3
D47-3/4t-11	0	6.0	0.004	5
D47-3/4t-12	0	3.0	0.001	3
D49-Bot-1	70	41.0	0.033	30
D49-Bot-2	70	62.0	0.051	45
D49-Bot-3	70	57.0	0.046	40
D49-Bot-4	70	47.0	0.036	35
D49-Bot-5	30	29.0	0.024	20
D49-Bot-6	30	25.0	0.021	15
D49-Bot-7	30	32.0	0.027	20
D49-Bot-8	30	25.0	0.020	15
D49-Bot-9	0	7.0	0.004	10
D49-Bot-10	0	3.0	0.000	5
D49-Bot-11	0	4.0	0.002	3
D49-Bot-12	0	3.0	0.001	3

Table 30 – CVN Test Results, Sample D.4-SE

Sample ID	Test Temperature (°F)	Absorbed Energy (ft-lb)	Lateral Expansion (in.)	Percent Shear
D41-Top-1	70	38	0.032	25
D41-Top-2	70	60	0.051	40
D41-Top-3	70	61	0.052	40
D41-Top-4	70	45	0.038	25
D41-Top-5	30	28	0.024	15
D41-Top-6	30	31	0.027	15
D41-Top-7	30	8	0.008	8
D41-Top-8	30	35	0.030	20
D41-Top-9	0	3	0.002	3
D41-Top-10	0	4	0.003	3
D41-Top-11	0	3	0.002	3
D41-Top-12	0	24	0.020	10
D43-1/4t-1	70	31	0.027	20
D43-1/4t-2	70	42	0.035	25
D43-1/4t-3	70	51	0.043	35
D43-1/4t-4	70	31	0.026	20
D43-1/4t-5	30	19	0.017	10
D43-1/4t-6	30	6	0.006	5
D43-1/4t-7	30	18	0.016	10
D43-1/4t-8	30	7	0.006	5
D43-1/4t-9	0	3	0.002	3
D43-1/4t-10	0	3	0.002	3
D43-1/4t-11	0	3	0.002	3
D43-1/4t-12	0	2	0.003	3
D45-1/2t-1	70	15	0.016	10
D45-1/2t-2	70	8	0.009	8
D45-1/2t-3	70	26	0.023	15
D45-1/2t-4	70	22	0.021	15
D45-1/2t-5	30	5	0.005	5
D45-1/2t-6	30	5	0.005	5
D45-1/2t-7	30	4	0.004	3
D45-1/2t-8	30	5	0.004	5
D45-1/2t-9	100	33	0.031	25
D45-1/2t-10	100	16	0.019	20
D45-1/2t-11	100	13	0.015	20
D45-1/2t-12	100	38	0.034	30

Table 30 Continued – CVN Test Results, Sample D.4-SE

Sample ID	Test Temperature (°F)	Absorbed Energy (ft-lb)	Lateral Expansion (in.)	Percent Shear
D47-3/4t-1	70	29	0.026	20
D47-3/4t-2	70	35	0.032	20
D47-3/4t-3	70	43	0.037	25
D47-3/4t-4	70	17	0.016	10
D47-3/4t-5	30	4	0.003	5
D47-3/4t-6	30	4	0.004	5
D47-3/4t-7	30	4	0.003	5
D47-3/4t-8	30	4	0.005	5
D47-3/4t-9	100	15	0.018	20
D47-3/4t-10	100	59	0.050	40
D47-3/4t-11	100	37	0.033	25
D47-3/4t-12	100	62	0.051	40
D49-Bot-1	70	54	0.047	35
D49-Bot-2	70	41	0.036	30
D49-Bot-3	70	48	0.042	30
D49-Bot-4	70	40	0.035	25
D49-Bot-5	30	8	0.008	5
D49-Bot-6	30	20	0.019	10
D49-Bot-7	30	30	0.026	15
D49-Bot-8	30	21	0.019	10
D49-Bot-9	0	3	0.002	3
D49-Bot-10	0	25	0.022	10
D49-Bot-11	0	37	0.031	20
D49-Bot-12	0	2	0.001	3

Table 31 – CVN Test Results, Sample E.6-NW

Sample ID	Test Temperature (°F)	Absorbed Energy (ft-lb)	Lateral Expansion (in.)	Percent Shear
E61-Top-1	70	54.0	0.044	40
E61-Top-2	70	57.0	0.049	40
E61-Top-3	70	56.0	0.048	40
E61-Top-4	70	46.0	0.037	30
E61-Top-5	30	10.0	0.009	10
E61-Top-6	30	32.0	0.027	20
E61-Top-7	30	34.0	0.028	20
E61-Top-8	30	7.0	0.006	10
E61-Top-9	0	5.0	0.005	5
E61-Top-10	0	8.0	0.007	5
E61-Top-11	0	4.0	0.004	5
E61-Top-12	0	2.0	0.002	5
E63-1/4t-1	70	38.0	0.032	30
E63-1/4t-2	70	31.0	0.027	20
E63-1/4t-3	70	8.0	0.008	15
E63-1/4t-4	70	12.0	0.012	15
E63-1/4t-5	30	29.0	0.025	15
E63-1/4t-6	30	4.0	0.002	5
E63-1/4t-7	30	22.0	0.019	15
E63-1/4t-8	30	26.0	0.022	15
E63-1/4t-9	0	3.0	0.002	3
E63-1/4t-10	0	3.0	0.002	3
E63-1/4t-11	0	3.0	0.002	3
E63-1/4t-12	0	2.0	0.001	3
E65-1/2t-1	70	18.0	0.015	15
E65-1/2t-2	70	8.0	0.007	10
E65-1/2t-3	70	34.0	0.028	30
E65-1/2t-4	70	21.0	0.018	15
E65-1/2t-5	30	4.0	0.002	3
E65-1/2t-6	30	5.0	0.004	3
E65-1/2t-7	30	4.0	0.002	3
E65-1/2t-8	30	4.0	0.002	5
E65-1/2t-9	100	30.0	0.027	30
E65-1/2t-10	100	43.0	0.036	40
E65-1/2t-11	100	33.0	0.027	30
E65-1/2t-12	100	33.0	0.027	30

Table 31 Continued – CVN Test Results, Sample E.6-NW

Sample ID	Test Temperature (°F)	Absorbed Energy (ft-lb)	Lateral Expansion (in.)	Percent Shear
E67-3/4t-1	70	28.0	0.024	20
E67-3/4t-2	70	36.0	0.031	30
E67-3/4t-3	70	18.0	0.017	15
E67-3/4t-4	70	41.0	0.036	30
E67-3/4t-5	30	9.0	0.008	5
E67-3/4t-6	30	40.0	0.034	30
E67-3/4t-7	30	21.0	0.019	10
E67-3/4t-8	30	5.0	0.004	5
E67-3/4t-9	0	3.0	0.001	3
E67-3/4t-10	0	3.0	0.002	3
E67-3/4t-11	0	4.0	0.003	3
E67-3/4t-12	0	4.0	0.003	3
E69-Bot-1	70	56.0	0.046	40
E69-Bot-2	70	55.0	0.045	40
E69-Bot-3	70	41.0	0.035	30
E69-Bot-4	70	40.0	0.033	30
E69-Bot-5	30	35.0	0.029	20
E69-Bot-6	30	7.0	0.006	10
E69-Bot-7	30	34.0	0.029	20
E69-Bot-8	30	5.0	0.004	8
E69-Bot-9	0	5.0	0.004	3
E69-Bot-10	0	3.0	0.002	5
E69-Bot-11	0	5.0	0.003	3
E69-Bot-12	0	6.0	0.006	3

Table 32 – CVN Test Results, Sample E.6-NE

Sample ID	Test Temperature (°F)	Absorbed Energy (ft-lb)	Lateral Expansion (in.)	Percent Shear
E61-Top-1	70	52	0.043	40
E61-Top-2	70	50	0.043	40
E61-Top-3	70	53	0.044	40
E61-Top-4	70	40	0.035	30
E61-Top-5	30	32	0.028	20
E61-Top-6	30	28	0.023	15
E61-Top-7	30	27	0.024	15
E61-Top-8	30	34	0.029	20
E61-Top-9	0	3	0.002	3
E61-Top-10	0	12	0.010	5
E61-Top-11	0	5	0.003	5
E61-Top-12	0	27	0.022	10
E63-1/4t-1	70	39	0.034	20
E63-1/4t-2	70	34	0.028	20
E63-1/4t-3	70	9	0.011	10
E63-1/4t-4	70	22	0.019	15
E63-1/4t-5	30	28	0.025	15
E63-1/4t-6	30	3	0.002	3
E63-1/4t-7	30	4	0.004	5
E63-1/4t-8	30	4	0.003	5
E63-1/4t-9	100	33	0.031	20
E63-1/4t-10	100	38	0.033	20
E63-1/4t-11	100	51	0.043	35
E63-1/4t-12	100	33	0.030	20
E65-1/2t-1	70	29	0.027	20
E65-1/2t-2	70	33	0.028	20
E65-1/2t-3	70	24	0.021	15
E65-1/2t-4	70	28	0.024	15
E65-1/2t-5	30	4	0.003	5
E65-1/2t-6	30	5	0.003	5
E65-1/2t-7	30	20	0.017	10
E65-1/2t-8	30	4	0.004	5
E65-1/2t-9	100	38	0.033	25
E65-1/2t-10	100	13	0.015	15
E65-1/2t-11	100	23	0.022	15
E65-1/2t-12	100	37	0.031	20

Table 32 Continued – CVN Test Results, Sample E.6-NE

Sample ID	Test Temperature (°F)	Absorbed Energy (ft-lb)	Lateral Expansion (in.)	Percent Shear
E67-3/4t-1	70	15	0.015	15
E67-3/4t-2	70	20	0.019	15
E67-3/4t-3	70	38	0.033	25
E67-3/4t-4	70	18	0.017	15
E67-3/4t-5	30	24	0.022	15
E67-3/4t-6	30	5	0.004	5
E67-3/4t-7	30	5	0.004	5
E67-3/4t-8	30	4	0.003	5
E67-3/4t-9	100	13	0.015	20
E67-3/4t-10	100	34	0.030	20
E67-3/4t-11	100	40	0.036	30
E67-3/4t-12	100	35	0.029	20
E69-Bot-1	70	51	0.046	40
E69-Bot-2	70	40	0.036	30
E69-Bot-3	70	37	0.033	25
E69-Bot-4	70	43	0.037	30
E69-Bot-5	30	26	0.023	10
E69-Bot-6	30	41	0.035	25
E69-Bot-7	30	6	0.006	5
E69-Bot-8	30	21	0.019	10
E69-Bot-9	0	3	0.002	3
E69-Bot-10	0	3	0.002	3
E69-Bot-11	0	5	0.004	5
E69-Bot-12	0	4	0.004	3

Table 33 – CVN Test Results, Sample E.6-SW

Sample ID	Test Temperature (°F)	Absorbed Energy (ft-lb)	Lateral Expansion (in.)	Percent Shear
E61-Top-1	70	53.0	0.041	40
E61-Top-2	70	54.0	0.042	40
E61-Top-3	70	54.0	0.044	40
E61-Top-4	70	49.0	0.039	35
E61-Top-5	30	28.0	0.022	15
E61-Top-6	30	24.0	0.019	15
E61-Top-7	30	41.0	0.034	25
E61-Top-8	30	34.0	0.028	20
E61-Top-9	0	14.0	0.013	5
E61-Top-10	0	10.0	0.008	5
E61-Top-11	0	3.0	0.000	3
E61-Top-12	0	29.0	0.024	15
E63-1/4t-1	70	30.0	0.025	20
E63-1/4t-2	70	41.0	0.034	30
E63-1/4t-3	70	24.0	0.021	20
E63-1/4t-4	70	12.0	0.011	20
E63-1/4t-5	30	13.0	0.011	8
E63-1/4t-6	30	5.0	0.004	5
E63-1/4t-7	30	29.0	0.024	15
E63-1/4t-8	30	11.0	0.009	5
E63-1/4t-9	0	2.0	0.001	3
E63-1/4t-10	0	5.0	0.004	5
E63-1/4t-11	0	3.0	0.002	3
E63-1/4t-12	0	3.0	0.001	3
E65-1/2t-1	70	6.0	0.005	8
E65-1/2t-2	70	23.0	0.019	10
E65-1/2t-3	70	6.0	0.005	5
E65-1/2t-4	70	5.0	0.004	5
E65-1/2t-5	30	5.0	0.003	5
E65-1/2t-6	30	4.0	0.003	5
E65-1/2t-7	30	3.0	0.002	3
E65-1/2t-8	30	3.0	0.002	5
E65-1/2t-9	100	13.0	0.013	10
E65-1/2t-10	100	25.0	0.021	20
E65-1/2t-11	100	31.0	0.025	25
E65-1/2t-12	100	30.0	0.023	25

Table 33 Continued – CVN Test Results, Sample E.6-SW

Sample ID	Test Temperature (°F)	Absorbed Energy (ft-lb)	Lateral Expansion (in.)	Percent Shear
E67-3/4t-1	70	40.0	0.033	30
E67-3/4t-2	70	25.0	0.022	20
E67-3/4t-3	70	38.0	0.032	30
E67-3/4t-4	70	42.0	0.035	30
E67-3/4t-5	30	8.0	0.006	5
E67-3/4t-6	30	22.0	0.019	10
E67-3/4t-7	30	28.0	0.024	15
E67-3/4t-8	30	5.0	0.003	5
E67-3/4t-9	0	3.0	0.001	3
E67-3/4t-10	0	3.0	0.002	3
E67-3/4t-11	0	3.0	0.001	3
E67-3/4t-12	0	3.0	0.001	3
E69-Bot-1	70	47.0	0.039	40
E69-Bot-2	70	46.0	0.038	35
E69-Bot-3	70	44.0	0.036	30
E69-Bot-4	70	64.0	0.054	45
E69-Bot-5	30	29.0	0.024	15
E69-Bot-6	30	47.0	0.039	30
E69-Bot-7	30	16.0	0.014	10
E69-Bot-8	30	11.0	0.010	8
E69-Bot-9	0	4.0	0.003	3
E69-Bot-10	0	4.0	0.002	3
E69-Bot-11	0	28.0	0.023	15
E69-Bot-12	0	21.0	0.018	10

Table 34 – CVN Test Results, Sample E.6-SE

Sample ID	Test Temperature (°F)	Absorbed Energy (ft-lb)	Lateral Expansion (in.)	Percent Shear
E61-Top-1	70	54	0.048	35
E61-Top-2	70	61	0.052	40
E61-Top-3	70	55	0.047	35
E61-Top-4	70	47	0.040	35
E61-Top-5	30	6	0.006	10
E61-Top-6	30	24	0.021	15
E61-Top-7	30	42	0.036	25
E61-Top-8	30	32	0.028	20
E61-Top-9	0	15	0.013	10
E61-Top-10	0	5	0.005	3
E61-Top-11	0	5	0.004	3
E61-Top-12	0	4	0.003	3
E63-1/4t-1	70	33	0.030	20
E63-1/4t-2	70	41	0.036	25
E63-1/4t-3	70	17	0.018	15
E63-1/4t-4	70	38	0.033	25
E63-1/4t-5	30	4	0.004	5
E63-1/4t-6	30	4	0.003	5
E63-1/4t-7	30	8	0.008	10
E63-1/4t-8	30	10	0.009	5
E63-1/4t-9	100	56	0.047	40
E63-1/4t-10	100	41	0.036	30
E63-1/4t-11	100	28	0.025	20
E63-1/4t-12	100	41	0.036	30
E65-1/2t-1	70	7	0.009	10
E65-1/2t-2	70	29	0.027	15
E65-1/2t-3	70	39	0.034	25
E65-1/2t-4	70	10	0.012	10
E65-1/2t-5	30	5	0.005	3
E65-1/2t-6	30	4	0.003	3
E65-1/2t-7	30	5	0.004	5
E65-1/2t-8	30	6	0.007	5
E65-1/2t-9	100	42	0.036	30
E65-1/2t-10	100	44	0.040	35
E65-1/2t-11	100	42	0.037	30
E65-1/2t-12	100	37	0.034	25

Table 34 Continued – CVN Test Results, Sample E.6-SE

Sample ID	Test Temperature (°F)	Absorbed Energy (ft-lb)	Lateral Expansion (in.)	Percent Shear
E67-3/4t-1	70	32	0.028	20
E67-3/4t-2	70	27	0.024	15
E67-3/4t-3	70	29	0.026	15
E67-3/4t-4	70	31	0.027	20
E67-3/4t-5	30	5	0.004	5
E67-3/4t-6	30	24	0.022	10
E67-3/4t-7	30	24	0.021	15
E67-3/4t-8	30	13	0.012	5
E67-3/4t-9	0	4	0.003	3
E67-3/4t-10	0	3	0.002	3
E67-3/4t-11	0	2	0.001	3
E67-3/4t-12	0	2	0.001	3
E69-Bot-1	70	49	0.041	40
E69-Bot-2	70	38	0.033	20
E69-Bot-3	70	45	0.038	40
E69-Bot-4	70	52	0.045	40
E69-Bot-5	30	20	0.018	10
E69-Bot-6	30	38	0.032	15
E69-Bot-7	30	12	0.012	8
E69-Bot-8	30	14	0.012	5
E69-Bot-9	0	7	0.007	3
E69-Bot-10	0	6	0.006	5
E69-Bot-11	0	4	0.002	3
E69-Bot-12	0	8	0.007	3

Table 35 – CVN Test Results, First Street Girder Flange Core Samples

Sample ID	Test Temperature (°F)	Absorbed Energy (ft-lb)	Lateral Expansion (in.)	Percent Shear
NE1-Top-1	70	58.0	0.046	50
NE1-Top-2	70	17.0	0.015	20
NE1-Top-3	30	28.0	0.023	15
NE1-Top-4	30	32.0	0.027	15
NE3-1/4t-1	70	14.0	0.014	20
NE3-1/4t-2	70	43.0	0.036	30
NE3-1/4t-3	30	4.0	0.003	5
NE3-1/4t-4	30	5.0	0.003	10
NE5-1/2t-1	70	41.0	0.036	30
NE5-1/2t-2	70	61.0	0.050	50
NE5-1/2t-3	30	6.0	0.004	10
NE5-1/2t-4	30	15.0	0.022	15
NE7-3/4t-1	70	47.0	0.042	35
NE7-3/4t-2	70	50.0	0.044	40
NE7-3/4t-3	30	5.0	0.003	10
NE7-3/4t-4	30	4.0	0.003	5
NE9-Bot-1	70	43.0	0.036	30
NE9-Bot-2	70	52.0	0.044	40
NE9-Bot-3	30	30.0	0.025	15
NE9-Bot-4	30	26.0	0.022	15
NW1-Top-1	70	55.0	0.044	35
NW1-Top-2	70	31.0	0.025	20
NW1-Top-3	30	36.0	0.031	20
NW1-Top-4	30	30.0	0.026	10
NW3-1/4t-1	70	35.0	0.028	30
NW3-1/4t-2	70	27.0	0.023	20
NW3-1/4t-3	30	16.0	0.014	10
NW3-1/4t-4	30	4.0	0.002	5
NW5-1/2t-1	70	10.0	0.008	10
NW5-1/2t-2	70	27.0	0.024	15
NW5-1/2t-3	30	7.0	0.006	5
NW5-1/2t-4	30	5.0	0.004	5
NW7-3/4t-1	70	42.0	0.035	30
NW7-3/4t-2	70	25.0	0.021	15
NW7-3/4t-3	30	4.0	0.002	5
NW7-3/4t-4	30	5.0	0.003	5

Table 35 Continued – CVN Test Results, First Street Girder Flange Core Samples

Sample ID	Test Temperature (°F)	Absorbed Energy (ft-lb)	Lateral Expansion (in.)	Percent Shear
NW9-Bot-1	70	56.0	0.046	35
NW9-Bot-2	70	64.0	0.049	40
NW9-Bot-3	30	33.0	0.029	15
NW9-Bot-4	30	39.0	0.033	15
SE1-Top-1	70	39.0	0.034	20
SE1-Top-2	70	47.0	0.039	35
SE1-Top-3	30	32.0	0.027	15
SE1-Top-4	30	26.0	0.022	10
SE3-1/4t-1	70	43.0	0.038	30
SE3-1/4t-2	70	42.0	0.036	30
SE3-1/4t-3	30	5.0	0.005	5
SE3-1/4t-4	30	4.0	0.003	5
SE5-1/2t-1	70	41.0	0.036	30
SE5-1/2t-2	70	58.0	0.050	35
SE5-1/2t-3	30	6.0	0.005	5
SE5-1/2t-4	30	4.0	0.004	5
SE7-3/4t-1	70	27.0	0.024	10
SE7-3/4t-2	70	46.0	0.039	30
SE7-3/4t-3	30	4.0	0.003	5
SE7-3/4t-4	30	5.0	0.002	5
SE9-Bot-1	70	34.0	0.029	15
SE9-Bot-2	70	35.0	0.029	15
SE9-Bot-3	30	59.0	0.041	50
SE9-Bot-4	30	33.0	0.028	15
SW1-Top-1	70	46.0	0.039	30
SW1-Top-2	70	40.0	0.034	30
SW1-Top-3	30	40.0	0.034	30
SW1-Top-4	30	25.0	0.021	15
SW3-1/4t-1	70	14.0	0.014	10
SW3-1/4t-2	70	29.0	0.025	20
SW3-1/4t-3	30	17.0	0.016	10
SW3-1/4t-4	30	5.0	0.005	5
SW5-1/2t-1	70	26.0	0.022	15
SW5-1/2t-2	70	6.0	0.006	5
SW5-1/2t-3	30	4.0	0.002	5
SW5-1/2t-4	30	4.0	0.002	5

Table 35 Continued – CVN Test Results, First Street Girder Flange Core Samples

Sample ID	Test Temperature (°F)	Absorbed Energy (ft-lb)	Lateral Expansion (in.)	Percent Shear
SW7-3/4t-1	70	35.0	0.029	25
SW7-3/4t-2	70	14.0	0.013	10
SW7-3/4t-3	30	5.0	0.004	5
SW7-3/4t-4	30	12.0	0.011	5
SW9-Bot-1	70	59.0	0.048	40
SW9-Bot-2	70	41.0	0.035	30
SW9-Bot-3	30	30.0	0.026	15
SW9-Bot-4	30	31.0	0.026	25

Table 36 – CVN Test Results, Fremont Street Hanger Core Sample N26

Sample ID	Test Temperature (°F)	Absorbed Energy (ft-lb)	Lateral Expansion (in.)	Percent Shear
N26-North-1	70	101	0.074	75
N26-North-2	70	86	0.067	70
N26-North-3	30	71	0.060	45
N26-North-4	30	79	0.066	50
N26-1/4t from North-1	70	61	0.054	40
N26-1/4t from North-2	70	77	0.064	50
N26-1/4t from North-3	30	54	0.049	25
N26-1/4t from North-4	30	57	0.050	25
N26-1/2t-1	70	79	0.066	60
N26-1/2t-2	70	32	0.032	30
N26-1/2t-3	30	22	0.020	15
N26-1/2t-4	30	31	0.028	15
N26-1/4t from South-1	70	98	0.076	75
N26-1/4t from South-2	70	90	0.071	70
N26-1/4t from South-3	30	49	0.044	30
N26-1/4t from South-4	30	52	0.045	30
N26-South-3	30	91	0.071	60
N26-South-4	30	86	0.071	50

Table 37 – CVN Test Results, Fremont Street Hanger Core Sample S26

Sample ID	Test Temperature (°F)	Absorbed Energy (ft-lb)	Lateral Expansion (in.)	Percent Shear
S26-North-1	70	118	0.078	75
S26-North-2	70	102	0.074	75
S26-North-3	30	88	0.068	50
S26-North-4	30	91	0.072	55
S26-1/4t from North-1	70	95	0.069	60
S26-1/4t from North-2	70	75	0.059	50
S26-1/4t from North-3	30	67	0.056	35
S26-1/4t from North-4	30	48	0.041	25
S26-1/2t-1	70	124	0.082	75
S26-1/2t-2	70	89	0.069	65
S26-1/2t-3	30	45	0.037	20
S26-1/2t-4	30	69	0.058	35
S26-1/4t from South-1	70	89	0.065	75
S26-1/4t from South-2	70	73	0.058	70
S26-1/4t from South-3	30	52	0.045	25
S26-1/4t from South-4	30	47	0.041	25
S26-South-1	70	96	0.071	75
S26-South-2	70	94	0.073	75
S26-South-3	30	80	0.067	50
S26-South-4	30	76	0.062	50

Table 38 – CVN Test Results, First Street Hanger Core Sample N18

Sample ID	Test Temperature (°F)	Absorbed Energy (ft-lb)	Lateral Expansion (in.)	Percent Shear
N18-North-1	70	104	0.077	70
N18-North-2	70	88	0.065	60
N18-North-3	30	78	0.064	50
N18-North-4	30	87	0.074	50
N18-1/4t from North-1	70	71	0.059	60
N18-1/4t from North-2	70	94	0.074	70
N18-1/4t from North-3	30	66	0.055	35
N18-1/4t from North-4	30	57	0.047	30
N18-1/2t-1	70	21	0.020	20
N18-1/2t-2	70	27	0.026	25
N18-1/2t-3	30	8	0.006	20
N18-1/2t-4	30	9	0.008	20
N18-1/4t from South-1	70	68	0.057	50
N18-1/4t from South-2	70	85	0.066	65
N18-1/4t from South-3	30	82	0.067	60
N18-1/4t from South-4	30	9	0.009	20
N18-South-1	70	111	0.078	70
N18-South-2	70	102	0.073	70
N18-South-3	30	80	0.065	50
N18-South-4	30	72	0.058	40

Table 39 – CVN Test Results, First Street Hanger Core Sample S18

Sample ID	Test Temperature (°F)	Absorbed Energy (ft-lb)	Lateral Expansion (in.)	Percent Shear
S18-North-1	70	99	0.073	75
S18-North-2	70	95	0.075	75
S18-North-3	30	77	0.063	50
S18-North-4	30	73	0.060	45
S18-1/4t from North-1	70	91	0.072	60
S18-1/4t from North-2	70	95	0.070	70
S18-1/4t from North-3	30	86	0.073	50
S18-1/4t from North-4	30	14	0.016	20
N18-1/2t-1	70	35	0.032	25
N18-1/2t-2	70	21	0.019	20
N18-1/2t-3	30	8	0.009	15
N18-1/2t-4	30	18	0.017	15
S18-1/4t from South-1	70	90	0.071	70
S18-1/4t from South-2	70	94	0.074	70
S18-1/4t from South-3	30	53	0.044	25
S18-1/4t from South-4	30	11	0.011	15
S18-South-1	70	94	0.073	75
S18-South-2	70	108	0.078	75
S18-South-3	30	98	0.076	65
S18-South-4	30	79	0.064	45

Table 40 – Melt U1588 CVN Test Results from Mill Cert [34]

Slab No.	Specimen Size	Test Temperature (°F)	Absorbed Energy (ft-lb)		
1	Full	70	17	35	45
3	Full	70	35	42	42

Table 41 – Longitudinal Tensile Test Results, D.4-S

Girder Sample ID	Tensile ID	Tensile Direction	Tensile Location	Yield Strength, 0.2 % offset (ksi)	Ultimate Tensile Strength (ksi)	Elongation, 2 in. gage length (%)	Reduction of Area
As Per ASTM A572, Grade 50				50 min.	60 min.	21 min.	-
D.4-SW	4-3-1	Longitudinal	¼ Thickness From Top	75	87	28.2	64.7
	4-3-2			60	87	26.3	63.0
	4-2-1		Mid-Thickness	63	91	27.8	63.7
	4-2-2			62	90	27.0	63.7
	4-1-1		¼ Thickness From Bottom	60	88	26.5	63.2
	4-1-2			61	88	27.6	62.7
D.4-SE	4-3-1		¼ Thickness From Top	62	88	26.3	62.3
	4-3-2			61	87	26.5	64.9
	4-2-1		Mid-Thickness	64	91	26.7	60.2
	4-2-2			63	90	26.5	63.4
	4-1-1		¼ Thickness From Bottom	61	87	27.5	62.9
	4-1-2			61	87	28.6	65.0

Table 42 – Longitudinal Tensile Test Results, E.6-S

Girder Sample ID	Tensile ID	Tensile Direction	Tensile Location	Yield Strength, 0.2 % offset (ksi)	Ultimate Tensile Strength (ksi)	Elongation, 2 in. gage length (%)	Reduction of Area
As Per ASTM A572, Grade 50				50 min.	60 min.	21 min.	-
E.6-SW	6-3-1	Longitudinal	¼ Thickness From Top	59	86	27.3	67.0
	6-3-2			60	87	26.1	65.6
	6-2-1		Mid-Thickness	66	95	24.9	61.8
	6-2-2			66	95	24.1	60.5
	6-1-1		¼ Thickness From Bottom	59	87	26.6	63.7
	6-1-2			59	86	27.3	65.8
E.6-SE	6-3-1		¼ Thickness From Top	61	87	27.4	64.2
	6-3-2			61	87	27.7	64.6
	6-2-1		Mid-Thickness	60	86	26.6	60.9
	6-2-2			59	86	27.7	60.5
	6-1-1		¼ Thickness From Bottom	60	86	27.6	62.5
	6-1-2			60	86	28.2	65.0

Table 43 – Longitudinal Tensile Test Results, D.4-NE & E.6-NE

Girder Sample ID	Tensile ID	Tensile Direction	Tensile Location	Yield Strength, 0.2 % offset (ksi)	Ultimate Tensile Strength (ksi)	Elongation, 2 in. gage length (%)	Reduction of Area
As Per ASTM A572, Grade 50				50 min.	60 min.	21 min.	-
D.4-NE	4-3-1	Longitudinal	¼ Thickness From Top	61	87	29.7	62.7
	4-3-2			60	87	30.5	64.7
	4-2-1		Mid-Thickness	60	86	27.2	60.5
	4-2-2			60	86	27.7	56.8
	4-1-1		¼ Thickness From Bottom	61	86	28.6	61.8
	4-1-2			60	87	29.6	63.3
E.6-NE	6-3-1		¼ Thickness From Top	62	88	26.5	62.7
	6-3-2			61	87	29.3	63.1
	6-2-1		Mid-Thickness	63	90	27.1	61.2
	6-2-2			63	90	26.3	59.7
	6-1-1		¼ Thickness From Bottom	61	87	28.2	64.3
	6-1-2			60	86	25.8	64.2

Table 44 – Transverse Tensile Test Results, D.4-N

Girder Sample ID	Tensile ID	Tensile Direction	Tensile Location	Yield Strength, 0.2 % offset (ksi)	Ultimate Tensile Strength (ksi)	Elongation, 2 in. gage length (%)	Reduction of Area
As Per ASTM A572, Grade 50				50 min.	60 min.	21 min.	-
D.4-NW	4-3-1	Transverse	¼ Thickness From Top	60	87	24.4	53.2
	4-3-2			60	87	26.4	58.0
	4-1-1		¼ Thickness From Bottom	60	87	25.6	56.9
	4-1-2			60	86	24.4	52.2
D.4-NE	4-3-1		¼ Thickness From Top	60	86	24.9	54.9
	4-3-2			60	86	26.7	57.6
	4-1-1		¼ Thickness From Bottom	61	87	24.4	54.4
	4-1-2			61	87	24.0	54.8

Table 45 – Transverse Tensile Test Results, D.4-S

Girder Sample ID	Tensile ID	Tensile Direction	Tensile Location	Yield Strength, 0.2 % offset (ksi)	Ultimate Tensile Strength (ksi)	Elongation, 2 in. gage length (%)	Reduction of Area
As Per ASTM A572, Grade 50				50 min.	60 min.	21 min.	-
D.4-SW	4-3-1	Transverse	¼ Thickness From Top	61	87	25.7	55.8
	4-3-2			61	87	26.6	54.8
	4-1-1		¼ Thickness From Bottom	60	87	25.0	56.1
	4-1-2			60	87	27.0	57.2
D.4-SE	4-3-1		¼ Thickness From Top	60	86	23.8	56.7
	4-3-2			60	86	26.6	58.5
	4-1-1		¼ Thickness From Bottom	60	86	29.1	58.9
	4-1-2			60	86	23.1	55.3

Table 46 – Transverse Tensile Test Results – E.6-N

Girder Sample ID	Tensile ID	Tensile Direction	Tensile Location	Yield Strength, 0.2 % offset (ksi)	Ultimate Tensile Strength (ksi)	Elongation, 2 in. gage length (%)	Reduction of Area
As Per ASTM A572, Grade 50				50 min.	60 min.	21 min.	-
E.6-NW	6-3-1	Transverse	¼ Thickness From Top	59	86	27.8	59.0
	6-3-2			60	86	27.5	57.6
	6-1-1		¼ Thickness From Bottom	60	85	27.2	58.7
	6-1-2			60	86	27.0	58.2
E.6-NE	6-3-1		¼ Thickness From Top	61	87	26.8	56.6
	6-3-2			61	86	27.7	59.1
	6-1-1		¼ Thickness From Bottom	60	86	27.6	58.0
	6-1-2			60	86	29.1	56.5

Table 47 – Transverse Tensile Test Results – E.6-S

Girder Sample ID	Tensile ID	Tensile Direction	Tensile Location	Yield Strength, 0.2 % offset (ksi)	Ultimate Tensile Strength (ksi)	Elongation, 2 in. gage length (%)	Reduction of Area
As Per ASTM A572, Grade 50				50 min.	60 min.	21 min.	-
E.6-SW	6-3-1	Transverse	¼ Thickness From Top	59	85	25.2	55.3
	6-3-2			60	86	23.3	55.8
	6-1-1		¼ Thickness From Bottom	59	86	23.1	54.3
	6-1-2			59	85	23.2	55.3
E.6-SE	6-3-1		¼ Thickness From Top	60	86	24.2	55.1
	6-3-2			60	86	26.1	56.6
	6-1-1		¼ Thickness From Bottom	59	85	27.2	56.4
	6-1-2			60	86	25.5	56.8

Table 48 – Macro-Section Hardness Testing Results, D.4-S & E.6-N (HRB)

ID	D.4-S	E.6-N	ID	D.4-S	E.6-N	ID	D.4-S	E.6-N	ID	D.4-S	E.6-N
1	90	90	**12**	92	90	**23**	87	88	**34**	87	87
2	88	89	**13**	91	91	**24**	87	89	**35**	87	87
3	91	88	**14**	91	92	**25**	90	91	**36**	89	89
4	93	91	**15**	95	95	**26**	94	99	**37**	91	93
5	85	90	**16**	89	88	**27**	87	90	**38**	89	87
6	84	88	**17**	90	87	**28**	89	90	**39**	90	91
7	85	92	**18**	89	89	**29**	87	91	**40**	87	87
8	93	97	**19**	95	95	**30**	97	96	**41**	98	90
9	88	88	**20**	91	90	**31**	91	89	**42**	86	87
10	88	90	**21**	87	87	**32**	88	87	**43**	87	87
11	90	91	**22**	87	87	**33**	86	85	**44**	86	86

Table 49 – Surface Hardness Testing, Weld Access Hole Radii (HRC)

ID	D.4-NW	D.4-NE	D.4-SW	D.4-Se	E.6-NW	E.6-NE	E.6-SW	E.6-SE
1	41	50	37	34	42	42	37	21
2	39	47	35	35	59	31	42	39
3	36	54	47	35	40	41	33	50
4	46	40	37	47	31	46	52	33
5	36	37	33	38	40	28	48	44
Average	40	46	38	38	42	38	42	37

Table 50 – Surface Hardness Testing, Girder Flange Sides (HRC)

ID	D.4-NW	D.4-NE	D.4-SW	D.4-Se	E.6-NW	E.6-NE	E.6-SW	E.6-SE
1 (Flange Top)	32	48	32	40	39	50	46	50
2	47	44	52	40	36	47	43	46
3	57	52	53	50	40	42	43	41
4	40	21	50	39	38	43	36	52
5 (Flange Bottom)	45	36	47	33	34	43	48	32
Average	44	40	47	40	37	45	43	44

Table 51 – Girder Flange Material Composition, Product Analysis (wt. %)

Element	Per ASTM A572 Grade 50	D.4-N		D.4-S	
		D.4-NE	D.4-NW	D.4-SE	D.4-SW
C	0.27 max.	0.21	0.25	0.20	0.22
Mn	1.46 max.	1.12	1.08	1.02	1.12
P	0.05 max.	0.02	0.02	0.02	0.02
S	0.06 max.	0.01	<0.01	<0.01	0.01
Si	0.10-0.45	0.26	0.26	0.25	0.25
Al		0.008	0.008	0.008	0.011
Cr		0.10	0.099	0.097	0.11
Cu		0.29	0.29	0.27	0.22
Mo		0.019	0.017	0.016	0.064
Nb		0.007	0.006	0.007	0.001
Ni		0.076	0.076	0.072	0.065
Ti		<0.001	<0.001	<0.001	0.001
V		0.041	0.038	0.037	0.042

Table 52 – Girder Flange Material Composition, Product Analysis (wt. %)

Element	Per ASTM A572 Grade 50	E.6-N		E.6-S	
		E.6-NE	E.6-NW	E.6-SE	E.6-SW
C	0.27 max.	0.21	0.20	0.20	0.25
Mn	1.46 max.	1.06	1.04	1.03	1.13
P	0.05 max.	0.02	0.02	0.02	0.02
S	0.06 max.	<0.01	<0.01	<0.01	0.01
Si	0.10-0.45	0.26	0.25	0.26	0.26
Al		0.008	0.009	0.008	0.010
Cr		0.099	0.096	0.097	0.11
Cu		0.28	0.27	0.28	0.22
Mo		0.017	0.016	0.017	0.064
Nb		0.006	0.006	0.006	0.001
Ni		0.075	0.071	0.074	0.068
Ti		<0.001	<0.001	<0.001	0.001
V		0.038	0.037	0.037	0.042

APPENDIX E. POP-IN CRACK INITIATION CLOSED-FORM K SOLUTION

The following closed form stress intensity factor (K) analysis was used to verify the initial residual stress distribution necessarily present to initiate the pop-in crack from a microcrack with a crack depth (a) of 0.06 in. and fracture toughness (K_{1c}) of approximately 30 ksi√in.

K for an elliptical surface flaw can be calculated from the following (Sneddon, Irwin, and Kobayashi [20, 21, 22]):

$$K = 1.12\,\sigma\sqrt{\frac{\pi a}{Q}}M_k$$

$$Q = \sqrt{\emptyset^2 - 0.212\left(\frac{\sigma^2}{\sigma_{ys}^2}\right)}$$

$$\emptyset = \frac{3\pi}{8} + \frac{\pi}{8}\frac{a^2}{c^2}$$

a = 0.06 in. x 2c = 1.5 in. → c = 0.75 in.

$$\emptyset = \frac{3\pi}{8} + \frac{\pi}{8}\frac{0.06^2}{0.75^2}$$

$$\emptyset = 1.180$$

Since residual stress at the access hole surface is at or above yield, then $(\sigma/\sigma_{ys})^2 = 1.0$

$$Q = 1.086$$

Since a << than the plate width (W) → $M_k \sim 1.0$

$$K = 1.12\,\sigma\sqrt{\frac{\pi(0.06)}{1.086}}\,(1.0)$$

At fracture initiation $K = K_{1c} \sim 30$ ksi√in.

$$\emptyset = 1.18$$

$$30 = 1.12\,\sigma\sqrt{\frac{\pi(0.06)}{1.086}}\ (1.0)$$

$\underline{\sigma = 64 \text{ ksi}}$

Note that this calculation is only for K and does not consider inelastic behavior accounted for in the FAD approach.

APPENDIX F. TPG3 GIRDER FE MODEL DIMENSIONS

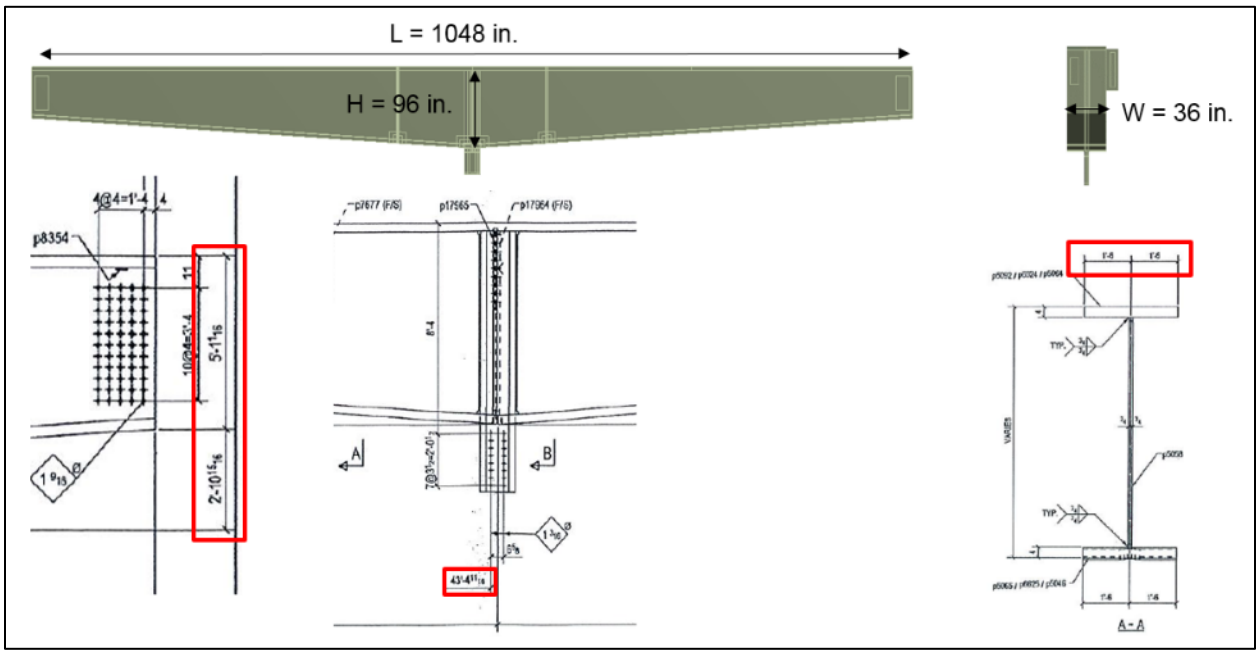

Fig. 237. Overall TPG3 girder dimensions shown on the 3D model with the appropriate reference dimensions, based on the shop drawings [25], highlighted.

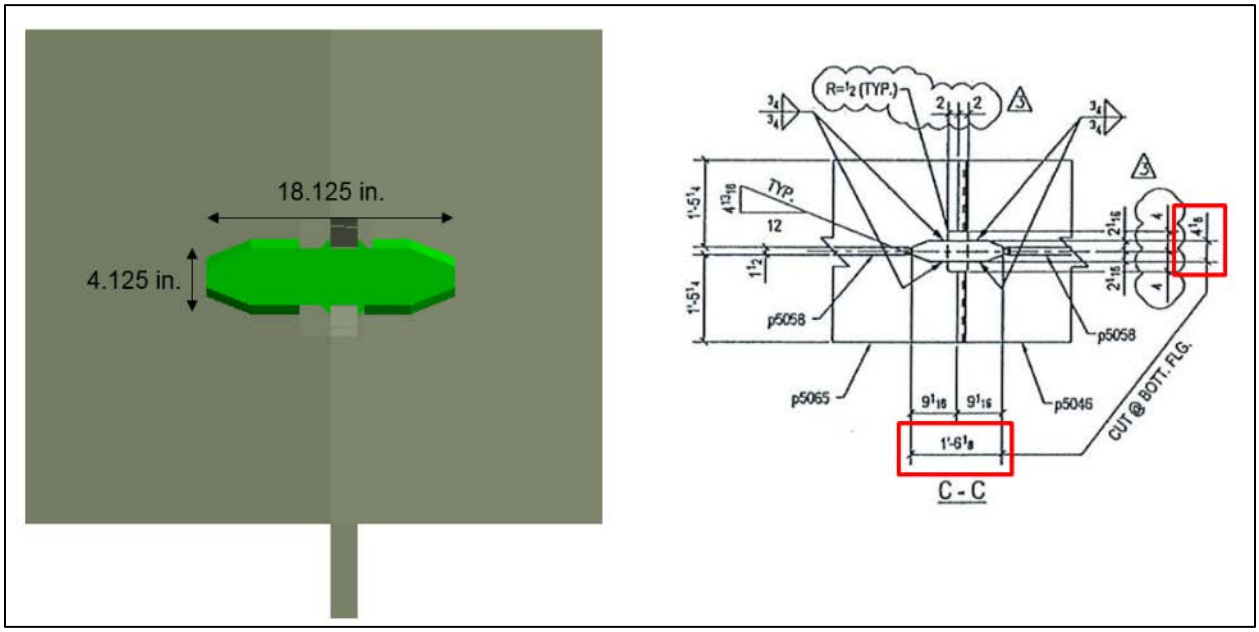

Fig. 238. Hanger dimensions shown on the 3D model with the appropriate reference dimensions, based on the shop drawings [25], highlighted.

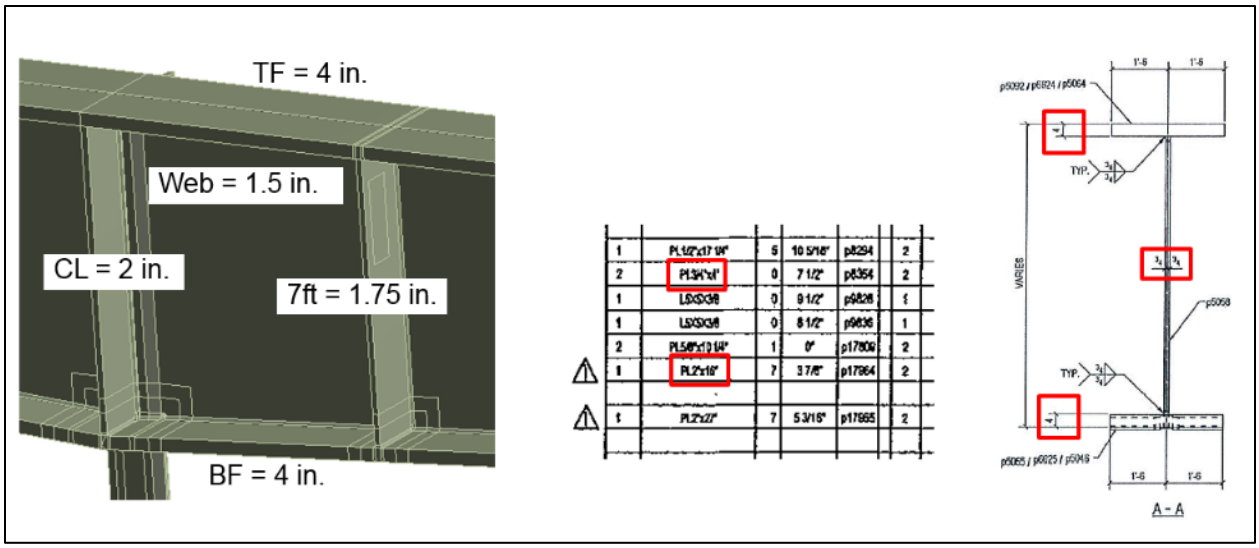

Fig. 239. Plate thicknesses shown on the 3D model with the appropriate reference dimensions, based on the shop drawings [25], highlighted.

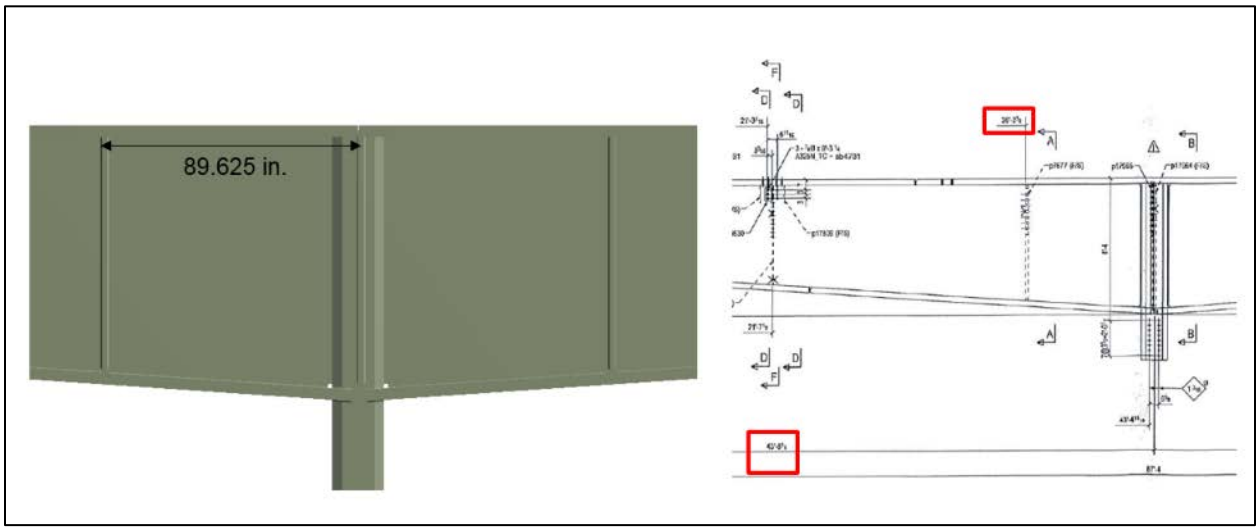

Fig. 240. Stiffener spacing shown on the 3D model with the appropriate reference dimensions, based on the shop drawings [25], highlighted.

APPENDIX G. FREMONT STREET D.4 TPG3 GIRDER FE RESULTS

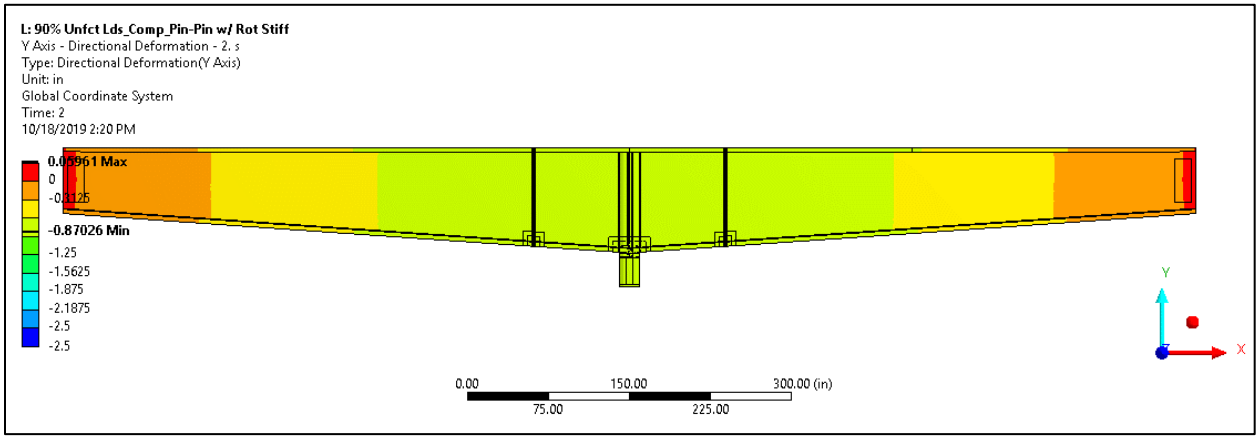

Fig. 241. Vertical deformation (in.) at 1.0×DL.

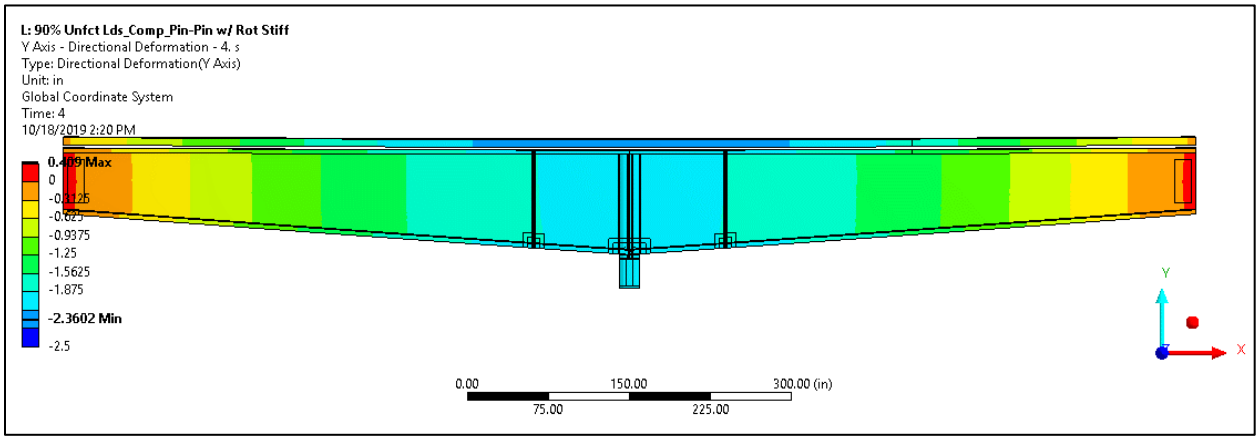

Fig. 242. Vertical deformation (in.) at 1.0×(DL+SDL).

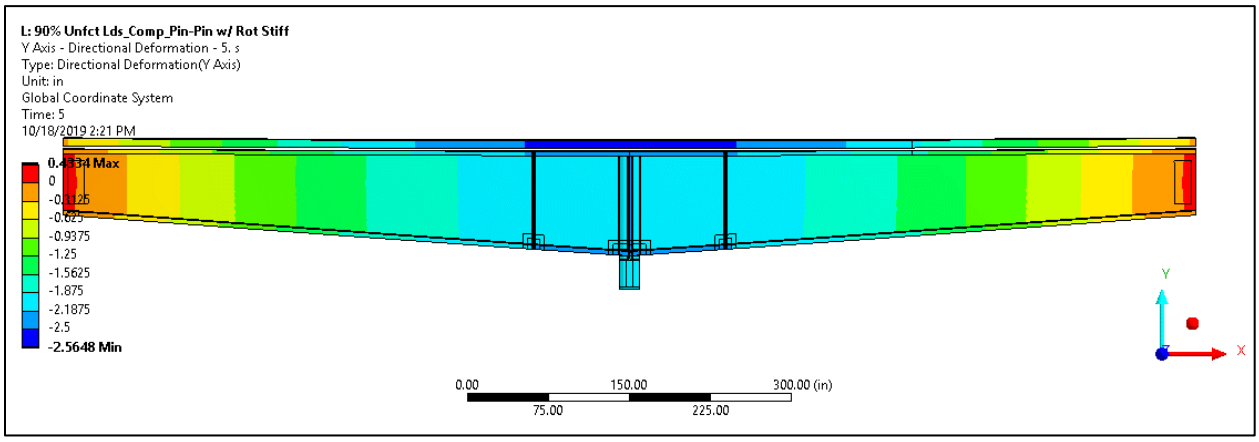

Fig. 243. Vertical deformation (in.) at 1.0×(DL+SDL)+1.0×LL.

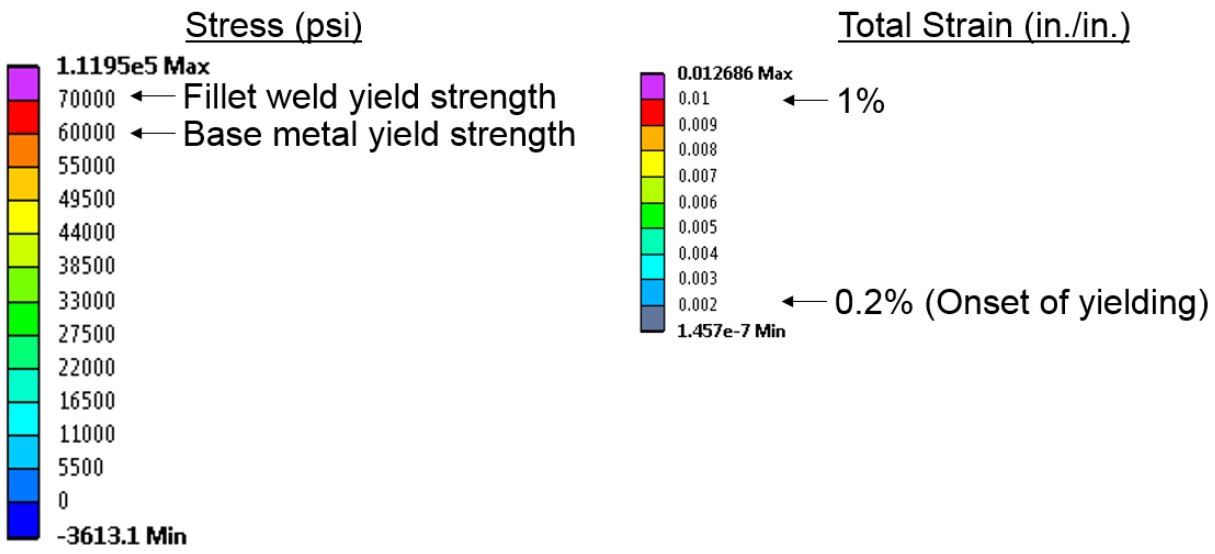

Fig. 244. Stress and strain contour bands for all proceeding FE result plots. Yield strengths shown are the assumed values at the time of fracture.

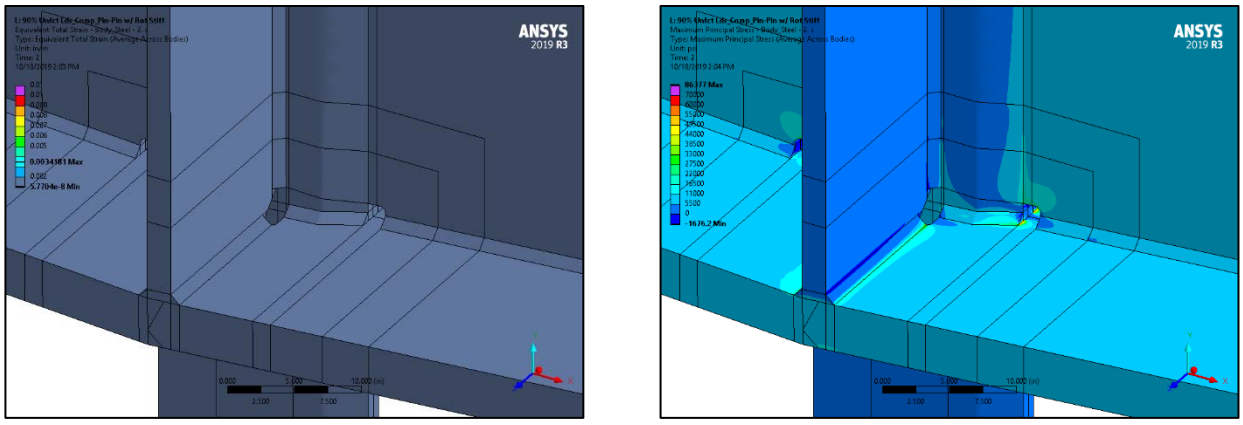

Fig. 245. Region of interest (top) total strain (in./in.) and maximum principal stress (psi) at 1.0×DL.

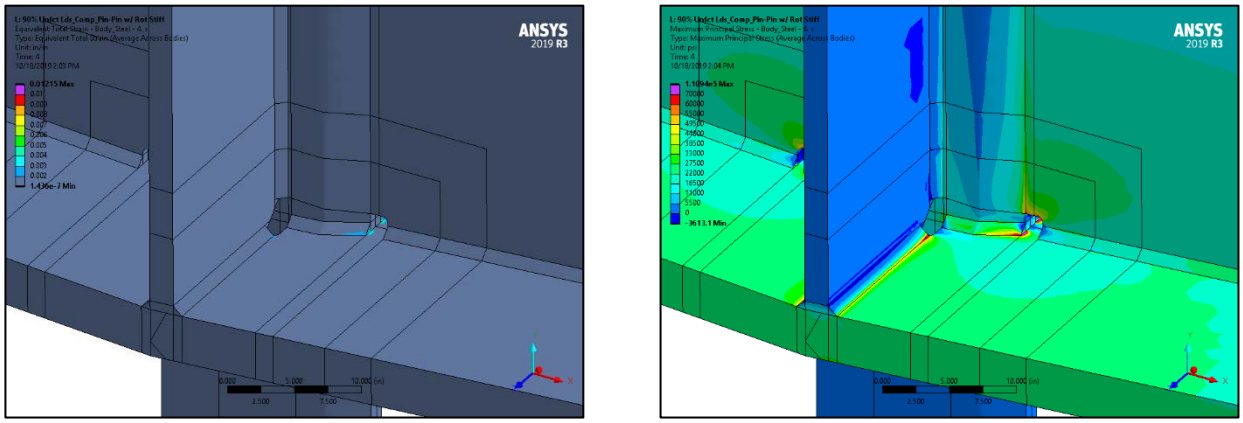

Fig. 246. Region of interest (top) total strain (in./in.) and maximum principal stress (psi) at 1.0×(DL+SDL).

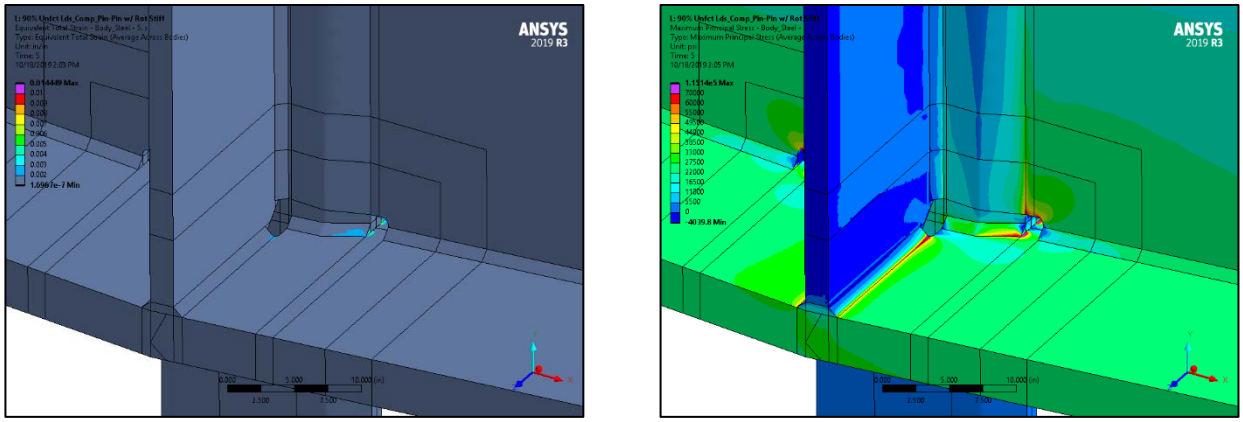

Fig. 247. Region of interest (top) total strain (in./in.) and maximum principal stress (psi) at 1.0×(DL+SDL)+1.0×LL.

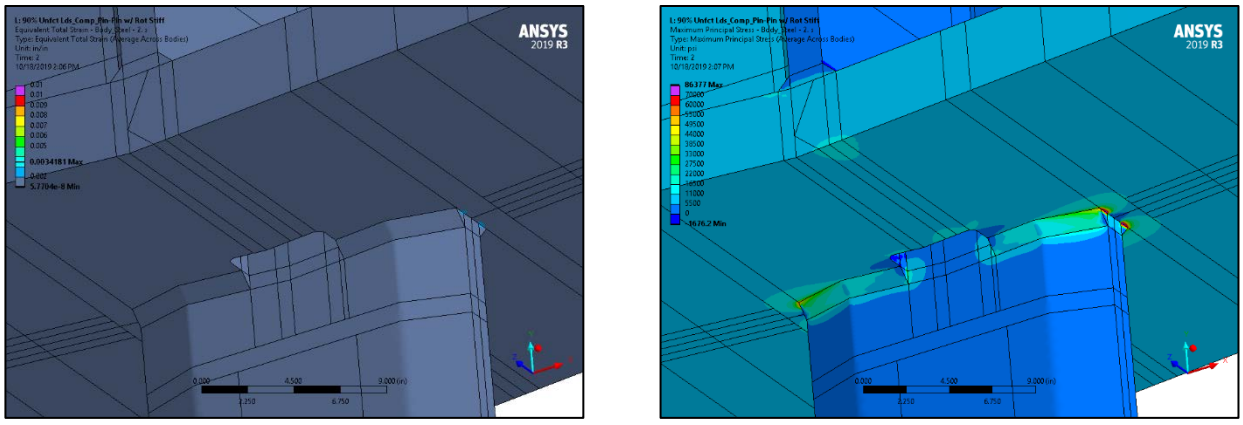

Fig. 248. Region of interest (bottom) total strain (in./in.) and maximum principal stress (psi) at 1.0×DL.

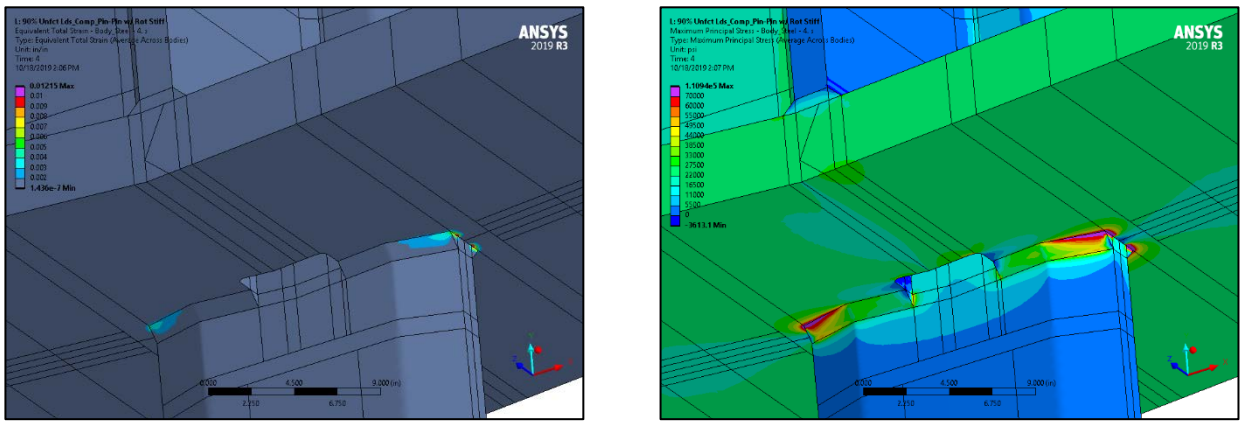

Fig. 249. Region of interest (bottom) total strain (in./in.) and maximum principal stress (psi) at 1.0×(DL+SDL).

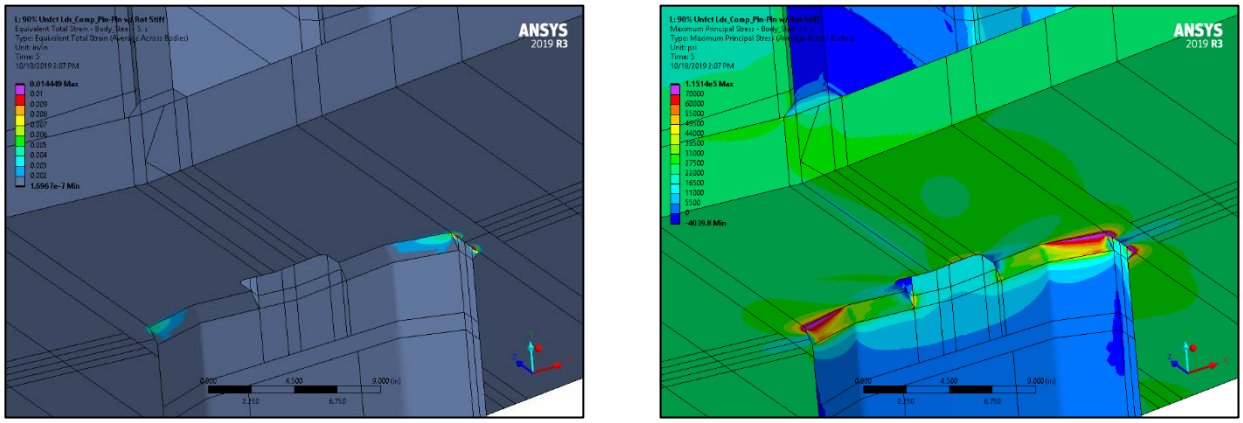

Fig. 250. Region of interest (bottom) total strain (in./in.) and maximum principal stress (psi) at 1.0×(DL+SDL)+1.0×LL.

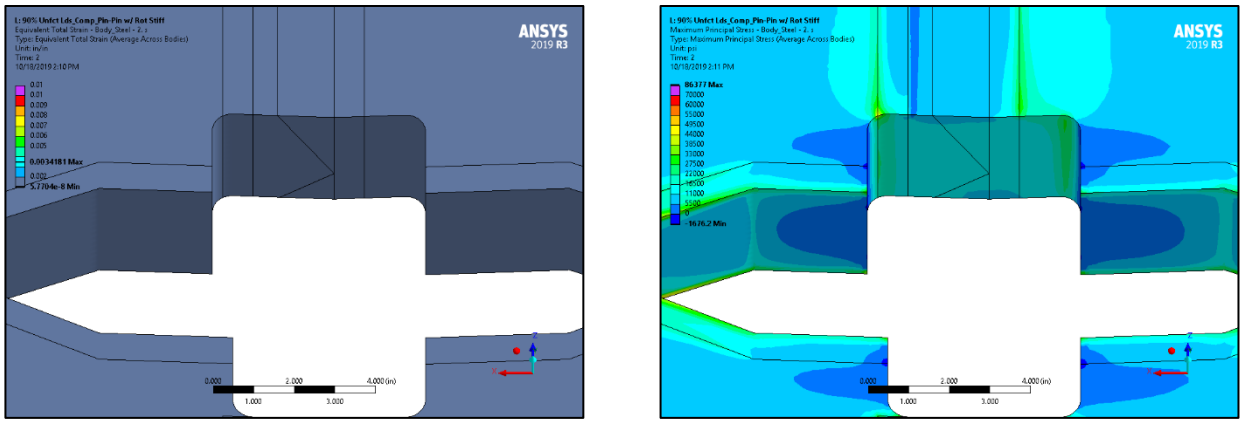

Fig. 251. Weld access hole (north) total strain (in./in.) and maximum principal stress (psi) at 1.0×DL.

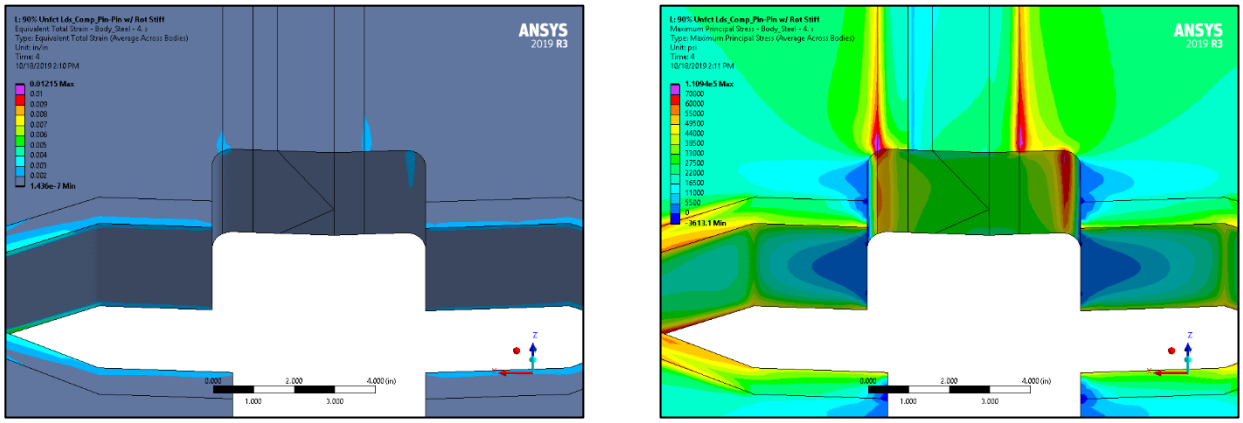

Fig. 252. Weld access hole (north) total strain (in./in.) and maximum principal stress (psi) at 1.0×(DL+SDL).

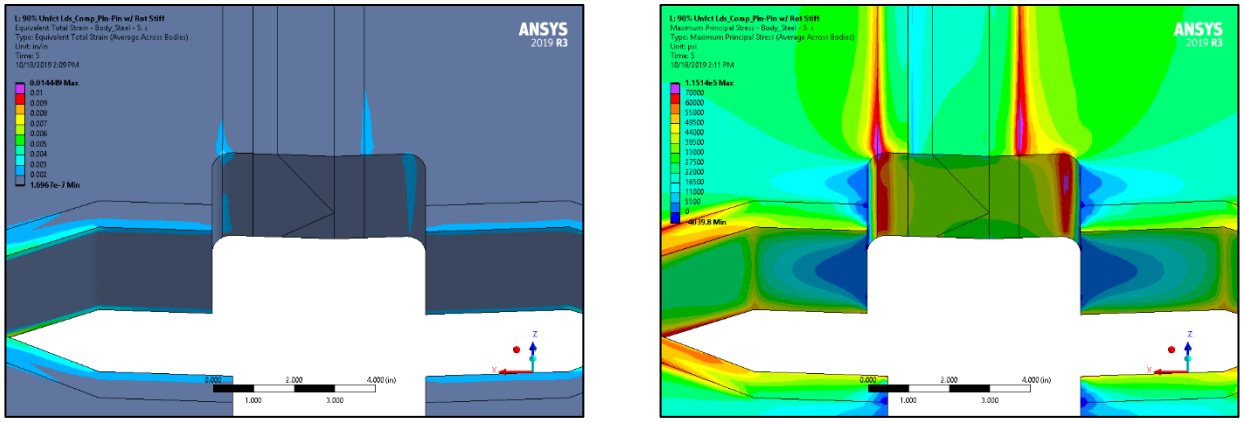

Fig. 253. Weld access hole (north) total strain (in./in.) and maximum principal stress (psi) at 1.0×(DL+SDL)+1.0×LL.

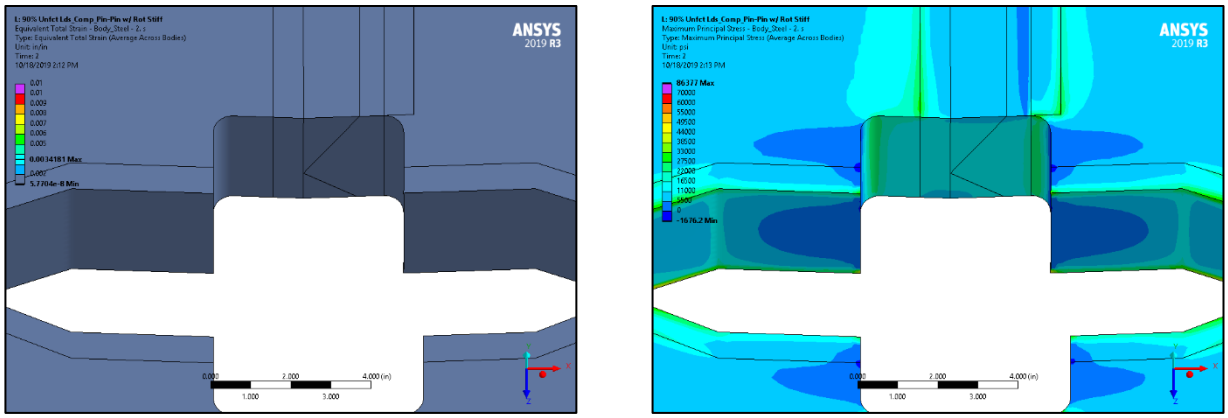

Fig. 254. Weld access hole (south) total strain (in./in.) and maximum principal stress (psi) at 1.0×DL.

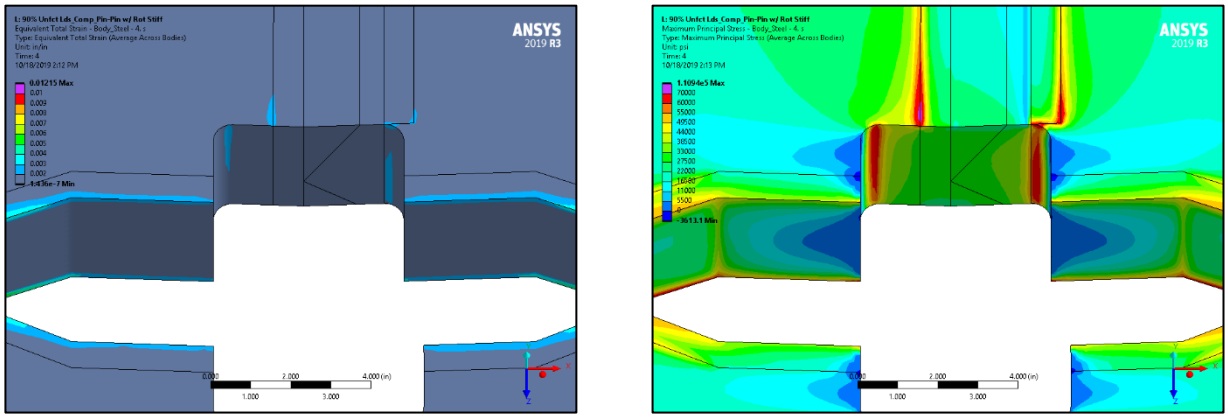

Fig. 255. Weld access hole (south) total strain (in./in.) and maximum principal stress (psi) at 1.0×(DL+SDL).

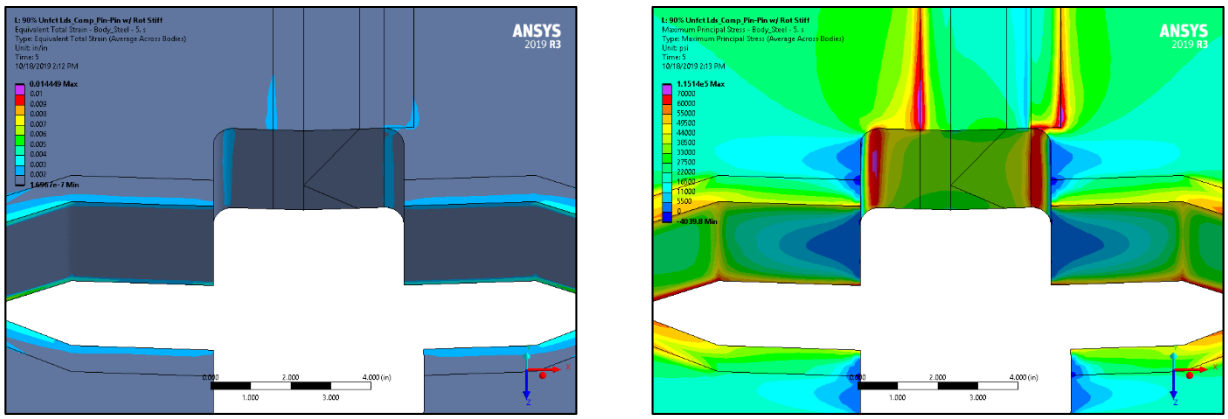

Fig. 256. Weld access hole (south) total strain (in./in.) and maximum principal stress (psi) at 1.0×(DL+SDL)+1.0×LL.

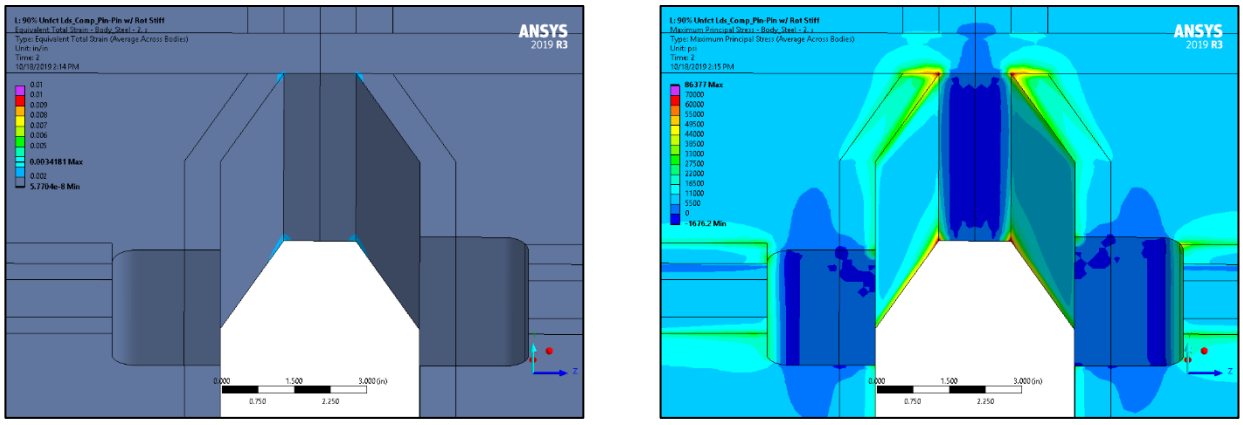

Fig. 257. Hanger slot (west) total strain (in./in.) and maximum principal stress (psi) at 1.0×DL.

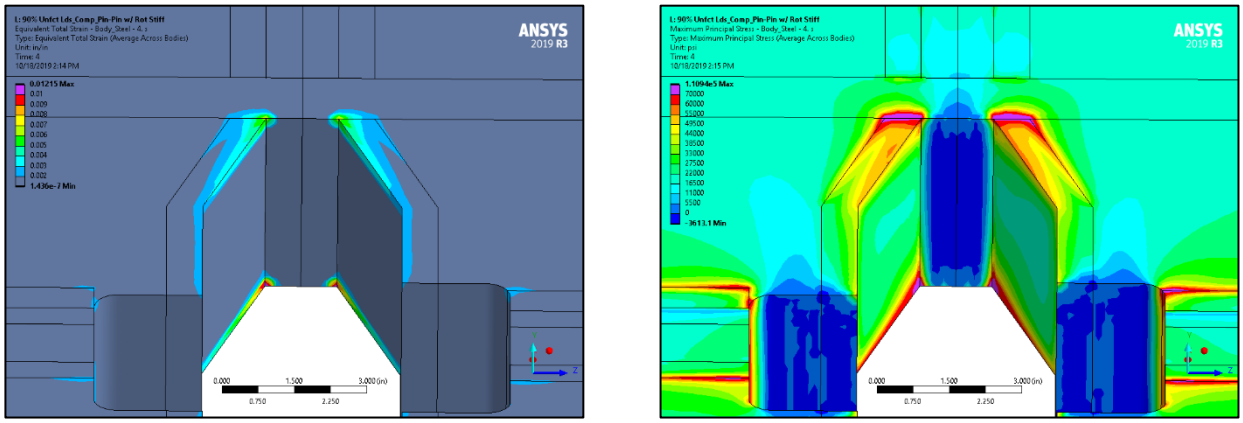

Fig. 258. Hanger slot (west) total strain (in./in.) and maximum principal stress (psi) at 1.0×(DL+SDL).

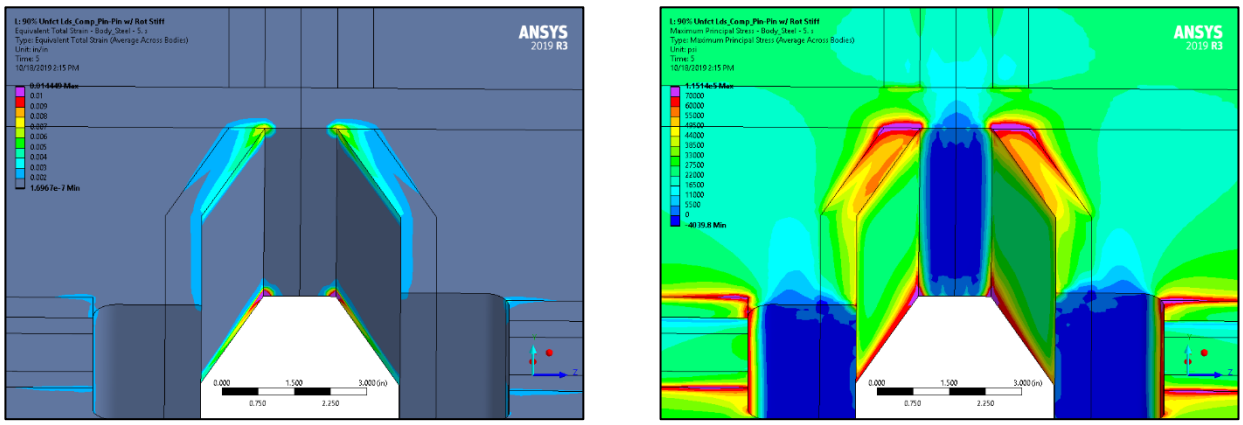

Fig. 259. Hanger slot (west) total strain (in./in.) and maximum principal stress (psi) at 1.0×(DL+SDL)+1.0×LL.

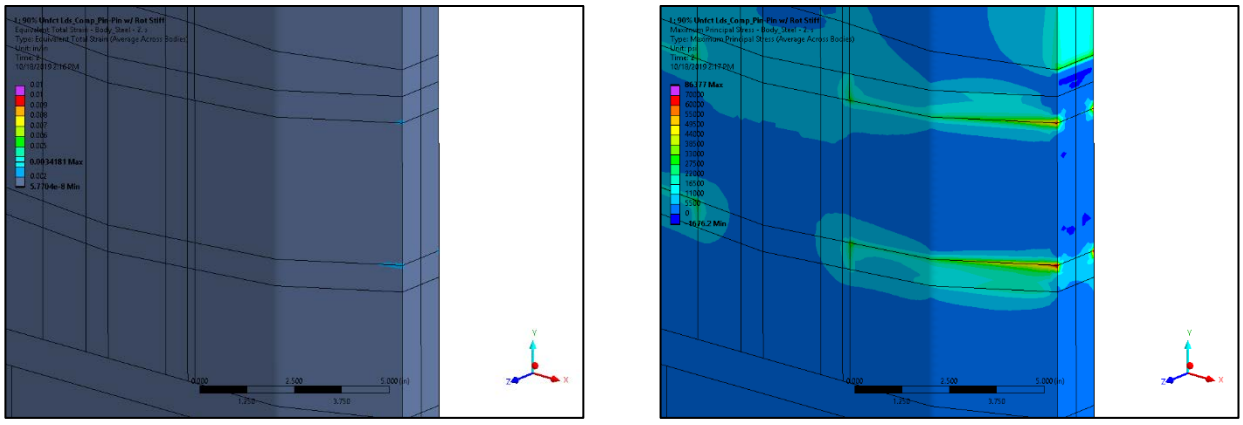

Fig. 260. Hanger plate (northwest) total strain (in./in.) and maximum principal stress (psi) at 1.0×DL.

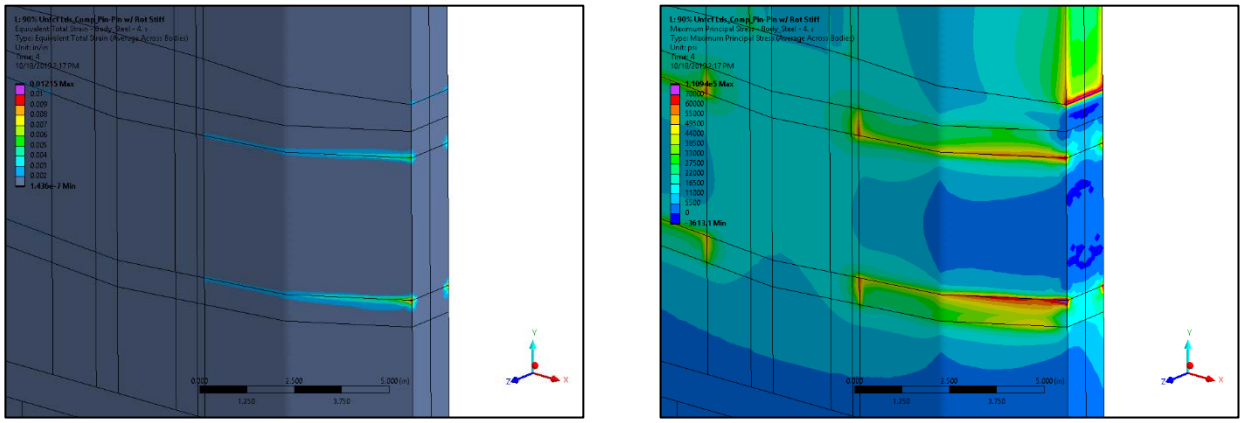

Fig. 261. Hanger plate (northwest) total strain (in./in.) and maximum principal stress (psi) at 1.0×(DL+SDL).

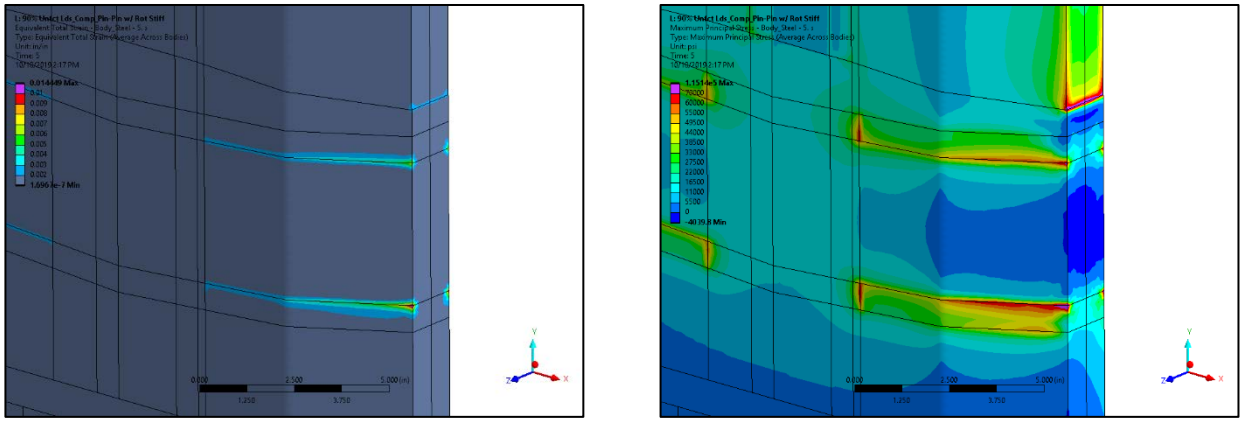

Fig. 262. Hanger plate (northwest) total strain (in./in.) and maximum principal stress (psi) at 1.0×(DL+SDL)+1.0×LL.

APPENDIX H. CORE SAMPLE METALLURGICAL EVALUATION – SUPPLEMENTAL IMAGES

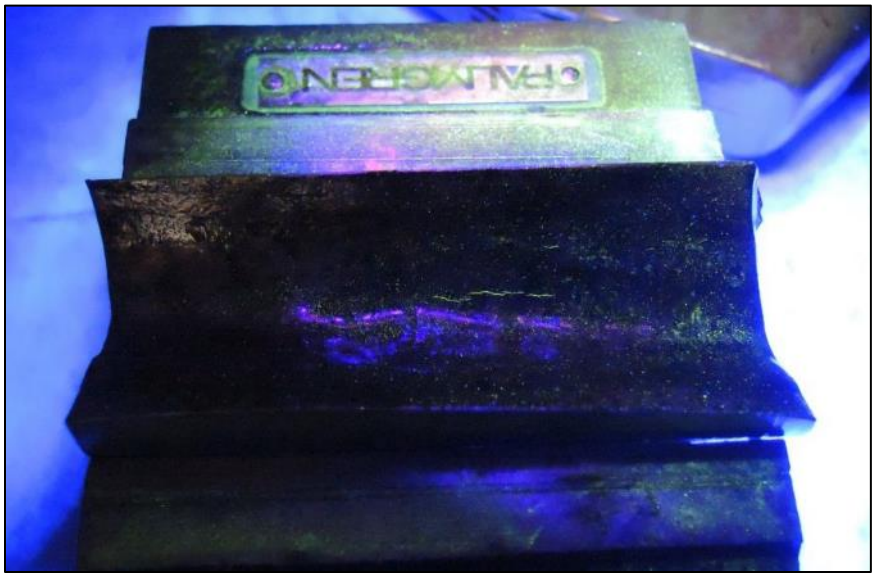

Fig. 263 Representative image of the flange weld access hole surface of core sample D-NE following wet fluorescent magnetic particle testing showing microcracks.

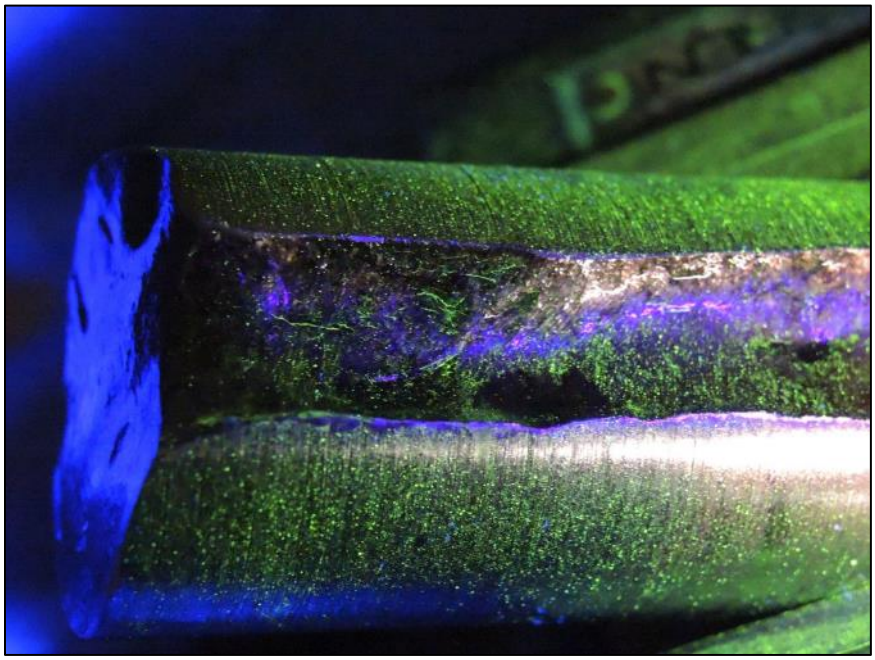

Fig. 264 Representative image of the flange weld access hole surface of core sample D-NW following wet fluorescent magnetic particle testing showing microcracks.

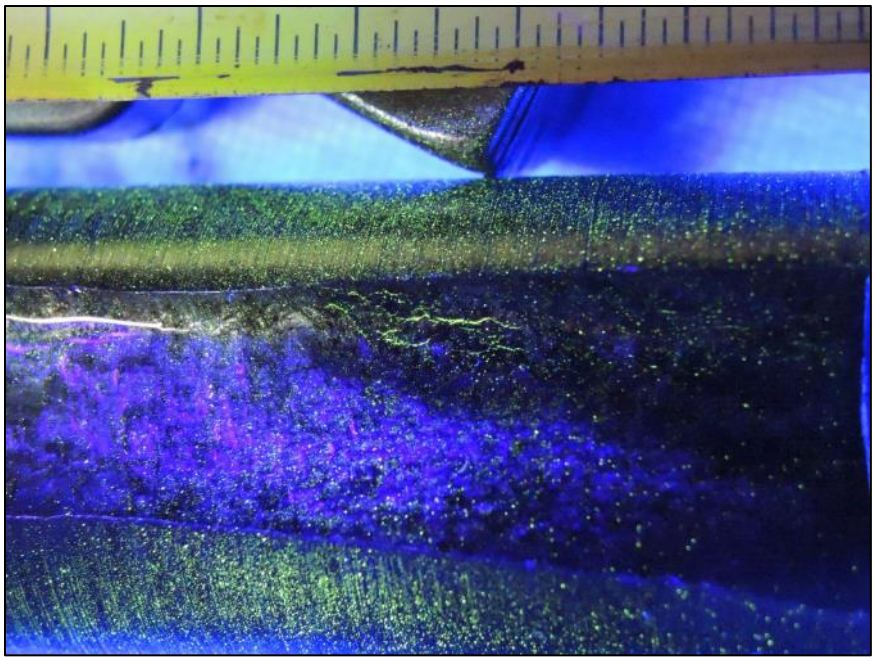

Fig. 265 Representative image of the flange weld access hole surface of core sample D-SW following wet fluorescent magnetic particle testing showing microcracks.

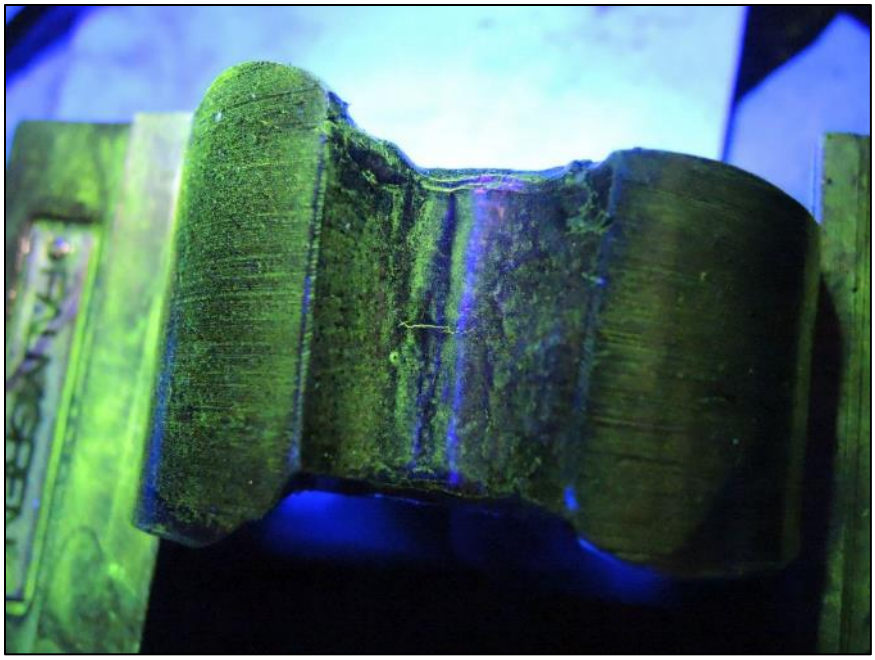

Fig. 266 Representative image of core sample F-W, which was removed to create the new web stress relief hole, following wet fluorescent magnetic particle testing showing a crack.

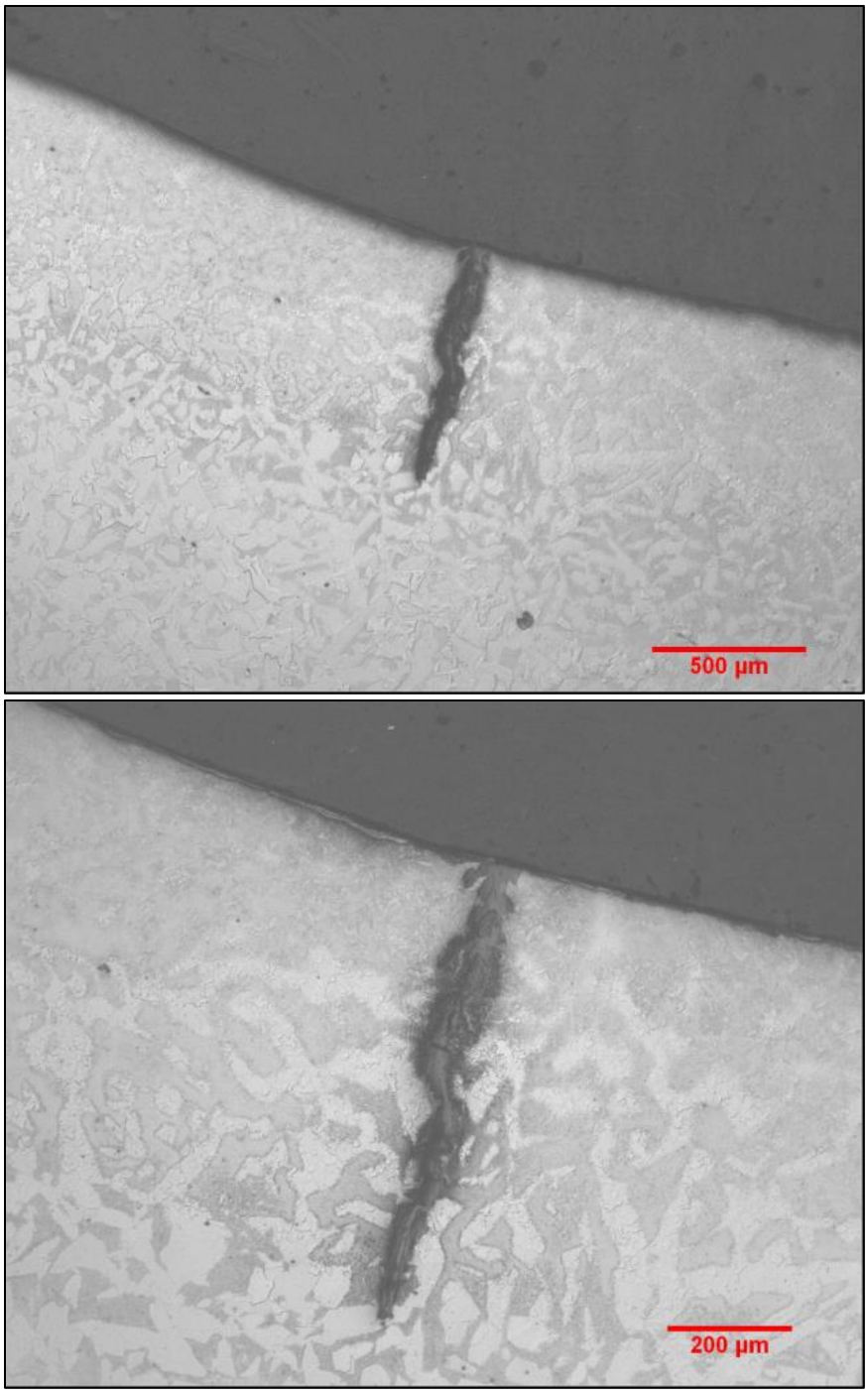

Fig. 267 Representative image of the flange weld access hole surface of core sample D-NE revealing a microcrack.

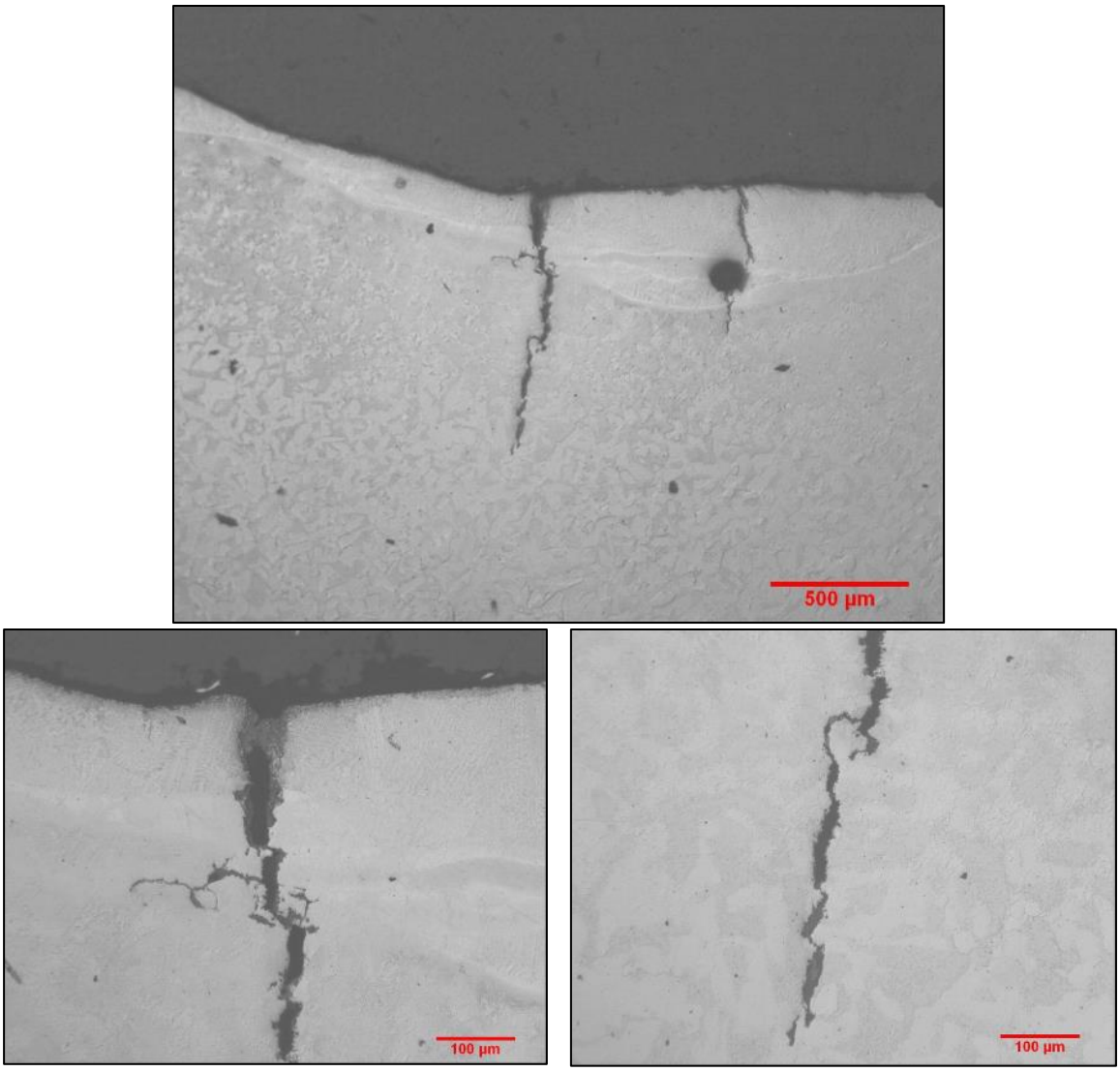

Fig. 268 Representative images of the flange weld access hole surface of core sample D-NW revealing microcracks.

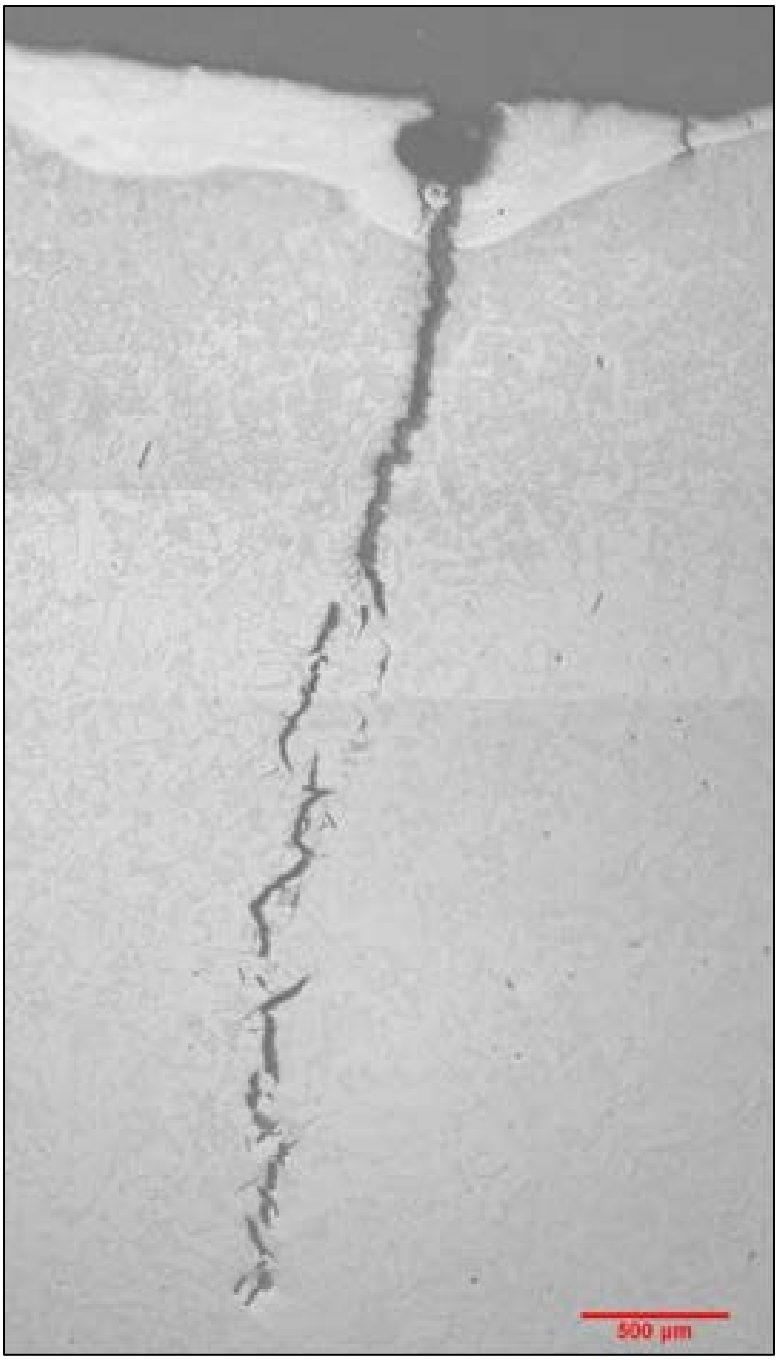

Fig. 269 Representative images of the flange weld access hole surface of core sample D-SW revealing microcracks.

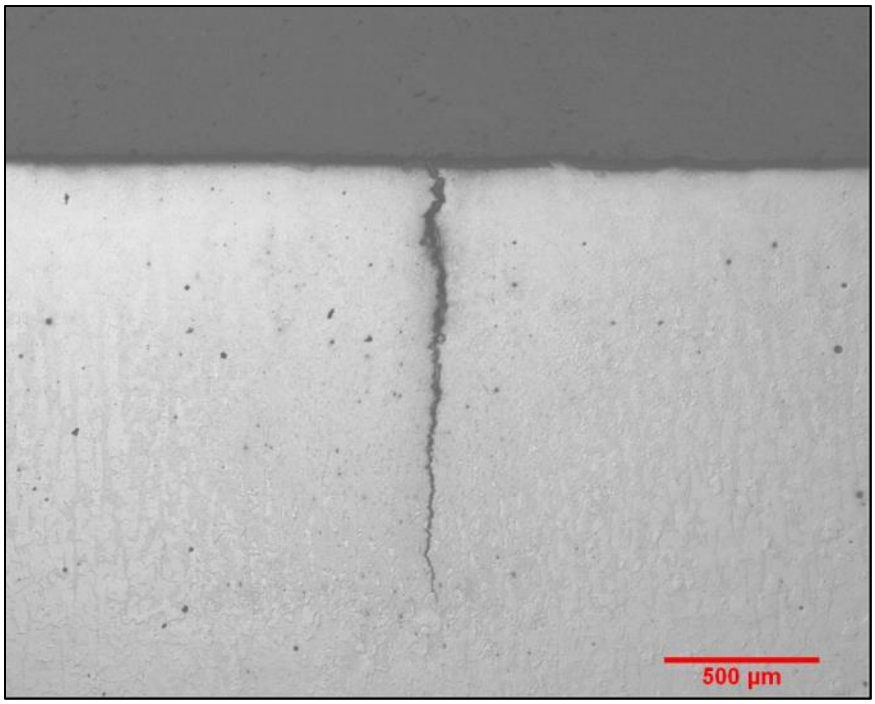

Fig. **270** Representative image of the original web access hole surface contained in core sample F-W revealing a crack (see **Fig. 266**).